# Mass-wasting episodes in the geological evolution of the Azores islands : timing, recurrence, mechanisms and consequences

Ana Cristina Goulart da Costa

▶ **To cite this version:**

Ana Cristina Goulart da Costa. Mass-wasting episodes in the geological evolution of the Azores islands : timing, recurrence, mechanisms and consequences. Volcanology. Université Paris Sud - Paris XI; Universidade de Lisboa. Faculdade de ciências, 2015. English. NNT : 2015PA112001 . tel-01417798

**HAL Id: tel-01417798**

**https://theses.hal.science/tel-01417798**

Submitted on 16 Dec 2016

**HAL** is a multi-disciplinary open access archive for the deposit and dissemination of scientific research documents, whether they are published or not. The documents may come from teaching and research institutions in France or abroad, or from public or private research centers.

L'archive ouverte pluridisciplinaire **HAL**, est destinée au dépôt et à la diffusion de documents scientifiques de niveau recherche, publiés ou non, émanant des établissements d'enseignement et de recherche français ou étrangers, des laboratoires publics ou privés.

UNIVERSITÉ PARIS-SUD

ÉCOLE DOCTORALE 534 :
MODÉLISATION ET INSTRUMENTATION EN PHYSIQUE, ÉNERGIES, GÉOSCIENCES ET ENVIRONNEMENT

Laboratoire : *GEOPS*

# THÈSE DE DOCTORAT

SCIENCES DE L'UNIVERS

par

**Ana Cristina Goulart da Costa**

# Mass-wasting episodes in the geological evolution of the Azores islands: timing, recurrence, mechanisms and consequences

**Date de soutenance : 09/02/2015**

**Composition du jury :**

| | | |
|---|---|---|
| Directeur de thèse : | Fernando Marques | Professeur (HDR) (Universidade de Lisboa) |
| Co-directeur de thèse : | Anthony Hildenbrand | Chargé de Recherche CNRS (HDR) (Université Paris-Sud) |
| Rapporteurs : | Valerio Acocella | Chercheur (University "Roma Tre") |
| | Sebastian Krastel | Professeur (Christian-Albrechts-Universität zu Kiel) |
| Examinateurs : | Xavier Quidelleur | Professeur (Université Paris-Sud) |
| | José Madeira | Professeur Assistant (Universidade de Lisboa) |

**FACULDADE DE CIÊNCIAS - UNIVERSIDADE DE LISBOA**
**DEPARTAMENTO DE GEOLOGIA**

**FACULTÉ DES SCIENCES D'ORSAY - UNIVERSITÉ PARIS-SUD**
ÉCOLE DOCTORALE 534:
MODÉLISATION ET INSTRUMENTATION EN PHYSIQUE, ÉNERGIES, GÉOSCIENCES ET ENVIRONNEMENT
Laboratoire: *GEOPS*
THÈSE DE DOCTORAT SCIENCES DE L'UNIVERS

# MASS-WASTING EPISODES IN THE GEOLOGICAL EVOLUTION OF THE AZORES ISLANDS: TIMING, RECURRENCE, MECHANISMS AND CONSEQUENCES

Ana Cristina Goulart da Costa

Doutoramento em Geologia

Especialidade em Geodinâmica Interna

**2014**

**FACULDADE DE CIÊNCIAS - UNIVERSIDADE DE LISBOA**
**DEPARTAMENTO DE GEOLOGIA**

**FACULTÉ DES SCIENCES D'ORSAY - UNIVERSITÉ PARIS-SUD**
ÉCOLE DOCTORALE 534:
MODÉLISATION ET INSTRUMENTATION EN PHYSIQUE, ÉNERGIES, GÉOSCIENCES ET ENVIRONNEMENT
Laboratoire: *GEOPS*
THÈSE DE DOCTORAT SCIENCES DE L'UNIVERS

# MASS-WASTING EPISODES IN THE GEOLOGICAL EVOLUTION OF THE AZORES ISLANDS: TIMING, RECURRENCE, MECHANISMS AND CONSEQUENCES

Ana Cristina Goulart da Costa

Tese co-orientada pelo Prof. Doutor Fernando Manuel Ornelas Guerreiro Marques (FCUL) e co-orientada pelo Prof. Doutor Anthony Hildenbrand (Université Paris-Sud), especialmente elaborada para a obtenção do grau de doutor em Geologia, Especialidade em Geodinâmica Interna

**2014**

# Mass-wasting episodes in the geological evolution of the Azores islands: timing, recurrence, mechanisms and consequences

Large-scale flank collapses are recurrent in the geological evolution of volcanic ocean islands. Such catastrophic episodes of destabilization can be voluminous and generate large tsunamis, which may cause considerable damage and thus represent extremely hazardous events.

The Azores islands east of the Mid-Atlantic Ridge are located on the Eurasia(Eu)/Nubia(Nu) plate boundary, and therefore subject to structural control and seismic activity (historical events of magnitude up to ca. 7). However, prior to MEGAHazards Project (PTDC/CTE-GIX/108149/2008, funded by FCT, Portugal), large-scale flank collapses in the Azores were considered to be lacking, mainly due to the small dimension of the volcanic edifices. Here, we conclude unequivocally on the occurrence of such events in the Azores.

The present PhD thesis addresses the evolution of the Pico-Faial steep volcanic ridge, which sits on a major normal fault associated with the Eu/Nu diffuse boundary, focusing especially on the large-scale flank failures in Pico Island. Based on high-resolution sub-aerial and submarine Digital Elevation Models, new structural and stratigraphic data, and high-resolution K-Ar dating on separated volcanic groundmass, we: (1) constrain the volcano stratigraphy of Pico; (2) reconstruct the major phases of growth and destruction in Pico and Faial islands in the last 200 kyr; (3) reconstruct the ca. 125 kyr evolution of the currently active large-scale slump in the SE of Pico Island; (4) provide new structural data/interpretations regarding the scarp that sharply cuts the S flank of Pico Stratovolcano; (5) report on the occurrence of large-scale failures in the N and S flanks of the Pico Island between ca. 125 and 70 ka, which generated large submarine debris deposits; and (6) propose that the role of the Pico-Faial ridge as a structure accommodating part of the extension on the diffuse Nu/Eu boundary has been consolidated in the last ca. 125 kyr.

Many factors favouring the development of such large-scale flank instabilities have been proposed in the literature, but their exact role and mutual contribution remain poorly understood. We here present an analytical solution for the cohesive Coulomb Critical Wedge theory applied to gravitational instabilities, and associated analogue simulations to test some structural implications of the model. We investigate the impact of several variables on the stability of volcanic flanks, including: wedge slope and dimensions, cohesion, internal friction along the basal detachment, and fluid overpressure. We conclude that: (1) the

steepening of the volcanic flanks and basal detachment lead to a decrease in the fluid overpressure ratio (fluid overpressure divided by lithostatic pressure) necessary to produce failure. (2) The decrease of the stabilizing effect of cohesion with increasing depth of the basal detachment favours the occurrence of deep-seated large-scale gravitational destabilization in basal detachments deeper than ca. 2000-2500 m (in volcanic edifices necessarily higher than 2500 m). For shallower basal detachments, the overpressure ratios required to induce failure are comparatively larger. For shallower basal detachments, steeper flanks and stronger edifice materials, shallow failure parallel to the edifice flank surface is favoured, instead of deep-seated deformation. (3) With increasingly deeper basal detachments (possible in larger volcanic edifices), while the impact of cohesion diminishes, the relative importance of basal internal friction for the stability of the edifice increases.

The investigation of the occurrence of large-scale mass-wasting in the Azores islands, and the modelling of the variables controlling the stability of the volcanic edifices are only at their first steps and will be further developed in the future.

***Keywords*:** Pico-Faial volcanic ridge; Azores Triple Junction; large-scale flank collapses; destabilizing factors, cohesive Critical Coulomb Wedge

# Mass-wasting episodes in the geological evolution of the Azores islands: timing, recurrence, mechanisms and consequences


## Extended Abstract

Large-scale flank collapses are recurrent in the geological evolution of volcanic ocean islands. Such catastrophic episodes of destabilization can be voluminous and generate large tsunamis, which may cause considerable damage and thus represent extremely hazardous events.

The Azores islands east of the Mid-Atlantic Ridge are located on the Eurasia(Eu)/Nubia(Nu) plate boundary, and therefore subject to structural control and seismic activity (historical events of magnitude up to ca. 7). However, prior to MEGAHazards Project (PTDC/CTE-GIX/108149/2008, funded by FCT, Portugal), large-scale flank collapses in the Azores were considered to be lacking, mainly due to the small dimension of the volcanic edifices. Here, we conclude unequivocally on the occurrence of such events in the Azores.

The present PhD thesis addresses the evolution of the Pico-Faial steep volcanic ridge, which sits on a major normal fault associated with the Eu/Nu diffuse boundary, focusing especially on the large-scale flank failures in Pico Island. Based on high-resolution sub-aerial and submarine Digital Elevation Models, new structural and stratigraphic data, and high-resolution K-Ar dating on separated volcanic groundmass we: (1) found evidence for large-scale flank collapses; (2) reconstructed with unprecedented resolution the growth and destruction of Pico and Faial islands, focusing specially on the large-scale flank failures that affected Pico Island during the last 200 kyr.

Pico Island comprises three main volcanic systems, from older to younger: (1) the Topo Volcano, (2) the Fissural System, and (3) the Pico Stratovolcano. (1) The Topo Volcano is partly exposed in Pico's SE flank, and is here dated between 186 ± 5 and 125 ± 4 ka or 115 ± 4 ka. It was significantly destroyed by a N-directed large-scale flank collapse between ca. 125 and 70 ka. Offshore, a debris deposit was identified and interpreted as corresponding to this flank collapse. The deposit has a maximum length of 20 km and covers an area of ca. 150 $km^2$. It comprises hectometre blocks, and has an exposed volume here estimated between 4 and 10 $km^3$, although the actual volume probably exceeds 10 $km^3$. During the same period, gradual deformation started in the SE flank of the Topo Volcano, producing a composite collapse structure: (1) a slump complex in the west, which is still active, and (2) a catastrophic flank collapse in the east. A first episode of deformation most probably occurred between ca. 125 and 115 ka, along the master fault of the slump. Between

ca. 115 and 75 ka, the scar was partially filled by volcanic products erupted from volcanic cones developed within the slump depression, and possibly from the early WNW-ESE Fissural System. Subsequent deformation in the slump area affected in part the filling units, leading to the individualization of secondary curved faults. Between ca. 125 and 69 ka, the eastern distal part of Topo Volcano's SE flank and the early sub-aerial sequence of the Fissural System experienced catastrophic flank collapse towards the S, which generated a large offshore debris deposit with a minimum run-out of ca. 17 km. More recent volcanic products have gradually masked the mass-wasting scars. The young Pico Stratovolcano grew in the westernmost sector of the island, at least since ca. 57 ka. Its southern flank has been partially destroyed by flank collapse(s), and subsequently covered by more recent volcano-sedimentary products.

The evolution of the Pico-Faial volcanic ridge in the last 200 kyr has been marked by simultaneous volcanic growth and destruction in both Pico and Faial islands. While the Topo Volcano grew in Pico (ca. 186-125 ka) and was partially destroyed (ca. 125-115 ka), in Faial Island the period defined for major deformation in the Faial graben ended (ca. 360-115 ka), and a central volcano started growing inside the graben (ca. 130-115 ka). This rapid and simultaneous evolution of Pico and Faial islands constitutes evidence for the accommodation of extension associated with the Nu-Eu plate boundary on this ridge during the last 200 kyr.

Many factors favouring the development of such large-scale flank instabilities have been proposed in the literature, but their exact role and mutual contribution remain poorly understood. We here present an analytical solution for the cohesive Coulomb Critical Wedge theory applied to gravitational instabilities, and associated analogue simulations to test some structural implications of the model. We investigate the impact of several variables including wedge geometry, cohesion, coefficient of internal friction and fluid overpressure ratio (fluid overpressure divided by lithostatic pressure) on wedge stability. We focus especially on how cohesion influences the stress regime within the wedge, by inhibiting deformation and constraining failure location. We show that the stability of a cohesive wedge under fluid overpressure is size-dependent (the influence of cohesion is more significant for smaller wedges), while the stability of a non-cohesive wedge under fluid overpressure is size-independent. The stabilizing effect of cohesion is more significant for the most superficial domain of the wedge. The thickness of this stable superficial layer decreases with increasing fluid overpressure ratio. Within the layer impacted by cohesion, the principal compressive stress rotates and the expected faults are listric. If the thickness limit expected for this layer is reached within the wedge (given the properties of the materials, the fluid overpressure ratio,

and the configuration of the wedge), the generated listric faults become parallel to the wedge's upper surface at the thickness limit. This limit means that the material strength reached the failure envelope.

We assess the stability of the wedge along a basal detachment, through comparison of the forces driving and resisting the downslope movement. We verify that the stabilizing effect of cohesion is accentuated in the foremost thin domain of the wedge, defining a required Minimum Failure Length (MFL). This MFL decreases for smaller cohesions, smaller coefficients of internal friction, larger fluid overpressure ratios, steeper upper surface and basal detachment of the wedge.

Although this analytical model does not integrate the local effects of topography in the stress field, we applied it to gravitational instabilities in volcanic systems, considering as variables: volcanic edifice slope and dimensions (volcanic flanks dipping 7-15°, basal detachment surfaces dipping 0-2°, maximum wedge height above the basal detachment up to 5500 m), cohesion (volcanic wedge: from 0 to 2.6 MPa; basal detachment: from 0 to 0.9 MPa), coefficient of internal friction (volcanic wedge: 0.45; basal detachment: 0.18 and 0.32), and fluid overpressure (ranging from null to higher than the lithostatic pressure). We conclude that: (1) the steepening of the volcanic flanks and basal detachment lead to a decrease in the fluid overpressure ratio necessary to produce failure; (2) the decrease of the stabilizing effect of cohesion with increasing depth of the basal detachment favours the occurrence of deep-seated large-scale gravitational destabilization in basal detachments deeper than ca. 2000-2500 m (in volcanic edifices necessarily higher than 2000-2500 m). For shallower basal detachments, the overpressure ratios required to induce failure are comparatively larger. For shallower basal detachments, steeper flanks and stronger edifice materials, shallow failure parallel to the edifice flank surface is favoured, instead of deep-seated deformation; (3) With increasingly deeper basal detachments (possible in larger volcanic edifices), while the impact of cohesion diminishes, the relative importance of basal internal friction for the stability of the edifice increases.

Besides the main work reported above, additional field and laboratory (K-Ar dating) works were performed in the scope of the MEGAHazards Project. The published works directly related to the subject of this thesis are included in this manuscript. These concern the reconstruction of Faial's volcano-tectonic evolution, and the study of current deformation in the large-scale slump that affects Pico's SE flank. The results of the GPS campaigns performed in Pico and Faial Islands were additionally included in published works regarding

the diffuse Nu-Eu plate boundary and the WSW-ENE associated transform structures. These published works are included as annex files.

The investigation of the occurrence of large-scale mass-wasting in the Azores islands, and the modelling of the variables controlling the stability of the volcanic edifices are only at their first steps, and will be further developed in the near future.

***Keywords*:** Pico-Faial volcanic ridge; Azores Triple Junction; large-scale flank collapses; destabilizing factors, cohesive Critical Coulomb Wedge

# Episódios de movimento de massa na evolução geológica das Ilhas Açorianas: idade, recorrência, mecanismos e consequências

Movimentos de massa de larga escala são recorrentes na evolução geológica das ilhas vulcânicas oceânicas. Quando catastróficos, estes episódios de destabilização podem ser volumosos e gerar grandes tsunamis, capazes de causar estragos consideráveis, e portanto constituem eventos de perigosidade considerável.

As ilhas dos Açores a Este da Crista Médio-Atlântica distribuem-se ao longo da fronteira de placas Euroasia(Eu)/Nubia(Nu), e estão por isso sujeitas a controlo estrutural e actividade sísmica (eventos históricos com magnitude até ca. 7). Contudo, antes do Projecto MEGAHazards (PTDC/CTE-GIX/108149/2008, financiado pela FCT, Portugal), considerava-se que os Açores não teriam sofrido colapsos de flanco catastróficos, devido às pequenas dimensões das ilhas. Aqui concluímos, inequivocamente, que os Açores sofreram colapsos catastróficos.

A presente tese de doutoramento aborda a evolução da íngreme crista vulcânica Pico-Faial, desenvolvida sobre uma importante falha normal associada à fronteira difusa Eu/Nu, dando especial atenção à ocorrência de grandes colapsos de flanco na ilha do Pico. Com base em Modelos Digitais de Terreno sub-aéreos e submarinos de alta resolução, novos dados de estratigrafia e tectónica, e datação K-Ar de alta resolução executada em matriz vulcânica, aqui apresentamos: (1) evidências para a ocorrência de grandes colapsos de flanco; (2) a reconstrução, com resolução sem precedentes, das fases de crescimento e destruição nas ilhas do Pico e Faial, focando especialmente a ocorrência de grandes colapsos de flanco no Pico nos últimos 200 kyr.

A ilha do Pico é constituída por três sistemas vulcânicos (do mais antigo para o mais recente): (1) o Vulcão do Topo; (2) o Sistema Fissural, e (3) o Estratovulcão do Pico. O Vulcão do Topo aflora parcialmente no flanco SE do Pico, e é aqui datado entre 186 ± 5 e 125 ± 4 ka ou 115 ± 4 ka. O flanco N deste edifício foi significativemte destruído por um grande colapso entre ca. 125 e 70 ka. No domínio submarino, um depósito foi identificado e interpretado como correspondente a este colapso de flanco. O depósito tem um comprimento máximo de 20 km e cobre uma área de ca. 150 $km^2$. Este depósito inclui blocos hectométricos, e um volume exposto aqui estimado entre 4 e 10 $km^3$, embora o volume real provavelmente ultrapasse os 10 $km^3$. Neste intervalo de tempo, de ca. 125 a 70 ka, o flanco SE do Vulcão do Topo começou a deformar-se gradualmente, gerando uma estrutura de

colapso compósita: (1) a Oeste, um *slump* de grande escala, ainda hoje activo, e (2) um colapso de flanco catastrófico a Este. O primeiro episódio de deformação ocorreu muito provavelmente entre ca. 125 e 115 ka, gerando a estrutura principal do *slump*. Entre ca. 115 ka e 75 ka, a cicatriz resultante foi parcialmente preenchida por produtos vulcânicos provenientes de cones localizados na depressão do *slump* e, provavelmente, de cones do Sistema Fissural. Posteriormente, a deformação na área do *slump* affectou parcialmente as unidades que preencheram a cicatriz, com a propagação de estruturas secundárias arqueadas. Entre ca. 125 e 69 ka, a parte distal do flanco SE do Vulcão do Topo e a sequência sub-aérea primordial do Sistema Fissural colapsaram catastroficamente para Sul, gerando um grande depósito *offshore*, com extensão mínima de ca. 17 km. As cicatrizes de colapso foram depois parcialmente cobertas por produtos vulcânicos. Desde há pelo menos ca. 57 ka o Estratovulcão do Pico tem-se desenvolvido no sector Oeste da ilha. O flanco S deste edifício foi parcialmente destruído por colapso(s) de flanco, e posteriormente coberto por produtos vulcano-sedimentares.

A evolução da crista vulcânica Pico-Faial nos últimos 200 kyr foi marcada por fases simultâneas de crescimento e destruição em ambas as ilhas. Enquanto o Vulcão do Topo crescia (ca. 186-125 ka) e era parcialmente destruído (ca. 125-115 ka) no Pico, no Faial terminava o período definido para a deformação significativa no graben (ca. 360-115 ka) e um vulcão central preenchia a depressão central deste (ca. 130-115 ka). Esta evolução rápida e simultânea das ilhas Pico e Faial aponta para a acomodação de extensão associada à fronteira de placas Eu/Nu ao longo desta crista nos últimos 200 kyr.

Muitos factores que favorecem o desenvolvimento de colapsos de flanco de larga escala têm sido propostos na literatura. Contudo, ainda não se compreende bem o papel específico de cada um destes factores, e como se relacionam entre si. Apresentamos aqui uma solução analítica para a teoria do Prisma Crítico de Coulomb coesivo, aplicada a destabilizações gravitacionais, complementada por testes de modelação análoga para verificar implicações estruturais da solução analítica. Averiguamos o impacto de variáveis como a geometria do prisma, coesão, coeficiente de atrito interno e rácio de sobrepressão de fluidos (sobrepressão de fluidos a dividir pela pressão litostática) no estado de estabilidade do prisma. Abordamos especialmente a influência que a coesão exerce no campo de tensões dentro do prisma, inibindo a deformação e condicionando a localização da ruptura. Concluímos que a estabilidade de um prisma coesivo sob a infuência de sobrepressão de fluidos depende das dimensões do prisma (a coesão do material do prisma tem um maior impacto em prismas de pequenas dimensões), enquanto a estabilidade de um prisma não

coesivo sob sobrepressão de fluidos é independente das dimensões do mesmo. O efeito estabilizador da coesão é mais significativo no domínio superficial do prisma. A espessura desta camada superficial diminui com o aumento do rácio de sobrepressão de fluidos. Dentro da camada influenciada pela coesão, a orientação da principal componente de tensão compressiva roda, esperando-se a geração de falhas lístricas. Se o limite de espessura desta camada é atingido no interior do prisma (para determinada resistência do material, rácio de sobrepressão de fluidos, e configuração do prisma), as falhas lístricas geradas tornam-se paralelas à superfície superior do prisma à profundidade correspondente a este limite de espessura. Este limite corresponde à chegada do material do prisma ao seu envelope de ruptura.

Avaliamos a estabilidade do prisma ao longo de um descolamento basal, ao confrontarmos as forças destabilizadoras e resistentes à deformação. Verificamos que o efeito estabilizador da coesão é mais acentuado no domínio frontal (menos espesso) do prisma, definindo um Comprimento Mínimo para a Ruptura (CMR). Este CMR diminui para menores valores de coesão e coefficiente de atrito interno, maiores rácios de sobrepressão de fluidos, e maiores inclinações da superfície superior do prisma e do descolamento basal.

Embora este modelo analítico não considere o efeito da topografia no campo de tensões, nós aplicamo-lo a destabilizações gravitacionais em sistemas vulcânicos, considerando como variáveis: inclinação dos flancos (7 e 15º), inclinação do descolamento basal (0 e 2º), dimensões do edifício (altura máxima da cunha vulcânica acima do descolamento basal até 5500 m), coesão (cunha vulcânica: de 0 a 2.6 MPa; descolamento basal: de 0 a 0.9 MPa), coeficiente de atrito interno (cunha vulcânica: 0.45; descolamento basal: 0.18 e 0.32), e sobrepressão de fluidos (de nula a superior à pressão litostática). Concluímos que: (1) o aumento da inclinação dos flancos e do descolamento basal conduz à diminuição do rácio de sobrepressão de fluidos necessário para provocar ruptura; (2) a diminuição do efeito estabilizador da coesão com o aumento da profundidade do descolamento basal favorece a ocorrência de destabilização gravitacional ao longo de descolamentos basais a profundidades superiores a ca. 2000-2500 m (edifícios vulcânicos com altitude superior a ca. 2000-2500 m). Para descolamentos mais superficiais, os rácios de sobrepressão necessários para induzir ruptura são comparativamente maiores. Para descolamentos mais superficiais, flancos mais inclinados e materiais vulcânicos mais coesivos, é favorecida a ocorrência de ruptura superficial paralela à superfície dos flancos vulcânicos; (3) Com o aumento da profundidade dos descolamentos basais (edifícios

vulcânicos de maiores dimensões), enquanto a importância da coesão diminui, a importância relativa do atrito ao longo do descolamento basal aumenta.

Para além do trabalho acima mencionado, foi executado trabalho de campo e laboratório (datação K-Ar) adicional, no âmbito do Projecto MEGAHazards. As publicações (em co-autoria) directamente relacionadas com o tema desta tese estão incluídas no manuscrito. Estas abordam a reconstrução vulcano-tectónica da ilha do Faial, e o estudo da deformação actual no slump de larga escala que affecta o flanco SE da ilha do Pico. Os resultados das campanhas de GPS executadas nas ilhas do Pico e Faial foram integrados em publicações que abordam a fronteira diffusa Eu/Nu e suas estruturas transformantes WNW-ENE. Estas publicações são apresentadas como ficheiros anexos.

A investigação da ocorrência de movimentos de massa de larga escala nas ilhas dos Açores, e a modelação das variáveis que controlam a estabilidade dos edifícios vulcânicos estão ainda num estado embrionário, e serão aprofundadas num futuro próximo.

***Palavras-Chave:*** crista vulcânica Pico-Faial; Junção Tripla dos Açores; colapsos de flanco de larga escala; factores destabilizadores, Prisma Crítico de Coulomb coesivo.

# Episodes de destruction gravitaire durant l'évolution géologique des îles Açores: âge, récurrence, mécanismes et conséquences

Les grands effondrements de flanc sont des phénomènes récurrents dans l'évolution géologique des îles océaniques. Ces épisodes de déstabilisation volumineux, le plus souvent catastrophiques, sont capables de générer d'importants tsunamis, qui peuvent causer des dommages considérables, et représentent donc des événements extrêmement dangereux.

Le îles des Açores à l'est de la Dorsale Médio-Atlantique sont situés sur la frontière de plaques diffuse entre l'Eurasie (Eu) et la Nubie (Nu), et donc sous l'influence d'un contrôle structural et d'une activité sismique importante (événements historiques de magnitude jusqu'à ca. 7). Avant le projet MEGAHazards (PTDC / CTE-GIX / 108149/2008, financé par FCT, Portugal), les effondrements de flanc à grande échelle ont été considérés comme inexistants aux Açores, principalement à cause de la petite dimension des édifices volcaniques. Ici, nous concluons sans équivoque que de tels événements se sont bien produits dans les Açores.

La thèse de doctorat concerne l'évolution de la ride volcanique escarpée de Pico-Faial, qui se trouve sur une faille normale majeur associée à la limite diffuse Nu/Eu. Nous nous concentrons particulièrement sur les grands effondrements de flanc qui ont affecté l'île de Pico. A partir de données topographiques à haute-résolution (modèle numérique aérien et données bathymétriques), de nouvelles données structurales et stratigraphiques, et de nouvelles datations K-Ar sur mésostase volcanique, nous avons: (1) mis en évidence des grands effondrements catastrophiques jusqu'alors non reconnus; (2) reconstruit avec une résolution temporelle sans précédent les phases majeures de croissance volcanique et de destruction dans les îles Pico et Faial, plus spécialement les instabilités qui ont affecté l'île de Pico, durant les derniers 200 ka.

L'île de Pico es constituée par trois systèmes volcaniques principaux, de l'ancien au plus jeune: (1) le Volcan Topo, (2) le Système Fissural, et (3) le Stratovolcan Pico. (1) Le Volcan Topo est partiellement exposé dans le flanc SE de l'île, et est daté ici entre 186 ± 5 et 125 ± 4 ka ou 115 ± 4 ka. Il a été significativement détruit par un effondrement de flanc de grande échelle vers le N, entre environ 125 et 70 ka. Au large, nous identifions une champ de de débris, interprété comme généré par cet effondrement sectoriel. Ce dépôt a une longueur maximale de 20 km et couvre une superficie d'environ 150 $km^2$. Il comporte des blocs hectométriques, et a un volume exposé estimé ici entre 4 et 10 $km^3$, bien que le volume réel dépasse probablement 10 $km^3$. Durant la même période, la déformation progressive a

commencé dans le flanc SE du Volcan Topo, générant une structure d'effondrement composite: (1) l'initiation d'un *slump complexe* à l'ouest, qui est toujours actif, et (2) un effondrement de flanc catastrophique plus à l'est. Le premier épisode de déformation a très probablement a eu lieu entre ca. 125 et 115 ka, le long de la faille majeure du *slump*. Entre 115 et 75 ka, la cicatrice a été partiellement remplie par les produits volcaniques issus de cônes volcaniques développés dans la dépression du *slump*, voire à l'axe du Système Fissural précoce, d'orientation principale ONO-ESE. La déformation ultérieure dans la zone du *slump* a affecté partiellement les unités de remplissage, conduisant à l'individualisation de failles secondaires courbes. Entre ca. 125 et 69 ka, la partie distale E du flanc SE du Volcan Topo et la première séquence sub-aérienne du Système Fissural ont été tronqués par un autre effondrement sectoriel catastrophique vers le S, ce qui a généré un grand dépôt de débris sous-marin avec une course minimale de 17 km. Les produits volcaniques plus récents ont masqué graduellement les cicatrices de destruction gravitaire. Le jeune Stratovolcan Pico s'est développé dans le secteur ouest de l'île, au moins depuis environ 57 ka. Son flanc sud a également été partiellement détruit par un ou plusieurs effondrements de flanc(s), et par la suite couvert par des produits volcano-sédimentaires plus récents.

L'évolution de la ride volcanique Pico-Faial dans les derniers 200 ka a été marquée par l'occurrence simultanée de croissance volcanique et de destruction dans les îles de Pico et Faial. Tandis que le Volcan sub-aérien de Topo se construisait à Pico (ca. 186-125 ka) puis était partiellement détruit (ca. 125-115 ka), une phase de déformation majeure se terminait sur l'ile voisine de Faial, donnant lieu au développement d'un large graben (ca. 360-115 ka), lui-même rempli par la croissance rapide d'un volcan central (ca. 130-115 ka). Cette évolution rapide et simultanée des îles Pico et Faial constitue un indice fort de l'accommodation de l'extension associé à la limite des plaques Nu/Eu le long de cette ride durant les derniers 200 ka.

De nombreux facteurs favorisant le développement des instabilités de flanc sur les îles volcaniques ont été proposés dans la littérature, mais leur rôle exact et leur contribution mutuelle restent mal compris. Nous présentons ici une solution analytique pour la théorie du Prisme Critique de Coulomb (*Critical Coulomb Wedge*) cohésif, appliquée à des instabilités gravitaires, et des simulations analogiques complémentaires pour tester certaines implications structurales du modèle. Nous étudions l'impact de plusieurs variables sur la stabilité du prisme, notamment la géométrie et les dimensions du prisme, la cohésion, le coefficient de friction interne et le rapport de surpression de fluide (surpression de fluide divisé par la pression lithostatique). Nous examinons particulièrement comment la cohésion influence le

régime de contraintes dans le prisme, inhibant la déformation et contraignant la localisation de la rupture. Nous montrons que la stabilité d'un prisme cohésif soumis à surpression de fluides dépend de sa taille (influence de la cohésion plus sensible dans les prismes plus petits), tandis que la stabilité d'un prisme non-cohésif sous l'effet de surpression de fluides est indépendante de la taille. L'effet stabilisateur de la cohésion est plus important pour le domaine le plus superficiel du prisme. L'épaisseur de cette couche superficielle stable diminue avec l'augmentation du rapport de surpression de fluide. Dans la couche influencée par la cohésion, l'orientation de la contrainte principale compressive tourne et les failles générées sont listriques. Si l'épaisseur critique pour cette couche est atteinte dans l'intérieur du prisme (en fonction des propriétés des matériaux, du ratio de surpression de fluide, et de la configuration du prisme), les failles listriques générées deviennent parallèles à la surface supérieure du prisme. Cette limite indique que le matériel du prisme atteint son enveloppe de rupture.

Nous évaluons la stabilité du prisme le long du décollement basal, grâce à la comparaison des forces motrices et des forces qui résistent au mouvement descendant. Nous vérifions que l'effet stabilisateur de la cohésion est accentué dans le front moins épais du prisme, définissant une Longueur Minimale pour la Rupture (LMR). Cette LMR diminue pour les cohésions plus faibles, pour les petits coefficients de friction interne, pour les rapports de surpression de fluide élevés, et pour des surfaces (supérieure et de décollement) du prisme plus inclinées.

Bien que ce modèle d'analyse n'intègre pas les effets locaux de la topographie sur le champ de contraintes, nous l'avons appliqué à des instabilités gravitaires dans les systèmes volcaniques. Nous avons considéré plusieurs variables: la pente des flancs et les dimensions de l'édifice (flancs volcaniques plongeant de 7-15 °, décollement basal incliné de 0 à 2°, hauteur maximale du prisme au-dessus du détachement basal jusqu'à 5500 m), la cohésion (prisme volcanique: de 0 à 2,6 MPa; décollement basal: 0 à 0,9 MPa), le coefficient de friction interne (prisme volcanique: 0.45; décollement basal : 0.18 et 0.32), et la surpression de fluides (entre zéro et supérieure à la pression lithostatique).

Nous concluons que: (1) l'augmentation de la pente des flancs du volcan et du décollement basal conduit à une diminution du rapport de surpression de fluide nécessaire pour produire la rupture; (2) la diminution de l'effet stabilisateur de la cohésion avec la profondeur du décollement basal favorise l'occurrence de déstabilisation gravitaire profonde à grande échelle pour des décollements plus profonds que 2000-2500 m. Pour des décollements basals plus superficiels, les ratios de surpression de fluide nécessaires pour induire la rupture

sont relativement supérieurs. Pour les décollements moins profonds, des flancs très inclinés et des matériaux très résistants, la rupture superficielle parallèle à la surface du flanc est favorisée, par rapport à la rupture profonde. (3) Pour des profondeurs supérieures à 2500 m (cas des grands édifices volcaniques), tandis que l'impact de la cohésion diminue, l'effet de la friction interne le long du décollement basal devient relativement plus importante.

Au delà du travail principal indiqué ci-dessus, des travaux supplémentaires, tan sur le terrain qu'en laboratoire (géochronologie K-Ar) ont été réalisés dans le cadre du projet MEGAHazards. Les articles publiés comme co-auteur, et directement liés au sujet de cette thèse, sont inclus dans le manuscrit. Ceux-ci concernent la reconstruction de l'évolution volcano-tectonique de Faial, et l'étude de la déformation actuelle dans le *slump* de grande échelle que affecte le flanc SE de Pico. Les résultats des campagnes GPS réalisées aux îles Pico et Faial Îles ont également été inclus dans travaux publiés comme co-auteur, concernant le limite diffuse Nu/Eu et les structures transformantes OSO-ENE associées. Ces travaux publiés sont inclus dans les fichiers annexes.

L'étude des grands effondrements de flanc dans les îles des Açores, et la modélisation des variables qui contrôlent la stabilité des édifices volcaniques ont fournit des résultats pertinents et importants pour la compréhension des instabilités gravitaires sur les îles volcaniques en général. Ces travaux demeurent cependant incomplets, et seront approfondis dans futur proche.

***Mots-Clés:*** ride volcanique Pico-Faial; Triple Junction des Açores; grands effondrements de flanc; facteurs déstabilisants; Prisme Critique de Coulomb cohésif

# Acknowledgments

I thank the juri members for accepting the invitation to review, evaluate and discuss the work here presented.

I thank the Universidade de Lisboa and Université Paris-Sud, for providing the conditions necessary to develop this PhD work. I thank FCT (Fundação para a Ciência e a Tecnologia, Portugal) for financing this work, through a PhD scholarship (SFRH/BD/68983/2010), and through the MEGAHazards Project (PTDC/CTE-GIX/108149/2008).

I thank:

Fernando Ornelas Marques, my supervisor, for inviting me to become part of the MEGAHazards Project. This PhD was the best opportunity I had in my life. In these 4 years, with his example of hard work, guidance and omnipresent support, I learned how to explore the geology of my home-islands in the Azores. Fernando usually says "*The eyes only see what the mind knows*". He taught me how to open my eyes. There are no words large enough to express my gratitude...

Anthony Hildenbrand, my co-supervisor, for giving me the opportunity to work in the *GEOPS* laboratory (Orsay, France). I thank Anthony for the lessons on strength and precision, learnt in the field and in the laboratory.

I'm deeply thankful to both my supervisors for the support, the valuable discussions, suggestions and multiple revisions of manuscripts, through the development of this work.

Régis Mourgues (Université du Maine, Le Mans), for the guidance and discussions regarding the modeling work presented in this thesis. His knowledge of Mechanics and availability to clarify countless doubts were (are) extremely valuable.

I thank the members of the MEGAHazards Project:

- Aurore Sibrant, for helping in the fieldwork and K-Ar dating, and for providing me the opportunity to participate in the fieldwork in S.Miguel and Sta. Maria;
- Cristina Catita, for clarifying any doubt regarding the Digital Elevation Models;
- João Catalão, for giving me the opportunity to participate in the GPS campaigns in Pico and Faial, and for being available to clarify any doubts;

- Vicente Soler, for giving me the opportunity to participate in the monitoring work in Pico Island, and (also) for being available to help in case of any difficulty;
- Thomas Boulesteix, for his precious help in the beginning of the modelling work and friendship.

I thank my FCUL family:

- the professors of the bachelor's degree in Geology. I would like to thank in particular Filipe Rosas, who introduced me to fieldwork, analogue modelling, and gave me the opportunity to learn in the LATTEX lab, with João Moedas, Sónia Matias and Pedro Terrinha. I also thank Línia Martins, Teresa Palácios and João Mata, who introduced me to magmatism; José Brandão and João Cabral, who introduced me to Structural Geology; and José Madeira, who introduced me to the geology of Pico-Faial volcanic ridge in his Geomorphology classes.

- my colleagues and friends, for the huge support through these years: Catarina Fernandes, Mónica Sousa, Inês Pereira, Sofia Pereira, Carlos Nogueira, Bernardo de Almeida. I thank specially Paula Marques Figueiredo, and her wonderful family, for being present when I needed most.

I thank my GEOPS family:

Julia Ricci, my friend, colleague member of the "3kg sledgehammer community", passionate for volcanoes and Italian pasta. Carlos Pallares and Claire Boukari, for the support. Xavier Quidelleur, for the interest demonstrated for the work here presented. I also thank Pierre-Yves Gillot, Pierre Lahitte, Kim Ho, Chantal Rock and Valérie Godard.

I thank my Le Mans family:

Aurélien Lacoste, Denis Bureau, Chrystelle Gruber, Jean-Baptiste Legland and Pierre Strzerzynski.

A special thanks to: Cédric Bulois, for the support in (and outside) the laboratory, and for always being ready to explode sand volcanoes; and to Cynthia Garibaldi, for the availability to run permeability models.

I thank my extended Azorean family:

First, I would like to thank Professors Zilda França and Victor-Hugo Forjaz, who officially presented me to Geology.

I thank the people that helped me in the fieldwork: José Dias (o Corvino), who took me in the first boat trip to observe the sea cliffs of Topo Volcano; Nílton Nunes, who helped me in the fieldwork in S. Caetano creek; José Alberto Costa, for helping me in a tempestuous GPS campaign in Faial; José Azevedo and José Gabriel Jorge and family, for assisting in the periodical maintenance of the monitoring networks.

I thank Manuel Paulino Costa, director of the Natural Park of Pico, for being always available to provide necessary information.

Finally, I thank my Family-Family:

Through these years I have had the opportunity to experience the huge magnitude of the support from my parents. My parents and brother have assisted me in the field work, either in sunny or cold/rainy days. My father started writing a novel about Topo, called *Milhafre do Arrife*, while I was working on the headwall of the slump. It is now published. My mother was a permanent source of moral support in these years, and I'll be forever grateful for her presence. My family members (living or already in transit through the Carbon cycle) are walking examples of hard work. I will always do my best to follow their steps. The most valuable lessons I learned were taught by them, while working in our vineyards in Pico.

This work gave me the opportunity to truly discover and appreciate my home-islands, Pico and Faial. It gave me the opportunity to meet and work with great people, and discover incredible places. It taught me lessons on geology, and tsunami lessons on all the great fields of life beyond it.

Peace, Love and Olivines

Ana

# Table of Contents

**Abstract** ..... **i**

**Abstract (Extended version)** ..... **iii**

**Resumo** ..... **vii**

**Résumé** ..... **xi**

**Acknowledgments** ..... **xv**

**Table of Contents** ..... **xix**

**PART I** ..... **1**

**Chapter 1 - Introduction** ..... **3**

**Chapter 2 - Geological setting** ..... **9**

**PART II - Long term evolution of the Pico-Faial volcanic ridge** ..... **25**

**Chapter 3 - Reconstructing the architectural evolution of volcanic islands from combined K/Ar, morphologic, tectonic, and magnetic data: The Faial Island example (Azores) - Hildenbrand et al.(2012a)** ..... 27

Abstract ..... 29

1. Introduction ..... 29

2. Geological background ..... 30

3. Fieldwork and sampling strategy ..... 31

4. Methods and results ..... 32

5. Discussion ..... 33

6. Conclusions ..... 37

**Chapter 4 - Large-scale catastrophic flank collapses in a steep volcanic ridge: The Pico-Faial Ridge, Azores Triple Junction - Costa et al. (2014)** ..... **39**

Abstract ..... 41

1. Introduction ..... 41

2. Geologic setting ..... 42

3. Morphological analysis ..... 42

4. Fieldwork ..... 45

5. K-Ar geochronology ..... 46

6. Discussion ..... 47

7. Conclusions ..... 53

Appendix A ..... 56

Appendix B ..... 60

Appendix C ..... 62

**Chapter 5 - Growth and collapse of Pico Island during its 200 kyr life time (Pico-Faial ridge, Azores Triple Junction) - Costa et al. (*submitted*) ..... 63**

Abstract ..... 65

1. Introduction ..... 66

2. Geological background ..... 69

3. Methods and results ..... 73

4. Discussion ..... 88

5. Conclusions ..... 100

Appendix A ..... 107

Appendix B ..... 118

**PART III - Current deformation in Pico Island ..... 121**

**Chapter 6 - Large-scale active slump of the southeastern flank of Pico Island, Azores - Hildenbrand et al. (2012b) ..... 123**

Abstract ..... 125

Introduction ..... 125

Slump geometry and kinematics ..... 125

Slump monitoring by GPS and radar interferometry ..... 126

Slump mechanisms and propagation ..... 127

Further evolution? ..... 127

Item DR1 ..... 129

Item DR2 ..... 130

Item DR3 ..... 131

**PART IV - Cohesive Coulomb Critical Taper Theory applied to gravitational instability: analytical solution and application to gravitational collapses in volcanic systems ..... 139**

**Chapter 7 - Gravitational instability in a cohesive granular material atop an overpressured detachment - analytical derivation and experimental testing - Costa et al. (*in prep a*) ..... 141**

Abstract ..... 143

1. Introduction ..... 144

2. The non-cohesive critical taper - a force equilibrium approach ..... 148

3. The cohesive critical taper - a force equilibrium approach ..... 150

4. Structural consequences of cohesion ..... 153

5. Experimental analogue modeling ..... 158

6. Cohesive wedge model - Minimal Failure Length (*MFL*) ..... 166

7. Conclusions ..... 168

Appendix A ..... 173

Appendix B ..... 177

**Chapter 8 - Cohesive Coulomb critical taper theory applied to gravitational collapses in overpressured volcanic systems: analytical/numerical modeling - Costa et al. (*in prep b*) ..... 181**

Abstract ..... 183

1. Introduction ..... 184

2. Cohesion of volcanic edifices ..... 186

3. Fluid overpressure in volcanic edifices ..... 187

4. Application of the cohesive model to volcanic system ..... 189

5. Discussion ..... 195

6. Conclusions ..... 201

7. Perspectives ..... 201

Appendix A ..... 207

**PART V** ..... **209**

**Chapter 9 - Conclusions** ..... **211**

**Chapter 10 - References** ..... **217**

**ANNEX I - Reply to the comment by Quartau and Mitchell on "Reconstructing the architectural evolution of volcanic islands from combined K/Ar, morphologic, tectonic, and magnetic data: The Faial Island example (Azores)" - Hildenbrand et al. (2013a)** ..... **241**

**ANNEX II - Reply to comment (Mitchell et al., 2013) on "Large-scale active slump of the southeastern flank of Pico Island, Azores" - Hildenbrand et al. (2013b)**..... **247**

**ANNEX III - GPS and tectonic evidence for a diffuse plate boundary at the Azores Triple Junction (Marques et al., 2013), and respective *corrigendum* (Marques et al., 2014a)** ..... **251**

**ANNEX IV - The 1998 Faial earthquake, Azores: Evidence for a transform fault associated with the Nubia-Eurasia plate boundary? - Marques et al. (2014b)** ..... **267**

# PART I

# Chapter 1

## Introduction

# Introduction

Large-scale gravitational destabilization is recurrent in the geological evolution of volcanic ocean islands. It has been known to occur within a spectrum of deformation mechanisms between gradual deformation along deep listric faults, as slumps, or catastrophic deformation, as debris avalanches (Moore et al., 1989, 1994a). Both gradual and catastrophic failures usually occur during the main eruptive history of a given island, and the volume of individual failure episodes partly depends on edifice size. For example, the most extreme debris-avalanches have been extensively recognized along the Hawaiian Emperor volcanic chain, which comprises by far the largest volcanic islands on Earth. These debris fields were shown to reach volumes up to thousands of $km^3$, run-outs up to hundreds of kms, and often result in the transport of blocks of kilometric dimensions. The most conspicuous example is the Nu'uanu debris avalanche on the NE of Oahu Island, Hawaii, which covers 23000 $km^2$, has an estimated volume of 2500-3500 $km^3$, a run-out of 220 km, and which involved the transport of a 30 km long/ 600 $km^3$ block along ca. 55 km (Moore et al., 1989; Normark et al., 1993; Moore and Clague, 2002; Satake et al., 2002).

Other giant catastrophic flank failure events (> 10 $km^3$) have been interpreted from evidence onshore and offshore all over the world: e.g. in Hawaii (Lipman et al., 1988; Moore et al., 1989,1994a; Moore and Clague, 2002), the Canary (Navarro and Coello, 1989; Carracedo et al., 1999; Krastel et al., 2001; Masson et al., 2002; Boulesteix et al., 2012; 2013), in Cape Verde (e.g., Day et al., 1999; Masson et al., 2008), along the Caribbean arc (Deplus et al., 2001; Le Friant et al., 2003; Samper et al., 2007; Germa et al., 2011), in French Polynesia in the Pacific (Clouard et al., 2001; Clouard and Bonneville, 2004; Hildenbrand et al., 2004; 2006), or in Reunion Island in the Indian Ocean (Duffield et al., 1982; Gillot et al., 2004; Kelfoun et al., 2010) .

Catastrophic episodes of destabilization can be voluminous and generate large tsunamis (Keating and McGuire, 2000): as shown by numerical modelling (Giachetti et al., 2011; Paris et al., 2011); and as evidenced by marine conglomerates identified onshore at high altitudes (e.g., Pérez-Torrado et al., 2006; Ferrer et al., 2013 in Canary Islands; Paris et al., 2011; Ramalho et al., 2013 in Cape Verde; Paris et al., 2013 for La Reunion; Moore and Moore, 1984,1988; Moore et al., 1994b; Moore, 2000; McMurty et al., 2004; for Hawaii). The large tsunamis generated may cause considerable damage and thus represent extremely hazardous events.

While for the large-scale events as the ones reported for the large Hawaii volcanic islands a recurrence between ca. 25 and 100 ka is estimated, small collapses in volcanic islands are generally considered more frequent (Lipman et al., 1988; Normark et al., 1993 in Keating and McGuire, 2000).

The Azores islands are of small dimensions when compared with the Hawaiian counterparts. For instance, the dimensions of the whole Faial Island are close to those of the Tuscaloosa seamount, the biggest block identified in the Nu'uanu debris avalanche, to the NE of Oahu Island. The Azores islands east of the Mid-Atlantic Ridge (MAR) are located on the Eurasia(Eu)/Nubia(Nu) diffuse plate boundary, along steep volcanic ridges bounded by major faults that accommodate the diffuse deformation (Marques et al., 2013, 2014a). Historic records attest the occurrence of volcanic growth episodes (Madeira and Brum da Silveira, 2003) and surface deformation events related to volcanic (e.g., Catalão et al., 2006) and seismic activity (magnitude up to ca. 7 - Fernandes et al., 2002; Madeira and Brum da Silveira, 2003; Borges et al., 2007; Marques et al., 2014b), constituting a real risk for the local population. Given the dimensions, configuration and tectonic setting of the islands, the flank collapses in the Azores islands are expected to be much less voluminous, but much more frequent than the typical cases studied in Hawaii. Despite the smaller volumes displaced, these more frequent events have been shown to still have potential for generation of tsunamis (Kelfoun et al., 2010; Giachetti et al., 2012). The consequences of such frequent events would be extremely damaging for the populations of the island (partially) destroyed, as well as for the populations of the islands nearby through tsunami propagation, as the islands are spatially close to one another, and the populations are concentrated near the coastlines. However, despite the active tectonic setting and the steep configuration of the islands, prior to MEGAHazards Project (PTDC/CTE-GIX/108149/2008, funded by FCT, Portugal), large-scale flank collapses in the Azores were considered to be lacking, mainly due to the small dimension of the volcanic edifices (e.g. Mitchell, 2003; Mitchell et al., 2008).

The present PhD thesis addresses the long term evolution and current gravitational deformation of the Pico-Faial steep volcanic ridge, which sits on a major normal fault associated with the Eu/Nu diffuse boundary. We focus especially on the large-scale flank failures in Pico Island.

Based on high-resolution sub-aerial and submarine Digital Elevation Models (DEM), new structural and stratigraphic data, and high-resolution K-Ar dating on separated volcanic groundmass, we: (1) reconstruct the volcanostratigraphy of Faial and Pico Islands; (2) identify and characterize onshore and offshore evidence for large-scale destruction events in

the Pico-Faial volcanic ridge; (3) constrain in time these occurrences, and analyse them in the context of the evolution of the islands; (4) reconstruct the evolution of the major phases of growth and destruction in the Pico-Faial ridge, and analyse its long term evolution in the context of the diffuse Eu/Nu plate boundary; (5) interpret currently active large-scale gravitational structures in Pico Island.

Many factors favouring the development of such large-scale flank instabilities have been proposed in the literature (e.g., McGuire, 1996; Keating and McGuire, 2000), but their exact role and mutual contribution remain poorly understood. Through analytical, numerical and analogue modelling (performed in Université du Maine, Le Mans, France, in collaboration with Dr. Régis Mourgues), we assess the roles of edifice geometry/configuration and dimensions, the strength of the volcanic materials and basal detachments (cohesion and internal friction), and fluid overpressure We focus especially on how cohesion influences the stress regime within the wedge, by inhibiting deformation and constraining failure location.

**Organization of the manuscript**

The introductory **Part I** includes the present chapter and, as **Chapter 2**, a concise geological setting of the study area.

The core of this manuscript is divided in three main parts (Parts II, III and IV). In each part, articles signed as first author (published, submitted or in preparation), or as co-author (published articles directly related to the subject of this thesis) are presented. The numbering of figures, tables and equations is independent for each paper. The references cited and the supplementary files of each article are properly presented at the end of each article.

**Part II** concerns the long term evolution of the Pico-Faial volcanic ridge. This part comprises:

- **Chapter 3,** which corresponds to the co-authored work on the reconstruction of the evolution of the Faial Island by Hildenbrand et al. (2012a). As **Annex I**, a reply to a comment by Quartau and Mitchell (2013) regarding this paper (Hildenbrand et al., 2013a) is presented.

**- Chapter 4,** where we show the occurrence of large-scale flank collapses in the N flank of Pico Island more than 70 ka ago (Costa et al., 2014).

- **Chapter 5**, which corresponds to a more complete work regarding the geological evolution of Pico Island, including the evolution of the large-scale slump structure on its SE flank and the analysis of the overall evolution of Pico-Faial ridge in the last 200 kyr (Costa et al., *submitted*).

**Part III** concerns the current deformation in Pico Island, and comprises:

- **Chapter 6**, which corresponds to a co-authored published work that reports on the current activity of a large-scale slump on the SE flank of Pico Island, based on GPS and InSAR data (Hildenbrand et al., 2012b). As **Annex II**, a reply to a comment by Mitchell et al. (2013) on this paper (Hildenbrand et al., 2013b) is presented.

**Part IV** comprises the modeling work regarding the impact of edifice configuration/dimension, cohesion, internal friction and fluid overpressure on gravitational destabilization. This part includes:

- **Chapter 7**, in which are presented: an analytical solution for the cohesive Coulomb Critical Wedge theory applied to gravitational instabilities, and associated analogue simulations to test some structural implications of the model (Costa et al., *in prep a*);

- **Chapter 8**, which corresponds to the application of the analytical solution to the occurrence of gravitational destabilization in volcanic flanks (Costa et al., *in prep b*).

Finally, in the final **Part V:**

**- Chapter 9**, in which the main conclusions of this PhD work are summarized;

- **Chapter 10**, in which a complete list of the references cited through this thesis is provided.

Additional published co-authored works, in the scope of MEGAHazards Project, are presented as annexes:

**Annex III** - "*GPS and tectonic evidence for a diffuse plate boundary at the Azores Triple Junction"*, by Marques et al. (2013), and respective *corrigendum* (Marques et al., 2014a);

**Annex IV**- "*The 1998 Faial earthquake, Azores: Evidence for a transform fault associated with the Nubia-Eurasia plate boundary?",* by Marques et al. (2014b).

# Chapter 2

## Geological setting

# Geological setting

The Azores Islands are located near the triple junction between North-America (Na), Eurasia (Eu) and Nubia (Nu) lithospheric plates, the so-called Azores Triple Junction (ATJ) (Fig. 1). The ATJ is diffuse, currently of rift-rift-rift type, and located between 38.3ºN, 30.3ºW and 39.4ºN, 29.7ºW along the Mid-Atlantic Ridge (MAR) (Marques et al., 2013a, presented as *Annex III*). This diffuse domain is marked by a decrease in the MAR seafloor spreading rates N and S of the ATJ (DeMets et al., 2010): from ca. 22.5 mm/yr N of latitude 40ºN (Na/Eu) to ca. 19.5mm/yr S of 38ºN (Na/Nu) (Marques et al., 2013a).

The islands located to the E of the MAR sit on a strongly fractured/anomalously elevated portion of the lithosphere, known as the "Azores Plateau", which is defined by the ca. 2000 m isobath (Krause and Watkins, 1970; Searle, 1980). These islands are distributed along the Eu/Nu plate boundary. Considering Eu stationary, the predicted GPS angular velocity of Nu is 4.6 ± 0.3 mm/yr toward S87.9º ± 3.3º (Marques et al., 2013a).

The western half of the Eu/Nu plate boundary is presently diffuse (Fig.1a, e.g. Lourenço et al., 1998; Luis et al., 1998; Miranda et al., 1998; Fernandes et al., 2006; Borges et al., 2007; Lourenço, 2007; Hildenbrand et al., 2008; Luis and Miranda, 2008; Marques et al., 2013a; 2014a ; Neves et al., 2013; Trippanera et al., 2014; Hildenbrand et al., 2014; Miranda et al., 2014). The deformation is mostly accommodated by several extensional structures in a ca. 140 km wide area (Marques et al., 2013a, 2014a, *Annex III*):

(1) the Terceira Rift (TR , Fig. 1, Machado, 1959; Krause and Watkins, 1970; Searle, 1980; Vogt and Jung, 2004);

(2) the ca. WNW-ESE graben-horst-graben structure to the SW of the TR (Fig. 1) (Marques et al., 2013a, 2014a), which is arranged *en échelon* at the scale of the diffuse boundary. It comprises the S. Jorge Graben (Lourenço, 2007) and the Faial Half-Graben, with an intervening horst, the S. Jorge/Faial Horst (Marques et al., 2013a, 2014a).

In this diffuse deformation area, have been recorded numerous volcanic eruptions have since the XVth century, and seismic events with magnitude up to ca.7 since 1939 (Madeira and Brum da Silveira, 2003; Borges et al., 2007). The registered seismic events with magnitude larger than 4 have involved predominantly normal kinematics (Marques et al., 2014b, *Annex IV*).

To the SW of the TR, the regional deformation has influenced the development of narrow and steep volcanic ridges, S. Jorge and Pico-Faial (Fig. 1), bounded by the major

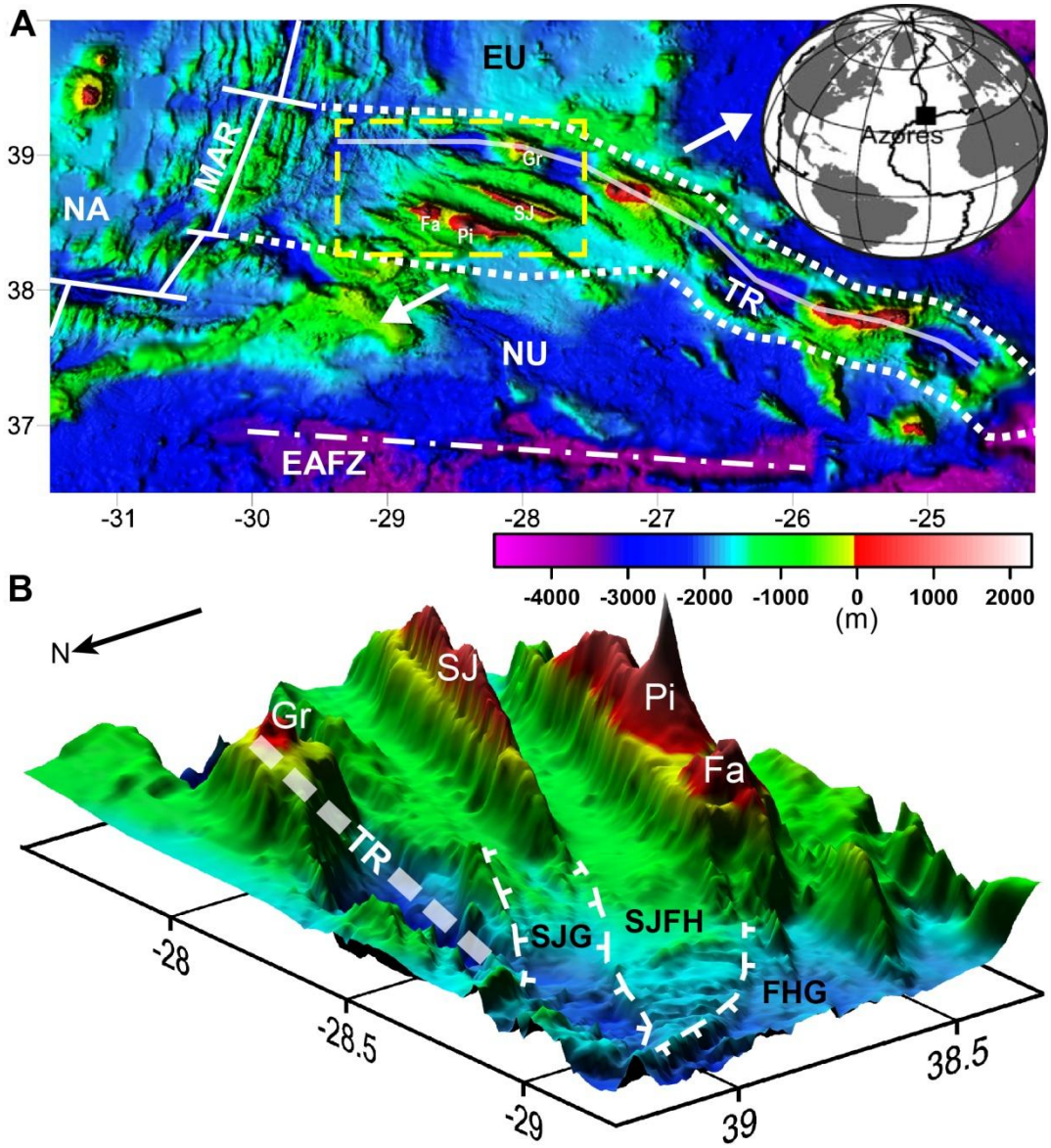


**Fig. 1.** (A) Location of the Azores archipelago on the triple junction between the North America (NA), Eurasia (EU) and Nubia (NU) plates (lighting from WSW). Main active structures represented as thick white lines (Middle Atlantic Ridge – MAR, Terceira Rift – TR); limits of the diffuse Eu/Nu plate boundary represented as dotted lines, and extension orientation indicated as thick white arrows; and the currently inactive East Azores Fracture Zone (EAFZ) as dashed-dot-dashed white line. Yellow dashed rectangle marks the area presented in B. (B) 3D surface (viewed from NW and lighting from E) of the sector that includes the WNW-ESE volcanic ridge studied in this thesis, composed of the Faial (Fa) and Pico (Pi) islands. TR marked as a thick dashed white line. The graben/horst structure SW of the TR is defined according to Marques et al. (2013a, 2014a). SJG - S. Jorge Graben; SJFH - S. Jorge/Faial Horst; FHG - Faial Half-Graben. SJ - S. Jorge Island; Gr - Graciosa Island. The bathymetric data are from Lourenço et al. (1998).

structures mentioned above in (2). These volcanic ridges are characterized by slopes commonly around 25-35º, locally reaching higher values along coastal cliffs. These ridges are characterized by a multi-stage development during the last 1.3 Myr (Féraud et al., 1980; Demande et al., 1982; Hildenbrand et al., 2008).

The origin of the volcanism in the Azores is still a controversial subject. Some authors advocate the existence of a mantle plume, from geochemical data (Schilling, 1975; White et al., 1976; Turner et al., 1997; Moreira et al., 1999; Bourdon et al., 2005; Madureira et al., 2005; 2011; Beier et al.,. 2012) and from seismic tomography (Silveira and Stutzmann, 2002; Montelli et al., 2004, 2006; Pilidou et al., 2005; Silveira et al., 2006; Yang et al., 2006; Adam et al., 2013; Saki et al., 2015). The so-called Azores plume is considered to have contributed to the formation of the Azores plateau (Gente et al., 2003), and to be presently at the end of its activity (Cannat et al., 1999; Silveira et al., 2006). Others consider that the magmatism in the Azores can be explained by an upper mantle source enriched in volatiles (Bonatti, 1990; Métrich et al., 2014), and/or propose that lithospheric deformation along the Eu/Nu plate boundary has largely controlled melt production and volcanic outputs (Neves et al., 2013; Hildenbrand et al., 2014; Métrich et al., 2014).

**1. Pico-Faial volcanic ridge**

The Pico-Faial volcanic ridge sits on the master fault bounding the Faial Half-Graben in the north, and is locally parallel to the orientation of the Eu/Nu plate boundary (Fig. 1b, Marques et al., 2013a, 2014a). This structure currently accommodates part of the inter-plate deformation (Marques et al., 2013a; Trippanera et al., 2014). The western and central sectors of the ridge are aligned WNW-ESE, parallel to the local orientation of the Eu/Nu plate boundary (Fig. 1a). Towards the E, the submarine prolongation of the ridge is oriented N150º (Stretch et al., 2006; Lourenço, 2007; Mitchell et al., 2012a).

The sub-aerial growth of the Pico-Faial ridge started prior to the Matuyama-Brunhes transition (789 ± 8 ka, Quidelleur et al., 2003). Negative magnetic anomalies were identified in Faial Island, located on the westernmost sector of the ridge, and on the submarine continuation of the ridge towards SE of Pico (Miranda et al., 1991; Lourenço, 2007; Hildenbrand et al., 2012a), where the oldest age was obtained for this ridge, ca. 1.5 Ma (Ar/Ar dating, Beier, 2006).

Although the WNW-ESE direction constitutes the most obvious structural trend, the

Pico-Faial ridge is punctuated by three WNW-ESE aligned central-type volcanoes, interpreted as a consequence of the intersection of structural trends oblique to WNW-ESE (e.g., Madeira, 1998). These secondary oblique structural trends are:

(a) NNW-SSE: this orientation is strongly represented in the structures interpreted from the bathymetry (Marques et al., 2013a,2014a) and in the solutions of focal mechanisms determined for historical seismic activity (Marques et al., 2014b). It is consistent with the orientation expected for the structures accommodating pure extension in the Nu-Eu plate boundary (Marques et al., 2014b, *Annex IV*). This trend was also interpreted on the flanks of the Pico Stratovolcano, from the alignment of the volcanic vents of the 1718 volcanic eruption (Madeira and Brum da Silveira, 2003);

(b) NNE-SSW: this is the orientation of faults, dykes and extension fractures recognized on the sub-aerial domain of the polygenic edifices in Faial Island (Trippanera et al., 2014); and interpreted as MAR-inherited (e.g., Chovelon, 1982)

(c) WSW-ENE: it coincides with the orientation of minor scarps interpreted in the submarine domain of the volcanic ridge (Lourenço, 2007; Marques et al., 2013a, 2014a); such orientation is also the one expected for transform structures associated with the present Eu/Nu plate boundary (Marques et al., 2014b, *Annex IV*).).

Here we address the long-term geological evolution of the islands along this ridge, Faial and Pico, focusing especially on what is known about the occurrence of major tectonic and gravitational deformation in these islands.

## 2. Faial Island

### *2.1. Volcanic stratigraphy*

Faial is located on the western sector of the Pico-Faial volcanic ridge (Fig. 1). Chovelon (1982) defined the following main volcanic units in Faial, from older to younger (Fig. 2a):

- the old Galego volcano, cropping out on the E sector of the island. The edifice was strongly dismantled by deformation in an island-scale graben (Machado, 1955). Nonetheless, a lateral correspondence between palaeosoil levels visible on the SE and on the NE of the island was assumed (Chovelon, 1982).

- a central-type edifice, the Central Volcano (CV), which developed inside the graben

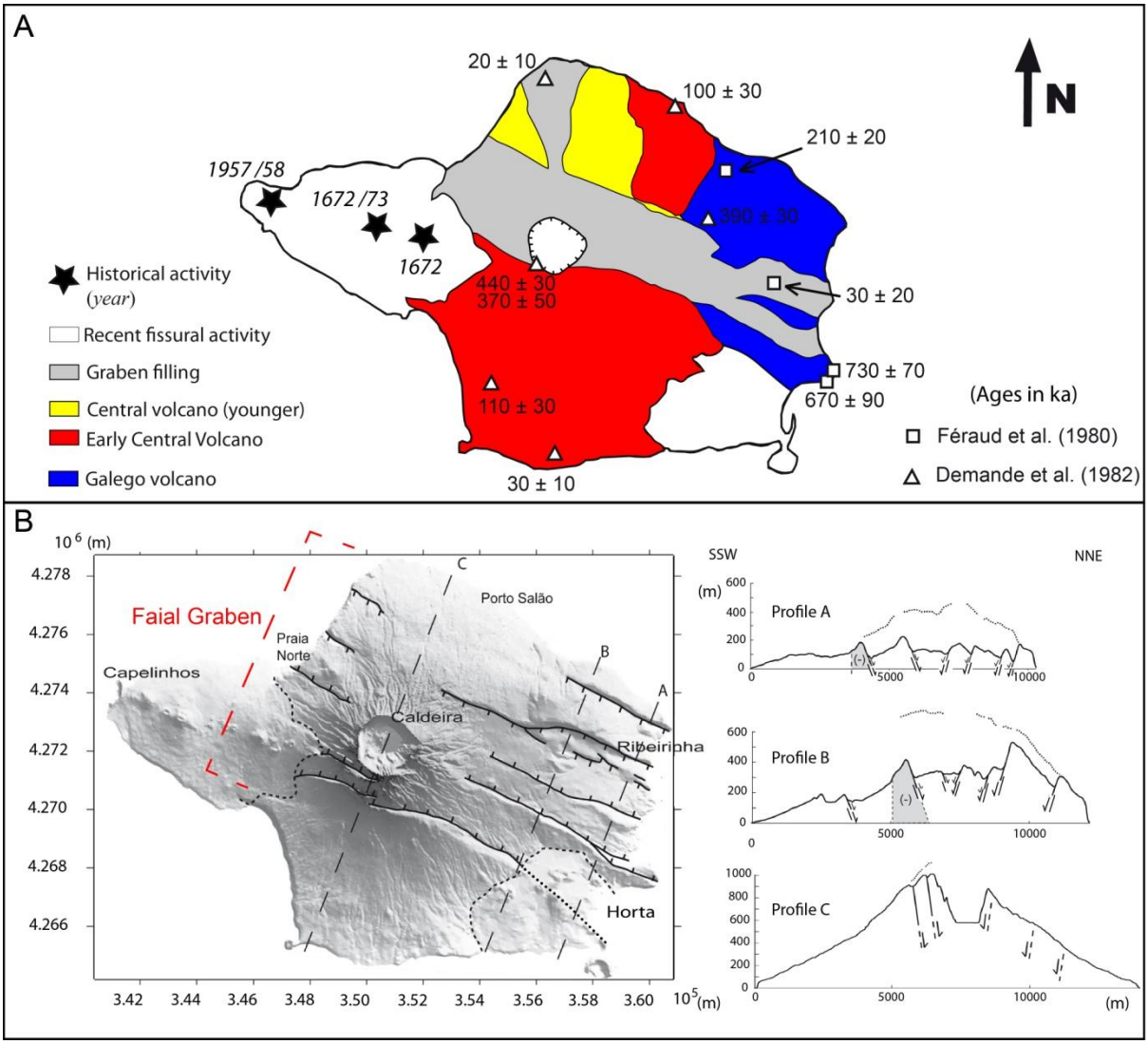


**Fig. 2**. (A) Simplified geological map of Faial (modified by Hildenbrand et al., 2012a after Chovelon, 1982). Presented K/Ar ages, in thousands of years (ka), from Féraud et al. (1980) and Demande et al. (1982), and the location/year of the historical eruptions. (B) Shaded relief of high-resolution DEM from Faial (lighting from N), with interpretation of graben structures and SSW-NNE profiles. Figures modified after Hildenbrand et al. (2012a).

and experienced at least two phases of activity (Fig. 2b, Féraud et al., 1980).

- volcanics filling the island-scale graben in the last 30 kyr;

- volcanics in the SE of the island, with small volcanic cones and basaltic lava flows.

- trachytic pumice deposits resulting from explosive activity in the CV (Chovelon, 1982; Serralheiro et al., 1989; Madeira et al., 1995). These deposits have covered extensive areas of the island during the last 10 kyr (dotted blue area in Fig. 3a, Serralheiro et al., 1989; Madeira, et al., 1995; Madeira, 1998 - with ages determined through radiocarbon dating).

- the volcanics from the WNW-ESE Capelo peninsula, on the westernmost sector of

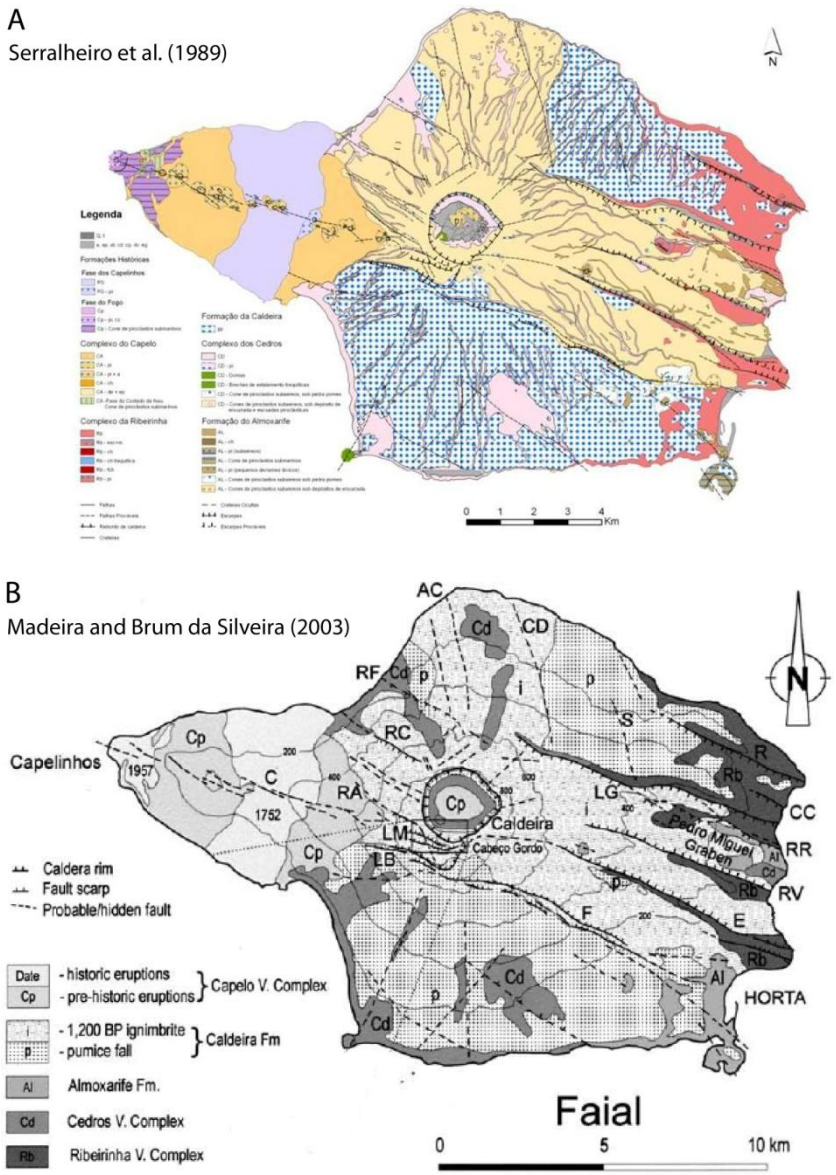


**Fig. 3.** Geological map of Faial presented by: (A) Serralheiro et al. (1989). Main units represented: Red - Ribeirinha Complex (equivalent to Galego volcano); Ligh yellow - Almoxarife Formation (equivalent to graben filling units); Light-rose and small green areas: Cedros Complex (equivalent to the first main growth phase of the Central Volcano); Blue-Dotted areas - sectors covered by deposits resulting from the explosive activity of the Central Volcano; Orange and purple areas on the Capelo peninsula - recent fissural vulcanism (Capelo Complex), including historical volcanic activity (purple). (B) Madeira and Brum da Silveira (2003) (after Serralheiro et al., 1989, and Madeira, 1998).

Faial. They consist mainly of basaltic scoriae cones and associated lavas erupted in the last 10 kyr. Two historical eruptions in this area occurred in 1672-1673, and 1957-1958 (Fig. 2a).

After Chovelon (1982), and prior to Hildenbrand et al. (2012a) (*Chapter 3*), several works focused on the reconstruction of Faial's evolution by more detailed cartographic work

and radiocarbon dating (Fig. 3, Serralheiro et al., 1989; Madeira et al., 1995; Madeira, 1998). However, these works relied always on the K/Ar data from Féraud et al. (1980) and Demande et al. (1982) regarding the age of the early phases of sub-aerial development of Faial (Fig. 3 - e.g., Serralheiro et al., 1989; Madeira, 1998; Pacheco, 2001; Madeira and Brum da Silveira, 2003). These previous ages acquired on whole-rock samples are scarce and fairly imprecise, and do not allow a clear calibration of the volcanic stratigraphy. For instance, there is an apparent overlap between the age range for the old Galego volcano (730 ± 70 ka to 210 ± 20 ka), which was heavily dismantled by the island-scale graben, and the age range for the main growth of the Central Volcano (440 ± 30 ka to 30 ± 10 ka), which was built inside the graben (Hildenbrand et al., 2012a).

### *2.2. The Faial Graben*

Faial is affected by an island-scale WNW-ESE graben (Fig. 2b, Machado, 1955), whose scarps are more developed in the E. Towards the W, the scarps have been masked by the successive deposits of the large polygenic CV, centred in the subsided central block of the graben (Féraud et al., 1980). This large volcanic edifice has been itself affected by the graben structures. Further W, the scarps continue in the offshore domain.

The fault scarps are generally oriented N110º-120º, with faults dipping 60-70º towards the SSW in the N, and towards the NNE in the S. Evidence for transtensional movement along the graben faults has been reported: normal dextral slip for the major WNW-ESE faults, and normal sinistral slip for the (less expressive) conjugate NNW-SSE faults (Madeira and Ribeiro, 1990; Madeira, 1998; Madeira and Brum da Silveira, 2003). More recently, Marques et al. (2014b) interpreted bends along the trace of the major WNW-ESE structures as evidences for sinistral slip along the WNW-ESE graben faults, instead of dextral.

Prior to Hildenbrand et al. (2012a), different ages have been proposed for the beginning of the graben activity: Féraud et al. (1980) suggested a maximum age of 670-730 ka (without considering the uncertainties of the data), Chovelon (1982) proposed a minimum age of 30 ka, and Madeira (1998) proposed that the graben activity began at 73-40 ka. Madeira and Brum da Silveira (2003), based on paleoseismological studies and radiocarbon dating, report on recurrent episodes of graben activity through the Holocene, until historical times.

Although the origin of this graben can be related to tectonics (Tazzief, 1959), its

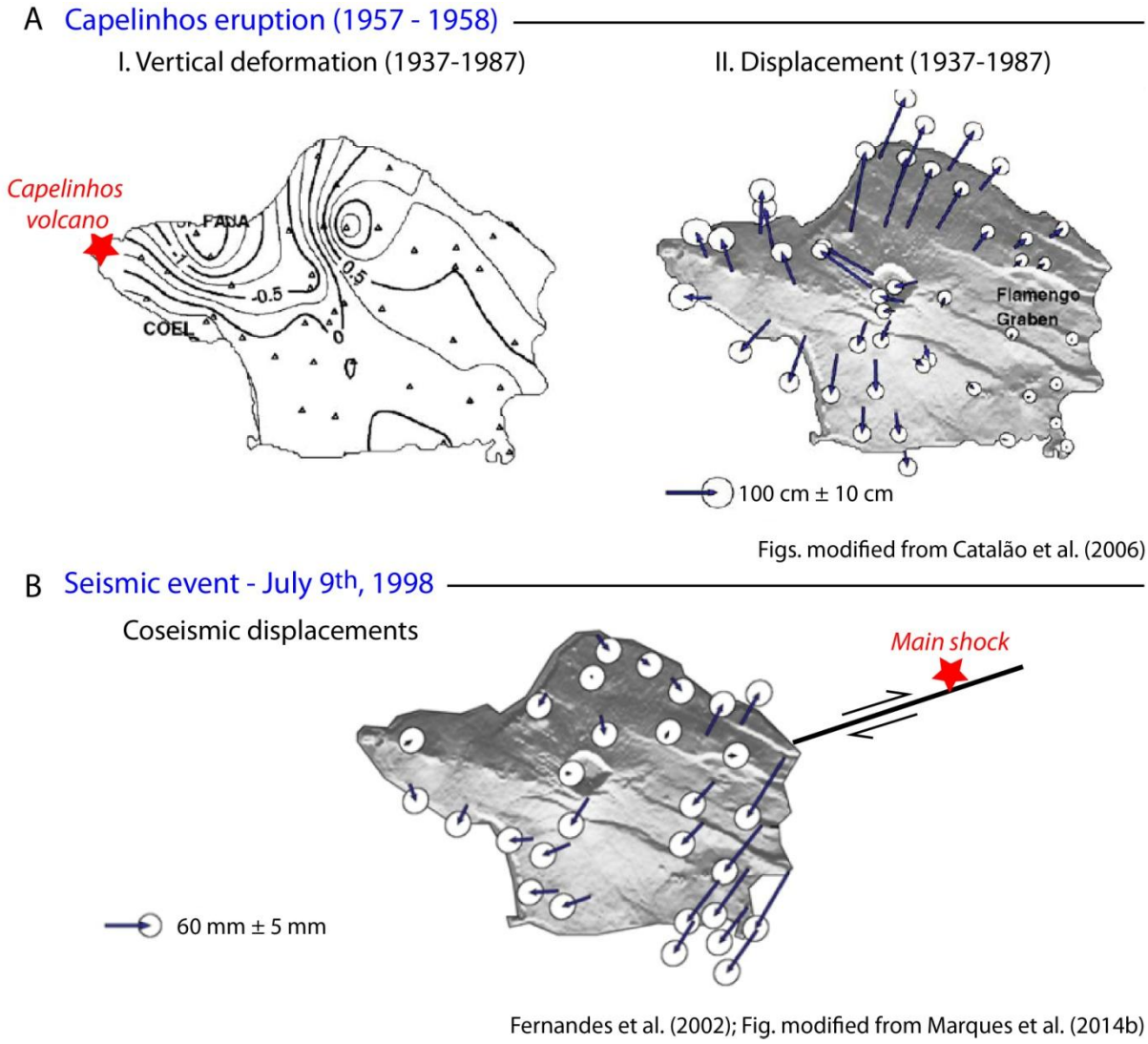


**Fig. 4.** (A) Vertical deformation (contours defined for 0.25 m spacing) (i) and displacement (ii) determined for the period 1937-1987, in Faial (Catalão et al., 2006). There is represented the location of Capelinhos volcano, resulting from the 1957-1958 eruption; (B) Coseismic displacements determined for the last large seismic event that affected the Pico-Faial ridge, at July 9$^{th}$ 1998 (Marques et al., 2014b, after Fernandes et al., 2002). The structure responsible for this seismic event, the associated kinematics and the location of the main shock are represented (Marques et al., 2014b).

development has been influenced by volcanic processes, as shown by the events of the seismic crisis in May-June of 1958, during the eruption of Capelinhos volcano (1957-1958) on the WNW end of the island (Fig. 2a). This seismic crisis generated the opening of fissures, with up to 1m vertical movements along the WNW-ESE graben faults (Tazzief, 1959; Zbyszewski and Da Veiga Ferreira, 1959; Machado et al., 1962; Madeira and Brum da

Silveira, 2003), and opening of N55º fractures inside the caldera of the central volcano with associated fumarolic/phreatic activity (Tazieff, 1959). Based on geodetic measurements carried out between 1937 and 1987, Catalão et al. (2006) concluded that the main surface deformation in Faial over this period probably corresponds to the deformation associated with the Capelinhos eruption (Fig. 4a). The results of this study show a maximum subsidence of -1.75 m on the NW of the island, for the mentioned period (Catalão et al., 2006).

The epicentre of the most recent major tectonic seismic event that affected the Pico-Faial ridge (July 9$^{th}$, 1998, with magnitude $M_L$ = 5.8 - Matias et al., 2007) was located on the offshore, 10 km to the NE of Faial (Fig. 4b). The main shock induced a clockwise rotation of Faial (Fig. 4b, Fernandes et al., 2002), with associated reactivation of (more superficial) major faults in the NE of Faial Graben (Marques et al., 2014b).

## 3. Pico Island

### *3.1. Volcanic stratigraphy*

Previous studies have shown that Pico comprises three main volcanic complexes (Fig. 5a, Zbyszewski et al., 1963a, 1963b; Forjaz, 1966; Woodhall, 1974): (1) the relicts of an old extinct volcano in the SE, generally referred to as the Topo Volcano; (2) a ca. WNW-ESE lineament of strombolian cones in the middle and eastern parts of the island, known as the Fissural System; and (3) the Pico Stratovolcano, peaking at 2351 m above sea level, which makes up the western half of the island.

According to previous geochronological data, the sub-aerial part of Pico has developed during the last ca. 300 kyr (250 ± 40 ka, in Demande et al., 1982, Fig. 5a). Pico's sub-aerial growth seems to have started in the east, with the growth of the Topo Volcano (Fig. 5a, Zbyszewski et al., 1963a; Forjaz, 1966; Woodhall, 1974; Madeira, 1998; Nunes, 1999; Nunes et al., 1999a), interpreted as a shield volcano by Woodhall (1974). The remnants of this early sub-aerial volcano have been partially covered unconformably by younger volcanic products poured from scattered scoria cones and WNW-ESE aligned cones of the sub-aerial Fissural System (Zbyszewski et al., 1963a, 1963b; Woodhall, 1974; Madeira, 1998; Nunes, 1999; Nunes et al., 1999b, Fig. 5a).

The latest stages of island growth comprise the development of the Fissural System and the Pico Stratovolcano, which have been active through the Holocene, up to historical times (Fig. 5a, e.g., Zbyszewski et al., 1963b; Forjaz, 1966; Woodhall, 1974; Madeira, 1998;

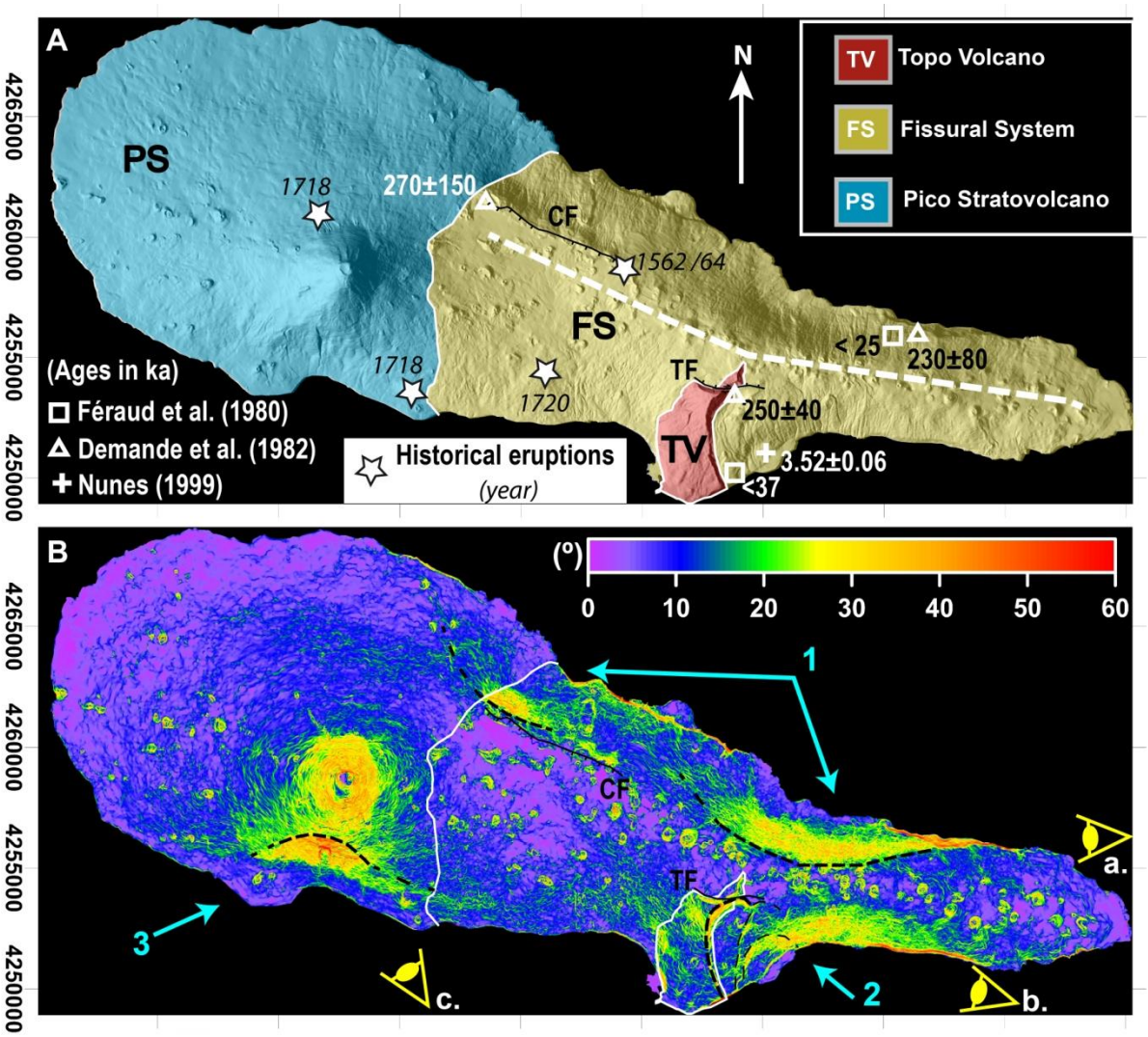


**Fig. 5.** (A) Shaded relief of the 10 m resolution DEM of Pico Island (lighting from ESE), with coordinates in metres UTM (zone 26N). White squares and triangles mark the K-Ar ages from Féraud et al. (1980) and Demande et al. (1982), respectively. Also shown a radiocarbon age (plus sign) from Nunes (1999). The ages are indicated in thousands of years (ka). Simplified geologic/physiographic map (modified after Madeira, 1998). Traces of the Capitão Fault (CF) and Topo Fault (TF) (after Madeira, 1998; Nunes et al., 1999; Madeira and Brum da Silveira, 2003). There are indicated the location and years of the historical eruptions; (B) Slope map of Pico Island built from the 10 m resolution DEM. Dashed black lines: scarps interpreted from zones of anomalously steep slopes, referred in the text as *1*, e *2* and *3*. Perspectives (yellow eyes) identified as *A*, *B* and *C* are presented as 3D surfaces in Fig. 6.

Nunes, 1999; Nunes et al., 1999a; Madeira and Brum da Silveira, 2003; Mitchell et al., 2008).

Available whole-rock K-Ar data from Féraud et al. (1980) and Demande et al. (1982) (Fig. 5a) are very scarce and do not allow the age calibration of Pico's volcano-stratigraphy.

For instance, one lava flow from the old Topo Volcano was previously dated at 250 ± 40 ka, whereas two lava flows sampled in the western and eastern sectors of the Fissural System yielded ages of 270 ± 150 ka and 230 ± 80 ka, respectively (Demande et al., 1982, Fig. 5a). These three ages overlap within their range of uncertainty, and thus are not precise enough to confidently reconstruct the evolution of the island. Ages estimated younger than 25 ka and 37 ka (Fig. 5a; Féraud et al., 1980) have been also obtained on lava flows from the northern and southern flanks of the island, respectively, but their geological significance remains elusive. A few radiocarbon data on charcoal fragments and/or paleosoils covered by lava flows help to constrain the age of some of the most recent eruptions (Madeira, 1998; Nunes, 1999). However, these data are of limited use to study the long-term evolution of the ridge due to the restricted applicability of the method (< ca. 50 kyr).

The lack of precise and representative isotopic ages in Pico (França, 2000), the lack of marked lithologic variability between main volcanic units (França, 2000; França et al., 2006), and the temporal partial overlap of the volcanic activity, all have hampered the definition of Pico's volcanic stratigraphy. The earlier works have relied greatly on the published K-Ar and radiocarbon ages, on the alteration degree of the volcanic deposits, and on local field relationships (e.g., Madeira, 1998; Nunes, 1999; Nunes et al., 1999a; França, 2000; França et al., 2000).

Two WNW-ESE faults have been recognized in Pico, and interpreted as normal dextral (Fig. 5; Madeira, 1998; Madeira and Brum da Silveira, 2003):

- The Topo Fault (*TF* in Fig. 5), evidenced by scarps with height up to 140 m, affects the old Topo Volcano (Woodhall, 1974; Madeira, 1998). Madeira (1998), based on morphological analysis and assuming that the N-S outcrop visible to the N of this fault was originally in continuity with the highest outcropping remnants of Topo in the S, interpreted the kinematics as predominantly dextral strike-slip (ca. 600 m), with a smaller dip slip component towards the N (ca. 44 m). Madeira (1998) considered that the Topo Fault remained active during the sub-aerial evolution of Pico (period of ca. 300 kyr);

- The Capitão Fault (*CF* in Fig. 5), dipping towards the S, and with a scarp up to 20 m high (Zbyszewski et al., 1963b; Forjaz, 1966; Madeira, 1998; Madeira and Brum da Silveira, 2003). This fault scarp was masked on the W by recent deposits of the Pico Stratovolcano, and on the E by recent volcanic cones (including the one involved in the historical eruption of 1562-1564, Fig. 5a), and has been considered active during the Holocene (Madeira, 1998; Madeira and Brum da Silveira, 2003).

*3.2. Mass-wasting structures in Pico Island*

Earlier studies in Pico have highlighted the existence of several structures affecting the various volcanic complexes (Figs. 5b and 6): (1) two concave steep zones on Pico's northern flank; (2) several nested scarps in SE Pico; and (3) a WNW-ESE scarp on the southern flank of the Pico Stratovolcano.

(1) On Pico's northern flank, two topographic embayments were considered by Mitchell (2003) as "*ambiguous candidates for landslides*" (Figs. 5b and 6a). Mitchell et al. (2008) identified a hummocky terrain area on the shallow bathymetry (depth up to of a few hundred meters) adjacent to a sub-aerial embayment (Fig. 2 in Mitchell et al., 2008, feature A), which was interpreted as a deposit resulting from either debris avalanche or repeated lava delta failure.

(2) The easternmost topographic embayment on the northern flank is mirrored in Pico's southern flank by another concave and steep main scarp and a series of less-pronounced scars (Figs. 5b and 6b). The main scarp has been variably interpreted as: a crater or caldera (Zbyszewski et al., 1963a), a "trap door" type caldera of the Topo Volcano (Woodhall, 1974), a landslide scar (Madeira, 1998; Madeira and Brum da Silveira, 2003; Mitchell, 2003), or a fault constituting the headwall of a slump structure (Nunes, 1999; França, 2000; Nunes, 2002). Nunes (1999, 2002) has proposed that this structure is younger than 37 ka, and inactive since the beginning of the Holocene. This hypothesis was later reinforced by Mitchell et al. (2012). These authors did not find evidence for deformation of the current coastal shelf by the slump structures, and considered that the lava delta was formed according to the present sea level.

(3) The WNW-ESE scarp on the southern flank of the Pico Stratovolcano (Figs. 5b and 6c) has been interpreted either as an avalanche scar (Woodhall, 1974; Madeira, 1998; Madeira and Brum da Silveira, 2003) or as a fault scarp (Forjaz, 1966; Machado et al., 1974; Chovelon, 1982, Forjaz et al., 1990; Nunes, 1999; Nunes et al., 1999a,b; Mitchell, 2003). This scarp has been described as being masked by more recent volcanic products from the Pico Stratovolcano (Chovelon, 1982; Madeira, 1998; Nunes, 1999), and its base covered by recent and thick colluvium deposits (Madeira, 1998; Nunes, 1999).

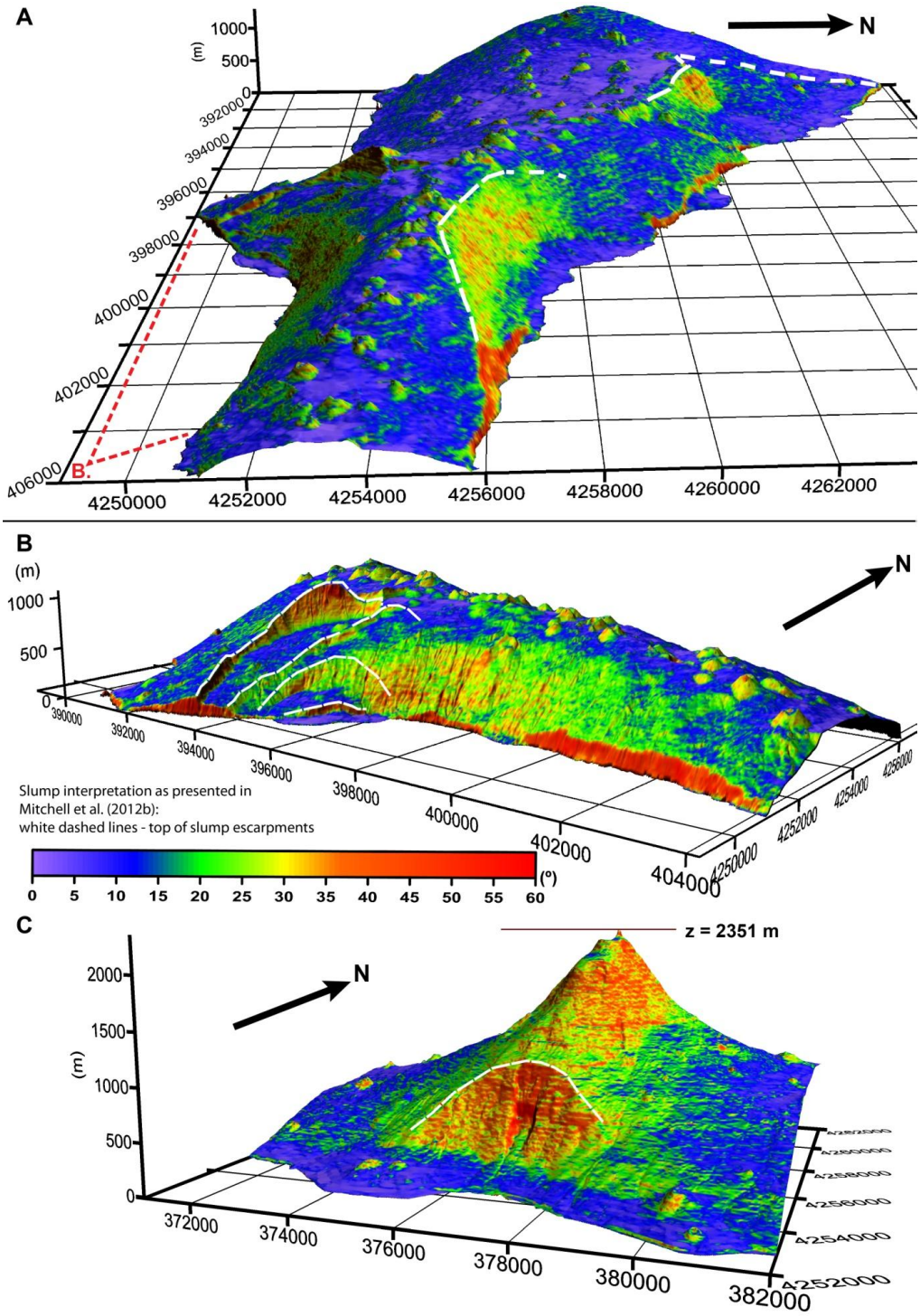


**Fig. 6.** Images obtained by superimposing the 3D view of Pico Island relief (vertical exaggeration: 2x) and the slope map image (shared color scale for slope angles), obtained from a 10 m resolution DEM. Perspectives presented A, B and C, are indicated in Fig. 5b by "a.", "b." and "c.", respectively. (A) Perspective from E (lighting from NW), of Pico Island's topography, with interpretation of the N and S flanks' main scarps as dashed white lines. (B) View from ESE of the slump structure's topography (lighting from SW). Scarps interpreted as white dashed lines (structures interpretation as presented in Mitchell et al., 2012b). (C) Perspective from SE of Pico stratovolcano's strongly dipping southern flank (lighting from SE).

Costa et al. (2014), *Chapter 4*, presented new data and interpretations regarding the embayments on the N flank mentioned in (1). Hildenbrand et al. (2012b), *Chapter 6*, focused on the slump structure mentioned in (2), providing the interpretation for its complex configuration and evidence for its current activity. Costa et al. (*submitted*), *Chapter 5*, provides the reconstruction of Pico Island, calibrated by high-resolution K-Ar data, constraining in time the structures referred to in (1) and (2), and provides new data/interpretations regarding the structure (3).

# PART II

## Long term evolution of the Pico-Faial volcanic ridge

# Chapter 3

## Reconstructing the architectural evolution of volcanic islands from combined K/Ar, morphologic, tectonic, and magnetic data: The Faial Island example (Azores)

## (Hildenbrand et al., 2012a)

Journal of Volcanology and Geothermal Research 241–242 (2012) 39–48

Contents lists available at SciVerse ScienceDirect

Journal of Volcanology and Geothermal Research

journal homepage: www.elsevier.com/locate/jvolgeores

# Reconstructing the architectural evolution of volcanic islands from combined K/Ar, morphologic, tectonic, and magnetic data: The Faial Island example (Azores)

A. Hildenbrand [a,b,*], F.O. Marques [c], A.C.G. Costa [a,c], A.L.R. Sibrant [a,c], P.F. Silva [d], B. Henry [e], J.M. Miranda [c], P. Madureira [f,g]

[a] Univ Paris-Sud, Laboratoire IDES, UMR8148, Orsay, F-91405, France
[b] CNRS, Orsay, F-91405, France
[c] Universida de Lisboa, IDL, Lisboa, Portugal
[d] ISEL/DEC and IDL/CGUL, Lisboa, Portugal
[e] Paleomagnetism, IPGP and CNRS, 4 Av. de Neptune, 94107 Saint-Maur cedex, France
[f] Centro de Geofísica de Évora and Dep. de Geociências da Univ. de Évora, R. Romão Ramalho, 59, 7000-671 Évora, Portugal
[g] Estrutura de Missão para os Assuntos do Mar, R. Costa Pinto, 165, 2770-047, Paço D'Arcos, Portugal

ARTICLE INFO

*Article history:*
Received 10 January 2012
Accepted 11 June 2012
Available online 21 June 2012

*Keywords:*
Faial
Volcanic construction
Mass-wasting
K/Ar
Tectonics
Magnetism
Azores triple junction

ABSTRACT

The morpho-structural evolution of oceanic islands results from competition between volcano growth and partial destruction by mass-wasting processes. We present here a multi-disciplinary study of the successive stages of development of Faial (Azores) during the last 1 Myr. Using high-resolution digital elevation model (DEM), and new K/Ar, tectonic, and magnetic data, we reconstruct the rapidly evolving topography at successive stages, in response to complex interactions between volcanic construction and mass wasting, including the development of a graben. We show that: (1) sub-aerial evolution of the island first involved the rapid growth of a large elongated volcano at ca. 0.85 Ma, followed by its partial destruction over half a million years; (2) beginning about 360 ka a new small edifice grew on the NE of the island, and was subsequently cut by normal faults responsible for initiation of the graben; (3) after an apparent pause of ca. 250 kyr, the large Central Volcano (CV) developed on the western side of the island at ca 120 ka, accumulating a thick pile of lava flows in less than 20 kyr, which were partly channelized within the graben; (4) the period between 120 ka and 40 ka is marked by widespread deformation at the island scale, including westward propagation of faulting and associated erosion of the graben walls, which produced sedimentary deposits; subsequent growth of the CV at 40 ka was then constrained within the graben, with lava flowing onto the sediments up to the eastern shore; (5) the island evolution during the Holocene involves basaltic volcanic activity along the main southern faults and pyroclastic eruptions associated with the formation of a caldera volcano–tectonic depression. We conclude that the whole evolution of Faial Island has been characterized by successive short volcanic pulses probably controlled by brief episodes of regional deformation. Each pulse has been separated by considerable periods of volcanic inactivity during which the Faial graben gradually developed. We propose that the volume loss associated with sudden magma extraction from a shallow reservoir in different episodes triggered incremental downward graben movement, as observed historically, when immediate vertical collapse of up to 2 m was observed along the western segments of the graben at the end of the Capelinhos eruptive crises (1957–58).

© 2012 Elsevier B.V. All rights reserved.

## 1. Introduction

The geological evolution of oceanic islands is generally marked by rapid volcanic growth alternating with destruction by a variety of mass-wasting processes including giant sector collapses, vertical caldera subsidence, fault generation/propagation, shallow landslides and coastal erosion (e.g., Moore et al., 1989; Mitchell, 1998; Hildenbrand et al., 2004, 2006, 2008a, 2008b; Quartau et al., 2010; Boulesteix et al., 2012). The study of such destruction events is of particular societal relevance, since they can cause considerable damage. The Azores volcanic islands in the Atlantic are particularly sensitive to mass-wasting processes. The region is characterized by intense deformation responsible for high magnitude earthquakes (e.g., Borges et al., 2007). Like the neighbouring islands of Pico, S. Jorge, Terceira and Graciosa in the central Azores, Faial is still active and is characterized by the localization of volcanism along N110°-trending eruptive fissures and vents. Faial is additionally marked by a large graben-like structure elongated along the same azimuth (N110°). The island thus offers a great opportunity

* Corresponding author at: Univ Paris-Sud, Laboratoire IDES, UMR8148, 91405 Orsay, F-91405, France. Tel.: +33 1 69 15 67 42; fax: +33 1 69 15 48 91.
*E-mail address:* anthony.hildenbrand@u-psud.fr (A. Hildenbrand).

0377-0273/$ – see front matter © 2012 Elsevier B.V. All rights reserved.
doi:10.1016/j.jvolgeores.2012.06.019

to study the interactions between volcanism and tectonics. We present here a new study aimed at reconstructing the architecture and the volcano–tectonic evolution of Faial during the last 1 Myr. Our approach combines new tectonic analysis, K/Ar dating and palaeomagnetic data on selected samples, which, together with high-resolution DEM data and analyses of magnetic anomalies carried out during an aerial survey (Miranda et al., 1991), provides valuable insight into the competition between volcanic construction and destruction by tectonic processes, mass-wasting, and erosion throughout the geological evolution of the island.

## 2. Geological background

The Central Azores islands (Fig. 1) were formed during the Quaternary on top of an oceanic plateau, the Azores Plateau, at the triple junction between the North American, Eurasian and Nubian lithospheric plates (e.g., Searle, 1980; Miranda et al., 1991; Luis et al., 1994; Lourenço et al., 1998; Vogt and Jung, 2004). The origin of the volcanism in the area is still controversial: some authors argue for an origin from volatile-enriched upper mantle domains (Schilling et al., 1980; Bonatti, 1990), whereas others, based on geochemical data (Schilling, 1975; White et al., 1979; Flower et al., 1976; Davies et al., 1989; Widom & Shirey, 1996; Turner et al., 1997; Moreira et al., 1999; Madureira et al., 2005; 2011) or seismic tomography (Silveira and Stutzmann, 2002; Montelli et al., 2004; Yang et al., 2006), consider the Azores volcanism to be related to a mantle plume. According to Silveira et al. (2006), the shallow S-wave negative anomaly (down to ~250 km) results from the presence of a dying and now untailed plume, the head of which was responsible for building of the Azores Plateau. Furthermore, regional deformation has largely controlled the distribution of volcanic vents, leading to the construction of submarine ridges with N150° and N110° main orientations (e.g., Lourenço et al., 1998; Stretch et al., 2006; Hildenbrand et al., 2008b; Silva et al., 2012). Most of the Azores islands have experienced historic volcanic activity. The most recent volcanic crisis on Faial, the Capelinhos eruption (1957–1958), was characterized by a surtseyan and strombolian activity, which increased the island area to the west (Machado et al., 1959; Zbyszewski and Veiga Ferreira, 1959; Machado et al., 1962).

Faial constitutes one of the emerged parts of a single main volcanic ridge, the Pico–Faial Ridge. This structure is roughly elongated along the N110° direction, but probably older N150° submarine ridges can be observed or are suspected offshore the eastern ends of both Faial and Pico (Fig. 1). The geology of Faial island has been divided by Chovelon (1982) into five main volcanic units (Fig. 2a): (i) the Galego volcano mapped in the east and northeast areas of the island, from north of Horta to the northern coast; (ii) a main volcanic edifice, the Central Volcano (CV), built on the western side of the Galego volcano, during at least two main phases of activity; (iii) recent volcanic units filling the graben, from 0.03 Ma to the present; (iv) basaltic units in the E (Horta) and W (Capelo). The Horta volcanism, located in the SE corner of the island, is characterized by a series of small scoria cones and associated basaltic lava flows. The Capelo volcanism corresponds to the most recent volcanic activity that formed a peninsula in the westernmost part of Faial. It was erupted during the last 10 kyr (Madeira et al., 1995), and is morphologically characterized by a series of volcanic cones aligned WNW-ESE that stretches the island towards the Capelinhos volcano, which emerged during the 1957–1958 eruption; (v) widespread trachytic pumice deposits generated by recent explosive activity of the Central Volcano over the last 10 kyr. Subsequently, other workers have conducted more detailed geological mapping, and have renamed the main units (e.g., Serralheiro et al., 1989; Madeira, 1998; Pacheco, 2001). These works were mostly based on the original geochronological framework established by Féraud et al. (1980) and Demande et al. (1982), which we therefore used as a basis for the present study.

The recent eruptive history of Faial has been quite well documented from radiocarbon dating on charcoal fragments collected in pyroclastic deposits and/or palaeosoils (e.g. Madeira et al., 1995). The earlier volcano–tectonic evolution of the island, however, remains unclear in the absence of sufficient reliable temporal constraints. Five K/Ar ages have been published in the early 1980s for the whole island, two of which are being related to very young volcanic episodes (Féraud et al., 1980). The remaining three samples have been collected along the eastern end of the island, in an area attributed to the Galego volcano. The results on these samples vary from 0.73 ± 0.07 Ma to 0.21 ± 0.02 Ma, which means that the sub-aerial part of the old volcanic system would have developed over a period of about 0.5 Myr. A few additional unpublished K/Ar determinations

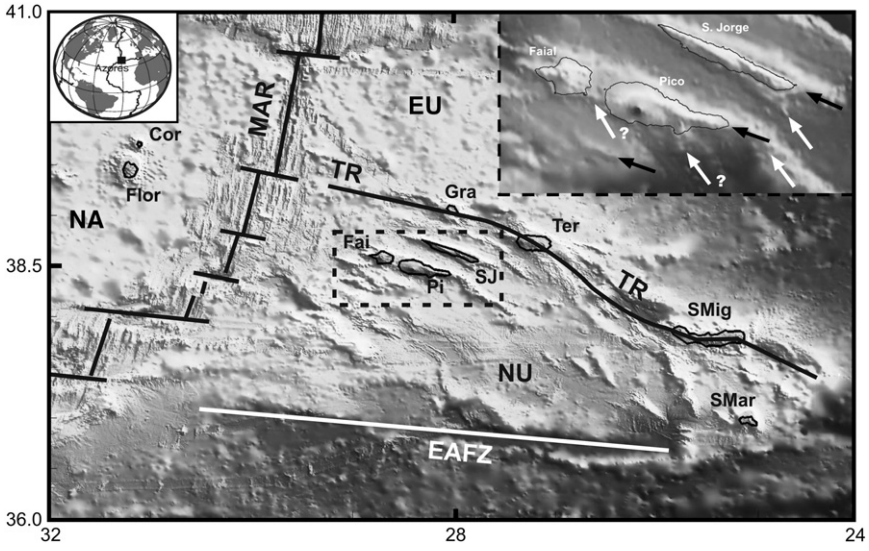


**Fig. 1.** Main figure: Location of the Azores volcanic archipelago near the triple junction between the North American (NA), the Eurasian (EU) and the Nubian (NU) plates. The dashed rectangle localizes the inset. Bold black lines show the Mid-Atlantic Ridge (MAR) and the Terceira Rift (TR), and the white line shows the East Azores Fracture Zone (EAFZ). SJ: S. Jorge; Gra: Graciosa; Ter: Terceira; Fai: Faial; Pi: Pico; Flor: Flores; Cor: Corvo; SMig: S. Miguel; SMar: Santa Maria. Background bathymetric data from Lourenço et al. (1998). Inset: Main submarine structures around Sao Jorge, Pico and Faial. Black and white arrows show linear submarine ridges with N110 and N150 directions, respectively. Modified from Hildenbrand et al. (2008b).

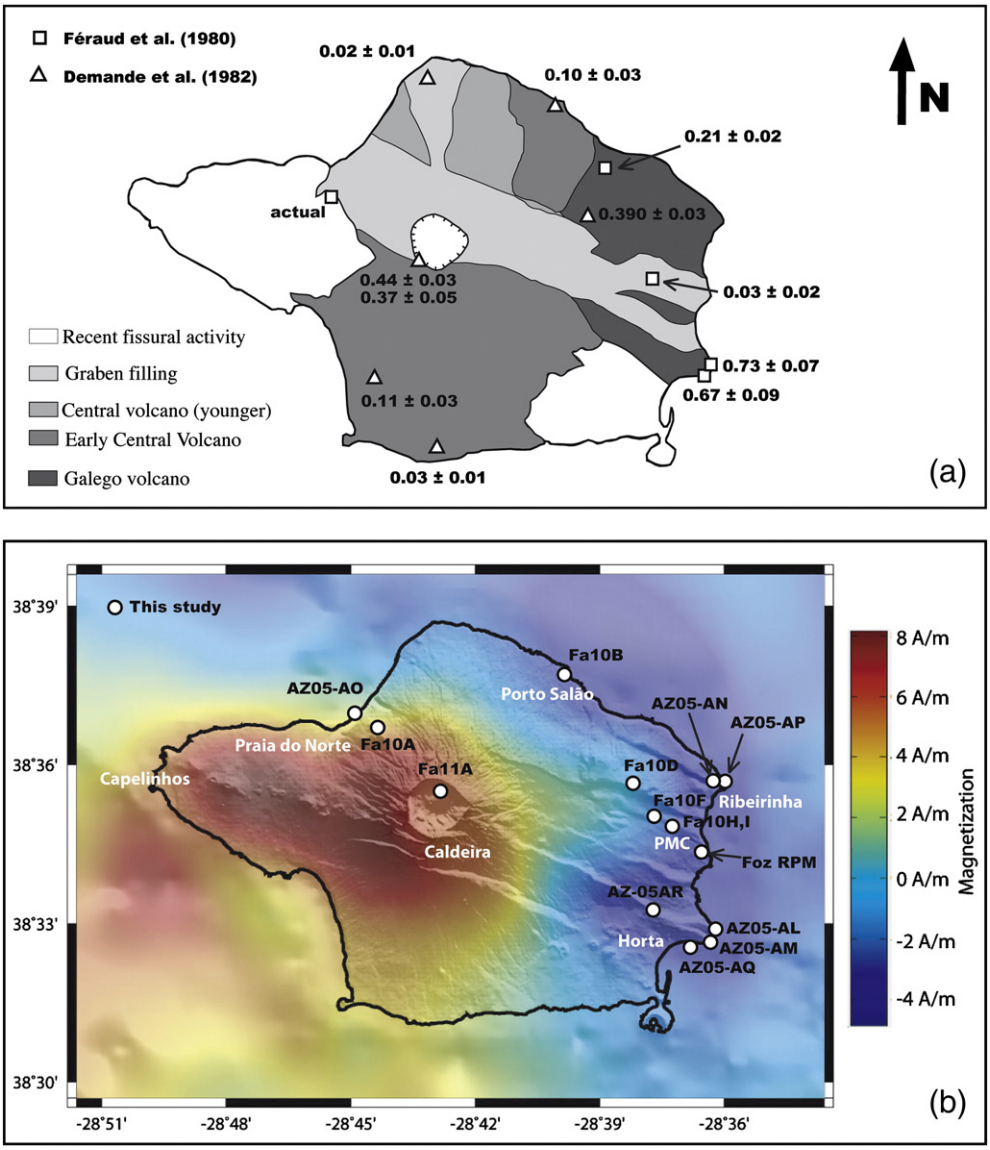


**Fig. 2.** (a) Geological map of Faial (modified after Chovelon, 1982). Previous K/Ar ages (in Ma) from Féraud et al. (1980) and Demande et al. (1982) are shown. (b) Magnetization map combined with a high-resolution digital elevation model (DEM) of the island. The colour scale shows the magnetization values. White dots with black circles show the location of our new samples collected for both K/Ar and magnetic analyses. Localities are shown in white. PMC: Pedro Miguel creek.

presented in a report (Demande et al., 1982) and a thesis (Chovelon, 1982) have been subsequently acquired on whole-rock samples from the central volcanism sampled in the northern and western parts of the island. They range in age between $0.44 \pm 0.03$ Ma and $0.03 \pm 0.01$ Ma. From the few previous K/Ar data available for Faial (Féraud et al., 1980; Chovelon, 1982; Demande et al., 1982), the two main volcanic systems would thus have experienced synchronous growth between $0.44 \pm 0.03$ Ma and $0.21 \pm 0.02$ Ma. This seems in apparent contradiction, since the main volume of the Central Volcano has apparently grown within the main graben cutting the Galego volcano (Fig. 2b). Therefore, the timing for graben initiation, and the relationships between volcanic construction and destruction, and tectonics remain insufficiently documented to allow the development of a coherent and comprehensive model.

## 3. Fieldwork and sampling strategy

The interactions between volcanic growth and partial destruction on volcanic islands such as Faial generally result in complex relationships of the different geological units, in response to a rapidly evolving topography. In such conditions, reconstructing the successive stages of construction and graben development requires strategic investigations on target areas. We first used available morphological and geophysical data to identify the zones of major interest for fieldwork and selective sampling. Such preliminary work includes the combination of a high-resolution DEM of Faial with a magnetization map built from magnetic data acquired during a previous aerial survey of the island (Miranda et al., 1991) merged with the aeromagnetic map of the Azores Platform (Luis et al., 1994) into a regular grid with a 0.005º step both in longitude and latitude (Fig. 2b). Magnetization was computed with the actual topography and using the 3D-inversion technique of Macdonald et al. (1980). This inversion procedure makes two main assumptions: (1) a constant thickness source layer (1.0 km), the upper surface of which is defined by the bathymetry, and (2) fixed values for the main field and the magnetization ($59.5\ A.m^{-1}$ and $-17\ A.m^{-1}$, respectively). A band pass filter (1.1–120 km) was applied to ensure convergence. The processing was made with the Mirone software suite (Luis, 2007).

The magnetization map evidences an area with high-magnitude negative values in the eastern side of the island. This zone coincides

with a narrow morphological relief, the northern part of which is affected by the main graben. Such sector retains crucial information, because the predicted magnetization may reflect volcanic construction during a period with reversed polarity of the magnetic field, e.g., during the Matuyama chron prior to 0.789 ± 0.008 Ma (Quidelleur et al., 2003). The lowermost and uppermost parts of this apparently old volcanic succession thus have been extensively sampled for geochronological and magnetic measurements (samples AZ05-AL, AM, AQ, AR). The parts of the faults exposed along the eastern shore have also been investigated carefully.

The NE part of the island attributed to the Galego volcanism in earlier studies shows a zone of low-magnitude negative magnetization roughly elongated in the N110 direction. This sector is additionally characterized by a prominent topographic high with relatively steep slopes towards the North. It is composed of a moderately thick volcanic succession, including porphyritic lavas with dominant plagioclase phenocrysts. This succession is cut by the northern fault of the main graben, and by an additional scarp farther North, near the village of Ribeirinha. The lower and upper distal parts of this succession were sampled close to shore level in the NE tip of Faial (samples AZ05-AN and AZ05-AP, respectively). A sample was also collected at an elevation of ca 500 m on the upper rim of the main fault near Galego (Fa10D) to constrain a maximum age for initiation of the graben. The geometry and kinematics of the eastern end of the main fault were additionally examined at the shore level.

The Central Volcano in the western half of the island is marked by an overall positive magnetization highlighted by yellow to red colours on the magnetization map (Fig. 2b). The maximum is centred close to the present caldera depression, but rapidly vanishes towards the distal parts, where slightly negative values are observed. A lava flow at the base of the volcanic succession exposed in the caldera walls was sampled at an altitude of 575 m to constrain the earliest accessible stage of edification of the Central Volcano (sample Fa11A). The external parts of the volcano overall have smooth and gentle slopes extending up to the northern and southern shores of the island, where they are cut by large coastal cliffs. We took advantage of these natural sections to collect lava flows at the base of the succession at Praia do Norte and Porto Salão (samples AZ05-AO and Fa10B, respectively). A lava flow from the upper part of the CV succession was additionally sampled at an altitude of ca 300 m uphill Praia do Norte (sample Fa 10A).

The central part of the CV has relatively steep slopes incised by recent narrow canyons. The canyons have a relatively radial distribution close to the eruptive centre, but they bifurcate close to recent scars apparently truncating the (previous) external slopes of the volcano. Such bifurcation is quite obvious in the eastern sector, where individual lava flows and erosion have apparently been geometrically constrained within the graben. Consequently, detailed field investigations were carried out in the graben depression, along the Pedro Miguel creek. These investigations allowed us to identify old lava flows (sample Fa10H) overlain in unconformity by sedimentary deposits, which in turn have been buried by more recent lava flows. Some of the young lava flows were sampled throughout the longitudinal section of the creek (samples Fa10F, Fa10I, Foz RPM), where they define morphological steps. However, they exhibit complex local architecture with important internal flow patterns and complex lateral overlap (Fig. 3), suggesting their channelling into a low topography, down to sea level.

## 4. Methods and results

### 4.1. K/Ar geochronology

After careful petrographic examination of the samples in thin-section, the micro-crystalline groundmass was selected for potassium–argon (K–Ar) analyses. Some of the samples are characterized by high amounts of plagioclase phenocrysts/glomerocrysts, which can amount up to 40% in volume. They also contain pyroxene, minor olivine and various oxides. Such minerals partially crystallized at a deep level in the magma chamber and thus are not representative of the age of eruption at the surface. They are also K-poor and may carry significant amount of inherited excess Ar. After crushing and sieving the samples to 125–250 μm, all the phenocrysts have been so systematically removed with heavy liquids. Narrow density spans generally in the range 2.95–3.05 have been achieved to select the freshest part of the groundmass and eliminate the fraction with a lower density, that is potentially affected by alteration and secondary zeolitisation.

K and Ar were measured on two separate aliquots of the selected grains, the former by flame absorption-spectrophotometry and the latter by mass spectrometry. K is determined with a 1% relative uncertainty from replicate analyses on standards (Gillot et al., 1992). The $^{40}Ar/^{36}Ar$ isotopic composition of Ar has been measured according to the Cassignol–Gillot unspiked technique (Gillot and Cornette, 1986; Gillot et al., 2006). With this particular technique, the $^{40}Ar$ and $^{36}Ar$ are simultaneously collected avoiding any potential drift associated with peak switching. The level of atmospheric contamination is then accurately determined by comparing

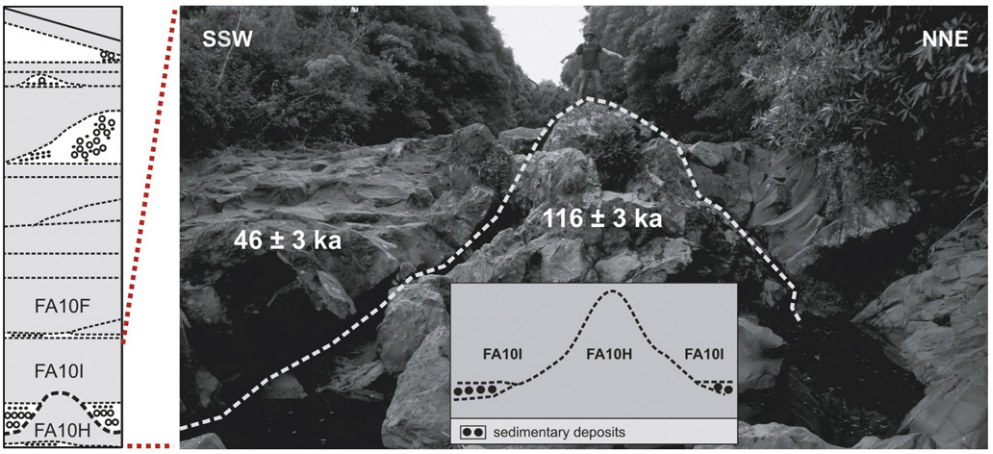


**Fig. 3.** Left: Schematic log showing the main geometrical relationships between the various units recognized in the Pedro Miguel creek. Light grey areas separated by thin dashed lines mark individual lava flows. White parts show sediments, with circles and dots representing coarse conglomerates and sandstones, respectively. The thick dashed line shows the main unconformity. Right: close up image on the main unconformity. The age of the lava flows below and above the unconformity reported here are shown.

the $^{40}Ar/^{36}Ar$ ratios of the sample and of an air pipette measured in strictly similar pressure conditions, allowing the detection of minute amounts of radiogenic Ar, as low as 0.1% (Gillot et al., 2006). The Cassignol–Gillot technique has been shown especially suitable to date low-K and high-Ca basalts and andesites of late Quaternary age with an uncertainty of only a few ka (e.g., Hildenbrand et al., 2003, 2008b; Quidelleur et al., 2008; Samper et al., 2009; Germa et al., 2010, 2011). For high-K lavas, it has been extended to the last millennium with an uncertainty of only a few centuries (Quidelleur et al., 2001). Both K and Ar were analysed at least twice in order to obtain a reproducible value within the range of uncertainties. The decay constants used are from Steiger and Jäger (1977). The results are presented in Table 1, where the uncertainties are quoted at the 1σ level.

The ages measured on our samples from Faial range between 848 ± 12 ka and 38 ± 1 ka. The results obtained on the different lava flows from the old volcanic succession are tightly clustered around 850 ka, and overlap within the range of uncertainties at the 1σ level. These results are significantly older than previous K/Ar determinations at 0.73 ± 0.07 Ma (Féraud et al., 1980). The new ages measured on lava flows from the distal part of the volcanic succession exposed on the NE corner of Faial (Ribeirinha) yield indistinguishable values of 358 ± 7 ka and 363 ± 8 ka (samples AZ05-AN and AZ05-AP, respectively). The lava flow sample collected on the same succession cut by the main graben is dated here at 389 ± 7 ka, which is similar to a previous age of 0.39 ± 0.03 Ma obtained by Demande et al. (1982) on an aphyric sample collected at a similar level to the West (Fig. 2).

The new ages measured on lava flows sampled at the base of the caldera wall and at the base of the coastal cliffs in the NE and N parts of the CV succession are very close to each other, ranging between 129 ± 2 ka and 118 ± 3 ka (samples Fa11 A and AZ05-AO, respectively). The age for the upper part of the same succession (sample Fa10A) yields a similar value of 118 ± 3 ka, showing that the CV has experienced a very rapid stage of sub-aerial growth at about 120 ka. The new age obtained on our sample Fa10H collected in the deepest parts of the Pedro Miguel creek is also dated at 116 ± 3 ka. The late phase of graben filling is finally constrained from dating successive young lava flows from Pedro Miguel creek between 46 ± 3 ka and 38 ± 1 ka. The oldest age is obtained on the lava flow (sample Fa10I) immediately covering sediments on top of the older lava flows here dated at 116 ± 3 ka (sample Fa10H), confirming therefore the existence of a major unconformity (Fig. 3).

**Table 1**
Results of the K–Ar dating on fresh groundmass separates. The ages are indicated in thousands of years (ka). The uncertainties are reported at the 1σ level.

| Sample | Long. | Lat. | K% | $^{40}Ar^*$ (%) | $^{40}Ar^*$ ($10^{12}$at/g) | Age (ka) | Unc. (ka) | Mean (ka) |
|---|---|---|---|---|---|---|---|---|
| AZ05-AM | −28.609 | 38.552 | 1.430 | 29.9 | 1.2630 | 845 | 12 | 848 ± 12 |
| | | | | 30.8 | 1.2704 | 850 | 12 | |
| AZ05-AQ | −28.613 | 38.543 | 1.694 | 28.3 | 1.4948 | 845 | 12 | 847 ± 12 |
| | | | | 35.4 | 1.5011 | 848 | 12 | |
| AZ05-AL | −28.609 | 38.552 | 1.585 | 43.0 | 1.3976 | 844 | 12 | 846 ± 12 |
| | | | | 40.1 | 1.4043 | 848 | 12 | |
| AZ05-AR | −28.625 | 38.553 | 1.863 | 33.3 | 1.6399 | 843 | 12 | 843 ± 12 |
| | | | | 39.5 | 1.6424 | 844 | 12 | |
| FA10D | −28.631 | 38.591 | 1.060 | 9.7 | 0.4349 | 393 | 7 | 389 ± 7 |
| | | | | 9.2 | 0.4262 | 385 | 7 | |
| AZ05-AN | −28.612 | 38.599 | 1.222 | 14.8 | 0.4651 | 364 | 6 | 363 ± 6 |
| | | | | 16.5 | 0.4618 | 362 | 6 | |
| AZ05-AP | −28.608 | 38.599 | 1.264 | 7.7 | 0.4739 | 359 | 7 | 358 ± 7 |
| | | | | 10.0 | 0.4727 | 358 | 6 | |
| Fa11A | −28.713 | 38.592 | 3.173 | 9.2 | 0.4332 | 131 | 2 | 129 ± 2 |
| | | | | 11.8 | 0.4217 | 127 | 2 | |
| FA10B | −28.658 | 38.626 | 1.539 | 4.9 | 0.2023 | 126 | 3 | 127 ± 3 |
| | | | | 5.0 | 0.2061 | 128 | 3 | |
| AZ05-AO | −28.750 | 38.613 | 1.827 | 4.3 | 0.2203 | 115 | 3 | 118 ± 3 |
| | | | | 3.7 | 0.2293 | 120 | 4 | |
| FA10A | −28.750 | 38.608 | 1.419 | 3.8 | 0.1754 | 118 | 4 | 118 ± 3 |
| | | | | 4.0 | 0.1750 | 118 | 3 | |
| FA10H | −28.620 | 38.577 | 1.785 | 4.7 | 0.2195 | 118 | 3 | 116 ± 3 |
| | | | | 5.2 | 0.2141 | 115 | 3 | |
| FA10I | −28.620 | 38.577 | 1.503 | 1.8 | 0.0716 | 46 | 3 | 46 ± 3 |
| | | | | 1.8 | 0.0735 | 47 | 3 | |
| Foz RPM | −28.612 | 38.578 | 2.225 | 3.2 | 0.0960 | 41 | 1 | 40 ± 1 |
| | | | | 3.6 | 0.0910 | 39 | 1 | |
| FA10F | −28.622 | 38.577 | 1.919 | 2.9 | 0.0778 | 39 | 1 | 38 ± 1 |
| | | | | 4.0 | 0.0757 | 38 | 1 | |

### 4.2. Paleomagnetic data

Silva et al. (2008, 2010, in preparation) performed a paleomagnetic study on Faial Island on 140 samples collected along 6 different sections that mostly correspond to the flows dated in this study. Rockmagnetic experiments identified magnetic carriers favourable for paleomagnetic study (presence of magnetite of Pseudo-Single Domain-Single Domain states). Demagnetizations have shown mostly the presence of a single stable magnetization component defining a characteristic remanent magnetization.

Virtual Geomagnetic Poles for 11 lava flows indicate a normal polarity of the Earth magnetic field and for 5 flows a reversed polarity. The reversed polarity is exclusively measured on the samples dated in this paper at about 0.85 Ma. This confirms that the phase of old volcano construction occurred at the final stages of the Matuyama reversed chron.

The other lava flows show a positive polarity, in accordance with their eruption during the Brunhes normal chron, i.e. during the last 0.789 ± 0.008 Myr (Quidelleur et al., 2003). When accessible, lava flows from the same lava pile generally exhibit very similar paleomagnetic directions, confirming the existence of massive pulses during volcano construction. We note, however, that data from 2 flows of the old volcanic sequence along the sea cliff show abnormal paleomagnetic direction with respect to the average values. This could be highlighting local tilting processes associated with differential movement along recent faults.

### 4.3. Tectonic analysis of fault geometry and kinematics

The most prominent tectonic feature in Faial is the central graben affecting the whole island. The graben fault scarps are clearly visible in successive topographic cross-sections (Fig. 4) but the actual fault surfaces are only visible locally along sea cliffs (Fig. 5). Faults and fault scarps strike N110° on average; some fault scarps dip 35–45º to the NNE or SSW, while others dip more steeply at the surface, at around 55–75º to the NNE or SSW. Tilting of the lavas in the hanging-wall block and steepness of faults at the Earth's surface indicate a listric geometry at depth. The observed fault striations are dip-slip, which means that they are normal faults. Fault displacement, as shown by the displacement of the topography, gradually increases away from the Central Volcano, especially to the E; this can mean that part of the older fault displacement has been gradually covered by CV eruptions. The few faults that presently show a significant displacement, even close to the south flank of the caldera, indicate that recent fault displacement has been greater in the south than elsewhere (Fig. 4). We dated the oldest rocks here at about 850 ka, so they are not associated with these southernmost faults bounding the graben. This implies that there was a south dipping topography of the old island, otherwise the southernmost fault would show the oldest rocks.

## 5. Discussion

### 5.1. Successive stages of volcano–tectonic evolution

#### 5.1.1. Rapid construction of a first main volcano

The old volcanic succession cropping out in the eastern side of the island is dated here between 848 ± 12 ka (sample AZ05-AM) at the base

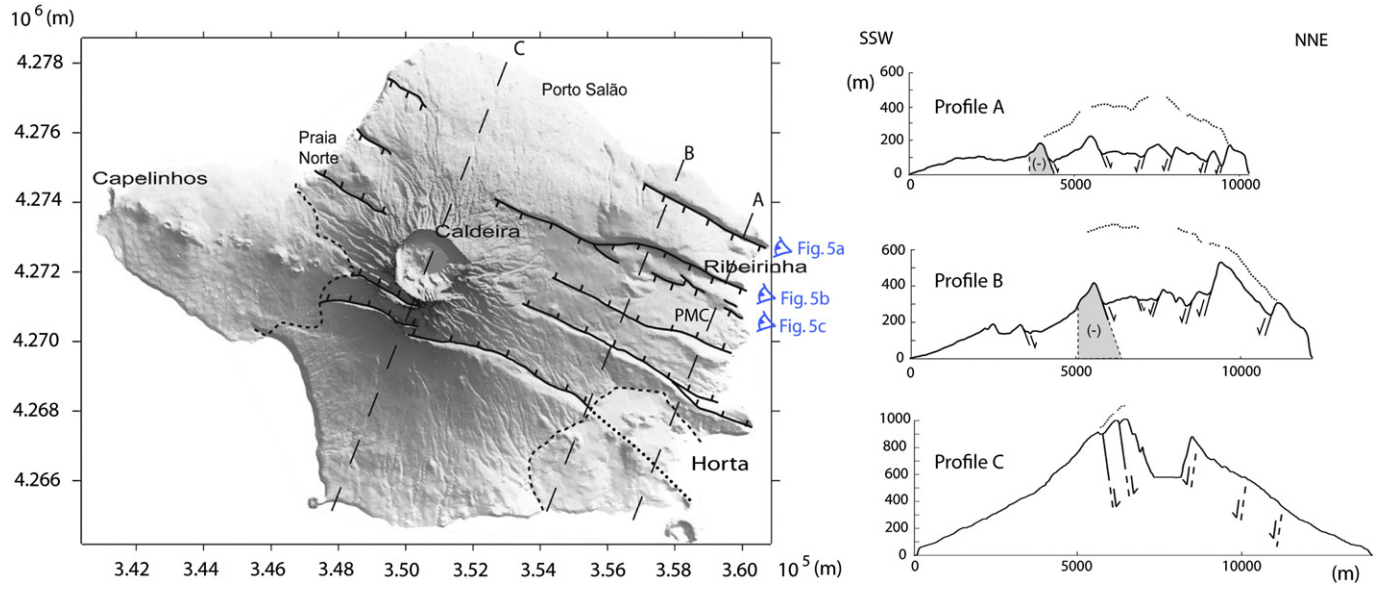


**Fig. 4.** Left: Shaded-relief map drawn from the high-resolution DEM (illumination from the North), showing the main topographical characteristics of the island. Thick black lines show the base of the various fault scarps, with ticks towards the footwall. The dotted line shows the inferred prolongation of the southern fault under recent basaltic volcanic cones in the Horta sector. Dashed lines localize the topographic profiles shown on the right. The eye symbols show the points of view from which the photographs in Fig. 5 have been taken. Right: Topographic cross-sections evidencing recent apparent fault displacements across the width of the Faial graben. Grey areas show the remnants of the volcanic system older than 850 ka (reversed magnetization). Thin dotted lines show the restored topography.

and 843 ± 12 ka (sample AZ05-AR) at the top, in full agreement with the reversed polarity recorded by the lava flows. These new ages overlap within the uncertainties, testifying to a rapid stage of growth prior to the end of the Matuyama period. Our new results are significantly older than previous K/Ar determinations of 0.73 ± 0.07 Ma and 0.67 ± 0.09 Ma acquired on whole-rock samples from the same area (Féraud et al., 1980). The latter value, despite its large uncertainty, is inconsistent with the reversed polarity here recorded for this sector. Such age under-estimation in earlier studies may result from the experimental procedure used previously. The samples dated by Féraud et al. (1980), were pre-degassed at ca 230 °C under vacuum for a period of up to 20 hours before analysis (Féraud, 1977). Such procedure, initially aimed at removing part of the atmospheric contamination adsorbed on the surface of the grains, is unsuitable because it can also result in partial diffusion and removal of radiogenic argon from the poorly retentive volcanic glass, which can in turn yield too young ages.

The initial geometry of the old volcanic system cannot be constrained precisely, because it was largely destroyed during a period of up to 500 kyr, and more recently was covered by volcanic activity and partly affected by tectonic activity and mass-wasting processes. However, the original dimensions can be estimated by combining all our data. Low magnitude negative magnetizations computed (light blue colour shades) for the eastern part of the island (Fig. 2) do not mean that the outcropping lavas have a reversed polarity, because the polarity measured on the samples collected in that area is normal. The inversion process we used computed a vertical average of the magnetization, interpreted to reflect a thin and young (<0.780 Ma) layer of rocks with normal polarity overlaying a deep and older layer of reversed polarity. Therefore, the thinner the layer of normal magnetic polarity lavas on top of the reversed polarity rocks is, the more the colour approaches deep blue. The persistence of the light blue area close to the island shore in the different sectors of Faial (except the SW) suggests that the original volcano is present underneath most of the recent lava units and therefore had a geographical extent encompassing most of the present island area (Fig. 2). The narrow sector presently cropping in the eastern sector (strong negative magnetizations evidenced by a deep blue colour, and measured ages of about 850 ka) must have been a persistent topographic high, which has not been covered by subsequent young lava flows. We can get a rough idea of the old topography (prior to present-day graben) by restoring surface displacements to their original position (Fig. 4). This shows that the topography prior to recent faulting was convex upward (topographic high), which is not favourable for blanketing by younger positive lava flows. Therefore, this area most likely coincides with a relatively high morphological crest in the eastern side of the original volcanic system. We note that the elongation of the inland negative magnetization is slightly oblique with respect to the present N110 axis of the island. High-magnitude negative values also extend offshore Faial to the northwest. This suggests that the old volcanic system possibly had a ridge-like morphology with a main axis closer to the northwest-southeast direction (Fig. 6a). Prolongation of such a volcanic edifice would thus extend into the Faial–S. Jorge channel as proposed by Miranda et al. (1991). An old volcanic edifice with such elongation is also compatible with the presence of northwest-southeast trending old ridges recognized at the scale of the Azores plateau, e.g., in the eastern part of S. Jorge (Hildenbrand et al., 2008b).

*5.1.2. Prolonged volcanic gap and construction of a small edifice in the NE part of Faial*

The oldest lava flows collected in the NE sector of the island are dated here at 387 ± 7 ka, revealing an apparent gap in volcanism of at least 450 kyr after the construction of the old volcano. Such a gap could reflect in part a sampling bias, i.e. un-investigated volcanic units could potentially be intercalated between the old volcanic succession and the lava pile here dated between 387 ± 7 ka and 358 ± 7 ka. However, this is not supported by the magnetization map, which shows low negative values in the NE sector reflecting a thin cover of lavas with normal polarity on top of the older units. The morphological surface in the NE tip of the island also supports lavas locally flowing from a small volcanic edifice towards the North and Northeast, on the partly preserved outer slopes of the Matuyama volcano (Fig. 6b).

Geomorphological data, however, do not support such lava flows on the southern and western sides of the island. Several authors have proposed that early sub-aerial construction of the CV could be

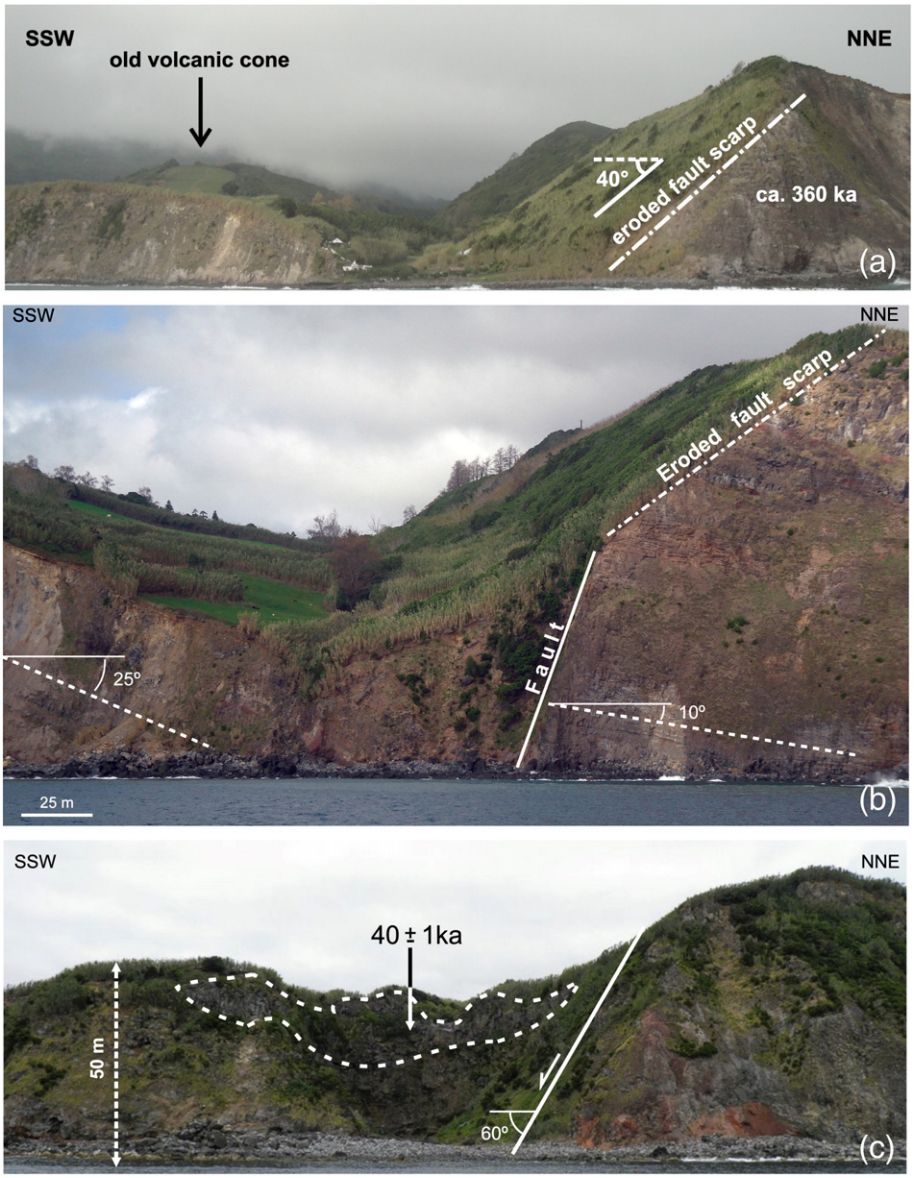


**Fig. 5.** Photographs taken from the sea showing the contrasted geometry of old and recent fault scarps. See Fig. 4 for localization.

as old as 0.47 Ma (Demande et al., 1982; Madeira and da Silveira, 2003; Quartau et al., 2010). Such an inference relies on a K/Ar whole-rock age of $0.44 \pm 0.03$ Ma obtained on a highly porphyric sample containing high amounts of olivine and pyroxene phenocrysts, which was sampled in the western wall of the caldera (Demande et al., 1982). Whole-rock dating on such porphyric and/or weathered samples in the Azores and elsewhere has been clearly shown to yield abnormaly old ages by incorporation of inherited excess argon and/or potassium removal by alteration processes (e.g., Johnson et al., 1998; Quidelleur et al., 1999; Hildenbrand et al., 2004). In contrast, the new age of $129 \pm 2$ ka obtained on the fresh-separated groundmass of our sample Fa11A from the base of the caldera succession shows that most of the CV has been built much later (see next section). Therefore, prior to such recent volcanic growth, the western side of the old volcano has most probably experienced a prolonged period of volcanic inactivity exceeding 500 kyr. Partial destruction of the original morphology by mass wasting processes, including coastal and stream erosion and tectonics, and subsequent blanketing by the CV on the western side of the island can thus explain the absence of the negative anomaly such as observed in the eastern sector.

*5.1.3. Initiation of the Faial graben and early development of the Central Volcano*

Early sub-aerial growth of the CV within a very short period is supported by our new age constraints obtained for samples from the base and uppermost parts of the thick succession exposed both in the caldera walls and at the northern part of the island near Praia do Norte. We note that two similar, though less precise ages, have been previously measured at $0.10 \pm 0.03$ Ma and $0.11 \pm 0.03$ Ma on sub-aphyric samples from the northern and southern coasts, near Porto Salão and Lombega, respectively (Demande et al., 1982). The positive anomalies observable on the magnetization map in the sector of Praia do Norte are consistent with emplacement of a thick lava cover immediately to the North of the main Caldera eruptive centre. A similar pattern, though less pronounced, is also visible as far as the southern coast of the island. In contrast, the persistence of negative anomalies in the sector of Porto de Salão indicates a more reduced thickness. There, the northern gentle slope of the CV also exhibits a clear morphological lateral contrast with the prominent unit here dated between $389 \pm 7$ ka and $358 \pm 7$ ka, which confirms that the latter had a restricted geographical extension.

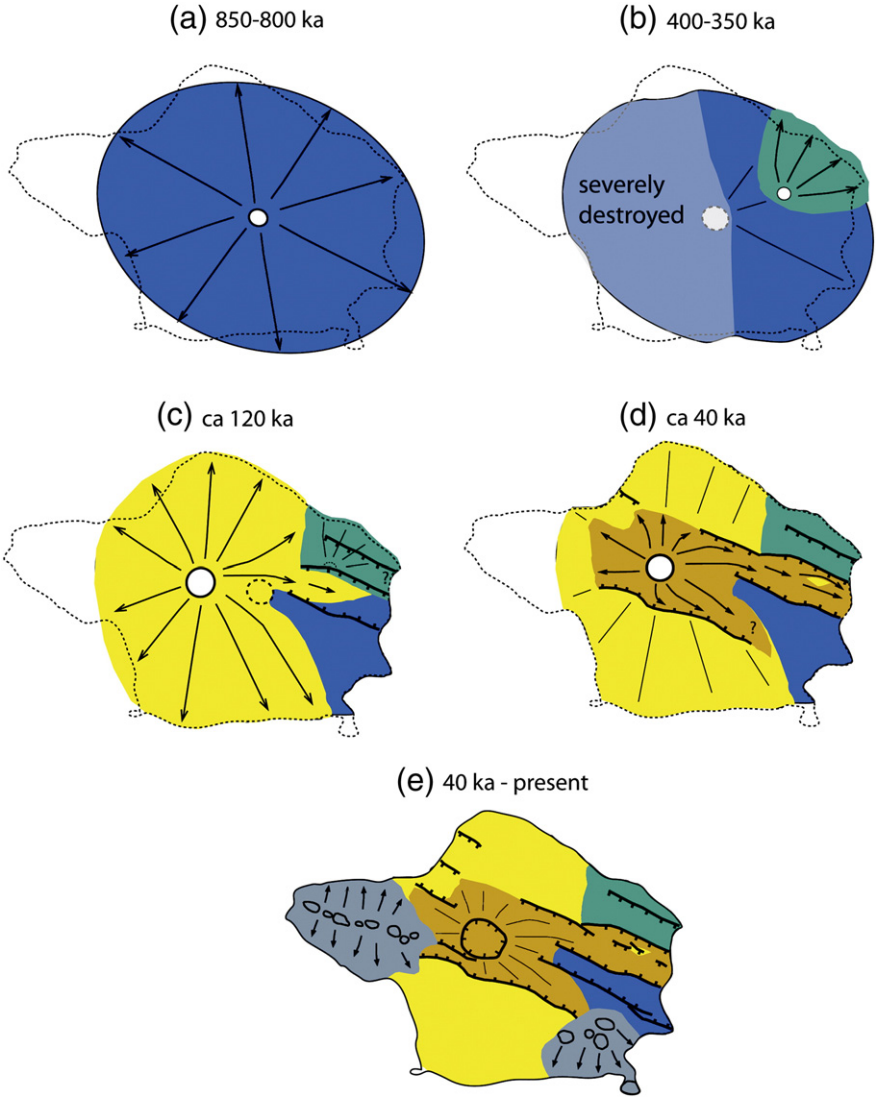


**Fig. 6.** Schematic model of evolution showing the main stages of volcanic construction separated by incremental fault migration and graben development.

Our new sample collected in the deeper parts of the graben is dated at 116 ± 3 ka, very much in agreement with the age we obtained for the upper northern flank of the CV (sample Fa10A, 118 ± 3 ka). This clearly shows that (1) the graben was already partly formed at that time, and (2) lava flows from the upper part of the CV were channelized in this prominent topographic low (Fig. 6c). Therefore, the eastern part of the graben experienced a significant phase of development between 390 ka and 120 ka, which is much older than previously thought. We note that the fault near Ribeirinha could have formed during this period, which could explain the eroded aspect of the scarp recognized in the field (Fig. 5a).

*5.1.4. Incremental evolution of the graben and further construction of the Central Volcano*

The several lava flows sampled on top of the unconformity in Pedro Miguel Creek range in age between 46 ± 3 ka and 38 ± 1 ka. These new ages do not overlap each other but attest to very rapid burying of the graben. Although a few scoria cones have developed recently within the graben, such massive filling was most probably fed by renewed activity at the Caldera eruptive centre, as revealed by the present prominent morphology of the volcano (Fig. 6d). The unconformity in Pedro Miguel creek shows an apparent volcanic gap of ca. 80 kyr, which can explain the deep erosion of the older lava flows and the local accumulation of sedimentary deposits on their remnants. The presence of large boulders (up to 1 m in size) most probably highlights morphological rejuvenation upstream, which can therefore be associated with significant vertical deepening of the graben between 120 ka and 40 ka. Furthermore, the younger succession shows that the pilling of lava flows was interrupted from time to time by smaller erosion surfaces and smaller grain-size conglomeratic deposits (see Fig. 3). We interpret these interruptions in the lava piling as times of movement along the adjacent normal faults, which could thus be linked with repeated eruptions at the CV. The scars developed on the southern side of the volcano have a very prominent surface expression, featuring high slopes and a significant vertical offset. This suggests recent reconfiguration of the deformation, with increasing displacement along the southern edge of the graben. The more prominent positive magnetization along these scars supports partial buttressing of the lava flows erupted from the CV against the southern faults.

*5.1.5. Late evolution during the last 40 kyr*

The young units of Faial Island previously dated by radiocarbon (<10 ka) are mainly related to the very recent explosive volcanic activity at the CV (Madeira et al., 1995). Several basaltic volcanic cones are additionally distributed along the southernmost fault of

the graben, suggesting that magma ascent was constrained along this mechanical discontinuity, but they do not give precise information as to whether the latter was active at that period, because a pre-existing fault could also have focussed magma ascent. The southern faults in the western sector do, however, affect the recent part of the CV, showing downward movement very recently, i.e., additional westward propagation of the graben during the last 40 kyr, and most probably during the last 10 kyr. Several recent basaltic cones and vents on the western tip of the island, including the historical eruptions, also occurred during the last 10 kyr (Madeira et al., 1995). The caldera could thus have experienced partial development in response to magma withdrawal associated with emptying of a shallow reservoir during the several differentiated pyroclastic eruptions and/or an additional phase of graben development (Fig. 6e), two processes which might be intimately linked, as discussed in the next section.

### 5.2. Links between regional deformation, volcano growth and graben development

Our new data show that volcanic activity on Faial has occurred through short periods of robust volcanic construction, each lasting less than 30 kyr and being separated from the others by prolonged hiatuses, up to 500 kyr in duration. This is similar to the case of the neighbouring island of S. Jorge, where multi-stage volcanic growth alternating with prolonged gaps have been recently shown by geochronological analyses on samples prepared according to the same procedure and analysed with the same technique (Hildenbrand et al., 2008b). Furthermore, comparison of these data with recent stepwise $^{40}Ar/^{39}Ar$ analyses on separated volcanic groundmass on Terceira (Calvert et al., 2006) shows synchronous short phases of volcanic construction on the three islands, e.g. between 400 ka and 350 ka, and probably throughout most of the last 300kyr. Recent magma outputs in the area thus have been concentrated along the N110 direction to develop simultaneously S. Jorge, Faial and Terceira, which most probably reflects significant episodes of intense regional deformation. Similarly, volcanic construction has been constrained by $^{40}Ar/^{39}Ar$ at about 850 ka in S. Miguel (Johnson et al., 1998), i.e., synchronous with the construction of the old volcano on Faial.

MacDonald (1972) concluded that the exact origin of the Faial graben was not known but proposed three mechanisms: (1) removal of magma from an underlying chamber, or (2) stretching of the surface of the volcano, or (3) stretching of the entire underlying crust due to spreading of the Atlantic Ocean basin. Our new data support the first hypothesis, and provide additional insight on the iterative development of the Faial graben in relation with the several volcanic pulses. The most conspicuous arguments for our interpretation are:

(1) The inward listric geometry of the faults responsible for local tilting of the island surface suggests their flattening at shallow depth, strongly indicative of the existence of (an) underlying magma chamber(s) developed within the volcanic edifice.
(2) Each of the short volcanic episodes here evidenced included the eruption of either highly porphyric lavas featuring plagioclase phenocrysts/glomerocrysts, or evolved lavas like mugearites, benmoreites and trachytes. Such characteristics support intermittent storage of the magma in a reservoir prior to their extraction to the surface.
(3) Each volcanic stage, at least during the last 400 kyr, has been followed by a period of graben development. Westward migration of volcanic construction has also been followed by systematic westward propagation of the graben faults, supporting dominant deflation above the main zone of magma withdrawal.
(4) The presence of sediments intercalated within the lava flows here dated at 120 ka and 40 ka suggests the morphologic rejuvenation of the scarps during the interval separating the two main periods of eruption, supporting incremental displacement along the main faults of the graben.
(5) Such a mechanism occurred in recent time during the Capelinhos eruption, where 1.5 m of vertical displacement were measured in 1958, late in the eruptive crisis that started in 1957 (Machado et al., 1959; Zbyszewski and Veiga Ferreira, 1959; Machado et al., 1962; Catalão et al., 2006).

## 6. Conclusions

This study shows the suitability of using complementary approaches for retrieving the architecture and understanding the evolution and development of oceanic islands in response to complex interactions between volcanic growth and partial destruction by a variety of mass-wasting processes. The combined use of precise K/Ar geochronology on separated groundmass, morpho-tectonic analyses, and magnetic data allow us to depict a step by step model emphasizing short stages of volcanic growth separated by long periods of inactivity during which the volcanic units were subjected to significant mass wasting, including coastal and stream erosion, possibly lateral collapse, and incremental normal faulting. Therefore, the present architecture of the island does not result from simply the coeval development of two main volcanic edifices that were synchronously active over long periods of time.

The successive phases of rapid volcano growth shown in this study have apparently been controlled by short volcanic pulses confined along the main lithospheric structures, triggered by brief episodes of regional deformation. In contrast, the gradual development of the Faial graben appears to be closely linked to the dynamics of magma extraction from ESE-WNW elongated magma chamber(s) at depth, which episodically loses volume and triggers passive gravitational collapse. Such a model is applicable to other oceanic islands, in the Azores and elsewhere.

## Acknowledgements

We thank two anonymous reviewers and two previous anonymous reviewers (earlier version of the manuscript) for their constructive remarks, which helped to significantly improve the paper. Fieldwork and isotope dating were in great part supported by TEAMINT (POCTI/CTE/48137/2002) and MEGAHazards (PTDC/CTE-GIX/108149/2008) research projects funded by FCT (Portugal). This is also a contribution to the project EVOLV (PTDC/CTE-GIN/71838/2006), and is LGMT contribution 102. We acknowledge J.C. Nunes for his reading of the manuscript and for discussions.

## References

Bonatti, E., 1990. Not so hot hot-spots in the oceanic mantle. Science 250, 107–111.
Borges, J.F., Bezzeghoud, M., Buforn, E., Pro, C., Fitas, A., 2007. The 1980, 1997 and 1998 Azores earthquakes and some seismo–tectonic implications. Tectonophysics 435, 37–54.
Boulesteix, T., Hildenbrand, A., Gillot, P.Y., Soler, V., 2012. Eruptive response of oceanic islands to giant landslides: new insights from the geomorphologic evolution of the Teide–Pico Viejo volcanic complex (Tenerife, Canary). Geomorphology 138 (1), 61–73.
Calvert, A.T., Moore, R.B., McGeehin, J.P., da Silva, A.M.R., 2006. Volcanic history and Ar-40/Ar-39 and C-14 geochronology of Terceira Island, Azores, Portugal. Journal of Volcanology and Geothermal Research 156, 103–115.
Catalão, J., Miranda, J.M., Lourenco, N., 2006. Deformation associated with the Faial (Capelinhos) 1957–1958 eruption: inferences from 1937–1997 geodetic measurements. Journal of Volcanology and Geothermal Research 155, 151–163.
Chovelon, P., 1982. Evolution volcanotectonique des iles de Faial et de Pico, thesis Univ. Paris-Sud, Orsay, 186 pp.
Davies, G.R., Norry, M.J., Gerlach, D.C., Cliff, R.A., 1989. A combined chemical and Pb-Sr-Nd isotope study of the Azores and Cape Verde hot-spots: the geodynamic implications. In: Saunders, M.J. (Ed.), Magmatism in the Ocean Basins: Geol. Soc. Special Publication, pp. 231–235.
Demande, J., Fabriol, R., Gérard, A., Iundt, F., 1982. Prospection géothermique des Iles de Faial et Pico (Açores). 82SGN003GTH. Bureau de recherches géologiques et minières, Orléans.

Féraud, G., 1977. Contribution à la datation du volcanisme de l'archipel des Açores par la méthode Potassium-Argon. Conséquences géodynamiques, thesis Univ. Paris VII, Paris.
Féraud, G., Kaneoka, I., Allègre, C.J., 1980. K/Ar ages and stress pattern in the Azores: geodynamic implications. Earth and Planetary Science Letters 46, 275–286.
Flower, M.F.J., Schmincke, H.-U., Bowman, H., 1976. Rare earth and other trace elements in historic Azorean lavas. Journal of Volcanology and Geothermal Research 1, 127–147.
Germa, A., Quidelleur, X., Gillot, P.Y., Tchilinguirian, P., 2010. Volcanic evolution of the back-arc Pleistocene Payun Matru volcanic field (Argentina). Journal of South American Earth Sciences 29, 717–730.
Germa, A., Quidelleur, X., Lahitte, P., Labanieh, S., Chauvel, C., 2011. The K-Ar Cassignol-Gillot technique applied to western Martinique lavas: a record of Lesser Antilles arc activity from 2 Ma to Mount Pelee volcanism. Quaternary Geochronology 6, 341–355.
Gillot, P.Y., Cornette, Y., 1986. The Cassignol technique for potassium–argon dating, precision and accuracy – examples from the late Pleistocene to recent volcanics from southern Italy. Chemical Geology 59, 205–222.
Gillot, P.Y., Cornette, Y., Max, N., Floris, B., 1992. Two reference materials, trachytes Mdo-G and Ish-G, for argon dating (K-Ar and Ar-40/Ar-39) of Pleistocene and Holocene rocks. Geostandards Newsletter 16, 55–60.
Gillot, P.Y., Hildenbrand, A., Lefèvre, J.C., Albore-Livadie, C., 2006. The K/Ar dating method: principle, analytical techniques and application to Holocene volcanic eruptions in southern Italy. Acta Vulcanologica 18, 55–66.
Hildenbrand, A., Gillot, P.Y., Soler, V., Lahitte, P., 2003. Evidence for a persistent uplifting of La Palma (Canary Islands), inferred from morphological and radiometric data. Earth and Planetary Science Letters 210, 277–289.
Hildenbrand, A., Gillot, P.Y., Le Roy, I., 2004. Volcano–tectonic and geochemical evolution of an oceanic intra-plate volcano: Tahiti-Nui (French Polynesia). Earth and Planetary Science Letters 217, 349–365.
Hildenbrand, A., Gillot, P.Y., Bonneville, A., 2006. Off-shore evidence for a huge landslide of the northern flank of Tahiti-Nui (French Polynesia). Geochemistry, Geophysics, Geosystems 7, 1–12.
Hildenbrand, A., Gillot, P.Y., Marlin, C., 2008a. Geomorphological study of long-term erosion on a tropical volcanic ocean island: Tahiti-Nui (French Polynesia). Geomorphology 93, 460–481.
Hildenbrand, A., Madureira, P., Ornelas Marques, F., Cruz, I., Henry, B., Silva, P., 2008b. Multi-stage evolution of a sub-aerial volcanic ridge over the last 1.3 Myr: S. Jorge Island, Azores Triple Junction. Earth and Planetary Science Letters 273, 289–298.
Johnson, C.L., Wijbrans, J.R., Constable, C.G., Gee, J., Staudigel, H., Tauxe, L., Forjaz, V.H., Salgueiro, M., 1998. Ar-40/Ar-39 ages and paleomagnetism of Sao Miguel lavas, Azores. Earth and Planetary Science Letters 160, 637–649.
Lourenço, N., Miranda, J.M., Luis, J.F., Ribeiro, A., Victor, L.A.M., Madeira, J., Needham, H.D., 1998. Morpho-tectonic analysis of the Azores Volcanic Plateau from a new bathymetric compilation of the area. Marine Geophysical Research 20, 141–156.
Luis, J.F., 2007. Mirone: a multi-purpose tool for exploring grid data. Computers and Geosciences 33, 31–41.
Luis, J.F., Miranda, J.M., Galdeano, A., Patriat, P., Rossignol, J.C., Victor, L.A.M., 1994. The Azores triple junction evolution since 10-Ma from an aeromagnetic survey of the Mid-Atlantic Ridge. Earth and Planetary Science Letters 125, 439–459.
MacDonald, G.A., 1972. Volcanoes. A Discussion of Volcanoes, Volcanic Products, and Volcanic Phenomena. Prentice-Hall, International, New Jersey. 510 pp.
Macdonald, K.C., Miller, S.P., Huestis, S.P., Spiess, F.N., 1980. 3-Dimensional modeling of a magnetic reversal boundary from inversion of deep-tow measurements. Journal of Geophysical Research 85, 3670–3680.
Machado, F., Nascimento, J.M., Denis, A.F., 1959. Evolução Topografica do cone Vulcanico dos Capelinhos, Le Volcanisme de l'ile de Faial. Serv. Geol. Portugal, Mem. 4, 65–71.
Machado, F., Parsons, W., Richards, A., Mulford, J.W., 1962. Capelinhos eruption of Fayal Volcano, Azores, 1957–1958. Journal of Geophysical Research 67, 3519–3529.
Madeira, J., 1998. Estudos de neotectónica nas ilhas do Faial, Pico e S. Jorge: Uma contribuição para o conhecimento geodinâmico da junção tripla dos Açores, PhD thesis. Faculdade de Ciencias, Univ. of Lisboa, 481 pp.
Madeira, J., da Silveira, A.B., 2003. Active tectonics and first paleoseismological results in Faial, Pico and S. Jorge islands (Azores, Portugal). Annals of Geophysics 46, 733–761.
Madeira, J., Soares, A.M.M., Da Silveira, A.B., Serralheiro, A., 1995. Radiocarbon dating recent volcanic activity on Faial Island (Azores). Radiocarbon 37, 139–147.
Madureira, P., Moreira, M., Mata, J., Allegre, C.J., 2005. Primitive neon isotopes in Terceira Island (Azores archipelago). Earth and Planetary Science Letters 233, 429–440.
Madureira, P., Mata, J., Mattielli, N., Queiroz, G., Silva, P., 2011. Mantle source heterogeneity, magma generation and magmatic evolution at Terceira Island (Azores archipelago): constraints from elemental and isotopic (Sr, Nd, Hf, and Pb) data. Lithos 126, 402–418.
Miranda, J.M., Freire Luis, J., Abreu, I., Mendes Victor, A., 1991. Tectonic framework of the Azores Triple Junction. Geophysical Research Letters 18, 1421–1424.
Mitchell, N.C., 1998. Characterising the irregular coastlines of volcanic ocean islands. Geomorphology 23, 1–14.
Montelli, R., Nolet, G., Dahlen, F.A., Masters, G., Engdahl, E.R., Hung, S.H., 2004. Finite-frequency tomography reveals a variety of plumes in the mantle. Science 303, 338–343.
Moore, J.G., Clague, D.A., Holcomb, R.T., Lipman, P.W., Normark, W.R., Torresan, M.E., 1989. Prodigious submarine landslides on the Hawaiian Ridge. Journal of Geophysical Research 94, 17,465–17,484.
Moreira, M., Doucelance, R., Kurz, M.D., Dupre, B., Allegre, C.J., 1999. Helium and lead isotope geochemistry of the Azores Archipelago. Earth and Planetary Science Letters 169, 189–205.
Pacheco, J.M.R., 2001. Processos associados ao desenvolvimento de erupções vulcânicas hidromagmáticas explosivas na ilha do Faial e sua interpretação numa perspectiva de avaliação do hazard e minimização do risco. PhD thesis. Azores University. Ponta Delgada. 300 pp.
Quartau, R., Trenhaile, A.S., Mitchell, N.C., Tempera, F., 2010. Development of volcanic insular shelves: insights from observations and modelling of Faial Island in the Azores Archipelago. Marine Geology 275, 66–83.
Quidelleur, X., Gillot, P.Y., Carlut, J., Courtillot, V., 1999. Link between excursions and paleointensity inferred from abnormal field directions recorded at La Palma around 600 ka. Earth and Planetary Science Letters 168, 233–242.
Quidelleur, X., Gillot, P.Y., Soler, V., Lefevre, J.C., 2001. K/Ar dating extended into the last millennium: application to the youngest effusive episode of the Teide volcano (Spain). Geophysical Research Letters 28, 3067–3070.
Quidelleur, X., Carlut, J., Soler, V., Valet, J.P., Gillot, P.Y., 2003. The age and duration of the Matuyama–Brunhes transition from new K–Ar data from La Palma (Canary Islands) and revisited Ar-40/Ar-19 ages. Earth and Planetary Science Letters 208, 149–163.
Quidelleur, X., Hildenbrand, A., Samper, A., 2008. Causal link between Quaternary paleoclimatic changes and volcanic islands evolution. Geophysical Research Letters 35.
Samper, A., Quidelleur, X., Komorowski, J.C., Lahitte, P., Boudon, G., 2009. Effusive history of the Grande Decouverte Volcanic Complex, southern Basse-Terre (Guadeloupe, French West Indies) from new K-Ar Cassignol-Gillot ages. Journal of Volcanology and Geothermal Research 187, 117–130.
Schilling, J.-G., 1975. Azores mantle blob – rare earth evidence. Earth and Planetary Science Letters 25, 103–115.
Schilling, J.-G., Bergeron, M.B., Evans, R., 1980. Halogens in the mantle beneath the North Atlantic. Philosophical Transactions of the Royal Society of London Series A 297, 147–178.
Searle, R., 1980. Tectonic pattern of the Azores spreading centre and triple junction. Earth and Planetary Science Letters 51, 415–434.
Serralheiro, A., Forjaz, V.H., Alves, C.A.M., Rodrigues, B., 1989. Carta Vulcanológica dos Açores – Ilha do Faial, Scale 1:15 000, Sheets 1, 2, 3 & 4. Centro de Vulcanologia do INIC, Serviço Regional de Protecção Civil dos Açores & Univ. of Azores (Ed.), Ponta Delgada.
Silva, P.F., Henry, B., Marques, F.O., Hildenbrand, A., Marques, F.O., 2008. New paleomagnetic and K/Ar on Faial Island (Azores Archipelago). Constraints on the spatio-temporal evolution of the on-land volcanism. : 11th Castle Meeting, Bojnice (Slovakia).
Silva, P.F., Henry, B., Hildenbrand, A., Madureira, P., Marques, F.O., Kratinová, Z., Nunes, J.C., 2010. Spatial/temporal evolution of Faial's onshore volcanism (Azores Archipelago). Joint AGU Meeting, Foz de Iguassu. .
Silva, P.F., Henry, B., Marques, F.O., Hildenbrand, A., Madureira, P., Mériaux, C.A., Kratinová, Z., 2012. Palaeomagnetic study of a sub-aerial volcanic ridge (São Jorge Island, Azores) for the past 1.3 Myr: evidences for the Cobb Mountain Subchron, volcano flank instability and tectono-magmatic implications. Geophysical Journal International 188, 959–978.
Silva, P.F., Miranda, J.M., Henry, B., Marques, F.O., Hildenbrand, A., Madureira, P., Kratinová, Z. in preparation. Paleomagnetic and magnetic study of Faial island (Azores Archipelago). Geophys. J. Int.
Silveira, G., Stutzmann, E., 2002. Anisotropic tomography of the Atlantic Ocean. Physics of the Earth and Planetary Interiors 132, 237–248.
Silveira, G., Stutzmann, E., Davaille, A., Montagner, J.P., Mendes-Victor, L., Sebai, A., 2006. Azores hotspot signature in the upper mantle. Journal of Volcanology and Geothermal Research 156, 23–34.
Steiger, R.H., Jäger, E., 1977. Subcommission on geochronology: convention on the use of decay constants in geo and cosmochronology. Earth and Planetary Science Letters 36, 359–362.
Stretch, R.C., Mitchell, N.C., Portaro, R.A., 2006. A morphometric analysis of the submarine volcanic ridge south-east of Pico Island, Azores. Journal of Volcanology and Geothermal Research 156, 35–54.
Turner, S., Hawkesworth, C., Rogers, N., King, P., 1997. U-Th isotope disequilibria and ocean island basalt generation in the Azores. Chemical Geology 139, 145–164.
Vogt, P.R., Jung, W.Y., 2004. The Terceira Rift as hyper-slow, hotspot-dominated oblique spreading axis: a comparison with other slow-spreading plate boundaries. Earth and Planetary Science Letters 218, 77–90.
White, W.M., Tapia, M.D.M., Schilling, J.-G., 1979. The petrology and geochemistry of the Azores Islands. Contributions to Mineralogy and Petrology 69, 201–213.
Widom, E., Shirey, S.B., 1996. Os isotope systematics in the Azores: implications for mantle plume sources. Earth and Planetary Science Letters 142, 451–465.
Yang, T., Shen, Y., van der Lee, S., Solomon, S.C., Hung, S.H., 2006. Upper mantle structure beneath the Azores hotspot from finite-frequency seismic tomography. Earth and Planetary Science Letters 250, 11–26.
Zbyszewski, G., Veiga Ferreira, O., 1959. Rapport de la Deuxième mission Géologique. Le Volcanisme de l' ile de Faial. : Serv. Geol. Portugal, Mem., vol. 4.

# Chapter 4

## Large-scale catastrophic flank collapses in a steep volcanic ridge: The Pico–Faial Ridge, Azores Triple Junction

## (Costa et al., 2014)

Author's personal copy

Journal of Volcanology and Geothermal Research 272 (2014) 111–125

Contents lists available at ScienceDirect

Journal of Volcanology and Geothermal Research

journal homepage: www.elsevier.com/locate/jvolgeores

# Large-scale catastrophic flank collapses in a steep volcanic ridge: The Pico–Faial Ridge, Azores Triple Junction

A.C.G. Costa [a,b,c,d,*], F.O. Marques [a], A. Hildenbrand [c,d], A.L.R. Sibrant [c,d], C.M.S. Catita [a,b]

[a] University of Lisbon, Lisbon, Portugal
[b] IDL, Lisbon, Portugal
[c] Univ. Paris-Sud, Laboratoire IDES, UMR8148, Orsay F-91405, France
[d] CNRS, Orsay F-91405, France

ARTICLE INFO

*Article history:*
Received 16 September 2013
Accepted 6 January 2014
Available online 17 January 2014

*Keywords:*
Large-scale flank collapse
Debris deposit
Steep volcanic ridge
Mass wasting
Pico Island
Azores

ABSTRACT

Large-scale flank collapses are common in the geological evolution of volcanic ocean islands in the Atlantic. To date, catastrophic lateral collapses in the Azores Islands have been difficult to identify, leading to suggestions that a lack of events may relate to the relatively small size of the islands. Here we show evidence for two major collapses on the northern flank of Pico Island (Pico–Faial volcanic ridge, central Azores), suggesting that this island had a collapse incidence similar to that of other Atlantic volcanic islands.

The study is based on the analysis of: (1) offshore and onshore high-resolution digital elevation models; (2) field data focused on the N flank; and (3) new K–Ar ages on selected lava flow samples.

Pico sub-aerial northern flank is marked by two conspicuous arcuate shaped depressions concave towards the sea, here interpreted as landslide scars. A main debris field is observed offshore the largest depression. This deposit has 20 km of maximum length, covers ca. 150 $km^2$, is composed of meter to hectometer blocks, and has an exposed volume here estimated between 4 and 10 $km^3$, though the actual volume probably exceeds 10 $km^3$. Debris flow towards the ESE was apparently determined by the slope of the narrow WNW–ESE S. Jorge channel.

Young lava flows cascade over the interpreted scars, thus concealing the older volcanic sequence(s) affected by the landslide(s). New K–Ar ages measured on these lava flows provide a minimum age of ca. 70 ka for the large-scale collapse(s) in Pico's northern flank.

© 2014 Elsevier B.V. All rights reserved.

## 1. Introduction

The destruction of volcanic islands occurs at small and large scales, gradually or suddenly on catastrophic events. Large-scale flank failure in volcanic islands can involve either gradual movement along deep listric faults (slump) or the generation of debris avalanche (Moore et al., 1989). These two mechanisms are not mutually exclusive, as a creeping slump may suddenly turn into a catastrophic debris avalanche. From on-land and offshore studies, catastrophic large-scale mass wasting has been identified on volcanic islands all over the world (e.g., Duffield et al., 1982; Moore et al., 1989; Gillot et al., 1994; Deplus et al., 2001; Krastel et al., 2001; Masson et al., 2002; Hildenbrand et al., 2006). In the Atlantic, more specifically, catastrophic failure episodes have been extensively documented, e.g. in the Canary (Navarro and Coello, 1989; Carracedo et al., 1999; Krastel et al., 2001; Masson et al., 2002; Boulesteix et al., 2012, 2013), in Cape Verde (e.g., Day et al., 1999; Masson et al., 2008), and along the Caribbean arc (Deplus et al., 2001; Le Friant et al., 2003; Samper et al., 2007; Germa et al., 2011).

To date, catastrophic flank collapses in the Azores Islands have been difficult to identify, leading to suggestions that a lack of collapses may relate to the relatively small volume of individual islands and volcanic ridges (e.g. Mitchell, 2003). Two topographic embayments on the southern flank of Pico Island have been related to lateral flank movement in the form of old catastrophic landslides or slumping processes (Woodhall, 1974; Madeira, 1998; Nunes, 1999, 2002; Madeira and Brum da Silveira, 2003; Hildenbrand et al., 2012b, 2013b; Mitchell et al., 2012, 2013), but none of these features is clearly and unambiguously associated with well-identified offshore deposits.

Here we put forward evidence of two major collapses, and respective submarine deposits, on Pico's northern flank, showing that the island has experienced episodes of flank instability like other Atlantic volcanic islands.

The identification of offshore debris deposits and the interpretation of onshore source zones in Pico's northern flank are here primarily based on morphological characterization, through combined analysis of a 10 m resolution sub-aerial digital elevation model (DEM) and the new 50 m resolution bathymetry of the narrow S. Jorge Channel (between Pico's northern flank and S. Jorge's southern flank). The analysis of the bathymetry also supports the discussion of the influence of channel morphology on the landslide submarine flow and deposition.

* Corresponding author at: University of Lisbon and IDL, Lisbon, Portugal. Tel.: +351 918318361.
*E-mail address:* acgcosta@fc.ul.pt (A.C.G. Costa).

0377-0273/$ – see front matter © 2014 Elsevier B.V. All rights reserved.
http://dx.doi.org/10.1016/j.jvolgeores.2014.01.002

Author's personal copy



In order to determine the age and recurrence of the failure events, we performed fieldwork focused on the establishment of volcanic stratigraphy/structure of the source zones, aiming at finding possible landslide scars/deposits and to sample the volcanic sequences affected by and covering the landslide related features. The sampled rocks were then processed according to the K–Ar Cassignol–Gillot unspiked technique.

## 2. Geologic setting

The Azores Islands are located about the triple junction between North-America, Eurasia and Nubia plates (Fig. 1). The study region is located on the locally diffuse Nubia/Eurasia plate boundary (Lourenço et al., 1998; Fernandes et al., 2006; Borges et al., 2007; Marques et al., 2013), where regional deformation has influenced the development of narrow and steep volcanic ridges (Fig. 1). The volcanic ridges of S. Jorge and Pico–Faial (Fig. 1) are characterized by slopes commonly around 25–35°, locally reaching higher values along coastal cliffs. These ridges are characterized by a multi-stage development during the last 1.3 Myr (Féraud et al., 1980; Demande et al., 1982; Hildenbrand et al., 2008, 2012a). This multi-stage development includes short periods of volcanic construction interrupted by long periods of island destruction. The island destruction processes are either gradual (e.g., erosion, graben development) or catastrophic like the events here reported. The growth of the sub-aerial Pico–Faial ridge started ca. 850 ka ago on the eastern part of Faial Island (Quartau et al., 2010, 2012; Hildenbrand et al., 2012a, 2013a; Quartau and Mitchell, 2013), with the growth of sub-aerial Pico during the last ca. 300 ka (Fig. 2, 250 ± 40 ka, in Demande et al., 1982). The oldest outcropping volcanic unit in Pico, the Topo Unit (TU), is located on its SE flank (Fig. 2), which is deeply affected by a currently active slump structure (Hildenbrand et al., 2012b) (Fig. 3, feature 1). A WNW–ESE fissural system (FS) developed N of Topo (Fig. 2), and a stratovolcano (Fig. 2, PS) constitutes the westernmost part of the island (Fig. 2, e.g., Forjaz 1966); both have been volcanically active through the Holocene and in historic times (Madeira, 1998; Nunes, 1999; Mitchell et al., 2008). Two topographic embayments on Pico's northern flank (Fig. 3) were considered by Mitchell (2003) as "ambiguous candidates for landslides". Mitchell et al. (2008) identified a hummocky terrain area on the shallow bathymetry (depth up to of a few hundred meters) adjacent to a sub-aerial embayment (Fig. 2 in Mitchell et al., 2008, feature A), which was interpreted as a deposit resulting from debris avalanche or repeated lava delta failure. Despite these evidences, to date the published works (e.g., Mitchell, 2003; Mitchell et al., 2008) do not conclude unequivocally on the occurrence of major landslides in Azores islands.

## 3. Morphological analysis

### 3.1. Construction of the DEMs

The submarine grid of the deepest sector of the Pico–S. Jorge channel (50 m resolution, Fig. A.1a) was constructed using the multibeam data acquired with a 12 kHz Kongsberg EM120 multibeam echo sounder system (Lourenço, personal communication). The depth accuracy (RMS) for this system is estimated as 0.2–0.5% of the water depth (Kongsberg, 2007). Considering that the maximum water depth in the study area is ca. 1300 m, the maximum RMS expected for this data set lies in the range 2.6–6.5 m.

The multibeam data were processed using the CARIS software, clean of noise and converted to an ASCII file (Lourenço, personal communication). Next, the 50 m resolution ASCII data were converted to a raster structure of 50 m spatial resolution, using a simple gridding method.

The onshore data used in this study was produced from a digital topographic map of Pico Island (Portuguese Army Geographic Institute, IGeoE). Photogrammetric methods led to the production of this information at the 1:25,000 scale. The vertical accuracy of these data is approximately 5 m (Afonso et al., 2002). The nodes and lines with three-dimensional coordinates (x, y and z) of the contour lines were then used to generate a TIN (Triangulated Irregular Network) model, which is a vector-based representation of the relief based on a network of non-overlapping triangles (Burrough and McDonnell, 1998). The conversion of the TIN model to a raster structure was then performed interpolating the cell z-values from the input TIN at the spatial resolution of 10 m and 50 m to produce the final onshore DEMs for Pico Island (10 m spatial resolution), S. Jorge and Faial Islands (50 m spatial resolution). To this purpose, we used the ArcGIS 9.3 software from ESRI with the 3D Analyst extension. For the final grid, we introduced in the no-data zone on Pico's northern coast (between the sub-aerial and submarine grids described above) the 100 m spaced contours obtained from photogrammetry of Fig. 2 in Mitchell et al. (2008). The final 50 m resolution grid was built through combination of the sub-aerial and submarine DEMs described above (Fig. 4), filling the no-data zone with a 200 m resolution interpolation that included the depth contours

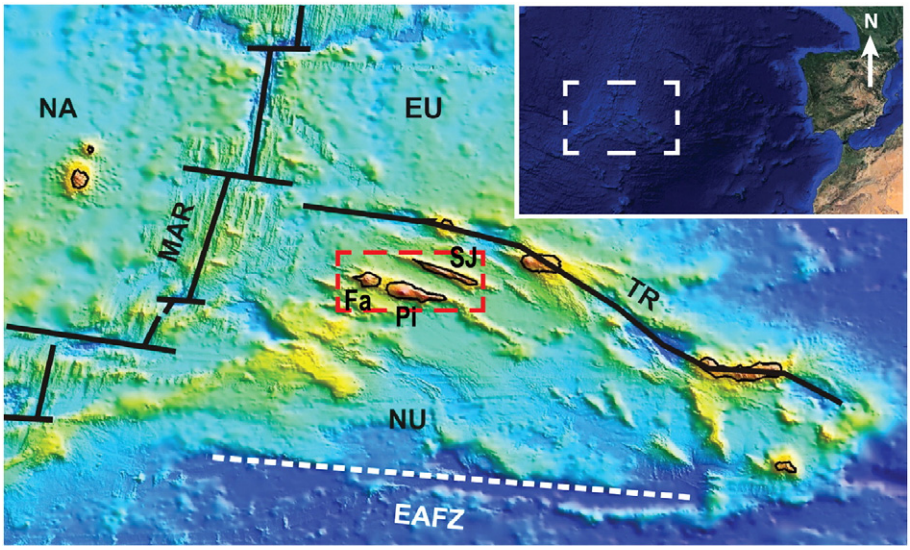


**Fig. 1.** Location of the Azores archipelago on the triple junction between the North America (NA), Eurasia (EU) and Nubia (NU) plates. Main active structures represented as thick black lines (Middle Atlantic Ridge — MAR, Terceira Rift — TR) and inactive structure as dashed white line (East Azores Fracture Zone — EAFZ). The white dashed rectangle encompassing the islands of Pico (Pi), S. Jorge (SJ) and Faial (Fa) limits the study area. Bathymetric data from Lourenço et al. (1998); Image available at http://w3.ualg.pt/~jluis/acores_plateau.htm. (right top rectangle) Inset for the location of the Azores Triple Junction (Google Earth image — 19-08-2013).

Author's personal copy



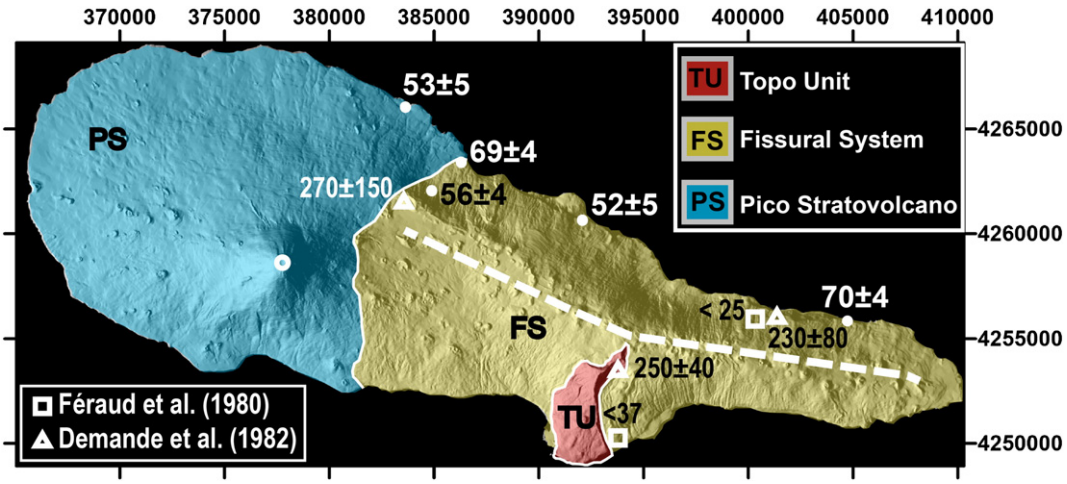


**Fig. 2.** Shaded relief of the 10 m resolution DEM of Pico Island (lighting from ESE), with coordinates in meters UTM (zone 26N). White dots and numbers along Pico's northern flank mark the location and the K–Ar ages presented in this study. White squares and triangles mark the K–Ar ages presented in Féraud et al. (1980) and Demande et al. (1982), respectively. The ages are indicated in thousands of years (ka). Simplified geologic/physiographic map (modified after Madeira, 1998).

extracted from Mitchell et al. (2008). Further details on the composition of the final DEM grid are provided in Appendix A.

For the construction of Pico's elevation gradient in the sub-aerial domain (Fig. 3), we took the original 10 m resolution elevation grid of the sub-aerial domain and created a final 10 m resolution terrain slope grid in the Surfer software (Golden Software, Inc.; software version 9.11.47). For each grid node, the angle of dip was calculated considering the elevation gradients between neighboring nodes in N–S and E–W directions (Golden Software, Inc., 2002, after Moore et al., 1993). Therefore, though the final slope grid presents values for 10 m spaced nodes, the calculation of the final values is based on the elevation gradient between nodes at a 20 m distance from each other (twice the horizontal resolution of the original DEM).

### 3.2. Pico's sub-aerial northern flank

On an elevation gradient map (Fig. 3), the northern flank is generally steeper than the southern flank. On the northern flank, the sub-aerial elevation gradient of the fissural system (Fig. 2, FS) reaches 30–45° on two sectors of concave profile, reaching ca. 800 m of maximum height (Fig. 3):

1. On the western sector of the fissural system, the 30–45° slopes are aligned WNW–ESE (Fig. 3, feature 2). They are masked in the west and in the east by more recent volcanic deposits erupted by the younger Pico stratovolcano and by the fissural system, respectively (Figs. 2 and 3).
2. On the eastern sector of the northern flank, the steep slopes define an arcuate topography, which is concave towards the sea and grossly parallel to the volcanic ridge axis (Fig. 3, feature 3).

### 3.3. S. Jorge Channel bathymetry

The building of the grid mosaic, combining sub-aerial and submarine grids, is described in Appendix A of the supplementary material.

Pico and S. Jorge islands are separated by a ca. 20 km wide WNW–ESE channel, known as the S. Jorge Channel (Fig. 4). The maximum depth along its axis varies between ca. −1230 m and −1270 m, with a basal surface defined around −1270 m, deepening towards its

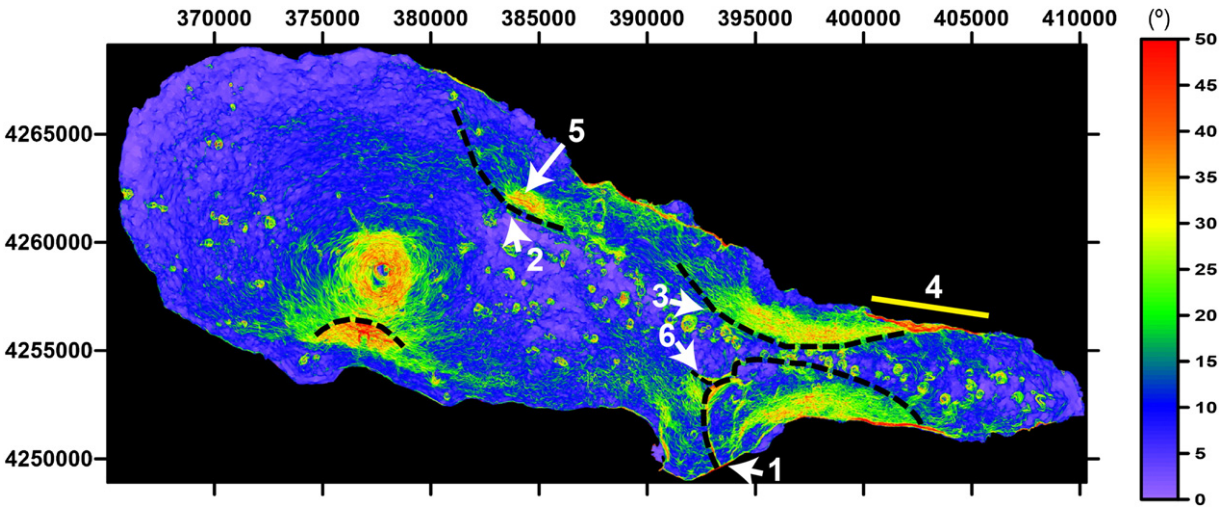


**Fig. 3.** Slope map of Pico Island built from the 10 m resolution DEM. Dashed black lines: scarps interpreted from zones of anomalously strong slopes. Numbered features: 1 — active slump; 2 — westernmost scar of Pico's N flank; 3 — easternmost scar of Pico's N flank coastal; 4 — coastal cliff mentioned in Section 4; 5 — location of the creeks referred to in Section 4; 6 — scarp that limits the outcropping TU to the N.

Author's personal copy



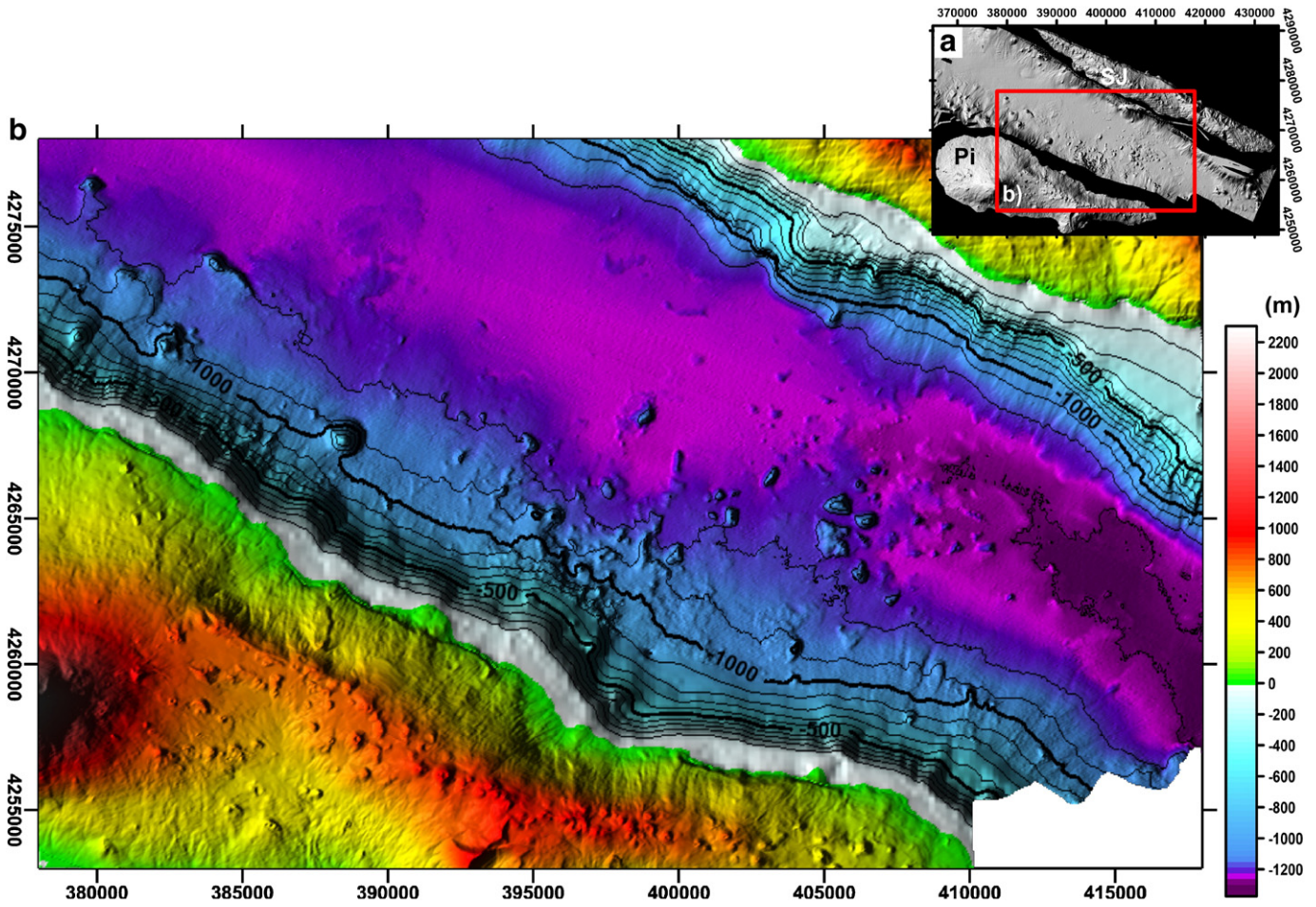


**Fig. 4.** Topographic grid used as basis for this study. (a) Shaded relief (50 m resolution, lighting from WNW) of Pico Island (Pi), S. Jorge Island (SJ) and bathymetry of S. Jorge channel. The red rectangle indicates the area comprised in b. (b) Final grid resulting from the combination of the DEMs presented in (a) and contours extracted from Mitchell et al. (2008) (50 m resolution, lighting from W). Contour levels for 100 m spaced depths are presented. A detailed description of the grid construction is presented in Appendix A.

WNW and ESE ends. On the bathymetry of the S. Jorge Channel (Fig. 5a), we identified:

1. The main feature in the central sector, a WSW–ENE elongated hummocky area, with a positive relief relative to the surrounding sea floor (Fig. 6a, feature "A"). It has a maximum visible length of 20 km (ca. 22 km, measured along a longitudinal profile) and spreads over an area of ca. 150 km$^2$. The grain size of the material at the surface of this positive-relief feature is generally too small to be distinguishable on this 50 m resolution DEM. The largest individual hummocks observed are located on the distal part of the deposit, at an average depth of −1240 m (Fig. 6a): the largest is 1700 m long, 1200 m wide and 100 m high (Fig. 6a, feature 1), and the second largest is 1000 m long, 600 m wide and 200 m high (Fig. 6a, feature 2). On the SE zone of the hummocky terrain, a homogeneous mass of, apparently, intermediate size debris material can be identified (Fig. 6a, feature "A", dashed yellow line). At the foot of Pico's submarine flank, on the surface of this homogeneous mass (high resolution bathymetry presented as Fig. 2 in Mitchell et al., 2008), there are visible lineaments perpendicular to the submarine flank. Uphill, on the submarine flank, there are two small arcuate scarps (Fig. 6a, red dashed lines).
2. A NNE–SSW elongated, lobate-shaped hummocky terrain on the western sector (Fig. 6a, feature "B"). Its maximum extent is ca. 8 km, measured from, and perpendicularly to, the base of Pico's submarine flank. It is generally composed of small debris, undistinguishable on the 50 m resolution DEM, but with some larger hummocks. The limits of the deposit are not well defined in the proximity of Pico's flank, covering a minimum area of 32 km$^2$.
3. A smaller deposit at the base of S. Jorge's southern flank (Fig. 6a, feature "C"), with 4 km of maximum length, measured from, and perpendicularly to, the base of S. Jorge's submarine flank, and covering an area of ca. 12 km$^2$. Upslope the submarine flank, there is an arcuate-shaped scar (Fig. 6a, red dashed line).
4. Lobate-shaped deposits visible along the base of Pico and S. Jorge's flanks. These deposits are generally composed of small size debris, undistinguishable on the 50 m resolution DEM, but with some larger hummocks.

### 3.4. Debris volume

The exposed volume of Pico's northern deposit (Fig. 6a, feature "A") was estimated considering solely the space between the actual topographic surface of the deposit and hypothetical basal surfaces (based on submarine flank profiles performed on deposit-free sectors). We built NNE–SSW cross sections of the original grid (perpendicular to the coastline on the zone where the deposit is thickest), spaced approximately 1.2 km, and covering the deposit area and the surrounding deposit-free area (Fig. 7). The origin considered for the horizontal distance of the cross sections is the −100 m contour line, roughly the limit of the Pico's shelf. For the calculation of the exposed volume, we assume that the upward limit of the deposit is at −100 m contour (we assume that it is limited to the extent visible on the bathymetry,

Author's personal copy



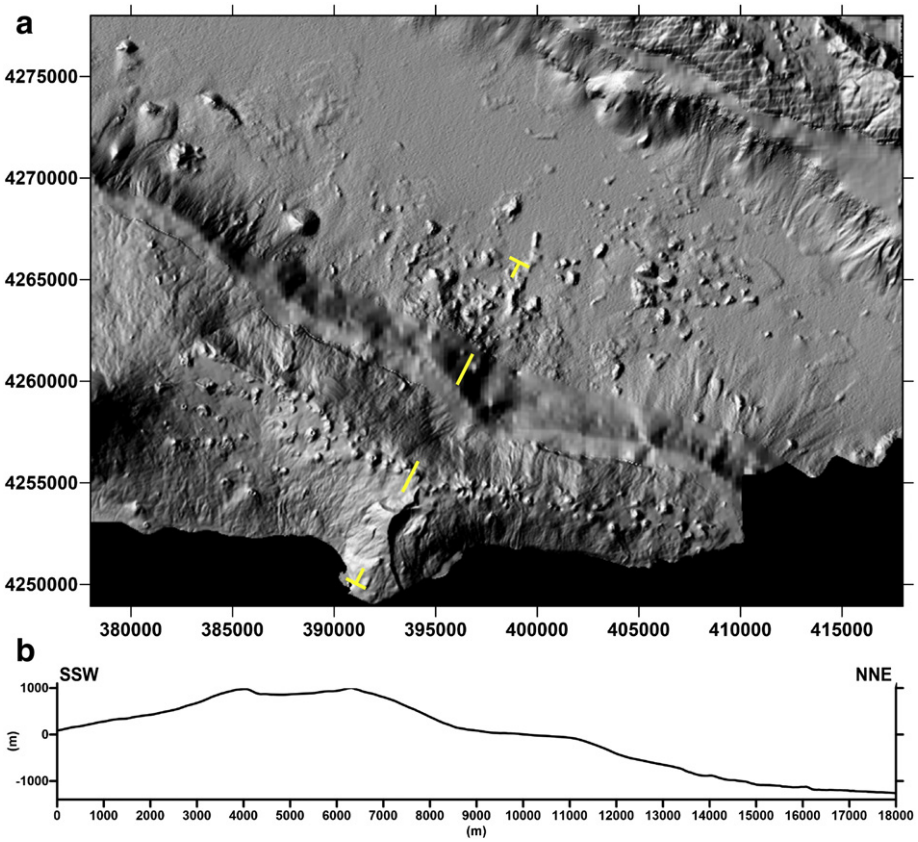


**Fig. 5.** (a) Shaded relief map of the S. Jorge channel, sub-aerial Pico and S. Jorge islands (lighting from ESE, 50 m resolution DEM). (b) Topographic profile across Pico Island's sub-aerial domain and submarine northern flank, presented as a yellow dashed line in (a).

not continuing landward), and we do not consider the effects of blanketing by more recent volcanic/sedimentary materials.

As the channel deepens and gets narrower towards the ESE (Fig. 4), the volume will be given as an interval: minimum volume estimated with a hypothetical basal profile representative of the WNW limit of the deposit, and maximum volume estimated with a hypothetical basal profile that considers the greater depths of the ESE limit of the deposit. The hypothetical basal profile from the WNW limit of the deposit (Fig. 7b, black dashed line) was determined from the average of closely spaced cross sections (Fig. 7a, full white line cross sections), on a zone relatively undisturbed by the presence of sedimentary deposits or volcanic cones. In order to build the hypothetical basal profile used for the determination of the maximum volume (Fig. 7b, red dashed line), we considered all the cross sections performed perpendicularly to the coast, and determined the maximum depth attained by the bulk of these cross sections for 1 km spaced horizontal distance values.

For the construction of each hypothetical basal surface, we introduced the values determined for the "normal profiles" in the blank area (Fig. 7a, area comprised by the green dashed line) and performed a 200 m resolution spatial interpolation (kriging) (Fig. 8a and b). The standard deviations associated with the interpolation method used have a maximum value of 25 m (Fig. B.1). These spatial interpolations have associated Root Mean Square (RMS) errors within a range of 4.7–5.6 m, and a maximum residue of 26.0 m, for the deposit's blanked area (Table B.1). Though the maximum residue obtained for the complete grid has a value of 145.1 m (Table B.1), this residue was obtained outside the deposit's blanked area, therefore outside the zone considered in the volume calculation (Fig. B.2). We built "deposit thickness" grids by subtracting each of the hypothetical basal surfaces from the real topographic surface (Fig. 8c and d). The maximum thickness of the deposit lies between ca. 238 and 304 m (Table 1). In Fig. 8c and d, it is visible that there are appreciable volumetric anomalies on the surroundings of the limits defined for the deposit, where it would be ideal to have a perfect fit between real and estimated basal surfaces. In order to partially eliminate these anomalies, the volume was calculated only for the deposit's area (Fig. 8c and d, area comprised by the dashed black line). The volume of the deposit visible on the bathymetry is, roughly, between 4 and 10 $km^3$ (Table 1, positive volume). If we consider that, for the hypothetical maximum depth basal surface, there are still zones on which the basal surface lies above the real topography (Table 1, negative volume), then the exposed volume of the deposit must be closer to 10 $km^3$ than to 4 $km^3$.

## 4. Fieldwork

In order to constrain the age of failure events on Pico's northern flank, we attempted to sample the volcanic sequence affected by the flank failure and the one covering the landslide scar(s). The fieldwork was focused on the zones where it would be more probable to reach the older volcanic sequence affected by the eventual flank failures, i.e., inside deep creeks incising the cascading lavas, and along coastal cliffs close to these features.

On the eastern sector of Pico's N flank, the high coastal cliff has a maximum height of ca. 400 m. It intersects the steep slope zone that defines the eastern embayment (Fig. 3, feature "4"). Along this coastal cliff, the outcropping sequence consists mainly of lava flows that dip to the N on the western sector, whereas lava flows dip to the NE on the eastern sector (Fig. 6a). No major unconformities have been observed on the outcropping sequence. Nevertheless, we sampled a lava flow (Table 2 and Fig. 2, sample Pi10X), as close as possible to the base of the outcropping sequence.

Author's personal copy



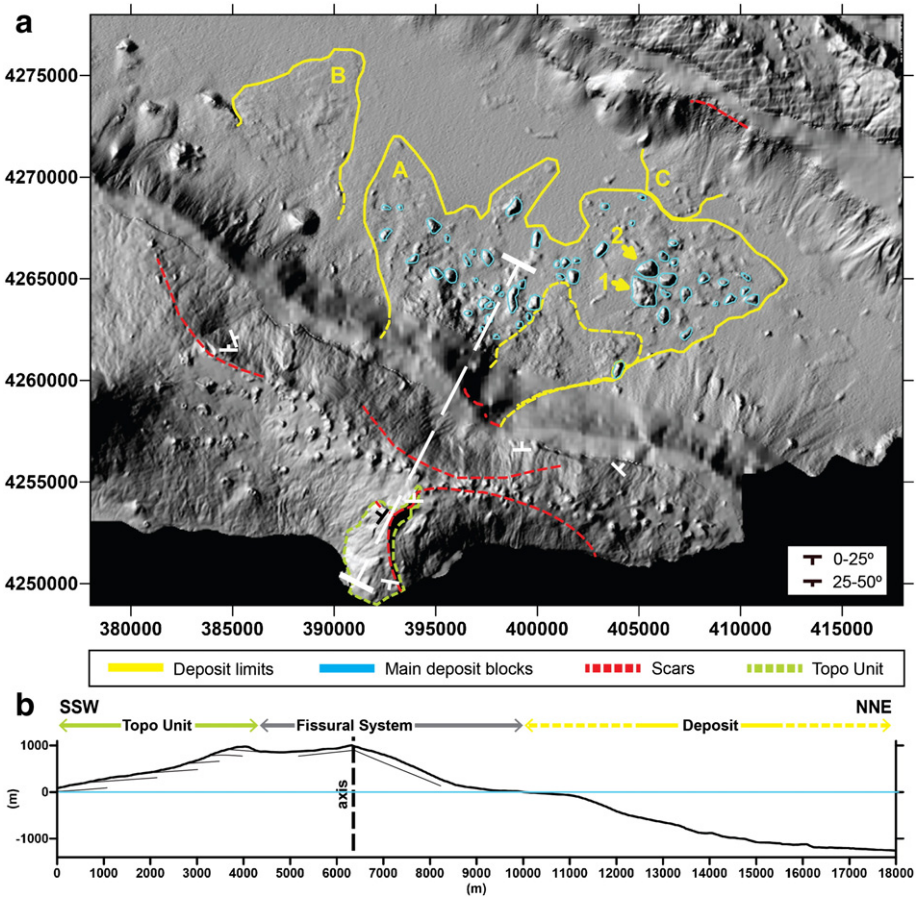


**Fig. 6.** (a) Shaded relief map of the S. Jorge channel, sub-aerial Pico and S. Jorge islands (lighting from ESE, 50 m resolution DEM), with interpretation of possible scars, blocks and limits of debris deposits. Yellow arrows indicate the biggest individual hummocks observed. Green dashed line indicates the extent of the TU. Dashed white line indicates the cross section presented in b. The lava flow orientations measured on the field are indicated. The non-interpreted version of this shaded relief map is presented as Fig. 5a. (b) Topographic profile across Pico Island and the proximal zone of the main debris deposit interpreted on the bathymetry. Representation of the main geometry of the deposits observed on the field. The non-interpreted version of this topographic profile is presented as Fig. 5b.

On the western sector of Pico's northern flank, we worked upstream along two creeks that incise the zone of steep slope (Fig. 3, feature 5). Here we observed cascading lava flows dipping 35–45° towards the sea (Fig. 6a), intercalated with pyroclastic and clastic sedimentary deposits. Again we could not observe a significant unconformity that could represent a landslide scar. Anyway, we sampled a lava flow at the base of this volcanic sequence (Table 2 and Fig. 2, sample Pi11N). Other samples were collected at the base of coastal cliffs along Pico's northern coast (Table 2 and Fig. 2, samples Pi10R, Pi10P, and Pi10U), in order to constrain the age of the fissural system volcanism.

The easternmost embayment identified on Pico's northern flank is located immediately to the N of the exposed remnants of TU (Figs. 2 and 6a). Additional fieldwork was performed on this sector, in the southern flank of the island (cut by the SSW–NNE cross section presented in Figs. 5 and 6). The observed TU deposits consist mainly of meter thick lava flows with dips in the range 0–25°, and a variation in maximum dip orientation (Fig. 6a). The outcropping TU lavas are limited in the N by a slightly arcuate W–E scarp, ca. 150 m high, whose maximum dip reaches 35–40° towards the N (Fig. 3, feature 6). Near this scarp, the TU lava flows dip 10° towards the NW (Fig. 6a).

## 5. K–Ar geochronology

The samples were prepared and dated by K–Ar at the IDES laboratory, Université Paris-Sud (Orsay, France). In order to check the unaltered state of the samples, thin sections were carefully observed under the microscope. The samples were crushed and sieved to a homogeneous size fraction (125–250 μm). As phenocrysts may carry inherited excess Ar, by crystallizing previously to the eruption under high pressures at depth, their presence in the analyzed sample may lead to the determination of an excessive age. Therefore, we systematically removed all the phenocrysts (olivine, pyroxene and plagioclase), through magnetic separation and heavy-liquid sorting. At the end of this process, we obtained a groundmass of homogeneous grain size (125–250 μm) and density (classically ranging between 2.95 g/cm$^3$ and 3.05 g/cm$^3$ for basaltic samples).

K was measured by flame absorption-spectrophotometry, with 1% uncertainty from systematic analysis of standards (Gillot et al., 1992). Ar was measured by mass spectrometry, according to the Cassignol–Gillot unspiked technique (Cassignol and Gillot, 1982; Gillot and Cornette, 1986; Gillot et al., 2006). The Cassignol–Gillot technique has been shown especially suitable to date low-K and high-Ca basalts and andesites of late Quaternary age with an uncertainty of only a few ka (e.g., Samper et al., 2007; Hildenbrand et al., 2008, 2012a; Germa et al., 2011; Boulesteix et al., 2012, 2013). With this technique, $^{40}$Ar and $^{36}$Ar are measured simultaneously, avoiding any potential signal drift. Also with this technique, the level of atmospheric contamination is accurately determined by comparison between the isotopic ratios of the sample and an air pipette at strictly similar $^{40}$Ar level. This allows the detection of tiny amounts of radiogenic $^{40}$Ar, as low as 0.1% (Gillot et al., 2006).

K and Ar were both measured at least twice to ensure the reproducibility of the results. The used decay constants are from Steiger and Jäger (1977). The obtained ages are presented in Fig. 2 and Table 2, where the uncertainties are quoted at the 1σ level. The various lava flows sampled in this study are dated between 70 ± 4 ka and 52 ± 5 ka. The oldest

Author's personal copy



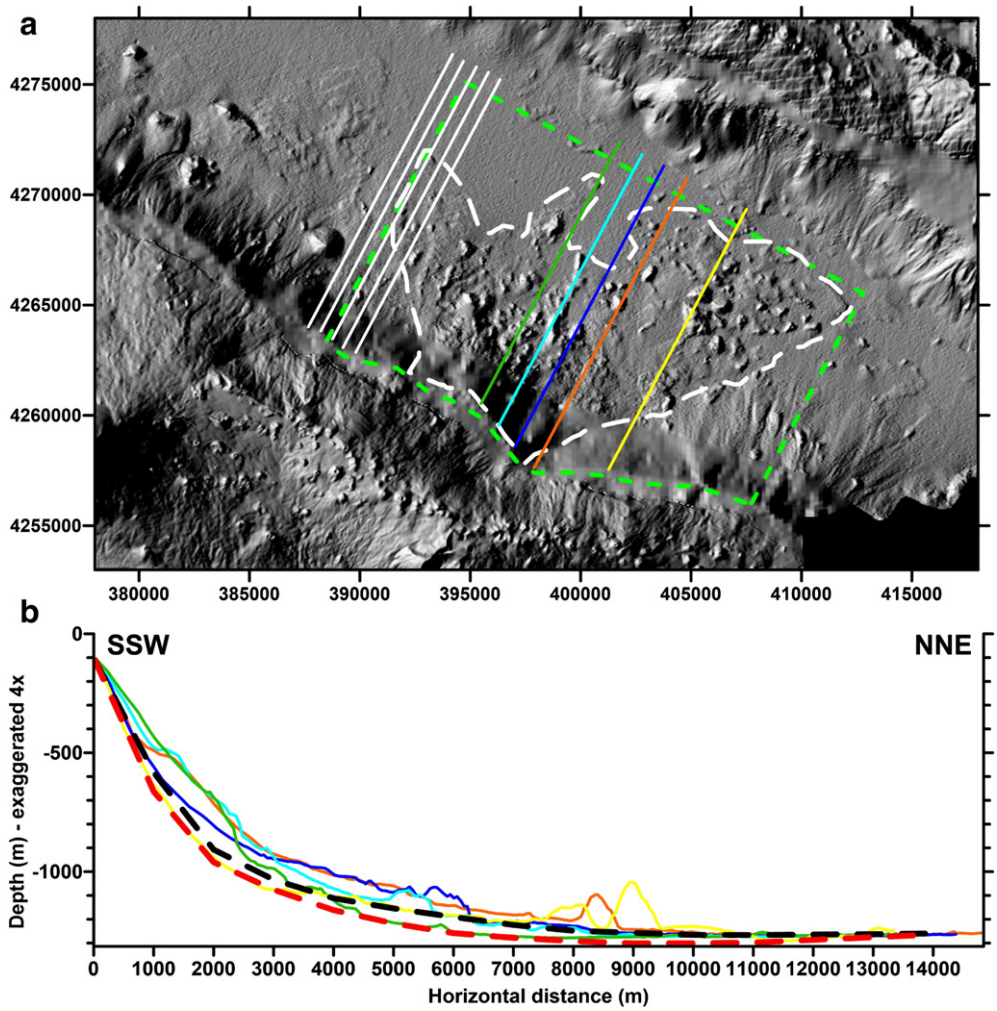


**Fig. 7.** (a) Full colored lines on the deposit area represent the most relevant NNE–SSW cross sections. Full white lines on the NW represent the cross sections considered for the calculation of the "normal" submarine profile, used in the estimation of minimum volume. Contour of debris deposit is represented by a dashed white line, and the contour of the area blanked for volume calculation purposes is defined by the green dashed line. (b) Plot of the most relevant SSW–NNE cross-sections on the deposit area (full lines) and of the hypothetical basal profiles built for the calculation of minimum volume (red dashed line) and maximum volume (black dashed line).

flows covering the western and eastern scars yield similar values of 70 ± 4 ka and 69 ± 4 ka (samples Pi10X and Pi10 R, respectively).

## 6. Discussion

### *6.1. Sub-aerial scarps on Pico's northern flank*

Although still very steep on the slope map, the two main curved scarps visible on Pico's sub-aerial N flank are presently smooth, due to blanketing by volcanic products that erupted from the fissural system and Pico stratovolcano. These younger volcanic deposits have therefore been deposited on top of a sharper and steeper scarp. Wide lava deltas have formed at the base of the curved scarps (Figs. 2 and 3), thus smoothing also part of the submarine scarp.

Following Mitchell (2003), who hypothesized a landslide related origin for these conspicuous scarps, we interpret these features as scars resulting from past failure events on Pico's northern flank.

### *6.2. Main debris deposit*

#### *6.2.1. Debris dimensions*

Some of the hummocks in the debris deposit A (Fig. 6a) are easily discernible on the shaded relief image due to the strong reflection/shadow contrast of their "soft" surfaces under the imposed lighting. As these hummocks generally have an irregular shape rather than being conical features, we interpret them as blocks rather than small volcanic edifices.

Despite its significant dimensions, the height of the biggest hummock identified (see Section 3.3) is very small when compared to its width/length, and the hummock's surface is extremely irregular and weakly reflects the imposed lighting (Fig. 6a, feature "1", see Section 3.3). We interpret this large hummock as evidence for either a big irregular block or an agglomerate of blocks, covered by smaller debris. The second largest hummock identified (Fig. 6a, feature "2", see Section 3.3) constitutes the biggest individual block observed on the surface of the deposit.

#### *6.2.2. Debris source(s) and number of failure events*

Based on the location, shape, and thickness spatial distribution, we interpret this hummocky terrain as a deposit of material resulting from partial collapse of Pico's northern flank. The deposit's shape and thickness spatial distribution at the foot of Pico's submarine flank suggest a source area of relatively small lateral extent (ca. 7 km). This source zone likely corresponds to the sub-aerial scar immediately upstream the deposit (Fig. 6a).

We interpret the homogeneous debris size domain on the SE of the deposit (Fig. 6a, feature A, yellow dashed line) as a deposit resulting from a more recent collapse of Pico's submarine flank. As suggested by the deposit's shape and the longitudinal flow structures visible on its

Author's personal copy



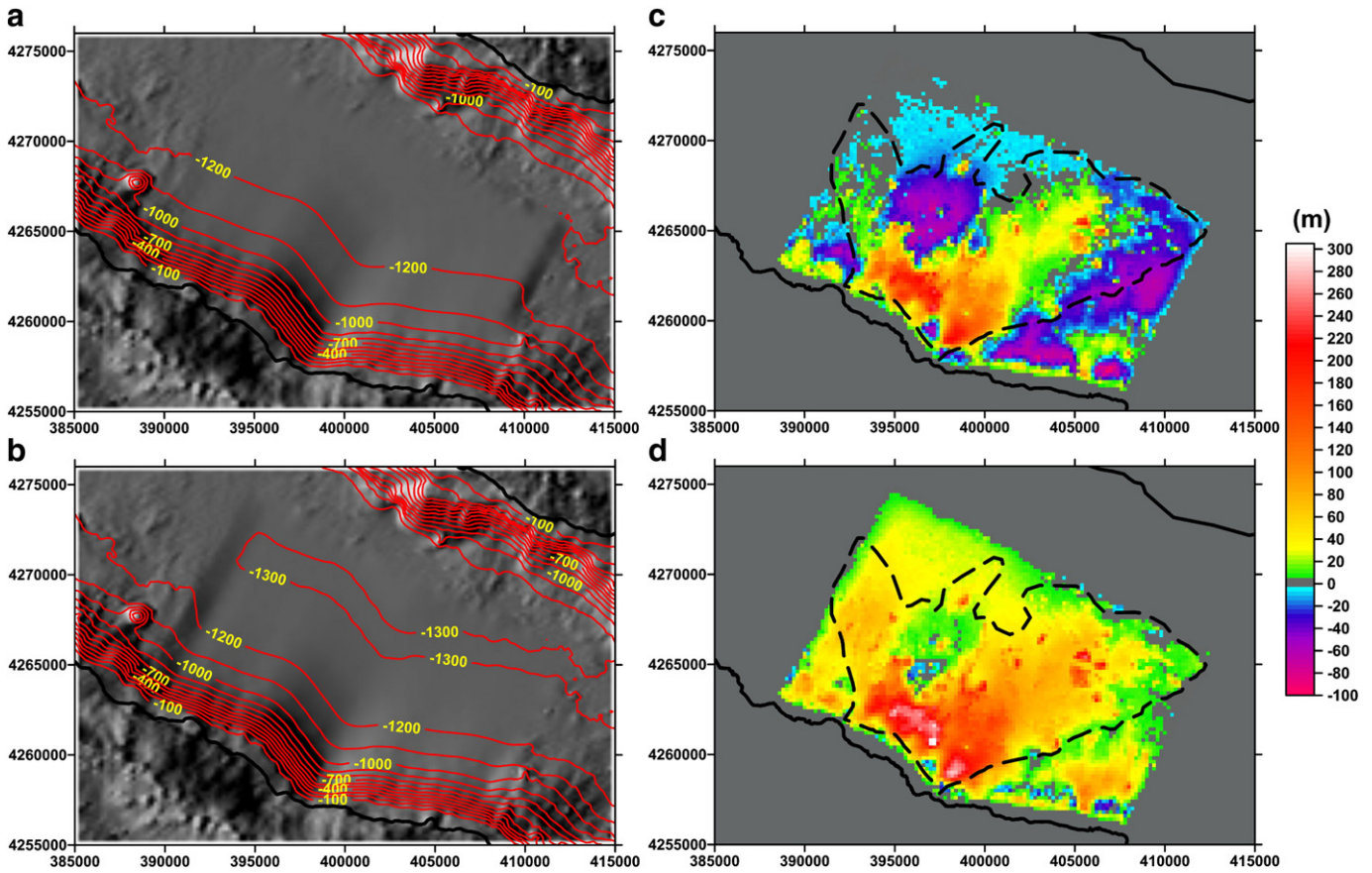


**Fig. 8.** Estimated basal surfaces for minimum volume (a) and maximum volume (b) calculations (grid lighting from WNW, 0 m contour lines of the surfaces plotted as full black lines). Grids of deposit thickness for the minimum volume (c) and maximum volume (d) (black dashed line limits the area considered for the volume calculations, and the full black lines represent the islands' coastlines). Color scale for the deposit thickness (c and d) is presented on the right.

surface (lineaments mentioned in Section 3.3, visible in Fig. 2 from Mitchell et al., 2008), the interpreted sources of this deposit's material are the two arcuate scarps uphill of the submarine deposit (Fig. 6a). The scars interpreted on the sub-aerial northern flank have been covered by more recent volcanic deposits. The significant protrusion near sea level observable in the area interpreted as source zone of the main deposit (Fig. 6) is interpreted as a consequence of more recent submarine flank reconstruction and lava delta accumulation (Mitchell et al., 2002, 2008; Mitchell, 2003), thus reshaping the scar left by the debris avalanche.

Therefore, it is impossible to assess directly (a) the landward continuity of the deposit (Fig. 9), (b) the exact configuration, at depth, of the scar associated with the failure (Fig. 9, yellow dashed line), and (c) which volcanic sequences were affected by the flank collapse. The possible scenarios for the sequences affected by the studied flank failure were constrained by the local topography (Fig. 6) and fieldwork data, and depend on the premises we assume for: (a) the continuity of the TU volcanic edifice towards the N, where it is masked by deposits of the more recent fissural system; (b) the actual configuration of the scar at depth; and (c) the possible development of a pre-collapse sequence of sub-aerial fissural system deposits.

Three main hypotheses can be put forward regarding the sequences that were affected by the major flank failure identified in this study:

1. The TU volcanic edifice was continuous and higher towards the N, and its northern flank collapsed catastrophically (Fig. 9a);
2. The TU volcanic edifice was shallower towards the N, on top of which a pre-collapse fissural system grew. Then failure occurred in the N, with catastrophic removal of deposits from both TU and pre-collapse fissural edifices (Fig. 9b).
3. The TU volcanic edifice was shallow towards the N, on top of which a thick sequence of pre-collapse fissural system deposits was emplaced. When the N flank failure occurred, only the pre-collapse fissural system was affected (Fig. 9c).

Though hypotheses 2 (Fig. 9b) and 3 (Fig. 9c) cannot be excluded, fieldwork observations on the scar did not allow the identification of a pre-collapse fissural system sequence. Therefore, scenario 1 (Fig. 9a), which considers the failure of TU volcanics only, is here considered as the soundest hypothesis.

Based on this hypothesis, we propose the following evolution for this sector of the volcanic ridge:

1. Growth of the TU volcanic edifice (Fig. 10a and b). The variation of the maximum dip orientation of the volcanic deposits observed in the field (Fig. 10a) suggests that the original summit of this volcanic edifice would be located in the area of the SE Pico active slump depression (Figs. 3 and 10). Such location had already been proposed for the core of the referred volcanic edifice by Nunes et al. (2006), from the interpretation of a major positive Bouger anomaly identified there.
2. Destruction of most of the TU volcanic edifice (Fig. 10c).

**Table 1**
Values of volume and thickness obtained for the models of minimum and maximum volumes. Positive volume is the volume between the surfaces, being the hypothetical basal surface under the actual topographic surface. Negative volume is the volume between the surfaces, being the hypothetical basal surface above the actual topographic surface.

| | Positive volume ($km^3$) | Negative volume ($km^3$) | Maximum thickness (m) |
|---|---|---|---|
| Minimum volume | 4.278 | 1.6 | 238 |
| Maximum volume | 10.242 | 0.015 | 304 |

Author's personal copy



**Table 2**
Results of the K–Ar dating on fresh-separated groundmass. The ages are indicated in thousands of years (ka). The uncertainties are reported at the 1σ level.

| Samples | UTM E | UTM N | K (%) | $^{40}Ar^*$ (%) | $^{40}Ar^*$ ($10^{10}$ at/g) | Age (ka) | Uncertainty (ka) | Mean (ka) |
|---|---|---|---|---|---|---|---|---|
| Pi10X | 26405050 | 4255843 | 0.897 | 1.7 | 6.378 | 68 | 4 | 70 ± 4 |
| | | | | 1.8 | 6.715 | 72 | 4 | |
| Pi10R | 26386933 | 4262897 | 1.057 | 2.3 | 7.823 | 71 | 3 | 69 ± 4 |
| | | | | 1.2 | 7.116 | 64 | 6 | |
| Pi11N | 26384950 | 4261825 | 0.913 | 1.9 | 5.602 | 59 | 3 | 56 ± 4 |
| | | | | 1.0 | 4.949 | 52 | 5 | |
| Pi10P | 26383509 | 4265958 | 0.831 | 0.5 | 4.116 | 47 | 9 | 53 ± 5 |
| | | | | 1.4 | 4.788 | 55 | 4 | |
| Pi10U | 26392413 | 4260735 | 0.961 | 1.0 | 5.523 | 55 | 5 | 52 ± 5 |
| | | | | 0.9 | 4.951 | 49 | 5 | |

The clear N–S scarp that affects this edifice's eastern sector (Fig. 3, feature "1") shows that part of the mass-wasting has been accommodated along the structure(s) that constitute the currently active large-scale slump structure (mass wasting structure not represented in Figs. 6 and 9, since it is not intersected by the cross section).

It is not possible to observe the continuation of TU edifice towards the N, due to large-scale flank destruction and masking of the remnants by the more recent fissural system deposits (Fig. 10d). The destruction of this edifice's northern flank would have occurred along the sub-aerial scar interpreted for the eastern sector of Pico, and originated the major submarine deposit here reported. The orientation and dip of the exposed north-facing scarp that constitutes the northern limit of TU's outcrops (Fig. 3, feature "6") are not concordant with the local orientation of volcanic deposits (see Section 4). This structure was previously interpreted as a fault scarp (Madeira and Brum da Silveira, 2003), and it might constitute the uppermost expression of a secondary structure located further S of the interpreted main sub-aerial scar (Fig. 10c and d, yellow dashed line with question marks). This interpreted structure could have accommodated non-catastrophic deformation of the TU's volcanic sequence to the S of the main scar.

3. Growth of the fissural system (Fig. 2, FS), masking the sub-aerial scar in TU edifice's northern flank (Fig. 10d). The real configurations of the interpreted scar and of the remnants of the TU volcanic edifice have been extensively masked by more recent volcanism. Therefore it is not possible to establish a detailed comparison between the configuration of the scars identified on Pico's northern flank with landslide scars exposed elsewhere.

Debris deposits resulting from the accumulation of multiple failures have been described in some oceanic islands (e.g. Urgeles et al., 1999; Watts and Masson, 2001; Masson et al., 2006; Hunt et al., 2011). In Pico, with the exception of the homogeneous debris field in the SE

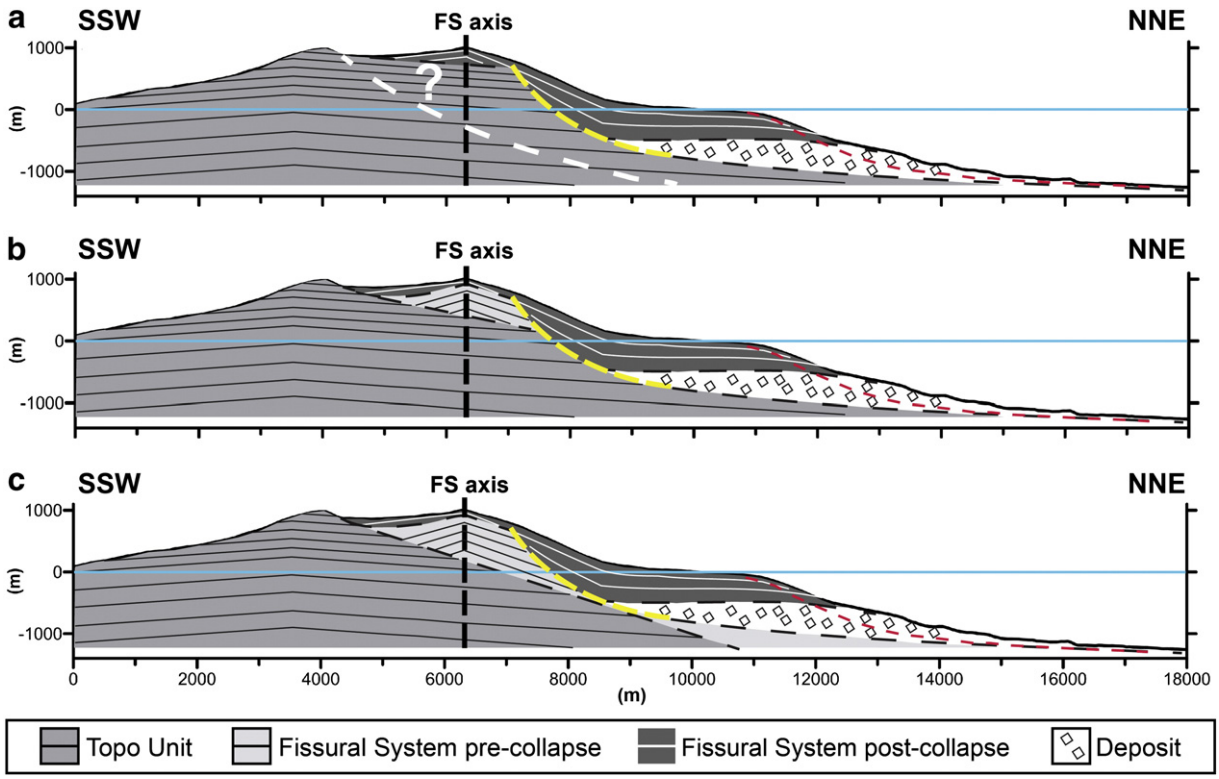


**Fig. 9.** Geological interpretation of the section marked in Figs. 5 and 6. Yellow dashed line marks the scar suggested as debris source. Red dashed line represents the basal surface considered in the estimation of the maximum volume. Black dashed lines indicate the suggested contacts between volcanic sequences and the deposit. White dashed line indicates a suggested secondary structure that affected TU volcanic sequence. Possible scenarios for the volcanic sequence(s) affected by the flank failure: (a) scar only affects TU deposits; (b) scar affects TU and fissural system deposits; (c) and scar only affects fissural system deposits.

Author's personal copy



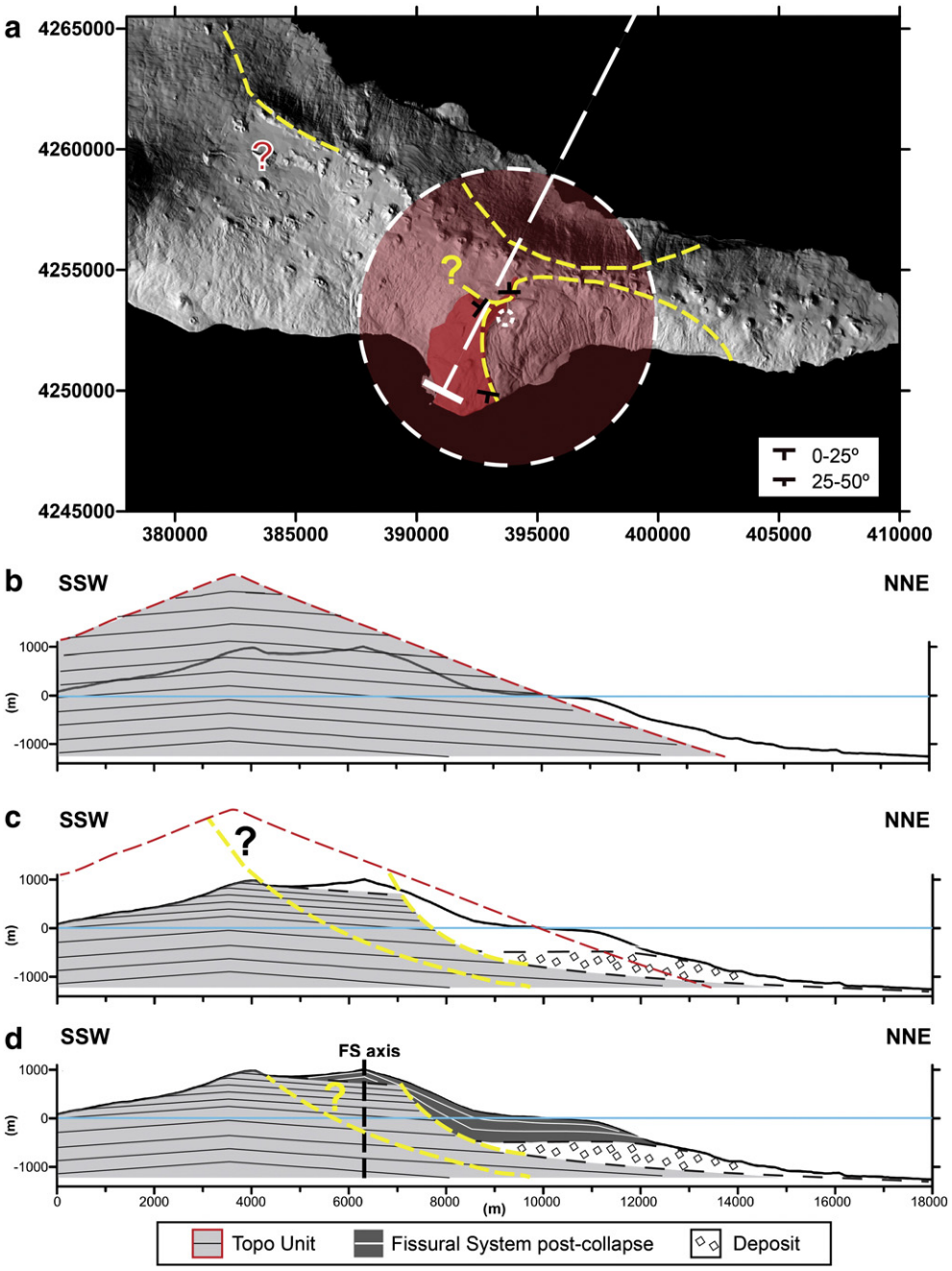


**Fig. 10.** Presentation of the hypothesis in which the failure that originated the main deposit only affected the TU sequence. (a) Map view of sub-aerial Pico with the representation of the actual extent of sub-aerial TU volcanic edifice (dark red area) and its lava flow orientations, the schematic configuration of the original TU edifice (semi-transparent light red area) and the location of its original crater (small white dashed line circle). SSW–NNE white dashed line represents the cross section interpreted. Yellow dashed lines represent the scarps interpreted in the study area. Schematic representation of the evolution of this volcanic ridge sector, across the SSW–NNE topographic profile: (b) original configuration of TU edifice. (c) TU's northern flank destruction; (d) current stage, with fissural system (FS) deposits concealing the scar of the failure event in study.

sector of the main deposit, and interpreted as resulting from the collapse of the submarine flank, we did not find morphological or chronological evidence supporting the formation of the debris deposit by accumulation of multiple failures. Therefore, we consider that the deposit results from a single failure event, with the exception of a subsequent small failure on the submarine flank.

*6.2.3. Debris volume*

The lack of data regarding the inner structure of the island (i.e. geophysical data) prevents us from assessing the extent of surface morphology change since the flank failure, due to factors like the partial filling of the topographic embayment by younger volcanic products. However, considering the geometrical constraints imposed by the topography, the geometry/location of the interpreted scar, the geometry of the observed deposit surface offshore, and field data (Fig. 6a), we provide simplified interpreted schemes (Fig. 9) for the inner structure of the island along the cross section presented in Figs. 5 and 6.

The constraints imposed by the location/geometry of the interpreted scar (Fig. 9, yellow dashed line) and by the northern flank topography represented in the cross section suggest the inland continuation of the debris deposit (Fig. 9). Therefore, we consider that even the maximum volume of 10 $km^3$ here estimated for the exposed part of the deposit (Fig. 9, red dashed line represents the basal surface considered in the

Author's personal copy



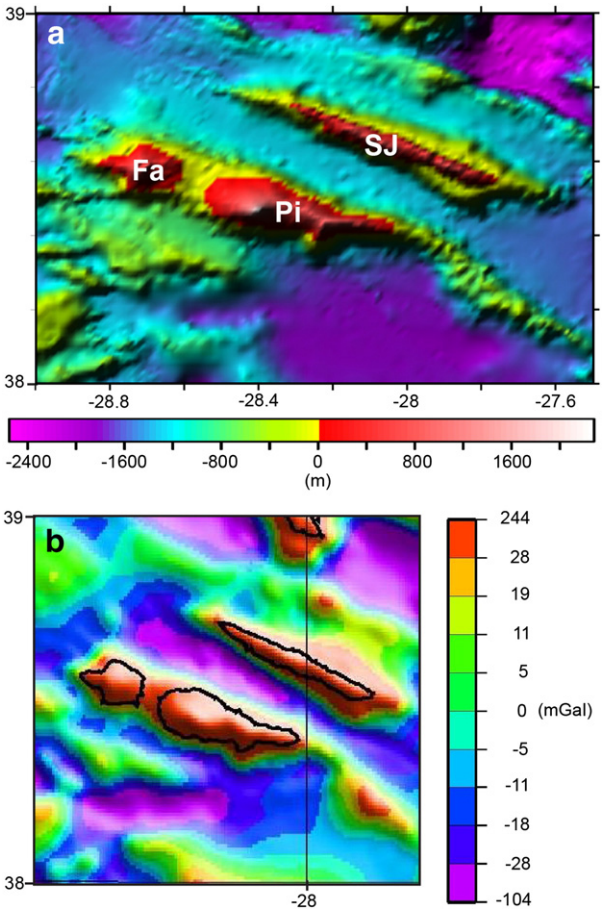


**Fig. 11.** (a) 1300 resolution DEM (lighting from NW) of the study area. Bathymetric data from Lourenço et al. (1998), available at http://w3.ualg.pt/~jluis/. Fa — Faial Island, Pi — Pico Island, SJ — S. Jorge Island. (b) Free air gravity anomaly map of the same area (extract of Fig. 3 from Catalão and Bos, 2008).

estimation of the maximum volume observable) will constitute an underestimation of the actual volume of the debris deposit.

Catalão and Bos (2008) present a free air gravity anomaly map of the Azores (Fig. 11b, extract of Fig. 3 in Catalão and Bos, 2008), produced from land gravity data, ship-borne gravity data, and a background grid of satellite altimeter-derived gravity data (model KMS02, from Andersen et al., 1999). In order to avoid possible anomalies of the satellite data near the steep coastlines of the islands, these data were not considered for offshore areas at less than 20 km from the coastlines (the coastlines were masked with a 20 km buffer on the offshore domain) (Catalão and Bos, 2008).

This map of the free air gravity anomaly (Fig. 11b) displays a strong negative anomaly in the S. Jorge Channel. However, it is clear from the bathymetry (Fig. 11a) that this area does not correspond to a strong topographic low. Note that the deep basins (magenta in Fig. 11a) correspond to strong negative gravity anomalies (magenta in Fig. 11b). Therefore, we interpret the contrasting association of high topography (green in Fig. 11a) and strong negative gravity anomaly as the result of accumulation of a rock with density much lower than basalt, most likely corresponding to thick accumulation of marine sediments (low density deposits). The thick accumulation of sediments may have blanketed the debris deposits, thus concealing their actual dimensions.

Therefore, considering the probable inland continuation of the deposit (Fig. 9) and the masking of the actual deposit by more recent blanketing by volcanic/sedimentary products, we conclude that the actual volume probably exceeds the estimated 10 km$^3$.

*6.2.4. Flow mobility and constraints*

The deposit's shape and the debris distribution in the deposit suggest that part of the debris flowed towards NNW and NNE, but the most significant part of the landslide material (including the biggest blocks) flowed towards greater depths towards the E. It was thus clearly conditioned by the submarine topography.

The mobility of a landslide can be expressed as a function of the ratio $H/L$ ($H$ — height between the topmost source zone of the material and the deposit; $L$ — maximum runout length), which represents the apparent coefficient of friction of the avalanche (e.g. Lipman et al., 1988; Hampton et al., 1996). This ratio decreases (mobility increases) for material volumes larger than 0.001 km$^3$ (Scheidegger, 1973, in Hampton et al., 1996). More recently, Legros (2002) argued that $L$ is mainly controlled by the volume ($V$) of the failed mass, instead of being controlled by $H$.

The estimated maximum volume of Pico's debris deposit is ca. 10 km$^3$, $L$ is ca. 22 km (measured along a longitudinal profile), and $H$ is ca. 2 km. The estimated volume is below, and the ratio $H/L$ is above the values given for volcanic submarine landslides in Legros (2002). The graphs in Fig. 12 show correlations between $H$, $L$, $V$ and $H/L$ data from several oceanic islands' landslide deposits (data presented in Table 3). From the graph in Fig. 12c it is clear that the mobility of Pico's debris deposit, the smallest deposit plotted, broadly fits the trend of decreasing $H/L$ for decreasing volume values. Though the control imposed by the buttressing S. Jorge flank is clear in the morphological analysis of the deposit, its effect on the landslide mobility (i.e., effect on the runout distance reached by the deposit) is not clear in the graphical analysis.

*6.2.5. Configuration, block dimensions and spatial distribution*

The general shape of the studied deposit is very similar to that of Güimar's debris deposit, resulting from the destabilization of a growing volcanic ridge on the SE flank of Tenerife Island (Canary Islands) (Krastel and Schmincke, 2002), and to that of Monte Amarelo's debris deposit, resulting from the destabilization of Fogo Island (Cape Verde) (Le Bas et al., 2007; Masson et al., 2008). Similarly to Pico, the landslide products in Tenerife and Fogo were mostly constrained by submarine channels: the Güimar landslide products were confined to the channel between Tenerife and Gran Canaria islands, and the Monte Amarelo's landslide products have been confined to the channel between Fogo and Santiago Islands. As recognized by Mitchell et al. (2008) for the sector of Pico's deposit most proximal to its source, the spatial distribution of debris is similar to one of the deposits on west La Palma, which resulted from the accumulation of debris from more than one landslide event (Playa de la Veta Debris Avalanche Complex, and Cumbre Nueva Debris Avalanche, Urgeles et al., 1999).

There are no clearly observed erosional chutes between the source zone and Pico's debris deposit, unlike many cases identified offshore some of the Canary and Hawaiian Islands (Mitchell et al., 2002). We consider that the absence of a well defined chute in Pico's deposit is due to the combination of a relatively small runout (imposed, at least in part, by the nearby topographic obstacle of the S. Jorge ridge), and the extensive masking of the source and proximal sector of the deposit by more recent volcanic products.

Though the maximum runout and volume of Pico's deposit are at least one order of magnitude lower than giant landslides recognized in other oceanic volcanoes (Canary, Hawaii), the largest block dimensions are similar to the ones observed in the Canaries (e.g.,; Masson, 1996; Krastel et al., 2001; Watts and Masson, 2001), but much smaller than the largest blocks exposed offshore the Hawaiian islands (e.g., Moore et al., 1995).

While in Güimar's deposit the largest blocks are observed in the most proximal sector of the deposit, the largest blocks visible in Pico's northern deposit are located on the distal sector of the deposit. A similar spatial arrangement of the blocks has been observed in other deposits found in Hawaii (e.g., South Kona deposit in the SW of Hawaii island —

Author's personal copy



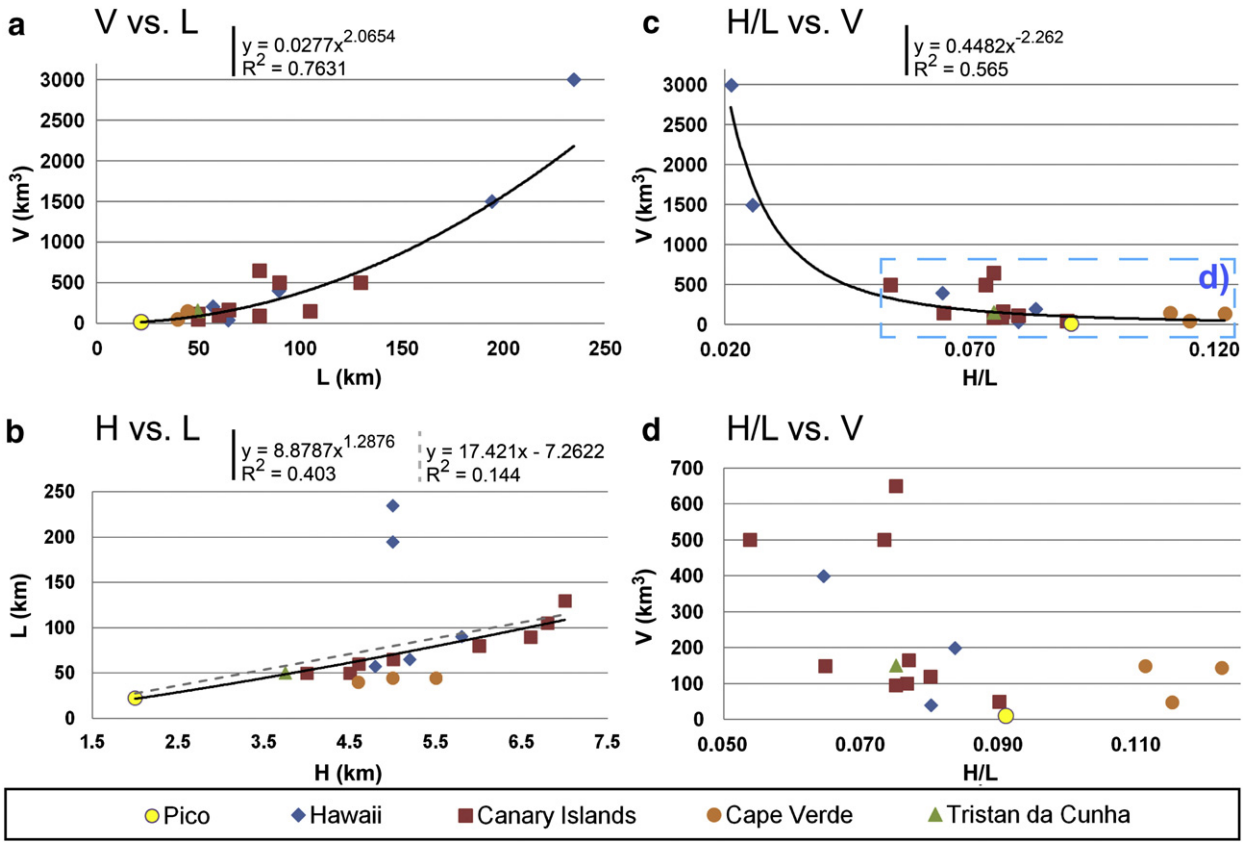


**Fig. 12.** Plots of correlation between maximum runout length ($L$) (km), height ($H$) (km), ratio $H/L$, and volume ($V$) (km$^3$) for volcanic landslides in oceanic islands. Values plotted (Hawaii Islands, Canary Islands, Tristan da Cunha, Cape Verde and Pico) and respective references are indicated in Table 3. Graphical representation, equation and coefficient of determination ($R^2$) of power law trend lines (full black lines) and linear trend line (gray dashed line).

**Table 3**
Data from landslides of Hawaii Islands, Canary Islands, Tristan da Cunha Island, Cape Verde Islands, and Pico Island, plotted in Fig. 12.

| Island | Landslide | Volume (km$^3$) | $L$ (km) | $H$ (km) | $H/L$ | References |
|---|---|---|---|---|---|---|
| *Azores Islands* | | | | | | |
| Pico | | >10 | 22 | 2 | 0.091 | This study |
| *Hawaii Islands* | | | | | | |
| Hawaii | Alika–1 | 400 | 80–100[a] | 5.8 | 0.064 | Lipman et al. (1988) |
| | Alika–2 | 200 | 55–60[a] | 4.8 | 0.083 | Lipman et al. (1988) |
| | Kae Lae slide | 40 | 65 | 5.2 | 0.080 | Legros (2002) |
| Molokai | Wailau slide | 1500 | <195 | 5 | 0.026 | Moore et al. (1989), Moore and Clague (2002), Satake et al. (2002) |
| Oahu | Nuuanu | 3000 | 235 | 5 | 0.021 | Moore et al. (1989), Moore and Clague (2002), Satake et al. (2002) |
| *Tristan da Cunha Islands* | | | | | | |
| Tristan da Cunha | | 150 | 50 | 3.75 | 0.075 | Hampton et al. (1996) |
| *Canary Islands* | | | | | | |
| El Hierro | El Golfo | 150–180[a] | 65 | 5 | 0.077 | Masson et al. (2002) |
| | Las Playas II | <50 | 50 | 4.5 | 0.090 | Masson et al. (2002) |
| | El Julan | 130 (?) | 60 | 4.6 | 0.077 | Masson et al. (2002) |
| La Palma | Cumbre Nueva | 95 | 80 | 6 | 0.075 | Masson et al. (2002) |
| | Playa de la Veta | 650 (?) | 80 | 6 | 0.075 | Masson et al. (2002) |
| Tenerife | Icod | 150 (?) | 105 | 6.8 | 0.065 | Masson et al. (2002) |
| | Roques de Garcia | 500 (?) | 130 | 7 | 0.054 | Masson et al. (2002) |
| | Orotava | 500 (?) | 90 | 6.6 | 0.073 | Masson et al. (2002) |
| | Güimar | 120 | > 50 | 4 | 0.080 | Masson et al. (2002) |
| *Cape Verde* | | | | | | |
| Fogo | Monte Amarelo | 130–160[a] | 45 | 5.5 | 0.122 | Day et al. (1999), Masson et al. (2008) |
| Santo Antão | Tope de Coroa 2 | 50 | 40 | 4.6 | 0.115 | Holm et al. (2006), Masson et al. (2008) |
| | Tope de Coroa 1 | 150 | 45 | 5 | 0.111 | Holm et al. (2006), Masson et al. (2008) |

[a] For dimensions given as intervals, the value plotted was the average of the interval range.

Author's personal copy



Moore et al., 1995) and Canary Islands (e.g., Icod deposit to the N of Tenerife, where relatively large blocks are concentrated along the margins of the deposit — Watts and Masson, 2001), which have been interpreted as evidence of the high velocity of the avalanches.

The comparatively smaller size of debris in the Canaries relative to Hawaii has been interpreted as being caused by several possible factors and processes: (1) block interaction and disintegration caused by confined flow along narrow chutes (Mitchell et al., 2002); (2) relatively more important component of failed sub-aerial material in Canary Islands, which would promote a more effective disintegration, due to a confining pressure lower in the sub-aerial domain than in the submarine domain (Mitchell et al., 2002); and (3) another factor that might influence the disintegration process is the higher proportion of pyroclastic material in the Canary, which will be more prone to disintegration than sequences constituted mainly by basaltic intrusive/extrusive rocks with a minor pyroclastic component (Mitchell et al., 2002, after Masson et al., 2002).

The debris transport in Pico's deposit was comparatively shorter and involved a smaller volume of material than the ones in Hawaii and the Canary (Fig. 12a). Moreover, the remnants of the edifice interpreted as the main source of northern Pico event(s) comprise a sequence mostly made of shallow dipping, meter thick lava flows, with no significant pyroclastic deposits. Therefore, the disintegration process in the Pico's event should be less effective than for the events in the Canary Islands.

### 6.3. Minor debris deposits

The shape of the "B" debris deposit (Fig. 6a) shows that it resulted from the accumulation of material transported from Pico's flank. However, it is not possible to define a source for this material as the limits of the deposit are undefined near Pico's submarine flank: it could result simply from the gradual accumulation of material from Pico's submarine flank; or it could be the relict of the deposit resulting from the collapse along the interpreted westernmost sub-aerial scar, now almost completely masked by the younger volcanic deposits.

The "C" debris deposit (Fig. 6a) is interpreted here as having resulted from a collapse of the uphill submarine flank of S. Jorge, where a scar is still visible (Fig. 6a, red dashed line).

### 6.4. Age of Pico's northern flank failure(s)

Previous K–Ar ages published on Pico (Féraud et al., 1980; Demande et al., 1982; Fig. 2) were acquired on a limited number of samples, and therefore do not constrain accurately the evolution of the island. Some of those previous ages also must be considered with caution, as they have been acquired on whole-rock samples, which can significantly bias the results, as discussed in Hildenbrand et al. (2012a).

On Pico's northern flank, we only observed outcrops of the volcanic deposits that cover the interpreted scar depressions (see Section 4), therefore the new K–Ar ages here obtained on fresh groundmass only provide a minimum age for the flank failure(s). The maximum age of 70 ± 4 ka and 69 ± 4 ka here obtained on the lava flows Pi10X and Pi10 R filling the sub-aerial scars (Fig. 2 and Table 2), provides a minimum age of ca. 70 ka for the occurrence of large-scale collapse(s) in Pico's northern flank.

Based on our data, we cannot establish if the two sub-aerial scarps here identified on Pico's northern flank were produced by two synchronous flank collapses. For the scar interpreted on the western sector of the fissural system (Fig. 3, feature "2"), there is not a corresponding major deposit offshore. As mentioned in Section 6.2, the flank failure deposits might appear masked by more recent volcanic/sedimentary products. As the deposit corresponding to the eastern sub-aerial scar is still clearly visible, this could suggest that the western scar is older than the eastern.

### 6.5. Possible causes and consequences

Given the geologic setting of the studied volcanic edifice, a steep volcanic ridge located on a tectonically active region, catastrophic failure of Pico northern flank may have been influenced/triggered from a variety of possible processes:

1. Progressive destabilization due to flank overload and oversteepening of TU edifice and/or along the tectonically controlled WNW–ESE volcanic ridge;
2. Triggering by NNE–SSW magma push (associated to the growth of Pico–Faial WNW–ESE volcanic ridge);
3. Fluid overpressure directly or indirectly associated with volcanic activity;
4. Local focusing of destabilization promoted by the physical discontinuity between the TU edifice surface and the fissural system deposits (Fig. 10).

Mitchell (2003) suggests a height threshold of ca. 2.5 km, above which large-scale landslides become common. Previously, Mitchell (2001) suggested that the transition between stable and unstable conditions for submarine volcanic edifices would occur gradually for an interval of edifice heights between 2 and 4 km. The height between Pico's highest point and the sea bottom is above this threshold, i.e. ca. 3.6 km. However, this maximum is attained for Pico stratovolcano, on the westernmost sector of the island, i.e. far from the studied failure. The current height between the topmost level of the source zone and the studied debris deposit is ca. 2 km. When discussing the edifice height at the time of the occurrence of a large-scale landslide, we should take into account that the current configuration of the island does not necessarily correspond to the configuration of the island at the time the landslide occurred. From the absolute ages here presented for Pico, it is not clear that the Pico stratovolcano was already developing by the time the studied flank collapse occurred. However, there was the TU volcano, whose original size and maximum altitude are not known. Therefore, the current height of ca. 2 km between the topmost sector of the source zone and the surrounding submarine floor probably constitutes an underestimation of the height at the time the flank collapse occurred. Considering that the height of the affected volcanic edifice relative to the surrounding sea floor was greater than ca. 2 km, the studied event supports the trend presented in Mitchell (2001).

One of the most important consequences of catastrophic flank collapses on volcanic ocean islands lies in their ability to trigger large tsunamis. Considering that S. Jorge lies to the north of Pico, only ca. 20 km apart, the sudden collapse of a sector several $km^3$ in dimension would have generated a large tsunami that most likely strongly impacted the southern coast of S. Jorge. Therefore, further investigations should focus on the southern coast of S. Jorge.

### 6.6. Flank failure in northern and southern Pico

The scar in northern Pico is mirrored in the S flank by a steep slope embayment that includes the currently active slump (Fig. 3, feature "1"). On the offshore area adjacent to this embayment on the southern flank there is a significant deposit whose debris were identified on side scan sonar data (Mitchell, 2003), and which constitutes a topographic bulge on the low resolution bathymetry (see Fig. C.1, in Appendix C). Therefore, both Pico's flanks have been affected by large-scale flank failure, highlighting the strong susceptibility of steep ridge-shaped edifices to flank failure.

## 7. Conclusions

From the new geomorphologic, stratigraphic, structural and geochronologic data acquired in the present study, we conclude that the evolution of the Pico Island volcanic ridge was marked by the

Author's personal copy



occurrence of flank failures in both N and S flanks. The landslide debris resulting from the collapse of Pico's N flank have accumulated on the ocean floor of the S. Jorge Channel, and their likely sources are two major scars standing out on Pico's slope map.

Here we conclude that, more than 70 ka ago, after the growth of the TU volcanic edifice, Pico's northern flank collapsed catastrophically, forming two steep and arcuate sub-aerial scars. The material mobilized from the eastern source zone likely exceeds 10 $km^3$, and consists of a mixture of meter to hectometer blocks. These flowed towards greater depths in the E, along the channel between Pico–Faial and S. Jorge volcanic ridges. The tsunami resulting from the $km^3$ collapse most probably rapidly traveled the ca. 20 km wide channel and violently impacted S. Jorge's southern flank. Since ca. 70 ka and until historic times, more recent deposits, volcanic products related to the growth of the WNW–ESE fissural system and Pico stratovolcano have been progressively filling the sub-aerial scars. These post-collapse volcanic products, and marine sediments as well, have been covering the island's submarine flanks, masking partially or completely the evidence of failure events.

The evolution of the Pico's sector in the Pico–Faial volcanic ridge was also marked by large-scale flank failure on the southern flank, generating a sub-aerial scar (symmetrical to the easternmost scar in the N flank) and a debris deposit observed on the offshore. Further investigations are being conducted, in order to constrain the evolution of this volcanic ridge.

Supplementary data to this article can be found online at http://dx.doi.org/10.1016/j.jvolgeores.2014.01.002.

## Acknowledgments

This is a contribution to Project MEGAHazards, funded by FCT (PTDC/CTE-GIX/108149/2008), Portugal. The first author has a PhD scholarship funded by FCT (SFRH/BD/68983/2010). We thank EMEPC (http://www.emepc.pt/), and Nuno Lourenço in particular, for making the bathymetric data available, without which this study would not have been possible. The final version of this paper benefited from the constructive and thorough comments by N. Mitchell.

## References

Afonso, A., Gomes, F., Fernandes, M., 2002. IGeoE: Cartografia de qualidade - a base de um SIG. Trib. das Autarquias 108, 13–14 (Jun. 2002).

Andersen, O.B., Knudsen, P., Kenyon, S., Trimmer, R., 1999. Recent improvement in the KMS global marine gravity field. Boll. Geofis. Teor. Appl. 40 (3–4), 369–377.

Borges, J.F., Bezzeghoud, M., Buforn, E., Pro, C., Fitas, A., 2007. The 1980, 1997 and 1998 Azores earthquakes and some seismo-tectonic implications. Tectonophysics 435 (1–4), 37–54. http://dx.doi.org/10.1016/j.tecto.2007.01.008.

Boulesteix, T., Hildenbrand, A., Gillot, P.Y., Soler, V., 2012. Eruptive response of oceanic islands to giant landslides: new insights from the geomorphologic evolution of the Teide–Pico Viejo volcanic complex (Tenerife, Canary). Geomorphology 138 (1), 61–73. http://dx.doi.org/10.1016/j.geomorph.2011.08.025.

Boulesteix, T., Hildenbrand, A., Soler, V., Quidelleur, X., Gillot, P.Y., 2013. Coeval giant landslides in the Canary Islands: implications for global, regional and local triggers of giant flank collapses on oceanic volcanoes. J. Volcanol. Geotherm. Res. 257, 90–98. http://dx.doi.org/10.1016/j.jvolgeores.2013.03.008.

Burrough, P.A., McDonnell, R.A., 1998. Principles of Geographical Information Systems. Oxford University Press, New York (333 pp.).

Carracedo, J.C., Day, S.J., Guillou, H., Torrado, F.J.P., 1999. Giant Quaternary landslides in the evolution of La Palma and El Hierro, Canary Islands. J. Volcanol. Geotherm. Res. 94 (1–4), 169–190. http://dx.doi.org/10.1016/S0377-0273(99)00102-X.

Cassignol, C., Gillot, P.Y., 1982. Range and effectiveness of unspiked potassium–argon dating: experimental groundwork and applications. In: Odin, G.S. (Ed.) Numerical Dating in Stratigraphy. John Wiley & Sons Ltd, Chichester, England, pp. 159–179.

Catalão, J., Bos, M.S., 2008. Sensitivity analysis of the gravity geoid estimation: a case study on the Azores plateau. Phys. Earth Planet. Inter. 168 (1–2), 113–124. http://dx.doi.org/10.1016/j.pepi.2008.05.010.

Day, S.J., Heleno da Silva, S.I.N., Fonseca, J.F.B.D., 1999. A past giant lateral collapse and present-day flank instability of Fogo, Cape Verde Islands. J. Volcanol. Geotherm. Res. 94 (1–4), 191–218. http://dx.doi.org/10.1016/S0377-0273(99)00103-1.

Demande, J., Fabriol, R., Gérard, A., Iundt, F., 1982. Prospection géothermique des Iles de Faial et Pico (Açores). Report 82SGN003GTH, Bureau de Recherches Géologiques et Minières, Orléans, France.

Deplus, C., Le Friant, A., Boudon, G., Komorowski, J.C., Villemant, B., Harford, C., Ségoufin, J., Cheminée, J.L., 2001. Submarine evidence for large-scale debris avalanches in the Lesser Antilles Arc. Earth Planet. Sci. Lett. 192 (2), 145–157. http://dx.doi.org/10.1016/S0012-821X(01)00444-7.

Duffield, W.A., Stieltjes, L., Varet, J., 1982. Huge landslide blocks in the growth of Piton de la Fournaise, La Réunion and Kilauea volcano, Hawaii. J. Volcanol. Geotherm. Res. 12 (1–2), 147–160. http://dx.doi.org/10.1016/0377-0273(82)90009-9.

Féraud, G., Kaneoka, I., Allègre, C.J., 1980. K/Ar ages and stress pattern in the Azores: geodynamic implications. Earth Planet. Sci. Lett. 46 (2), 275–286. http://dx.doi.org/10.1016/0012-821X(80)90013-8.

Fernandes, R.M.S., Bastos, L., Miranda, J.M., Lourenço, N., Ambrosius, B.A.C., Noomen, R., Simons, W., 2006. Defining the plate boundaries in the Azores region. J. Volcanol. Geotherm. Res. 156 (1–2), 1–9. http://dx.doi.org/10.1016/j.jvolgeores.2006.03.019.

Forjaz, V.H., 1966. Carta geológica do sistema vulcânico Faial-Pico-S. Jorge. Escala 1:200 000. In: Machado, F., Forjaz, V.H. (Eds.),A actividade vulcânica na ilha do Faial (1957-67), 1968. Comissão de Turismo da Horta, 89 pp.

Germa, A., Quidelleur, X., Lahitte, P., Labanieh, S., Chauvel, C., 2011. The K–Ar Cassignol–Gillot technique applied to western Martinique lavas: a record of Lesser Antilles arc activity from 2 Ma to Mount Pelée volcanism. Quat. Geochronol. 6 (3–4), 341–355. http://dx.doi.org/10.1016/j.quageo.2011.02.001.

Gillot, P.Y., Cornette, Y., 1986. The Cassignol technique for potassium–argon dating, precision and accuracy: examples from the Late Pleistocene to Recent volcanics from southern Italy. Chem. Geol. Isot. Geosci. Sect. 59, 205–222. http://dx.doi.org/10.1016/0168-9622(86)90072-2.

Gillot, P.Y., Cornette, Y., Max, N., Floris, B., 1992. Two reference materials, trachytes MDO-G and ISH-G, for Argon dating (K–Ar and $^{40}Ar/^{39}Ar$) of Pleistocene and Holocene rocks. Geostand. Newslett. 16 (1), 55–60. http://dx.doi.org/10.1111/j.1751-908X.1992.tb00487.x.

Gillot, P.Y., Lefèvre, J.C., Nativel, P.E., 1994. Model for the structural evolution of the volcanoes of Réunion Island. Earth Planet. Sci. Lett. 122 (3–4), 291–302. http://dx.doi.org/10.1016/0012-821X(94)90003-5.

Gillot, P.Y., Hildenbrand, A., Lefèvre, J.C., Albore-Livadie, C., 2006. The K/Ar dating method: principle, analytical techniques and application to Holocene volcanic eruptions in Southern Italy. Acta Vulcanol. 18, 55–66.

Golden Software, Inc., 2002. Surfer 8: contouring and 3D surface mapping for scientists and engineers—user guide. In: Golden Software, Incorporated (Ed.). 640 pp.

Hampton, M.A., Lee, H.J., Locat, J., 1996. Submarine landslides. Rev. Geophys. 34 (1), 33–59. http://dx.doi.org/10.1029/95RG03287.

Hildenbrand, A., Gillot, P.Y., Bonneville, A., 2006. Offshore evidence for a huge landslide of the northern flank of Tahiti–Nui (French Polynesia). Geochemistry Geophysics Geosystems 7 (3), Q03006. http://dx.doi.org/10.1029/2005GC001003.

Hildenbrand, A., Madureira, P., Ornelas Marques, F., Cruz, I., Henry, B., Silva, P., 2008. Multi-stage evolution of a sub-aerial volcanic ridge over the last 1.3 Myr: S. Jorge Island, Azores Triple Junction. Earth Planet. Sci. Lett. 273 (3–4), 289–298. http://dx.doi.org/10.1016/j.epsl.2008.06.041.

Hildenbrand, A., Marques, F.O., Costa, A.C.G., Sibrant, A.L.R., Silva, P.M.F., Henry, B., Miranda, J.M., Madureira, P., 2012a. Reconstructing the architectural evolution of volcanic islands from combined K/Ar, morphologic, tectonic, and magnetic data: the Faial Island example (Azores). J. Volcanol. Geotherm. Res. 241–242, 39–48. http://dx.doi.org/10.1016/j.jvolgeores.2012.06.019.

Hildenbrand, A., Marques, F.O., Catalão, J., Catita, C.M.S., Costa, A.C.G., 2012b. Large-scale active slump of the southeastern flank of Pico Island, Azores. Geology 40 (10), 939–942. http://dx.doi.org/10.1130/G33303.1.

Hildenbrand, A., Marques, F.O., Costa, A.C.G., Sibrant, A.L.R., Silva, P.F., Henry, B., Miranda, J.M., Madureira, P., 2013a. Reply to the comment by Quartau and Mitchell on "Reconstructing the architectural evolution of volcanic islands from combined K/Ar, morphologic, tectonic, and magnetic data: the Faial Island example (Azores)", J. Volcanol. Geotherm. Res. 241–242, 39–48, by Hildenbrand et al. (2012). J. Volcanol. Geotherm. Res. 255, 127–130. http://dx.doi.org/10.1016/j.jvolgeores.2013.01.015.

Hildenbrand, A., Marques, F.O., Catalão, J., Catita, C.M.S., Costa, A.C.G., 2013b. Large-scale active slump of the southeastern flank of Pico Island, Azores: reply. Geology 41 (12), e302. http://dx.doi.org/10.1130/G34879Y.1.

Holm, P.M., Wilson, J.R., Christensen, B.P., Hansen, L., Hansen, S.L., Hein, K.M., Mortensen, A.K., Pedersen, R., Plesner, S., Runge, M.K., 2006. Sampling the Cape Verde mantle plume: evolution of melt compositions on Santo Antão, Cape Verde Islands. J. Petrol. 47 (1), 145–189. http://dx.doi.org/10.1093/petrology/egi071.

Hunt, J.E., Wynn, R.B., Masson, D.G., Talling, P.J., Teagle, D.A.H., 2011. Sedimentological and geochemical evidence for multistage failure of volcanic island landslides: a case study from Icod landslide on north Tenerife, Canary Islands. Geochem. Geophys. Geosyst. 12 (12), Q12007. http://dx.doi.org/10.1029/2011GC003740.

Kongsberg, S., 2007. EM 120 Multibeam Echo Sounder, Product Description. Kongsberg Maritime AS, Norway, Bremerhaven, Pangaea 44 p. (available at http://epic.awi.de/26725/1/Kon2007a.pdf).

Krastel, S., Schmincke, H.U., 2002. The channel between Gran Canaria and Tenerife: constructive processes and destructive events during the evolution of volcanic islands. International Journal of Earth Sciences 91 (4), 629–641. http://dx.doi.org/10.1007/s00531-002-0285-8.

Krastel, S., Schmincke, H.U., Jacobs, C.L., Rihm, R., Le Bas, T.P., Alibés, B., 2001. Submarine landslides around the Canary Islands. J. Geophys. Res. 106 (B3), 3977–3997. http://dx.doi.org/10.1029/2000JB900413.

Le Bas, T.P., Masson, D.G., Holtom, R.T., Grevemeyer, I., 2007. Slope failures on the flanks of the southern Cape Verde Islands. In: Lykousis, V., Sakellariou, D., Locat, J. (Eds.), Submarine Mass Movements and Their Consequences. Springer, Dordrecht, Netherlands, pp. 337–345.

Le Friant, A., Boudon, G., Deplus, C., Villemant, B., 2003. Large-scale flank collapse events during the activity of Montagne Pelée, Martinique, Lesser Antilles. J. Geophys. Res. Solid Earth 108 (B1), 2055. http://dx.doi.org/10.1029/2001JB001624.

Author's personal copy



Legros, F., 2002. The mobility of long-runout landslides. Eng. Geol. 63 (3–4), 301–331. http://dx.doi.org/10.1016/S0013-7952(01)00090-4.
Lipman, P.W., Normark, W.R., Moore, J.G., Wilson, J.B., Gutmacher, C.E., 1988. The giant submarine Alika debris slide, Mauna Loa, Hawaii. J. Geophys. Res. Solid Earth 93 (B5), 4279–4299. http://dx.doi.org/10.1029/JB093iB05p04279.
Lourenço, N., Miranda, J.M., Luis, J.F., Ribeiro, A., Mendes Victor, L.A., Madeira, J., Needham, H.D., 1998. Morpho-tectonic analysis of the Azores Volcanic Plateau from a new bathymetric compilation of the area. Mar. Geophys. Res. 20 (3), 141–156. http://dx.doi.org/10.1023/A%3A1004505401547.
Madeira, J., 1998. Estudos de neotectónica nas ilhas do Faial, Pico e S. Jorge: Uma contribuição para o conhecimento geodinâmico da junção tripla dos Açores. PhD thesis Faculdade de Ciências, Univ, Lisboa, Portugal (481 pp.).
Madeira, J., Brum da Silveira, A., 2003. Active tectonics and first paleoseismological results in Faial, Pico and S. Jorge islands (Azores, Portugal). Ann. Geophys. 46 (5), 733–761. http://dx.doi.org/10.4401/ag-3453.
Marques, F.O., Catalão, J.C., DeMets, C., Costa, A.C.G., Hildenbrand, A., 2013. GPS and tectonic evidence for a diffuse plate boundary at the Azores Triple Junction. Earth and Planetary Science Letters 381, 177–187. http://dx.doi.org/10.1016/j.epsl.2013.08.051.
Masson, D.G., 1996. Catastrophic collapse of the volcanic island of Hierro 15 ka ago and the history of landslides in the Canary Islands. Geology 24 (3), 231–234. http://dx.doi.org/10.1130/0091-7613(1996)024<0231:CCOTVI>2.3.CO;2.
Masson, D.G., Watts, A.B., Gee, M.J.R., Urgeles, R., Mitchell, N.C., Le Bas, T.P., Canals, M., 2002. Slope failures on the flanks of the western Canary Islands. Earth Sci. Rev. 57 (1–2), 1–35. http://dx.doi.org/10.1016/S0012-8252(01)00069-1.
Masson, D.G., Harbitz, C.B., Wynn, R.B., Pedersen, G., Lovholt, F., 2006. Submarine landslides: processes, triggers and hazard prediction. Phil. Trans. R. Soc. A 364, 2009–2039. http://dx.doi.org/10.1098/rsta.2006.1810.
Masson, D.G., Le Bas, T.P., Grevemeyer, I., Weinrebe, W., 2008. Flank collapse and large-scale landsliding in the Cape Verde Islands, off West Africa. Geochem. Geophys. Geosyst. 9 (7), Q07015. http://dx.doi.org/10.1029/2008GC001983.
Mitchell, N.C., 2001. The transition from circular to stellate forms of submarine volcanoes. J. Geophys. Res. Solid Earth 106 (B2), 1987–2003. http://dx.doi.org/10.1029/2000JB900263.
Mitchell, N.C., 2003. Susceptibility of mid-ocean ridge volcanic islands and seamounts to large-scale landsliding. J. Geophys. Res. 108 (B8), 2397. http://dx.doi.org/10.1029/2002JB001997.
Mitchell, N.C., Masson, D.G., Watts, A.B., Gee, M.J.R., Urgeles, R., 2002. The morphology of the submarine flanks of volcanic ocean islands: a comparative study of the Canary and Hawaiian hotspot islands. J. Volcanol. Geotherm. Res. 115 (1–2), 83–107. http://dx.doi.org/10.1016/S0377-0273(01)00310-9.
Mitchell, N.C., Beier, C., Rosin, P.L., Quartau, R., Tempera, F., 2008. Lava penetrating water: submarine lava flows around the coasts of Pico Island, Azores. Geochem. Geophys. Geosyst. 9 (3), Q03024. http://dx.doi.org/10.1029/2007GC001725.
Mitchell, N.C., Quartau, R., Madeira, J., 2012. Assessing landslide movements in volcanic islands using near-shore marine geophysical data: south Pico Island, Azores. Bull. Volcanol. 74 (2), 483–496. http://dx.doi.org/10.1007/s00445-011-0541-5.
Mitchell, N.C., Quartau, R., Madeira, J., 2013. Large-scale active slump of the southeastern flank of Pico Island, Azores: comment. Geology 41 (12), e301. http://dx.doi.org/10.1130/G34006C.1.
Moore, J.G., Clague, D.A., 2002. Mapping the Nuuanu and Wailau Landslides in Hawaii. In: Takahashi, E., Lipman, P.W., Garcia, M.O., Naka, J., Aramaki, S. (Eds.),Hawaiian volcanoes: deep underwater perspectives. Geophysical Monograph Series, 128. American Geophysical Union, Washington D.C., pp. 223–244. http://dx.doi.org/10.1029/GM128.
Moore, J.G., Clague, D.A., Holcomb, R.T., Lipman, P.W., Normark, W.R., Torresan, M.E., 1989. Prodigious submarine landslides on the Hawaiian Ridge. J. Geophys. Res. Solid Earth 94 (B12), 17465–17484. http://dx.doi.org/10.1029/JB094iB12p17465.
Moore, I.D., Lewis, A., Gallant, J.C., 1993. Terrain properties: estimation methods and scale effects. In: Jakeman, A.J., Beck, M.B., MCaleer, M.J. (Eds.),Modelling Change in Environmental Systems. John Wiley and Sons, New York.
Moore, J.G., Bryan, W.B., Beeson, M.H., Normark, W.R., 1995. Giant blocks in the South Kona landslide, Hawaii. Geology 23 (2), 125–128. http://dx.doi.org/10.1130/0091-7613(1995) 023<0125:GBITSK>2.3.CO;2.
Navarro, J.M., Coello, J., 1989. Depressions Originated by Landslide Processes in Tenerife. ESF Meeting on Canarian Volcanism, Lanzarote 150–152.
Nunes, J.C., 1999. A actividade vulcânica na ilha do Pico do Plistocénico Superior ao Holocénico: Mecanismo eruptivo e hazard vulcânico. PhD thesis Universidade dos Açores, Ponta Delgada, Portugal (356 pp.(available at: http://www.jcnunes.uac.pt/principal.htm)).
Nunes, J.C., 2002. Lateral collapse structures in Pico Island (Azores): mechanism, constraints and age. 3ª Assembleia Luso Espanhola de Geodesia e Geofísica, Valencia, pp. 731–735.
Nunes, J.C., Camacho, A., França, Z., Montesinos, F.G., Alves, M., Vieira, R., Velez, E., Ortiz, E., 2006. Gravity anomalies and crustal signature of volcano-tectonic structures of Pico Island (Azores). J. Volcanol. Geotherm. Res. 156 (1–2), 55–70. http://dx.doi.org/10.1016/j.jvolgeores.2006.03.023.
Quartau, R., Mitchell, N.C., 2013. Comment on "Reconstructing the architectural evolution of volcanic islands from combined K/Ar, morphologic, tectonic, and magnetic data: the Faial Island example (Azores)" by Hildenbrand et al. (2012) [J. Volcanol. Geotherm. Res. 241–242 (2012) 39–48]. Journal of Volcanology and Geothermal Research 255, 124–126. http://dx.doi.org/10.1016/j.jvolgeores.2012.12.020.
Quartau, R., Trenhaile, A.S., Mitchell, N.C., Tempera, F., 2010. Development of volcanic insular shelves: insights from observations and modelling of Faial Island in the Azores Archipelago. Mar. Geol. 275 (1–4), 66–83. http://dx.doi.org/10.1016/j.margeo.2010.04.008.
Quartau, R., Tempera, F., Mitchell, N.C., Pinheiro, L.M., Duarte, H., Brito, P.O., Bates, C.R., Monteiro, J.H., 2012. Morphology of the Faial Island shelf (Azores): the interplay between volcanic, erosional, depositional, tectonic and mass-wasting processes. Geochem. Geophys. Geosyst. 13, Q04012. http://dx.doi.org/10.1029/2011GC003987.
Samper, A., Quidelleur, X., Lahitte, P., Mollex, D., 2007. Timing of effusive volcanism and collapse events within an oceanic arc island: Basse–Terre, Guadeloupe archipelago (Lesser Antilles Arc). Earth Planet. Sci. Lett. 258 (1–2), 175–191. http://dx.doi.org/10.1016/j.epsl.2007.03.030.
Satake, K., Smith, J.R., Shinozaki, K., 2002. Three-dimensional reconstruction and tsunami model of the Nuuanu and Wailau giant landslides, Hawaii. In: Takahashi, E., Lipman, P.W., Garcia, M.O., Naka, J., Aramaki, S. (Eds.),Hawaiian Volcanoes: Deep Underwater Perspectives. Geophysical Monograph Series 128. American Geophysical Union, Washington D.C., pp. 333–346. http://dx.doi.org/10.1029/GM128.
Scheidegger, A.E., 1973. On the prediction of the reach and velocity of catastrophic landslides. Rock Mech. 5 (4), 231–236. http://dx.doi.org/10.1007/BF01301796.
Steiger, R.H., Jäger, E., 1977. Subcommission on geochronology: convention on the use of decay constants in geo- and cosmochronology. Earth Planet. Sci. Lett. 36 (3), 359–362. http://dx.doi.org/10.1016/0012-821X(77)90060-7.
Urgeles, R., Masson, D.G., Canals, M., Watts, A.B., Le Bas, T., 1999. Recurrent large-scale landsliding on the west flank of La Palma, Canary Islands. J. Geophys. Res. Solid Earth 104 (B11), 25331–25348. http://dx.doi.org/10.1029/1999JB900243.
Watts, A.B., Masson, D.G., 2001. New sonar evidence for recent catastrophic collapses of the north flank of Tenerife, Canary Islands. Bull. Volcanol. 63 (1), 8–19.
Woodhall, D., 1974. Geology and volcanic history of Pico Island Volcano, Azores. Nature 248, 663–665. http://dx.doi.org/10.1038/248663a0.

## Appendix A. DEM – grid building

We composed a 50 m resolution mosaic grid with the bathymetric data grid, the 10 m resolution topographic grid of Pico, and the 50 m resolution topographic grids of Faial and S. Jorge Islands (Fig. A.1a).

For the shallow submarine zone, we integrated data from Fig. 2 in Mitchell et al. (2008), showing the shallow depth bathymetry of Pico's northern flank, as a contour map with 100 m spaced contour lines. On this map, the wide coastal shelf is visible. The non-consideration of this shallow, low-slope feature would impact directly on the surfaces interpolated, submarine profiles and, consequently, on the analysis of the deposits proximal to the island´s flank.

In order to extract the data from Mitchell et al.'s (2008) map: (a) the figure was georeferenced (1st order polynomial transformation, with an accuracy of ± 8.9 m RMS, and a maximum residual of 19.56 m); (b) the compatibility between data sets was verified by superimposing the contour maps from both data sets and comparing the contour lines on overlapping areas; (c) the contour lines were individually digitized from the georeferenced Mitchell et al.'s (2008) map for the no-data zone of our study area, the respective depth values were attributed, and these contour lines were integrated in our general grid data file (Fig. A.1b).

Afterwards, we performed a 200 m resolution spatial interpolation (kriging) for the study area (Fig. A.2a). The standard deviations associated with the interpolation method used are presented in Fig. A.2b. Though the maximum standard deviation value obtained on the whole grid area is 170 m, on the area of interest for this study the standard deviation values in heights range between 0 m and 25 m. For this kriging operation, considering the Z-value

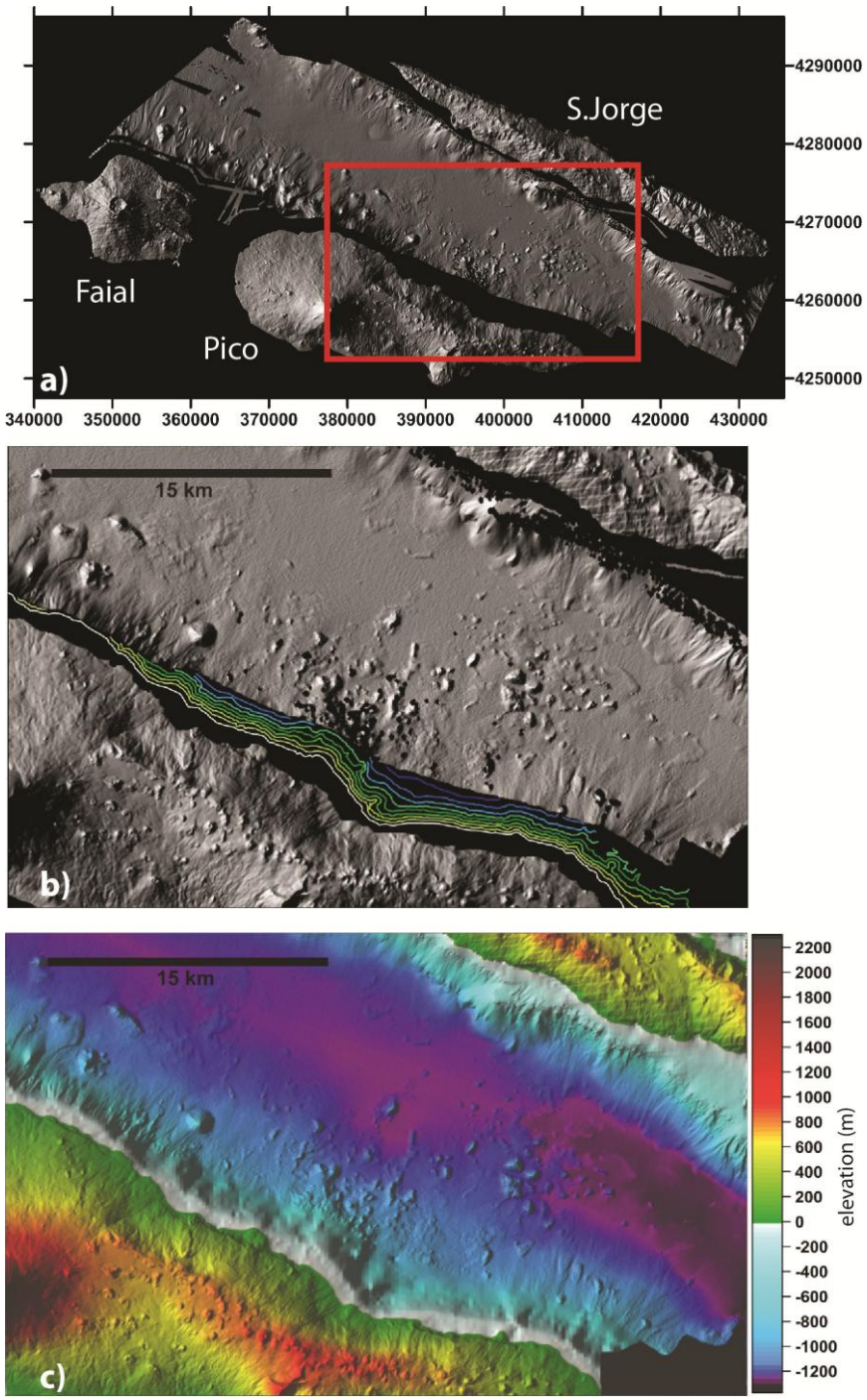


**Fig. A.1. (a)** initial 50 m resolution grid mosaic with topography of Pico, Faial and S. Jorge, and deep bathymetry (lighting from ENE). Red rectangle: study area (Figs. b and c). **(b)** zoom on the initial grid mosaic (lighting from ENE) with plot of the 100 m spaced contour lines extracted from Mitchell et al. (2008). **(c)** Surface resulting from the filling of the originally no-data zones (b) with 200 m resolution spatial interpolation data, considering the contour lines extracted from Mitchell et al. (2008) (lighting from ENE).

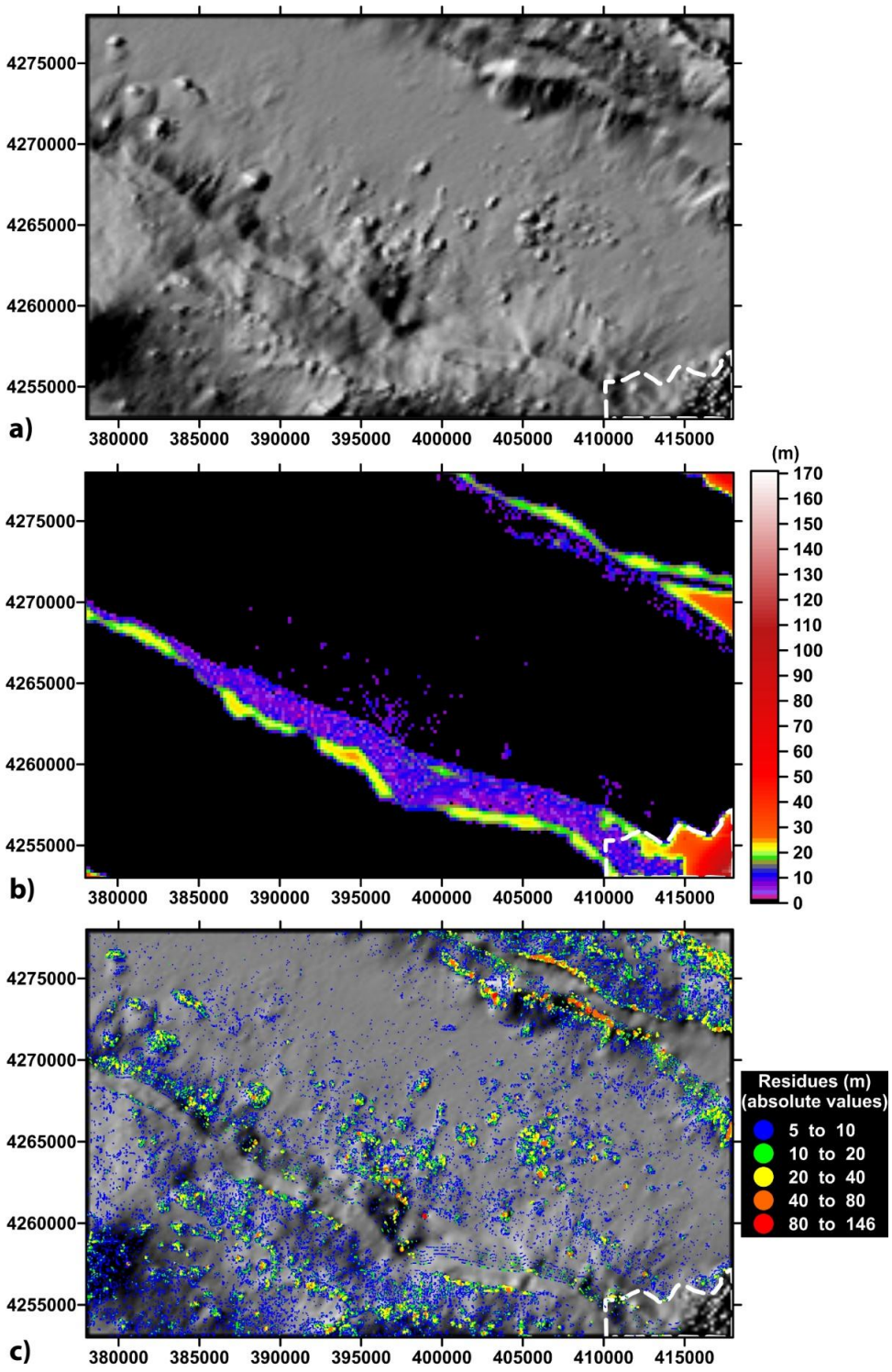


**Fig. A.2. (a)** Shaded relief of the 200 m resolution DEM, considering the data from the original grids and the data extracted from Mitchell et al's (2008) figure (lighting from ENE). White dashed line at the right bottom corner comprises the area blanked afterwards due to strong artifacts; **(b)** Standard deviations associated with the spatial interpolation performed in the building of the 200 m resolution DEM presented in (a); **(c)** Map of the residues between the 200 m resolution interpolated surface and the data input.

residues between the interpolated surface and the data input for interpolation (Fig. A.2c), an accuracy of 5.4 m RMS was obtained, with a residue's maximum absolute value of 125.0 m.

Then, a 50 m resolution mosaic was built for the study area, from the general 50 m resolution mosaic (Fig. A.1c), filling the no-data zones with the data from the 200 m resolution grid previously built.

**Reference cited in Appendix A:**

Mitchell, N.C., Beier, C., Rosin, P., Quartau, R., Tempera, F., 2008. Submarine lava flows around the coasts of Pico Island, Azores. Geochemistry, Geophysics, Geosystems 9, Q03024, doi:10.1029/2007GC001725.

## Appendix B. Volume and Maximum Thickness of Main Debris Deposit

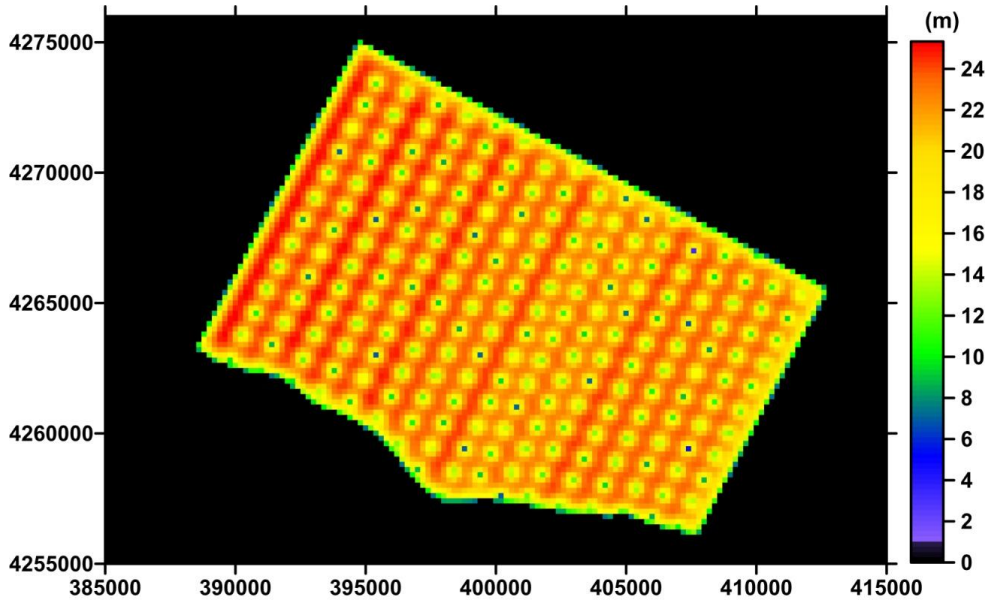


**Fig. B.1.** Standard deviations associated with the spatial interpolations performed in the building of the theoretical basal surfaces for volume calculation.

**Table B.1.** Root Mean Square (RMS) errors associated with the kriging interpolation performed to build the theoretical basal surfaces used in the volume estimation. In "Complete Grid" we consider the residuals of Z values between the interpolated surface and all the data points considered in the interpolation. In "Deposit's blanked area" we consider only the residuals of Z values between the interpolated surface and the "theoretical" data points inserted in the deposit's blanked area (Fig. B.1, black dashed line).

| | **Complete Grid** | | **Deposit's blanked area** | |
|---|---|---|---|---|
| **Theoretical Basal Surfaces** | RMS (m) | Maximum residue (absolute value) (m) | RMS (m) | Maximum residue (absolute value) (m) |
| **Minimum volume** | 5.5 | 145.1 | 4.7 | 22.9 |
| **Maximum volume** | 5.5 | 145.1 | 5.6 | 26.0 |

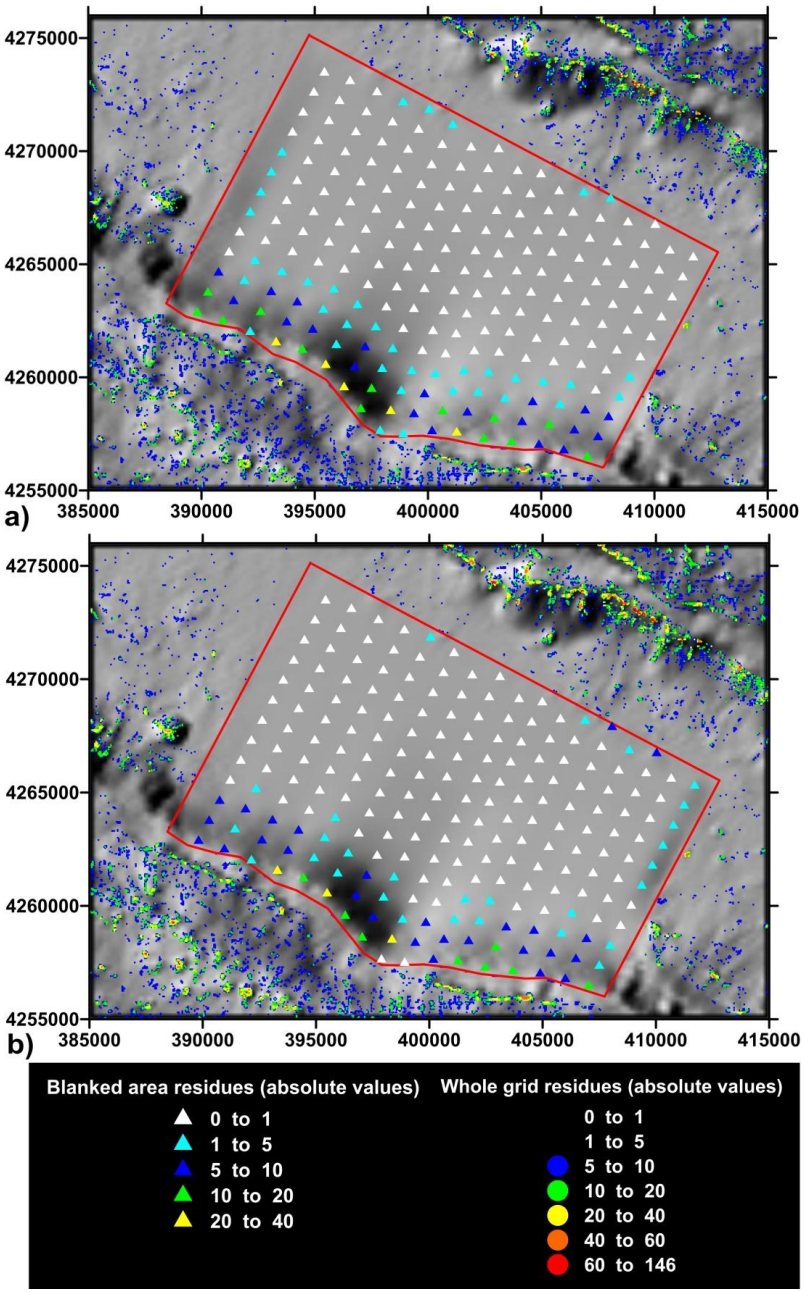


**Fig. B.2.** Maps of the residues absolute values (values in meters) for the basal surface used in the maximum volume calculation **(a)**, and for the basal surface used in the minimum volume calculation **(b)**. The area blanked for the construction of the basal surfaces is indicated as a full red line. In order to obtain clearer maps, the residual values lower than ± 5 m are not represented outside the blanked area.

## Appendix C - Debris deposit on Pico's southern flank

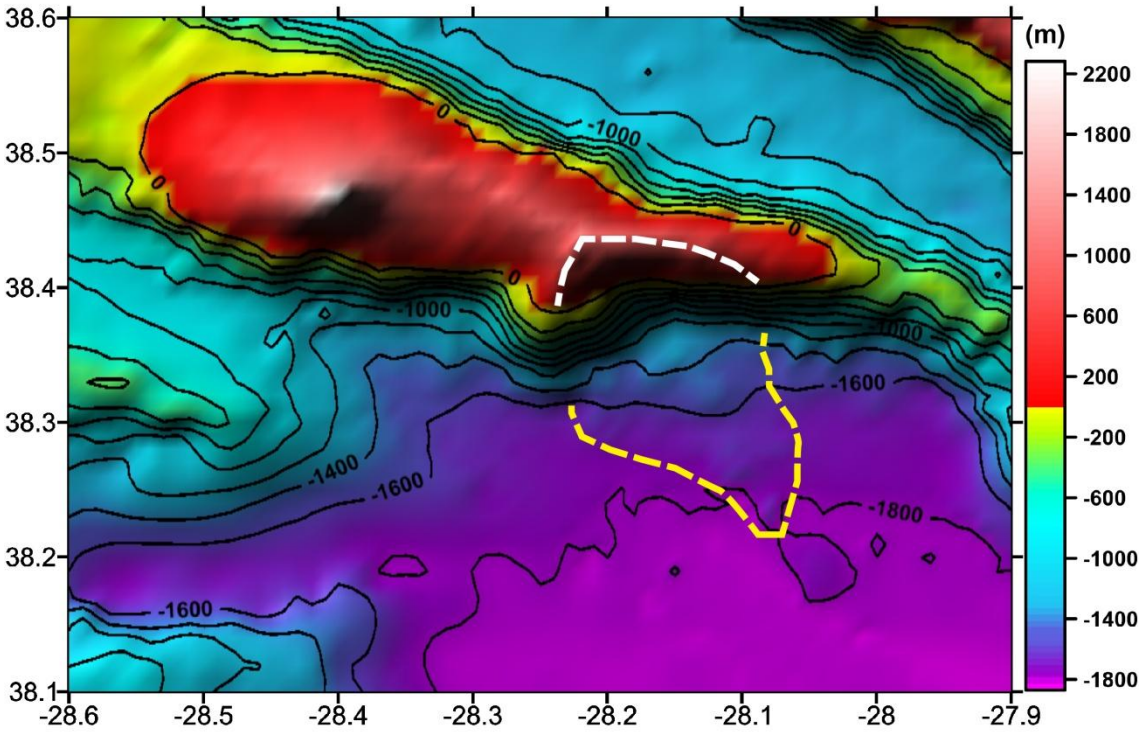


**Fig. C.1.** Shaded surface of Pico Island and surrounding sea floor (lighting from E). 1300 m resolution DEM, from Lourenço et al. (1998), available at http://w3.ualg.pt/~jluis/. White dashed line - sub-aerial embayment in the S flank. Yellow dashed line - limits of the debris deposit interpreted on the offshore.

## Reference cited in Appendix C:

Lourenço, N., Miranda, J.M., Luis, J.F., Ribeiro, A., Mendes Victor, L.A., Madeira, J., Needham, H.D., 1998. Morpho-tectonic analysis of the Azores Volcanic Plateau from a new bathymetric compilation of the area. Marine Geophysical Researches 20 (3), 141-156. http://dx.doi.org/10.1023/A%3A1004505401547.

# Chapter 5

## Growth and collapse of Pico Island during its 200 kyr life time (Pico-Faial ridge, Azores Triple Junction)

## (Costa et al., *submitted*)

# Growth and collapse of Pico Island during its 200 kyr life time (Pico-Faial ridge, Azores Triple Junction)

*(submitted)*

**A.C.G. Costa[1,2*], A. Hildenbrand[2,3], F.O. Marques[4], A.L.R. Sibrant[2], A. Santos de Campos[5]**

(1) Universidade de Lisboa and IDL, Lisboa, Portugal
(2) Univ. Paris-Sud, Laboratoire GEOPS, UMR8148, Orsay, F-91405
(3) CNRS, Orsay, F-91405
(4) Universidade de Lisboa, Lisboa, Portugal
(5) EMEPC, Paço de Arcos, Portugal

**Abstract**

The Pico Island constitutes the easternmost sub-aerial domain of a steep WNW-ESE volcanic ridge, which has developed within the Nubia-Eurasia diffuse plate boundary (Azores Triple Junction). The island comprises three volcanic systems, from older to younger: the Topo Volcano, the Fissural System, and the Pico Stratovolcano. From a high-resolution Digital Elevation Model (10 m), and new bathymetric, stratigraphic, structural, and high-precision K-Ar data, we reconstruct the main successive stages of growth and partial destruction of the island over the last 200 kyr. The Topo Volcano is partly exposed in Pico SE flank and is here dated between 186 ± 5 and 115 ± 4 ka. It was significantly destroyed by a N-directed large-scale flank collapse between ca. 125 and 70 ka. During the same period, gradual deformation started in the southern flank, producing a slump complex that is still active. A first episode of deformation occurred between ca. 125 and 115 ka along the master fault of the slump. Between ca. 115 and 75 ka, the scar was partially filled by volcanic products erupted from volcanic cones developed within the slump depression, and possibly also from the early WNW-ESE Fissural System. Subsequent deformation in the slump area affected in part the filling units, leading to the individualization of secondary curved faults. Between ca. 125 and 69 ka, the distal part of the southern flank , the scar filling units and the early sub-aerial sequence of the Fissural System

experienced catastrophic flank collapse towards the S, which generated a large debris-avalanche deposit with a minimum run-out of ca. 17 km. Recent volcanic products have gradually masked the mass-wasting scars. The young Pico Stratovolcano grew in the westernmost sector of the island, at least since ca. 57 ka. Its southern flank has been significantly destroyed by flank collapse(s), and subsequently covered by more recent volcano-sedimentary rocks. The evolution of the Pico-Faial volcanic ridge in the last 200 kyr has been marked by simultaneous volcanic growth and destruction in both Pico and Faial islands. While the Topo Volcano grew in Pico (ca. 186-125 ka) and was partially destroyed (ca. 125-115 ka), in Faial Island the period defined for major deformation in the Faial graben ended (ca. 360-115 ka), and a central volcano started growing inside the graben (ca. 130-115 ka). This rapid and simultaneous evolution of Pico and Faial islands constitutes evidence for the accommodation of extension associated with the Nu-Eu plate boundary on this ridge during the last 200 kyr.

***Keywords:*** large-scale mass wasting; volcanic construction; flank collapse; active slump; K-Ar dating; Pico-Faial volcanic ridge; Azores Triple Junction

## 1. Introduction

The evolution of oceanic islands is generally marked by the interplay between volcanic construction and repeated destruction by a variety of mass-wasting processes. Large-scale lateral flank instabilities, especially, have been recognized as a ubiquitous and potentially highly destructive geological phenomenon documented around many volcanic islands worldwide, e.g. in Hawaii (Lipman et al., 1988; Moore et al., 1989,1994; Moore and Clague, 2002), in the Cape Verde archipelago (e.g., Day et al., 1999; Masson et al., 2008), in French Polynesia (Clouard et al., 2001; Clouard and Bonneville, 2004; Hildenbrand et al., 2004; 2006), and in the Canary Islands (e.g., Carracedo. 1994; Krastel et al., 2001; Masson et al., 2002). Two main types of movement are classically distinguished: slow and gradual rotational movement along a deep detachment, often referred to as “slump”, and (2) catastrophic rupture of an island flank, yielding the sudden generation of voluminous debris-avalanches, which can trigger destructive tsunamis (Moore et al., 1989; Satake et al., 2002). Both types usually occur during the main eruptive history of a given island, and the volume of individual failure episodes partly depends on edifice size. For instance, the most extreme debris-avalanches have been extensively recognized along the Hawaiian Emperor volcanic chain, which comprises by far the largest volcanic islands on Earth. The most extreme events have mobilized huge amounts of material, up to several

thousands of $km^3$, and generated debris-avalanches with impressive run-out, sometimes exceeding 100 km (e.g. Moore et al., 1989; 1994). However, such episodes appear quite infrequent, with an estimated recurrence of about 100 kyr (Normark et al., 1993). In contrast, smaller volcanic islands seem to experience smaller but more frequent destabilization events, which still can amount to several cubic kilometres and generate large tsunamis (e.g. Keating and McGuire, 2000). Therefore, studying the link between volcanic construction and repeated destabilization in relatively small volcanic islands like Pico is of particular societal relevance.

Here we focus on the evolution of the Pico-Faial volcanic ridge in the Azores, which comprises the islands of Pico (main focus) and Faial. Both are much smaller than the Canary or Hawaiian islands, but, in contrast, located in an active tectonic setting. Like the other volcanic islands in the Central Azores, the Pico-Faial Ridge is located on the diffuse boundary between the North America (NA), Eurasia (Eu) and Nubia (Nu) plates (Fig. 1a), and sits on an anomalously elevated portion of the Mid-Atlantic Ridge (MAR, Fig. 1a) known as the Azores Plateau. The western end of the Nu-Eu plate boundary is presently diffuse (Fig.1a, e.g. Lourenço et al., 1998; Luis et al., 1998; Miranda et al., 1998; Fernandes et al., 2006; Borges et al., 2007; Lourenço, 2007; Hildenbrand et al., 2008; Luis and Miranda, 2008; Marques et al., 2013a; 2014a ; Neves et al., 2013; Trippanera et al., 2014; Hildenbrand et al., 2014; Miranda et al., 2014). The deformation is mostly accommodated by several extensional structures in a ca. 140 km wide area: (1) the Terceira Rift (TR, Fig. 1), and (2) the ca. WNW-ESE graben-horst-graben structure to the SW of the TR (Fig. 1b), which comprises the 200 m deep S. Jorge Graben (Lourenço, 2007) and the Faial Half-Graben, with an intervening horst, the S. Jorge/Faial Horst (Marques et al., 2013a, 2014a).

While the S. Jorge volcanic ridge developed apparently inside a graben, the Pico-Faial ridge developed in great part on the master fault bounding in the north the Faial half-graben (Fig. 1). The sub-aerial growth of this ridge started ca. 850 ka ago on the eastern part of Faial (Fig. 1, Hildenbrand et al., 2012a). Faial Island evolved by short periods of voluminous volcanic construction intercalated with longer periods of major destruction by large-scale mass wasting. The evolution of these steep volcanic ridges appears intimately related to tectonic deformation, which may partly control the successive stages of volcanic growth and repeated episodes of destabilization, mostly through large catastrophic sector collapses (Woodhall, 1974; Madeira, 1998; Nunes, 1999; Mitchell, 2003; Mitchell et al., 2008; Costa et al., 2014) or large-scale slumping (Nunes, 1999; Mitchell et al., 2012a; Hildenbrand et al., 2012b).

Despite the relatively small volume of the Azorean islands, increasing evidence for large-scale catastrophic destruction in the form of lateral flank collapses has been accumulated

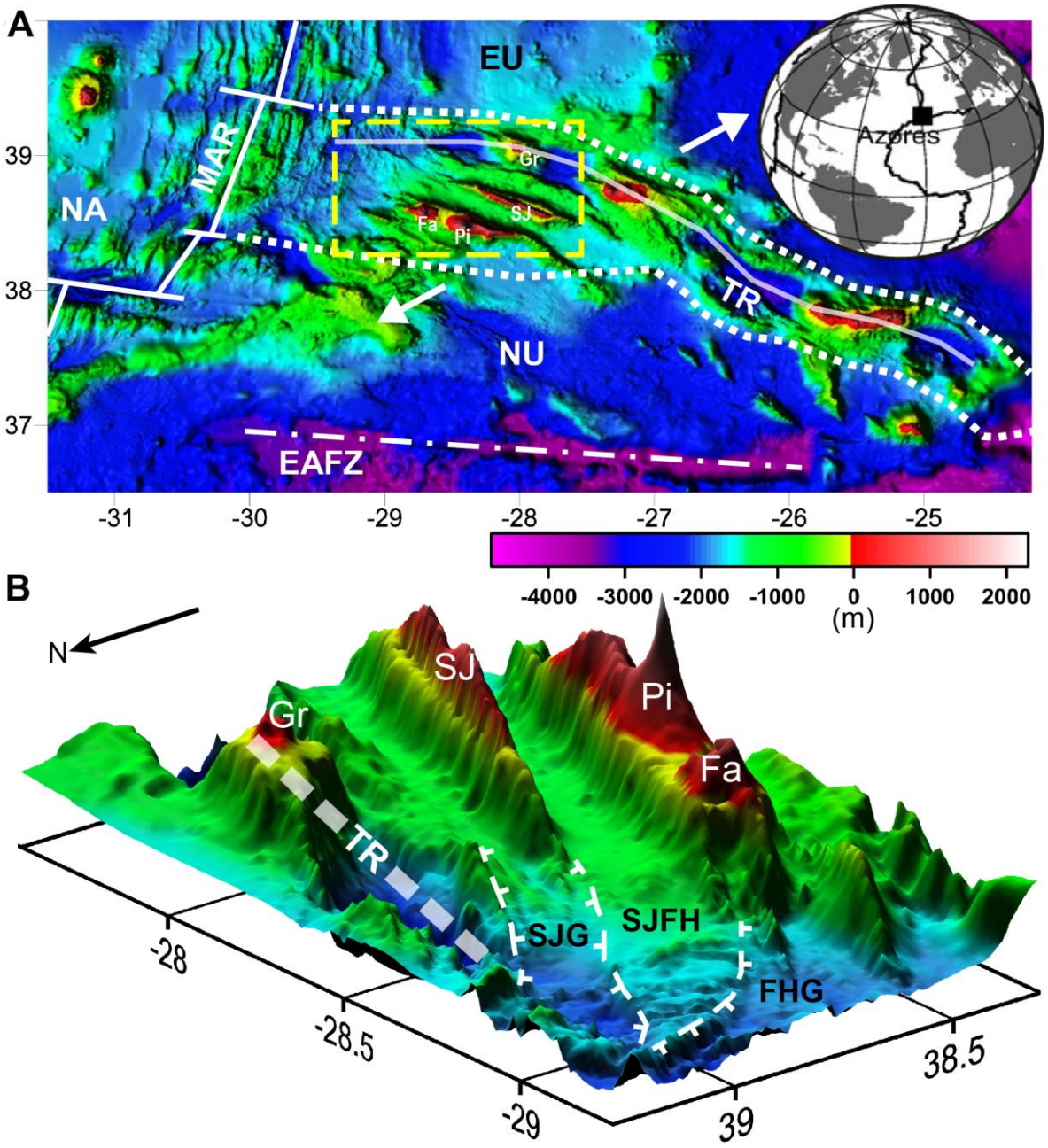


**Fig. 1**. (A) Location of the Azores archipelago on the diffuse boundary between the North America (NA), Eurasia (EU) and Nubia (NU) plates (lighting from WSW). Main active structures represented as thick white lines (Mid-Atlantic Ridge – MAR, Terceira Rift – TR); limits of the diffuse Nu-Eu plate boundary represented by dotted lines and extension orientation indicated by thick white arrows; and inactive structure as dashed-dot-dashed white line (East Azores Fracture Zone – EAFZ). Yellow dashed rectangle marks the area presented in B. (B) 3D surface (viewed from NW and lighting from E) of the sector that includes the WNW-ESE Pico (Pi)-Faial (Fa) volcanic ridge studied in this paper. TR marked by thick dashed white line. The graben/horst structure SW of the TR is defined according to Marques et al. (2013a, 2014a). SJG - S. Jorge Graben; SJFH - S. Jorge/Faial Horst; FHG - Faial Half-Graben. SJ - S. Jorge Island; Gr - Graciosa Island. Bathymetric data from Lourenço et al. (1998).

(Marques et al., 2013b; Sibrant et al., 2014), particularly in Pico Island (Costa et al., 2014).

Furthermore, evidence of current activity of a large-scale creeping slump in Pico's SE flank has been reported in Hildenbrand et al. (2012b). The integration of the data here presented with previously published data on Pico and Faial (Madeira, 1998; Nunes, 1999; Hildenbrand et al., 2012a; Costa et al., 2014) will allow us to reconstruct the main stages of sub-aerial evolution of the ridge and discuss the influence of regional deformation on the successive episodes of volcanic construction and destruction.

The present study is based on the analysis and interpretation of a high-resolution Digital Elevation Model (DEM), detailed stratigraphic and structural observations and measurements, and high-precision K-Ar dating: (1) the geomorphological analysis from high-resolution sub-aerial and submarine DEMs allowed the interpretation of volcanic complexes, mass-wasting scars and offshore debris deposits; (2) the detailed stratigraphic observation along sea cliffs and major canyons allowed the recognition of the main volcano-stratigraphic unconformities, and therefore to distinguish the main volcanic systems and their geometry; (3) the structural study, with the recognition and measurement of attitudes of faults, dykes and lava flows showed where the main structural discontinuities are, and their effects on the overall structure and evolution of the island; (4) the stratigraphic and structural data were used to carry out strategic sampling for K-Ar isotopic dating, which provides an accurate temporal framework to constrain the timing of volcanic construction and destruction episodes.

## 2. Geological background

### *2.1. Pico's volcanic stratigraphy*

Previous studies have shown that Pico comprises three main volcanic complexes (Fig.1): (1) the relicts of an old extinct volcano in the SE, generally referred to as the Topo Volcano; (2) a ca. WNW-ESE linear chain of strombolian cones in the middle and eastern parts of the island, known as the Fissural System; and (3) the impressive Pico Stratovolcano, peaking at 2351 m above sea level, which makes up the western half of the island (Fig. 2a). According to previous geochronological data, the sub-aerial part of Pico has developed during the last ca. 300 kyr (250 ± 40 ka, in Demande et al., 1982, Fig. 2a). Pico's sub-aerial growth seems to have started in the east, with the growth of the Topo Volcano (Fig. 2a, Zbyszewski et al., 1963; Forjaz, 1966; Woodhall, 1974; Madeira, 1998; Nunes, 1999; Nunes et al., 1999a), interpreted as a shield volcano by Woodhall (1974). Remnants of this early sub-aerial volcano have been

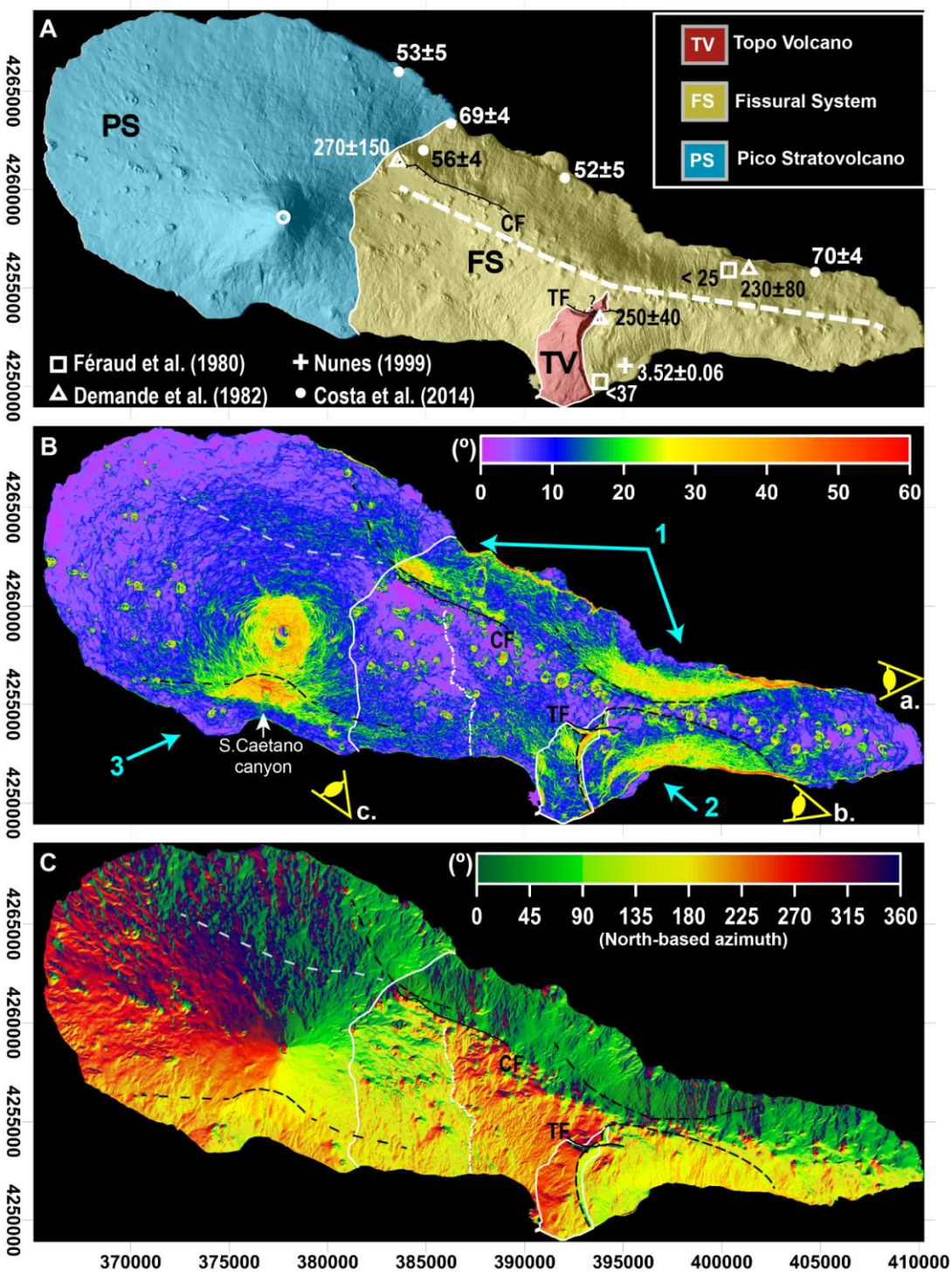


**Fig. 2**. (A) Shaded relief of the 10 m resolution DEM of Pico Island (lighting from ESE), with coordinates in metres UTM (zone 26N). White squares, triangles and circles mark the K-Ar ages from Féraud et al. (1980), Demande et al. (1982) and Costa et al. (2014), respectively. Also shown a radiocarbon age (plus sign) from Nunes (1999). The ages are indicated in thousands of years. Simplified geologic/physiographic map (modified after Madeira, 1998). Traces of the Capitão Fault (CF) and Topo Fault (TF) (after Madeira, 1998; Nunes et al., 1999; Madeira and Brum da Silveira, 2003). (B) Slope map of Pico Island built from the 10 m resolution DEM. Dashed black lines: scarps interpreted from zones of anomalously steep slopes. Grey dashed line: gentle slope anomaly oriented WNW-ESE on the N flank of Pico Stratovolcano. Perspectives

(yellow eyes) identified as *A*, *B* and *C* are presented as 3D surfaces in Fig. A2 (Supplementary Data - Appendix A). The white arrow in the southern flank of Pico Stratovolcano locates a canyon along which part of the fieldwork was done, the S. Caetano canyon. (C) Surface map of Pico Island built from the 10 m resolution DEM, indicating the North-based azimuth of strongest dip. Dash-dot white line marks the boundary between two domains of the Fissural Complex with different azimuths of strongest dip. The clean version of this figure is provided as Fig. A1 (Supplementary Data - Appendix A).

unconformably covered by younger volcanic products poured from scattered scoria cones and WNW-ESE aligned cones making up the sub-aerial Fissural System (Zbyszewski et al., 1963; Woodhall, 1974; Madeira, 1998; Nunes, 1999; Nunes et al., 1999b, Fig. 2). The latest stages of island growth comprise the development of the Fissural System and the Pico Stratovolcano, which have been active through the Holocene, up to historical times (Fig. 2a, e.g., Zbyszewski et al., 1963; Forjaz, 1966; Woodhall, 1974; Madeira, 1998; Nunes, 1999; Nunes et al., 1999a; Madeira and Brum da Silveira, 2003; Mitchell et al., 2008).

Available whole-rock K-Ar data from Féraud et al. (1980) and Demande et al. (1982) (Fig. 2a) are very scarce and do not allow the age calibration of Pico's volcano-stratigraphy. For instance, one lava flow from the old Topo Volcano was previously dated at 250 ± 40 ka, whereas two lava flows sampled in the western and eastern sectors of the Fissural System yielded ages of 270 ± 150 ka and 230 ± 80 ka, respectively (Demande et al., 1982, Fig. 2a). These three ages overlap within their range of uncertainty and thus are not precise enough to confidently reconstruct the evolution of the island. Ages estimated younger than 25 ka and 37 ka (Fig. 2a; Féraud et al., 1980) have been also obtained on lava flows from the northern and southern flanks, respectively, but their geological significance remains elusive. A few radiocarbon data on charcoal fragments and/or paleosoils covered by lava flows help to constrain the age of some of the most recent eruptions (Madeira, 1998; Nunes, 1999). However, these data are of limited use to study the long-term evolution of the ridge due to the restricted applicability of the method (< ca. 50 kyr).

The lack of precise and representative isotopic ages in Pico (França, 2000), the lack of marked lithologic variability between main volcanic units (França, 2000; França et al., 2006), and the temporal partial overlap of volcanic activity, have hampered the definition of Pico's volcanic stratigraphy. The earlier works relied greatly on the published K-Ar and radiocarbon ages, on the alteration degree of the volcanic deposits, and on local field relationships (e.g., Madeira, 1998; Nunes, 1999; Nunes et al., 1999a; França, 2000; França et al., 2000).

*2.2. Mass-wasting in Pico Island*

Earlier studies in Pico have highlighted the existence of several large structures affecting the various volcanic complexes (Fig. 2b): (1) two concave steep zones on Pico's northern flank; (2) several nested scarps in SE Pico; and (3) a WNW-ESE scarp on the southern flank of the Pico Stratovolcano. (1) On Pico's northern flank, a detailed analysis of high-resolution bathymetry, coupled with fieldwork and K-Ar dating on Pico's northern flank, led Costa et al. (2014) to identify a 4 to 10 $km^3$ submarine debris deposit interpreted as resulting from a northwards catastrophic flank collapse of the old Topo Volcano, prior to ca. 70 ka. (2) The easternmost scarp on the northern flank is mirrored in Pico's southern flank by another concave and steep main scarp and a series of less-pronounced scars (Fig. 2b). The main scarp (Figs. 4 and 5) has been variably interpreted as: a crater or caldera (Zbyszewski et al., 1963), a "trap door" type caldera of Topo Volcano (Woodhall, 1974), a landslide scar (Madeira, 1998; Madeira and Brum da Silveira, 2003; Mitchell, 2003), or a fault constituting the headwall of a slump structure (Nunes, 1999; França, 2000; Nunes, 2002; Hildenbrand et al., 2012b). Nunes (1999, 2002) proposed that this structure is younger than 37 ka and inactive since the beginning of the Holocene. This hypothesis was later reinforced by Mitchell et al. (2012a). These authors did not find evidence for deformation of the current coastal shelf by the slump structures, and considered that the lava delta was formed according to the present sea level. However, GPS data acquired between 2001 and 2006, and InSAR data acquired between 2006 and 2009, indicate that this structure is currently active, with horizontal movement of 1.6 ± 1.3 mm/yr, and subsidence ranging between 5 and 12 mm/yr (Hildenbrand et al., 2012b, 2013). Here we will argue that the landslide scar in SE Pico is much bigger than the portion of the active slump, and therefore constitutes the scar of a major catastrophic flank collapse, with the respective debris deposit at the ocean bottom, here newly reported. (3) The WNW-ESE scarp on the southern flank of the Pico Stratovolcano (Fig. 2b) has been interpreted either as an avalanche scar (Woodhall, 1974; Madeira, 1998; Madeira and Brum da Silveira, 2003) or as a fault scarp (Forjaz, 1966; Machado et al., 1974; Chovelon, 1982, Forjaz et al., 1990; Nunes, 1999; Nunes et al., 1999a,b; Mitchell, 2003). This scarp has been described as being masked by more recent volcanic products from the Pico Stratovolcano (Chovelon, 1982; Madeira, 1998; Nunes, 1999), and its base covered by recent and thick colluvium deposits (Madeira, 1998; Nunes, 1999). Here we present a description of the observations made along a creek incising the scarp.

## 3. Methods and results

### *3.1. Geomorphological analysis*

A 10 m resolution sub-aerial DEM was complemented with bathymetric data acquired offshore Pico's SE flank. The submarine data include previously published data (Lourenço et al., 1998; Mitchell et al., 2012a) and new high-resolution bathymetric data with a spatial resolution between 50 m and 250 m, aimed at identifying potential debris deposits generated by mass wasting episodes in SE Pico. All these data were merged into a single grid. Details about the data sources and grid construction are provided in the supplementary material (Appendix A).

Shaded-relief and slope maps constructed from the synthetic grid allowed us to distinguish important morphological features at both island and more local scales. Pico has a general WNW-ESE orientation, but is continued in the east by a NW-SE submarine ridge (e.g. Stretch et al., 2006; Lourenço, 2007; Mitchell et al., 2012b). Pico Island has a maximum length of ca. 46 km and maximum width of ca. 16 km. Its overall linear morphology is interrupted by two central-type volcanoes, with constructional slopes reaching more than 15º, especially in the upper part of the Pico Stratovolcano. Much higher slopes are locally observed over the island, which correspond to (1) coastal sectors, where impressive sub-vertical cliffs (maximum height of ca. 400 m on the northern flank) cut the various volcanic successions, and (2) scarps related to mass-wasting/faulting. These sub-aerial scarps are often strongly masked by more recent volcanic deposits (Chovelon, 1982; Madeira, 1998; Nunes, 1999; Mitchell et al., 2008; Hildenbrand et al., 2012b; Mitchell et al., 2012a; Costa et al., 2014). The steep submarine flanks of the island have been considered to fit the profile expected for constructional slopes (Mitchell et al., 2008, after Mitchell et al., 2002).

The interpretation of the shaded reliefs, slope maps and surface map (Figs. 2 to 6, A.1 to A.4) allowed us to distinguish and characterize different morpho-structural sectors.

The remnants of the Topo Volcano are partly exposed in the central part of the island. They constitute a prominent cape making up the southernmost sector of the island (Figs. 3 and 4). In this area, the remnants of Topo Volcano have been partly masked by more recent volcanic cones (Fig. 4b). The Topo Volcano remnants are located to the S of the axis of the Fissural System, and masked on the W, N and E by more recent volcanic products (Fig. 4b). Close to the Main Scarp headwall, Topo's sub-aerial SW sector presents steep slopes up to 20-25º (Fig. 3b). There, the older volcanic sequence crops out, and the topographic surface truncates the volcanic sequence, suggesting that significant erosion has occurred (Figs. A.3c and A.3d). Downslope,

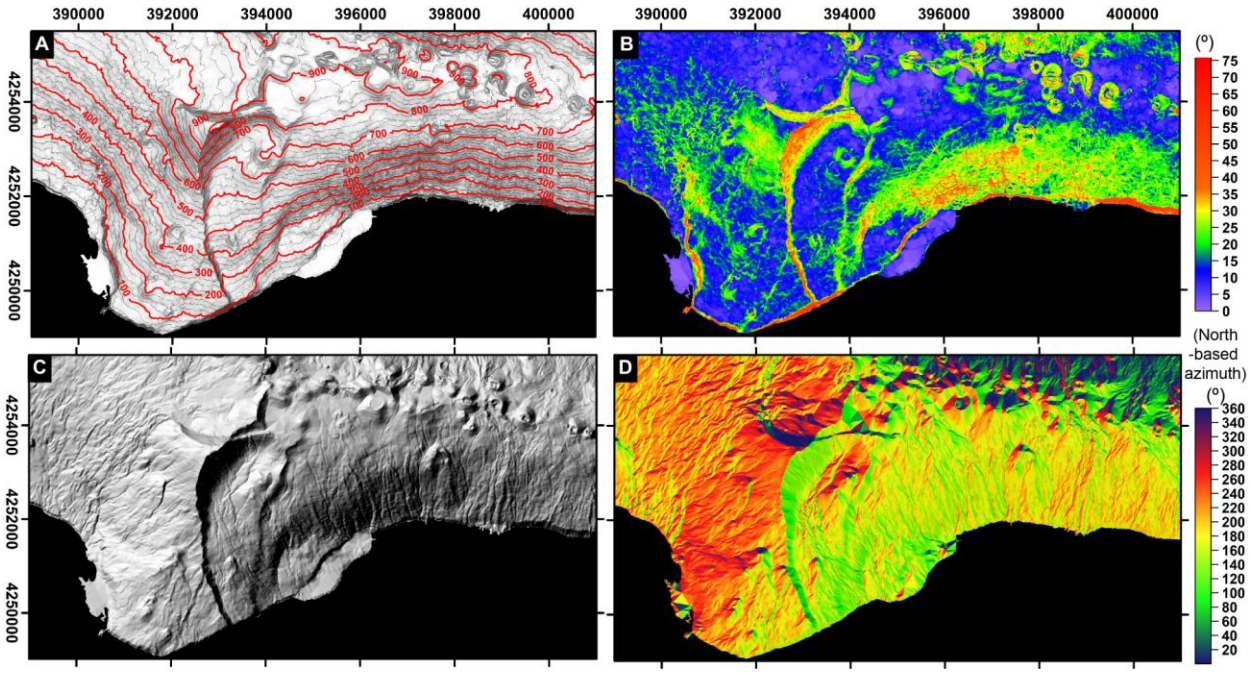


**Fig. 3**. Map views of the SE sector of Pico Island based on the 10 m resolution DEM. (A) Shaded relief (vertical lighting), with contour lines spaced 25 m. (B) Slope map. (C) Shaded relief with lighting from NW. (D) Surface map (north-based azimuth of the strongest dip). All the images show conspicuous curved NNE-SSW scarps in the west, and (older) less obvious curved E-W scarps covered by more recent volcanic deposits.

more recent volcanic materials from parasitic cones aligned SSW-NNE blanket the slopes and partially cover a small NNW-SSE scarp (*1* in Fig.4a). Despite the more recent volcanic cover, it is clear that the sub-aerial remnants of the Topo Volcano are affected in the N and E by prominent scarps (Fig. 4a). In the SE, the Topo Volcano is also cut by a 5 km long prominent and straight WSW-ENE sea cliff (*2* in Fig.4a, height up to 160 m above sea level, only locally interrupted by a lava delta). The Topo remnants are bounded in the N by a N-facing scarp (*3* in Fig. 4a), and the lineament that continues further E, which have been interpreted by Madeira (1998) as the Topo Fault (*TF* in Fig.4). Both blocks involved in this fault are affected by the headwall of the slump (*Main Scarp* in Fig. 4a). This scarp defines the eastern limit of the sub-aerial remnants of the Topo Volcano. It trends between NNW-SSE in the south and E-W in the north, and is thus concave to the SSE. Within the Main Scarp, several smaller scarps are nested in one another, and also concave to the SSE, and are designated Sn. S1 presents a general SSW-NNE orientation, and its height and slope vanish towards the N. S2 extends further E than the area that accommodates the current slump activity constrained by Hildenbrand et al. ( 2012b) (Fig. 3b). Its trend is parallel to S1 in the W (SSW-NNE) and parallel to the Fissural System axis

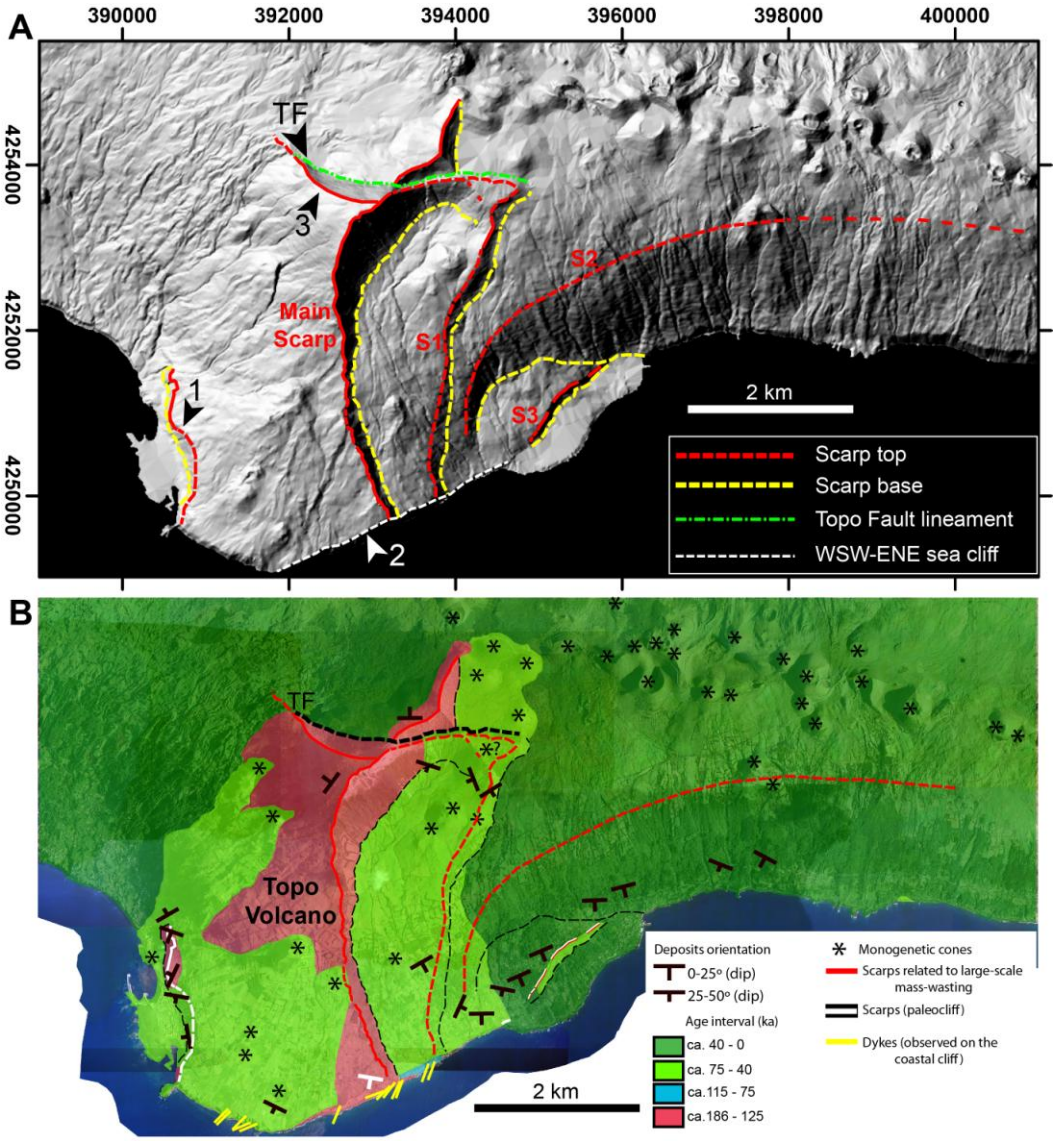


**Fig. 4**. (A) Shaded relief presented in Fig. 3c, with interpretation of the top (red dashed lines) and base (yellow dashed lines) of the scarps (numbered features addressed in the main text). We follow the designations attributed to the arcuate scarps of the slump in Hildenbrand et al. (2012b), but we identify as *Main Scarp* the conspicuous scarp limiting the slump area. (B) Simplified geologic map (complete version presented as Fig. 13).

in the north (E-W). The slope reaches 40º in the central area of the slump (Hildenbrand et al., 2012b), but S2 vanishes towards W and E (Figs. 2b and 3b). S3 is oriented SW-NE and vanishes towards the SW. Towards the NE, S3 meets S2 (Figs. 3b and 4a). The slump scarps are partially masked by volcanic deposits erupted from monogenetic cones formed along the axial zone of the Fissural System or aligned along the slump scarps (Fig. 4b).

The orientation of the sub-aerial Fissural System changes from W-E in the E to WNW-ESE in the W. Such inflection roughly occurs near the Topo volcano (Nunes, 1999; França,

2000). The axis of the Fissural System is well-defined and narrow to the E of Topo volcano, whereas it becomes wider, with a flatter top (slope dip < 5-10º) towards the Pico Stratovolcano. To the S of the inferred Capitão Fault (*CF* in Fig.2c, Madeira and Brum da Silveira, 2003), the topographic surface of the Fissural System dips towards the eastern quadrant. This domain has been integrated in the Pico Stratovolcano complex by previous authors (França et al., 1995 in França, 2000; Nunes et al., 1999a). Immediately to the east, the slope of the Fissural System dips towards the W (Fig. 2c). The northern flank of the Fissural System presents two steep scarps with headwalls oriented parallel to the axial zone (Fig. 2b). The topographic expression of these scarps is subdued, as they are strongly masked by volcanic products erupted from the axis of the Fissural System and from cones located on the scarp, and by the eastern sub-aerial flank of the Pico Stratovolcano.

The western half of the island is dominated by the Pico Stratovolcano, with quite a regular conical morphology all around except in the southern flank, where a conspicuous scarp is visible. The centre of the Pico Stratovolcano is located S of the longitudinal axis of the island, but it is part of a major alignment comprising the Caldera Volcano in Faial, the Pico Stratovolcano and the Topo Volcano, which is parallel to the underlying normal fault in the basement, bounding, in the north, the Faial half-graben. The southern flank of the Pico Stratovolcano is characterized by a sharp slope break oriented ca. WNW-ESE (*3* in Fig. 2b), which seems to continue laterally towards both WNW and ESE. The central part of the scarp is incised by a deep canyon (*S. Caetano canyon* in Fig. 2b). The upper part of this canyon has slopes that exceed 60º. Along the foot of this scarp, a prominent lava platform is visible. It is covered by a few scoria cones. The northern flank of the Pico Stratovolcano is less steep than the southern. Nevertheless, a slight WNW-ESE slope break is visible (Fig. 2b). The general distribution of the parasitic cones on the flanks of the Pico Stratovolcano suggests a predominance of the WNW-ESE lineaments.

The morphology of Pico's NE flank is marked by two WNW-ESE prominent and arcuate scarps facing N, whose details are given in Costa et al. (2014). The easternmost part of the island has the common shape of a narrow and straight volcanic ridge, made up of many WNW-ESE aligned scoria cones.

Offshore, the WSW-ENE to SW-NE direction of the straight coast and dykes measured along the SE coast is also suggested by the presence of submarine alignments of volcanic cones with trends ranging from SSW-NNE to SW-NE (light blue dashed lines in Fig. 5). Offshore the slump area (Figs. 5 and 6)**,** the new high-resolution bathymetric data show a protuberant area of hummocky terrain extending up to 17 km from the coast, along the NW-SE direction. From the

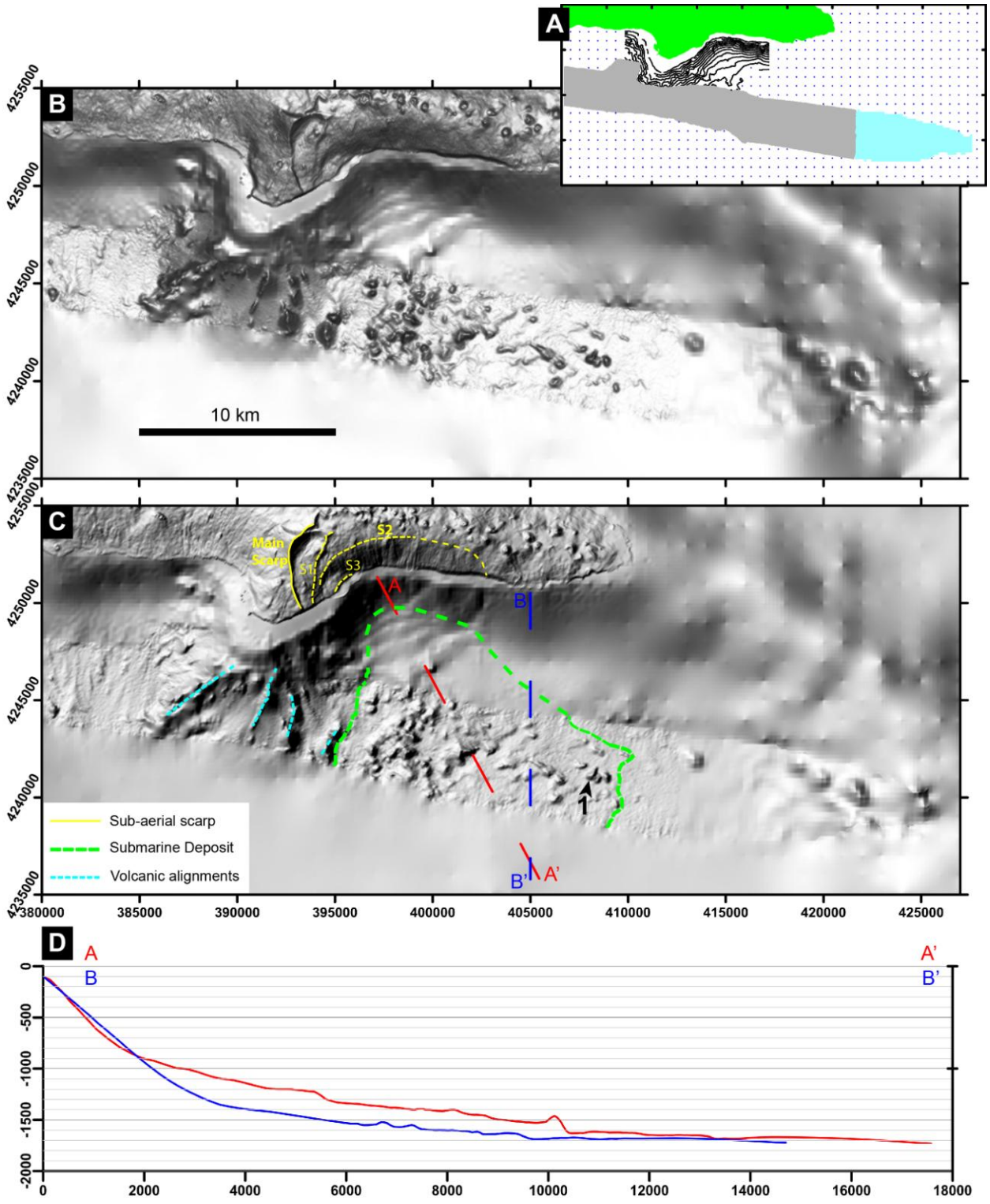


**Fig. 5**. (A) Different data sets used to compose the 50 m resolution grid presented in (B): green – 10 m resolution sub-aerial DEM; turquoise – 250 m resolution bathymetry; grey – 50 m resolution bathymetry; black lines – depth contours from Fig. 1b in Mitchell et al. (2012a); blue dots – bathymetric data extracted from the 1000 m resolution grid from Lourenço et al. (1998). (B) and (C) are shaded reliefs from the 50 m resolution grid, with vertical lighting and lighting from WNW, respectively. In C we interpreted the outline of the proximal sector of the hummocky terrain area (green dashed line), and the biggest block identified (*1*). We also indicate the alignments of submarine cones observed to the SW of Topo (light blue dashed lines), and the

scars (yellow lines) identified in the sub-aerial sector adjacent to the submarine debris deposit. The apparent WSW-ENE lineaments visible in the area of interpolation of contours extracted from Mitchell et al. (2012a) constitute interpolation artefacts. A clean version of this figure is provided as Fig. A.4. (D) Cross sections of the submarine flank indicated in (C).

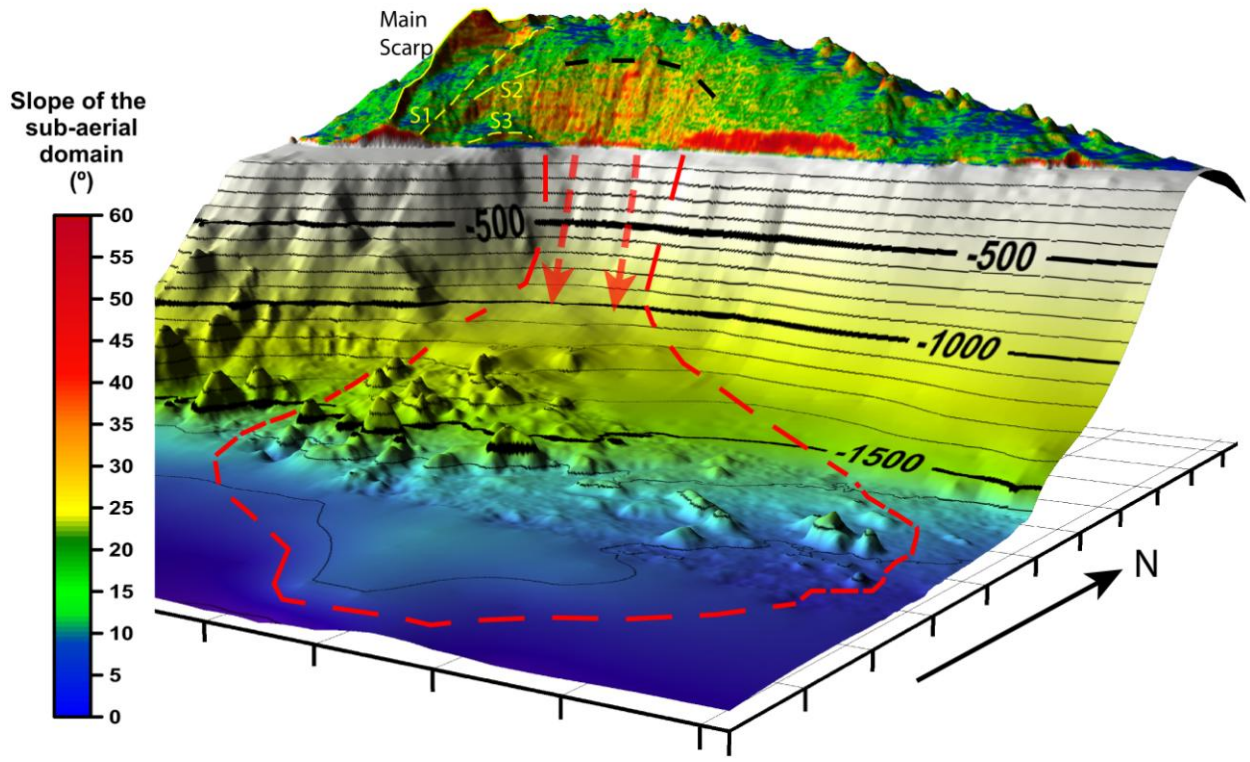


**Fig. 6**. 3D surface of the area represented in Fig. 5 viewed from SE, with elevation exaggerated 3x, and with lighting from SW. The sub-aerial domain is presented as a slope map. The extended outline and source of the deposit is interpreted with red dashed line and arrows. The interpreted sub-aerial source area for the debris material interpreted offshore is delimited by a black dashed line.

bathymetric mosaic that includes the low-resolution data, the deposit reaches depths of ca. 1700 m, but apparently extends farther South, beyond the high-resolution stripe (Fig. 6). The large hummocks are significantly masked by smaller size material, especially in the domain closer to Pico's submarine slope (in agreement with Mitchell et al., 2012a, 2013). The imposed lightings in Figs. 5b and 5c highlight the irregular shape of these hummocks, here interpreted as large blocks. These are especially clear in the distal part of the deposit, where the largest block is ca. 850 m long (*1* in Fig. 5c).

*3.2. Fieldwork and sampling*

Our fieldwork investigations and sampling strategy were devised to constrain in time the main phases of volcanic growth and partial destruction of the ridge. We concentrated our observations and sampling on the steep scarps, in deep canyons, and along the high coastal cliffs where the exposure of the geological units is maximal. Otherwise the exposure is very scarce. Figure 7 shows a synthetic illustration of the sampling strategy within the central part of the island, including the active slump area. Figure 8 additionally shows the location and identification of the samples collected, as well as the most relevant observations made in the field.

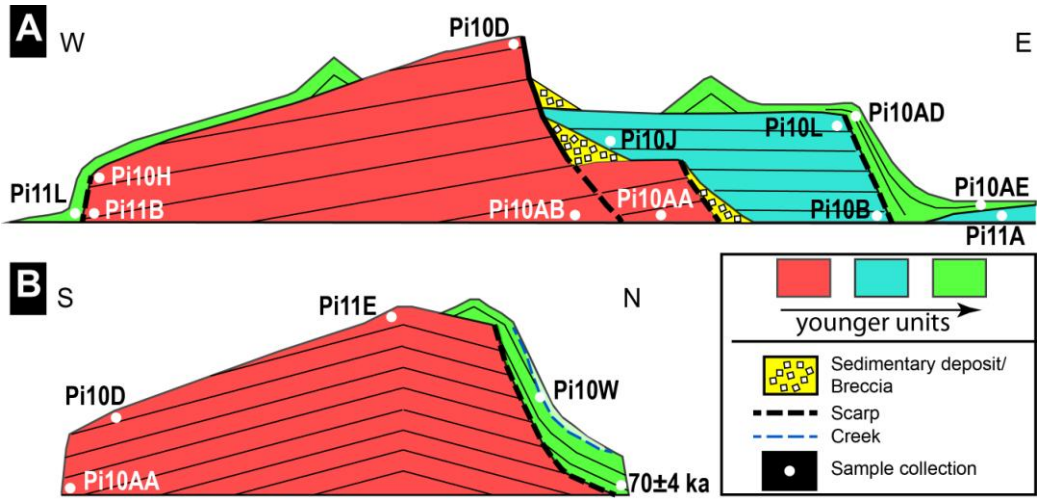


**Fig. 7**. Schematic illustration of the sampling strategy for (A) the Topo Complex/ SE active slump (especially along the WSW-ENE sea cliff), and (B) the scars on the northern flank. The position of some of the key samples is shown as white dots (exact position presented in Fig. 8).

The volcanic sequence of the Topo Volcano is partly exposed in the small SW scarp, the southern sea cliff and in the Main Scarp. On the small SW scarp of the Topo Volcano, we observed a basal sequence of lava flows gently dipping towards the W sector, overlain unconformably by lava flows and pyroclastic deposits. We sampled the basal sequence (Pi11B, Pi10H, Pi11K) and a lava flow from the overlying sequence (Pi11L). The southern sea cliff comprises a succession of metre to decametre thick lava flows locally dipping towards the SW, and cut by sub-vertical dykes striking between N040° and N070° (Figs. 8b and 8c). We collected the lowermost accessible lava flows at the base of the sea cliff (samples Pi10AA, Pi10AB) and

the uppermost ones at the top of the scarp (Pi10D, Pi12A, Pi11E). These samples should constrain the period of growth of the Topo volcano and the maximum age of the collapses towards the N and towards the SE. On the WSW-ENE sea cliff (Figs. 8c, A.5 to A.7), the Topo rocks are intruded by dykes near the "step" between Pi10AA and Pi10AB sampling sites, and are locally covered by a recent rock slide deposit. The Main Scarp shows breccia/coarse talus deposits at the base (Figs. 8c and 9), which are overlain by a younger thick sequence of S-dipping lava flows. The basal lava flows of this overlying sequence are generally very thin (up to 1m thick) on the E, except at the contact with the basal breccia deposit (Fig. 9b), where a pahoehoe lava flow shows significant local thickening and onlaps the basal topographic step of the Main Scarp (Fig. 8c). In contrast, the uppermost lava flows that cover the mid-slope talus deposit are generally massive and up to 10 m thick. These lava flows wedge out laterally against the main scarp (Fig. 9a). Although we did not observe erosive truncation, the separation between these distinct basal and upper lavas may constitute an unconformity (dash-dotted line in Fig. 8c, and supplementary Figs. A.6 and A.7). This sequence covering the Main Scarp is cut by NNE-SSW thin sub-vertical dykes and, in the E, is affected by the sharp S1. We sampled the lowermost (Pi10B) and the uppermost lava flows (Pi10L, Pi10J, Pi10O) of this sequence covering the Main Scarp. These samples should provide the minimum age for the generation of the Main Scarp, the maximum ages for the formation of the breccia/talus deposits, and the maximum age for the propagation of S1. S1 is masked by cascading lava flows, except inland on its topmost sector, where it cuts metre thick lava flows. East of S1, the small sea cliff comprises a sequence of sub-horizontal lava flows intercalated with paleosoils (Fig. 8c). We sampled the basal and topmost lava flows of the coastal cliff at the foot of S1 (Pi11A and Pi10AE, respectively), and a lava flow cascading over S1 (Pi10AD), which should constrain the minimum age of the formation of S1.

Towards the E, along S2, we only observed volcanic deposits (mostly lava flows) strongly dipping towards the sea. The eastern sector of S3 consists of a monotonous sequence of metre thick lava flows, with apparent dip of 10º towards the E-ENE, apparently corresponding to the lava flows that cascaded over S2 (Fig. 8b). We sampled a lava flow from this sequence (Pi11G, Fig. A.8), which should provide the minimum age for the formation of S2 and the maximum age for the formation of S3.We also sampled the basal and topmost lava flows of the sequence cropping out on the sea cliff E of the slump area (Pi11P and Pi12H, respectively), which should constrain the minimum age for the formation of S2. On the western sector of S3, the height and slope of the scarp decrease, and a sequence of thin cascading lava flows covers

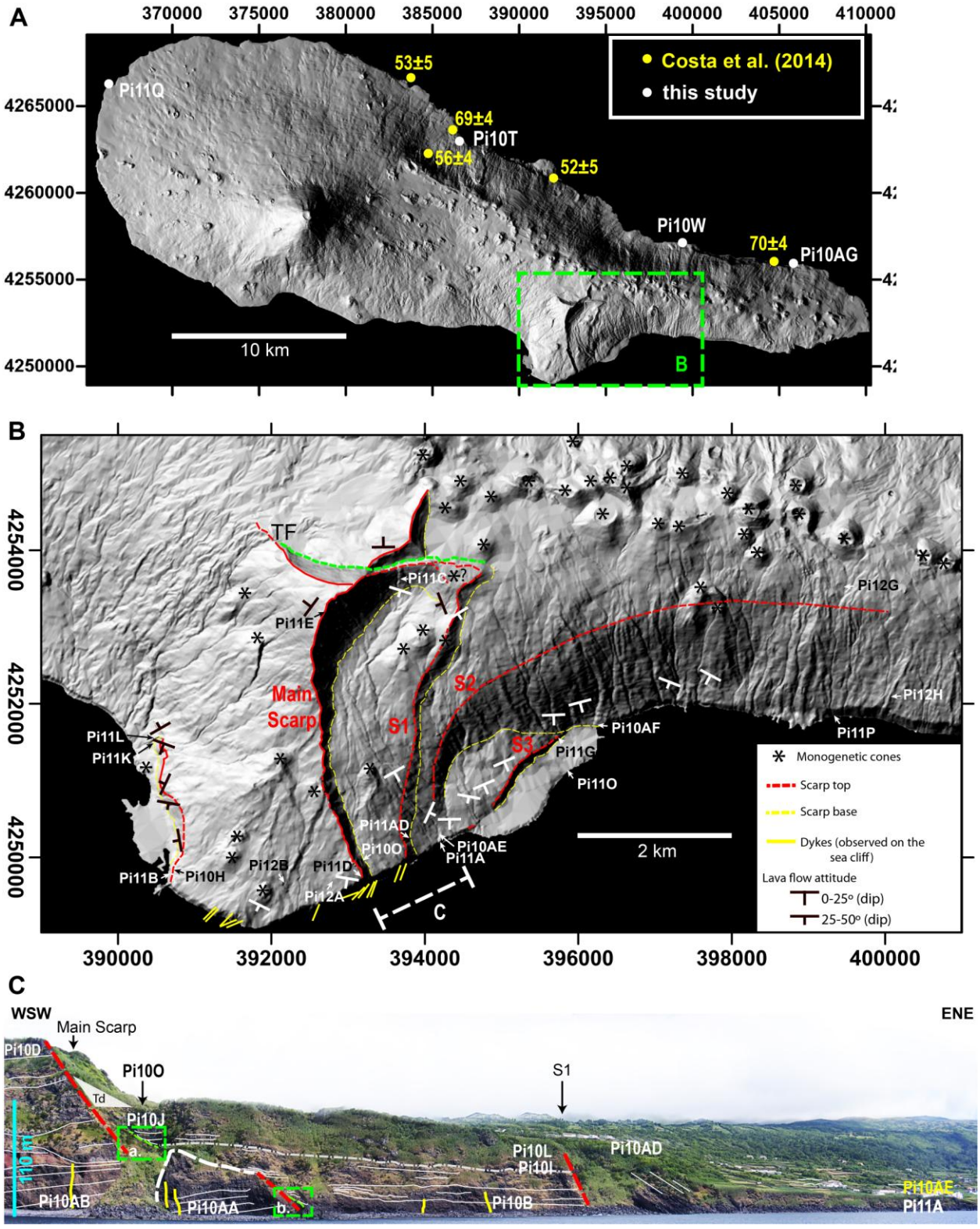


**Fig. 8**. Shaded reliefs (lighting from ESE in A., and from NW in B.), and image of the coastal section marked with c in B. (A) Ages from Costa et al. (2014) (in yellow), and sample location/identification of the new samples (in white). (B) Zoom of the slump sector, with indication of top and base of the scarps, identification of the scarps inside the slump area, indication of the attitude of lava flows, and location/identification of the new samples. (C) WSW-ESE view of the coastal cliff marked c in B. Thin white lines – local orientation of the

volcanic deposits as observed on the sea cliff. Grey dash-dotted line - possible unconformity. Red dashed lines - structural surfaces. Location/identification of the samples collected on (and in the proximities of) the sea cliff. Yellow lines - dykes. Green dashed lines – top of the observed fossilized talus/breccia deposits. Green dashed rectangles *a* and *b* mark the zoomed images of the sedimentary deposits presented in Figs. 9a and b, respectively. *Td* - Recent talus deposit. A clean version of this figure is provided as Fig. A.5 (Supplementary Data - Appendix A). Zoom in figures of the sea cliff section are provided as Figs. A.6 and A.7 (Supplementary Data - Appendix A).

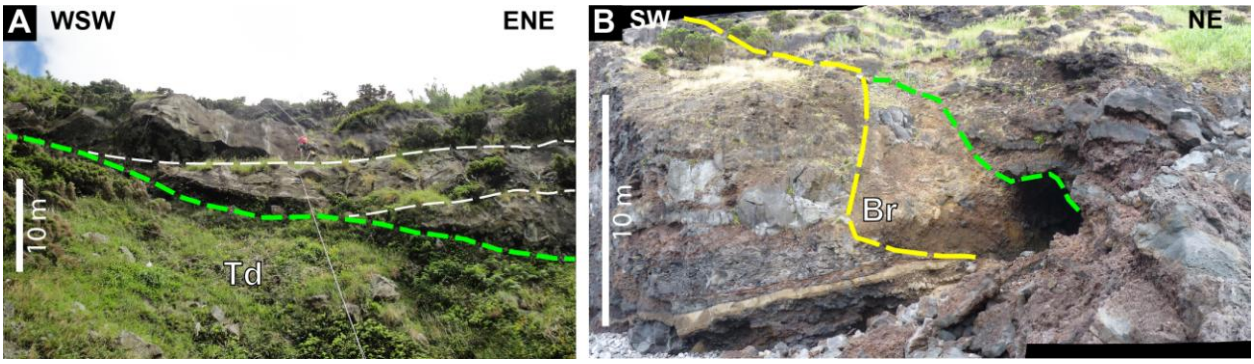


**Fig. 9**. (A) and (B) are zoomed pictures of the areas limited by the red rectangles *a* and *b* in Fig.8c, respectively. (A) Detail of the wedge-shaped talus deposit (Td), covered by lava flows (green dashed line). (B) Breccia (Br) covering the eastern edge of the footwall block (yellow dashed line), and overlain by a lava flow sequence (green dashed line).

S3, towards the current lava delta. We sampled a lava flow from the lava delta (Pi11O).

Despite Pico's northern flank being cut by deep canyons, we did not manage to observe the sequences affected by the flank collapses that generated the identified sub-aerial scars (Costa et al., 2014). Additionally to the samples presented in Costa et al. (2014), we sampled other rocks from the lava flows masking the scars in the N flank: Pi10T and Pi10W (Fig. 8a).

The Pico Stratovolcano stratigraphy is poorly exposed, as most of the lava flows at the surface have been generated by very young volcanic eruptions, especially during the historical period. The coastal cliffs around the volcano are very short, and therefore do not allow the observation and sampling of the earlier phases of volcano growth. Nevertheless, we sampled a lava flow from the NW sector of the Pico Stratovolcano: Pi11Q (Fig. 8a).

Further fieldwork on the island was restricted to the scarp that affects its southern flank, and observations were made along the S. Caetano canyon (Figs. 10 and 11). On the mouth sector we observed meter to decametre thick debris deposits covering sequences of lava flows. At the base of the scarp we observed, from bottom to top (Figs. 10 and 11):

A – Lava flows dipping towards downslope (*L1* to *L3*, Fig. 11a), intercalated with

sedimentary deposits (*D1* to *D3*, Fig.11a), overlain by a several meters thick and coarse (boulders) talus deposit (*D4*, Fig. 11a). Though there are coarse deposits related to the current canyon erosion, we observed that the metre thick deposits are overlain by, at least, one lava flow.

B – Several meters thick sequence of volcano-sedimentary material intercalated with lava flows, and intruded by dykes that strike N88-130º, mostly steeply dipping towards downstream (examples in Figs. 11b to 11e). The thickness of the dykes generally ranges between decimetres and metres. The thinner ones are sometimes disposed *en échelon*, with average strike of N120º and dip of 50-65º towards the SW (Fig. 11c).

The stratigraphic relationship between the sequences described in A and B is not clear. However, the coarse talus deposit *D4* in A (Fig. 11a) seems to cover also the downslope limit of the sequence described in B (Fig. 11b).

We did not observe an unconformity surface that could correspond to the failure surface of the S. Caetano scar. Unfortunately, the volcanic deposits observed did not present the conditions favourable for K-Ar dating, because the lava flows observed were extremely vesicular.

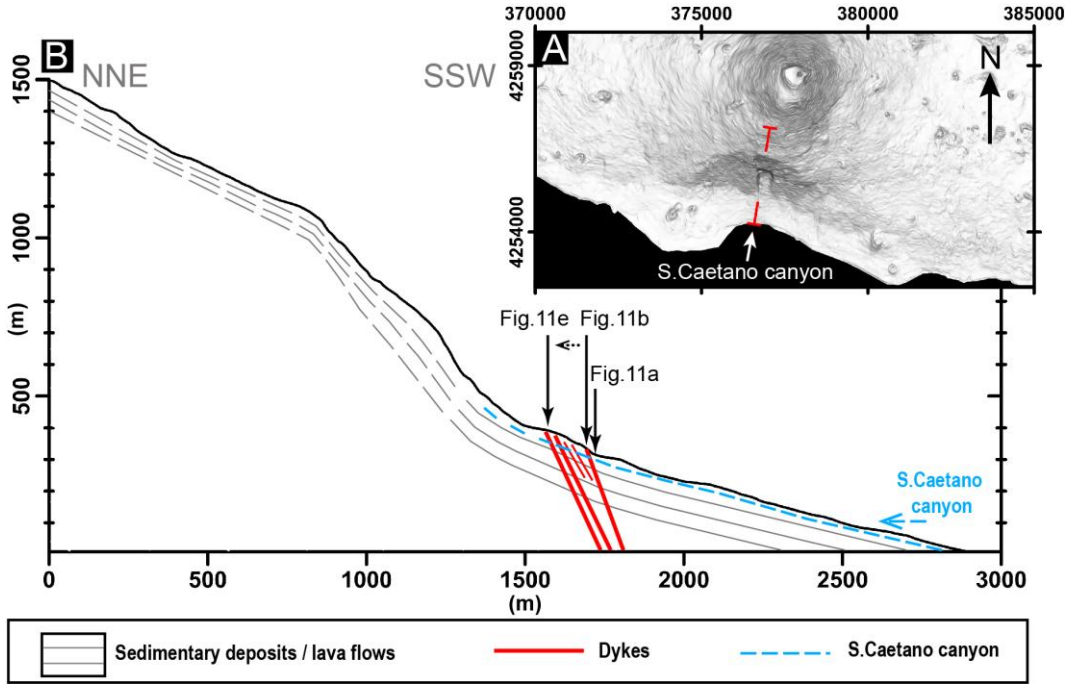


**Fig. 10**. (A) Shaded relief of the Pico Stratovolcano's S flank (vertical lighting), with indication of the trace of the cross section presented in (B), cut along the S. Caetano canyon. (B) Topographic profile along the S. Caetano canyon (no vertical exaggeration). The locations of the photographs presented in Fig. 11 are indicated, and the local orientations of the observed dykes and lava flows/sedimentary deposits represented.

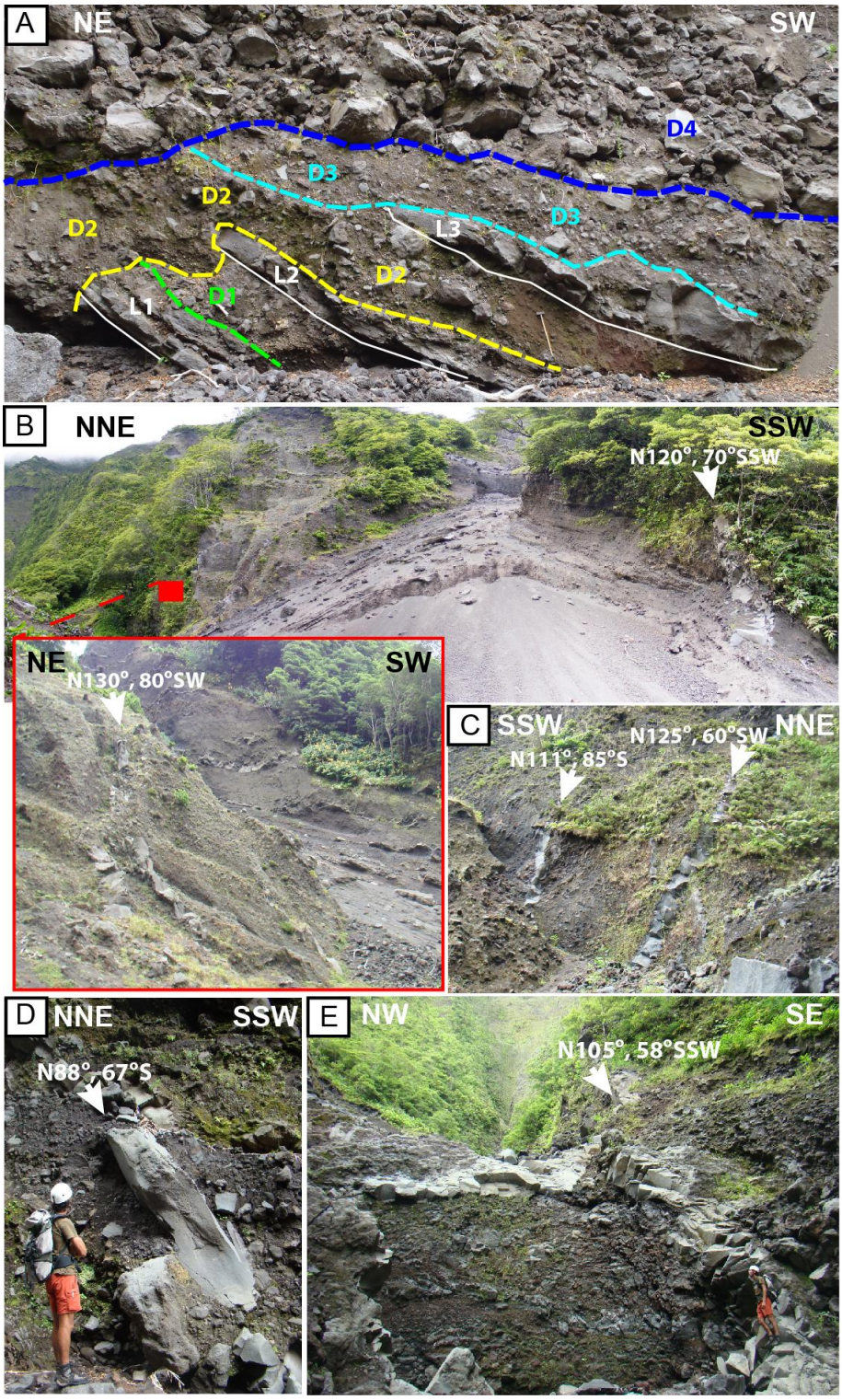


**Fig. 11**. Photographs taken in the S. Caetano canyon (order according to upslope observations). (A) Lava flows intercalated with sedimentary deposits. (B) Thick small grained volcaniclastic (pyroclastic) sequence with some thin lava flows intercalated and cut by steeply dipping dykes. Zoom in: view of the dykes located near the red square. (C) Small-grained volcaniclastic sequence intruded by *en échelon* dykes. (D) and (E) Metre thick dykes steeply dipping towards downslope, cutting the sequence of lava flows and volcano-sedimentary material. The dykes and their orientations are indicated with white arrows. A clean version of this figure is provided as Fig. A.9 in Appendix A (Supplementary Data).

3.3. *K-Ar dating*

We here present 28 new high-precision K-Ar ages (Fig.12 and Table 1), which together with the 5 ages acquired by Costa et al. (2014) constitute an unprecedented dataset to reconstruct the main successive stages of growth and partial destruction of the island over its whole eruptive history (Fig. 12). Our lava flow samples are fresh, aphyric to porphyric basalts (olivine, pyroxene and plagioclase phenocrysts), with low vesicular content. Dating precisely such young and mafic products requires the capability to measure extremely small amounts of radiogenic argon ($^{40}$Ar*, in Table 1). The Cassignol-Gillot technique, developed at Lab. GEOPS (University Paris-Sud, Orsay) is particularly suitable for such purpose (Gillot et al., 2006). It allows dating young, even K-poor, volcanic rocks with uncertainties of only a few ka (e.g., Samper et al., 2007; Hildenbrand et al., 2008, 2012a; Germa et al., 2011; Boulesteix et al., 2012, 2013; Costa et al., 2014).

The sample preparation included the following steps: (1) Careful observation of thin sections under a microscope to check that the samples have not suffered significant alteration; (2) crushing and sieving of the samples in order to obtain an homogeneous granulometry in the range 125-250 μm; (3) systematic removal of the phenocrysts through magnetic and heavy liquid sorting in order to extract the microlitic groundmass, which in the case of such basaltic samples is the only phase representative of the eruption age; (4) observation of the resulting sample under the binocular magnifier in order to attest its homogeneity. The groundmass samples obtained with this procedure present homogeneous size (125-250 μm) and density (2950-3050 kg/m$^3$for basaltic samples).

For each sample, K and Ar were both measured at least twice on distinct aliquotes of the homogeneous groundmass preparation by flame spectrophotometry and mass spectrometry, respectively. Details on the analytical procedure can be found elsewhere (Cassignol and Gillot, 1982; Gillot and Cornette, 1986; Gillot et al., 2006). The decay constants considered are from Steiger and Jäger (1977), and the age uncertainties are quoted at the 1σ level.

The oldest age obtained for the Topo volcano is 186 ± 5 ka, for the Fissural System is 70 ± 4 ka, and for the Pico Stratovolcano is 53 ± 5 ka (Fig. 12 and Table 1). The Topo volcano is extinct, but both the Fissural System and the Pico Stratovolcano are still active.

The volcanic sequence on the sea cliff cutting the Topo rocks was dated between 186 ± 5 ka and 125 ± 4 ka (Fig. 12). This old sequence is blanketed on the SW by younger volcanics erupted from parasitic cones, here dated between 60 ± 2 and 57± 2 ka.

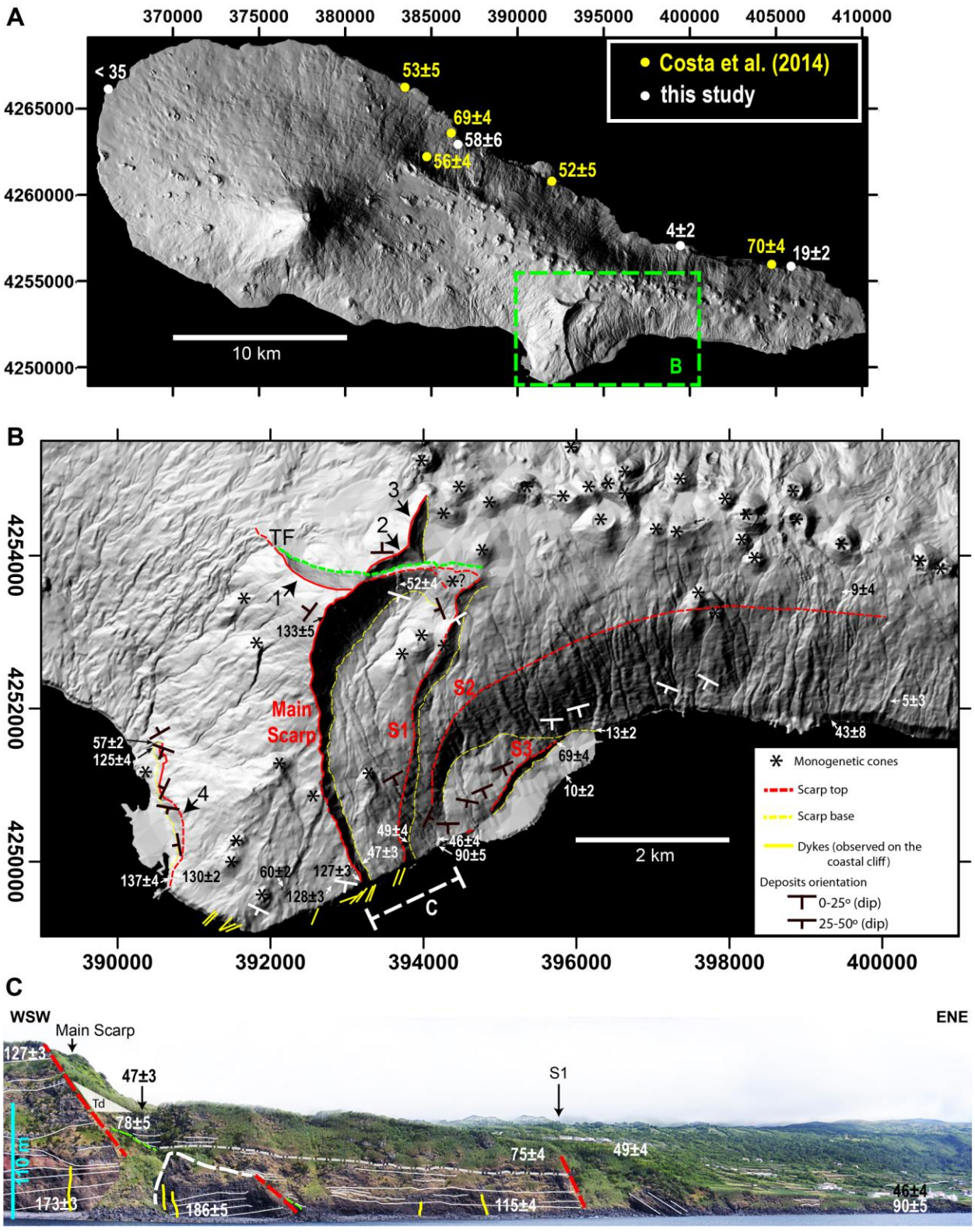


**Fig. 12**. Ages (in ka) obtained for the samples indicated in Fig. 8. Further details of this figure are provided in the caption of Fig. 8.

**Table 1**. Results of the K-Ar dating in the present study. The ages are presented in thousands of years (ka). The results are reported at the 1σ level. For sample Pi11E, the two Ar analyses did not overlap at 1σ, and therefore the uncertainty on the mean ages is obtained from the standard deviation to the average.

| Samples | UTM E | UTM N | K (%) | $^{40}$Ar* (%) | $^{40}$Ar* ($10^{10}$at/g) | Age (ka) | Uncertainty (ka) | Mean (ka) |
|---|---|---|---|---|---|---|---|---|
| **Pi10AA** | 26393459 | 4249592 | 0.864 | 4.9 | 16.479 | 183 | 5 | **186 ± 5** |
| | | | | 5.1 | 17.048 | 189 | 5 | |
| **Pi10AB** | 26393316 | 4249531 | 0.811 | 7.5 | 14.452 | 171 | 3 | **173 ± 3** |
| | | | | 8.0 | 14.771 | 174 | 3 | |
| **Pi11B** | 26390763 | 4249755 | 1.042 | 3.7 | 14.619 | 134 | 4 | **137 ± 4** |
| | | | | 3.5 | 15.303 | 141 | 5 | |
| **Pi11E** | 26392854 | 4253249 | 1.084 | 6.8 | 15.482 | 137 | 3 | **133 ± 5** |
| | | | | 6.8 | 14.716 | 130 | 3 | |
| **Pi10H** | 26390851 | 4249857 | 1.227 | 8.6 | 16.832 | 131 | 2 | **130 ± 2** |
| | | | | 8.2 | 16.589 | 129 | 2 | |
| **Pi12A** | 26392889 | 4249607 | 1.04 | 7.1 | 14.163 | 130 | 3 | **128 ± 3** |
| | | | | 7.3 | 13.724 | 126 | 2 | |
| **Pi10D** | 26393271 | 4249709 | 1.223 | 4.8 | 15.951 | 125 | 3 | **127 ± 3** |
| | | | | 5.3 | 16.440 | 129 | 3 | |
| **Pi11K** | 26390641 | 4251460 | 1.102 | 3.6 | 14.291 | 124 | 4 | **125 ± 4** |
| | | | | 4.0 | 14.452 | 126 | 4 | |
| **Pi10B** | 26393790 | 4249778 | 1.029 | 3.7 | 12.375 | 115 | 3 | **115 ± 4** |
| | | | | 3.6 | 12.437 | 116 | 4 | |
| **Pi11A** | 26394364 | 4250173 | 1.096 | 2.1 | 10.414 | 91 | 5 | **90 ± 5** |
| | | | | 1.9 | 10.152 | 89 | 5 | |
| **Pi10J** | 26393403 | 4249657 | 2.025 | 1.7 | 16.183 | 77 | 5 | **78 ± 5** |
| | | | | 1.4 | 16.646 | 79 | 6 | |
| **Pi10L** | 26393814 | 4249872 | 1.085 | 2.9 | 8.399 | 74 | 3 | **75 ± 4** |
| | | | | 1.4 | 8.544 | 75 | 6 | |
| **Pi11G** | 26395876 | 4251479 | 0.717 | 1.7 | 5.247 | 70 | 4 | **69 ± 4** |
| | | | | 1.9 | 5.153 | 69 | 4 | |
| **Pi12B** | 26392279 | 4249613 | 1.153 | 3.0 | 7.174 | 60 | 2 | **60 ± 2** |
| | | | | 3.8 | 7.297 | 61 | 2 | |
| **Pi10T** | 26386690 | 4263257 | 0.889 | 1.1 | 5.559 | 60 | 6 | **58 ± 6** |
| | | | | 1.0 | 5.179 | 56 | 6 | |
| **Pi11L** | 26390641 | 4251460 | 1.074 | 2.4 | 6.587 | 59 | 3 | **57 ± 2** |
| | | | | 2.6 | 6.251 | 56 | 2 | |
| **Pi11C** | 26393748 | 4253573 | 1.453 | 4.9 | 8.342 | 55 | 1 | **52 ± 4** |
| | | | | 5.7 | 7.576 | 50 | 1 | |
| **Pi10AD** | 26394024 | 4250211 | 0.912 | 1.2 | 4.552 | 48 | 4 | **49 ± 4** |
| | | | | 1.7 | 4.693 | 49 | 3 | |
| **Pi10AE** | 26394268 | 4250217 | 0.942 | 1.1 | 4.715 | 48 | 4 | **46 ± 4** |
| | | | | 1.1 | 4.283 | 44 | 4 | |
| **Pi10O** | 26393298 | 4249923 | 1.12 | 1.3 | 5.862 | 50 | 4 | **47 ± 3** |
| | | | | 2.1 | 5.267 | 45 | 2 | |
| **Pi11P** | 26399484 | 4251796 | 1.067 | 0.6 | 4.830 | 43 | 8 | **43 ± 8** |
| | | | | 0.5 | 4.794 | 43 | 9 | |
| **Pi10AG** | 26405991 | 4255709 | 1.513 | 1.0 | 3.095 | 20 | 2 | **19 ± 2** |
| | | | | 0.8 | 2.749 | 17 | 2 | |
| **Pi10AF** | 26396362 | 4251625 | 1.077 | 0.7 | 1.481 | 13 | 2 | **13 ± 2** |
| | | | | 0.5 | 1.309 | 12 | 2 | |
| **Pi11O** | 26395881 | 4251008 | 1.278 | 0.4 | 0.951 | 7 | 2 | **10 ± 2** |
| | | | | 0.5 | 1.651 | 12 | 3 | |
| **Pi12G** | 26399372 | 4253385 | 1.109 | 0.1 | 0.687 | 6 | 5 | **9 ± 4** |
| | | | | 0.3 | 1.199 | 10 | 4 | |
| **Pi12H** | 26400154 | 4251895 | 1.15 | 0.1 | 0.208 | 2 | 3 | **5 ± 3** |
| | | | | 0.2 | 0.691 | 6 | 3 | |
| **Pi10W** | 26399674 | 4256931 | 1.476 | 0.1 | 0.482 | 3 | 2 | **4 ± 2** |
| | | | | 0.2 | 0.657 | 4 | 2 | |

Immediately east of the Main Scarp, the lava pile comprises ages between 115 ± 4 and 75 ± 4 ka (Fig. 12c). A lava flow sampled from the top of this sequence, at the foot of the Main Scarp, yields an age of 47 ± 3 ka (Figs. 12b and 12c). S1 is partially covered by a 49 ± 4 ka lava flow (Fig. 12b). The volcanic sequence at the foot of S1 was dated between 90 ± 4 and 46 ± 4 ka (Fig. 12c). A lava flow cropping out on the eastern sector of S3, and apparently cascading over S2, was dated as 69 ± 4 ka. Towards the E, other lavas cascading over S2 were dated between 43 ± 8 ka and 5 ± 3 ka. The lava flow that forms the eastern sector of the delta yields an age of 10 ± 2 ka.

The oldest ages determined for the northern slope of the Fissural System, published in Costa et al. (2014), correspond to the base of a prominent coastal cliff in the E, which was dated at 70 ± 4 ka, and to a lava flow masking an interpreted landslide scar in the W, which was dated at 69 ± 4 ka (Fig. 12a). Younger ages were measured on samples collected along the coastal cliffs and one canyon, ranging between 58 ± 6 and 4 ± 2 ka.

For Pico Stratovolcano, an age of 53 ± 5 ka was obtained in its NE flank (Fig. 12a, Costa et al., 2014). Unfortunately, it was not possible to determine precisely the age of the sample collected in the NW flank (Pi11Q). The Ar analysis was attempted 4 times, but there was no satisfactory convergence of results, which ranged between 0 and 35 ka. Therefore, we consider that the age of this sample is just indicative, but overall supports volcanism younger than 35 ka.

## 4. Discussion

The new K-Ar ages here presented, complemented by the data published in Costa et al. (2014), are fully consistent with our field observations, and allow the age calibration of Pico's volcano-stratigraphy for the last 200 kyr. The new data further show that the island has experienced several phases of rapid volcanic growth and episodic lateral destabilization.

### *4.1. Geological evolution of Pico*

#### *4.1.1. Early construction of the island*

The sub-aerial growth of the Topo Volcano is here constrained between ca. 186 ± 5 and 125 ± 4 or 115 ± 4 ka (Figs. 13, 14 and 15). Given the present morphology of the Topo sector and the attitude of the lava flows (Figs 12 and 13), the summit of the Topo Volcano should have been originally located in the topographically depressed area bounded by the Main Scarp, which

is consistent with the positive gravity anomaly detected in this area (Nunes et al., 2006).

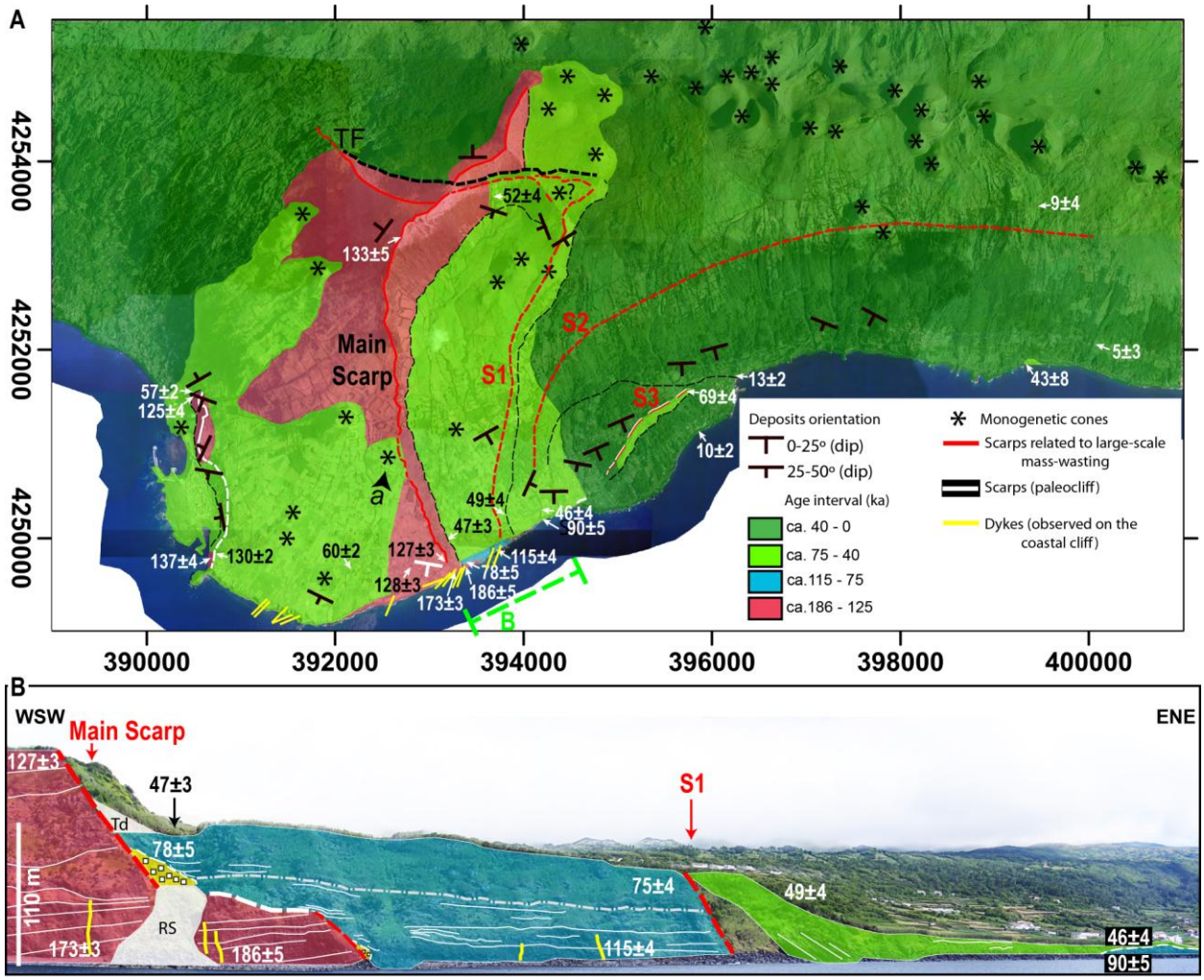


**Fig, 13**. (A) Geologic map built from the field observations and the new K-Ar data, with units defined as a function of the main unconformities observed in the field, and calibrated by the isotopic ages. Geology drawn on shaded relief with 10 m resolution DEM. (B) Interpreted profile of the coastal cliff indicated by green dashed line in (A). Grey dash-dotted line shows possible unconformity. Yellow lines represent dykes. *RS* corresponds to a recent small rockslide. *Td* corresponds to a recent talus deposit. Yellow wedge with embedded squares marks a talus deposit covered by the 78 ka lavas.

### *4.1.2. Destruction of the early edifice*

The several scars that affect the central/eastern part of the island point to repeated large-scale episodes of lateral destabilization, which may have occurred either in a gradual and/or in a catastrophic way. The new ages here reported on the lava successions affected by and/or concealing the main failures provide important new insights into the nature and the possible sequential development of these flank instabilities.

In the uppermost sector of the Topo volcano, the lateral contrast between the blocks to

the South and North of the inferred Topo Fault (Fig. 13a) support the existence of a fault that accommodated subsidence of the northern block (Madeira, 1998), but we could not find evidence for a strike-slip component (as proposed by Madeira, 1998). Costa et al. (2014) suggested that the destruction of Topo's N flank involved gradual deformation along this structure, coupled with catastrophic failure towards the N more than ca. 70 ka ago. The youngest possible age of 115 ± 4 ka obtained for the Topo volcanic succession provides a new temporal bound, which now constrains the occurrence of the northern catastrophic flank collapse between ca. 115 and 70 ka.

In Pico's SE flank, the collapse structure is much more complex than in Pico´s N flank, in terms of geometry, unconformities, faults, type of collapse, and ages. Most importantly, the collapse structure in the SE seems composite, i.e., with an earlier catastrophic collapse and a still active slump, in great contrast to the northern collapses. Therefore, it deserves a more detailed discussion before coming to the conclusions.

At the shore level, an apparent discontinuity between samples Pi10AA and Pi10AB (Fig. 8c) exists in the (downward) prolongation of the Main Scarp. This discontinuity can thus be interpreted as a fault segment (*Fault 1*, Fig. 14). However, the ages of the lava flows on the base of the sequences affected by this possible fault show an older age on the hanging wall, seemingly inconsistent with a normal fault. Given the E-W orientation of the Main Scarp's headwall, and that the lava flows dip to the SW, the ca. N-S part of the scarp must have a dextral strike-slip component that can justify the ages obtained to each side of the fault.

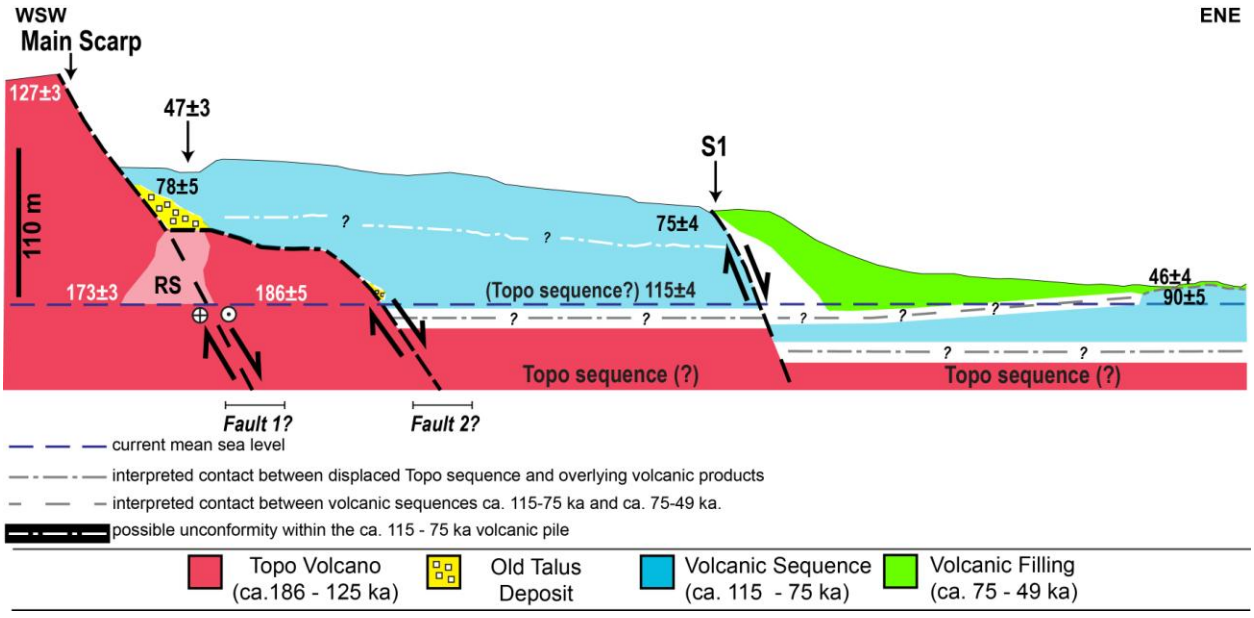


**Fig. 14**. Interpretative scheme of the slump structure.

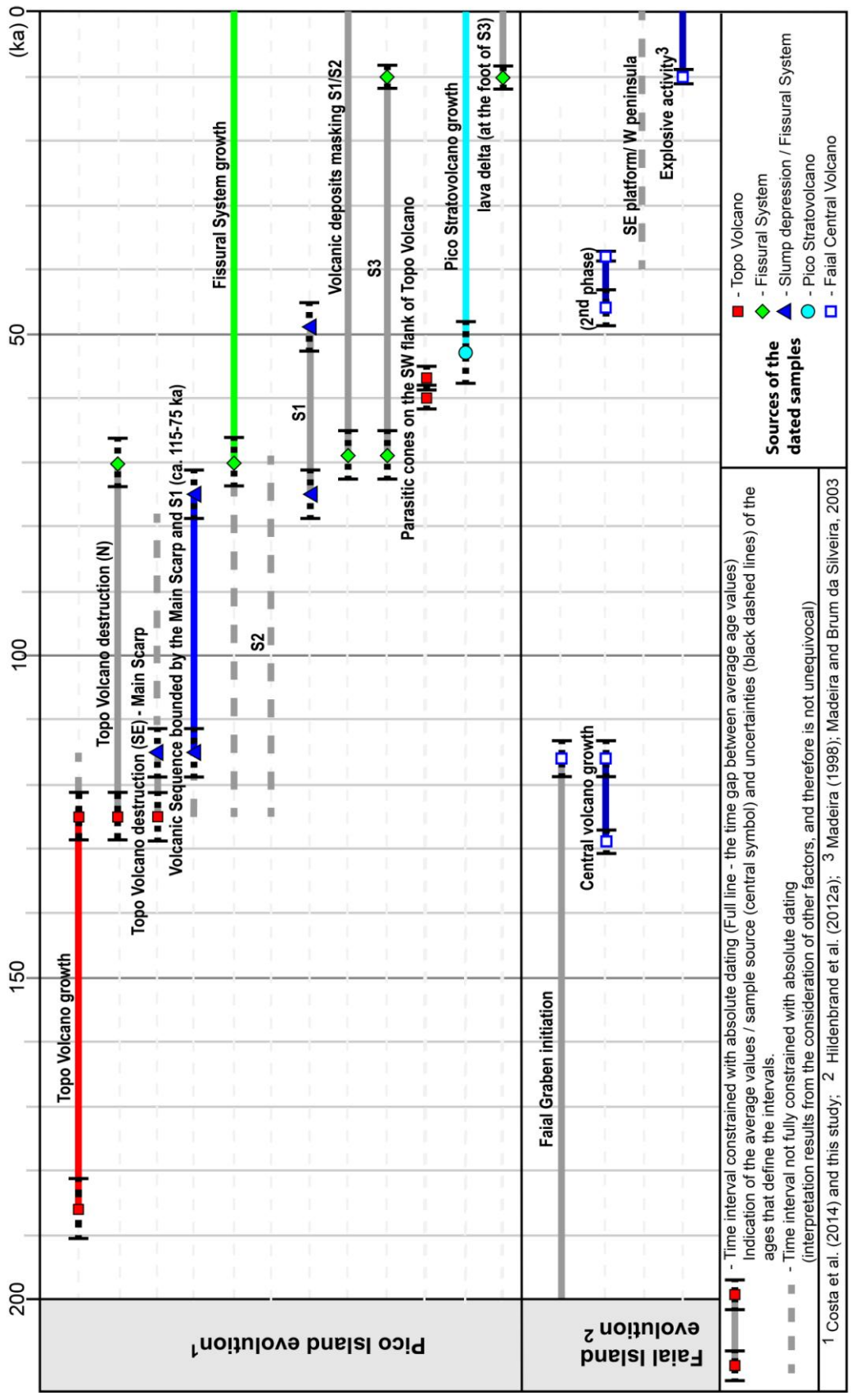


**Fig. 15**. Time line of the evolution of Pico and Faial in the last 200 kyr.

Some tens of meters farther east, the discontinuity interpreted as *Fault 2* (Fig. 14) presents an irregular geometry and is apparently connected to the Main Scarp. *Fault 2* is overlain by old breccia/talus deposits, and it separates two volcanic sequences of distinct ages (ca. 186 – 127 in the foot wall, and ca. 115 – 75 ka in the hanging wall). The age of 115 ± 4 ka obtained on a lava flow exposed at the base of the sequence in the hanging wall almost overlaps within the range of uncertainties with the age of 125 ± 4 ka measured on the uppermost lava flows from the Topo Volcano . Therefore, the lava flow here dated at ca. 115 ka may either constitute (1) the top of Topo Volcano edifice displaced by a (normal) fault, or (2) the base of a volcanic sequence filling a low topography created during an early phase of destruction of Topo Volcano (Fig. 15).

(1) In the first hypothesis, gradual displacement along *Fault 2* would imply a cumulative vertical displacement of at least 200 m (current difference in altitude plus erosion of the top of Topo) during a maximum period of 115 kyr, which gives an average conservative rate of ca 2 mm/yr. Such value is a minimum, because the lava flows onlapping the midslope talus deposit at the foot of the Main Scarp are here dated at ca 78 ka. This suggests that significant movement on *Fault 2* occurred between ca. 115 ka and 78 ka, which would indicate an average rate of downward displacement closer to 5 mm/yr. Noticeably, the two rates here estimated are similar to present vertical displacements recorded by GPS and InSAR data within the SE Pico slump (Hildenbrand et al., 2012b). This scenario implies that the upper displaced sequence of Topo is presently under sea level, and without any unconformity separating the 125 from the 115 ka lavas.

(2) In the second hypothesis, an early phase of destruction affected the Topo Volcano between ca. 125 and 115 ka, with these younger lavas sitting unconformably on the younger lavas of the Topo Volcano (ca. 125 ka) in the hanging wall. A catastrophic collapse seems unlikely, because the submarine slopes offshore *Fault 2* seem globally preserved, though slightly disrupted (Fig. 6). Therefore, we prefer the hypothesis of a gradual downward movement of the island flank close to the Main Scarp. This scenario is thus similar to hypothesis 1, but it implies that the upper displaced sequence of Topo is presently under sea level, and with an unconformity separating the 125 from the 115 ka lavas. It also means that initiation of the slump between 125 ka and 115 ka was followed by significant volcanism filling part of the former SE depression at ca. 115 ka. This supports a significant eruptive response to flank movement, as observed on other oceanic islands (e.g., Manconi et al., 2009; Boulesteix et al., 2012). However, in our case, early slumping was not followed by the growth of a large, well-individualized post-collapse edifice. The attitude and the dip of the 115 ka lava flows filling the depression could suggest that

they were erupted from small cones located on the headwall zone, but these feeders have not been found. We note that the dip of the 115 lava flows, after removal of the probable rotation over a listric fault, would be consistent with the dip of the Topo Volcano's southern flank.

The ca.115-75 ka volcanic sequence is bounded in the E by a steep scarp corresponding to S1, which is covered by a cascading lava flow equivalent to our sample Pi10AD, here dated at 49 ± 4 ka. This suggests that S1 accommodated significant deformation between ca. 75 and 49 ka (Figs. 14 and 15). The lava flow sampled at the base of the S1's hanging wall is here dated at 90 ± 5 ka, which is very close to the age of one of the uppermost lavas from the ca. 115 - 75 ka succession (sample Pi10J, age of 78 ± 5 ka), within the range of uncertainties. This suggests that, like the Main Scarp, S1 developed in a gradual rather than catastrophic way. Consequently, it seems reasonable to infer that, locally, the displaced flank of the old volcano is under present sea level, immediately at the foot of S1.

In contrast, the submarine flank of the island is clearly interrupted by a large embayment offshore S2 (Fig.6). The debris field recognized on the distal submarine slope also closely matches the inland extension of S2. This supports the creation of the S2 arcuate structure by a catastrophic flank collapse, which generated large debris-avalanche deposits. Despite careful inland investigation, we could not observe the volcanic sequence cut by S2. Instead, the scar has been extensively covered by more recent cascading lava flows. In the western portion of S2, especially, cascading lava flows partly formed a sub-aerial platform which is nowadays cut by S3. One of these lavas sampled at the base of the S3 cliff (sample Pi11G) is here dated as 69 ± 4 ka (Fig. A.6). Another lava flow cascading on the eastern part of S2 (our sample Pi11D) yields a K/Ar age of 43 ± 8 ka. From these new data, the catastrophic sector collapse here proposed occurred prior to ca 69 ka. The maximum age of the collapse is more difficult to establish, especially as the possible connection between S1 and S2 remains enigmatic. As S2 affects a domain previously occupied by Topo Volcano, we establish ca. 125 ka as maximum age for S2 formation (Fig. 15). The sub-aerial part of S2 truncates the previous lava succession(s) up to a height of ca. 600 m. From the volcanic pile(s) exposed immediately to the west of S1, it seems plausible that the collapse removed not only the whole flank of the old volcanic edifice, but also part of the filling succession here dated between 115 ka and 75 ka. In such hypothesis, the catastrophic flank collapse here proposed possibly occurred between 75 ka and 69 ka. This narrow time interval coincides with the development of widespread volcanism along the whole Fissural System, as massive lava flows concealing the scars in the northern sector of the island yield similar ages (Costa et al., 2014). Parasitic scoria cones also developed close to the main scarp, upon the eroded remnants of the Topo Volcano, ca 60 ka ago. Such apparent synchronicity

support a close link between volcanism and deformation along the various structures affecting the central part of the island. More recently, volcanic cones grew on S2, which coupled with the current distribution of subsidence in the slump area suggest that S2 has accommodated gradual subsidence recently (Hildenbrand et al., 2012b). Similarly, the steepness of the Main Scarp suggests that it accommodated movement recently.

Finally, S3 constitutes a steep curvilinear scarp (Fig. 13a), whose orientation is compatible with the general orientation of the slump structures previously described. This scar cuts lava flows here dated at 69 ± 4 ka, and is partially blanketed in the west by volcanic deposits that form the lava delta here dated at 10 ± 2 ka (Fig. 13a). From the bathymetric data, it appears quite clear that this portion of the island flank partly sits on the submarine embayment associated with S2, and therefore that it may be quite unstable. Therefore, we cannot exclude that the arcuate scarp S3 formed by repeated detachment of coastal segments, prior to ca 10 ka.

It is acknowledged that the evolution of a slump structure can lead to catastrophic destabilization (e.g., Moore et al., 1989, 1994; Urgeles et al., 1999). From the step-by-step evolution here presented, we conclude that Pico's SE flank slump evolved mostly through gradual deformation during the last 125 kyr, with the occurrence of a catastrophic flank collapse along S2 between ca. 75 and 69 ka (Fig. 15). The consecutive local development of faults most probably potentiated the current focus of subsidence (Keating and McGuire, 2000; Hildenbrand et al., 2012b).

### *4.1.3. Growth and destruction of the Pico Stratovolcano*

The onset of Pico Stratovolcano sub-aerial growth remains poorly constrained in time. The age obtained by Costa et al. (2014) on a lava sampled in a small cliff (NE of the main edifice), and the results obtained from our sample Pi11Q from the northwest part of the island (≤ 35 ka), both suggest that the volcano developed during the last 50 kyr, and more specifically during the last 35 kyr. This points to a concentration of the volcanism in the western side of the island, yielding the fast construction of a robust (still active) edifice within only a few tens of kyr. However, our data show that recent (synchronous?) volcanic activity also occurred along the main Fissural System, and in the slump area ca 40-50 ka ago, and during the last 15 kyr.

Regarding the WNW-ESE scarp on the southern flank of Pico Stratovolcano, previous published works only mentioned that this scarp was covered by volcanic deposits from the stratovolcano, and that there are significant recent colluvium deposits along the base of the scarp (Chovelon, 1982; Madeira, 1998; Nunes, 1999; Nunes et al., 1999a). Our field observations add

to the published knowledge regarding this scarp. In the S. Caetano canyon, as we did not observe a large-scale unconformity, we propose that the sequences observed on the scarp are concealing a large-scale failure surface (Fig. 16). These sequences of volcano-sedimentary material and lava flows are cut by numerous dykes disposed *en échelon*, which strike parallel to the main scarp orientation and dip downstream (Figs. 11 and 16).

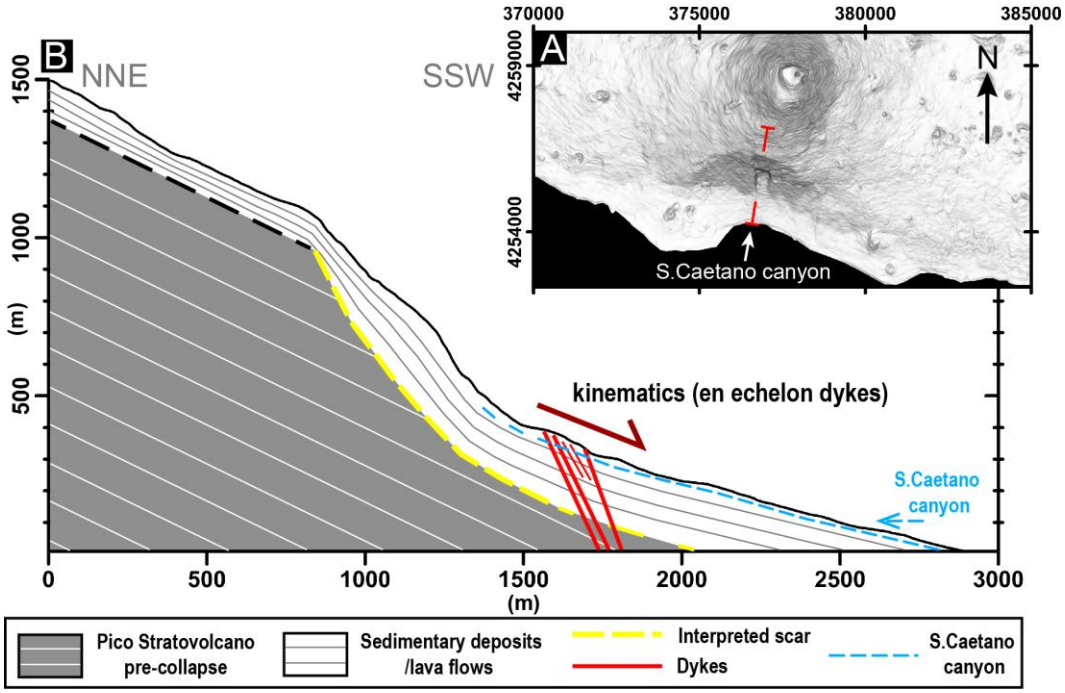


**Fig. 16**. Interpretation of the topographic profile and observations presented in Fig.10.

The overall intrusion of the dykes along the scar alignment may have been conditioned by: (1) the deflection of magma ascent towards an orientation sub-parallel to the scarp, possibly caused by the influence of the Pico Stratovolcano's topographic load on the stress field (McGuire and Pullen, 1989; Acocella and Neri, 2009; Maccaferri et al., 2011); (2) the structural control of an hypothetical deep WNW-ESE fault (Nunes, 1999); (3) the discontinuity of the scar, at least close to the surface.

The local *en échelon* arrangement of the dykes suggests that the intruded volcano-sedimentary sequence was undergoing shear deformation at the moment of intrusion (Fig. 16), most likely as a slump. Furthermore, the possibility of future structurally controlled dyke intrusions along this scarp, as Pico Stratovolcano has been historically active, suggest that this sector is prone to landslide occurrence triggered by dyke intrusion. A parallel may be established with the case of Fogo Island (Cape Verde), where historic volcanic events led to the opening of *en échelon* fissures in the filling sequence, regarded as evidence for progressive destabilization of the affected flank (Day et al., 1999). The local steepness of the topography and even the

sporadic strong discharge of stream water along the deeply incised creek reinforce the idea that this scarp is highly prone to further landslide occurrence.

*4.2. Evolution of the Pico-Faial ridge during the last 200 kyr*

From our new data, the volcanism in Pico occurred through short episodes of volcanic construction and repeated destabilization during the last 200 kyr. Our data additionally suggest that the growth of the island and its repeated destruction have occurred along preferential directions, i.e. NNE-SW, ENE-WSW and WNW-ESE. These directions correspond to major regional tectonic structures in the lithosphere.

The NNE-SSW direction is a major regional trend, which is parallel to the local orientation of the MAR (Fig. 1a). The NE-SW to ENE-WSW trend is a transform direction associated with the present Eu/Nu plate boundary (DeMets et al., 2010), and has been recently recognized by Marques et al. (2014b) and Sibrant et al. (2014) in Faial-Pico volcanic ridge and Graciosa island, respectively. The WNW-ESE trend corresponds to the major horst/graben and volcanic ridge structures in central Azores. These main trends can all be found in Pico: the dykes along the coastline range in strike between NNE-SSW and ENE-WSW (Fig. 13a); the sea cliff and the marine platform that limits the sub-aerial remnants of Topo Volcano to the E is oriented ENE-WSW (Fig. 5); Pico is elongated WNW-ESE, and the Caldera (Faial), the Pico and the Topo volcanoes follow the same trend. Based on the position of these three main volcanoes, the main lithospheric trends, and recently recognized faults (e.g. Marques et al., 2014b), we conclude that the main central-type volcanoes developed at the intersection of major lithospheric faults.

In Faial, the oldest sub-aerial volcanism was dated at ca. 850 ka by Hildenbrand et al. (2012a). It was followed by ca. 500 kyr period of destruction of the original edifice (see also Appendix B). Around 360 ka, a new smaller edifice was growing in NE Faial. The equivalent of this construction/destruction activity in Faial was not found in Pico, despite belonging to the same volcanic ridge.

Based on the data/interpretations here presented and on previous works (mainly Hildenbrand et al., 2012a; Costa et al., 2014), we propose the following evolution of the Pico-Faial ridge for the last 200 kyr (Figs. 15 and 17). The schemes provided in Fig. 17 were drawn on a 3D perspective of the ridge provided as Fig. B.1.

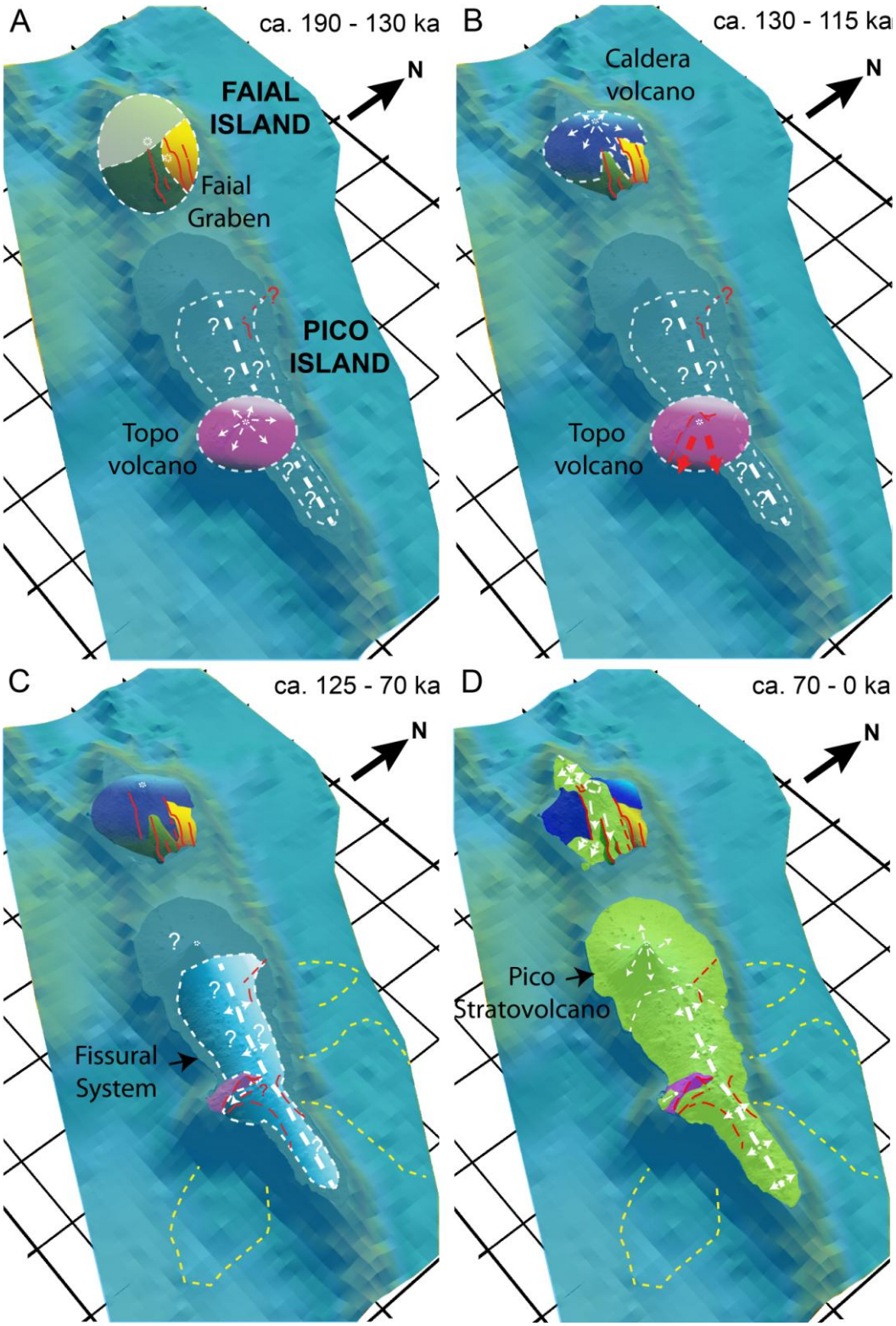


**Fig. 17**. Step-by-step evolution of the Pico-Faial volcanic ridge in the last 200 kyrs. (A) Simultaneous development of the island-scale graben in Faial and growth of the Topo volcano (pink coloured edifice) in Pico. (B) Growth of a central volcano in Faial, partially filling the Faial Graben, and partial destruction of Topo in Pico, forming the main scarp of the slump structure. (C) Volcanic growth hiatus in Faial, with development of the graben structure, while

there was widespread growth of the Fissural System in Pico, with failure(s) on the N and S flanks, generating significant debris deposits indicated by yellow dashed lines. (D) Growth of the Fissural System, parasitic cones on Topo's flanks, and development of the Pico Stratovolcano in Pico. Volcanic growth in Faial, with partial filling of the graben structure, growth of the southeastern volcanic platform and western peninsula, with volcanic growth phases associated with gradual development of the graben structures.

(1) In Faial, a WNW-ESE island-scale graben, the Faial Graben, developed between ca. 350 and 130 ka (Hildenbrand et al., 2012a). Meanwhile, the sub-aerial Topo Volcano was growing in Pico (ca. 186-125 ka) (Figs. 15 and 17a).

(2) While Topo was reaching its final stages of growth in Pico and being dismantled (ca. 125-115 ka), a central-type volcano (the Caldera Volcano) was growing in Faial (ca. 130-115 ka, Hildenbrand et al., 2012a), partially filling the central depression of the Faial Graben (Figs. 15 and 17b).

(3) Between ca. 125 and 70 ka, there was considerable sub-aerial growth and destabilization of the Fissural System in Pico. The volcanics from the Fissural System partially masked the scar(s) affecting the Topo Volcano (Figs. 15 and 17c). Two major catastrophic flank collapses occurred prior to 70 ka, and produced debris deposits now identified in the ocean bottom.

(4) Since ca. 70 ka (Figs. 15 and 17d), volcanic products have erupted from the Fissural System in Pico, and partially masked the earlier collapse scars. Around ca. 60 ka, parasitic cones developed on Topo Volcano's SW flank, covering it unconformably. The Pico Stratovolcano has been growing on the westernmost sector of the island, at least since ca. 53 ka. The S flank of this stratovolcano has suffered a partial flank collapse. In the last 10 kyr, extended volcanic activity has occurred in both Pico Stratovolcano, the Fissural System, and as parasitic activity on Topo's SW flank. A slump is currently active in SE Pico (Hildenbrand et al., 2012b). In Faial, since ca. 46 ka, newly erupted materials have partially filled the Faial Graben, extending the surface of the island towards the SE. Since ca. 10 ka, a WNW-ESE sub-aerial fissural system grew towards the W, and episodes of explosive activity occurred in the central volcano (Madeira and Brum da Silveira. 2003; Hildenbrand et al., 2012a, Figs. 15 and 17d).

From this reconstruction, we notice that: (a) the growth of Topo Volcano's sub-aerial edifice in Pico occurred at the end of the time interval defined for the major development of the Faial Graben in Faial (Figs. 14 and 17a); (b) the time span for the final stage of Topo Volcano's growth, its destruction towards the SE, and the probable beginning of the Fissural System growth

in Pico, coincides with the growth of the Caldera Volcano in Faial (Figs. 14 and 17b). These moments reflect particularly well the dynamics of growth and destruction in the evolution of the Pico-Faial volcanic ridge.

The Pico-Faial volcanic ridge sits on top of a master fault, locally parallel to the orientation of the Nu-Eu plate boundary (Fig.1b), which currently accommodates part of the inter-plate deformation (Marques et al., 2013a, 2014a). In the last 200 kyr, the ridge has been punctuated by three WNW-ESE aligned central-type volcanoes, as a consequence of the intersection of structural trends oblique to WNW-ESE. These structural trends are expressed by: (a) the orientation of the submarine alignments, dykes and SE coastal cliff cutting the Topo volcano (ranging between the MAR-inherited ca. NNE-SSW orientation, and the WSW-ENE orientation of the transforms of the Nu-Eu plate boundary); (b) the NNW-SSE fracture in Pico Stratovolcano, interpreted from the alignment of the volcanic vents of the 1718 volcanic eruption (Madeira and Brum da Silveira, 2003), the orientation expected for the structures accommodating pure extension in the Nu-Eu plate boundary (Marques et al., 2014b); (c) the NNE-SSW faults, dykes and extension fractures recognized on the sub-aerial domain of the polygenic edifices in Faial Island (Trippanera et al., 2014); (d) minor scarps interpreted in the submarine domain of the volcanic ridge, oriented according to the structural trends mentioned above (Lourenço, 2007). The marked dynamics of growth/destruction in both islands in the last 200 kyr is here considered to be intimately connected to the recent deformation in this diffuse plate boundary.

The sub-aerial fissural system in the S. Jorge ridge started to develop at ca 1.3 Myr, much earlier than the beginning of the sub-aerial growth of Faial (ca. 850 ka). The bulk of the sub-aerial S. Jorge was already built before sub-aerial Pico started to grow. According to Hildenbrand et al. (2008; 2014), the volcanic sequence in S. Jorge Island is younger than ca. 750 kyr, contemporaneous with the development of the sub-aerial Pico-Faial ridge, and was marked by lower degrees of partial melting than the 1.3-1.2 Ma sequence. Furthermore, the widespread sub-aerial growth of Pico-Faial fissural systems in the last ca.125 kyr contrasts with the reduced recent volcanic growth recorded for S. Jorge Island (Hildenbrand et al., 2008). These evidences suggest that the accommodation of the extension associated with the Nu-Eu plate boundary along these two ridges (Marques et al., 2013a, 2014a) changed from a state of main extension accommodated along the S. Jorge ridge (previous to ca. 850 ka), to a state of extension accommodated by both volcanic ridges (in the last ca. 850 kyr), with reinforcement of the Pico-Faial ridge as a structure accommodating extension in the last ca. 125 kyr.

## 5. Conclusions

From the data/interpretations here presented, coupled with the results/interpretations presented in Costa et al. (2014), we propose the following evolution for Pico Island (Fig. 15):

A – The sub-aerial development of Topo Volcano lasted between ca. 186 and 115 ka.

B – The destruction of Topo Volcano's N flank occurred between ca. 125 and 70 ka, with gradual subsidence along the Topo Fault and catastrophic deformation further N (probably already affecting deposits from the Fissural System, with associated generation of the submarine debris deposit reported in Costa et al., 2014). The gradual destruction of Topo's SE flank occurred between ca. 125 and 115 ka, generating the Main Scarp of the currently active slump (Hildenbrand et al., 2012a). Between ca. 125 and 69 ka, the distal sector of this flank was affected by a major catastrophic collapse.

C – Between ca. 125 and 69 ka, the sub-aerial Fissural System grew substantially. In the same period, this fast growing edifice suffered catastrophic flank collapses: (1) on the westernmost and easternmost sectors of the Fissural System's N flank, with the occurrence of collapses directed towards the N, older than ca. 69 ka ago and constrained between ca. 125 and 70 ka, respectively (Costa et al., 2014, and this study); (2) on the Fissural System's S flank, propagating the eastern sector of S2 (affecting the most distal sector of the subsided SE flank of Topo volcano) and generating the large debris deposit on the offshore, between ca. 125 and 69 ka.

D – Since ca. 70 ka, volcanic products erupted from the Fissural System, blanketing in great part the collapse scars. Around ca. 60 ka, parasitic cones developed unconformably on the SW flank of the Topo Volcano.

E – The Pico Stratovolcano has been growing on the westernmost sector of the island, at least since ca. 53 ka. The S flank of this stratovolcano has suffered a partial flank collapse. The interpreted failure surface was afterwards covered by more recent volcano-sedimentary deposits, which have been repeatedly intruded by dykes parallel to the scarp surface and disposed *en échelon*. This scarp is considered to be highly prone to landslide occurrence.

F – A slump is currently active in SE Pico, re-activating in-depth older mass-wasting structures, as there was shown clear evidence for movement along S2 (Hildenbrand et al., 2012a).

The development of Pico and Faial islands during the last 200 kyr illustrates the strong dynamic competition between volcanic construction and destruction in such active tectonic settings, with evidence for simultaneous occurrence of large-scale destruction in one island while

there was significant volcanic growth in the other. The comparison of the evolution of the Pico-Faial ridge and the evolution of the neighbouring S. Jorge ridge suggests that the role of Pico-Faial ridge as a structure accommodating part of the extension on the diffuse Nu-Eu boundary has been consolidated in the last ca. 125 kyr.

**Acknowledgments**

This is a contribution to Project MEGAHazards (PTDC/CTE-GIX/108149/2008), funded by FCT, Portugal. ACGC has a PhD scholarship funded by FCT (SFRH/BD/68983/2010). ACGC wishes to acknowledge Judite Costa, José Costa, José Dias and Nílton Nunes for the support in the fieldwork. We acknowledge EMEPC for providing the high-resolution bathymetric data used here.

**References**

Acocella, V., Neri, M., 2009. Dike propagation in volcanic edifices: Overview and possible developments. Tectonophysics 471, 67─77. http://dx.doi.org/10.1016/j.tecto.2008.10.002

Borges, J. F., Bezzeghoud, M., Buforn, E., Pro, C., Fitas, A., 2007. The 1980, 1997 and 1998 Azores earthquakes and some seismo-tectonic implications. Tectonophysics 435 (1─4), 37 –54. http://dx.doi.org/10.1016/j.tecto.2007.01.008.

Boulesteix, T., Hildenbrand, A., Gillot, P.Y., Soler, V., 2012. Eruptive response of oceanic islands to giant landslides: new insights from the geomorphologic evolution of the Teide–Pico Viejo volcanic complex (Tenerife, Canary). Geomorphology 138 (1), 61–73. http://dx.doi.org/10.1016/j.geomorph.2011.08.025.

Boulesteix, T., Hildenbrand, A., Soler, V., Quidelleur, X., Gillot, P.Y., 2013. Coeval giant landslides in the Canary Islands: implications for global, regional and local triggers of giant flank collapses on oceanic volcanoes. J. Volcanol. Geotherm. Res. 257, 90–98. http://dx.doi.org/10.1016/j.jvolgeores.2013.03.008

Carracedo, J.C., 1994. The Canary Islands: an example of structural control on the growth of large oceanic-island volcanoes. Journal of Volcanology and Geothermal Research 60, 225-241.

Cassignol, C., Gillot, P.Y., 1982. Range and effectiveness of unspiked potassium–argon dating: experimental groundwork and applications. In: Odin, G.S. (Ed.) Numerical Dating in Stratigraphy. John Wiley & Sons Ltd, Chichester, England, pp. 159–179.

Chovelon, P., 1982. Evolution volcanotectonique des iles de Faial et de Pico. Ph.D. Thesis.Univ. Paris-Sud, Orsay, France, 186 pp.

Clouard, V., Bonneville, A., 2004. Submarine Landslides in French Polynesia, In: Hekinian, R., Stoffers, P, Cheminé, J.-L. (Eds.), Oceanic Hotspots: intraplate submarine magmatism and tectonism. Springer-Verlag, pp. 209-238.

Clouard, V., Bonneville, A., Gillot, P.Y., 2001. A giant landslide on the southern flank of Tahiti Island, French Polynesia. Geophys. Res. Lett. 28, 2253–2256.

Costa, A.C.G., Marques, F.O., Hildenbrand, A., Sibrant, A.L.R., Catita, C.M.S., 2014. Large-

scale catastrophic flank collapses in a steep volcanic ridge: The Pico–Faial Ridge, Azores Triple Junction. J. Volcanol. Geotherm. Res. 272, 111 –125, http://dx.doi.org/10.1016/j.jvolgeores.2014.01.002.

Day, S.J., Heleno da Silva, S.I.N., Fonseca, J.F.B.D., 1999. A past giant lateral collapse and present-day flank instability of Fogo, Cape Verde Islands. J. Volcanol. Geotherm. Res. 94 (1–4), 191–218. http://dx.doi.org/10.1016/S0377-0273(99)00103-1.

Demande, J., Fabriol, R., Gérard, A., Iundt, F., 1982. Prospection géothermique des Iles de Faial et Pico (Açores). Report 82SGN003GTH, Bureau de Recherches Géologiques et Minières, Orléans, France.

DeMets, C., Gordon, R.G., Argus, D.F., 2010. Geologically current plate motions. Geo-phys. J. Int. 181,1–80. http://dx.doi.org/10.1111/j.1365-246X.2009.04491.x

Féraud, G., Kaneoka, I., Allègre, C.J., 1980. K/Ar ages and stress pattern in the Azores: geodynamic implications. Earth Planet. Sci. Lett. 46 (2), 275–286. http://dx.doi.org/10.1016/0012-821X(80)90013-8.

Fernandes, R.M.S., Bastos, L., Miranda, J.M., Lourenço, N., Ambrosius, B.A.C., Noomen, R., Simons, W., 2006. Defining the plate boundaries in the Azores region. J. Volcanol. Geotherm. Res. 156 (1–2), 1–9. http://dx.doi.org/10.1016/j.jvolgeores.2006.03.019.

Forjaz, V.H., 1966. Carta geológica do sistema vulcânico Faial-Pico-S. Jorge. Escala 1:200 000. In: Machado, F., Forjaz, V.H., (Eds.), A actividade vulcânica na ilha do Faial (1957-67), 1968, Comissão de Turismo da Horta, Portugal, 89 pp.

Forjaz, V.H., Serralheiro, A., Nunes, J.C., 1990. Carta vulcanológica dos Açores - Grupo Central. Escala 1:200000. Serviço Regional de Protecção Civil, Universidade dos Açores e Centro de Vulcanologia INIC, Ponta Delgada, Portugal.

França, Z., 2000. Origem e evolução petrológica e geoquímica do vulcanismo da ilha do Pico. Açores. Ph.D. Thesis, Univ. Açores, Ponta Delgada, Portugal.

França, Z., Rodrigues, B., Cruz, J.V., Carvalho, M.R., Nunes, J.C., 1995. Ensaio de orientação para o estudo petrológico e geoquímico das lavas históricas da ilha do Pico - Açores. IV Congresso Nacional de Geologia, Porto, Mem. Mus. Geol. Fac. Ciências Porto 4, 723-724.

França, Z., Nunes, J.C., Cruz, J.V., Carvalho, M.R, Serralheiro, A., 2000. Carta de distribuição petrográfica da ilha do Pico (Açores) e mapa de amostragem. In: França, Z. (Eds.) Origem e evolução petrológica e geoquímica do vulcanismo da ilha do Pico - Açores, 2002, Câmara Municipal de São Roque do Pico, Portugal, 391 pp.

França, Z.T.M., Tassinari, C.C.G., Cruz, J.V., Aparicio, A.Y., Araña, V., Rodrigues, N.R., 2006. Petrology, geochemistry and Sr-Nd-Pb isotopes of the volcanic rocks from Pico Island - Azores (Portugal). J. Volcanol. Geotherm. Res. 156 (1–2), 71–89. http://dx.doi.org/10.1016/j.jvolgeores.2006.03.013

Germa, A., Quidelleur, X., Lahitte, P., Labanieh, S., Chauvel, C., 2011. The K–Ar Cassignol Gillot technique applied to western Martinique lavas: a record of Lesser Antilles arc activity from 2 Ma to Mount Pelée volcanism. Quat. Geochronol. 6 (3–4), 341–355. http://dx.doi.org/10.1016/j.quageo.2011.02.001.

Gillot, P.Y., Cornette, Y., 1986. The Cassignol technique for potassium–argon dating, precision and accuracy: examples from the Late Pleistocene to Recent volcanics from southern Italy. Chem. Geol. Isot. Geosci. Sect. 59, 205–222. http://dx.doi.org/10.1016/0168-9622(86)90072-2.

Gillot, P.Y., Hildenbrand, A., Lefèvre, J.C., Albore-Livadie, C., 2006. The K/Ar dating method: principle, analytical techniques and application to Holocene volcanic eruptions in Southern Italy. Acta Vulcanol. 18, 55–66.

Hildenbrand, A., Gillot, P.Y., Le Roy, I., 2004. Volcano-tectonic and geochemical evolution of an oceanic intra-plate volcano: Tahiti-Nui (French Polynesia), Earth Planet. Sci. Lett., 217 (3-4), 349-365. http://dx.doi.org/10.1016/S0012-821X(03)00599-5

Hildenbrand, A., Gillot, P.Y., Bonneville, A., 2006. Offshore evidence for a huge landslide of the northern flank of Tahiti–Nui (French Polynesia). Geochemistry Geophysics Geosystems 7 (3), Q03006. http://dx.doi.org/10.1029/2005GC001003.

Hildenbrand, A., Madureira, P., Ornelas Marques, F., Cruz, I., Henry, B., Silva, P., 2008. Multi-stage evolution of a sub-aerial volcanic ridge over the last 1.3 Myr: S. Jorge Island, Azores Triple Junction. Earth Planet. Sci. Lett. 273 (3–4), 289–298. http://dx.doi.org/10.1016/j.epsl.2008.06.041.

Hildenbrand, A., Marques, F.O., Costa, A.C.G., Sibrant, A.L.R., Silva, P.M.F., Henry, B., Miranda, J.M., Madureira, P., 2012a. Reconstructing the architectural evolution of volcanic islands from combined K/Ar, morphologic, tectonic, and magnetic data: the Faial Island example (Azores). J. Volcanol. Geotherm. Res. 241–242, 39–48. http://dx.doi.org/10.1016/j.jvolgeores.2012.06.019.

Hildenbrand, A., Marques, F.O., Catalão, J., Catita, C.M.S., Costa, A.C.G., 2012b. Large-scale active slump of the southeastern flank of Pico Island, Azores. Geology 40 (10), 939–942. http://dx.doi.org/10.1130/G33303.1.

Hildenbrand, A., Marques, F.O., Catalão, J., Catita, C.M.S., Costa, A.C.G., 2013. Large-scale active slump of the southeastern flank of Pico Island, Azores: reply. Geology 41(12), e302. http://dx.doi.org/10.1130/G34879Y.1.

Hildenbrand, A., Weis, D., Madureira, P., Marques, F.O., 2014. Recent plate re-organization at the Azores Triple Junction: Evidence from combined geochemical and geochronological data on Faial, S. Jorge and Terceira volcanic islands. Lithos 210-211, 27-39. doi:10.1016/j.lithos.2014.09.009

Keating, B.H., McGuire, W.J., 2000. Island Edifice Failures and Associated Tsunami Hazards. Pure appl. geophys. 157 (6–8), 899–955.

Krastel, S., Schmincke, H.U., Jacobs, C.L., Rihm, R., Le Bas, T.P., Alibés, B., 2001. Submarine landslides around the Canary Islands. J. Geophys. Res. 106 (B3), 3977–3997. http://dx.doi.org/10.1029/2000JB900413.

Lipman, P.W., Normark, W.R., Moore, J.G., Wilson, J.B., Gutmacher, C.E., 1988. The giant submarine Alika debris slide, Mauna Loa, Hawaii. J. Geophys. Res. Solid Earth 93 (B5), 4279–4299. http://dx.doi.org/10.1029/JB093iB05p04279.

Lourenço, N., 2007. Tectono-magmatic Processes at the Azores Triple Junction. Ph.D. Thesis, Univ. Algarve, Faro, Portugal, 239 pp.

Lourenço, N., Miranda, J.M., Luis, J.F., Ribeiro, A.,Mendes Victor, L.A., Madeira, J., Needham, H.D., 1998. Morpho-tectonic analysis of the Azores Volcanic Plateau from a new bathymetric compilation of the area. Mar. Geophys. Res. 20 (3), 141–156. http://dx.doi.org/10.1023/A%3A1004505401547.

Luis, J.F., Miranda, J.M., 2008. Reevaluation of magnetic chrons in the North Atlantic between 35ºN and 47ºN:Implications for the formation of the Azores Triple Junction and associated

plateau. J. Geophys. Res.113 (B10), B10105. http://dx.doi.org/10.1029/2007JB005573

Luis, J.F., Miranda, J.M., Galdeano, A., Patriat, P., 1998. Constraints on the structure of the Azores spreading center from gravity data. Mar. Geophys. Res. 20 (3), 157–170. http://dx.doi.org/10.1023/A:1004698526004

Maccaferri, F., Bonafede, M., Rivalta, E., 2011. A quantitative study of the mechanisms governing dike propagation, dyke arrest and sill formation. J. Volcanol. Geotherm. Res. 208, 39–50. doi:10.1016/j.jvolgeores.2011.09.001

Machado, F., Trêpa, M.V., Férin, C., Nunes, J.C., 1974. Crise sísmica do Pico (Açores), Nov. 1973. Comunicações dos Serviços Geológicos de Portugal 57, 229–242.

Madeira, J., 1998. Estudos de neotectónica nas ilhas do Faial, Pico e S. Jorge: Uma contribuição para o conhecimento geodinâmico da junção tripla dos Açores. Ph.D. Thesis. Univ. Lisboa, Portugal, 481 pp.

Madeira, J., Brum da Silveira, A., 2003. Active tectonics and first paleoseismological results in Faial, Pico and S. Jorge islands (Azores, Portugal). Ann. Geophys. 46 (5), 733–761. http://dx.doi.org/10.4401/ag-3453.

Manconi, A., Longpre, M.A., Walter, T.R., Troll, V.R., Hansteen, T.H., 2009. The effects of flank collapses on volcano plumbing systems. Geology 37 (12), 1099–1102. http://dx.doi.org/10.1130/G30104A.1

Marques, F.O., Catalão, J.C., DeMets, C., Costa, A.C.G., Hildenbrand, A., 2013a. GPS and tectonic evidence for a diffuse plate boundary at the Azores Triple Junction. Earth Planet. Sci. Lett. 381, 177–187. http://dx.doi.org/10.1016/j.epsl.2013.08.051.

Marques, F.O., Sibrant, A.L.R., Hildenbrand, A., Costa, A.C.G., 2013b. Large-scale sector collapses in the evolution of Santa Maria Island, Azores. Abstract Meeting AGU, 2013.

Marques, F.O., Catalão, J.C., DeMets, C., Costa, A.C.G., Hildenbrand, A., 2014a. Corrigendum to " GPS and tectonic evidence for a diffuse plate boundary at the Azores Triple Junction" [Earth Planet. Sci. Lett. 381 (2013) 177-187]. Earth Planet. Sci. Lett. 387, 1–3. http://dx.doi.org/10.1016/j.epsl.2013.11.029.

Marques, F.O., Catalão, J., Hildenbrand, A., Costa, A.C.G., Dias, N.A., 2014b. The 1998 Faial earthquake, Azores: Evidence for a transform fault associated with the Nubia-Eurasia plate boundary? Tectonophysics. http://dx.doi.org/10.1016/j.tecto.2014.06.024.

Masson, D.G., Watts, A.B., Gee, M.J.R., Urgeles, R., Mitchell, N.C., Le Bas, T.P., Canals, M., 2002. Slope failures on the flanks of the western Canary Islands. Earth Sci. Rev. 57 (1–2), 1–35. http://dx.doi.org/10.1016/S0012-8252(01)00069-1.

Masson, D.G., Le Bas, T.P., Grevemeyer, I., Weinrebe, W., 2008. Flank collapse and largescale landsliding in the Cape Verde Islands, off West Africa. Geochem. Geophys. Geosyst. 9 (7), Q07015. http://dx.doi.org/10.1029/2008GC001983.

McGuire, W.J., Pullen, A.D., 1989. Location and orientation of eruptive fissures and feeder-dykes at Mount Etna: influence of gravitational and regional stress regimes. J. Volcanol. Geotherm. Res. 38 (3–4), 325–344. http://dx.doi.org/10.1016/0377-0273(89)90046-2

Miranda, J.M., Mendes Victor, L.A., Simões, J.Z., Luis, J.F., Matias, L., Shimamura, H., Shiobara, H., Nemoto, H., Mochizuki, H., Hirn, A., Lépine, J.C., 1998. Tectonic setting of the Azores Plateau deduced from a OBS survey. Mar. Geophys. Res. 20, 171–182.

Miranda, J.M., Luis, J.F., Lourenço, N., Goslin, J., 2014. Distributed deformation close to the Azores Triple "Point". Mar. Geol. 355, 27–35.

http://dx.doi.org/10.1016/j.margeo.2014.05.006
Mitchell, N.C., 2003. Susceptibility of mid-ocean ridge volcanic islands and seamounts to large-scale landslding. J. Geophys. Res. 108 (B8), 2397. http://dx.doi.org/10.1029/2002JB001997.
Mitchell, N.C., Masson, D.G., Watts, A.B., Gee, M.J.R., Urgeles, R., 2002. The morphology of the submarine flanks of volcanic ocean islands: a comparative study of the Canary and Hawaiian hotspot islands. J. Volcanol. Geotherm. Res. 115 (1–2), 83–107. http://dx.doi.org/10.1016/S0377-0273(01)00310-9.
Mitchell, N.C., Beier, C., Rosin, P.L., Quartau, R., Tempera, F., 2008. Lava penetrating water: submarine lava flows around the coasts of Pico Island, Azores. Geochem. Geophys. Geosyst. 9 (3), Q03024. http://dx.doi.org/10.1029/2007GC001725.
Mitchell, N.C., Quartau, R., Madeira, J., 2012a. Assessing landslide movements in volcanic islands using near-shore marine geophysical data: south Pico Island, Azores. Bull. Volcanol. 74 (2), 483–496. http://dx.doi.org/10.1007/s00445-011-0541-5.
Mitchell, N.C., Stretch, R., Oppenheimer, C., Kay, D., Beier, C., 2012b. Cone morphologies associated with shallow marine eruptions: east Pico Island, Azores. Bull. Volcanol. 74 (10), 2289–2301. http://dx.doi.org/10.1007/s00445-012-0662-5
Mitchell, N.C., Quartau, R., Madeira, J., 2013. Large-scale active slump of the southeastern flank of Pico Island, Azores: comment. Geology 41 (12), e301. http://dx.doi.org/10.1130/G34006C.1.
Moore, J.G., Clague, D.A., 2002.Mapping the Nuuanu andWailau Landslides in Hawaii. In: Takahashi, E., Lipman, P.W., Garcia, M.O., Naka, J., Aramaki, S. (Eds.),Hawaiian volcanoes: deep underwater perspectives. Geophysical Monograph Series, 128. American Geophysical Union, Washington D.C., pp. 223–244. http://dx.doi.org/10.1029/GM128.
Moore, J.G., Clague, D.A., Holcomb, R.T., Lipman, P.W., Normark,W.R., Torresan, M.E., 1989. Prodigious submarine landslides on the Hawaiian Ridge. J. Geophys. Res. 94 (B12), 17465–17484. http://dx.doi.org/10.1029/JB094iB12p17465.
Moore, J.G., Normark, W.R., Holcomb, R.T., 1994. Giant Hawaiian landslides. Annu. Rev. Earth Planet. Sci. 22, 119–144. http://dx.doi.org/10.1146/annurev.ea.22.050194.001003.
Neves, M.C., Miranda, J.M., Luis, J.F., 2013. The role of lithospheric processes on the development of linear volcanic ridges in the Azores. Tectonophysics 608, 376–388. http://dx.doi.org/10.1016/j.tecto.2013.09.016.
Normark, W.R., Moore, J.G., Torresan, M.E., 1993. Giant Volcano-Related Landslides and the Development of the Hawaiian Islands. In: Schwab, W.C., Lee, H.J., Twichell, D.C., Submarine Landslides: Selected Studies in the U.S. Exclusive Economic Zone, 2002, U.S. Geological Survey Bulletin, pp. 184-196.
Nunes, J.C., 1999. A actividade vulcânica na ilha do Pico do Plistocénico Superior ao Holocénico: Mecanismo eruptivo e hazard vulcânico. Ph.D. Thesis. Univ. Açores, Ponta Delgada, Portugal, 356 pp.(available at: http://www.jcnunes.uac.pt/principal.htm)
Nunes, J.C., 2002. Lateral collapse structures in Pico Island (Azores): mechanism, constraints and age. 3a Assembleia Luso Espanhola de Geodesia e Geofísica, Valencia, pp. 731–735.
Nunes, J.C., França, Z., Cruz, J.V., Carvalho, M.R., Serralheiro, A., 1999a, Carta Vulcanológica da Ilha do Pico (Açores), In: Nunes, J.C., (Eds.), A actividade vulcânica na ilha do Pico do Plistocénico Superior ao Holocénico: Mecanismo eruptivo e hazard vulcânico, 1999, Ph.D.

Thesis. Univ. Açores, Ponta Delgada, Portugal, 356 pp.

Nunes, J.C., França, Z., Cruz, J.V., Carvalho, M.R., Serralheiro, A., 1999b, Carta Morfo-tectónica da Ilha do Pico (Açores), In: Nunes, J.C., (Eds.), A actividade vulcânica na ilha do Pico do Plistocénico Superior ao Holocénico: Mecanismo eruptivo e hazard vulcânico, 1999, Ph.D. Thesis. Univ. Açores, Ponta Delgada, Portugal, 356 pp.

Nunes, J.C., Camacho, A., França, Z., Montesinos, F.G., Alves, M., Vieira, R., Velez, E., Ortiz, E., 2006. Gravity anomalies and crustal signature of volcano-tectonic structures of Pico Island (Azores). J. Volcanol. Geotherm. Res. 156 (1–2), 55–70. http://dx.doi.org/10.1016/j.jvolgeores.2006.03.023.

Samper, A., Quidelleur, X., Lahitte, P., Mollex, D., 2007. Timing of effusive volcanism and collapse events within an oceanic arc island: Basse–Terre, Guadeloupe archipelago (Lesser Antilles Arc). Earth Planet. Sci. Lett. 258 (1–2), 175–191. http://dx.doi.org/10.1016/j.epsl.2007.03.030.

Satake, K., Smith, J.R., Shinozaki, K., 2002. Three-dimensional reconstruction and tsunami model of the Nuuanu and Wailau giant landslides, Hawaii. In: Takahashi, E., Lipman, P.W., Garcia, M.O., Naka, J., Aramaki, S. (Eds.), Hawaiian Volcanoes: Deep Underwater Perspectives. Geophysical Monograph Series 128. American Geophysical Union, Washington D.C., pp. 333–346. http://dx.doi.org/10.1029/GM128.

Sibrant, A.L.R., Marques, F.O., Hildenbrand, A., 2014. Construction and destruction of a volcanic island developed inside an oceanic rift: Graciosa Island, Terceira Rift, Azores. J. Volcanol. Geotherm. Res. 284, 32-45. http://dx.doi.org/10.1016/j.jvolgeores.2014.07.014

Steiger, R.H., Jäger, E., 1977. Subcommission on geochronology: convention on the use of decay constants in geo- and cosmochronology. Earth Planet. Sci. Lett. 36 (3), 359–362. http://dx.doi.org/10.1016/0012-821X(77)90060-7.

Stretch, R., Mitchell, N.C., Portaro, R.A., 2006. A morphometric analysis of the submarine volcanic ridge of Pico Island. J. Volcanol. Geotherm. Res. 156(1–2), 35–54. http://dx.doi.org/10.1016/j.jvolgeores.2006.03.009

Trippanera, D., Porreca, M., Ruch, J., Pimentel, A., Acocella, V., Pacheco, J., Salvatore, M., 2014. Relationships between tectonics and magmatism in a transtensive/transform setting: An example from Faial Island (Azores, Portugal). Geological Society of America Bulletin 126 (1-2), 164-181. http://dx.doi.org/10.1130/B30758.1

Urgeles, R., Masson, D.G., Canals, M., Watts, A.B., Le Bas, T., 1999. Recurrent large-scale landsliding on the west flank of La Palma, Canary Islands. J. Geophys. Res. Solid Earth 104 (B11), 25331–25348. http://dx.doi.org/10.1029/1999JB900243.

Woodhall, D., 1974. Geology and volcanic history of Pico Island Volcano, Azores. Nature 248, 663–665. http://dx.doi.org/10.1038/248663a0.

Zbyszewski, G., Ribeiro Ferreira, C., Veiga Ferreira, O., Torre de Assunção, C., 1963. Notícia explicativa da Folha "B" da Ilha do Pico (Açores). Carta Geológica de Portugal na escala 1/50 000. Serviços Geológicos de Portugal. Lisbon, Portugal. 21 pp.

## APPPENDIX A

### DEM origin and construction

The sub-aerial topographic data here presented were produced from the digital topographic map of Pico Island (Portuguese Army Geographic Institute), of 1:25,000 scale and vertical accuracy of ca. 5 m (Afonso et al., 2002). Details on the sub-aerial DEM construction are provided in Costa et al. (2014). The DEMs presented for Pico and Faial islands have spatial resolution of 10 and 50 m, respectively.

The 50-250m resolution submarine data here presented resulted from a swath bathymetry survey with a 12 kHz Kongsberg EM120 multibeam echo sounder system. The estimated depth accuracy (RMS, Root Mean Square) is 0.2-0.5% of the water depth (Kongsberg, 2007). As the maximum depth of the presented high-resolution area is ca. 1750 m, the maximum RMS estimated for these data ranges between 3.5-8.75 m. The data were processed using CARIS software, clean of noise and converted to an ASCII file. Afterwards, these data were converted to a raster structure of either 50 m or 250 m spatial resolution, using kriging spatial interpolation. The grid displaying these submarine data (Figs. 5 and 6) was built from a composition of data from different sources and of different resolutions (Fig. 5a): (a) the sub-aerial data of 10 m resolution (green area in Fig.5a); (b) the submarine 50 and 250 m data (grey and light blue areas, respectively, in Fig. 5a); (c) 100 m spaced depth contours for the shallow depths adjacent to the scar on Pico's SE flank (Fig.4), obtained from photogrammetry of Fig. 1a in Mitchell et al. (2012) (black lines in Fig.5a); (d) 1000 m resolution bathymetric data (blue dots in Fig. 5a, Lourenço et al.,1998). First we performed a spatial interpolation of 200 m resolution on the submarine domain, considering the data distribution represented in Fig. 5a. The WSW-ESE apparent alignments visible on the shaded reliefs from Figs. 5b and 5c, are artefacts related to the spatial interpolation of the contour levels (Fig. 5a). Afterwards, we composed the final 50 m resolution grid mosaic, considering preferentially the 50/250 m resolution bathymetric data and the 10 m resolution sub-aerial data, and filling the remaining space with the 200 m resolution data from the interpolation performed previously.

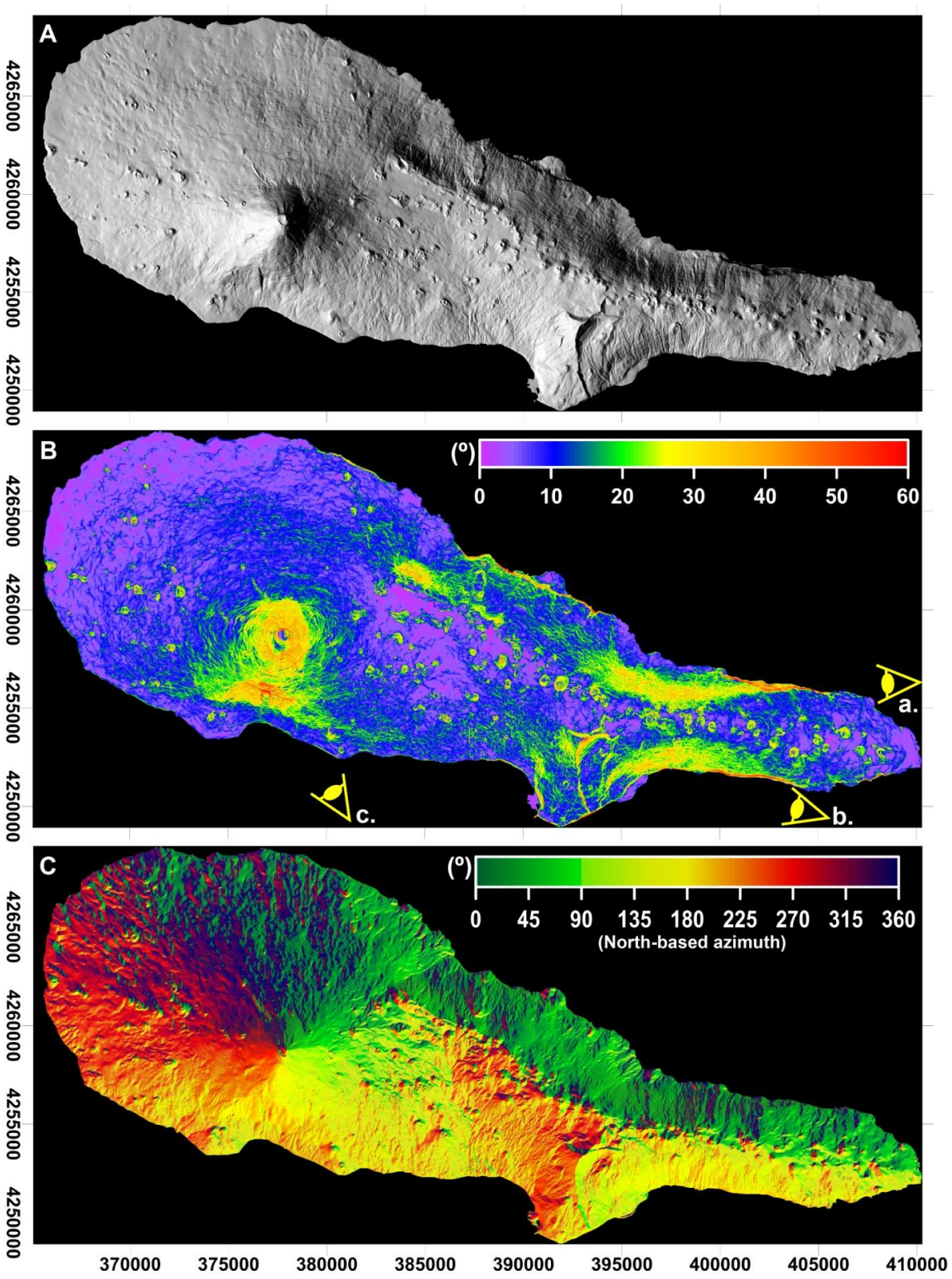


**Fig. A.1. (A)** Shaded relief of the 10 m resolution DEM of Pico Island (lighting from ESE), with coordinates in metres UTM (zone 26N). **(B)** Slope map of Pico Island built from the 10 m resolution DEM. 3D perspectives indicated as yellow eyes are presented in Fig. A.2. "a" - view presented in Fig. 3a. Perspective "B." - view presented in Fig. 3b. Perspective "C." - view presented in Fig. 3c. **(C)** Surface map of Pico Island built from the 10 m resolution DEM, indicating the North-based azimuth of strongest dip.

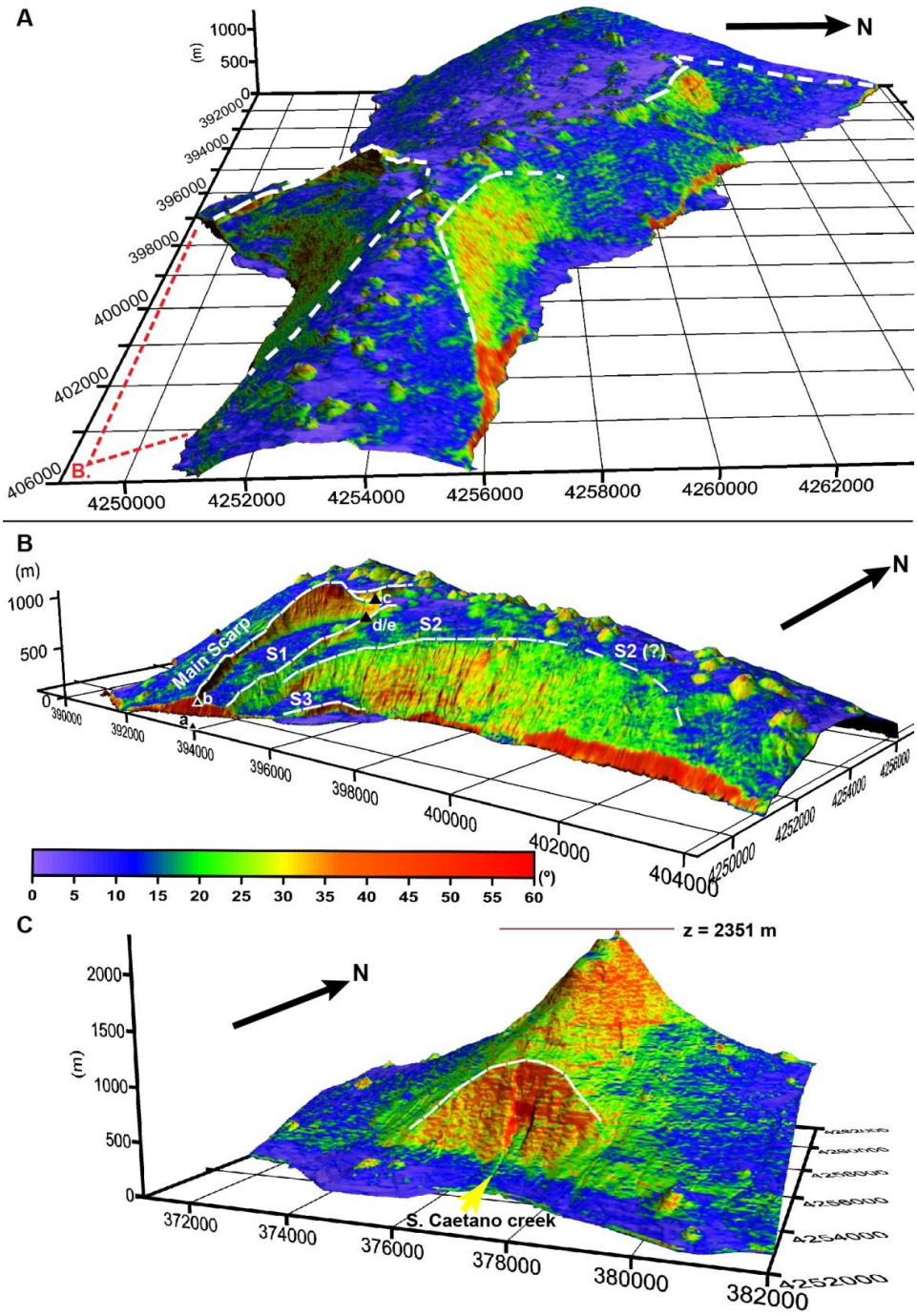


**Fig. A.2.** Images obtained by superimposing the 3D view of Pico Island relief (vertical exaggeration: 2x) and the slope map image (shared color scale for slope angles), obtained from a 10 m resolution DEM. Perspectives presented A, B and C, are indicated in Fig. 2b by "A.", "B." and "C.", respectively. **(A)** Perspective from E (lighting from NW), of Pico Island's topography, with interpretation of the N and S flanks' main scarps as dashed white lines. **(B)** View from ESE of the slump structure's topography (lighting from SW). Scarps interpreted as white dashed lines (structures identification and interpretation modified after Hildenbrand et al., 2012). Black triangles identified as *a*, *b*, *c*, *d* and *e* indicate the observation spots of the corresponding panoramic pictures presented in Fig. A3 (Appendix A). **(C)** Perspective from SE of Pico stratovolcano's strongly dipping southern flank (lighting from SE).

**Fig. A.3.** Panoramic views of the slump structure scarps. Observation spots of the pictures are indicated and identified on **Fig. A2** (black triangles). Scarps are identified and interpreted as yellow lines.

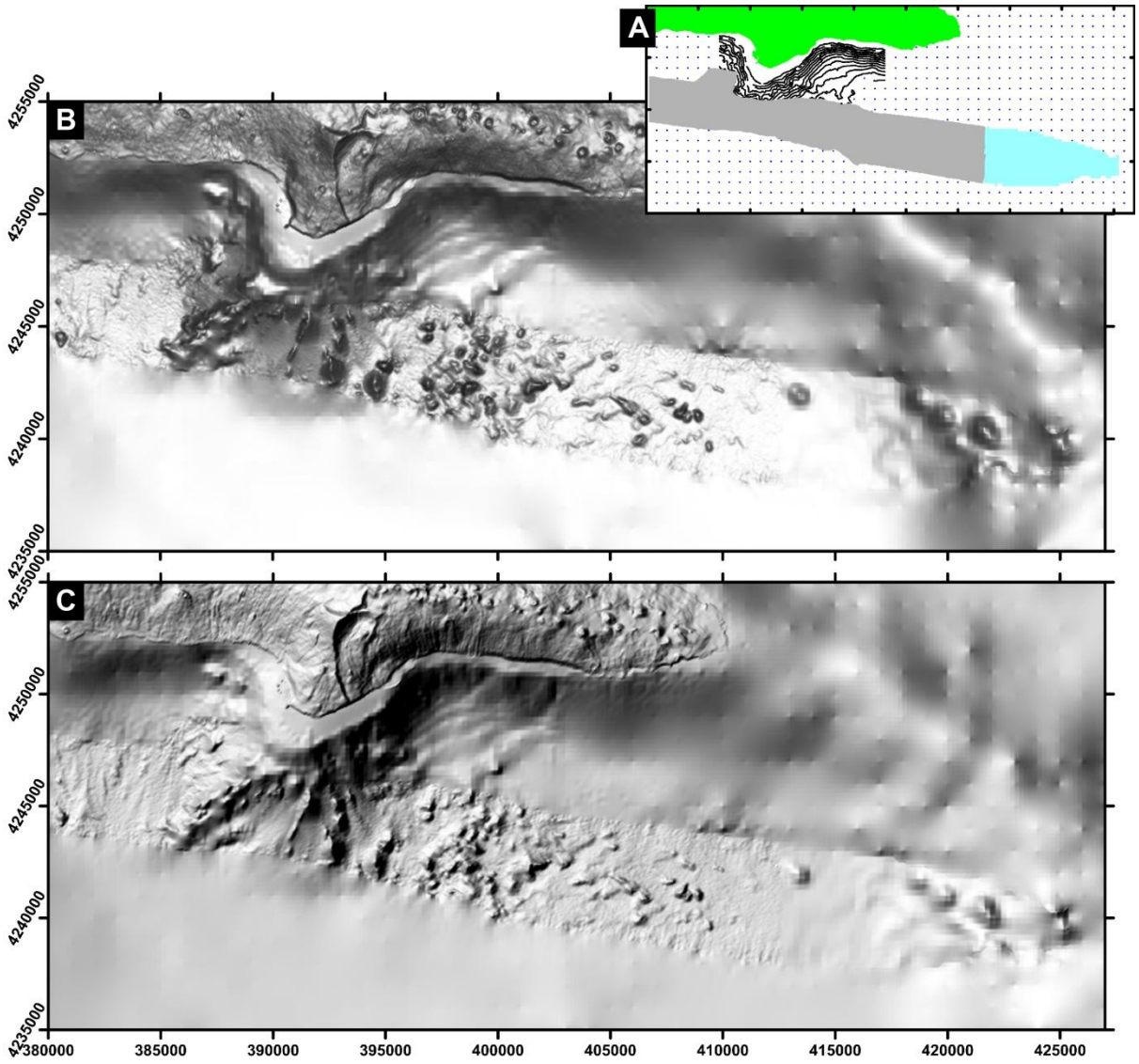


**Fig. A.4.** **(A)** Different elements used to composed the 50m resolution grid presented below: green - 10 m resolution sub-aerial DEM; blue - 250m resolution bathymetric data (made available by EMEPC); grey - 50m resolution bathymetric data (made available by EMEPC); black lines - depth contours from Fig. 1b in Mitchell et al. (2012); blue dots - bathymetric data extracted from the 1000 m resolution grid from Lourenço et al. (1998), available at http://w3.ualg.pt/~jluis/acores_plateau.htm. **(B)** and **(C)** constitute shaded reliefs from the 50m resolution grid composed as described in (A), with vertical lighting and lighting from WNW, respectively. The apparent WSW-ENE lineaments visible in the area of interpolation of contours extracted from Mitchell et al. (2012) constitute interpolation artefacts.

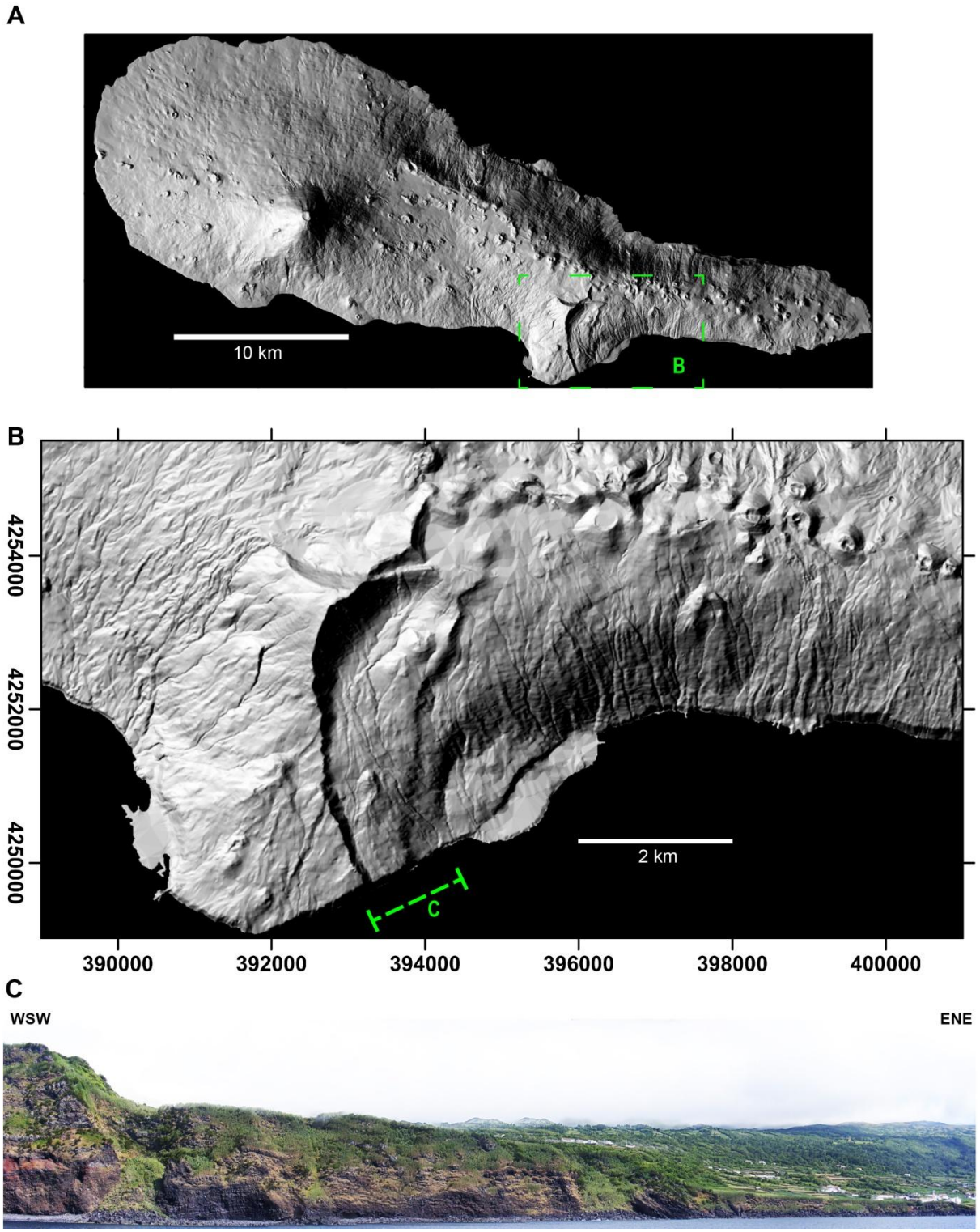


**Fig. A.5. (A)** Shaded relief of Pico Island from a 10 m resolution DEM (lighting from ESE). **(B)** Shaded relief of Pico Island from a 10 m resolution DEM (lighting from NW). **(C)** WSW-ESE view of the sea cliff whose extent is indicated as a green dashed line in (B).

**Fig. A.6.** Zoom in on the sea cliff presented as Fig. A.5c.

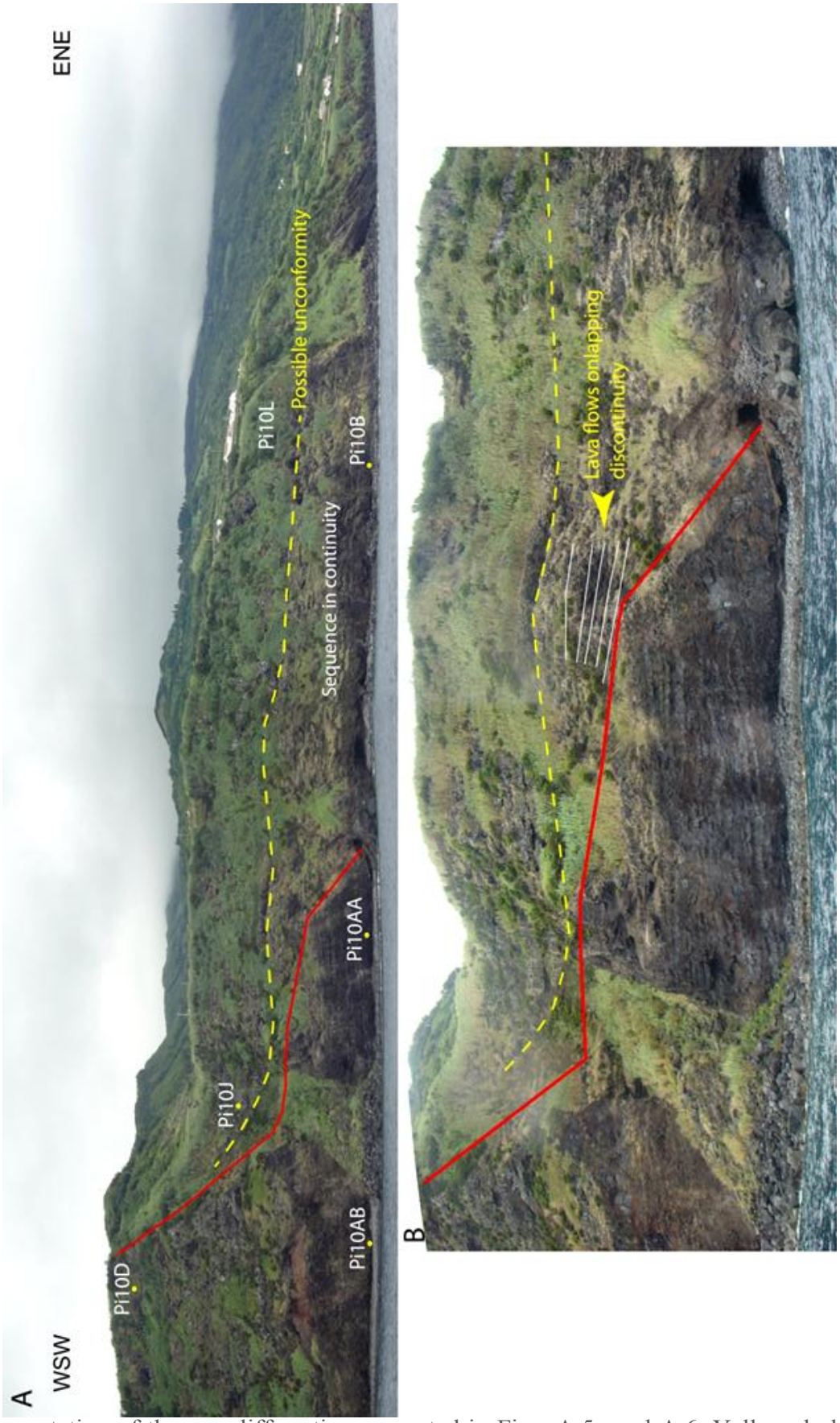


**Fig. A.7.** Interpretation of the sea cliff section presented in Figs. A.5c and A.6. Yellow dashed line indicates possible unconformity. Full red line represents a main physical discontinuity. The samples collected on this sea cliff are indicated in **A**.

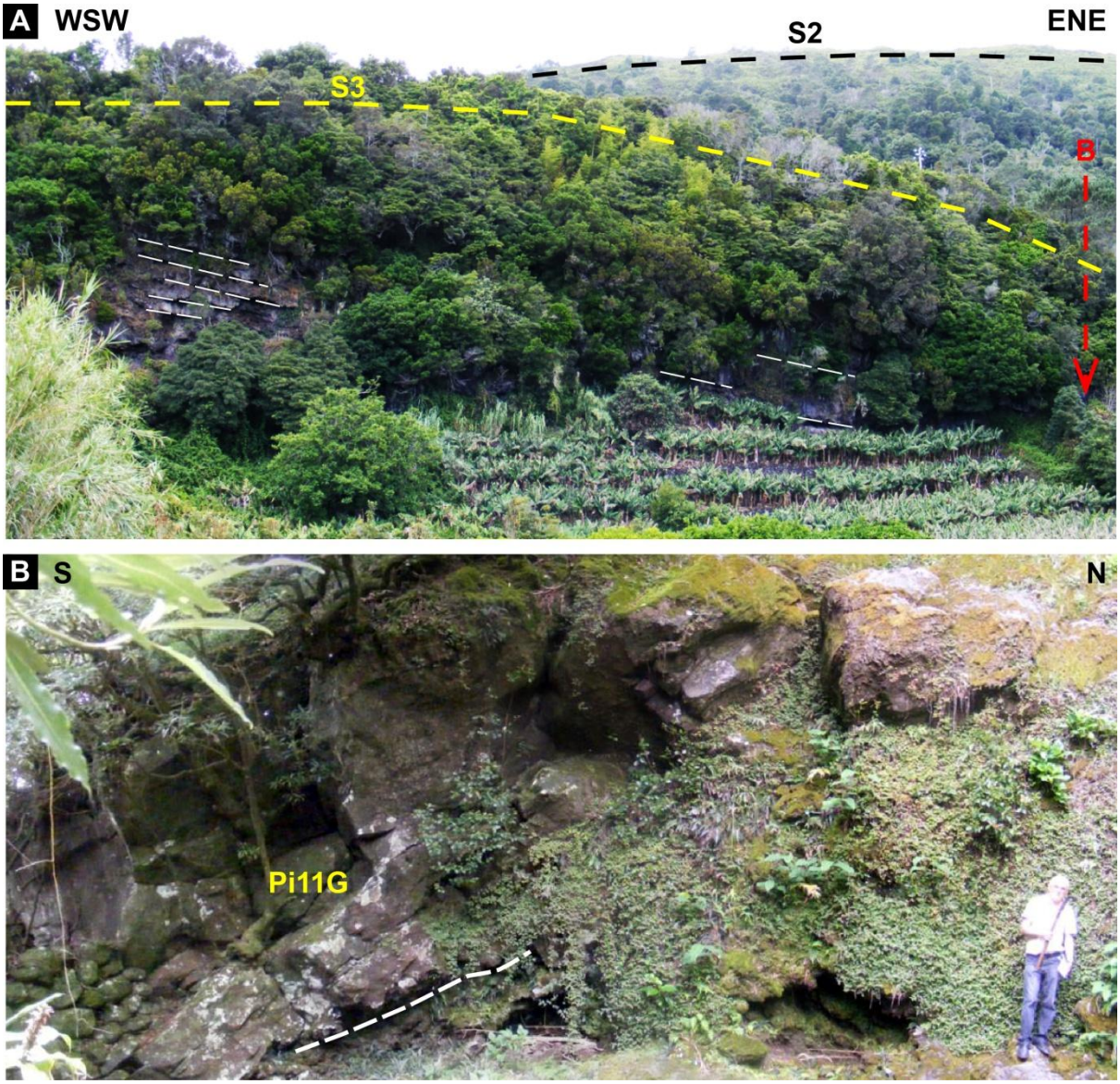


**Fig. A.8. (A)** View of the easternmost sector of S3. The outcropping sequence locally apparently dips towards E. **(B)** Location of sampling of Pi11G. The lava flow is laterally continuous to the sequence visible on (A).

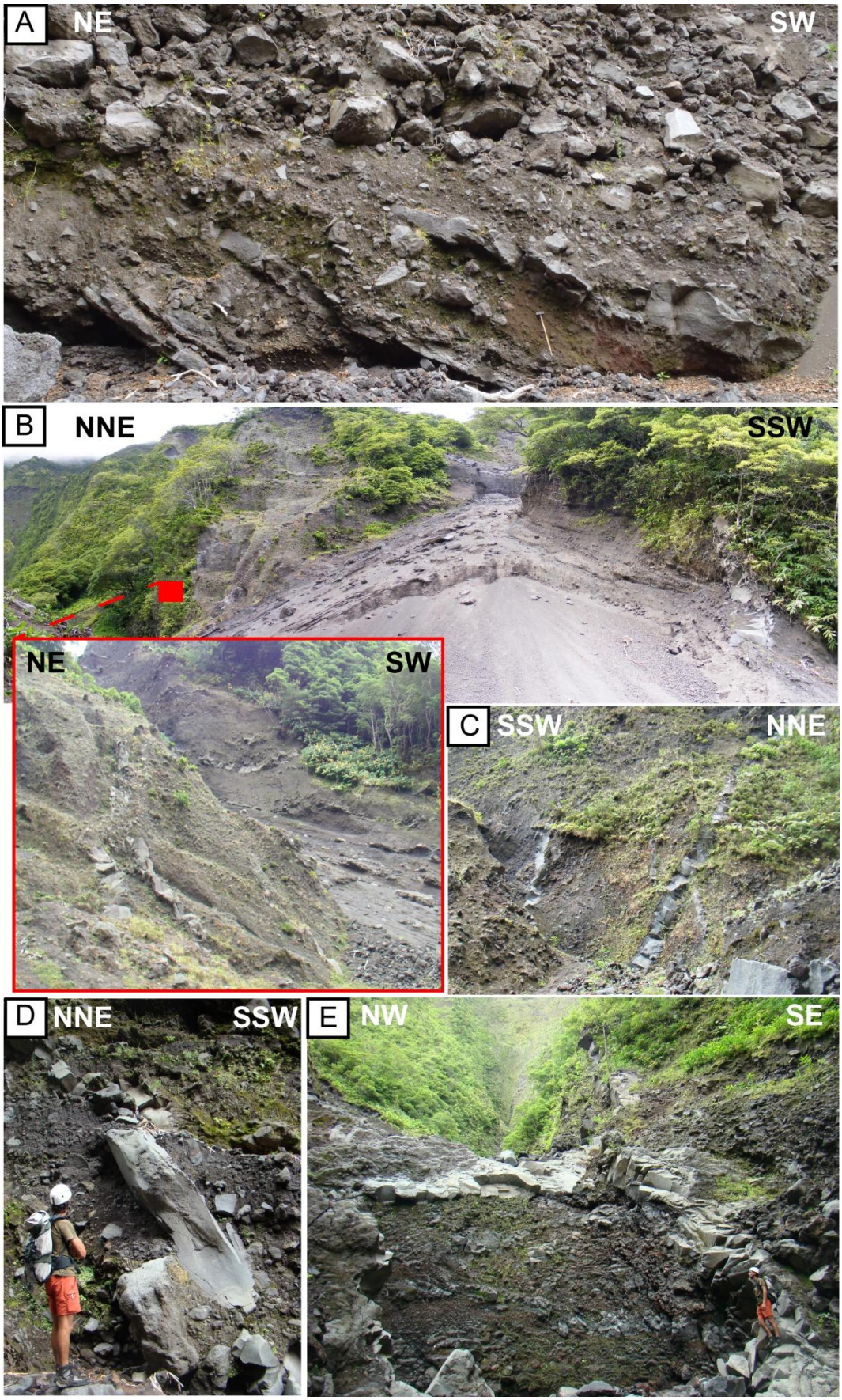


**Fig. A.9.** Photos from S.Caetano creek (order according to upslope observations): **(A)** lava flows intercalated with sedimentary deposits, and overlain by a thick coarser deposit with decimetric

boulders; **(B)** Thick small grained volcaniclastic (pyroclastic) sequence with some thin lava flows intercalated and cut by strongly dipping dykes. Zoom in: view of the dykes located on the red square zone.; **(C)** Small grained volcaniclastic sequence cut by *en echelon* dykes (strongly inclined dyke on the right cutting a small dyke); **(D)** and **(E)** Metric thick/ strongly inclined dykes towards downslope, cutting the sequence.

**References**


Afonso, A., Gomes, F., Fernandes,M., 2002. IGeoE: Cartografia de qualidade - a base de um SIG. Trib. das Autarquias 108, 13–14 (Jun. 2002).

Costa, A.C.G., Marques, F.O., Hildenbrand, A., Sibrant, A.L.R., Catita, C.M.S., 2014. Large-scale catastrophic flank collapses in a steep volcanic ridge: The Pico–Faial Ridge, Azores Triple Junction. J. Volcanol. Geotherm. Res. 272, 111-125, http://dx.doi.org/10.1016/j.jvolgeores.2014.01.002.

Hildenbrand, A., Marques, F.O., Catalão, J., Catita, C.M.S., Costa, A.C.G., 2012a. Large-scale active slump of the southeastern flank of Pico Island, Azores. Geology 40 (10), 939–942. http://dx.doi.org/10.1130/G33303.1.

Kongsberg, S., 2007. EM 120 Multibeam Echo Sounder, Product Description. Kongsberg Maritime AS, Norway, Bremerhaven, Pangaea 44 p. (available at http://epic.awi.de/26725/1/Kon2007a.pdf).

Lourenço, N., Miranda, J.M., Luis, J.F., Ribeiro, A., Mendes Victor, L.A., Madeira, J., Needham, H.D., 1998. Morpho-tectonic analysis of the Azores Volcanic Plateau from a new bathymetric compilation of the area. Mar. Geophys. Res. 20 (3), 141-156. http://dx.doi.org/10.1023/A%3A1004505401547.

Mitchell, N.C., Quartau, R., Madeira, J., 2012. Assessing landslide movements in volcanic islands using near-shore marine geophysical data: south Pico Island, Azores. Bull. Volcanol. 74 (2), 483–496. http://dx.doi.org/10.1007/s00445-011-0541-5.

## APPPENDIX B

### Evolution of the Pico - Faial ridge previous to 200 kyrs

Here we resume the evolution of the Pico-Faial ridge previous to 200 kyrs:

(1) The distribution of magnetic anomalies along the ridge shows evidence for the development of the Pico-Faial ridge on the Faial sector and on the submarine domain to the SE of Pico, previous to the Matuyama- Brunhes transition (Miranda et al., 1991; Lourenço, 2007; Hildenbrand et al., 2012), at 789±8ka (Quidelleur et al., 2003).

(2) Between ca. 850─800 ka, a volcanic edifice grew on the SE sector of Faial Island (Figs. B.1 and B.2a), followed by a volcanic hiatus between ca. 800─400 ka, during which this edifice was heavily dismantled (Hildenbrand et al. 2012, Fig. B.2b);

(3) Between ca. 400─350 ka, newly erupted volcanic material masked Faial Island's NE sector (Fig. B.2c);

(4) In Faial Island, a WNW-ESE island-scale graben propagated between ca. 350─130 ka (Fig. B.2d) (Hildenbrand et al., 2012). Meanwhile, towards ESE (Pico Island), sub-aerial Topo Volcano started to grow (ca. 186─125 ka) (Fig. 17a).

The volcanic growth in NE Faial in (3) and graben development in (4) coincide in time with the volcanic growth of the westernmost sector of S.Jorge Island (Hildenbrand et al., 2008).

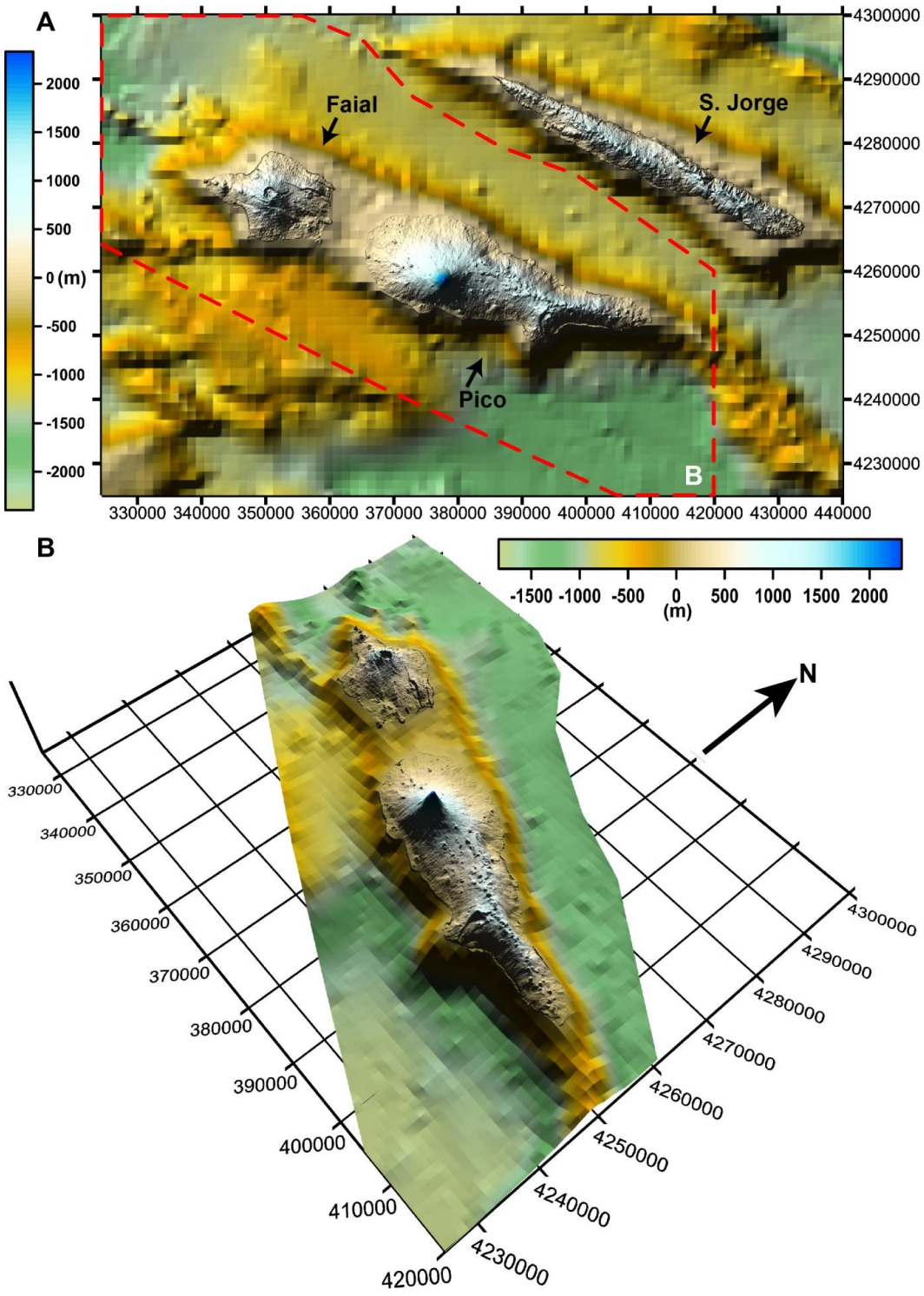


**Fig. B.1. (A)** Map view of the topographic surface from the area comprising Pico-Faial and S. Jorge ridges. The observed topographic surface resulted from the combination of 50 m resolution DEMs for Pico, Faial and S. Jorge Islands and a 1 km resolution DEM of the submarine domain. Bathymetric data from Lourenço et al., (1998) , available at http://w3.ualg.pt/~jluis/. **(B)** 3D perspective (view from ESE) of the Pico-Faial volcanic ridge, used as a base for the representation of the ridge evolutionary steps presented in Figs. 9 and 10.

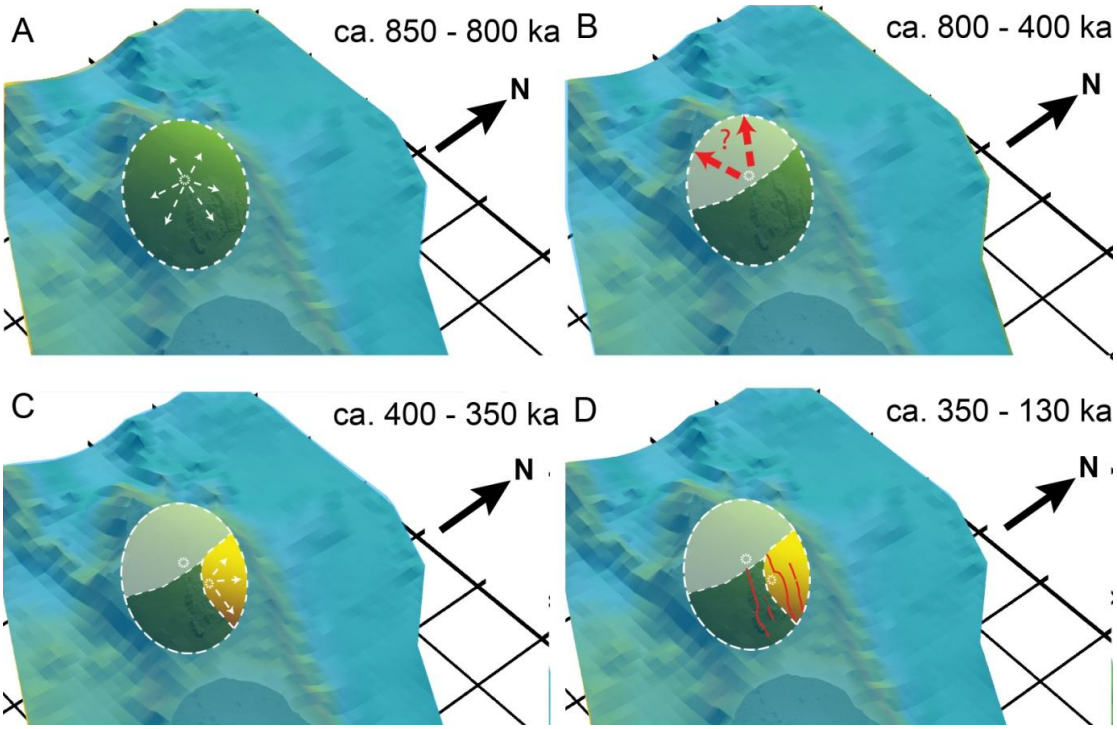


**Fig. B.2.** Schematic step-by-step evolution of the Pico-Faial volcanic ridge, following the data and interpretations presented in Hildenbrand et al., (2012). The theoretical schemes presented are superimposed with a 3D perspective of the ridge DEM (Fig. B.1). (A) Beginning of the sub-aerial development of the volcanic ridge with growth of a volcanic edifice on Faial Island sector (ca. 850 - 800 ka). (B) Partial destruction of the volcanic edifice referred in (A) (ca. 800 - 400 ka). (C) Volcanic growth phase on the northern sector of Faial Island (ca. 400 - 350 ka). (D) Development of a WNW-ESE island-scale graben structure (ca. 350 - 130 ka). Graben scarps represented as red lines.

**References**

Hildenbrand, A., Madureira, P., Ornelas Marques, F., Cruz, I., Henry, B., Silva, P., 2008. Multi-stage evolution of a sub-aerial volcanic ridge over the last 1.3 Myr: S. Jorge Island, Azores Triple Junction. Earth Planet. Sci. Lett. 273 (3–4), 289–298. http://dx.doi.org/10.1016/j.epsl.2008.06.041.

Miranda, J.M., Freire Luis, J., Abreu, I., Mendes Victor, L.A., 1991. Tectonic framework of the Azores triple junction. Geophys. Res. Lett.18 (8), 1421-1424.

Lourenço, N., 2007. Tectono-magmatic Processes at the Azores Triple Junction. PhD thesis. Universidade do Algarve, Faro, Portugal, 239pp.

Lourenço, N., Miranda, J.M., Luis, J.F., Ribeiro, A., Mendes Victor, L.A., Madeira, J., Needham, H.D., 1998. Morpho-tectonic analysis of the Azores Volcanic Plateau from a new bathymetric compilation of the area. Mar. Geophys. Res. 20 (3), 141-156. http://dx.doi.org/10.1023/A%3A1004505401547.

Quidelleur, X., Carlut, J., Soler, V., Valet, J.P., Gillot, P.Y., 2003. The age and duration of the Matuyama–Brunhes transition from new K–Ar data from La Palma (Canary Islands) and revisited Ar-40/Ar-19 ages. Earth Planet. Sci. Lett. 208, 149–163. http://dx.doi.org/10.1016/S0012-821X(03)00053-0

# PART III

## Current deformation in Pico Island

# Chapter 6

## Large-scale active slump of the southeastern flank of Pico Island, Azores

## (Hildenbrand et al., 2012b)

# Large-scale active slump of the southeastern flank of Pico Island, Azores

A. Hildenbrand[1,2,*], F.O. Marques[3], J. Catalão[4], C.M.S. Catita[4], and A.C.G. Costa[1,4]
[1]Univ Paris-Sud, Laboratoire IDES, UMR8148, Orsay, F-91405, France
[2]CNRS, Orsay, F-91405, France
[3]Universidade Lisboa, 1749-016 Lisboa, Portugal
[4]Universidade Lisboa and IDL, 1749-016 Lisboa, Portugal

## ABSTRACT

**We report evidence for ongoing lateral slump of part of the southeastern flank of the Pico volcanic ridge in the Azores. Data from a high-resolution digital elevation model, field work, GPS, and radar interferometry show that: (1) the slumping sector is several cubic kilometers in size; (2) the structure involves several curved scars with normal fault kinematics; (3) the central part is undergoing little horizontal displacement toward the southeast (1.6 ± 1.3 mm/yr), but significant downward movement (5–12 mm/yr); and (4) the outer part of the southeastern flank of Pico is subsiding faster than the inner parts; this likely reflects recent individualization of a steep seaward-dipping fault in the moving mass. The slump shares similarities with active slumps recognized elsewhere, although the studied area may represent only the proximal part of a much larger complex potentially affecting the deep submarine base of the island. Displacement of the subaerial part of the southeastern flank of Pico seems to be accommodated by the movement and rotation of large blocks along listric normal faults.**

## INTRODUCTION

The growth of volcanic islands is generally punctuated by large lateral flank failures, which can trigger destructive tsunamis (Keating and McGuire, 2000; McMurtry et al., 2004). Giant sector collapses have been recognized around numerous islands worldwide, e.g., in Hawaii (Lipman et al., 1988; Moore et al., 1994; Morgan et al., 2000), French Polynesia (Clouard and Bonneville, 2004; Hildenbrand et al., 2006), the Canary Islands (Krastel et al., 2001; Walter and Schmincke, 2002; Boulesteix et al., 2012), Reunion Island (Duffield et al., 1982; Gillot et al., 1994), and the Caribbean arc (Le Friant et al., 2003; Samper et al., 2007). A number of triggering factors have been proposed over the past 20 years (e.g., McGuire, 1996; Elsworth and Day, 1999; McMurtry et al., 1999, 2004; Klüge l et al., 2005; Quidelleur et al., 2008), including concentration of dikes along rift zones and associated fluid pressurization by heating and/or compression of groundwater trapped between dikes, ground shaking by large regional earthquakes, gravitational spreading of the volcanoes along weak geological layers, or sea-level variations associated with climatic changes.

Contrasting types of sector collapse have been distinguished (Moore et al., 1994): (1) slow-moving rotational landslides along a deep-sea detachment fault, often called slumps; and (2) catastrophic landslides produced by the rapid detachment of the island flank, which may release fast-moving debris avalanches. These two kinds of processes are not mutually exclusive; part of a slump may suddenly collapse and trigger a tsunami (e.g., Tilling et al., 1976; Moore et al., 1994).

The Azores archipelago, in the Atlantic Ocean, comprises nine active volcanic islands and numerous linear submarine ridges developed close to the triple junction between the North American, Eurasian, and African lithospheric plates (Fig. 1), in an area characterized by important regional deformation and recurrent high-magnitude earthquakes (Borges et al., 2007). The islands are marked by a multistage evolution, including fast-growing phases and multiple destruction events, such as vertical caldera collapse, lateral landslides, and rock fall of various sizes (Mitchell, 2003; Calvert et al., 2006; Hildenbrand et al., 2008; Silva et al., 2012).

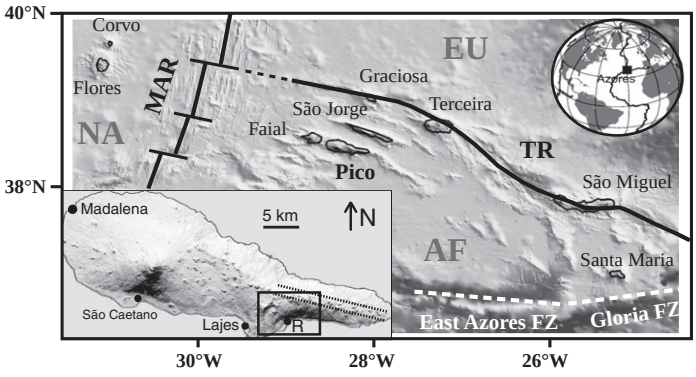


**Figure 1. Location of Azores volcanic archipelago near triple junction between North American (NA), Eurasian (EU), and African (AF) plates. Bold lines show Mid-Atlantic Ridge (MAR) and Terceira Rift (TR). FZ—fracture zone. Inset: Shaded relief map showing main morphology of Pico Island. Dotted lines highlight axis of main N110° rift zone. Two main landslide failures affect southern flank of island. Rectangle shows geographical extension of studied southeastern collapse area (Fig. 2). R is Ribeiras town.**

Pico Island is a narrow and steep volcanic ridge, formed by magma concentration along the N110° trend (Fig. 1). The oldest volcanic units are exposed in the central and eastern parts of the island, whereas more recent volcanic activity produced the Pico volcano, which occupies the western third of the island (Woodhall, 1974; Nunes, 1999).

Due to its steep topography, Pico Island is particularly sensitive to flank instability. The southern flank of the ridge shows several curved structures that are concave toward the ocean (Fig. 1), previously interpreted as reflecting early caldera development, faulting, or ancient lateral collapse (Woodhall, 1974; Nunes, 1999; Mitchell, 2003; Nunes et al., 2006). Knowledge of the geometry, volume, and kinematics of these structures, and understanding of their recent evolution and susceptibility to further movement, are critical for risk and hazard assessment, but remain poorly constrained. Our study focuses on the unstable southeastern part of the ridge; data from a high-resolution digital elevation model (DEM), field work, GPS, and radar interferometry show that part of the flank is currently being displaced toward the ocean, accommodated by the motion of large blocks that may eventually detach, with catastrophic consequences.

## SLUMP GEOMETRY AND KINEMATICS

Using cartographic data and maps generated in 2005 by the Portuguese Army Institute (scale 1:25,000), we developed a DEM with 10 m spatial resolution and a vertical accuracy of 2 m. It was used to produce a shaded relief map (Fig. 2A), a slope map, and topographic cross sections

*E-mail: anthony.hildenbrand@u-psud.fr.


© 2012 Geological Society of America. For permission to copy, contact Copyright Permissions, GSA, or editing@geosociety.org.

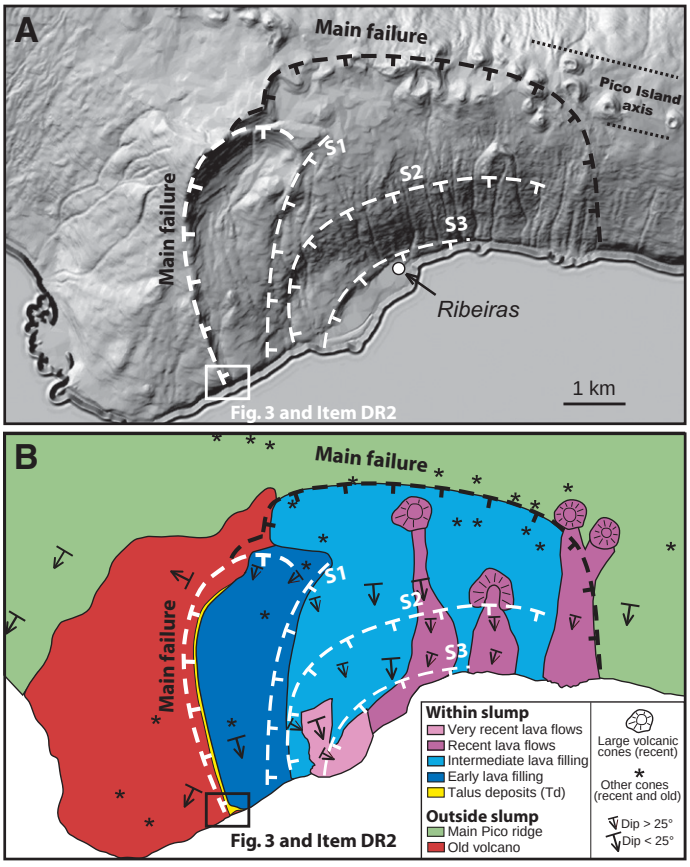


**Figure 2. A: Main morphostructural units within southeastern slump area. Main scars here recognized are highlighted by white dashed lines. Black line indicates inferred continuation of main structure extending to southern part of axial rift zone. B: Simplified geologic map of studied area. Modified after Nunes (1999).**

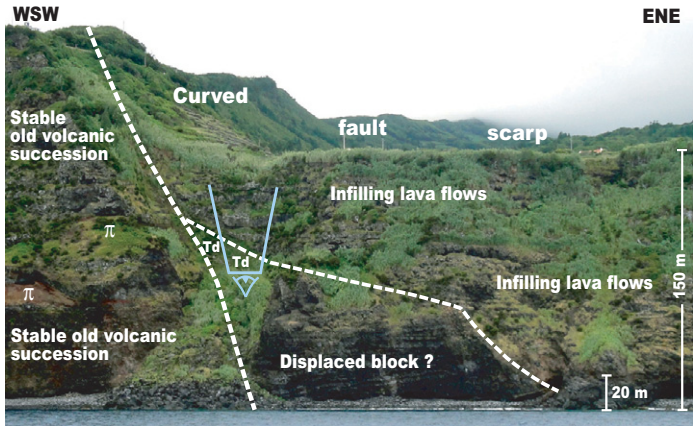


**Figure 3. Photograph taken from sea showing geometric relationships between main geological units exposed along southern end of main collapse rim at shore level. Td—talus deposits; pi symbols—levels of Strombolian fallout deposits; blue outline and symbol show point of view from which photo exposed in Item DR2 (see footnote 1) was taken (upward).**

(Fig. DR1 in GSA Data Repository[1]), which, together with geologic data (Figs. 2B and 3), provide important new constraints on the geometry of the failure.

1. The main collapse rim is exposed as an arcuate scarp open to the southeast. It forms a 300-m-high prominent headwall with steep slopes dipping as much as 60°. The northern part of this structure has been partly covered by recent lava flows, but discontinuous unburied segments can be identified, suggesting an overall horseshoe-shape geometry.

2. The inner portion of the collapse sector is marked by a morphological plateau with gentle slopes. The upper part of the plateau is composed of recent lava flows erupted from small cones developed at the base of the main failure.

3. The plateau is interrupted by slope breaks; from west to east, three main scarps can be identified (S1, S2, and S3, Fig. 2; Item DR1 in the Data Repository). S1 occurs along a lineament roughly parallel to the southern end of the main failure. Its northern end is apparently connected with the main scar. S2 extends over a large area as an arcuate structure affecting the outer part of the plateau. It has a geometry typical of lateral failures, starting with a north-south rim at sea level, then bifurcating eastward and becoming almost parallel to the main axis of the island. This scarp is characterized by a steep seaward dip of as much as 45°. Farther east, the slope is smoothed by recent lava flows erupted from volcanic cones located along the main rift zone, and from parasitic cones developed within the collapse sector. The S3 scarp has been previously interpreted as fossil coastal cliffs (Nunes, 1999); however, it defines a clear embayment partly covered by recent lava flows, which cascaded down to the sea and formed a lava delta.

The architecture and kinematics of the slump are further constrained by field data (Fig. 3; Item DR2). The in situ old volcanic sequence is exposed along coastal cliffs as a pile of thin lava flows, including red levels of Strombolian fallout deposits (π symbol in Fig. 3). This succession is interrupted by a main scarp making up the western rim of the slump (Fig. 3). To the east of this major discontinuity, a different volcanic succession crops out. It likely defines the top of a large downthrown block, which would therefore indicate a minimum vertical offset of ~300 m. This large block is overlain by a thick layer of poorly sorted talus deposits (Td in Fig. 3), including angular lava blocks exceeding 1 m in size, that imply rapid infilling of a steep-sided canyon by large blocks probably shed from the main slump scar. The talus unit is covered by a suite of thick volcanic lava flows wedging out toward the main fault scarp (Fig. 3; Item DR2). All the field data suggest that the main collapse rim has acted as a major fault with normal kinematics. Gradual downward movement resulted in the persistence of a narrow drainage system, which was filled by lava flows and significant amounts of debris. Recent movement can also be suspected from the active development of a narrow debris fan remobilizing the talus deposits along the main scar (Fig. 3).

## SLUMP MONITORING BY GPS AND RADAR INTERFEROMETRY

In the framework of the research projects SARAÇORES (Deformation Partition in Azores using interferometric SAR Images; Catita et al., 2005) and TANGO (TransAtlantic Network for Geodesy and Oceanography; Fernandes et al., 2004), a dense GPS network was installed in Faial and Pico Islands (details in Item DR3). It consists of 31 stations, distributed mostly along the coastlines. One station (PRIB) is located near sea level in the central part of the collapse area, close to the town of Ribeiras. Four GPS campaigns were carried out on Faial and Pico Islands between 1999 and 2006. Measurements were made in survey mode, with a minimum of three sessions (24 h consecutive observation each) per station. The data set was complemented by synthetic aperture radar (SAR) data, aimed at producing interferograms and quantifying vertical displacements between 2006 and 2009 (for details, see the Data Repository and Catalão

[1]GSA Data Repository item 2012264, Item DR1 (detailed morphology of Pico southeastern slump), Item DR2 (thick lava flows overlying the talus deposits), and Item DR3 (methods and data processing; GPS and InSAR), is available online at www.geosociety.org/pubs/ft2012.htm, or on request from editing@geosociety.org or Documents Secretary, GSA, P.O. Box 9140, Boulder, CO 80301, USA.

et al. [2011]). The GPS horizontal surface velocities of Pico were used to estimate the parameters of the rigid body motion model associated with regional plate tectonics. The residuals between the rigid body motion and the geodetic data are attributed to intra-island deformation and are a good measure of local variations of the strain field.

Residual velocities computed at PRIB (2σ uncertainties) show a slight southeast displacement, with an average value of 1.6 ± 1.3 mm/yr, and a significant average vertical subsidence of 7.1 ± 1.9 mm/yr. Such downward vertical motion is consistent with the values obtained from radar interferometry (Fig. 4), although those data were acquired between 2006 and 2009 and show slightly higher rates of subsidence. The InSAR (In—interferometric) data show that the sectors outside of the collapse area are rather stable, with no significant vertical movement or little subsidence (<5 mm/yr), whereas downward vertical movement in the collapse area reaches 12 mm/yr, i.e., a net subsidence of 7 to 12 mm/yr. The highest rates are observed in the central part of the collapse, whereas the sector bounded by the main fault scar shows values between 5 and 8 mm/yr.

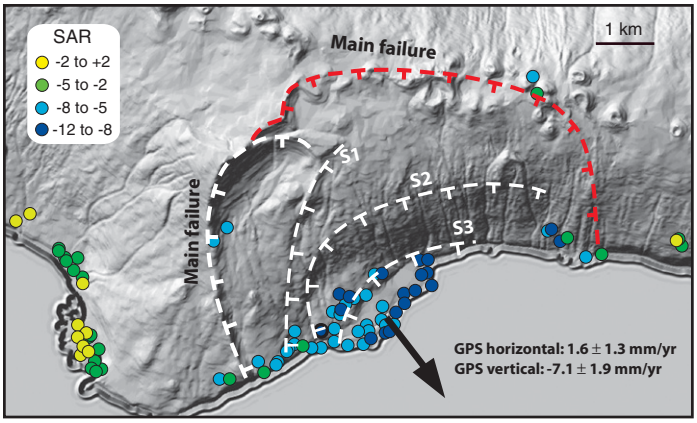


**Figure 4. Horizontal and vertical displacement rates within collapse area derived from GPS and synthetic aperture radar (SAR) data acquired from 2001–2006 and 2006–2009, respectively. Distinct colors for various rates of average vertical displacements are in mm/yr. Negative values and positive values are for downward and upward movements, respectively.**

## SLUMP MECHANISMS AND PROPAGATION

Previous studies have considered that the present configuration of the southeastern flank of Pico could reflect vertical caldera collapse (Woodhall, 1974; Mitchell et al., 2011). This is inconsistent with observed geology and our data, because (1) the horseshoe shape of the failures supports lateral movement; (2) central caldera collapse should have cut the east and west flanks of the old volcano in a symmetrical way, but its eastern flank is not exposed on land; and (3) present-day vertical motion is inconsistent with caldera collapse of the oldest volcanic lavas of the island. Lateral collapse has been proposed, but is considered as currently inactive (Nunes, 1999; Nunes et al., 2006; Mitchell et al., 2011); this is inconsistent with our data. One may argue that the measured displacements could result from active movements along strike-slip faults coinciding with the main axis of the island (Madeira and Brum da Silveira, 2003), with possible development of a pull-apart structure between such faults. However, such right-lateral movement would imply compression along the north-south main collapse rim, which is inconsistent with the measured flank spreading.

The main scar extends to the eastern parts of the ridge main axis, where numerous young cones have developed. The localization of the main failure surface thus may have been influenced by dike intrusion and magma push along the main rift zone, a mechanism frequently advocated to explain the development of flank instability on volcanic islands (Moore et al., 1994; Elsworth and Day, 1999; Hildenbrand et al., 2006).

The initiation of the failure is not well constrained in time, because there are insufficient geochronological data. Extrapolating the measured rate of subsidence along the main rim (net value of 5 mm/yr on average) suggests gradual downward movement during the past 60 k.y., but displacement rates may not have been constant through time. Nevertheless, the several curved scars developed farther east show less vertical offset and affect younger lava flows erupted from vents that apparently migrated sequentially eastward. This suggests recent eastward propagation of the failure within the central outer parts of the moving mass. The development of volcanic cones along the trace of the several secondary curved scars thus probably reflects the opening of lateral cracks, which served as local pathways for recent magma ascent. Although our InSAR data do not record present differential movement along S3, the formation of this arcuate scarp is here interpreted as resulting from recent deformation close to the island shore, which yielded the recurrent detachment of coastal segments. This is consistent with the presence of a moderate-sized debris field on the southern submarine slope of the ridge, identified from marine geophysical surveys (Mitchell, 2003).

Our new geodetic data show that the present deformation affects a significant part of the southeastern flank of Pico Island, and not solely the central lava delta. Therefore, other causes of subsidence such as recent lava cooling or compaction of underlying sediments cannot adequately explain the recorded movement, especially as a similar recent lava delta developed west of the collapse area does not show any appreciable downward movement (Fig. 4). Differential deformation at the foot of the various scars identified here also suggests the discrete displacement of large blocks along several curved faults with typical normal kinematics, as recognized or suspected on the Hilina fault system in Hawaii (Smith et al., 1999), the Cumbre Vieja western sector collapse on La Palma in the Canary Islands (Hildenbrand et al., 2003; González et al., 2010), or on the east flank of the dormant Damavand volcano in northern Iran (Shirzaei et al., 2011). The rates of subsidence reported here are significantly higher than the rates measured on the western slope of La Palma, but they are one order of magnitude lower than the values recorded on the southern mobile flank of Kilauea volcano in Hawaii (Owen et al., 2000). With a subaerial volume estimated as ~10 $km^3$, the southeastern collapse of Pico also appears to be significantly smaller than typical Hawaiian giant landslides (Moore et al., 1994), but the structures on Pico may evidence only the proximal part of a much larger complex potentially affecting the deep base of the submarine flank.

## FURTHER EVOLUTION?

The lack of volcanic eruptions or detectable inflation of the volcanic ridge over the period of geodetic monitoring implies that active downward displacement of the southeastern mobile flank of Pico Island is not a direct result of forceful magma intrusion along the rift zone. In addition, the lack of detected shallow earthquakes within the collapse area during this geodetic monitoring time interval suggests that creep is currently the main mode of deformation.

The higher rates of current vertical displacement measured near sea level possibly reflect cumulative displacements along the main rim of the collapse, and additional displacements along the more recent outer failures, especially S2 (Fig. 4). By this hypothesis, vertical displacements in the outer flank reach an average value of ~3–5 mm/yr, which is similar to or slightly higher than the maximum horizontal displacement rate derived from our GPS station (2.9 mm/yr), when uncertainties are accounted for. Such data support the fact that the distal part of the ridge is currently moving along a steep fault with a minimum dip of 45° toward the southeast. This is consistent with the exposed geometry of the outer arcuate structure S2, which therefore constitutes a priority target for further monitoring and hazard assessment, e.g., eventual block detachment and associated potential tsunami.

**ACKNOWLEDGMENTS**

This study has been in great part supported by FCT (Fundação para a Ciência e a Tecnologia, Portugal) through MEGAHazards ("Mass-wasting Episodes in the Geological Evolution of the Azores islands: timing, recurrence, mechanisms and consequences"; PTDC/CTE-GIX/108149/2008). This is LGMT (Laboratoire de Géochronologie Multi-Techniques) contribution 103. We thank T. Walter, N. Mitchell, and four anonymous reviewers for their valuable remarks.

**REFERENCES CITED**

Borges, J.F., Bezzeghoud, M., Buforn, E., Pro, C., and Fitas, A., 2007, The 1980, 1997 and 1998 Azores earthquakes and some seismo-tectonic implications: Tectonophysics, v. 435, p. 37–54, doi:10.1016/j.tecto.2007.01.008.

Boulesteix, T., Hildenbrand, A., Gillot, P.Y., and Soler, V., 2012, Eruptive response of oceanic islands to giant landslides: New insights from the geomorphologic evolution of the Teide–Pico Viejo volcanic complex (Tenerife, Canary): Geomorphology, v. 138, p. 61–73, doi:10.1016/jge omorph .2011.08.025.

Calvert, A.T., Moore, R.B., McGeehin, J.P., and Rodrigues da Silva, A.M., 2006, Volcanic history and $^{40}Ar/^{39}Ar$ and $^{14}C$ geochronology of Terceira Island, Azores, Portugal: Journal of Volcanology and Geothermal Research, v. 156, p. 103–115, doi:10.1016/jjv olgeores.2006.03.016.

Catalão, J., Nico, G., Hanssen, R., and Catita, C., 2011, Merging GPS and atmospherically corrected InSAR data to map 3D terrain displacement velocity: IEEE Transactions on Geoscience and Remote Sensing, v. 49, p. 2354–2360, doi:10.1109/TGRS.2010.2091963.

Catita, C., Feigl, K.L., Catalão, J., Miranda, J.M., and Victor, L.M., 2005, InSAR time series analysis of the 9 July 1998 Azores earthquake: International Journal of Remote Sensing, v. 26, p. 2715–2729, doi:10.1080/014311605 12331337835.

Clouard, V., and Bonneville, A., 2004, Importance of submarine landslides in French Polynesia, *in* Hekinian, R., ed., Oceanic hotspots: Intraplate submarine magmatism and tectonism: Berlin, Springer, p. 209–238.

Duffield, W.A., Stieljes, L., and Varet, J., 1982, Huge landslide blocks in the growth of Piton de la Fournaise, La Réunion and Kilauea volcano, Hawaii: Journal of Volcanology and Geothermal Research, v. 12, p. 147–160, doi:10.1016/0377-0273(82)90009-9.

Elsworth, D., and Day, S.J., 1999, Flank collapse triggered by intrusion: The Canarian and Cape Verde archipelagoes: Journal of Volcanology and Geothermal Research, v. 94, p. 323–340, doi:10.1016/S0377-0273(99)00110-9.

Fernandes, R.M.S., Bastos, L., Ambrosius, B.A.C., Noomen, R., Matheussen, S., and Baptista, P., 2004, Recent geodetic results in the Azores Triple Junction region: Pure and Applied Geophysics, v. 161, p. 683–699, doi:10.1007 /s00024-003-2469-y.

Gillot, P.Y., Lefèvre, J.C., and Nativel, P.E., 1994, Model for the structural evolution of the volcanoes of Réunion Island: Earth and Planetary Science Letters, v. 122, p. 291–302, doi:10.1016/0012-821X(94)90003-5.

González, P.J., Tiampo, K.F., Camacho, A.G., and Fernández, J., 2010, Shallow flank deformation at Cumbre Vieja volcano (Canary Islands): Implications on the stability of steep-sided volcano flanks at oceanic islands: Earth and Planetary Science Letters, v. 297, p. 545–557, doi:10.1016/j .epsl.2010.07.006.

Hildenbrand, A., Gillot, P.Y., Soler, V., and Lahitte, P., 2003, Evidence for a persistent uplifting of La Palma (Canary Islands), inferred from morphological and radiometric data: Earth and Planetary Science Letters, v. 210, p. 277–289, doi:10.1016/S0012-821X(03)00133-X.

Hildenbrand, A., Gillot, P.Y., and Bonneville, A., 2006, Off-shore evidence for a huge landslide of the northern flank of Tahiti-Nui (French Polynesia): Geochemistry Geophysics Geosystems, v. 7, p. 1–12, doi:10.1029/2005GC001003.

Hildenbrand, A., Madureira, P., Marques, F.O., Cruz, I., Henry, B., and Silva, P., 2008, Multi-stage evolution of a sub-aerial volcanic ridge over the last 1.3 Myr: S. Jorge Island, Azores Triple Junction: Earth and Planetary Science Letters, v. 273, p. 289–298, doi:10.1016/je psl.2008.06.041.

Keating, B.H., and McGuire, W.J., 2000, Island edifice failures and associated tsunami hazards: Pure and Applied Geophysics, v. 157, p. 899–955, doi:10.1007/s000240050011.

Klügel, A., Walter, T.R., Schwarz, S., and Geldmacher, J., 2005, Gravitational spreading causes en-echelon diking along a rift zone of Madeira Archipelago: An experimental approach and implications for magma transport: Bulletin of Volcanology, v. 68, p. 37–46, doi:10.1007/s00445-005-0418-6.

Krastel, S., Schmincke, H.U., Jacobs, C.L., Rihm, R., Le Bas, T.P., and Alibes, B., 2001, Submarine landslides around the Canary Islands: Journal of Geophysical Research, v. 106, p. 3977–3997, doi:10.1029/2000JB900413.

Le Friant, A., Boudon, G., Deplus, C., and Villemant, B., 2003, Large-scale flank collapse events during the activity of Montagne Pelee, Martinique, Lesser Antilles: Journal of Geophysical Research, v. 108, 2055, doi:10.1029/2001JB001624.

Lipman, P.W., Normak, W.R., Moore, J.G., Wilson, J.B., and Gutmacher, C.E., 1988, The giant submarine Alika debris slide, Mauna Loa, Hawaii: Journal of Geophysical Research, v. 93, p. 4279–4299, doi:10.1029/JB093iB05p04279.

Madeira, J., and Brum da Silveira, A., 2003, Active tectonics and first palaeoseismological results in Faial, Pico and Sao Jorge Islands (Azores, Portugal): Annals of Geophysics, v. 46, p. 733–761.

McGuire, W.J., 1996, Volcano instability: A review of contemporary themes, *in* McGuire, W.J., et al., eds., Volcano instability on Earth and other planets: Geological Society of London Special Publication 110, p. 1–23, doi:10.1144/GSL.SP.1996.110.01.01.

McMurtry, G.M., Herrero-Bervera, E., Cremer, M.D., Smith, J.R., Sherman, C., and Torresan, M.E., 1999, Stratigraphic constraints on the timing and emplacement of the Alika 2 giant Hawaiian submarine landslide: Journal of Volcanology and Geothermal Research, v. 94, p. 35–58, doi:10.1016 /S0377-0273(99)00097-9.

McMurtry, G.M., Fryer, G.J., Tappin, D.R., Wilkinson, I.P., Williams, M., Fietzke, J., Garbe-Schoenberg, D., and Watts, P., 2004, Megatsunami deposits on Kohala volcano, Hawaii, from flank collapse of Mauna Loa: Geology, v. 32, p. 741–744, doi:10.1130/G20642.1.

Mitchell, N.C., 2003, Susceptibility of mid-ocean ridge volcanic islands and seamounts to large-scale landsliding: Journal of Geophysical Research, v. 108, 2397, doi:10.1029/2002JB001997.

Mitchell, N.C., Quartau, R., and Madeira, J., 2011, Assessing landslide movements in volcanic islands using near-shore marine geophysical data: South Pico Island, Azores: Bulletin of Volcanology, v. 74, p. 483–496, doi:10.1007/s00445-011-0541-5.

Moore, J.G., Normark, W.R., and Holcomb, R.T., 1994, Giant Hawaiian landslides: Annual Review of Earth and Planetary Sciences, v. 22, p. 119–144, doi:10.1146/annurev.ea.22.050194.001003.

Morgan, J.K., Moore, G.F., Hills, D.J., and Leslie, S., 2000, Overthrusting and sediment accretion along Kilauea's mobile south flank, Hawaii: Evidence for volcanic spreading from marine seismic reflection: Geology, v. 28, p. 667–670, doi:10.1130/0091-7613(2000)28667:O ASAAK2.0.C O;2.

Nunes, J.C., 1999, A actividade vulcânica na ilha do Pico do Plistocénico Superior ao Holocénico: Mecanismo eruptivo e hazard vulcânico [Ph.D . thesis] Ponta Delgada, Portugal, Universade dos Açores, 356 p.

Nunes, J.C., Camacho, A., Franca, Z., Alves, M., Vieira, R., Velez, E., and Ortiz, E., 2006, Gravity anomalies and crustal signature of volcano-tectonic structures of Pico Island (Azores): Journal of Volcanology and Geothermal Research, v. 156, p. 55–70, doi:10.1016/jjv olgeores.2006.03.023.

Owen, S., Segall, P., Lisowski, M., Miklius, A., Denlinger, R., and Sako, M., 2000, Rapid deformation of Kilauea volcano: Global positioning system measurements between 1990 and 1996: Journal of Geophysical Research, v. 105, p. 18,983–18,998, doi:10.1029/2000JB900109.

Quidelleur, X., Hildenbrand, A., and Samper, A., 2008, Causal link between Quaternary paleoclimatic changes and volcanic islands evolution: Geophysical Research Letters, v. 35, L02303, doi:10.1029/2007GL031849.

Samper, A., Quidelleur, X., Lahitte, P., and Mollex, D., 2007, Timing of effusive volcanism and collapse events within an oceanic arc island: Basse Terre, Guadeloupe archipelago (Lesser Antilles Arc): Earth and Planetary Science Letters, v. 258, p. 175–191, doi:10.1016/je psl.2007.03.030.

Shirzaei, M., Walter, T.R., Nankali, H.R., and Holohan, E., 2011, Gravity-driven deformation of Damavand volcano, Iran, detected through InSAR time series: Geology, v. 39, p. 251–254, doi:10.1130/G31779.1.

Silva, P.F., Henry, B., Marques, F.O., Hildenbrand, A., Madureira, P., Mériaux, C.A., and Kratinová, Z., 2012, Palaeomagnetic study of a sub-aerial volcanic ridge (São Jorge Island, Azores) for the past 1.3 Myr: Evidence for the Cobb Mountain Subchron, volcano flank instability and tectono-magmatic implications: Geophysical Journal International, v. 188, p. 959–978, doi:10.1111/j 1365-246X.2011.05320.x.

Smith, J.R., Malahoff, A., and Shor, A.N., 1999, Submarine geology of the Hilina slump and morpho-structural evolution of Kilauea volcano, Hawaii: Journal of Volcanology and Geothermal Research, v. 94, p. 59–88, doi:10.1016 /S0377-0273(99)00098-0.

Tilling, R.I., Koyanagi, R.Y., Lipman, P.W., Lockwood, J.P., Moore, J.G., and Swanson, D.A., 1976, Earthquake and related catastrophic events, island of Hawaii, November 29, 1975: A preliminary report: U.S. Geological Survey Circular 740, 33 p.

Walter, T.R., and Schmincke, H.U., 2002, Rifting, recurrent landsliding and Miocene structural reorganization on NW-Tenerife (Canary Islands): International Journal of Earth Sciences, v. 91, p. 615–628, doi:10.1007/s00531 -001-0245-8.

Woodhall, D., 1974, Geology and volcanic history of Pico Island Volcano, Azores: Nature, v. 248, p. 663–665, doi:10.1038/248663a0.

Manuscript received 13 February 2012
Revised manuscript received 27 April 2012
Manuscript accepted 11 May 2012

Printed in USA

**Item DR1:** Maps detailing the morphology of Pico SE slump

**(A)** Shaded-relief map and morphology of the main scars here identified

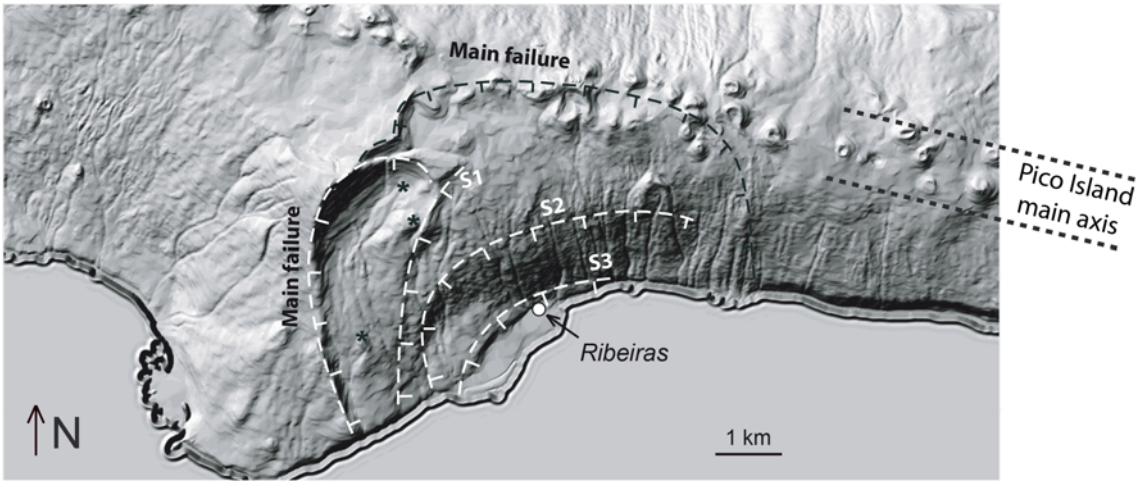


**(B)** Topographic contour map and cross-section (vertical exageration of a factor 2)

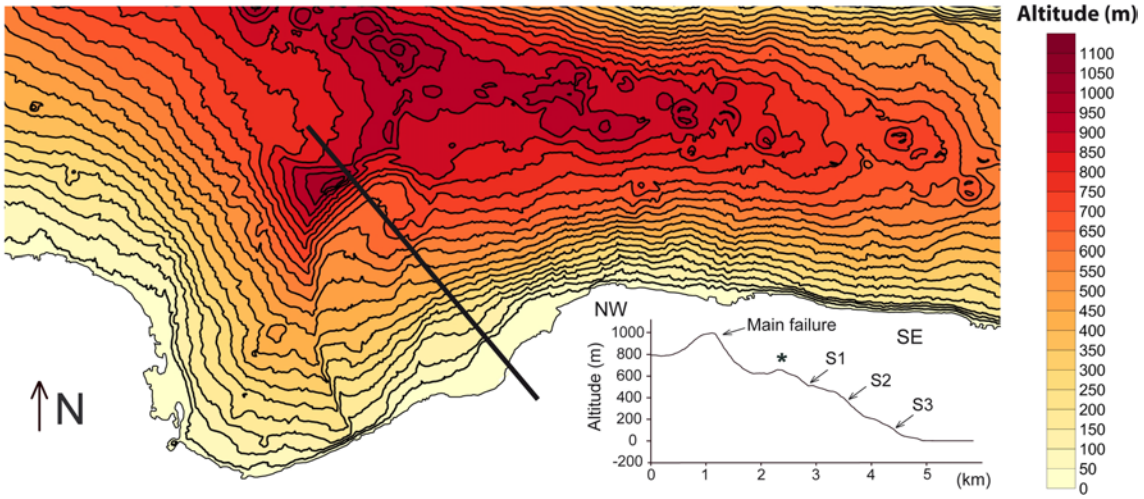


**(C)** Slope map

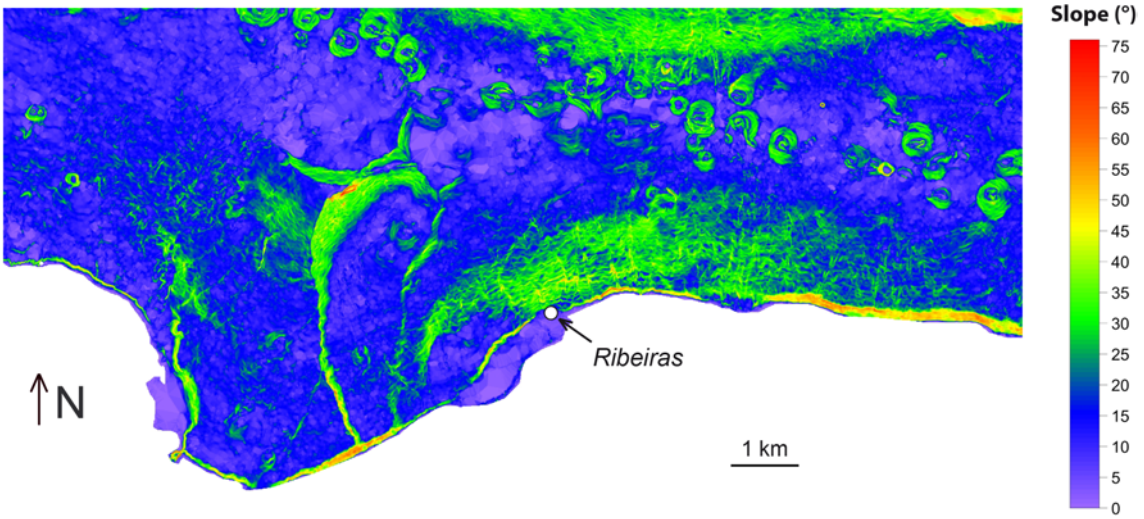

**Item DR2:** Photograph showing the thick lava flows overlying the Td. The geometry of individual lava flows evidence their buttressing against the main lateral discontinuity of the sector collapse. Geologist in the center of the picture for scale.

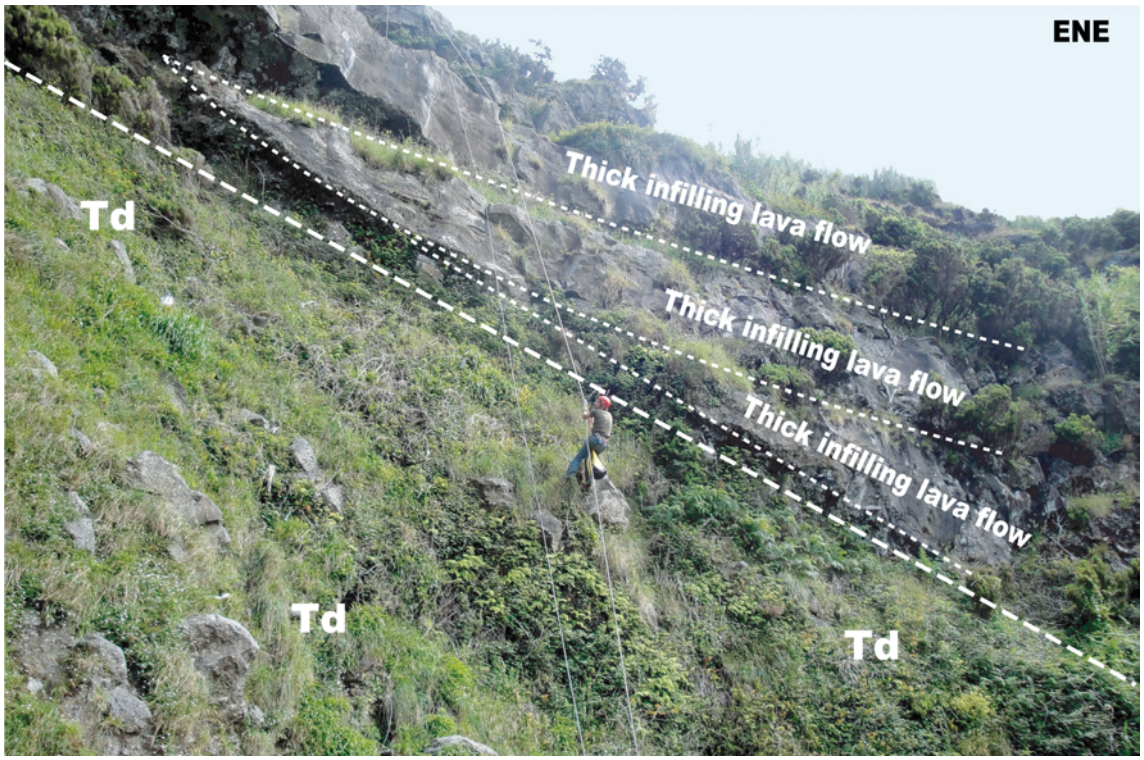

**Item DR3:** Details on the methods and data processing (GPS and InSAR)

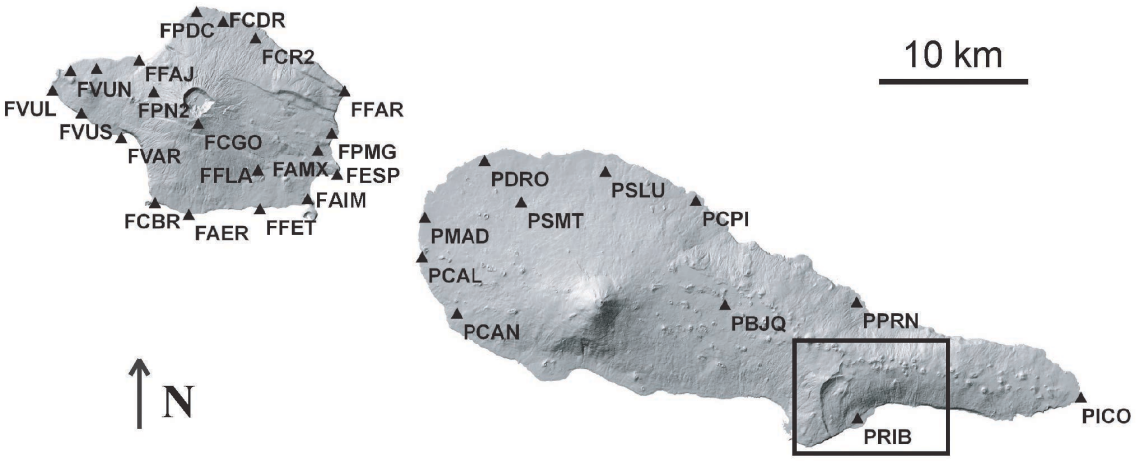


*Figure DR3A. Localization of the GPS stations on Faial and Pico islands*

## 1. GPS data acquisition and processing

In 2001 a dense GNSS network was installed in the central Azores, including 20 and 11 sites on Faial and Pico, respectively. This network was designed as a densification of the existing TANGO-OA/DEOS network originally consisting in only six stations per island (Fernandes et al., 2004). All sites were set up with metallic benchmarks installed in outcrops of solid rock. Four GPS campaigns were conducted from 1999 to 2006 (1999, 2001, 2003 and 2006). The reference campaign is 2001 when all the 31 stations were observed. On the other campaigns, only a subset of the network was observed but ensuring that every station was measured at least three times. The observation protocol was maintained in all surveys: each site was surveyed for 12 to 24 hours per day over an average of 3 consecutive days while the receiver installed in FAIM site (Faial Island) operated in continuous mode during the whole period. All the surveys were performed using dual-frequency GPS receivers, collecting data every 30 sec.

We analyzed all GPS data using GAMIT/GLOBK software (Herring, 2003; King and Bock, 2002). The data analysis involves two major procedures, as described elsewhere (Feigl et al., 1993; McClusky et al., 2000). The first procedure uses GAMIT to estimate parameters such as station position and orbital trajectory on a daily basis for a given 24-hour interval, from the union of the campaign stations and 9 global IGS stations. This daily procedure is completely standard and detailed in McClusky et al. (2000). A priori hydrostatic and wet models from Saastamoinen (1972) and Niell's (1996) mapping function were used to model the troposphere. Tropospheric parameters were estimated at each station every three hours. A linear picewise estimation model was used to estimate the zenith delay. The a priori estimates of the satellites' orbital parameters come from the precise trajectories computed at the Scripps Orbit and Permanent Array Center at SIO (Bock et al., 1997). In the second procedure, we combine the daily solutions with 3 global IGS subnetworks (IGS, IGS3 and EURO), using GLOBK software (Herring, 2003) in a regional stabilization approach (McClusky et al., 2000). This stabilization procedure defined a reference frame by minimizing, in a least squares sense, the departure from a priori values based on the International Terrestrial Reference Frame 2008 (Altamimi et al., 2011), of the positions and velocities for a set of 26 globally distributed stations. These stations thus move in a "no net rotation" reference frame approximately aligned with the ITRF2008. The average GPS station velocities were calculated from the GPS time series by linear regression of the survey position estimates generated using the GLOBK software. PRIB station time series are shown in figure DR3B. The estimated velocity for this station is: easting 10.1 ± 0.5 mm/yr, northing 13.4 ± 0.5 mm/yr and up -7.1±1.9 mm/yr.

a)

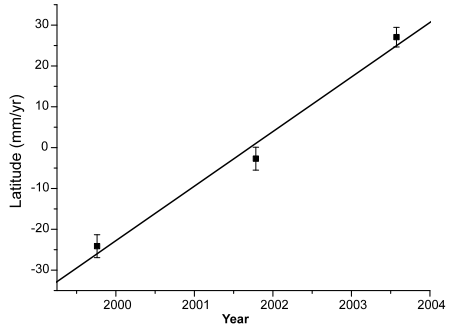


b)

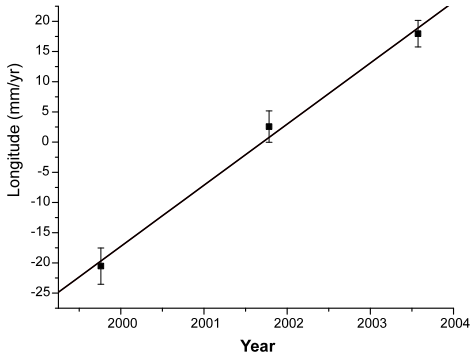


c)

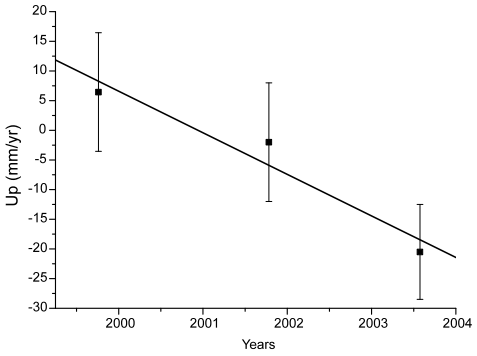


*Figure DR3B. Time series for PRIB GPS station showing displacements relative to ITRF2008: (a) north, (b) east, and (c) up.*

*Error bars on station positions reported at 2σ. The lines show linear fit to the data.*

The horizontal velocities, computed with GPS data from 1999 to 2006, were used to estimate the rigid body motion represented by the three components of the Euler vector ($\omega_x$, $\omega_y$, $\omega_z$). The rigid body motion is associated with the regional plate tectonics. The residual displacement for each GPS station was computed as the difference between the estimated rigid body motion and the GPS station velocity. The residual displacement is associated to the intra-island deformation related with local deformation effects.

The PRIB station has a residual horizontal motion outwards with a velocity of 1.6 ± 1.3 mm/yr and an average downward vertical displacement of 7.1 ±1.9 mm/yr.

## 2. INSAR data acquisition and processing

The interferometric dataset consisted of 57 ENVISAT-ASAR images covering Faial, Pico and S. Jorge islands, from 2006 March to 2009 January. Twenty-nine images were acquired along the descending pass and 28 along the ascending one. The perpendicular baseline range from -756m to 944m with a mean value of 126 m. The master image was chosen to minimize both the temporal and perpendicular baseline.

The DORIS software (Delft University of Technology, Kampes et al., 2003) was used for interferometric processing. A mask over sea was applied to the original data improving considerably the coregistration and interferometric processing. In the Azores, the coherence of interferograms is markedly low and the Persistent Scatterers approach seems to be the only reliable technique to extract useful information from interferograms. STAMPS software (Hooper et al., 2007) was used to determine the Permanent Scatterers using the stack of interferograms already processed for the ascending and descending passes.

The InSAR technique has two main limitations: first, it measures only the displacement along the radar line of sight (LOS) and second the measured displacement contains information on both the surface displacement and the temporal changes of the atmospheric phase delay. Concerning the first limitation, it is worth mentioning that 3-D terrain displacement is difficult to measure even in the case of InSAR measurements taken along both ascending and descending satellite passes. In fact, even in this case, there would be three unknown velocity components and just two independent InSAR LOS velocity measurements. For that, we have used a methodology to merge InSAR

point-like estimations, from both ascending and descending passes, and repeated GPS measurements of terrain displacement velocity to derive accurate maps of 3-D terrain displacement. A four-parameter trigonometric polynomial, representing a bias and a tilt, is computed by minimizing, separately for the ascending and descending passes, a cost function. It was observed that the merging of PS-InSAR and GPS data reduces the velocity dispersion of PS falling within the circular area around each GPS station from 7.2 $mm \cdot yr^{-1}$ to 2.1 $mm \cdot yr^{-1}$ on Pico Island. The complete description of the method and data can be found in Catalao et al. (2011).

As far as the second limitation is concerned the geodetic and atmospheric signals in INSAR data were disentangle using high-resolution numerical weather models. For any SAR image acquisition, the 3-D refractivity field and radar phase delay is computed using the high-resolution Weather Research and Forecasting (WRF) model to generate forecasts of the atmospheric parameters at a 1-km horizontal resolution and at the same time of SAR acquisitions. Synthetic interferograms corresponding to the atmospheric phase delays were then obtained as the difference between the atmospheric phase delays computed at the acquisition times of the master and slave SAR images. Before applying the PS-InSAR processing, atmospheric artifacts were mitigated by removing the corresponding synthetic interferogram of atmospheric phase delay from each SAR interferogram of the time series. The use of the WRF model further reduces the dispersion of estimates to 1.5 $mm.yr^{-1}$ almost everywhere on both islands. It was observed that the mitigation of atmospheric artifacts reduces the spatial dispersion of velocity estimates up to 30%. The INSAR time series for PSs within a radii of 200 m centered in PRIB is plotted in figure DR3C. A seasonal effect is seen on the time series interpreted as the response to soil water content variation. The mean precipitation in Azores islands is very high and can induce seasonal apparent vertical deformation. This

effect can be filtered out with a time series longer that an annual meteorological cycle. In our case, we have three years of SAR data and a tendency can be derived by linear regression of the relative position estimates. The estimated trend for the set of PS's close to PRIB is -6.1 mm/yr with an error of 1.3 mm/yr.

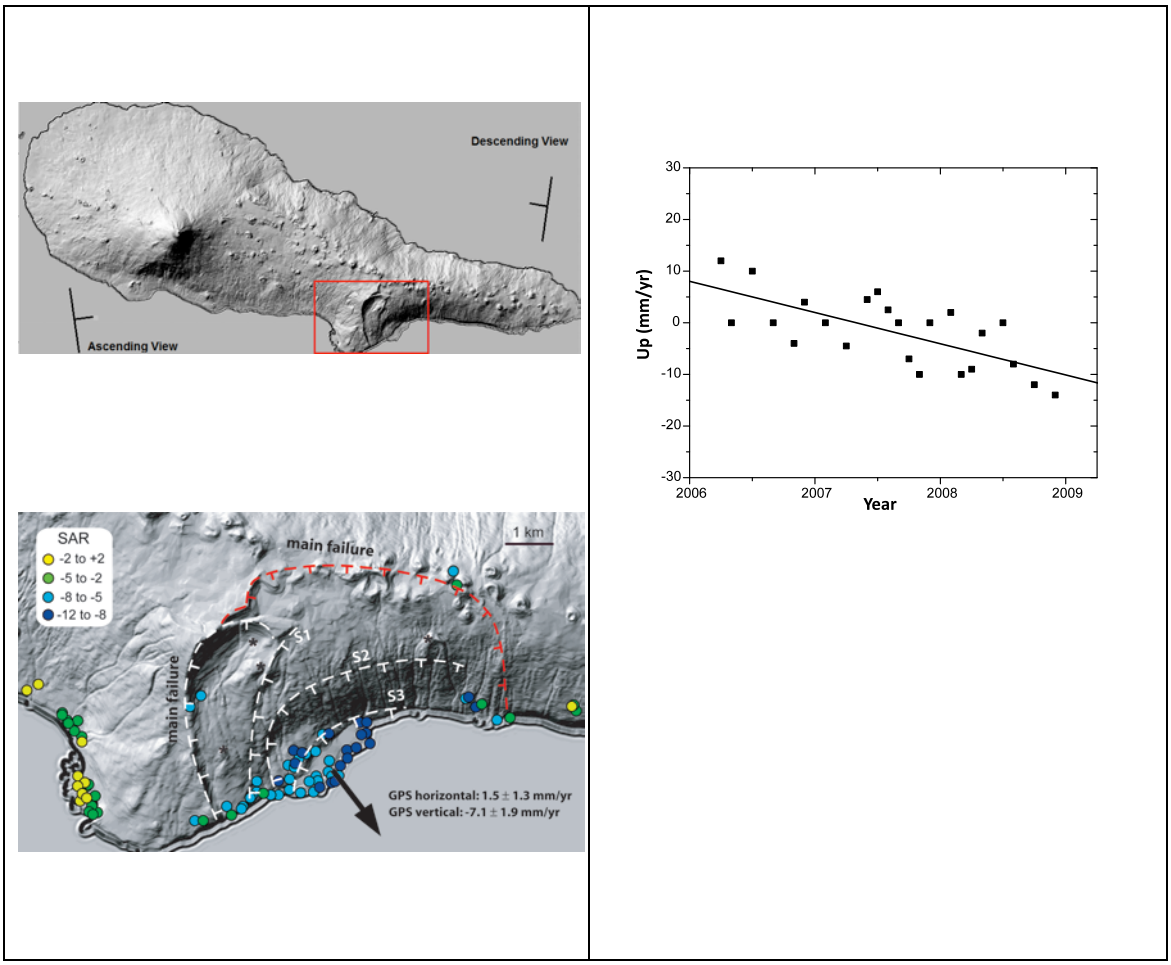


*Figure DR3C. Time series for Persistent Scatters on a radii of 200 m around PRIB station.*

**References cited in DR3**

Altamimi Z., Collilieux, X., and Métivier, L., 2011, ITRF2008: an improved solution of the International Terrestrial Reference Frame: J. Geodesy, vol. 85, p. 457-473.

Bock, Y., Wdowinski, S., Fang, P., Zhang, J., Behr, J., Genrich, J., Williams, S., Agnew, D., Wyatt, F., Johnson, H., Stark, K., Oral, B., Hudnut, K., Dinardo, S., Young, W., Jackson, D., and Gurtner, W., 1997, Southern California Permanent GPS Geodetic Array: Continuous measurements of regional crustal deformation between the 1992 Landers and 1994 Northridge earthquakes: J. Geophys. Res., v. 102, p. 18,013- 18,033.

Catalão, J., Nico, G., Hanssen, R., and Catita, C., 2011, Merging GPS and atmospherically corrected InSAR data to map 3D terrain displacement velocity: IEEE Transactions on Geoscience and Remote Sensing, doi:10.1109/TGRS.2010.2091963.

Catita, C., Feigl, K.L., Catalão, J., Miranda, J.M., and Victor, L.M., 2005, Time series analysis of SAR data applied to the study of the co-seismic deformation of the 9th July 1998 Pico-Faial (Azores) earthquake: Int. J. Remote Sensing, vol. 26, p. 2715-2729.

Feigl, K., Agnew, D., Bock, Y., Dong, D., Donnellan, A., Hager, B., Herring, T., Larsen, D.,, Larson, K., Murray, M., Shen, Z., and Webb, F., 1993, Space geodetic measurement of the velocity field of central and southern California, 1984-1992: J. Geophys. Res., v. 98, p. 21677-21712.

Fernandes, R.M.S., Bastos, L., Ambrosius, B.A.C., Noomen, R., Matheussen, S., Baptista, P., 2004. Recent geodetic results in the Azores Triple Junction region. Pure and Applied Geophysics 161 (3), 683–699.

Herring, T.A., 2003, GLOBK: Global Kalman Filter VLBI and GPS Analysis Program, Version 10.1.: Cambridge, Mass. Inst. Technology.

King, R.W., and Bock, Y., 2002, Documentation for the GAMIT analysis software, release 10.1: Cambridge, MA, Massachusetts Institute of Technology.

McClusky, S., Balassanian, S., Barka, A., Demir, C., Ergintav, S., Georgiev, I., Gurkan, O., Hamburger, M., Hurst, K., Kahle, H., Kastens, K., Kekelidze, G., King, R., Kotzev, V., Lenk, O., Mahmoud, S., Mishin, A., Nadariya, M., Ouzounis, A., Paradissis, D., Peter, Y., Prilepin, M., Reilinger, R., Sanli, I., Seeger, H., Tealeb, A., Toksoz, M., and Veis, G., 2000, Global positioning system constraints on plate kinematics and dynamics in the eastern Mediterranean and Caucasus: J. Geophys. Res., v. 105, p. 5695-5719.

Niell, A.E., 1996, Global mapping functions for the atmosphere delay at radio wavelengths: J. Geophys. Res., vol. 101, p. 3227–3246.

Saastamoinen, J., 1972, Atmospheric correction for the troposphere and stratosphere in radio ranging of satellites: in The Use of Artificial Satellites for Geodesy, Geophys. Monograph, v. 15, p. 247–251.

B. Kampes, R. Hanssen, and Z. Perski, “Radar interferometry with public domain tools,” in *Proc. FRINGE*, Frascati, Italy, Dec. 1–5, 2003.

A. Hooper, P. Segall, and H. Zebker, “Persistent scatterer interferometric synthetic aperture radar for crustal displacement analysis, with application to Volcano Alcedo, Galapagos,” *J. Geophys. Res.-Solid Earth*, vol. 112, no. B7, p. B07407, 2007.

# PART IV

## Cohesive Coulomb Critical Taper Theory applied to gravitational instability: analytical solution and application to gravitational collapses in volcanic systems

# Chapter 7

## Gravitational instability in a cohesive granular material atop an overpressured detachment – analytical derivation and experimental testing

## (Costa et al., *in prep a*)

# Gravitational instability in a cohesive granular material atop an overpressured detachment – analytical derivation and experimental testing

**(*in prep a*)**

**Costa, A.C.G. [1,2*], Mourgues, R.[3], Marques, F.O.[4], Lacoste, A.[5], Garibaldi, C.[3], Bulois, C.[3], Hildenbrand, A.[2,6], Boulesteix, T[7].**

(1) Universidade de Lisboa and IDL, Lisboa, Portugal
(2) Univ. Paris-Sud, Laboratoire GEOPS, UMR8148, Orsay, F-91405
(3) 1LUNAM, L.P.G.N., UMR 6112, Faculty of Science, Université du Maine, Le Mans, France
(4) Universidade de Lisboa, Lisboa, Portugal
(5) GeHCO, E.A.6293, Université de Tours, Tours, France
(6) CNRS, Orsay, F-91405
(7) Université de Lorraine, CNRS, CREGU, GeoRessources laboratory, Vandoeuvre les Nancy, F-54500, France

## Abstract

The critical taper theory of Coulomb wedges has been traditionally applied to compressive regimes (accretionary prisms/ fold-and-thrust belts), but more recently it has been applied to gravitational instabilities. The works using this theory either assume a non-cohesive wedge, or do not provide a simple analytical solution for the cohesive system. Here we derive an analytical solution for the cohesive critical wedge, and compare with results of analogue experiments. We focus on the role of cohesion on the stability state of the wedge, and analyze how cohesion conditions the stress regime within the wedge, by inhibiting deformation and conditioning failure location. We investigate the roles of wedge geometry, cohesion, and fluid overpressure. Structural implications of the analytical model were analyzed through analogue modeling carried out during the present study. We show that the stability of a cohesive wedge under fluid overpressure is size-dependent (the influence of

cohesion is more significant for smaller wedges), while the stability of a non-cohesive wedge under fluid overpressure is independent of its size. The stabilizing effect of cohesion is significant for the most superficial domain of the wedge. The thickness of this more stable superficial layer decreases with increasing fluid overpressure ratio. Within this layer, the principal compressive stress rotates and the expected structures are listric. If the limit of the thickness expected for this layer is reached within the wedge (given the material's properties, fluid overpressure ratio and wedge configuration), the generated listric structures become parallel to the wedge's upper surface at this limit. This limit marks the reach of the failure envelope for the wedge's material. In terms of the wedge's stability along a basal detachment, the stabilizing effect of cohesion is accentuated in the foremost thin domain of the wedge, defining a required Minimum Failure Length (MFL). This MFL decreases for: smaller cohesions, smaller coefficients of internal friction, larger fluid overpressure ratios, steeper upper and basal surfaces of the wedge.

***Keywords***

Critical taper theory; Coulomb wedges; cohesion; gravitational instabilities; gravitational spreading; shallow landsliding

## 1. Introduction

Events of large-scale gravitational destabilization occur in a wide range of geological settings (e.g., Moore et al., 1989; Haflidason et al., 2004; Lacoste et al., 2009), and in many cases only the surface deformations or the scar/deposits of the landslide are detectable (e.g., Hildenbrand et al., 2012; Costa et al., 2014). Geophysical methods allow the interpretation of the basal detachment and the characterization of the internal deformation of the displaced volume (Morgan et al., 2003; Haflidason et al., 2004).

Landsliding results from progressive changes of physical parameters critical for the stability state of slopes (e.g., decrease of the material's strength and surface morphology due to weathering/erosion, sedimentation, tectonics, changes of pore pressure) (e.g., Voight and Elsworth, 1997; Masson et al., 2006). The identification and study of the factors that lead to the decrease of the material stability and/or trigger landslide events are of high interest in many areas of geosciences with direct social implications (e.g., geotechnics and civil engineering, volcanology, oil industry).

Abnormal pore pressure (fluid overpressure) is a critical destabilization factor involved in numerous gravitational instabilities with low-dip slopes in sub-aerial and submarine structures at various scales: e.g., large-scale flank collapses in volcanic islands (Iverson, 1995; Day, 1996), sub-aerial landslides in active margins associated with river incision (Waitawhiti landslides, New Zealand - Lacoste et al., 2009, 2011), submarine landslides affecting passive margins (Amazon Fan - Cobbold et al., 2004; Mourgues et al., 2009; Gulf of Mexico - Flemings et al., 2008; 3000 $km^3$ Storegga slide - North Sea Fan - Kvalstad et al., 2005). Fluid overpressure is generated through several mechanisms, such as compaction disequilibrium (Walder and Nur, 1984; Day, 1996), mechanical and thermal pressurization of the porous medium (e.g., direct effect of magmatic intrusion, and associated effect of magmatic degassing - Iverson, 1995; Day, 1996; Elsworth and Voight, 1996; Voight and Elsworth, 1997; Reid, 2004), seismic loading (Elsworth and Voight, 1996), changing sea level (Iverson, 1995; Quidelleur et al., 2008; Smith et al., 2013), groundwater flow of meteoric water (Reid, 2004), and hydrocarbon generation (e.g., Cobbold et al., 2004, 2013; Zanella et al., 2014a, 2014b). Fluid overpressure is an important factor to take into consideration when addressing the global hydrological dynamics of a sedimentary basin, and with important implications for the oil industry (hydrocarbon maturation and risks associated to the drilling phase) (e.g., Nadeau, 2011).

In the last decades, much has been done to achieve a better understanding of these processes through numerical, analytical and analogue modeling (e.g., Reid, 2004; Mourgues et al., 2014; Zanella et al., 2014b). The simplification of the process inherent to modeling, often requires the neglect of variables that can be important for the understanding of the studied process (e.g., cohesion of the material), and often the formulation or results are too complex to allow for a clear and simple view of the role of each variable tested.

Cohesion of the materials conditions failure in compressive (accretionary wedges and thrust-and-fold belts - Davis et al., 1983; Dahlen et al., 1984) and extensional settings (e.g., it affects the depth of gravitational failure in volcanic edifices - del Potro et al., 2013). Even though its impact decreases with increasing depth (Dahlen et al., 1984; Iverson, 1995), two major landslide examples in submarine settings present large blocks of undisrupted material in their deposits and preserved steep scars: the Storegga slide, affected a sediment volume of 2400-3200 $km^3$ in the continental platform in the North Sea, developed retrogressively, with lateral spreading of large scale blocks (Toreva blocks) along 1.1-1.4º dipping failure surfaces, and generation and maintenance of a currently stable headwall scar with 20-45º dip (Haflidason et al., 2004; Bryn et al., 2005; Kvalstad et al., 2005a, 2005b); the Nu'uanu debris

avalanche, affected a volume of 2500-3500km$^3$ in the NE of O'ahu Island in Hawaii archipelago, and involved the transport of a 30km long/ 600 km$^3$ block (Tuscaloosa seamount) along ca. 55 km (Moore et al., 1989; Moore and Clague, 2002; Satake et al., 2002). The association of these major collapse events to fluid overpressure (Iverson, 1995, Kvalstad et al., 2005a), highlights the interest of studying the occurrence of gravitational destabilization in cohesive materials with intervention of fluid overpressure.

Through detailed structural analysis (e.g., from seismic data) and application of mathematical models efficient in describing the deformation, it is possible to reach an indirect estimation of some mechanical properties of the sediments. Among the analytical models used in tectonics, the critical taper model developed by Davis, Dahlen and co-authors (Davis et al.,1983; Dahlen et al.,1984; Dahlen, 1984, 1990) is one of the most known. It has been widely applied to the shape of accretionary wedges and thrust-and-fold belts, and used to estimate the weakness (often related to high pore fluid pressure) of the basal detachment. The basis of the critical taper theory in Coulomb wedges have been set in a series of papers: Davis et al. (1983); Dahlen et al. (1984) and Dahlen (1984, 1990). A wedge of Coulomb material under lateral compression will deform internally until a critical taper is reached. At this state, the prism and the basal detachment are everywhere on the verge of shear failure. The deformation will proceed with the growth of the wedge (self-similar growth, for non-cohesive material), through accretion of new material to the toe/ internal deformation, thus maintaining the critical taper and sliding along the basal detachment (Davis et al., 1983; Dahlen, 1984; Dahlen et al.,1984).

The mathematical formulation has multiple solutions, depending on the shear orientation on the basal detachment and the state of stress within the wedge (i.e., compressive or extensional, respectively, Fig. 1). Mourgues et al. (2014) pointed out that few studies focused on the applicability of the solution to gravitational spreading and gliding along passive margins, where elevated pore-fluid pressure is common in sediments and where numerous gravitational structures, such as landslides and debris flows, are identified (e.g., Storegga slide, Norway, Kvalstad et al., 2005; Demerara Rise, French Guiana, Pattier et al., 2011). They investigated the applicability of the solution to gravitational instabilities triggered by high pore-fluid pressure, in the absence of any external compressive or extensional forces, for non-cohesive material. They also proposed an expression alternative to the one presented in Dahlen (1984), better suited to the study of slope instabilities (Mourgues et al., 2014) and verified the predictions of the analytical model by using physical experiments in which compressed air was applied at the base of dry sand wedges to trigger

gravitational instabilities (Mourgues and Cobbold, 2006a, 2006b; Lacoste et al., 2012). In their analysis, Mougues et al. (2014) neglected the cohesion of the wedge, as it was initially postulated in Davis et al. (1983) and Dahlen (1984). However, cohesion is the main parameter of rock's strength that allows steep slopes and vertical cliffs to be stable and it cannot be reasonably neglected in stability analysis. Cohesion was introduced in-depth in the critical taper model by Dahlen et al. (1984). These authors predict that cohesion has a strong effect in the thinnest part of the wedge, while the deformation of the thickest part is similar to that of non-cohesive material (Davis et al., 1983; Dahlen et al., 1984). This implies that the upper surface of a Coulomb wedge will be concave: flatter in the foremost thinner sector more resistant to deformation, and steeper in the thicker sector where the slope tends towards the expected for a non-cohesive wedge (Davis et al., 1983).

Following the initial hypothesis of Coulomb critical taper theory, we reformulate the analytical approach presented in Mourgues et al. (2014) in order to study the occurrence of gravitational destabilization in a cohesive wedge with planar upper surface. We show that cohesion has clearly visible structural effects. It introduces a minimal length of sliding, and listric faults are formed (flat if high pore pressures are present in the cohesive cover). This last prediction is verified with physical experiments involving pore fluids in cohesive and permeable granular materials.

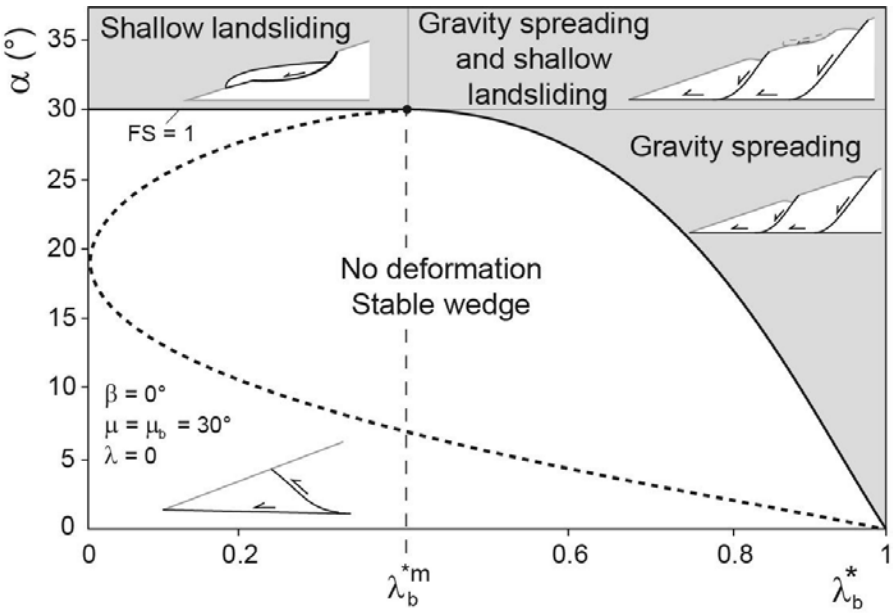


**Fig.1**. Gravitational deformation of a non-cohesive wedge. From Mourgues et al. (2014).

## 2. The non-cohesive critical taper – a force equilibrium approach

The critical taper theory is based on the assumption that the internal state of stress of a homogeneous wedge composed of material deforming following the Mohr-Coulomb criterion is on the verge of failure everywhere (Davis et al., 1983). The shape of the wedge, growing self-similarly, depends on the strength of the material and on the relative magnitude of the resistance to sliding at the base.

### *2.1. Solutions derived from the equilibrium of internal stresses*

Dahlen (1984) provides an exact solution for non-cohesive wedges by expressing the total taper angle of the critical wedge (expressed as the sum of the critical surface slope, $\alpha$, and the basal detachment, $\beta$) as a function of pore pressure ratios (considered as constant) along the basal detachment, $\lambda_b$, and within the wedge, $\lambda$, coefficients of sliding friction along the basal detachment, $\mu_b$, and within the wedge, $\mu$:

$$\alpha + \beta = \Psi_o + \Psi_b \quad (1)$$

Where $\Psi o + \Psi b$ are the angles between the maximum principal stress and the upper surface/ basal detachment, respectively. These two angles are written more explicitly:

$$\Psi_o = 0.5 \arcsin\left(\frac{sin\alpha}{sin}\right) - 0.5\alpha \quad (2)$$

$$\text{with } \alpha = \arctan\left(\frac{1}{1-\lambda^*} tan\alpha\right) \quad (3)$$

$$\Psi_b = 0.5 \arcsin\left(\frac{sin\ _b}{sin}\right) - 0.5\ _b \quad (4)$$

With the angle of friction of the wedge and $'_b$ the effective angle of friction on the detachment defined by Dahlen (1984) as:

$$\mu_b = tan\phi_b = \frac{1-\lambda_b^*}{1-\lambda^*}\mu_b \quad (5)$$

Recently, Mourgues et al. (2014) provided an alternative formulation of Dahlen's expression (Dahlen, 1984) and Lehner's graphical solution (Lehner, 1986). Their expression allows a direct calculation of the fluid pressure (or the basal friction) required for sliding on

the basal detachment, whereas Dahlen's critical taper exact solution required the resolution of an equation. Mourgues et al. (2014) expressed the fluid overpressure ratio required for the wedge to slide on a basal low-resistance layer as:

$$\lambda_b^* = 1 - (1 - \lambda^*)\frac{E_2}{\mu_b E_1} \quad (6)$$

With

$$E_1 = (1 - \lambda^*)\{Y + (1 - Y)\cos[2(\alpha-\beta)]\} + \tan(\alpha)\sin[2(\alpha-\beta)] \quad (7)$$

$$E_2 = (1 - \lambda^*)\{(Y - 1)\sin[2(\alpha-\beta)]\} + \tan(\alpha)\cos[2(\alpha-\beta)] \quad (8)$$

$$Y = \frac{1-\sin\phi\sqrt{1-FS^2}}{\cos^2\phi} \quad \text{for extensional state of stress} \quad (9)$$

$$Y = \frac{1+\sin\phi\sqrt{1-FS^2}}{\cos^2\phi} \quad \text{for compressive state of stress} \quad (10)$$

And

$$FS = \frac{\tan\alpha}{(1-\lambda^*)\tan\phi} \quad (11)$$

This solution is better suited to the study of slope instabilities (Mourgues et al.,2014) and it provides important indications on the stability of the surface slope and the potential triggering of shallow slumps through the expression of the factor of safety *FS* (Eq.7).

### *2.2. Solution derived from the balance of external forces applied on a triangular segment of the wedge*

Expressions 1 and 6 are derived from the equilibrium of internal stresses within the wedge. An alternative solution can be found by considering the balance of external forces applied on a triangular segment of the wedge. Dahlen used this approach in his review paper (Dahlen, 1990) to introduce the critical theory through a pedagogical approach but he used a simplified state of stresses and he did not derive the exact solution this way. In such an approach, the balance of forces applied on a triangular segment of length *l* and acting in the $x_1$ direction (Fig. 2b) is

$$F_\sigma + F_w + F_S + F_b = 0 \quad (12)$$

$F_\sigma$ is the force exerted by $\sigma_{x1}$ on the sidewall of the wedge. $F_w$ is the $x_1$ component of the gravitational body force. $F_s$ is the net $x_1$ component of the force resulting from the pore fluid pressure (seepage force, SF), and $F_b$ is the frictional force exerted at the base. Detailed expressions of these forces are given in appendix. An exact solution of Eq. 6 can be found for a non-cohesive wedge by considering the state of stresses defined by Dahlen (1984) and expressions derived by Mourgues et al. (2014):

$$\lambda_b^* = 1 - \frac{1-\lambda^*}{E_1 \mu_b}\left[(E_3 + \lambda^*)\tan(\alpha - \beta) + \frac{sin\beta}{cos\alpha \cos(\alpha-\beta)}\right] \quad (13)$$

with

$$E_3 = (1 - \lambda^*)(Y + (Y-1)\cos 2(\alpha-\beta)) - \tan\alpha \sin 2(\alpha-\beta) \quad (14)$$

Solutions 1, 6 and 13 are numerically strictly identical. Wang et al. (2006) and Mourgues et al. (2014) pointed out that the use of an effective angle of friction $'_b$ (Eq.5) introduced by Dahlen is erroneous because of an error introduced in the reference coordinate used to defined λ. Mourgues et al(2014) proposed a corrected value of the effective basal friction:

$$\mu_b = \mu_b \left(1 + \frac{\lambda^* - \lambda_b^*}{E_1}\right) \quad (15)$$

and gave a second solution for the critical taper referred as Model II. By using this corrected friction, Equation 13 becomes:

$$\lambda_b^* = E_1 + \lambda^* - \frac{1}{\mu_b}\left[(E_3 + \lambda^*)\tan(\alpha - \beta) + \frac{sin\beta}{cos\alpha \cos(\alpha-\beta)}\right] \quad (16)$$

## 3. The cohesive critical taper – a force equilibrium approach

The model developed here is based on Mourgues et al. (2014), but considering a non-negligible cohesion (Dahlen et al., 1984). Following the critical Coulomb wedge theory, we assume that the wedge is everywhere on the verge of failure, including along the basal detachment. Like in Mourgues et al. (2014), we consider that the model is not affected by external extensional or compressive forces, but is affected by pore fluid pressure.

We consider a wedge (Fig. 2a) with an upper surface angle α and basal surface angle β, both surfaces dipping in the same sense, and thus both angles are considered as positive. The Cartesian coordinate system *x,z* is defined with components parallel (*x*) and perpendicular (*z*) to the wedge's upper surface. The Cartesian coordinate system $x_1$,$z_1$ is defined with components parallel ($x_1$) and perpendicular ($z_1$) to the wedge's basal surface. The maximum prism length (*L*) and height (*H*) are defined perpendicularly to the wedge's basal surface.

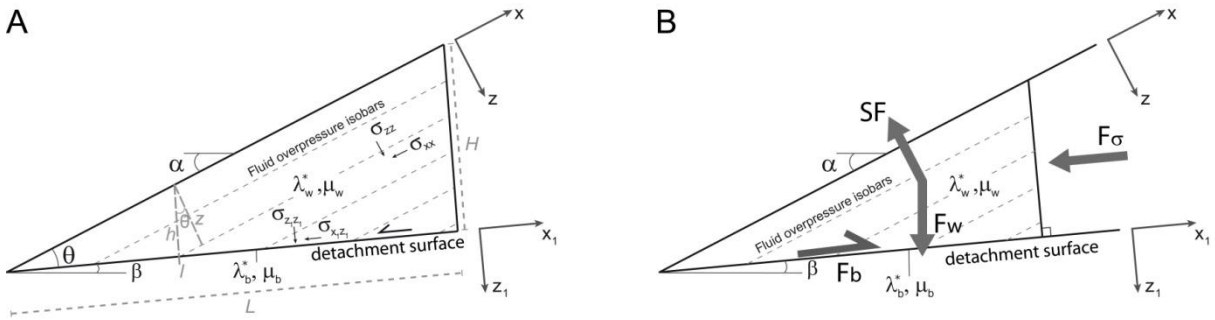


**Fig. 2**. (A) Representation of the wedge's configuration, Cartesian coordinate systems and variables. (B) Representation of the forces considered in the assessment of the wedge's stability along the basal detachment.

The detailed step-by-step formulation of the stress components within the wedge is presented in Appendix A.

Following Mourgues et al. (2014), we establish the equations of static equilibrium for the system relative to the Cartesian coordinate system *x,z*, and we define as boundary conditions that: (1) there is no variation of stresses along the *x* axis; (2) for $z = 0$ the effective stress components are null; (3) the fluid overpressure ratio $\lambda^*$ (Shi and Wang, 1988; Saffer and Bekins, 1998) is constant within the wedge (the pore fluid pressure is assumed to increase linearly with z).

$$\lambda^* = \frac{P_{ov}}{\rho\, gz \cos\alpha} \qquad (17)$$

in which $\sigma'$ is the effective stress, $\rho'$ is the density corrected for hydrostatic buoyancy, *g* is the gravitational acceleration, and $P_{ov}$ is the fluid overpressure (Hubbert and Rubey, 1959).

Considering the effective stress components $\sigma'_{xz}$ and $\sigma'_{zz}$ determined with the equations of static equilibrium, and that the wedge is on the verge of failure everywhere, the analysis of the Mohr diagram allows the determination of $\sigma'_{xx}$, and the integration of the parameter cohesion (*Co*) in the analytical expressions.

Afterwards, we imposed a rotation of the Cartesian coordinates from the *x,z* coordinate system to the $x_1,z_1$ coordinate system, in order to proceed to the stability analysis of the wedge along the basal detachment. The assessment of the stability state of the wedge is made through the balance between the forces driving (*Fd*) and inhibiting (*Fb*) the downslope movement along the basal detachment (Fig. 2b). The detailed step-by-step formulation of the considered forces is presented in Appendix B.

*Fd* for a given point *l* along the basal detachment is the result of the sum of the force components (Fig. 2b):

$$Fd = F_\sigma + F_w + F_s \quad (18)$$

a) $F_\sigma$ corresponds to the integral of $\sigma_{xx_1}$ along the local wedge height ($h$, along the $z_1$ axis), representing the effect of cohesion:

$$F = \int_0^h \sigma_{xx_1} dz_1 \quad (19)$$

b) $F_w$ at a point along the basal detachment of length $l$ and height $h$ corresponds to the gravitational load of the wedge section comprehended between that point and the wedge tip ($l = 0$, and $h = 0$). Considering a unitary width wedge slice:

$$F_w = \rho\, g \sin\beta \frac{hl}{2} \quad (20)$$

in which $\rho'$ is the density corrected for hydrostatic buoyancy, and $g$ is the gravitational acceleration.

c) $F_s$ is the component of the seepage force (*SF*) parallel to $x_1$, considering a wedge slice of unitary width:

$$F_s = \lambda^* \rho\, g \cos\alpha \cos\theta \frac{h^2}{2} \quad (21)$$

in which $\lambda^*$ is the fluid overpressure ratio within the wedge, and $\theta = \alpha$-$\beta$.

*Fb*, at a given point *l* on the basal detachment corresponds to the integral of the basal friction between *l* and the wedge tip ($l = 0$, $h = 0$):

$$Fb = \int_0^l \mu_b \times \sigma_n + Co_b \, dx_1 \quad (22)$$

with

$$\sigma_n = \sigma_{zz_1} + (\lambda^* - \lambda_b^*)\rho\, gl \sin\theta \cos\alpha \qquad (23)$$

in which $\mu_b$, $Co_b$ and $\lambda^*_b$ correspond to the internal friction coefficient, the cohesion, and the fluid overpressure ratio along the basal detachment, respectively. $\sigma'_n$ is the effective stress component normal to the basal surface of the wedge, taking into account a possible discrepancy between $\lambda^*$ and $\lambda^*_b$.

## 4. Structural consequences of cohesion

From the expressions derived for the effective stress components relative to the x,z coordinate system (Eqs. A5, A6 and A12), we observe that *Co* impacts on $\sigma'_{xx}$ only, while $\lambda^*$ affects $\sigma'_{zz}$ and $\sigma'_{xx}$. The variation of these effective stress components as a function of z, shows that $\sigma'_{xz}$ and $\sigma'_{zz}$ increase linearly with depth (Fig. 3). The gradient of $\sigma'_{zz}$ with depth is smaller for higher values of $\lambda^*$.

On the other hand, $\sigma'_{xx}$ is negative for small z values due to cohesion, and increases non-linearly with depth, with ever increasing gradients, surpassing the values of $\sigma'_{xz}$ and $\sigma'_{zz}$. The increment in gradient is more accentuated for higher values of $\lambda^*$. For high values of $\lambda^*$, $\sigma'_{xx}$ reaches a solution limit for critical depth limit ($Z_c$), which is shallower for higher $\lambda^*$.

The analysis of the Mohr diagram shows that this $Z_c$ of $\sigma'_{xx}$ is reached when the plot of $\sigma'_{xz}$ and $\sigma'_{zz}$ (x,z coordinate system) coincides with the $\sigma'_n$ and $\tau$ of the Mohr-Coulomb failure envelope of the wedge material (Fig.4a, grey line). This indicates that the expected failure surface at $Z_c$ would be perpendicular to the $\sigma'_{zz}$ axis, parallel to the wedge's upper surface.

We determined the variation of the maximum compression $\sigma_1$ and generated fracture orientations relative to the z axis, as a function of depth z, using the following expressions from Mourgues and Cobbold (2003) (Fig. 5):

$$\tan(2\omega) = -2\sigma_{xz}/(\sigma_{xx} - \sigma_{zz}) \qquad (24)$$

$$\gamma = 45 - \phi/2 \qquad (25)$$

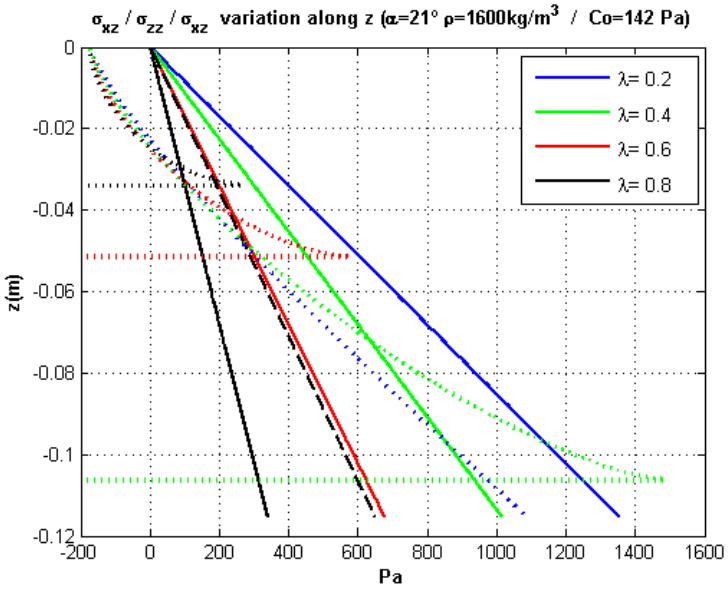


**Fig. 3**. Variation of the effective stress components in function of depth *z*, for different values of $\lambda^*$. Dotted line - $\sigma'_{xx}$ ; Full line - $\sigma'_{zz}$; Dashed line - $\sigma'_{xz}$. The horizontal dotted lines represent the *Zc* for each value of $\lambda^*$ (*Zc* decreases for increasing $\lambda^*$).

is no

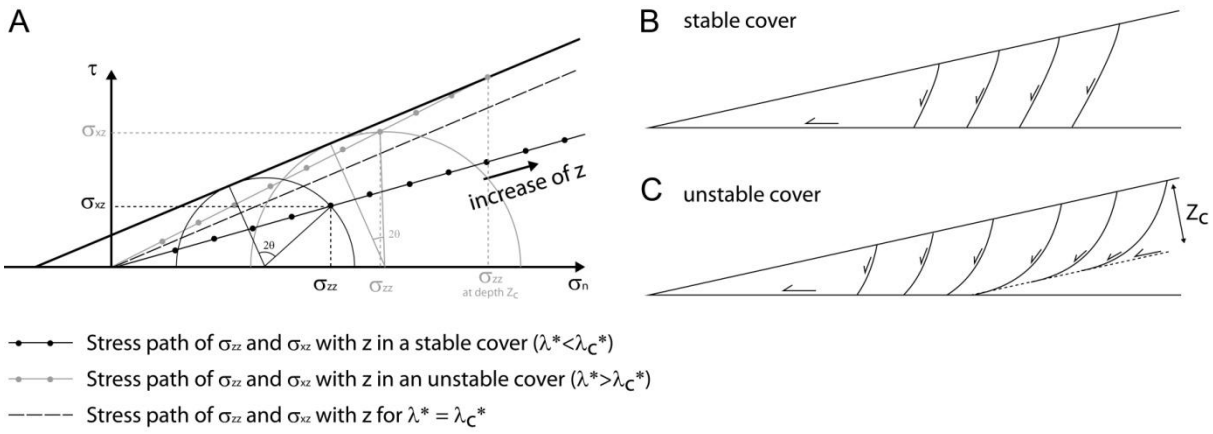


**Fig. 4.** (A) Representation of the Mohr diagram for $\lambda^*$ below, equal or above a critical $\lambda^*$ value ($\lambda_c^*$). (B) For $\lambda^* < \lambda_c^*$, Zc is not attained within the wedge, and the faults propagated do not become parallel to the wedge's upper surface. C. For $\lambda^* > \lambda_c^*$, Zc is attained within the wedge, and the faults propagated become parallel to the wedge's upper surface.

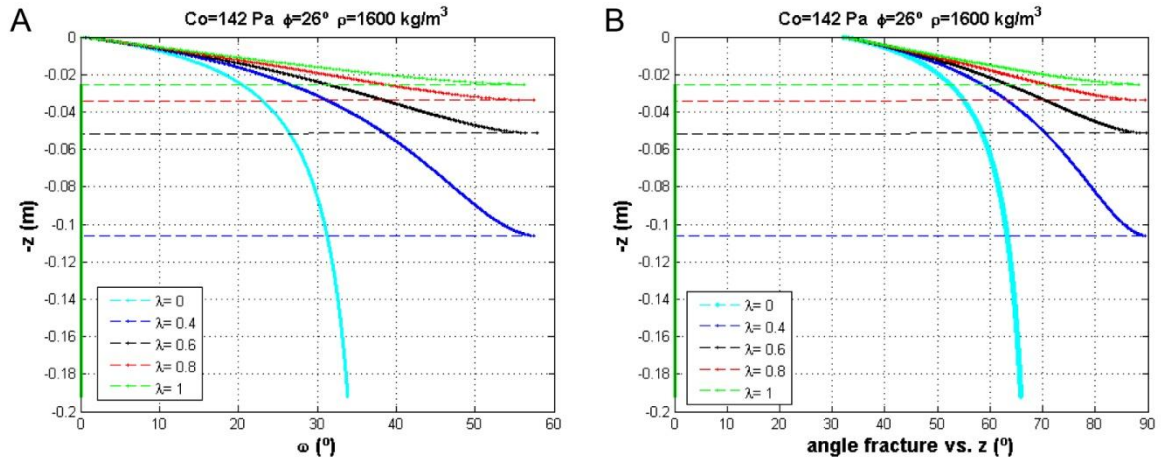


**Fig.5.** (A) Variation of the angle (ω) between $\sigma_1$ and the z axis with depth, for different $\lambda^*$ values. (B) Variation of the angle ($\gamma$) between the generated fracture and the z axis with depth, for different $\lambda^*$ values.

in which $\omega$ is the angle between $\sigma_1$ and the z axis, and $\gamma$ is the angle between $\sigma_1$ and the generated fracture.

We confirm that for $0 \leq z \leq Z_c$, there is a rotation of the orientation of $\sigma_1$ with increasing $z$, stronger for high $\lambda^*$, becoming progressively closer to the orientation of the upper surface of the wedge (Fig. 5a). Consequently, the generated fractures will be listric (curved like a shovel), becoming parallel to the upper surface of the wedge at $Z_c$ (Fig.5b).

Dahlen et al. (1984) had already predicted that cohesion would induce a change in orientation of the principal stresses within the wedge, contrary to the non-cohesive wedge for which was expected a non-variation of the principal stresses' orientation.

From the coincidence between $\sigma'_{xz}$ and $\sigma'_{zz}$ (x,z coordinate system) and $\sigma'_n$ and $\tau$ (the Mohr-Coulomb failure envelope) for $Z_c$ (Fig. 4a, grey line), we have:

$$\rho\, g Z_c \sin\alpha = (1-\lambda^*)\rho\, g Z_c \cos\alpha \tan\phi + Co \qquad (26)$$

$$Z_c = \frac{Co}{\rho\, g(\sin\alpha - (1-\lambda^*)\tan\phi\cos\alpha)} \qquad (27)$$

The thickness $Z_c$ of the layer, within which the rotation of $\sigma_1$ orientation occurs, increases with increasing cohesion ($Co$) of the material, and is null for non-cohesive materials (Figs. 6a and 6b). As stated previously, $Z_c$ decreases for increasing $\lambda^*$, but the previous equation also shows that $\lambda^*$ is more effective in decreasing $Z_c$ for large values of the angle $\alpha$ (Fig. 6c).

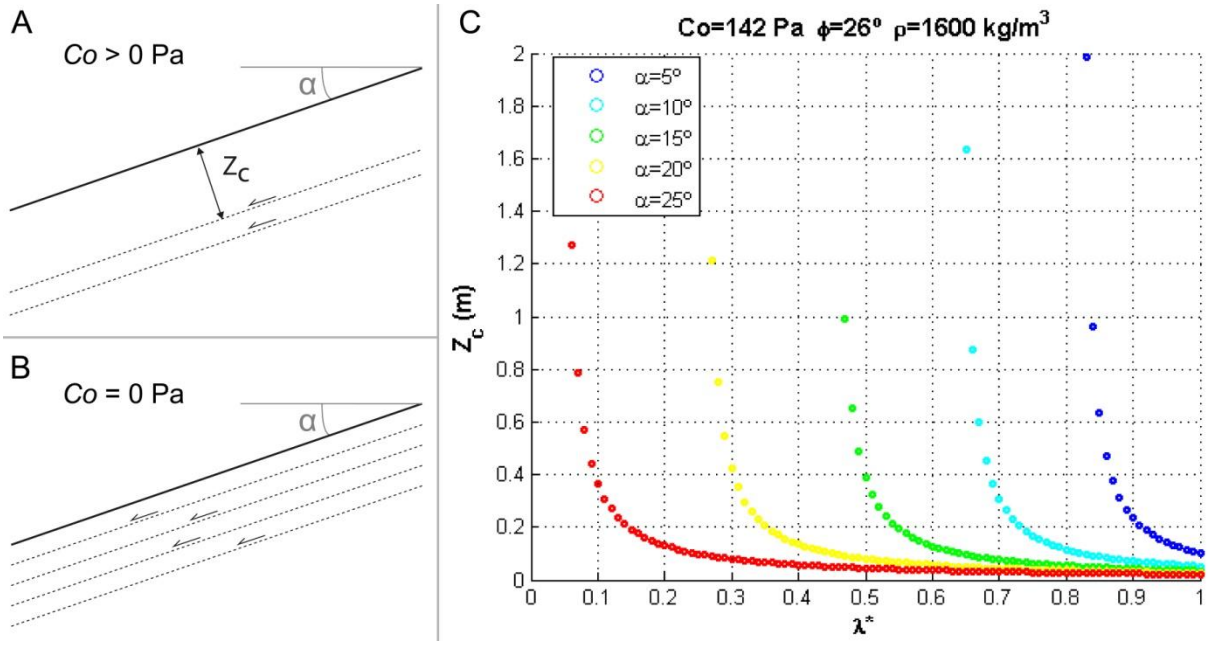


**Fig. 6.** (A) For a cohesive material with $\lambda^* > \lambda_c^*$, there is a superficial *Zc* thick layer, within which the generated fractures will be listric, and beyond which the generated fractures will be parallel to the wedge's upper surface. (B) For a non-cohesive material with $\lambda^* > \lambda_c^*$, the generated fractures will be parallel to the wedge's upper surface. (C) The thickness Zc of the upper layer for cohesive material (Co= 142 Pa), as a function of λ*, and of the angle α.

A parallel can be established between this cohesion-dependent critical depth $Z_c$ and the discussion made by Dahlen et al. (1984) on the relationship between wedge deformation and material's cohesion, stating the existence of an "*upper boundary layer in which cohesion plays a dominant role even near the back of the wedge*". His expression estimating the critical thickness of this upper layer (expression derived from Eq. (23) in Dahlen et al. (1984) is very similar to Eq. (11), even though a dependency on the angle $\alpha$ is not expressed.

The intersection of the failure envelope at $Z_c$ indicates that, if a cohesive wedge is big enough so that $Z_c$ is reached within it, the cohesive wedge is internally unstable (Fig. 4c). From the Mohr-Coulomb diagram, we observe that the intersection (or not) of the failure envelope of the material is highly dependent on the value of $\lambda^*$:

(a) if $\lambda^*$ is below or equal to a critical value $\lambda_c^*$, the failure envelope is not reached (Fig. 4a), and the orientation of the maximum compression/generated fractures tends to stabilize towards higher depths, not rotating towards an orientation that would imply the generation of fractures parallel to the wedge's upper surface (Fig. 4b).

(b) If $\lambda^*$ is above $\lambda_c^*$, then $Z_c$ is attained within the wedge, the failure envelope is reached (Fig. 4a), and the orientation of the generated fractures tends to rotate as a function of

depth, towards an orientation that would imply the generation of fractures parallel to the wedge's upper surface at $Z_c$ (Fig. 4c).

In order to determine the $\lambda_c^*$ beyond which the $Z_c$ is attained within a cohesive wedge of maximum height $H$ (with $Zc = H \times \cos\theta$), we reformulated Eq. (26):

$$\lambda_c^* = 1 - \frac{\tan\alpha}{\tan\phi} + \frac{Co}{\rho\, gH \cos\theta\ \cos\alpha \tan\phi} \tag{28}$$

For a non-cohesive material, we obtain, from Eq. (28), the expression by Hubbert and Rubey (1959) for the $\lambda^*$ necessary for the propagation of fractures parallel to the wedge's upper surface:

$$\tan\alpha = (1 - \lambda_c^*)\tan\phi \tag{29}$$

$$\lambda_c^* = 1 - \frac{\tan\alpha}{\tan\phi}$$

From Eq. (28), it is clear that a cohesive wedge is internally more stable than a non-cohesive wedge. However, the relative importance of $Co$ for the stability state of the wedge depends on the wedge's dimensions and configuration: its importance decreases for bigger wedges ($H$) and smaller $\alpha$ and $\theta$. In the limiting case of an extremely large wedge, $\lambda_c^*$ would tend to the one predicted for a non-cohesive wedge.

The stability of a non-cohesive wedge under fluid overpressure is independent of its size, while the increased stability of a cohesive wedge under fluid overpressure is size-dependent (the influence of cohesion is more significant for smaller wedges).

## 5. Experimental analogue modeling

### *5.1. Experimental setup and procedure*

Experimental studies have successfully applied fluid overpressure through injection of compressed air (e.g., Cobbold and Castro, 1999; Mourgues and Cobbold, 2003,2006a, 2006b; Lacoste et al., 2011, 2012; Mourgues et al., 2014).

Mourgues and Cobbold (2003) performed tests in tilted tabular models of homogeneous non-cohesive materials (fine sand), under extension and with upward injection of compressed air perpendicularly to the base of the model, in order to verify the structural consequences of pore fluid pressures.

We performed similar tests for cohesive materials, in order to verify the formation of listric faults predicted by the analytical model for cohesive material. We built a tilted tabular model of cohesive granular material (Fig. 7), over an equally large sieve (*sieve 1* in Fig. 7), and laterally constrained by acrylic walls. Then, a predetermined pore fluid pressure was imposed to the model, by injection of compressed air through the basal sieve. Afterwards, extension was applied to the model, by moving the downslope mobile wall attached to a basal sieve (*sieve 2* in Fig. 7) that created a velocity discontinuity at the base of the model.

We used as cohesive material glass microbeads (Table 1). The cohesion and coefficient of internal friction were determined with a series of direct shear tests on the material compacted to $\rho$ = 1600 kg/m$^3$ (initially $\rho$ = 1360 kg/m$^3$). We built the layer sequence up to a thickness of 6 cm, by gradually laying 0.5 and 1 cm thick layers of microbeads. The microbeads layers were intercalated with thin dark marker layers of Silicon carbide - grain 120 (BROTLAB) laid near the front wall (to serve as markers of deformation and visualization only). The model construction required the compaction of the sequence, in order to attain the density of 1600 kg/m$^3$. During this compaction, the dark silicon carbide markers were significantly distorted.

The whole sequence was then tilted 21°, a value below the angle of internal friction of the microbeads ($\phi$ = 26º). The tilt value was chosen in order for the critical depth (predicted depth at which the generated fault becomes parallel to the upper surface of the model) to coincide with the base of the tabular model, for a fluid pressure value attainable by our compressed air mechanism. If we had used a model of higher cohesion and/or lower tilt of the model, we would need much higher fluid pressures and a model much thicker to be able to see the listric shape of the fault.

For the different tests, different pore fluid pressures were imposed: 0 Pa ($\lambda^* = 0$), 200 Pa ($\lambda^* = 0.2275$) and 400 Pa ($\lambda^* = 0.4550$). These pressures correspond to $\lambda^*$ values below the $\lambda_c^* = 0.5441$ calculated for this 21º tilted, 6 cm thick tabular model.

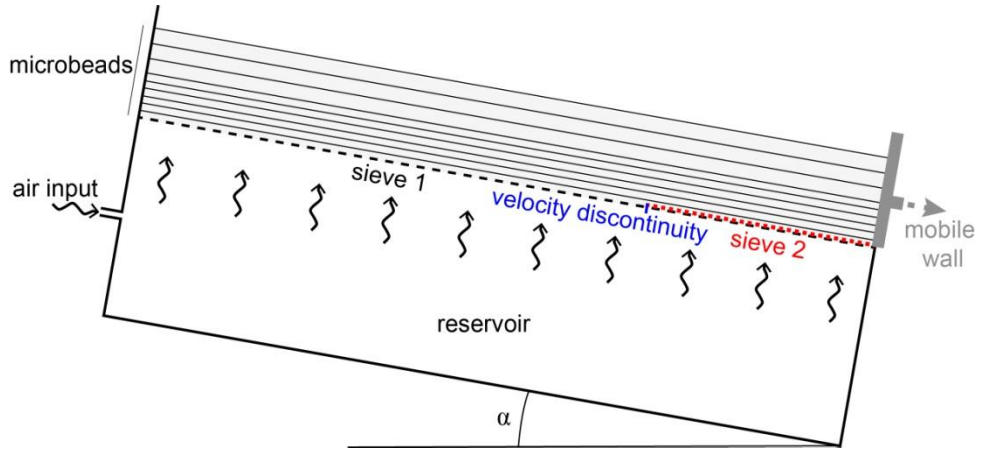


**Fig.7**. Experimental setup. The free edge of sieve 2 works as a velocity discontinuity.

**Table 1.** Properties of the material used in the analogue modeling, and considered in the presented analytical model simulations. The properties indicated were determined for a density of 1600 kg/m$^3$.

| | Grain size (μm) | Bulk density (kg/m$^3$) | Angle of internal friction (°) | Coefficient of internal friction (μ) | Permeability (m$^2$) | Cohesion (Pa) |
|---|---|---|---|---|---|---|
| Glass microbeads | 0 ─ 50 | 1600 | 26 | 0.49 | $6\times10^{-14}$ | 142 |

*5.2. Results*

In Figs. 8 to 10 we present the interpreted photographs taken during the experiments (the photographs are tilted 21º, parallel to the experiment device). The fault length (length between surface scarp and root of the fault, measured along the base of the model) of the fault first developed in the model, and the approximate dihedral angle between the first set of conjugate faults formed at each experiment are presented in Table 2.

For null pore fluid pressure, the first fault rooted at the basal velocity discontinuity (Fig. 8a). The deformation progressed with forward propagation of new structures near the velocity discontinuity (Figs. 8b and 8c): steep normal faults dipping downslope, and respective conjugate faults (steep normal faults dipping upslope).

For an intermediate pore fluid pressure (ca. 200 Pa), the first fault rooted at the basal velocity discontinuity (Fig. 9a). The deformation proceeded with backwards propagation of normal faults, and their steep conjugates (sub-vertical to reverse, considering the 21º tilt of the photographs in Fig. 9) near the velocity discontinuity (Fig. 9b), with the deformation extending afterwards to the upslope domains of the model ( with reverse conjugate fault, considering the 21º tilt of the model, Fig. 9c). The listric geometry is not obvious in the early stages for some of the faults, but it becomes clearer with the progressive rotational deformation of the kinematic markers near the base of the model.

At the highest value of fluid pressure (ca. 400 Pa), the first fault propagated from near the back wall of the model, did not root at the velocity discontinuity, and encompassed a slab with a length equal to that of the entire model (Fig. 10a). The deformation proceeded with further development of the initial low-angle normal fault and with the generation of its conjugate, a steep reverse fault (Fig. 10b).

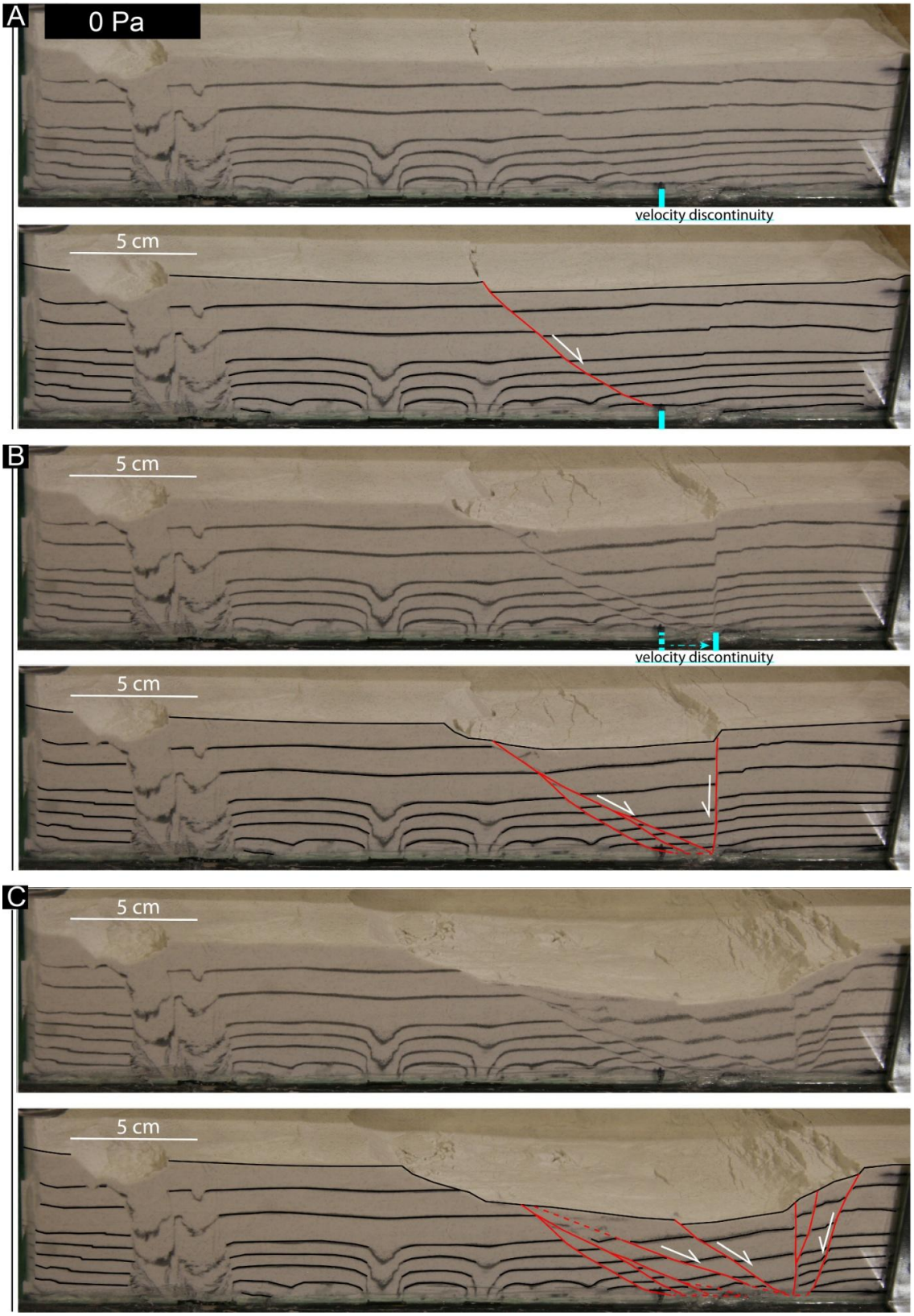


**Fig. 8.** Photographs (clean and interpreted) from the experiment with fluid $P = 0$ Pa ($\lambda^* = 0$). The base of the photos was aligned to the base of the model (21º tilt in reality). (A) First structure formed. (B) and (C) portrait the progression of the deformation.

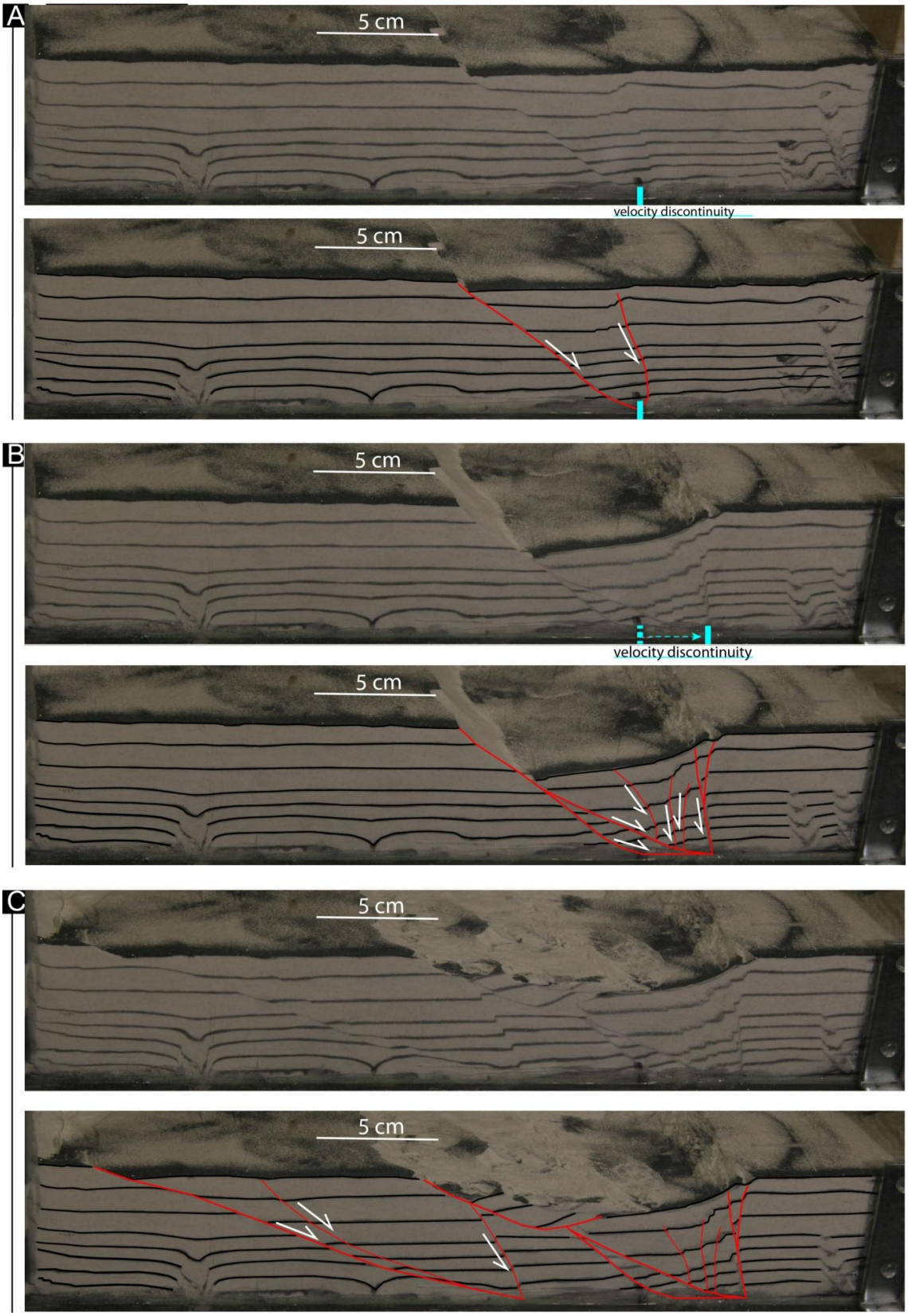


**Fig. 9.** Photographs (clean and interpreted) from the experiment with fluid P ≈ 200 Pa ($\lambda^* = 0.2275$). The base of the photos was aligned to the base of the model (21º tilt in reality). (A) First structures formed. (B) and (C) portrait the progression of the deformation.

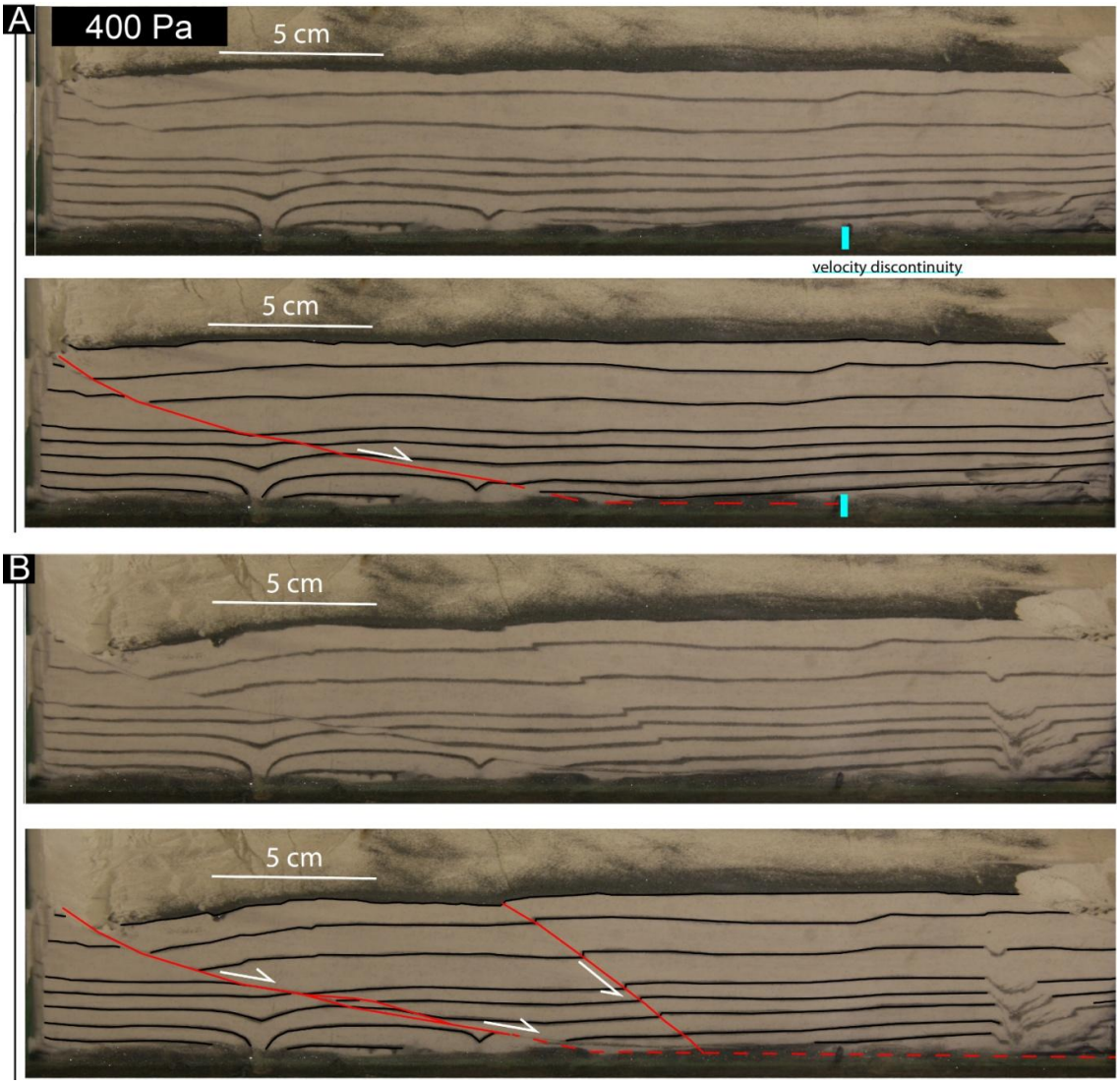


**Fig.10.** Photographs (clean and interpreted) from the experiment at fluid $P \approx 400$ Pa ($\lambda^* = 0.4550$). The base of the photos was aligned to the base of the model (21° tilt in reality). (A) First structure formed. (B) portraits the progression of the deformation.

**Table 2.** Measurements from the physical modeling experiments and predictions from the analytical model.

| | **Physical Model** | | **Analytical model** |
|---|---|---|---|
| | **Fault Length (m)** | **Dihedral angle between first set of conjugate faults (°)** | **Fault Length (m)** |
| **0 Pa** ($\lambda^*$=0) | 0.067 | ≈ 65 | 0.0635 |
| **≈ 200 Pa** ($\lambda^*$=0.2275) | 0.068 | ≈ 45 | 0.0732 |
| **≈ 400 Pa** ($\lambda^*$=0.4550) | 0.166 | ≈ 30 | 0.0954 |
| **Pc ≈ 478 Pa** ($\lambda_c^*$=0.5441) | | | 0.1287 |

*5.3. Discussion of the experimental results and comparison with the predictions of the analytical model*

The length of the faults increases for higher values of fluid pore pressure, because the general dip of the faults decreases, and therefore the faults nucleate closer to the back wall (Table 2). The dihedral angle between the first formed set of conjugate faults decreases for higher values of fluid pore pressure (Table 2).

Similar extension experiments presented in Mourgues and Cobbold (2003) for non-cohesive materials show that for non-cohesive material the faults have a rectilinear profile, and the dip of the normal faults decreases for increasing pore fluid pressure. For high values of pore fluid pressure, the dip of the normal fault dipping towards the moving wall can be so low that its conjugate becomes a reverse fault. The dihedral angle between the normal fault and its conjugate decreases with increase in fluid pressure. Similarly to Mourgues and Cobbold (2003), we verify that the fault dip and dihedral angle between conjugate faults decreased with increasing fluid pressure. However, our experiments with a cohesive material show that the faults generated are listric, in accordance with the predictions of the analytical model (Section 4).

Based on the analytical model, we determined the fault profiles expected for the different experimental tests ( $\lambda^* < \lambda_c^*$ ) and for $\lambda_c^*$ (Fig.11a). The maximum pore fluid pressure simulated corresponds to the $\lambda_c^*$ predicted to generate a detachment along the base of the model ($Z_c$ equivalent to the model thickness). The expected fault profile for the test without upward injection of fluid ($\lambda^* = 0$) is only slightly listric, with steep fault dip near the base of the model. For increasing fluid pore pressure, the expected fault profile becomes more clearly listric, longer, with decreasing angle between the fault surface and the base of the model. The predicted fault lengths for the different $\lambda^*$ values are presented in Table 2.

For most of the experimental tests, the generated faults are clearly listric. The faults become longer for higher pore fluid pressure, as generally predicted by the analytical model. The experimental length of the faults obtained for the lower pore fluid pressures (0 Pa, 200 Pa) are very close to the ones predicted by the analytical model (Table 2). However, that was not the case for the 400 Pa test. Even though the extension was imposed to the model only after a stable value of pore fluid pressure was reached, there were variations of the measured fluid pressure during deformation.

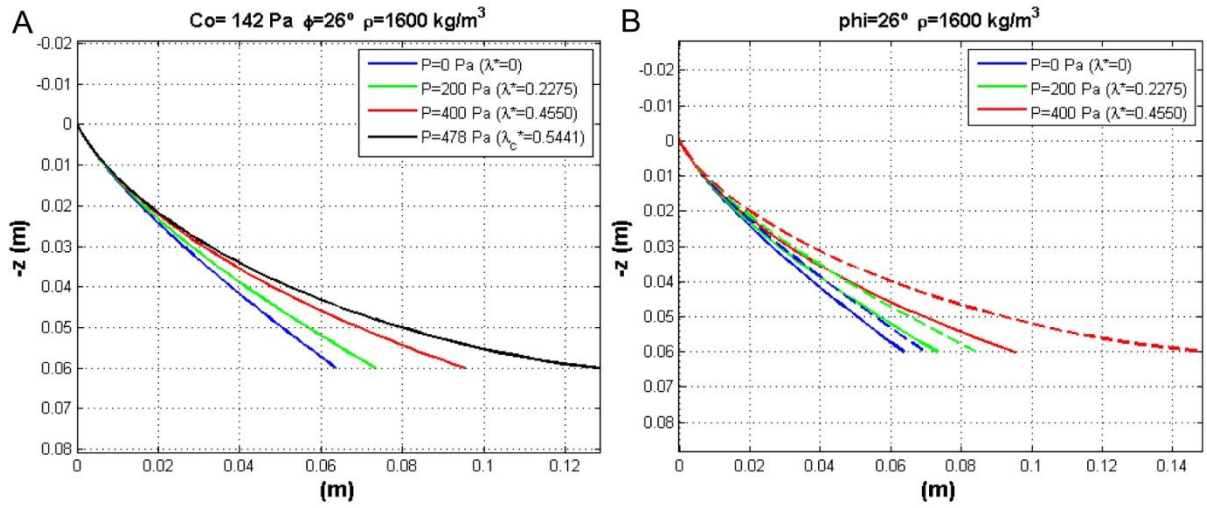


**Fig.11.** (A) Shape of the predicted faults for different fluid pore pressure values. (B) Shape of the predicted faults for $C_o \approx 142$ Pa (solid lines) and hypothetical lower Co ≈ 102 Pa (dashed lines). We observe a more marked impact of variable material cohesion at higher pore fluid pressures.

The compaction of the model in order to attain $\rho = 1600$ kg/m$^3$ (density for which was determined the cohesion and coefficient of internal friction of the material) most probably generated heterogeneities in the properties of the material, especially along the perpendicular to the model's base. Changes in the properties of the material can impact greatly on the shape of the generated fractures, especially for high values of pore fluid pressure, because:

- Variable density and permeability can impact on the distribution of fluid pore pressure, generating differently shaped faults (Fig. 11a). The effects of a heterogeneous distribution of permeability of the material are expected to be greater for higher values of pore fluid pressure.

- The cohesion presented in Table 1 was determined for a closely packed $\rho = 1600$ kg/m$^3$ material. A more loosely packed material with $\rho = 1360$ kg/m$^3$ is most probably associated with lower cohesion. In Fig. 11b we observe that the variation of cohesion impacts on the shape of the generated fracture, especially for larger values of pore fluid pressure.

We therefore conclude that the differences between the expected fault profiles predicted by the analytical model and the results of the experimental tests for high pore fluid pressure are justified by the heterogeneity of the physical model, contrasting with the homogeneity assumed in the analytical model.

Despite the differences between the results of analytical and analogue modeling, we confirmed:

a) the generation of listric faults in cohesive materials;

b) the influence of $\lambda^*$ in the geometry of the generated structures, in accordance with the interpretations presented in Mourgues and Cobbold (2003) for non-cohesive materials.

## 6. Cohesive wedge model – Minimal Failure Length (*MFL*)

As stated in Section 3, the stability state of the cohesive wedge along the basal detachment is here determined through the confrontation between the force driving the downslope movement (*Fd*) and the force inhibiting it (*Fb*), along the basal detachment (parallel to $x_1$). It was assumed that the cohesive wedge is everywhere on the verge of failure, including along the basal detachment. However, the plots of these forces for wide ranges of conditions guaranteeing instability along the basal detachment show that, for values of $l$ below a critical value $l_c$ (near the front tip of the wedge), *Fd* is lower than *Fb* (wedge stable along the basal detachment), and that, for $l > l_c$, *Fb* is higher than *Fd* (wedge unstable along the basal detachment) (Fig. 12a). Therefore, the failure of the wedge along the basal detachment occurred for $l$ values equal or exceeding this $l_c$, hereafter referred to as *MFL* (*Minimum Failure Length*). In Fig. 13a we present the evolution of the *Fd* and *Fb* curves for increasing $\lambda^*$, for a cohesive wedge composed of the material used in the analogue modeling (Table 1). For non-cohesive wedge materials and basal detachment, this *MFL* is undefined, because *Fd* and *Fb* converge towards a wide overlap for increasing values of $\lambda^*_w$ and $\lambda^*_b$, instead of an intersection at a single point (Figs. 12b and 13b).

The higher stability of the foremost thin part of the wedge is directly related to the variation of the stress components as discussed in Section 4, and consistent with Davis et al. (1983) and Dahlen et al. (1984), with the cohesion of the material inducing a higher strength to the most superficial layer of the wedge.

The estimation of *MFL* cannot be made through a simple equation, depending on numerical models that calculate the values of *Fd* and *Fb* and determine the intersection between the resulting curves.

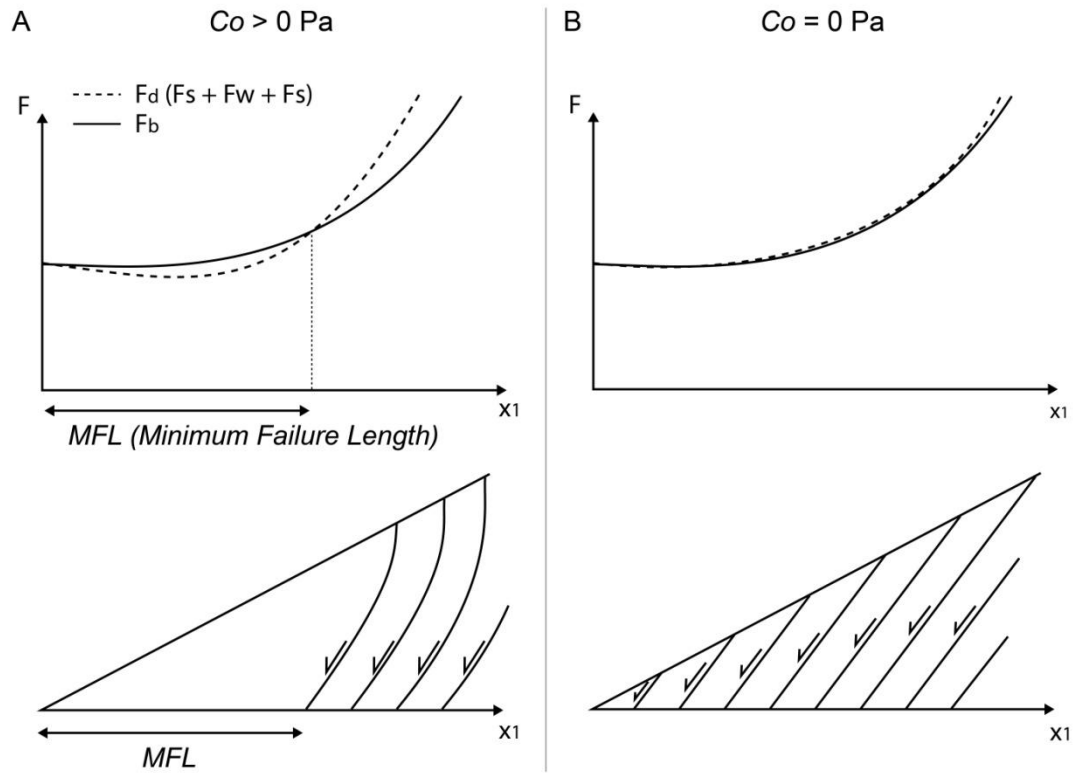


**Fig.12.** (A) Balance between *Fd* and *Fb* for a cohesive wedge, and schematic representation of the stable domain of the wedge (with a characteristic Main Failure Length - *MFL*) and unstable domains in the wedge. (B) Confrontation of *Fd* and *Fb* for a non-cohesive wedge, without the *MFL* long stable front.

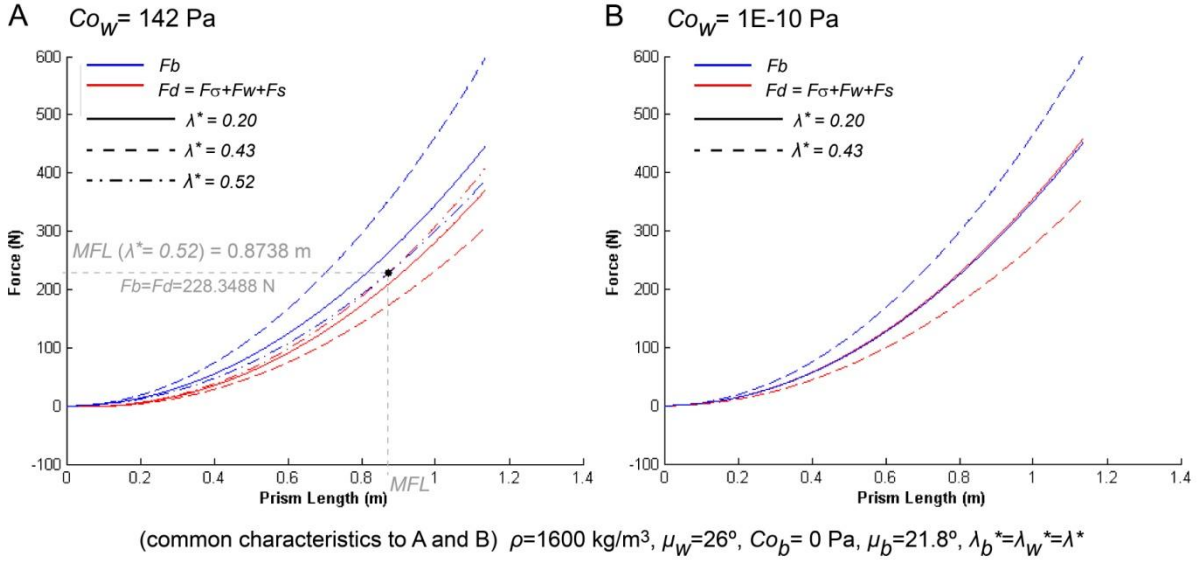


**Fig.13.** Balance between *Fd* and *Fb* for different $\lambda^*$, considering a wedge composed of the material in Table 1. (A) The material's actual cohesion (142 Pa) is considered. (B). Practically null cohesion. α=15º and β=5º (angles of the upper and basal surfaces of the wedge, respectively).

The *MFL* varies as a function of several factors:

-The *MFL* increases with increasing cohesion values in the wedge ($Co_w$) and along the basal detachment ($Co_b$).

- The *MFL* increases with increasing $\mu$ values in the wedge ($\mu_w$) and along the basal detachment ($\mu_b$).

- The *MFL* decreases with increasing $\lambda^*$ values in the wedge ($\lambda^*_w$) and along the basal detachment ($\lambda^*_b$).

-The *MFL* increases with decreasing $\alpha$ and $\beta$.

For a set of conditions of $Co$, $\mu$, $\lambda^*$, $\alpha$ and $\beta$, there is an *MFL* value that is constant for any maximum dimensions attributed to the wedge. Thus, for a cohesive wedge internally stable ($\lambda^* < \lambda_c^*$), if the maximum length of the wedge ($L$) is not greater than *MFL*, the wedge remains stable along the basal detachment. For a cohesive wedge internally stable ($\lambda^* < \lambda_c^*$), but for which the maximum length of the wedge ($L$) is greater than *MFL*, the wedge becomes unstable along the basal detachment, and listric faults are generated rooting in the basal detachment at $l > MFL$. A deeply rooted slump system is created (Fig. 4b). When the fluid overpressure ratios are high ($\lambda^* > \lambda_c^*$), the cohesive wedge becomes internally unstable: the failure envelope of the material is reached within the wedge, generating listric faults that tend to become parallel to the upper surface of the wedge at depth ($Zc$), as discussed in section 4. A shallow slump system is created, rooted at $z = Zc$ (Fig. 4c).

## 7. Conclusions

We show that the stability of a cohesive wedge under fluid overpressure is size-dependent (the influence of cohesion is more significant for smaller wedges), while the stability of a non-cohesive wedge under fluid overpressure is independent of its size. The stabilizing effect of cohesion is significant for the most superficial domain of the wedge. The thickness of this more stable superficial layer decreases with increasing fluid overpressure ratio. Within this layer, the principal compressive stress rotates and the expected structures are listric. If the limit of the thickness expected for this layer is reached within the wedge (given the material's properties, fluid overpressure ratio and wedge configuration), the generated listric structures become parallel to the wedge's upper surface at this limit. This limit marks the reach of the failure envelope for the wedge's material. In terms of the wedge's stability along a basal detachment, the stabilizing effect of cohesion is accentuated in the foremost thin domain of the wedge, defining a required Minimum Failure Length (*MFL*).

This *MFL* decreases for: smaller cohesion, smaller coefficient of internal friction, larger fluid overpressure ratio, steeper upper and basal surfaces of the wedge.

**Acknowledgments**

This is a contribution to Project MEGAHazards (PTDC/CTE-GIX/108149/2008), funded by FCT, Portugal. ACGC benefits from a PhD scholarship funded by FCT (SFRH/BD/68983/2010). We thank Christelle Gruber for the support in the experimental work.

**References**

Bryn, P., Berg, K., Forsberg, C.F., Solheim, A., Kvalstad, T.J., 2005. Explaining the Storegga Slide. Marine and Petroleum Geology 22, 11-19. doi:10.1016/j.marpetgeo.2004.12.003

Cobbold, P.R., Castro, L., 1999. Fluid pressure and effective stresses in sandbox models. Tectonophysics, 301, 1-19.

Cobbold, P.R., Mourgues, R., Boyd, K., 2004. Mechanism of thin-skinned detachment in the Amazon fan: assessing the importance of fluid overpressure and hydrocarbon generation. Marine and Petroleum Geology 21, 1013-1025.

Cobbold, P.R., Zanella, A., Rodrigues, N., Loseth, H., 2013. Bedding-parallel fibrous veins (beef and cone-in-cone): Worldwide occurrence and possible significance in terms of fluid overpressure, hydrocarbon generation and mineralization. Marine and Petroleum Geology 43, 1-20. http://dx.doi.org/10.1016/j.marpetgeo.2013.01.010

Costa, A.C.G., Marques, F.O., Hildenbrand, A., Sibrant, A.L.R., Catita, C.M.S., 2014. Large-scale catastrophic flank collapses in a steep volcanic ridge: The Pico–Faial Ridge, Azores Triple Junction. J. Volcanol. Geotherm. Res. 272, 111 –125, http://dx.doi.org/10.1016/j.jvolgeores.2014.01.002.

Dahlen, F.A., 1984. Noncohesive critical coulomb wedges: An exact solution. Journal of Geophysical Research 89(B12), 10125–10133.

Dahlen, F.A., 1990. Critical taper model of fold-and-thrust belts and accretionary wedges. Annu. Rev. Earth. Planet. Sci. 18, 55-99.

Dahlen, F.A., Suppe, J., Davis, D., 1984. Mechanics of Fold-and-Thrust Belts and Accretionary Wedges: Cohesive Coulomb Theory. Journal of Geophysical Research 89 (B12), 10087-10101.

Davis, D., Suppe, J., Dahlen, F.A., 1983. Mechanics of fold-and-thrust belts and accretionary wedges. Journal of Geophysical Research 88 (B2), 1153–1172.

Day, S.J., 1996. Hydrothermal pore fluid pressure and the stability of porous, permeable volcanoes. In: McGuire, W.J., Jones, A.P., Neuberg, J. (Eds.), Volcano Instability on the Earth and Other Planets. Geological Society Special Publication, London, 77–93.

del Potro, R., Hürlimann, M., Pinkerton, H., 2013. Modelling flank instabilities on stratovolcanoes: Parameter sensitivity and stability analyses of Teide, Tenerife.

Journal of Volcanology and Geothermal Research 256, 50-60. http://dx.doi.org/10.1016/j.jvolgeores.2013.02.003

Elsworth, D., Voight, B., 1996. Evaluation of volcano flank instability triggered by dyke intrusion. In: McGuire, W.J., Jones, A.P., Neuberg, J. (Eds.), Volcano Instability on the Earth and Other Planets. Geological Society Special Publication, London, 45-53.

Flemings, P.B., Long, H., Dugan, B., Germaine, J., John, C.M., Behrmann, J.H., Sawyer, D., IODP Expedition 308 Scientists, 2008. Pore pressure penetrometers document high overpressure near the seafloor where multiple submarine landslides have occurred on the continental slope, offshore Louisiana, Gulf of Mexico. Earth and Planetary Science Letters 269 (3-4), 309-325.http://dx.doi.org/10.1016/j.epsl.2007.12.005.

Haflidason, H., Sejrup, H.P., Nygard, A., Mienert, J., Bryn, P., Lien, R., Forsberg, C.F., Berg, K., Masson, D., 2004. The Storegga Slide: architecture, geometry and slide development. Marine Geology 213, 201-234. doi:10.1016/j.margeo.2004.10.007

Hildenbrand, A., Marques, F.O., Catalão, J., Catita, C.M.S., Costa, A.C.G., 2012. Large-scale active slump of the southeastern flank of Pico Island, Azores. Geology 40 (10), 939–942. http://dx.doi.org/10.1130/G33303.1.

Hubbert, M. K., and W. W. Rubey (1959), Role of fluid pressure in mechanics of overthrust faulting, Geol. Soc. Am. Bull., 70, 115–166.

Iverson, R.M., 1995. Can magma-injection and groundwater forces cause massive landslides on Hawaiian volcanoes? Journal of Volcanology and Geothermal Research 66, 295-308.

Kvalstad, T.J., Andresena, L., Forsberga, C.F., Bergb, K., Brynb, P., Wangen, M., 2005a. The Storegga slide: evaluation of triggering sources and slide mechanics. Marine and Petroleum Geology 22, 245-256.

Kvalstad, T.J., Nadim, F., Kaynia, A.M., Mokkelbost, K.H., Bryn, P., 2005b. Soil conditions and slope stability in the Ormen Lange area. Marine and Petroleum Geology 22, 299-310. doi:10.1016/j.marpetgeo.2004.10.021

Lacoste, A., Loncke, L., Chanier, F., Bailleul, J., Vendeville, B.C., Mahieux, G., 2009. Morphology and structure of a landslide complex in an active margin setting: The Waitawhiti complex, North Island, New Zealand. Geomorphology 109, 184-196. doi:10.1016/j.geomorph.2009.03.001

Lacoste, A., B. C. Vendeville, and L. Loncke (2011), Influence of combined incision and fluid overpressure on slope stability: Experimental modelling and natural applications, J. Struct. Geol., 33, 731–742.

Lacoste, A., B. C. Vendeville, R. Mourgues, L. Loncke, and M. Lebacq (2012), Gravitational instabilities triggered by fluid overpressure and downslope incision—Insights from analytical and analogue modelling, J. Struct. Geol., 42, 151–162.

Lehner, F. K., 1986. Comments on "noncohesive critical Coulomb wedges: An exact solution" by F.A. Dahlen. J. Geophys. Res. 91(B1), 793‐796.

Mandl, G., Crans,W., 1981. Gravitational gliding in deltas. In: McClay, K.R., Price, N.J. (Eds.), Thrust and Nappe Tectonics. Geological Society Special Publication, vol. 9, pp. 41-54.

Masson, D.G., Harbitz, C.B., Wynn, R.B:, Pedersen, G., Lovholt,F., 2006. Submarine landslides: processes, triggers and hazard prediction. Phil. Trans. R. Soc. A 364, 2009-2039. doi: 10.1098/rsta.2006.1810

Moore, J.G., Clague, D.A., 2002.Mapping the Nuuanu and Wailau Landslides in Hawaii. In: Takahashi, E., Lipman, P.W., Garcia, M.O., Naka, J., Aramaki, S. (Eds.),Hawaiian volcanoes: deep underwater perspectives. Geophysical Monograph Series, 128. American Geophysical Union, Washington D.C., pp. 223–244. http://dx.doi.org/10.1029/GM128.

Moore, J.G., Clague, D.A., Holcomb, R.T., Lipman, P.W., Normark,W.R., Torresan, M.E., 1989. Prodigious submarine landslides on the Hawaiian Ridge. J. Geophys. Res. Solid Earth 94 (B12), 17465–17484. http://dx.doi.org/10.1029/JB094iB12p17465.

Morgan, J. K., McGovern, P. J. (2005), Discrete element simulations of gravitational Volcanic deformation: 2. Mechanical analysis, J. Geophys. Res., 110, B05403, doi:10.1029/2004JB003253.

Morgan, J.K., Moore, G.F., Clague, D.A., 2003. Slope failure and volcanic spreading along the submarine south flank of Kilauea volcano, Hawaii. Journal of Geophysical Research 108 (B9), 2415. doi:10.1029/2003JB002411

Mourgues, R., and P. R. Cobbold (2003), Some tectonic consequences of fluid overpressures and seepage forces as demonstrated by sandbox modeling, Tectonophysics, 376, 75–97.

Mourgues, R., and P. R. Cobbold (2006a), Sandbox experiments on gravitational spreading and gliding in the presence of fluid overpressures, J. Struct. Geol., 28, 887–901.

Mourgues, R., and P. R. Cobbold (2006b), Thrust wedges and fluid overpressures: Sandbox models involving pore fluids, J. Geophys. Res., 111, B05404, doi:10.1029/2004JB003441.

Mourgues, R., Lecomte, E., Vendeville, B., Raillard, S., 2009. An experimental investigation of gravity-driven shale tectonics in progradational delta. Tectonophysics 474, 643-656.

Mourgues, R., Lacoste, A., Garibaldi, C., 2014. The Coulomb critical taper theory applied to gravitational instabilities. Journal of Geophysical Research (Solid Earth) 119 (1), 754-765. DOI: 10.1002/2013JB010359

Nadeau, P.H., 2011. Lessons Learned from the Golden Zone Concept for Understanding Overpressure Development, and Drilling Safety in Energy Exploration. Deepwater Horizon Study Group, Working Paper, 1-18, (available at: http://risk.berkeley.edu/pdfs_papers/DHSGWorkingPapersFeb16-2011/LessonsLearnedFromGoldenZoneConcept-PHN_DHSG-Jan2011-1.pdf)

Owen, S., Segall, P., Lisowski, M., Miklius, A., Denlinger, R., Sako, M., 2000. Rapid deformation of Kilauea Volcano: Global Positioning System measurements between 1990 and 1996. Journal of Geophysical Research 105 (B8), 18983-18998.

Pattier, F., Loncke, L., Gaullier, V., Vendeville, B., Maillard, A., Basile, C., Patriat, M., Roest, W.R., Loubrieu, B., 2011. Mass movements in a transform margin setting: The example of the Eastern Demerara Rise, in Submarine Mass Movements and Their Consequences, Advances in Natural and Technological Hazards Research, vol. 31, edited by Y. Yamada et al., pp. 331–339, Springer, Berlin, Germany.

Quidelleur, X., Hildenbrand, A., Samper, A., 2008. Causal link between Quaternary paleoclimatic changes and volcanic islands evolution. Geophysical Research Letters 35, L02303, doi:10.1029/2007GL031849.

Reid, M.E., 2004. Massive collapse of volcano edifices triggered by hydrothermal pressurization. Geology 32 (5), 373–376. doi: 10.1130/G20300.1

Saffer, D. M., and B. A. Bekins (1998), Episodic fluid flow in the Nankai accretionary complex: Timescale, geochemistry, flow rates, and fluid budget, J. Geophys. Res., 103(B12), 30,351–30,370.

Satake, K., Smith, J.R., Shinozaki, K., 2002. Three-dimensional reconstruction and tsunami model of the Nuuanu and Wailau giant landslides, Hawaii. In: Takahashi, E., Lipman, P.W., Garcia, M.O., Naka, J., Aramaki, S. (Eds.),Hawaiian Volcanoes: Deep Underwater Perspectives. Geophysical Monograph Series 128. American Geophysical Union, Washington D.C., pp. 333–346. http://dx.doi.org/10.1029/GM128.

Shi, Y., and C. Wang (1988), Generation of high pore pressures in accretionary prisms: Inferences from the Barbados subduction complex, J. Geophys. Res., 93(B8), 8893–8909.

Smith, D.E., Harrison, S., Jordan, J.T., 2013. Sea level rise and submarine mass failure on open continental margins. Quaternary Science Reviews 82, 93-103. http://dx.doi.org/10.1016/j.quascirev.2013.10.012

Voight, B., Elsworth, D., 1997. Failure of volcano slopes. Géotechnique 47 (1), 1-31.

Walder, J., Nur, A., 1984. Porosity reduction and crustal pore pressure development. Journal of Geophysical Research 89 (B13), 11539-11548.

Zanella, A., Cobbold, P.R., Rojas, L., 2014a. Beef veins and thrust detachments in Early Cretaceous source rocks, foothills of Magallanes-Austral Basin, southern Chile and Argentina: Structural evidence for fluid overpressure during hydrocarbon maturation. Marine and Petroleum Geology 55, 250-261. http://dx.doi.org/10.1016/j.marpetgeo.2013.10.006

Zanella, A., Cobbold, P.R., Le Carlier de Veslud, C., 2014b. Physical modelling of chemical compaction, overpressure development, hydraulic fracturing and thrust detachments in organic rich source rock. Marine and Petroleum Geology 55, 262-274. http://dx.doi.org/10.1016/j.marpetgeo.2013.12.017

## APPENDIX A - Determination of the stress components for a cohesive wedge

The equations of static equilibrium determined for the cartesian coordinates *x,z* are:

**(A1)**

$$\frac{\partial \sigma'_{xx}}{\partial x} + \frac{\partial \sigma'_{xz}}{\partial z} = \rho' g \sin\alpha - \frac{\partial P_{ov}}{\partial x}$$

**(A2)**

$$\frac{\partial \sigma'_{zz}}{\partial z} + \frac{\partial \sigma'_{xz}}{\partial x} = \rho' g \cos\alpha - \frac{\partial P_{ov}}{\partial z}$$

In which $\sigma'$ is the effective stress, $\rho'$ is the density corrected from hydrostatic buoyancy, $g$ is the constant acceleration of gravity and $P_{ov}$ is the fluid overpressure (Hubbert and Rubey, 1959).

We establish as boundary conditions:

(1) Following the infinite slope model, we assume that there is no stress variation along x axis, provided that "compaction is invariant along the slope and that the principal axes of the permeability tensor are approximately parallel and perpendicular to the free surface" (Lacoste et al.,2012, referring to Mandl and Crans,1981).

**(A3)**

$$\frac{\partial}{\partial x} = 0$$

(2) For the upper surface of the prism (z=0):

**(A4)**

$$\sigma'_{xz} = \sigma'_{zz} = 0$$

Here we ignore the effect of the water column weight for a submarine setting.

(3) the fluid overpressure ratio ($\lambda^*$, Eq. 17) is constant within the wedge (the pore fluid pressure is assumed to increase linearly with depth ($z$).

Considering the boundary conditions, the expressions (Eqs. A3 and A4) become:

**(A5)**

$$\sigma'_{xz} = \rho' g z \sin\alpha$$

**(A6)**

$$\sigma'_{zz} = \rho' gz \cos\alpha - P_{ov} = (1 - \lambda^*)\rho' gz \cos\alpha$$

From geometric analysis of the Mohr diagram, assuming that the prism material is on the verge of shear failure everywhere, and for known $\sigma'_{xz}$ and $\sigma'_{zz}$ (Fig. A.1):

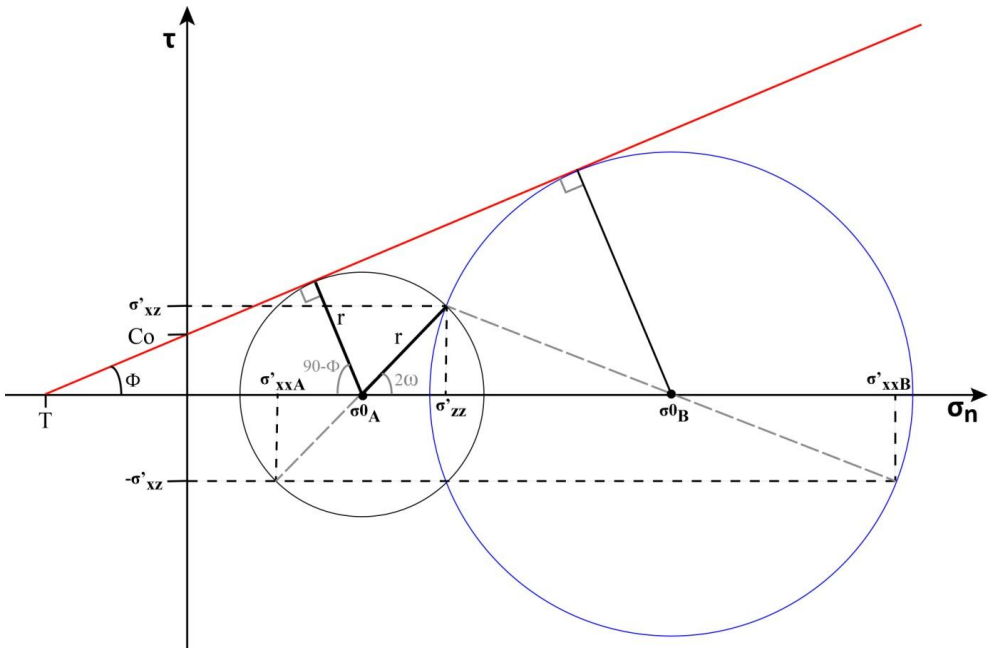


**Fig. A.1.** Mohr diagram, assuming that the prism material is on the verge of failure everywhere.

**(A7)**

$$\sin\phi = \frac{r}{T + \sigma_0} \Leftrightarrow r = T\sin\phi + \sigma_0 \sin\phi$$

**(A8)**

$$r^2 = (\sigma'_{zz} - \sigma_0)^2 + {\sigma'_{xz}}^2 = {\sigma'_{zz}}^2 + {\sigma_0}^2 - 2\sigma'_{zz}\sigma_0 + {\sigma'_{xz}}^2$$

In which $r$ is the radius of the Mohr circle, $_0$ is the center of the Mohr circle (average value of the maximum and minimum normal stresses), $T$ is the tension strength and $\phi$ is the angle of internal friction. As we consider that the failure of the material will obey to the rectilinear Coulomb failure criterion, the $T$ value will be directly related to the cohesion ($Co$) of the wedge material as:

**(A9)**

$$T = Co\tan\phi$$

From the equivalence between Equation A7 and the square of Equation A8, we obtain an expression that allows the determination of two $\sigma_0$ solutions:

**(A10)**

$$A = \sin^2\phi - 1$$

$$B = 2T\sin^2\phi + 2\sigma'_{zz}$$

$$C = T^2\sin^2 - \sigma'^{2}_{zz} - \sigma'^{2}_{xz}$$

$$\delta = B^2 - 4AC$$

$$\sigma_0 = \frac{-B \pm \sqrt{\delta}}{2A}$$

Considering the solution for $_0$ of the lateral extensional domain of Mohr circle, and knowing that:

**(A11)**

$$\sigma_0 = \frac{\sigma'_{zz} - \sigma'_{xx}}{2} + \sigma'_{xx}$$

$\sigma'_{xx}$ can be determined:

**(A12)**

$$\sigma'_{xx} = 2\sigma_0 - \sigma'_{zz}$$

With $_0$ as the center of the Mohr circle (average value of the maximum and minimum normal stresses) of the lateral extension domain.

As this analytical model is especially focused on the stability conditions along the basal detachment, it is necessary to transform the stress components from x,z coordinate system to $x_1$,$z_1$ coordinate system .This transformation consists in a rotation of $\theta°$ ($\alpha$ - $\beta$):

**(A13)**

$$\begin{cases} \sigma'_{xx_1} = \dfrac{\sigma'_{xx} + \sigma'_{zz}}{2} + \dfrac{\sigma'_{xx} - \sigma'_{zz}}{2}\cos(-2\theta) + \sigma'_{xz}\sin(-2\theta) \\ \sigma'_{zz_1} = \dfrac{\sigma'_{xx} + \sigma'_{zz}}{2} - \dfrac{\sigma'_{xx} - \sigma'_{zz}}{2}\cos(-2\theta) - \sigma'_{xz}\sin(-2\theta) \\ \sigma'_{xz_1} = \dfrac{\sigma'_{xx} + \sigma'_{zz}}{2}\sin(-2\theta) + \sigma'_{xz}\cos(-2\theta) \end{cases}$$

**References cited in Appendix A:**

Hubbert, M. K., and W. W. Rubey (1959), Role of fluid pressure in mechanics of overthrust faulting, Geol. Soc. Am. Bull., 70, 115–166.

Lacoste, A., B. C. Vendeville, R. Mourgues, L. Loncke, and M. Lebacq (2012), Gravitational instabilities triggered by fluid overpressure and downslope incision—Insights from analytical and analogue modelling, J. Struct. Geol., 42, 151–162.

Mandl, G., Crans,W., 1981. Gravitational gliding in deltas. In: McClay, K.R., Price, N.J. (Eds.), Thrust and Nappe Tectonics. Geological Society Special Publication, vol. 9, pp. 41-54.

## APPENDIX B - Assessment of the wedge stability along the basal detachment - Balance of forces

The stability of the wedge along the basal detachment will be analyzed as a confrontation between the resulting of the forces inducing and resisting the downslope movement (*Fd* and *Fb*, respectively), for each point along the basal detachment (of given *h* and *l*).

*Fd* at a given point of the basal detachment constitutes the resulting of the following force components:

**(B1)**

$$Fd = F_\sigma + F_w + F_s$$

$F_\sigma$ results from the integration of $\sigma'_{xxl}$ along the local wedge height ($h$ , along $z_1$ axis), incorporating the effect of the wedge material's cohesion (Fig. A.2).

**(B2)**

$$F_\sigma = \int_0^h \sigma'_{xx_1}\, dz_1$$

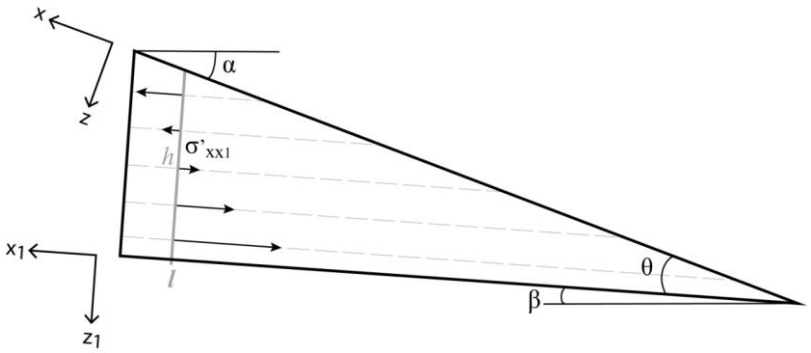


**Fig. A.2.** Representation of the wedge and variation of $\sigma'_{xxl}$ along the local wedge height.

$F_w$ at a point along the basal detachment of length *l* and height *h* will correspond to the gravitational load of the wedge section comprehended between that point and the wedge tip (*l* = *h* =0) (Fig. A.3):

**(B3)**

$$F_w = \iiint_V \rho' g \sin\beta \, dv$$

if considering a unitary width wedge slice:

**(B4)**

$$F_w = \rho' g \sin\beta \frac{hl}{2}$$

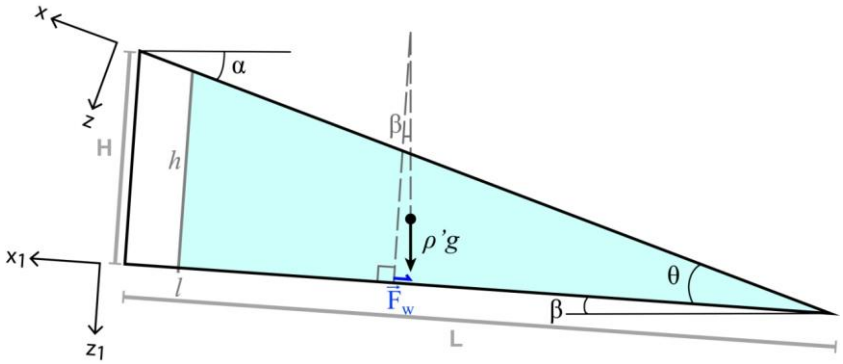


**Fig. A.3.** Respresentation of the wedge and $F_w$. $F_w$ at a point along the basal detachment corresponds to the gravitational load of the wedge section comprehended between that point and the wedge tip ($l = h = 0$).

A seepage force ($SF$) results from the drag exerted by moving fluid on the solid framework of a porous material, while under the effect of fluid overpressure gradient (Mourgues and Cobbold, 2003) (Fig. A.4). As this frictional drag caused by a moving fluid will not be applied simply to a determined surface, but rather acts pervasively on the whole mass, the seepage force will be expressed as a body force (an integral considering the three dimensions), similarly to $F_w$.

The seepage force expression considered in our calculations ($F_s$) will be constituted solely the component parallel to the basal detachment ($SF^{x1}$, Fig. A.4), as the component acting perpendicularly to the basal detachment ($SF^{z1}$) is already considered in the calculation of the effective stresses ($\sigma'_{zz1}$).

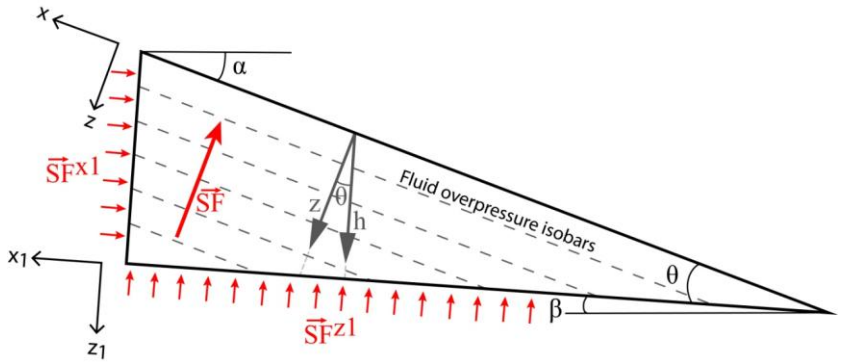


**Fig. A.4.** Representation of the wedge and Seepage Force components.

**(B5)**

$$SF = \iiint_V \text{grad } P_f \, dv$$

With *Pf* as the pore fluid pressure. Considering a wedge slice of unitary width, and Eq. 17 for $\lambda^*$:

**(B6)**

$$SF = \lambda^* \rho' g \cos\alpha \frac{hl}{2}$$

as the local wedge length (*l*) can be expressed in function of the wedge height *(h*):

**(B7)**

$$l = \frac{h}{\tan\theta}$$

**(B8)**

$$SF = \lambda^* \rho' g \cos\alpha \frac{h^2 \cos\theta}{2 \sin\theta}$$

Determining the component parallel to the basal detachment ($SF^{x1}$):

**(B9)**

$$SF^{x1} = F_s = \lambda^* \rho' g \cos\alpha \cos\theta \frac{h^2}{2}$$

Finally, the resisting force *Fb* is the integration of basal friction between a given point of the basal detachment (*l*) and the wedge tip (*l* = *h* =0):

**(B10)**

$$Fb = \int_0^l \tau \; dx_1$$

Considering that the wedge is on the verge of failure, according to Coulomb failure criterion:

**(B11)**

$$\tau = \mu_b \times \sigma'_n + Co_b$$

Taking $\mu_b$ as the internal friction coefficient of the basal detachment, $\sigma'_n$ as the effective normal stress component, and $Co_b$ as the basal detachment cohesion.

**(B12)**

$$Fb = \int_0^l \mu_b \times \sigma'_n + Co_b \; dx_1$$

with

**(B13)**

$$\sigma'_n = \sigma'_{zz_1} + P_{ov_{prism}} - P_{ov_{basal}}$$

Considering again Eq. 17 and that $z = h \times \cos\theta$:

**(B14)**

$$\sigma'_n = \sigma'_{zz_1} + (\lambda^* - \lambda_b^*)\rho' g h \cos\theta \cos\alpha$$

or rather considering that $l \times \sin\theta = h \times \cos\theta$, as $Fb$ is expressed as an integral along the wedge's length (Eq. B8):

**( B15)**

$$\sigma'_n = \sigma'_{zz_1} + (\lambda^* - \lambda_b^*)\rho' g l \sin\theta \cos\alpha$$

With $\lambda^*$ as the fluid overpressure ratio in the wedge, and $\lambda^*_b$ as the fluid overpressure ratio along the basal detachment.

**Reference cited in Appendix B:**

Mourgues, R., and P. R. Cobbold (2003), Some tectonic consequences of fluid overpressures and seepage forces as demonstrated by sandbox modeling, Tectonophysics, 376, 75–97.

# Chapter 8

## Cohesive Coulomb critical taper theory applied to gravitational collapses in overpressured volcanic systems: analytical/numerical modeling

## (Costa et al., *in prep b*)

# Cohesive Coulomb critical taper theory applied to gravitational collapses in overpressured volcanic systems: analytical/numerical modeling

***(in prep b)***

**Costa, A.C.G.[1,2*], Mourgues, R.[3], Marques, F.O.[4], Hildenbrand, A.[2,5], Boulesteix, T.[6], Garibaldi, C.[3]**

(1) Universidade de Lisboa and IDL, Lisboa, Portugal
(2) Univ. Paris-Sud, Laboratoire GEOPS, UMR8148, Orsay, F-91405
(3) 1LUNAM, L.P.G.N., UMR 6112, Faculty of Science, Université du Maine, Le Mans, France
(4) Universidade de Lisboa, Lisboa, Portugal
(5) CNRS, Orsay, F-91405
(6) Université de Lorraine, CNRS, CREGU, GeoRessources laboratory, Vandoeuvre les Nancy, F-54500, France

**Abstract**

The Coulomb Critical Wedge (CCW) theory has been most commonly applied to overpressured systems in compressive regimes, and more recently applied to gravitational instabilities. Here we present the application of a new analytical solution for the cohesive CCW theory to gravitational instabilities in volcanic edifices. We investigate the impact of several variables on the stability of the flanks of volcanoes, including: wedge slope and dimensions, cohesion, internal friction along the basal detachment, and fluid overpressure. We conclude that: (1) the steepening of the volcanic flanks and basal detachment leads to a decrease in the fluid overpressure ratio (fluid overpressure divided by lithostatic pressure) necessary to produce failure. (2) The decrease of the stabilizing effect of cohesion with increasing depth of the basal detachment favours the occurrence of deep-seated large-scale gravitational destabilization in basal detachments deeper than ca. 2000-2500 m (in volcanic edifices necessarily higher than 2500 m). (3) For shallower basal detachments, the

overpressure ratios required to induce failure are comparatively larger. (4) In edifices with steeper flanks and stronger materials, shallow failure parallel to the edifice flank surface is favoured, instead of deep-seated deformation. (5) With increasingly deeper basal detachments (possible in larger volcanic edifices), while the impact of cohesion diminishes, the relative importance of internal friction on the stability of the edifice increases. We then discuss the results of the model, and the implications regarding the stability of volcanic edifices in various settings, and with diverse configurations/dimensions (Hawaii, Canary and the smaller Azores islands).

***Keywords***
Coulomb critical taper theory; cohesion; fluid pressure distribution; gravitational instabilities; volcanic edifices; fluid overpressure4

## 1. Introduction

The susceptibility of volcanic edifices to large-scale flank failure is dependent on a number of internal and external factors (e.g., McGuire, 1996; Keating and McGuire, 2000). Factors intrinsic to the growth and evolution of each volcano include the geometry and architecture of the edifice (Siebert, 1984), the existence and development of potential volcano-tectonic discontinuities (dykes and faults)( Elsworth and Voight, 1996), the properties of the materials that constitute the edifice (e.g. strength, permeability, layering)(Mitchell, 2003; Oehler et al., 2005), their change in time (e.g., through hydrothermal or meteoric alteration) (Siebert, 1984; López and Williams, 1993; van Wyk de Vries, et al., 2000), and gradual deformation (e.g. Reid et al., 2010). On the other hand, "external" factors include seismic activity (Elsworth and Voight, 1996; Keating and McGuire, 2000), the eventual presence of thick and weak sedimentary layers below the edifice (Dieterich, 1988; Iverson, 1995; van Wyk de Vries and Borgia, 1996), and climatic changes, e.g., through eustatic variations of the sea level (Iverson, 1995; Quidelleur et al., 2008.

The fluid overpressure was already considered as being more important for the stability state of volcanic edifices than coefficient of internal friction or cohesion (Day, 1996), and has been considered as a partial justification to the large-scale destabilization of low-slope shield volcanoes (sub-aerial dip between 4 and 8º - Walker, 1999) and the long runout of associated debris avalanches (López and Williams, 1993; Iverson, 1995; Elsworth and Voight, 1996; Morgan and Clague, 2003). The increase of fluid overpressure has been

shown to push the volcanic edifice towards the stability limit, and lead to the deepening of the potential failure surfaces (Thomas et al., 2004a), producing an effect similar to a decrease in the basal strength (Morgan and McGovern, 2005a).

In volcanic islands, the role of cohesion in the gravitational destabilization is not consensual: either as negligible (Iverson, 1995) or of minor importance (Day, 1996); however:

(a) coherent pillow lavas, and not the much weaker hyaloclastites, are the major constituent of the submarine sector of volcanic oceanic edifices (Garcia and Davis , 2001, opposed to the interpretation presented in Moore and Chadwick, 1995; and about the relative weakness of hyaloclastites - Nielson and Stiger, 1996; Schiffman et al., 2006; Thompson et al., 2008, Table A.1). Several factors highlight the need to study the destabilizing effect of fluid overpressure build-up in domains with strength contrasts (e.g., cohesion): (1) the strength contrast between hyaloclastites (that can be practically non-cohesive - Nielson and Stiger, 1996) and lavas; (2) the susceptibility of hyaloclastites to become impermeable through compaction and hydrothermal alteration (Mitchell, 2003; Walton and Schiffman, 2003; Schiffman et al., 2006); (3) the widely recognized consequences of the hyaloclastites/lavas interface for the stability of the volcanic edifices (Mitchell, 2003; Schiffman et al., 2006); and (4) the contrast between the materials in the volcanic edifice and the underlying pelagic sediments (e.g., Iverson, 1995).

(b) in numerical modeling, the cohesion of the rocks in the volcanic edifice has been shown to affect the resulting deformation (e.g., Morgan and McGovern, 2005a), relatively to the cohesion along the basal detachment.

(c) cohesion has been considered to have an impact on failure depth (del Potro et al., 2013).

(d) the largest submarine debris deposit resulting from flank collapse(s) on volcanic islands (Nu'uanu debris avalanche, Hawaii, with estimated volume of 2500-3500km$^3$) apparently involved the transport of a 600 km$^3$ block (Tuscaloosa seamount) along ca. 55 km (Moore et al., 1989; Moore and Clague, 2002; Satake et al., 2002), suggesting that the cohesion should not be disregarded when studying large-scale failure events.

(e) from observation of volcanic edifices located near mid-ocean ridges, some authors (e.g. Mitchell, 2003) proposed that large-scale flank failure becomes common for edifices higher than 2500 m. Such height threshold would coincide with the beginning of the development of well-defined rift zones, which would potentiate the destabilization of the edifice through dyke intrusion (Mitchell, 2003). Furthermore, the size-dependency of flank

collapse occurrence could also reflect the change of material strength with the growth of the volcanic edifice, associated with decreasing water depth: the composition of the materials tends towards increasing vesicularity and relative importance of the volcaniclastic component, with progressive incorporation of the resulting deposits in the structure of the growing edifice (Fornari et al., 1979; Staudigel and Schminke, 1984; Batiza and White, 1999; Schmidt and Schminke, 1999; DePaolo et al., 2001; Garcia and Davis, 2001; Mitchell, 2003; Oehler et al., 2005; Garcia et al., 2007). The conclusion by Costa et al. (*in prep*) on the decrease of the cohesion impact with the increasing size of the volcanic edifice is consistent with the apparent dependency of the large-scale flank collapses on the size of the volcanic edifice.

The above mentioned arguments suggest an effective impact of fluid overpressure and cohesion on the development of large flank collapses in volcanic edifices. However, the exact role of these various factors and their mutual interactions remain in most cases poorly assessed quantitatively.

In Costa et al. (i*n prep*), the Coulomb Critical Wedge (CCW) theory is applied to gravitational destabilization in cohesive materials under the effect of fluid overpressure. The present study applies the model of Costa et al. (i*n prep*) to volcanic edifices, and especially aims at better defining the conditions for which the cohesion plays a major role or not, considering different volcanic edifice sizes, geometry (steepness of the flanks), material strength and fluid overpressure.

## 2. Cohesion of volcanic edifices

The overall cohesion of a volcanic edifice in previous modeling works has been considered to reach either 1 MPa (van Wyk de Vries et al., 2000; Cecchi et al., 2005), up to 10 MPa (e.g., Donnadieu and Merle, 1998, for a silicic stratovolcano; Oehler et al., 2005 for shield volcanoes), or even up to 100 MPa (Delcamp et al., 2008). Thomas et al. (2004b) refers to previous works estimating the general cohesion of volcanic edifices: of approximately 1 MPa (Jaeger and Cook, 1979; Voight et al., 1983 in Thomas et al., 2004b); within the range of 0.6-6 MPa for basaltic volcanic edifices (Schultz, 1995, 1996 in Thomas et al., 2004b); in the range 0-0.4 MPa for altered rocks in stratovolcanoes (Watters et al., 2000).

The cohesion values obtained through tests on intact rock samples (e.g., Schiffman et al., 2006) cannot be assumed to be equal to those of the general edifice, as the latter is

generally highly affected by physical discontinuities, such as for instance successive lava flows (layering), sub-vertical dykes, columnar jointing, and pervasive fracturing. The shear strength values determined for natural joints (Thompson et al., 2008) fall within the range 0-10 MPa, which is smaller than the results from tests performed in intact rock samples (Schiffman et al., 2006; Thompson et al., 2008), but closer to the range of values considered in the above mentioned works.

As indicated by Iverson (1995), the relevance of cohesion decreases with depth, i.e. with increasing lithostatic load. For instance, the maximum cohesion value of 8.6 MPa determined in the shear tests on natural joints (Thompson et al., 2008, Table A.1 in Appendix A) would be equivalent to 60-70% of the lithostatic load for a depth of 500 m, and equivalent to only 3-4% of the lithostatic load at depths of 9-10 kms. This decrease of the relative importance of cohesion with depth, being relevant for superficial zones of the wedge, has been addressed by Davis et al. (1983), Dahlen et al.(1984) and further developed in Costa et al. (*in prep*).

When extrapolating the strength values from intact rock to large-scale fractured rock-masses, the maximum strength values are even smaller. Based on Rock Mass-Rating and Hoek-Brown criterion, and from strength data of volcanic rock samples ("lava flows, dykes and airfall tuffs"), Thomas et al. (2004b) concluded that the general strength of the volcanic edifice is up to 96% smaller than the strength determined on intact rock samples. The estimated cohesion values for a volcanic edifice lie within the range 0.44 - 4.8 MPa, with an average of 1.3 MPa for the basaltic volcanic units on Tenerife (Canary Islands). The internal friction angles lie within the range of 28-38º (corresponding to coefficients of internal friction, $\mu$, in the range 0.53-0.78). The consideration of an additional disturbance parameter (e.g., removal of lithostatic load) would imply a maximum decrease in cohesion of ca. 30%.

## 3. Fluid overpressure in volcanic edifices

Fluid overpressure is the pressure of a fluid above the expected hydrostatic pressure (weight of a water column) at equivalent depth. It is commonly expressed as a "fluid overpressure ratio" ($\lambda^*$, fluid overpressure divided by the lithostatic pressure).

In volcanic systems, $\lambda^*$ can present a large range of values, from practically equivalent to hydrostatic ($\lambda^* = 0$) to above the lithostatic pressure ($\lambda^* > 1$), depending on the permeability, the strength of the medium and on the pressurization of fluid at the source (Day, 1996).

Studying the effects of the fluid overpressure on the destabilization of oceanic islands is pertinent, because there are: (a) great amounts of fluids (the edifices are saturated in sea and meteoric water); (b) internal and external factors capable of increasing the fluid pressure through mechanic and thermal processes; (c) potential sealing layers of low hydraulic conductivity in the structure of (or underlying) the volcanic edifices. These seal layers are developed due to reduction of the porosity of materials (e.g., Walder and Dun, 1984; Day, 1996), through pore-collapse possibly enhanced through seismic loading, deformation (with fluid circulation along faults), and/or after mechanical degradation of the volcanic deposits due to hydrothermal alteration.

The build-up of fluid overpressures within a volcanic edifice is conditioned by the balance between generation/diffusion of the fluid overpressures within a volcanic edifice (permeability high enough to allow the spatial propagation of the pressurized fluid and a permeability low enough to prevent the fluid escape), by the distribution and contrasts in strength of the materials constituting the volcanic edifice, and by the deformation of the edifice (e.g., fracturing, changes in the stress field) (Day, 1996, Reid et al., 2004).

Internal and external mechanisms often considered as generators of fluid overpressure within volcanic edifices are: (1) magmatic degassing along the conduit of the edifice (Day, 1996; Sparks, 1997; Thomas et al., 2004a). (2) Immediate mechanical effect of magma intrusions (Iverson, 1995; Elsworth and Voight, 1995,1996; Voight and Elsworth, 1997). (3) thermal heating of pore fluid due to magma intrusion (Elsworth and Voight, 1995,1996; Day, 1996; Voight and Elsworth, 1997). The build-up of fluid overpressures associated with magmatic intrusions depends on the location, the configuration/geometry and the temperature of the intrusion (Reid et al., 2004). Thermal heating has an effect that lasts longer than the immediate mechanical effect of dike intrusion (Day, 1996; Elsworth and Voight, 1996; Voight and Elsworth, 1997; Reid et al., 2004). Despite this, the mechanical effect of intrusion in highly permeable media can be more efficient in generating fluid overpressure than thermal heating (Day, 1996). (4) Seismic loading (Elsworth and Voight, 1996; del Poltro et al., 2013), as strong fluid overpressure gradients have been shown to generate low-magnitude seismicity (Terakawa. et al., 2013). (5) Groundwater flow of infiltrated meteoric water, which has the potential for generation of shallow landsliding in a steep stratovolcano (Reid et al., 2004). (6) Changing sea-level associated with (paleo-)climatic changes (Iverson, 1995; Quidelleur et al., 2008).

The generation of fluid overpressure is naturally connected to hydrothermal alteration, as both are consequences of fluid circulation within a volcanic edifice, and because

hydrothermal alteration has a deep effect on the permeability structure and strength distribution within the edifice. The impact of hydrothermal alteration in the stability of the edifice is more complex than the simple reduction of the edifice's strength with increasing degree of alteration (e.g., Siebert, 1984; López and Williams, 1993; van Wyk de Vries, et al., 2000). Hydrothermal alteration varies spatially in the edifice (Watters et al., 2000) and the location of the altered masses has an impact on the stability of the edifice (Reid et al., 2001; Cecchi et al., 2005). Depending on the type of hydrothermal alteration and secondary minerals formed, there can be a more significant decrease of the strength of materials for smaller degrees of alteration (del Potro and Hürlimann, 2009). In some cases hydrothermal alteration may even strengthen the edifice, e.g. through silicification and cementation (Watters et al., 2000; Zimbelman et al., 2004). A decrease in porosity/permeability and an increase of the strength with increasing degree of alteration has been reported (Walton and Schiffman, 2003; Schiffman et al., 2006; Thompson et al., 2008), but the opposite effect has been reported as well (Pola et al.,2012, 2014), with clear opposite implications for the potential generation of fluid overpressure within the edifice.

## 4. Application of the cohesive model to volcanic systems

### *4.1. Definition of variables and parameters*

The maximum height of the volcanic sequence above the basal detachment (*H*, measured perpendicular to the basal detachment as seen in Figs. 1 and 2) can either represent: (a) the full height of the volcanic edifice (*H)*, which therefore deforms along its basal surface; (b) the maximum height of a volcanic sequence above a more superficial basal detachment, e.g., rooted over a hyaloclastite layer. Here we use a maximum value of 5500m for *H*. This particular value would be equivalent to the approximate height of Mauna Loa's upper volcanic sequence, which sits over a thick layer of hyaloclastites, as supported by the drill-hole HSDP (DePaolo et al., 2001; Table A.1). Smaller values of H are tested (*H* = 1000 m and *H* = 2500 m), in order to assess the variation of the conditions necessary for failure to occur along basal detachments at different heights (Fig. 2).

The slope values of the wedge's upper surface ($\alpha$) here used are: 7º, which is average of the lava dip values presented in Morgan and McGovern, 2005a for Kilauea, Hawaii; and 15º, which is the dip expected for volcanic ridges as seen in the Azores (e.g., Costa et al., 2014, *submitted*) and in the Canary Islands (e.g., Mitchell et al., 2002).

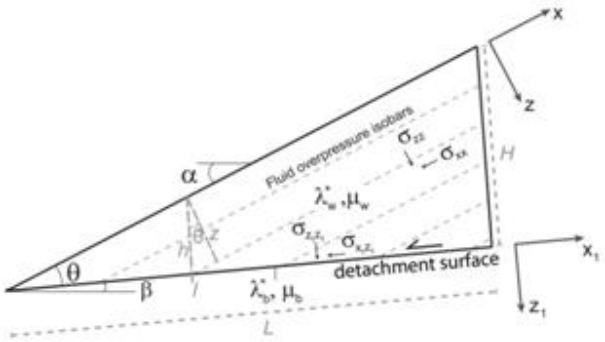


**Fig. 1.** Representation of the configuration of the wedge, Cartesian coordinate system, and variables. Excerpt of Fig.2 in Costa et al. (*in prep*).

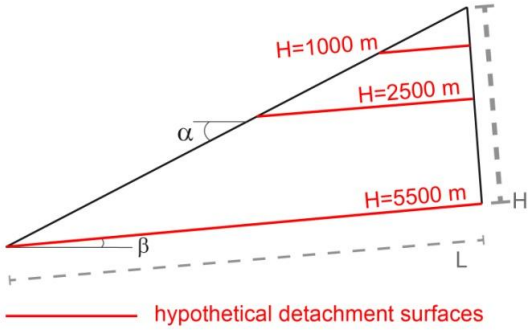


**Fig. 2**. Tested dimensions of the wedge, defined by the maximum height above the basal detachment (*H*).

We consider as basal surface angles ($\beta$): 0º (first column of Fig. 3) and 2º (second and third columns of Fig. 3). For the null value, *H* is equivalent to the maximum vertical height of the volcanic sequence. For $\beta$ = 2º, the discrepancy between *H* and the maximum vertical height of the volcanic sequence negligible (*H* = 5500 m measured perpendicularly to a basal surface tilted 2º, is equivalent to a vertical height of 5497 m). These two values are applied merely to illustrate the effect of tilting the basal detachment along which the wedge will deform.

The used fluid overpressure ratios $\lambda^*$ are the same within the wedge and along the basal detachment. The values considered for $\lambda^*$ range from 0 (null fluid overpressure) to higher than 1 (fluid overpressure higher than lithostatic pressure).

The value of the coefficient of internal friction ($\mu$) for the wedge ($\mu_w$) was 0.45 (angle of internal friction $\phi_w$ = 24.2º), which is the value determined with the direct shear test on natural joints of sub-aerial lava flows by Thompson et al. (2008) (Table A.1, tests performed in samples from HSDP core, Hawaii). The $\mu$ values used for the basal detachment ($\mu_b$) were obtained from the results by Thompson (Table A.1) for: the uppermost hyaloclastite deposit,

0.32 ($\phi_b$ = 17.6º), and the smallest value determined for the hyaloclastite deposits, 0.18 ($\phi_b$ = 10.2º) (Thompson et al., 2008).

The overall density of the volcanic edifice is considered to be 2500 kg/m$^3$ (Oehler et al., 2005).

For each configuration, we tested different values of cohesion for both the wedge ($Co_w$) and the basal detachment ($Co_b$). The values used here were obtained from different approaches and altogether define distinct scenarios regarding the strength of the edifice:

**Scenario 1** - practically non-cohesive wedge and basal detachment ($Co_w$ = $Co_b$ = 0.01 Pa) - Figs. 3a to 3c. This scenario constitutes a reference that allows the assessment of the overall influence of non-negligible cohesion on the deformation of the edifice.

**Scenario 2 -** relatively small cohesion values: $Co_w$ = 1 MPa (approximate value estimated for the basaltic rock masses by Thomas et al., 2004b), and $Co_b$ = 0.08 MPa (cohesion value within the range determined for altered material - Watters et al., 2000 in Thomas et al., 2004b) - Figs. 3d to 3f.

**Scenario 3** - Larger cohesion values determined from direct shear tests on natural joints of samples from HSDP core, Hawaii (Thompson et al., 2008, Table A.1): $Co_w$ = 2.6 MPa (value determined for the sub-aerial lava flows), and $Co_b$= 0.9 MPa (value determined for the uppermost hyaloclastite deposit) - Figs. 3g to 3i.

*4.2. Application of the cohesive model: results*

Through repeated comparison between the forces driving, *Fd*, and resisting, *Fb*, the downslope movement along the prescribed basal detachment, we determined the minimum $\lambda$* required for failure to occur along the basal detachment ($\lambda$* required for *Fd* > *Fb*) (Figs. 3 and 4). In Fig. 4, the dots correspond to the minimum $\lambda$* required for *Fd* > *Fb*: for an hypothetical basal detachments at deeper or shallower levels in the volcanic edifice (plotted at *H* = 1000 m; *H* = 2500 m; *H* = 5500 m), for different $\mu_b$ (different symbols), for different $Co_w$ (different colours of the symbols), for $\alpha$ = 7º (Fig. 4a), and $\alpha$ = 15º (Fig. 4b).

Through application of the expression presented in Costa et al. (*in prep*), we plot the values of $\lambda_c$* required to trigger internal failure of the wedge, parallel to the upper slope (α), as a function of maximum depth *H* (Eq. 1, colored curves in Fig. 4):

(1)

$$\lambda_c^*(H) = 1 - \frac{\tan \boldsymbol{\alpha}}{\tan \phi} + \frac{Co_w}{\rho' g H \cos\theta \ \cos\alpha \tan\phi}$$

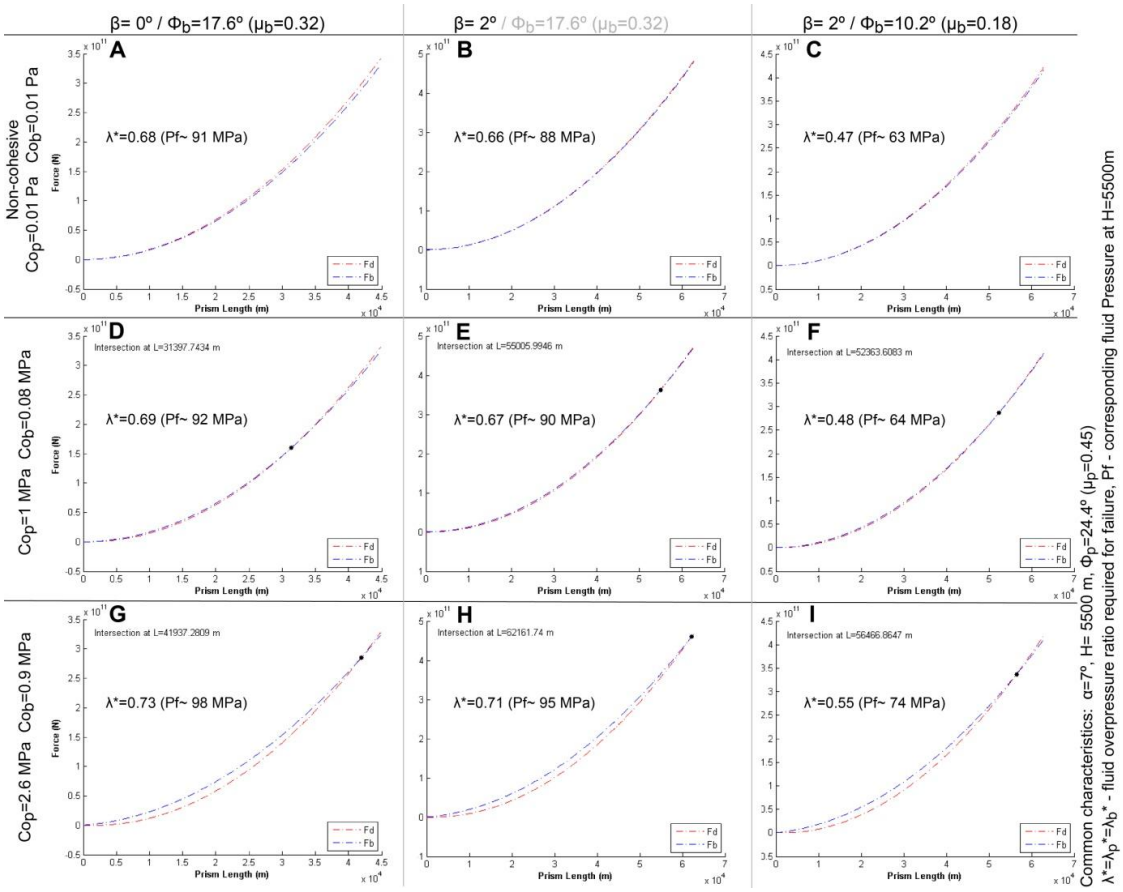


**Fig. 3. C**omparison of forces driving (*Fd*) and resisting (*Fb*) the movement along the basal detachment: minimum $\lambda^*$ required for failure to occur along the basal detachment. Presented scenarios with different cohesion, $\alpha$, $\beta$ and $\mu_b$. Theoretical schemes presented as Fig. 12 in Costa et al. (*in prep a*).

If $\lambda_c^*$ determined for a given $H$ is higher than the $\lambda^*$ required for failure along the basal detachment at depth $H$, the failure will occur along the basal detachment (Costa et al., *in prep*, Fig. 5a). If $\lambda_c^*$ determined for a given $H$ value is lower than the $\lambda^*$ required for failure along the basal detachment at depth $H$, the wedge will fail internally along shallower surfaces, ultimately parallel to the upper surface of the wedge (Costa et al., *in prep*, Fig. 5b).

Thus, the plot of the conditions of $\lambda^*$ required for failure along the basal detachment and within the wedge will determine the conditions for which deep-seated or shallow detachments are favored. The curves of $\lambda_c^*$ as a function of $H$ are presented in different colors depending on the cohesion of the wedge material ($Co_w$), for $\alpha$ = 7º (Fig. 4a) and $\alpha$ = 15º (Fig. 4b).

Regarding the non-cohesive Scenario 1, as $\lambda^*$ rises the *Fd* and *Fb* curves approach, until they overlap (Figs. 3a to 3c). Thus, the failure could occur at any point of the basal

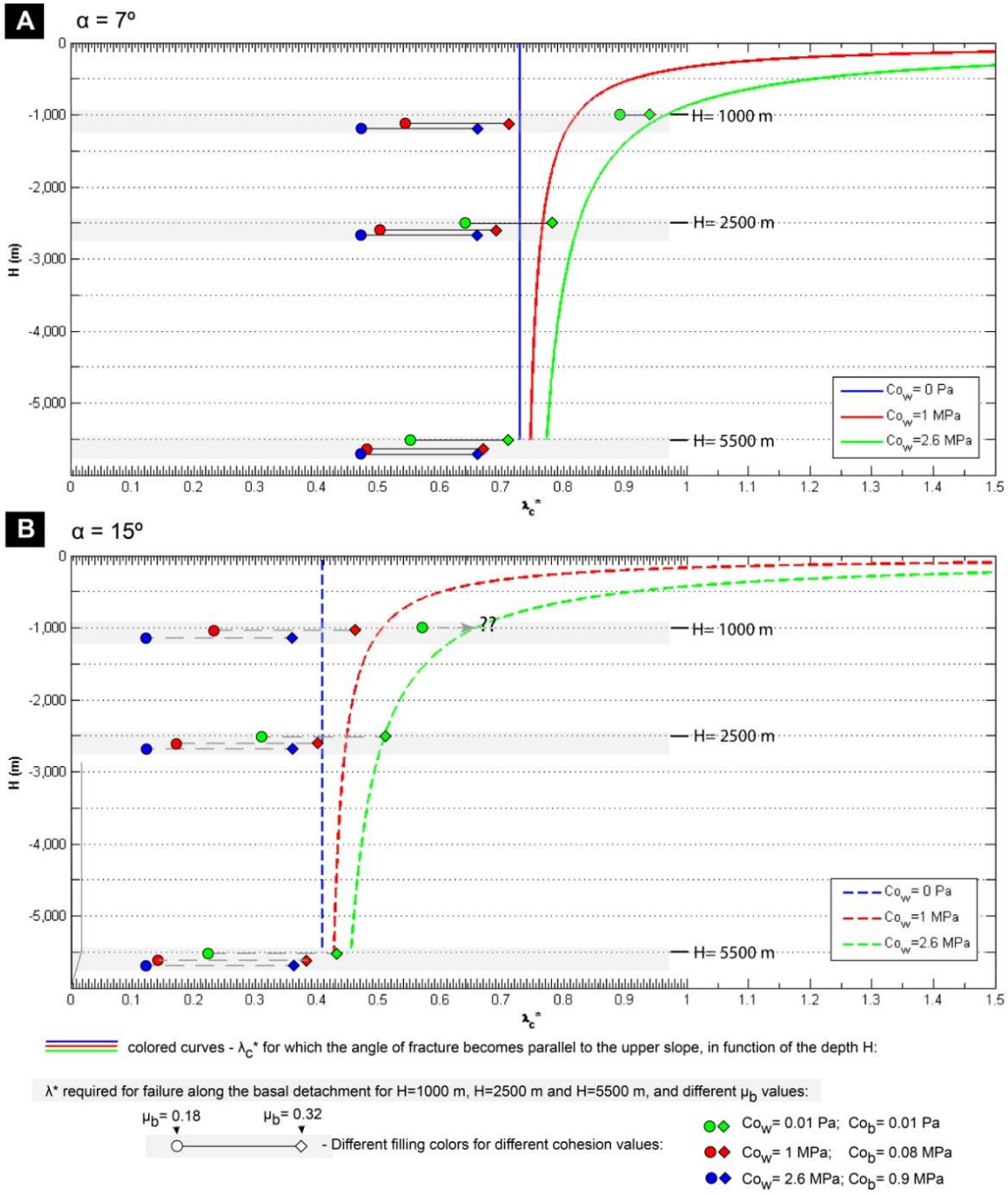


**Fig. 4.** Variation of $\lambda_c$* required for the fracture angle to become parallel to the upper surface of the wedge (slope $\alpha$), as a function of depth $H$. We plot the results for different cohesion values (coloured lines). We plot the hypothetical depths of basal detachment $H$ = 1000 m, $H$ = 2500 m and $H$ = 5500 m, and the $\lambda$* required for failure to occur along the basal detachment (coloured symbols), considering: different values of the wedge's cohesion (colours of the symbols), and different values of $\mu_b$ ($\mu_b$ = 0.18 - circles; $\mu_b$ = 0.32 - diamonds). (A) Plots for $\alpha$ = 7º. (B) Plots for $\alpha$ = 15º. For all the scenarios presented in this figure, we consider $\beta$ = 2º, $\rho'$ = 2500 kg/m$^3$, $\phi_w$ = 24.2º as constants.

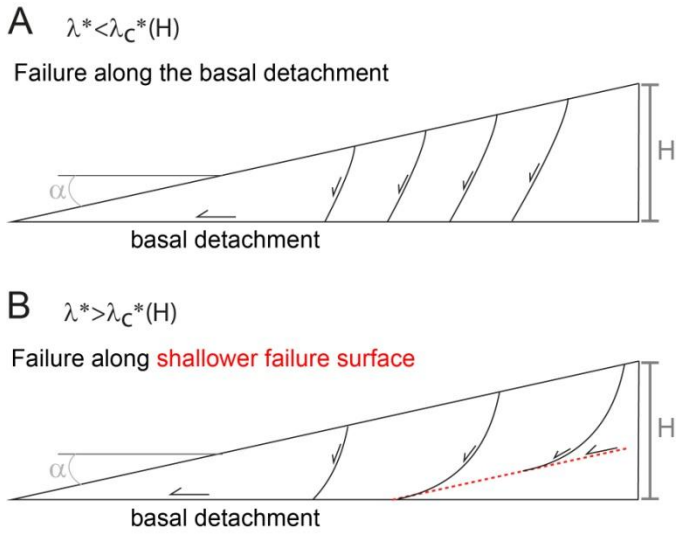


**Fig. 5.** (A) For $\lambda^* < \lambda_c^*$, the faults do not become parallel to the wedge's upper surface, and the failure will be deep-seated, along the basal detachment. (B) For $\lambda^* > \lambda_c^*$, the faults become parallel to the wedge's upper surface, and the failure is shallower. Adapted from Costa et al. (*in prep*).

detachment. In the non-cohesive system, the $\lambda^*$ required for failure along the basal detachment or $\lambda_c^*$ are independent of depth (Fig. 4).

For the cohesive Scenarios 2 and 3, the *Fd* and *Fb* curves approach and intersect as λ* increases, instead of overlapping (Fig. 3). These curves define a "stable" domain in the thinner part of the wedge, where *Fb* > *Fd*, making the failure to root in the thicker domains of the wedge, where *Fd* > Fb (beyond the Minimum Failure Length, in Fig. 12 of Costa et al., *in prep*).

We note that, for increasing depth, the difference in $\lambda^*$ and $\lambda_c^*$ between materials with different cohesion decreases with increasing depth (Fig. 4). Within the span of the cohesion value,s and for the α values here considered, we observe an accentuated decrease of $\lambda_c^*$ between the surface and H = 2500 m (Fig. 4). Beyond *H* = 2500 m, for cohesive materials, $\lambda_c^*$ is still higher than for a non-cohesive material, but the difference in values is minimal, and the value becomes practically stable as a function of depth.

The decrease of $\mu_b$ ( Fig. 4) results in the decrease of the fluid overpressure required to trigger failure. For increasing depths, we observe that the effect of changing $\mu_b$ becomes more important than the effect of changing cohesion (Fig. 5, see horizontal spacing between $\lambda^*$ values for different cohesions, comparatively to spacing between values of different $\mu_b$).

The increase in the tilt of the basal surface ($\beta$, Fig. 3) results in the decrease of the fluid overpressure required for failure to occur.

When changing the upper surface angle of the wedge $\alpha$ from 7º to 15º (Figs. 4a and 4b, respectively), the decrease in the $\lambda^*$ required to produce failure along the basal detachment and within the wedge is very significant. For the scenarios with $\alpha$ = 7º (Fig. 5a), the value of $\lambda^*$ required for failure along the basal detachment is always smaller than $\lambda_c^*$. However, for the steepened flank ($\alpha$ = 15º, Fig. 4b), for the strongest $Co_w$ and $\mu_b$, and if $H$ < 2500 m, the $\lambda^*$ required for failure along the basal detachment is higher than $\lambda_c^*$ (question marks in Fig. 4b).

## 5. Discussion

### *5.1. Model interpretations and relevance to Hawaii, Canary and Azores islands*

For higher values of cohesion of the wedge's material and basal detachment, a higher $\lambda^*$ value is required for failure to occur within the length of the basal detachment (Figs. 3 and 4).

The convergence of required $\lambda^*$ and $\lambda_c^*$ between materials of different cohesions for increasing depth (Fig. 4) reflects the decrease of the influence of cohesion on the stability of the wedge for increasing depth, as discussed in Costa et al. (*in prep*).

The pronounced decrease of $\lambda_c^*$ between the surface and $H$ = 2500 m, and the stability of $\lambda_c^*$ for different cohesions towards larger depths (Fig. 4) suggests that the stabilizing effect of cohesion decreases significantly for basal detachments up to 2500 m deep, becoming negligible for basal detachments deeper than 2500 m. The variable influence of cohesion as a function of depth suggests that it would be easier to generate deep-seated flank failures if the basal detachment were deeper, and, therefore, if the volcanic edifice were higher than ca. 2000 - 2500 m (Fig. 4). From several examples of volcanic edifices in islands and seamounts that grew on young oceanic lithosphere, Mitchell (2003) suggested that large-scale flank collapses would be more frequent in volcanic islands that surpassed a threshold height of ca. 2500 m. Here, just considering the effect of cohesion as a function of depth, without considering the possible effect of "external forces" as the ones induced by dyke intrusions or enrichment in weaker materials in larger volcanic edifices, we reach a similar threshold of critical volcanic edifice dimensions.

We observe that the effect of changing $\mu_b$ becomes more important than the effect of changing cohesion (Fig. 4, see horizontal spacing between $\lambda^*$ values for different cohesions,

comparatively to spacing between values of different $\mu_b$). This was expected given the much higher values of lithostatic load at these depths, comparatively to the cohesion values (Eq. 2).

(2)

$$\tau = \mu_b \times \sigma_n + Co_b$$

The tests with different $\alpha$ values illustrate the effect of over-steepening, and the different conditions required for failure in low-slope shield volcanoes and steeper volcanic ridges and stratovolcanoes (Figs. 4a and 4b). The substantially smaller $\lambda^*$ required to produce failure in the test with the strongest slopes of 15º (Fig. 4b) illustrates the easier attainment of failure in the volcanic edifices with steep slopes than in flat shield volcanoes.

For the scenarios with $\alpha$ = 7º (Fig. 4a), the value of $\lambda^*$ required for failure along the basal detachment was always smaller than $\lambda_c^*$, and thus the failure of the edifice would occur more easily along the basal detachment (Fig. 5a). However, for the steepened flank of α = 15º (Fig. 4b), for the strongest cohesion value and $\mu_b$, and if $H$ < 2500 m, the $\lambda^*$ required for failure along the basal detachment would be higher than $\lambda_c^*$ (question marks in Fig. 4b). Under these conditions, it would be more likely for shallower internal failure to occur, instead of failure along the basal detachment (Fig. 5b). The interpretation of the more likely occurrence of shallow landsliding in steeper volcanic ridges is compatible with the usual comparisons between the flatter shield volcanoes in Hawaii, affected by deep-seated collapses, and the steeper volcanic ridges in Canary Islands, with shallower flank failures (Carracedo, 1999; Mitchell et al., 2002; Morgan and McGovern, 2005a).

Although the smaller $\lambda^*$ required for failure in steep volcanic ridges suggests the potential for more frequent large-scale landslides in these edifices, it is necessary to take into account the different capacities for build-up of fluid overpressure in the different geological settings: e.g., the higher rate of volcanic growth in Hawaii (Carracedo, 1999), and the differences in composition of the sedimentary material underlying the volcanic edifices (Mitchell et al., 2002) suggest a higher potential for build-up of fluid overpressure than in the Canary Islands (Morgan and McGovern, 2005a).

The dimensions of the Azores Islands are much smaller than the dimensions of the Hawaii or Canary islands. Based on our model interpretations, the $\lambda^*$ values necessary to induce deep-seated gravitational destabilization in these small islands would be larger than those required in the larger Canary or Hawaiian edifices.

Despite the larger values of $\lambda^*$ required, large-scale collapses in the Azores islands have been increasingly recognized, and generally affect both shield volcanoes and volcanic

ridges that barely reach the threshold heights of ca. 2000-2500 m (e.g. Mitchell, 2003; Hildenbrand et al., 2012; Costa et al., 2014; Costa et al., *submitted*; Marques et al., 2013; Sibrant et al., 2014).

We saw for the steepest flanks ($\alpha$ = 15º), for the strongest cohesion and $\mu_b$, and $H$ < 2500 m (question marks in Fig. 4b), that it would be more likely for shallower failure parallel to the flank surface to occur, instead of failure along a basal detachment (Fig. 5b). Such is the case of Azores, where the volcanic edifices are not only steep (as discussed for Canary Islands), but also barely reach the threshold heights of ca. 2000-2500.

We consider that the seismic activity associated with the tectonic setting in the Azores may have compensated the effect of the small dimensions of the edifices, allowing the occurrence of fluid overpressure "peaks" (Elsworth and Voight, 1996), and thus allowing the flank collapses to develop even in such relatively small volcanic edifices.

The quick development of the volcanic edifices for the Pico-Faial volcanic ridge (Costa et al., *submitted*), especially the growth of the volcanic ridge segment that suffered catastrophic collapses (Costa et al., 2014), suggests the occurrence of periods of intense volcanic activity, with potentially fast build-up of fluid overpressure within the edifices. Furthermore, the effect of dike intrusion, deeply explored in the literature but not considered in this model, should play an important role and could have also contributed to the destabilization of the Azorean volcanic edifices.

### *5.2. Implications/ limitations of the model and the application presented*

#### *5.2.1. Scale (in)dependency of deformation - applied vs. gravitational forces*

Works on fluid overpressures associated with magma intrusion, using a rigid-wedge approach, without considering cohesion (Iverson, 1995), or just considering it implicit in an apparent angle of friction ($\phi$ = 20-60º, Elsworth and Voight, 1996), report the scale-dependency of the deformed mass as a function of the fluid overpressure. For mechanical effects of the magma intrusion, Iverson (1995) alerted that, for non-negligible fluid overpressure, the safety factor (resisting forces divided by driving forces) decreases with increasing fluid overpressure, and this overpressure is directly proportional to the length of the deformed wedge. Considering both mechanical and thermal effects of the magmatic intrusion, Elsworth and Voight (1996) observed that the safety factor decreases exponentially with increasing width of the wedge. An exception was found for mechanically-induced

overpressures. Considering large intrusion rates, and for extremely wide wedges, the safety factor rises with increasing wedge width (Elsworth and Voight, 1996).

This interpretation of scale-dependency between deformed wedge and fluid overpressure, from rigid-wedge models in which the influence of cohesion is ignored or not explicitly considered, is not comparable with the interpretations resulting from the adaptation of the CCW to gravitational instabilities in a non-cohesive wedge (Mourgues et al., 2014). In this case, the CCW points to scale-independency of the deformation.

Both approaches are different, with different assumptions: e.g., Iverson (1995) (mechanical pressurization of fluids) and Elsworth and Voight (1996) (mechanical and thermal pressurization of fluids) address the destabilizing effect of a source of pressurization "external" to the rigid-wedge, i.e. magmatic intrusion on the backwall of the wedge. In turn,, the CCW adaptation to gravitational destabilization from Mourgues et al. (2014) just considers gravitational forces, and does not take into account forces external to the wedge. Therefore, these approaches are not directly comparable. Like Mourgues et al. (2014), we just consider gravitational forces, but we consider cohesive wedges (Costa et al., *in prep*). A major difference between our cohesive model and the non-cohesive model by Mourgues et al. (2014) is that in a cohesive wedge, the deformation involving gravitational forces alone becomes scale-dependent.

### *5.2.2. Topographic stresses*

Morgan and McGovern (2005b) showed a variation of the orientation of the maximum compressive stress ($\sigma_1$) within the volcanic edifice: $\sigma_1$ is sub-vertical below the axis of the edifice and progressively rotates outwards, towards the more distal domains of the volcanic edifice (Fig. 6a). This variation in $\sigma_1$ orientation is attributed to the effect of a triangular topography in cross-section (Morgan and McGovern, 2005b, in agreement with Fiske and Jackson, 1972; Dieterich, 1988). It implies an increment of the shear stress relatively to normal stress (increasing $\tau/\sigma_n$) towards the distal part of the edifice.

We here consider the following alternative expression of Amonton's Law for the basal surface:

$$\tau/\sigma_n = \mu_b + Co_b/\sigma_n \quad (3)$$

Along the basal surface, a critical value of $\tau/\sigma_n$ can be reached, resulting in the gravitational destabilization limited to thinner/more distal domains, while the core of the edifice remains stable. We define this critical point as the Maximum Failure Length. As can be seen in Eq. 3, the critical value of $\tau/\sigma_n$ is smaller for simulations with smaller basal strength, leading to failures rooted more deeply in the edifice.

However, the original works on non-cohesive CCW by Davis, Dahlen and co-authors, as well as the recent reformulation presented in Mourgues et al. (2014) and the approximation of our cohesive analytical model to a practically null cohesion, show an orientation of $\sigma_1$ constant within the wedge (Fig. 6b). The ratio $\tau/\sigma_n$ is constant along the basal surface, thus not constraining the location of failure along the basal detachment.

For a non-negligible cohesion, the model of Costa et al. (*in prep*) shows a variation of $\sigma_1$ orientation contrary to the variation induced by the topography (Morgan and McGovern, 2005b), which is steeper in the front of the wedge and progressively less inclined towards the thicker sector of the wedge (Fig. 6c). As stated in Costa et al. (*in prep*), the effect of cohesion implies the stabilization of the most superficial/thinner sectors of the wedge (defining a Minimum Failure Length), an implication contrary to that of the topographic effect.

Mourgues et al. (2014) and Costa et al. (*in prep*) follow the assumption that the slope is infinite, not considering the effect of the peaked configuration on the stress field. Thus, although the wedge configuration corresponds geometrically to a slice of a volcanic edifice (Figs. 6b and 6c), it cannot be directly studied as a full edifice's flank.

Topography and cohesion have opposite effects on the spatial localization of the failure: topography imposes a Maximum Failure Length, i.e. contributes to a stable core and unstable distal domains, whereas cohesion imposes a Minimum Failure Length, and thus contributes to an unstable core and stable distal domains. The integration of the topography effect in the cohesive analytical model of the wedge (Costa et al., *in prep*), would: (a) improve the spatial constrain of the unstable domains in a cohesive edifice, constrained between the Maximum and Minimum Failure Lengths within the flank; (b) allow the study of the impact of fluid overpressure on this unstable domain.

As the topography effect inhibits the failure in the thickest part of the wedge, the minimum fluid overpressure ratio values required to trigger failure along the basal detachment in the cohesive scenario would be even higher than the values here presented.

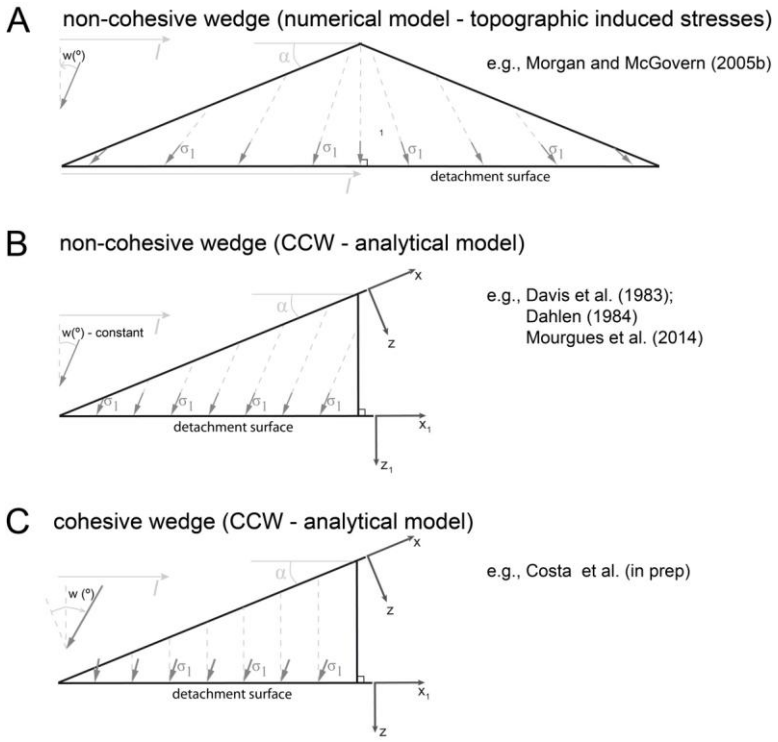


**Fig. 1**. Orientation of the maximum compressive stress ($\sigma_1$) within the volcanic edifice for: (A) Topographically-induced stresses; (B) non-cohesive CCW applied to gravitational destabilization; (C) cohesive CCW applied to gravitational destabilization.

*5.2.3. Constant/Variable fluid overpressure ratio values for wedge and basal detachment*

In the tests presented above, the $\lambda^*$ was considered as constant for the basal detachment and wedge. The use of different $\lambda^*$ values for the basal detachment and wedge, would allow the determination of the impact of permeability contrasts to the stability of the edifice.

In the model presented in Costa et al. (i*n prep*), it was initially established that there would be no stress gradients along the *x* axis, parallel to the wedge's upper surface. The properties defined for the material/surface (i.e., fluid overpressure ratio - $\lambda^*$, coefficient of internal friction - $\mu$) can be different for the wedge and for the basal detachment, but do not vary within the wedge or along the basal detachment.

The establishment of these properties as constant seems far from the expected scenarios in volcanic systems, where lateral changes of basal strength (e.g., roughness) and fluid overpressure can be produced (increment or decrease of fluid overpressure ratio towards the core of the edifice) (Morgan and McGovern, 2005a). The variation of the fluid overpressure ratio along the basal detachment is dependent on: the edifice configuration,

permeability contrasts within the edifice, source location/shape, and rate of injected fluid. The application of a constant fluid overpressure ratio to the whole domain of the model would imply an underevaluation of the stability conditions in the domains (actually) not affected by such a high pore fluid pressure (del Potro et al., 2013).

## 6. Conclusions

Under the values used in this work for the slope of the volcanic flanks ($\alpha$ = 7º and 15º), the dip of the basal detachment ($\beta$ between 0º and 2°), the height of the maximum wedge above the basal detachment (*H,* up to 5500 m), the cohesion of the volcanic wedge ($Co_w$, from 0 to 2.6 MPa), the cohesion in the basal detachment ($Co_b$ from 0 to 0.9 MPa), the coefficient of internal friction of the volcanic wedge ($\mu_w$ = 0.45), the coefficient of internal friction of the basal detachment ($\mu_b$ in the range 0.18 and 0.32), and the fluid overpressure ratio ($\lambda$*, ranging from 0 to higher than 1), we conclude that:

- The steepening of $\alpha$ and $\beta$ lead to a decrease in the $\lambda$* necessary to produce failure.
- The accentuated decrease of the stabilizing effect of $Co_w$ with increasing depth favors the occurrence of deep-seated large-scale gravitational destabilization in volcanic edifices higher than ca. 2000-2500 m. For smaller volcanic edifices, the $\lambda$* required to induce failure are comparatively larger and, for steep and stronger volcanic edifices, the occurrence of shallow failure is favored (parallel to the edifice flank surface), instead of deep-seated failure.
- With increasing *H*, while the relative importance of $Co_w$ for the stability of the edifice decreases, the relative importance of $\mu_b$ increases.

## 7. Perspectives

Add external forces to the model (e.g., lateral magma push).

Test the effect of contrasting permeabilities along the basal detachment and within the wedge. This would reflect the permeability contrasts observed in the nature.

Test the impact of laterally varying fluid overpressure ratio and internal friction along the basal detachment on the stability of the edifice.

Assess the impact of different mechanical properties of the sediments underlying the volcanic edifice (Hawaii vs. Canary Islands vs. Azores).

Determine the potential to build-up fluid overpressure in shield-volcanoes and steep volcanic ridges, considering differences in the constituting materials (e.g., more abundance of

pyroclastic/porous/easily altered materials in steep volcanic ridges), different rates of volcanic growth and tectonic setting.

**Acknowledgments**

This is a contribution to Project MEGAHazards (PTDC/CTE-GIX/108149/2008), funded by FCT, Portugal. ACGC benefits from a PhD scholarship funded by FCT (SFRH/BD/68983/2010).

**References**

Batiza, R., White, J.D.L., 1999. Submarine lavas and hyaloclastite. In: Sigurdsson, H., Houghton, B., McNutt, S.R., Rymer, H., Stix, J. (Eds.), Encyclopedia of Volcanoes. Academic Press, pp. 361─382.

Carracedo, J.C., 1999. Growth, structure, instability and collapse of Canarian volcanoes and comparisons with Hawaiian volcanoes. Journal of Volcanology and Geothermal Research 94, 1-19.

Cecchi, E., van Wyk de vries, B., Lavest, J.-M., 2005. Flank spreading and collapse of weak-cored volcanoes. Bulletin of Volcanology 67, 72-91. http://dx.doi.org/10.1007/s00445-004-0369-3

Costa, A.C.G., Marques, F.O., Hildenbrand, A., Sibrant, A.L.R., Catita, C.M.S., 2014. Large-scale catastrophic flank collapses in a steep volcanic ridge: The Pico–Faial Ridge, Azores Triple Junction. J. Volcanol. Geotherm. Res. 272, 111 –125, http://dx.doi.org/10.1016/j.jvolgeores.2014.01.002.

Costa, A.C.G., Hildenbrand, A., Marques, F.O., Sibrant, A.L.R., Santos de Campos, A., *submitted*.Growth and collapse of Pico Island during its 200 kyr life time (Pico-Faial ridge, Azores Triple Junction).

Costa, A.C.G., Mourgues, R., Marques, F.O., Lacoste, A., Garibaldi, C., Bulois, C., Hildenbrand, A., Boulesteix, T., *in prep*. Gravitational instability in a cohesive granular material atop an overpressured detachment - analytical derivation and experimental testing.

Dahlen, F.A., Suppe, J., Davis, D., 1984. Mechanics of Fold-and-Thrust Belts and Accretionary Wedges: Cohesive Coulomb Theory. Journal of Geophysical Research 89 (B12), 10087-10101.

Davis, D., Suppe, J., Dahlen, F.A., 1983. Mechanics of fold-and-thrust belts and accretionary wedges. Journal of Geophysical Research 88 (B2), 1153–1172.

Day, S.J., 1996. Hydrothermal pore fluid pressure and the stability of porous, permeable volcanoes. In: McGuire, W.J., Jones, A.P., Neuberg, J. (Eds.), Volcano Instability on the Earth and Other Planets. Geological Society Special Publication, London, 77–93.

del Potro, R., Hürlimann, M., 2009. The decrease in the shear strength of volcanic materials with argillic hydrothermal alteration, insights from the summit region of Teide stratovolcano, Tenerife. Engineering Geology 104, 135-143.

del Potro, R., Hürlimann, M., Pinkerton, H., 2013. Modelling flank instabilities on stratovolcanoes: Parameter sensitivity and stability analyses of Teide, Tenerife. Journal of Volcanology and Geothermal Research 256, 50-60. http://dx.doi.org/10.1016/j.jvolgeores.2013.02.003

Delcamp, A., van Wyk de Vries, B., James, M.R., 2008. The influence of edifice slope and substrata on volcano spreading. Journal of Volcanology and Geothermal Research 177, 925–942. http://dx.doi.org/10.1016/j.jvolgeores.2008.07.014

DePaolo, D., E. Stolper, and D. Thomas (2001), Deep drilling into a Hawaiian volcano, Eos Trans. AGU, 82, 149.

Dieterich, J. H., 1988. Growth and persistence of Hawaiian volcanic rift zones, J. Geophys. Res. 93, 4258– 4270.

Donnadieu, F., Merle, O., 1998. Experiments on the indentation process during cryptodome intrusions: New insights into Mount St. Helens deformation. Geology 26,79–82.

Elsworth, D., Voight, B., 1995. Dike intrusion as a trigger for large earthquakes and the failure of volcano flanks. Journal of Geophysical Research 100 (B4), 6005-6024.

Elsworth, D., Voight, B., 1996. Evaluation of volcano flank instability triggered by dyke intrusion. In: McGuire, W.J., Jones, A.P., Neuberg, J. (Eds.), Volcano Instability on the Earth and Other Planets. Geological Society Special Publication, London, 45-53.

Fiske, R.S., Jackson, E.D., 1972. Orientation and Growth of Hawaiian Volcanic Rifts: The Effect of Regional Structure and Gravitational Stresses. Proc. R. Soc. Lond. A 329, 299-326. http://dx.doi.org/10.1098/rspa.1972.0115

Fornari, D.J., Malahoff, A., Heezen, B.C., 1979. Submarine slope micro-morphology and volcanic substructure of the Island of Hawaii inferred from visual observations made from U.S. Navy deep-submergence vehicle (DSV) "Sea Cliff": Marine Geology 32 (1-2), 1–19. http://dx.doi.org/10.1016/0025-3227(79)90143-9

Garcia, M.O., Davis, M.G., 2001. Submarine growth and internal structure of ocean island volcanoes based on submarine observations of Mauna Loa volcano, Hawaii. Geology, 29 (2), 163 – 166.

Garcia, M. O., Haskins, E.H., Stolper, E.M., Baker, M., 2007. Stratigraphy of the Hawai‘i Scientific Drilling Project core (HSDP2): Anatomy of a Hawaiian shield volcano, Geochem. Geophys. Geosyst., 8, Q02G20, http://dx.doi.org/10.1029/2006GC001379.

Hildenbrand, A., Marques, F.O., Catalão, J., Catita, C.M.S., Costa, A.C.G., 2012. Large-scale active slump of the southeastern flank of Pico Island, Azores. Geology 40 (10), 939–942. http://dx.doi.org/10.1130/G33303.1.

Iverson, R.M., 1995. Can magma-injection and groundwater forces cause massive landslides on Hawaiian volcanoes? Journal of Volcanology and Geothermal Research 66, 295-308.

Jaeger, J.C., Cook, N.G.W., 1979. Fundamentals of Rock Mechanics. Chapman and Hall, New York.

López, D.L., Williams, S.N., 1993. Catastrophic Volcanic Collapse: Relation to Hydrothermal Processes. Science (New Series) 260, No. 5115, 1794-1796.

Marques, F.O., Sibrant, A., Hildenbrand, A., Costa, A.C.G., 2013. Large-scale Sector Collapses in the Evolution of Santa Maria Island, Azores. AGU Fall Meeting 2013, Abstract V51D-2719, San Francisco, California, 9-13 Dec.

McGuire, W.J., 1996. Volcano instability: a review of contemporary themes. In: McGuire, W.J., Jones, A.P., Neuberg, J. (Eds.), Volcano Instability on the Earth and Other Planets. Geological Society Special Publication, London, 1–23.

Mitchell, N.C., 2003. Susceptibility of mid-ocean ridge volcanic islands and seamounts to large-scale landsliding. J. Geophys. Res. 108 (B8), 2397. http://dx.doi.org/10.1029/2002JB001997.

Mitchell, N.C., Masson, D.G., Watts, A.B., Gee, M.J.R., Urgeles, R., 2002. The morphology of the submarine flanks of volcanic ocean islands A comparative study of the Canary and Hawaiian hotspot islands. Journal of Volcanology and Geothermal Research 115, 83-107.

Moore, J.G., 2001. Density of basalt core from Hilo drill hole, Hawaii. Journal of Volcanology and Geothermal Research 112, 221-230.

Moore, J.G., and Chadwick Jr., W.W., 1995. Offshore geology of Mauna Loa and adjacent area, Hawaii, In: Rhodes, J.M., and Lockwood, J.P. (Eds.), Mauna Loa revealed: Structure, Composition, History and Hazards. Geophysical Monograph 92, American Geophysical Union, Washington DC, pp. 21–44.

Moore, J.G., Clague, D.A., 2002.Mapping the Nuuanu and Wailau Landslides in Hawaii. In: Takahashi, E., Lipman, P.W., Garcia, M.O., Naka, J., Aramaki, S. (Eds.),Hawaiian volcanoes: deep underwater perspectives. Geophysical Monograph Series, 128. American Geophysical Union, Washington D.C., pp. 223–244. http://dx.doi.org/10.1029/GM128.

Moore, J.G., Clague, D.A., Holcomb, R.T., Lipman, P.W., Normark,W.R., Torresan, M.E., 1989. Prodigious submarine landslides on the Hawaiian Ridge. J. Geophys. Res. 94 (B12), 17465–17484. http://dx.doi.org/10.1029/JB094iB12p17465.

Mourgues, R., Lacoste, A., Garibaldi, C., 2014. The Coulomb critical taper theory applied to gravitational instabilities. Journal of Geophysical Research (Solid Earth) 119 (1), 754-765. http://dx.doi.org/10.1002/2013JB010359

Morgan, J.K., Clague, D.A., 2003. Volcanic spreading on Mauna Loa volcano, Hawaii: Evidence from accretion, alteration, and exhumation of volcaniclastic sediments. Geology 31 (5), 411-414.

Morgan, J. K., McGovern, P.J., 2005a. Discrete element simulations of gravitational volcanic deformation: 1. Deformation structures and geometries, J. Geophys. Res. 110, B05402. http://dx.doi.org/10.1029/2004JB003252.

Morgan, J. K., McGovern, P.J., 2005b. Discrete element simulations of gravitational volcanic deformation: 2. Mechanical analysis, J. Geophys. Res. 110, B05403. http://dx.doi.org/10.1029/2004JB003253.

Nielson, D. L., Stiger, S.G., 1996. Drilling and evaluation of Ascension #1, a geothermal exploration well on Ascension Island, South Atlantic Ocean. Geothermics 25 (4/5), 543–560, 1996.

Oehler, J.F., van Wyk de Vries, B., Labazuy, P., 2005. Landslides and spreading of oceanic hot-spot and arc shield volcanoes on Low Strength Layers (LSLs): an analogue modelling approach. Journal of Volcanology and Geothermal Research 144, 169-189. http://dx.doi.org/10.1016/j.jvolgeores.2004.11.023.

Pola, A., Crosta, G., Fusi, N., Barberini, V., Norini, G., 2012. Influence of alteration on physical properties of volcanic rocks. Tectonophysics 566-567, 67-86. http://dx.doi.org/10.1016/j.tecto.2012.07.017

Pola, A., Crosta, G.B., Fusi, N., Castellanza, R., 2014. General characterization of the mechanical behaviour of different volcanic rocks with respect to alteration. Engineering Geology 169, 1-13. http://dx.doi.org/10.1016/j.enggeo.2013.11.011

Quidelleur, X., Hildenbrand, A., Samper, A., 2008. Causal link between Quaternary paleoclimatic changes and volcanic islands evolution. Geophysical Research Letters 35, L02303. http://dx.doi.org/10.1029/2007GL031849.

Reid, M.E., 2004. Massive collapse of volcano edifices triggered by hydrothermal pressurization. Geology 32 (5), 373–376. http://dx.doi.org/10.1130/G20300.1

Reid, M.E., Sisson, T.W., Brien, D.L., 2001. Volcano collapse promoted by hydrothermal alteration and edifice shape, Mount Rainier, Washington. Geology 29, 779-782.

Reid, M.E., Keith, T.E.C., Kayen, R.E., Iverson, N.R., Iverson, R.M., Brien, D.L., 2010. Volcano collapse promoted by progressive strength reduction: new data from Mount St. Helens. Bull Volcanol 72, 761-766. http://dx.doi.org/10.1007/s00445-010-0377-4

Satake, K., Smith, J.R., Shinozaki, K., 2002. Three-dimensional reconstruction and tsunami model of the Nuuanu and Wailau giant landslides, Hawaii. In: Takahashi, E., Lipman, P.W., Garcia, M.O., Naka, J., Aramaki, S. (Eds.), Hawaiian Volcanoes: Deep Underwater Perspectives. Geophysical Monograph Series 128. American Geophysical Union, Washington D.C., pp. 333–346. http://dx.doi.org/10.1029/GM128.

Schiffman, P., Watters, R.J., Thompson, N., Walton, A.W., 2006. Hyaloclastites and the slope stability of Hawaiian volcanoes: insights from the Hawaiian Scientific Drilling Project's 3-km drill core. Journal of Volcanology and Geothermal Research 151 (1–3), 217–228.

Schmidt, R., Schminke, H.U., 1999. Seamounts and island building. In: Sigurdsson, H., Houghton, B., McNutt, S.R., Rymer, H., Stix, J. (Eds.), Encyclopedia of Volcanoes. Academic Press, pp. 383─402.

Schultz, R.A., 1995. Limits on strength and deformation properties of jointed basaltic rock masses. Rock Mechanics and Rock Engineering 28 (1), 1–15.

Schultz, R.A., 1996. Relative scale and the strength and deformability of rock masses. Journal of Structural Geology 18 (9), 1139–1149.

Sibrant, A.L.R., Marques, F.O., Hildenbrand, A., 2014. Construction and destruction of a volcanic island developed inside an oceanic rift: Graciosa Island, Terceira Rift, Azores. J. Volcanol. Geotherm. Res. 284, 32-45. http://dx.doi.org/10.1016/j.jvolgeores.2014.07.014

Siebert, L., 1984. Large volcanic debris avalanches: characteristics of source areas, deposits and associated eruptions. J. Volcanol. Geotherm. Res. 22, 163–197.

Sparks, R.S.J., 1997. Causes and consequences of pressurisation in lava dome eruptions. Earth and Planetary Science Letters 150, 177-189.

Staudigel, H., Schmincke, H.-U., 1984. The Pliocene Seamount Series of La Palma/Canary Islands. Journal of Geophysical Research 89 (B13), 11125-11215.

Terakawa, T., Yamanaka, Y., Nakamichi, H., Watanabe, T., Yamazaki, F., Horikawa, S., Okuda, T., 2013. Effects of pore fluid pressure and tectonic stress on diverse seismic

activities around the Mt. Ontake volcano, central Japan. Tectonophysics 608, 138-148. http://dx.doi.org/10.1016/j.tecto.2013.10.005.

Thomas, M.E., Petford, N., Bromhead, E.N., 2004a. The effect of internal gas pressurization on volcanic edifice stability: evolution towards a critical state. Terra Nova 16, 312-317. http://dx.doi.org/10.1111/j.1365-3121.2004.00567.x

Thomas, M.E., Petford, N., Bromhead, E.N., 2004b. Volcanic rock-mass properties from Snowdonia and Tenerife: implications for volcano edifice strength. Journal of the Geological Society, London, vol. 161, 1-8.

Thompson, N., Watters, R.J., Schiffman, P., 2008. Stability analysis of Hawaiian Island flanks using insight gained from strength testing of the HSDP core. Journal of Volcanology and Geothermal Research 171, 163–177. http://dx.doi.org/10.1016/j.jvolgeores.2007.11.008

van Wyk de Vries, B., Borgia, A., 1996. The role of basement in volcano deformation. In: McGuire, W.J., Jones, A.P., Neuberg, J. (Eds.), Volcano Instability on the Earth and Other Planets. Geological Society Special Publication, London, 95–110.

van Wyk de Vries, B., Kerle, N., Petley, D., 2000. Sector collapse forming at Casita volcano, Nicaragua. Geology 28 (2), 167-170. http://dx.doi.org/10.1130/0091-7613(2000)28<167:SCFACV>2.0.CO;2

Voight, B., Elsworth, D., 1997. Failure of volcano slopes. Géotechnique 47 (1), 1-31.

Voight, B., Elsworth, D., 2000. Instability and collapse of hazardous gas-pressurized lava domes. Geophysical Research Letters 27 (1), 1-4.

Voight, B., Janda, R.J., Glicken, H., Douglass, P.M. 1983. Nature and mechanics of the Mt. St. Helens rockslide–avalanche of 18th May 1980. Géotechnique 33, 243–227.

Walder, J., Nur, A., 1984. Porosity reduction and crustal pore pressure development. Journal of Geophysical Research 89 (B13), 11539-11548.

Walker, G.P.L., 1999. Basaltic volcanoes and volcanic systems. In: Sigurdsson, H., Houghton, B., McNutt, S.R., Rymer, H., Stix, J. (Eds.), Encyclopedia of Volcanoes. Academic Press, pp. 283─290.

Walton, A.W., Schiffman, P., 2003. Alteration of hyaloclastites in the HSDP 2 Phase 1 Drill Core: 1. Description and paragenesis. Geochemistry, Geophysics, Geosystems 4 (5), 8709. http://dx.doi.org/10.1029/2002GC000368.

Watters, R.J., Zimbelman, D.R., Bowman, S.D., Crowley, J.K., 2000. Rock mass strength assessment and significance to edifice stability, Mount Rainier and Mount Hood, Cascade Range Volcanoes. Pure appl. geophys. 157, 957–976.

Zimbelman, D.R., Watters, R.J., Firth, I.R., Breit, G.N., Carrasco-Nunez, G., 2004. Stratovolcano stability assessment methods and results from Citlaltépetl, Mexico. Bull Volcanol 66, 66-79. http://dx.doi.org/10.1007/s00445-003-0296-8

## Appendix A

**Table A.1**. Data from Thompson et al. (2008) regarding the shear strength on natural joints. Tests performed on the core samples from the 3098m deep drill-hole in Hawaii Island (DePaolo et al., 2001), cutting sub-aerial lava flows from Mauna Loa and sub-aerial/submarine deposits from Mauna Kea. Expected lithostatic stress for the samples' depth and considering two limit values for overall density of the rock column (minimum ρ=2500 kg/m$^3$ - e.g., Oehler et al., 2005, and a maximum of ρ=2900 kg/m$^3$ - considering Moore, 2001, that measured high density lava flows). Relative importance of the presented cohesion values determined by Thompson et al. (2008), comparatively to the values of lithostatic stress presented.

| Thompson et al. (2008) -Shear test on natural joints | | | | | Lithostatic stress (MPa) | | % of Cohesion vs. lithostatic | |
|---|---|---|---|---|---|---|---|---|
| Rock type | Alteration zone | Depth(m) | **Cohesion (Mpa)** | Friction angle (º) | ρ= 2500 kg/m$^3$ | ρ= 2900 kg/m$^3$ | ρ= 2500 kg/m$^3$ | ρ= 2900 kg/m$^3$ |
| Sub-aerial basalt flow (aa) | Not altered | 1064.9 | **2.6** | 24.4 | 26.12 | 30.30 | **9.96** | 8.58 |
| Hyaloclastite | Incipient | 1321.5 | **0.9** | 17.6 | 32.41 | 37.60 | **2.78** | 2.39 |
| | Smectitic | 1437.1 | **2.6** | 10.2 | 35.24 | 40.88 | **7.38** | 6.36 |
| | | 1472.2 | **1.2** | 15.8 | 36.11 | 41.88 | **3.32** | 2.87 |
| | | 1577.7 | **0.8** | 19.1 | 38.69 | 44.88 | **2.07** | 1.78 |
| | Palagonitic | 1582.4 | **2** | 14.1 | 38.81 | 45.02 | **5.15** | 4.44 |
| | | 1933.5 | **4.3** | 11.4 | 47.42 | 55.01 | **9.07** | 7.82 |
| Submarine pillow basalt | Not altered | 2116.3 | **8.6** | 13.5 | 51.90 | 60.21 | **16.57** | 14.28 |
| Hyaloclastite | Palagonitic | 2179.4 | **2.8** | 13 | 53.45 | 62.00 | **5.24** | 4.52 |
| Submarine pillow basalt | Not altered | 2368.1 | **4.7** | 23.4 | 58.08 | 67.37 | **8.09** | 6.98 |
| Hyaloclastite | Palagonitic | 2751 | **3.5** | 16.4 | 67.47 | 78.26 | **5.19** | 4.47 |

**References cited:**


DePaolo, D., E. Stolper, and D. Thomas (2001), Deep drilling into a Hawaiian volcano, Eos Trans. AGU, 82, 149.

Moore, J.G., 2001. Density of basalt core from Hilo drill hole, Hawaii. Journal of Volcanology and Geothermal Research 112, 221-230.

Oehler, J.F., van Wyk de Vries, B., Labazuy, P., 2005. Landslides and spreading of oceanic hot-spot and arc shield volcanoes on Low Strength Layers (LSLs): an analogue

modelling approach. Journal of Volcanology and Geothermal Research 144, 169-189. http://dx.doi.org/10.1016/j.jvolgeores.2004.11.023.

Thompson, N., Watters, R.J., Schiffman, P., 2008. Stability analysis of Hawaiian Island flanks using insight gained from strength testing of the HSDP core. Journal of Volcanology and Geothermal Research 171, 163–177. http://dx.doi.org/10.1016/j.jvolgeores.2007.11.008

# PART V

# Chapter 9

# Conclusions

# Conclusions

Despite the steep configuration and the active tectonic setting of the Azores islands, prior to MEGAHazards Project (PTDC/CTE-GIX/108149/2008, funded by FCT, Portugal) large-scale flank failures were considered to be lacking. The present PhD work was focused on the steep Pico-Faial volcanic ridge, which sits on a major normal fault associated with the diffuse Nubia/Eurasia plate boundary.

Based on high-resolution sub-aerial and submarine Digital Elevation Models, new structural and stratigraphic data, and high-resolution K-Ar dating on separated volcanic groundmass we: (1) conclude unequivocally on the occurrence of large-scale flank collapses in the Pico-Faial volcanic ridge; (2) reconstruct with unprecedented resolution the growth and destruction of Pico and Faial islands, focusing specially on the large-scale flank failures that affected Pico Island during the last 200 kyr.

*The Pico-Faial volcanic ridge*

The new volcanic stratigraphy, established during field work and calibrated with K/Ar dating, confirms that Pico Island comprises three main volcanic systems, from older to younger: (1) the Topo Volcano, (2) the Fissural System, and (3) the Pico Stratovolcano. (1) The Topo Volcano is partly exposed on Pico's SE flank, and is here dated between 186 ± 5 and 125 ± 4 or 115 ± 4 ka. It was significantly destroyed by a N-directed large-scale flank collapse between ca. 125 and 70 ka. Offshore, a debris deposit is here identified and interpreted as corresponding to this flank collapse. The deposit has a maximum length of 20 km and covers an area of ca. 150 $km^2$. It comprises hectometre blocks, it has an exposed volume here estimated between 4 and 10 $km^3$, although the actual volume probably exceeds 10 $km^3$, and was channelized between the Pico-Faial and S.Jorge volcanic ridges. During the same period, gradual deformation started in the SE flank of the Topo Volcano, producing a composite collapse structure: (1) a slump complex in the west, which is still active, and (2) a catastrophic flank collapse in the east. A first episode of deformation most probably occurred between ca. 125 and 115 ka, along the master fault of the slump. Between ca. 115 and 75 ka, the scar was partially filled by volcanic products erupted from volcanic cones developed within the slump depression, and possibly from the early WNW-ESE Fissural System. Subsequent deformation in the slump area affected in part the filling units, leading to the

individualization of secondary curved faults. Between ca. 125 and 69 ka, the eastern distal part of Topo's SE flank and the early sub-aerial sequence of the Fissural System experienced a catastrophic flank collapse towards the S, which generated a large offshore debris deposit here identified with a minimum runout of ca. 17 km. More recent volcanic products have gradually masked the mass-wasting scars. The young Pico Stratovolcano grew in the westernmost sector of the island, at least since ca. 57 ka. Its southern flank has been partially destroyed by flank collapse(s), and subsequently covered by more recent volcano-sedimentary products.

The evolution of the Pico-Faial volcanic ridge in the last 200 kyr has been marked by simultaneous volcanic growth and destruction in both Pico and Faial islands. While the Topo Volcano grew in Pico (ca. 186-125 ka) and was partially destroyed (ca. 125-115 ka), in Faial Island the period defined for major deformation in the Faial graben ended (ca. 360-115 ka), and a central volcano started growing inside the graben (ca. 130-115 ka). This rapid and simultaneous evolution of Pico and Faial islands constitutes evidence for the accommodation of extension associated with the Nu-Eu plate boundary on this ridge during the last 200 kyr.

*Analytical and analogue modeling of flank instabilities*

We here present an analytical solution for the cohesive Coulomb Critical Wedge theory applied to gravitational instabilities, and associated analogue simulations to test some structural implications of the model. We investigated the impact of several variables on wedge stability, including: wedge configuration and dimensions, cohesion, coefficient of internal friction and fluid overpressure ratio (fluid overpressure divided by lithostatic pressure), focusing especially on the roles of cohesion and fluid overpressure. We conclude that: (1) the stability of a cohesive wedge under fluid overpressure is size-dependent (the influence of cohesion is more significant for smaller wedges), while the stability of a non-cohesive wedge under fluid overpressure is size-independent. (2) The stabilizing effect of cohesion is more significant for the most superficial domain of the wedge. The thickness of this stable superficial layer decreases with increasing fluid overpressure ratio. (3) Within the layer impacted by cohesion, the principal compressive stress rotates and the expected faults are listric. If the thickness limit expected for this layer is reached within the wedge (given the properties of the materials, the fluid overpressure ratio, and the configuration of the wedge),

the generated listric faults become parallel to the wedge's upper surface at the thickness limit. This limit means that the material strength reached the failure envelope.

We assessed the stability of the wedge along a basal detachment, through comparison of the forces driving and resisting the downslope movement. We verified that the stabilizing effect of cohesion is accentuated in the foremost thin domain of the wedge, defining a required Minimum Failure Length (*MFL*). This *MFL* decreases for smaller cohesions, smaller coefficients of internal friction, larger fluid overpressure ratios, steeper upper surface and basal detachment of the wedge.

Although this analytical model does not integrate the effects of topography in the stress field, we applied it to gravitational instabilities in volcanic systems, considering as variables: slope and dimensions of the volcanic edifice (volcanic flanks dipping 7-15°, basal detachment surfaces dipping 0-2°, maximum wedge height above the basal detachment up to 5500 m), cohesion (volcanic wedge: from 0 to 2.6 MPa; basal detachment: from 0 to 0.9 MPa), coefficient of internal friction (volcanic wedge: 0.45; basal detachment: 0.18 and 0.32), and fluid overpressure (ranging from null to higher than the lithostatic pressure). We conclude that: (1) the steepening of the volcanic flanks and basal detachment lead to a decrease in the fluid overpressure ratio necessary to produce failure. (2) The decrease of the stabilizing effect of cohesion with increasing depth favours the occurrence of deep-seated large-scale gravitational destabilization in basal detachments deeper than (volcanic edifices higher than) ca. 2000-2500 m. For shallower basal detachments, the overpressure ratios required to induce failure are comparatively larger. For shallower basal detachments, steeper flanks and stronger edifice materials, shallow failure parallel to the flank surface is favoured, instead of deep-seated deformation. (3) With increasingly deeper basal detachments (possible in larger volcanic edifices), while the impact of cohesion diminishes, the relative importance of basal internal friction for the stability of the edifice increases.

This work is a contribution to MEGAHazards Project. The investigation of the occurrence of large-scale mass-wasting in the Azores islands, and the modelling of the variables controlling the stability of the volcanic edifices are only at their first steps, and will be further developed in the near future.

# Chapter 10

# References

# References


Acocella, V., Neri, M., 2009. Dike propagation in volcanic edifices: Overview and possible developments. Tectonophysics 471, 67─77. http://dx.doi.org/10.1016/j.tecto.2008.10.002

Adam, C., Madureira, P., Miranda, J.M., Lourenço, N., Yoshida, M., Fitzenz, D., 2013. Mantle dynamics and characteristics of the Azores plateau. Earth and Planetary Science Letters 362, 258–271.

Afonso, A., Gomes, F., Fernandes, M., 2002. IGeoE: Cartografia de qualidade - a base de um SIG. Tribuna das Autarquias 108 (Jun. 2002), 13-14.

Altamimi Z., Collilieux, X., Métivier, L., 2011. ITRF2008: an improved solution of the International Terrestrial Reference Frame. J. Geodesy 85, 457-473.

Andersen, O.B., Knudsen, P., Kenyon, S., Trimmer, R., 1999. Recent improvement in the KMS global marine gravity field. Bollettino Geofisica Teorica ed Applicata 40 (3-4), 369–377.

Batiza, R., White, J.D.L., 1999. Submarine lavas and hyaloclastite. In: Sigurdsson, H., Houghton, B., McNutt, S.R., Rymer, H., Stix, J. (Eds.), Encyclopedia of Volcanoes. Academic Press, pp. 361─382.

Beier, C., 2006. The magmatic evolution of oceanic plateaus: a case study from the Azores(Ph.D. thesis) University of Kiel, Germany.

Beier, C., Haase, K.M., Turner, S.P., 2012. Conditions of melting beneath the Azores. Lithos 144–145, 1–11. http://dx.doi.org/10.1016/j.lithos.2012.02.019

Bock, Y., Wdowinski, S., Fang, P., Zhang, J., Behr, J., Genrich, J., Williams, S., Agnew, D., Wyatt, F., Johnson, H., Stark, K., Oral, B., Hudnut, K., Dinardo, S., Young, W., Jackson, D., Gurtner, W., 1997. Southern California Permanent GPS Geodetic Array: Continuous measurements of regional crustal deformation between the 1992 Landers and 1994 Northridge earthquakes: J. Geophys. Res. 102, 18,013- 18,033.

Bonatti, E., 1990. Not So Hot Hot-Spots in the Oceanic Mantle. Science 250, 107-111.

Borges, J. F., Bezzeghoud, M., Buforn, E., Pro, C., Fitas, A., 2007. The 1980, 1997 and 1998 Azores earthquakes and some seismo-tectonic implications. Tectonophysics 435 (1-4), 37 –54. http://dx.doi.org/10.1016/j.tecto.2007.01.008.

Boulesteix, T., Hildenbrand, A., Gillot, P.Y., Soler, V., 2012. Eruptive response of oceanic islands to giant landslides: New insights from the geomorphologic evolution of the Teide–Pico Viejo volcanic complex (Tenerife, Canary). Geomorphology 138 (1), 61–73. http://dx.doi.org/10.1016/j.geomorph.2011.08.025.

Boulesteix, T., Hildenbrand, A., Soler, V., Quidelleur, X., Gillot, P.Y., 2013. Coeval giant landslides in the Canary Islands: Implications for global, regional and local triggers of giant flank collapses on oceanic volcanoes. Journal of Volcanology and Geothermal Research 257, 90-98. http://dx.doi.org/10.1016/j.jvolgeores.2013.03.008.

Bourdon, B., Turner, S.P., Ribe, N.M., 2005. Partial melting and upwelling rates beneath the Azores from a U-series isotope perspective. Earth and Planetary Science Letters 239 (1–2), 42–56. http://dx.doi.org/10.1016/j.epsl.2005.08.008

Bryn, P., Berg, K., Forsberg, C.F., Solheim, A., Kvalstad, T.J., 2005. Explaining the Storegga Slide. Marine and Petroleum Geology 22, 11-19. doi:10.1016/j.marpetgeo.2004.12.003

Burrough, P.A., McDonnell, R.A., 1998. Principles of Geographical Information Systems. Oxford University press, New York, 333 pp.Carracedo, J.C., Day, S.J., Guillou, H., Torrado, F.J.P., 1999. Giant Quaternary landslides in the evolution of La Palma and El Hierro, Canary Islands, Journal of Volcanology and Geothermal Research 94 (1–4), 169-190. http://dx.doi.org/10.1016/S0377-0273(99)00102-X.

Calvert, A.T., Moore, R.B., McGeehin, J.P., Rodrigues da Silva, A.M., 2006. Volcanic history and $^{40}Ar/^{39}Ar$ and $^{14}C$ geochronology of Terceira Island, Azores, Portugal. Journal of Volcanology and Geothermal Research 156, 103–115. doi:10.1016/j.jvolgeores.2006.03.016.

Calvert, A.T., Moore, R.B., McGeehin, J.P., da Silva, A.M.R., 2006. Volcanic history and Ar-40/Ar-39 and C-14 geochronology of Terceira Island, Azores, Portugal. J. Volcanol. Geotherm. Res. 156, 103-115.

Cannat, M., Briais, A., Deplus, C., Escartin, J., Georgen, J., Lin, J., Mercouriev, S., Meyzen, C., Muller, M., Pouliquen, G., Rabain, A., da Silva, P., 1999. Mid-Atlantic Ridge-Azores hotspot interactions: along-axis migration of a hotspot-derived event of enhanced magmatism 10 to 4 Ma ago. Earth and Planetary Science Letters 173 (3), 257–269. http://dx.doi.org/10.1016/S0012-821X(99)00234-4

Carracedo, J.C., 1994. The Canary Islands: an example of structural control on the growth of large oceanic-island volcanoes. Journal of Volcanology and Geothermal Research 60, 225-241.

Carracedo, J.C., 1999. Growth, structure, instability and collapse of Canarian volcanoes and comparisons with Hawaiian volcanoes. Journal of Volcanology and Geothermal Research 94, 1-19.

Cassignol, C., Gillot, P.Y., 1982. Range and effectiveness of unspiked potassium–argon dating: experimental groundwork and applications. In: Odin, G.S. (Ed.), Numerical Dating in Stratigraphy. John Wiley & Sons Ltd, Chichester, England, pp. 159–179.

Catalão, J., Bos, M.S., 2008. Sensitivity analysis of the gravity geoid estimation: A case study on the Azores plateau. Physics of the Earth and Planetary Interiors 168 (1-2), 113-124. http://dx.doi.org/10.1016/j.pepi.2008.05.010.

Catalão, J., Miranda, J.M., Lourenço, N., 2006. Deformation associated with the Faial (Capelinhos)1957–1958 eruption: Inferences from 1937–1997 geodetic measurements. Journal of Volcanology and Geothermal Research 155, 151-163. http://dx.doi.org/10.1016/j.jvolgeores.2006.03.028

Catalão, J., Nico, G., Hanssen, R., Catita, C., 2011. Merging GPS and atmospherically corrected InSAR data to map 3D terrain displacement velocity: IEEE Transactions on Geoscience and Remote Sensing 49, 2354–2360. doi:10.1109/TGRS.2010.2091963.

Catita, C., Feigl, K.L., Catalão, J., Miranda, J.M., Victor, L.M., 2005. Time series analysis of SAR data applied to the study of the co-seismic deformation of the 9th July 1998 Pico-Faial (Azores) earthquake. International Journal of Remote Sensing 26, 2715–2729. doi:10.1080/01431160512331337835.

Cecchi, E., van Wyk de vries, B., Lavest, J.-M., 2005. Flank spreading and collapse of weak-cored volcanoes. Bulletin of Volcanology 67, 72-91. http://dx.doi.org/10.1007/s00445-004-0369-3

Chovelon, P., 1982. Evolution volcanotectonique des iles de Faial et de Pico. Ph.D. Thesis.Univ. Paris-Sud, Orsay, France, 186 pp.

Clouard, V., Bonneville, A., 2004. Submarine Landslides in French Polynesia, In: Hekinian, R., Stoffers, P, Cheminé, J.-L. (Eds.), Oceanic Hotspots: intraplate submarine magmatism and tectonism. Springer-Verlag, pp. 209-238.

Clouard, V., Bonneville, A., Gillot, P.Y., 2001. A giant landslide on the southern flank of Tahiti Island, French Polynesia. Geophys. Res. Lett. 28, 2253–2256.

Cobbold, P.R., Castro, L., 1999. Fluid pressure and effective stresses in sandbox models. Tectonophysics, 301, 1-19.

Cobbold, P.R., Mourgues, R., Boyd, K., 2004. Mechanism of thin-skinned detachment in the Amazon fan: assessing the importance of fluid overpressure and hydrocarbon generation. Marine and Petroleum Geology 21, 1013-1025.

Cobbold, P.R., Zanella, A., Rodrigues, N., Loseth, H., 2013. Bedding-parallel fibrous veins (beef and cone-in-cone): Worldwide occurrence and possible significance in terms of fluid overpressure, hydrocarbon generation and mineralization. Marine and Petroleum Geology 43, 1-20. http://dx.doi.org/10.1016/j.marpetgeo.2013.01.010

Costa, A.C.G., Marques, F.O., Hildenbrand, A., Sibrant, A.L.R., Catita, C.M.S., 2014. Large-scale catastrophic flank collapses in a steep volcanic ridge: The Pico–Faial Ridge, Azores Triple Junction. J. Volcanol. Geotherm. Res. 272, 111 –125, http://dx.doi.org/10.1016/j.jvolgeores.2014.01.002.

Costa, A.C.G., Hildenbrand, A., Marques, F.O., Sibrant, A.L.R., Santos de Campos, A., *submitted*.Growth and collapse of Pico Island during its 200 kyr life time (Pico-Faial ridge, Azores Triple Junction).

Costa, A.C.G., Mourgues, R., Marques, F.O., Lacoste, A., Bulois, C., Hildenbrand, A., Boulesteix, T., *in prep a*. Gravitational instability in a cohesive granular material atop an overpressured detachment - analytical derivation and experimental testing.

Costa, A.C.G., Mourgues, R., Marques, F.O., Hildenbrand, A., Boulesteix, T., Garibaldi, C., *in prep b*. Cohesive Coulomb critical taper theory applied to gravitational collapses in overpressured volcanic systems: analytical/numerical modeling.

Dahlen, F.A., 1984. Noncohesive critical coulomb wedges: An exact solution. Journal of Geophysical Research 89(B12), 10125–10133.

Dahlen, F.A., 1990. Critical taper model of fold-and-thrust belts and accretionary wedges. Annu. Rev. Earth. Planet. Sci. 18, 55-99.

Dahlen, F.A., Suppe, J., Davis, D., 1984. Mechanics of Fold-and-Thrust Belts and Accretionary Wedges: Cohesive Coulomb Theory. Journal of Geophysical Research 89 (B12), 10087-10101.

Davis, D., Suppe, J., Dahlen, F.A., 1983. Mechanics of fold-and-thrust belts and accretionary wedges. Journal of Geophysical Research 88 (B2), 1153–1172.

Davies, G.R., Norry, M.J., Gerlach, D.C., Cliff, R.A., 1989. A combined chemical and Pb-Sr-Nd isotope study of the Azores and Cape Verde hot-spots: The geodynamic

implications, in: M.J. Saunders (Ed), Magmatism in the ocean basins. Geol. Soc. Special Publication, pp. 231-235.

Day, R., Fuller, M., Schmidt, V.A., 1977. Hysteresis properties of titanomagnetites: Grain size and compositional dependence. Phys. Earth Planet. Inter. 13, 260-267.

Day, S.J., 1996. Hydrothermal pore fluid pressure and the stability of porous, permeable volcanoes. In: McGuire, W.J., Jones, A.P., Neuberg, J. (Eds.), Volcano Instability on the Earth and Other Planets. Geological Society Special Publication, London, 77–93.

Day, S.J., Heleno da Silva, S.I.N, Fonseca, J.F.B.D., 1999. A past giant lateral collapse and present-day flank instability of Fogo, Cape Verde Islands, Journal of Volcanology and Geothermal Research 94 (1–4), 191-218, http://dx.doi.org/10.1016/S0377-0273(99)00103-1.

del Potro, R., Hürlimann, M., 2009. The decrease in the shear strength of volcanic materials with argillic hydrothermal alteration, insights from the summit region of Teide stratovolcano, Tenerife. Engineering Geology 104, 135-143.

del Potro, R., Hürlimann, M., Pinkerton, H., 2013. Modelling flank instabilities on stratovolcanoes: Parameter sensitivity and stability analyses of Teide, Tenerife. Journal of Volcanology and Geothermal Research 256, 50-60. http://dx.doi.org/10.1016/j.jvolgeores.2013.02.003

Delcamp, A., van Wyk de Vries, B., James, M.R., 2008. The influence of edifice slope and substrata on volcano spreading. Journal of Volcanology and Geothermal Research 177, 925–942. http://dx.doi.org/10.1016/j.jvolgeores.2008.07.014

Demande, J., Fabriol, R., Gérard, A., Iundt, F., 1982. Prospection géothermique des Iles de Faial et Pico (Açores). Report 82SGN003GTH, Bureau de Recherches Géologiques et Minières, Orléans, France.

DeMets, C., Gordon, R.G., Argus, D.F., 2010. Geologically current plate motions. Geo-phys. J. Int. 181(1), 1–80. http://dx.doi.org/10.1111/j.1365-246X.2009.04491.x

DePaolo, D., E. Stolper, and D. Thomas (2001), Deep drilling into a Hawaiian volcano, Eos Trans. AGU, 82, 149.

Deplus, C., Le Friant, A., Boudon, G., Komorowski, J.C., Villemant, B., Harford, C., Ségoufin, J., Cheminée, J.L., 2001. Submarine evidence for large-scale debris avalanches in the Lesser Antilles Arc. Earth and Planetary Science Letters 192 (2), 145-157. http://dx.doi.org/10.1016/S0012-821X(01)00444-7.

Dieterich, J. H., 1988. Growth and persistence of Hawaiian volcanic rift zones, J. Geophys. Res. 93, 4258– 4270.

Donnadieu, F., Merle, O., 1998. Experiments on the indentation process during cryptodome intrusions: New insights into Mount St. Helens deformation. Geology 26,79–82.

Duffield, W.A., Stieljes, L., Varet, J., 1982. Huge landslide blocks in the growth of Piton de la Fournaise, La Réunion and Kilauea volcano, Hawaii. Journal of Volcanology and Geothermal Research 12, 147–160. doi:10.1016/0377-0273(82)90009-9.

Elsworth, D., Voight, B., 1995. Dike intrusion as a trigger for large earthquakes and the failure of volcano flanks. Journal of Geophysical Research 100 (B4), 6005-6024.

Elsworth, D., Voight, B., 1996. Evaluation of volcano flank instability triggered by dyke intrusion. In: McGuire, W.J., Jones, A.P., Neuberg, J. (Eds.), Volcano Instability on the Earth and Other Planets. Geological Society Special Publication, London, 45-53.

Elsworth, D., Day, S.J., 1999. Flank collapse triggered by intrusion: the Canarian and Cape Verde archipelagoes. Journal of Volcanology and Geothermal Research 94, 323- 340.

Feigl, K., Agnew, D., Bock, Y., Dong, D., Donnellan, A., Hager, B., Herring, T., Larsen, D., Larson, K., Murray, M., Shen, Z., Webb, F., 1993. Space geodetic measurement of the velocity field of central and southern California, 1984-1992. J. Geophys. Res. 98, 21677-21712.

Féraud, G., 1977. Contribution à la datation du volcanisme de l'archipel des Açores par la méthode Potassium-Argon. Conséquences géodynamiques, thesis Univ. Paris VII, Paris.

Féraud, G., Kaneoka, I., Allègre, C.J., 1980. K/Ar ages and stress pattern in the Azores: Geodynamic implications. Earth and Planetary Science Letters 46 (2), 275–286. http://dx.doi.org/10.1016/0012-821X(80)90013-8.

Fernandes, R.M.S., Miranda, J.M., Catalão, J., Luis, J.F., Bastos, L., Ambrosius, B., 2002. Coseismic displacements of the Mw = 6.1, July 9, 1998, Faial earthquake (Azores, North Atlantic). Geophys. Res. Lett. 29. http://dx.doi.org/10.1029/2001GL014415.

Fernandes, R.M.S., Bastos, L., Ambrosius, B.A.C., Noomen, R., Matheussen, S., Baptista, P., 2004. Recent geodetic results in the Azores Triple Junction region. Pure and Applied Geophysics 161, 683–699. http://dx.doi.org/10.1007/s00024-003-2469-y.

Fernandes, R.M.S., Bastos, L., Miranda, J.M., Lourenço, N., Ambrosius, B.A.C., Noomen, R., Simons, W., 2006. Defining the plate boundaries in the Azores region. Journal of Volcanology and Geothermal Research 156 (1–2), 1-9, http://dx.doi.org/10.1016/j.jvolgeores.2006.03.019.

Ferrer, M., González de Vallejo, L., Seisdedos, J., Coello, J.J., García, J.C:, Hernández, L.E., Casillas, R., Martín, C., Rodríguez, J.A., Madeira, J., Andrade, C., Freitas, M.C., Lomoschitz, A., Yepes, J., Meco, J., Betancort, J.F., 2013. Güímar and La Oratava Mega-Landslides (Tenerife) and Tsunamis Deposits in Canary Islands. In: Margottini, C., Canuti, P., Sassa, K. (Eds.), Landslide Science and Practice, Volume 5: Complex Environment. Springer-Verlag. pp. 27-33.

Fiske, R.S., Jackson, E.D., 1972. Orientation and Growth of Hawaiian Volcanic Rifts: The Effect of Regional Structure and Gravitational Stresses. Proc. R. Soc. Lond. A 329, 299-326. http://dx.doi.org/10.1098/rspa.1972.0115

Flemings, P.B., Long, H., Dugan, B., Germaine, J., John, C.M., Behrmann, J.H., Sawyer, D., IODP Expedition 308 Scientists, 2008. Pore pressure penetrometers document high overpressure near the seafloor where multiple submarine landslides have occurred on the continental slope, offshore Louisiana, Gulf of Mexico. Earth and Planetary Science Letters 269 (3-4), 309-325.http://dx.doi.org/10.1016/j.epsl.2007.12.005.

Flower, M.F.J., Schmincke, H.-U., Bowman, H., 1976. Rare earth and other trace elements in historic Azorean lavas. J. Volcanol. Geotherm. Res. 1, 127-147.

Forjaz, V.H., 1966. Carta geológica do sistema vulcânico Faial-Pico-S. Jorge. Escala 1:200 000. In: Machado, F., Forjaz, V.H., (Eds.), A actividade vulcânica na ilha do Faial (1957-67), 1968, Comissão de Turismo da Horta, Portugal, 89 pp.

Forjaz, V.H., Serralheiro, A., Nunes, J.C., 1990. Carta vulcanológica dos Açores - Grupo Central. Escala 1:200000. Serviço Regional de Protecção Civil, Universidade dos Açores e Centro de Vulcanologia INIC, Ponta Delgada, Portugal.

Fornari, D.J., Malahoff, A., Heezen, B.C., 1979. Submarine slope micro-morphology and volcanic substructure of the Island of Hawaii inferred from visual observations made from U.S. Navy deep-submergence vehicle (DSV) "Sea Cliff": Marine Geology 32 (1-2), 1–19. http://dx.doi.org/10.1016/0025-3227(79)90143-9

França, Z., 2000. Origem e evolução petrológica e geoquímica do vulcanismo da ilha do Pico. Açores. Ph.D. Thesis, Univ. Açores, Ponta Delgada, Portugal.

França, Z., Rodrigues, B., Cruz, J.V., Carvalho, M.R., Nunes, J.C., 1995. Ensaio de orientação para o estudo petrológico e geoquímico das lavas históricas da ilha do Pico - Açores. IV Congresso Nacional de Geologia, Porto, Mem. Mus. Geol. Fac. Ciências Porto 4, 723-724.

França, Z., Nunes, J.C., Cruz, J.V., Carvalho, M.R, Serralheiro, A., 2000. Carta de distribuição petrográfica da ilha do Pico (Açores) e mapa de amostragem. In: França, Z. (Eds.) Origem e evolução petrológica e geoquímica do vulcanismo da ilha do Pico - Açores, 2002, Câmara Municipal de São Roque do Pico, Portugal, 391 pp.

França, Z.T.M., Tassinari, C.C.G., Cruz, J.V., Aparicio, A.Y., Araña, V., Rodrigues, N.R., 2006. Petrology, geochemistry and Sr-Nd-Pb isotopes of the volcanic rocks from Pico Island - Azores (Portugal). J. Volcanol. Geotherm. Res. 156 (1–2), 71–89. http://dx.doi.org/10.1016/j.jvolgeores.2006.03.013

Garcia, M.O., Davis, M.G., 2001. Submarine growth and internal structure of ocean island volcanoes based on submarine observations of Mauna Loa volcano, Hawaii. Geology, 29 (2), 163 – 166.

Garcia, M. O., Haskins, E.H., Stolper, E.M., Baker, M., 2007. Stratigraphy of the Hawai‘i Scientific Drilling Project core (HSDP2): Anatomy of a Hawaiian shield volcano, Geochem. Geophys. Geosyst., 8, Q02G20, http://dx.doi.org/10.1029/2006GC001379.

Gente, P., Dyment, J.,Maia, M., Goslin, J., 2003. Interaction between the Mid-Atlantic Ridge and the Azores hotspot during the last 85 Myr: emplacement and rifting of the hotspot-derived plateaus. Geochemistry, Geophysics, Geosystems 4 (10), 8514. http://dx.doi.org/10.1029/2003GC000527

Germa, A., Quidelleur, X., Gillot, P.Y., Tchilinguirian, P., 2010. Volcanic evolution of the back-arc Pleistocene PayunMatru volcanic field (Argentina). J. South. Amer. Earth Sci. 29, 717-730.

Germa, A., Quidelleur, X., Lahitte, P., Labanieh, S., Chauvel, C., 2011. The K-Ar Cassignol-Gillot technique applied to western Martinique lavas: A record of Lesser Antilles arc activity from 2 Ma to Mount Pelée volcanism. Quaternary Geochronology 6 (3-4), 341-355. http://dx.doi.org/10.1016/j.quageo.2011.02.001.

Giachetti, T., Paris, R., Kelfoun, K., Pérez-Torrado, F.J., 2011. Numerical modelling of the tsunami triggered by the Güìmar debris avalanche, Tenerife (Canary Islands): Comparison with field-based data. Marine Geology 284 (1–4), 189-202. http://dx.doi.org/10.1016/j.margeo.2011.03.018.

Giachetti, T., Paris, R., Kelfoun, K., Ontowirjo, B., 2012. Tsunami hazard related to a flank collapse of Anak Krakatau Volcano, Sunda Strait, Indonesia. In: Terry, J.P., Goff, J., (Eds.), Natural Hazards in the Asia-Pacific Region. Geological Society, London, Special Publications 361, 79-90. http://dx.doi.org/10.1144/SP361.7.

Gillot, P.Y., Cornette, Y., 1986. The Cassignol technique for potassium–Argon dating, precision and accuracy: Examples from the Late Pleistocene to Recent volcanics from southern Italy. Chemical Geology: Isotope Geoscience section, 59, 205–222. http://dx.doi.org/10.1016/0168-9622(86)90072-2.

Gillot, P.Y., Cornette, Y., Max, N., Floris, B., 1992. Two reference materials, trachytes MDO-G and ISH-G, for Argon dating (K-Ar and $^{40}Ar/^{39}Ar$) of Pleistocene and Holocene rocks. Geostandards Newsletter 16 (1), 55–60. http://dx.doi.org/10.1111/j.1751-908X.1992.tb00487.x.

Gillot, P.Y., Lefèvre, J.C., Nativel, P.E., 1994. Model for the structural evolution of the volcanoes of Réunion Island. Earth and Planetary Science Letters 122 (3–4), 291-302. http://dx.doi.org/10.1016/0012-821X(94)90003-5

Gillot. P.Y., Hildenbrand, A., Clouard, V., 2004. Comments on "Epiclastic deposits and "horseshoe-shaped" caldeiras in Tahiti (Society Islands) and Ua Huka (Marquesas Archipelago), French Polynesia" by Clément et al. (2003). J. Volcanol.Geotherm. Res.136 (1-2), 159-163.

Gillot, P.Y., Hildenbrand, A., Lefèvre, J.C., Albore-Livadie, C., 2006. The K/Ar Dating Method: Principle, Analytical Techniques and Application to Holocene Volcanic Eruptions in Southern Italy. Acta Vulcanologica 18, 55–66.

Golden Software, Inc., 2002. Surfer 8: Contouring and 3D Surface Mapping for Scientists and Engineers-user Guide. Editor Golden Software, Incorporated, 640 pp.

González, P.J., Tiampo, K.F., Camacho, A.G., Fernández, J., 2010. Shallow flank deformation at Cumbre Vieja volcano (Canary Islands): Implications on the stability of steep-sided volcano flanks at oceanic islands. Earth and Planetary Science Letters 297, 545–557. http://dx.doi.org/10.1016/j.epsl.2010.07.006.

Haflidason, H., Sejrup, H.P., Nygard, A., Mienert, J., Bryn, P., Lien, R., Forsberg, C.F., Berg, K., Masson, D., 2004. The Storegga Slide: architecture, geometry and slide development. Marine Geology 213, 201-234. doi:10.1016/j.margeo.2004.10.007

Hampton, M.A., Lee, H.J., Locat, J., 1996. Submarine landslides. Reviews of Geophysics 34 (1), 33-59. http://dx.doi.org/10.1029/95RG03287. Hildenbrand, A., Gillot, P.Y., Bonneville, A., 2006. Offshore evidence for a huge landslide of the northern flank of Tahiti-Nui (French Polynesia). Geochemistry Geophysics Geosystems 7 (3), Q03006, http://dx.doi.org/10.1029/2005GC001003.

Herring, T.A., 2003. GLOBK: Global Kalman Filter VLBI and GPS Analysis Program, Version 10.1.: Cambridge, Mass. Inst. Technology.

Hildenbrand, A., Gillot, P.Y., Soler, V., Lahitte, P., 2003. Evidence for a persistent uplifting of La Palma (Canary Islands), inferred from morphological and radiometric data. Earth and Planetary Science Letters 210, 277–289. http://dx.doi.org/10.1016/S0012-821X(03)00133-X.

Hildenbrand, A., Gillot, P.Y., Le Roy, I., 2004. Volcano-tectonic and geochemical evolution of an oceanic intra-plate volcano: Tahiti-Nui (French Polynesia), Earth Planet. Sci. Lett., 217 (3-4), 349-365. http://dx.doi.org/10.1016/S0012-821X(03)00599-5

Hildenbrand, A., Gillot, P.Y., Bonneville, A., 2006. Offshore evidence for a huge landslide of the northern flank of Tahiti–Nui (French Polynesia). Geochemistry Geophysics Geosystems 7 (3), Q03006. http://dx.doi.org/10.1029/2005GC001003.

Hildenbrand, A., Gillot, P.Y., Marlin, C., 2008. Geomorphological study of long-term erosion on a tropical volcanic ocean island: Tahiti-Nui (French Polynesia). Geomorphology 93, 460-481.

Hildenbrand, A., Madureira, P., Ornelas Marques, F., Cruz, I., Henry, B., Silva, P., 2008. Multi-stage evolution of a sub-aerial volcanic ridge over the last 1.3 Myr: S. Jorge Island, Azores Triple Junction. Earth and Planetary Science Letters 273 (3-4), 289-298. http://dx.doi.org/10.1016/j.epsl.2008.06.041

Hildenbrand, A., Marques, F.O., Costa, A.C.G., Sibrant, A.L.R., Silva, P.M.F., Henry, B., Miranda, J.M., Madureira, P., 2012a. Reconstructing the architectural evolution of volcanic islands from combined K/Ar, morphologic, tectonic, and magnetic data: The Faial Island example (Azores). Journal of Volcanology and Geothermal Research 241-242, 39-48. http://dx.doi.org/10.1016/j.jvolgeores.2012.06.019.

Hildenbrand, A., Marques, F.O., Catalão, J., Catita, C.M.S., Costa, A.C.G., 2012b. Large-scale active slump of the southeastern flank of Pico Island, Azores. Geology 40 (10), 939–942. http://dx.doi.org/10.1130/G33303.1.

Hildenbrand, A., Marques, F.O., Costa, A.C.G., Sibrant, A.L.R., Silva, P.F., Henry, B., Miranda, J.M., Madureira, P., 2013a. Reply to the comment by Quartau and Mitchell on "Reconstructing the architectural evolution of volcanic islands from combined K/Ar, morphologic, tectonic, and magnetic data: The Faial Island example (Azores)", J. Volcanol. Geotherm. Res. 241–242, 39–48, by Hildenbrand et al. (2012). Journal of Volcanology and Geothermal Research 255, 127-130. http://dx.doi.org/10.1016/j.jvolgeores.2013.01.015.

Hildenbrand, A., Marques, F.O., Catalão, J., Catita, C.M.S., Costa, A.C.G., 2013b. Large-scale active slump of the southeastern flank of Pico Island, Azores: REPLY. Geology 41 (12), e302. http://dx.doi.org/10.1130/G34879Y.1

Hildenbrand, A., Weis, D., Madureira, P., Marques, F.O., 2014. Recent plate re-organization at the Azores Triple Junction: Evidence from combined geochemical and geochronological data on Faial, S. Jorge and Terceira volcanic islands. Lithos 210-211, 27-39. doi:10.1016/j.lithos.2014.09.009

Holm, P.M., Wilson, J.R., Christensen, B.P., Hansen, L., Hansen, S.L., Hein, K.M., Mortensen, A.K., Pedersen, R., Plesner, S., Runge, M.K., 2006. Sampling the Cape Verde Mantle Plume: Evolution of Melt Compositions on Santo Antão, Cape Verde Islands. Journal of Petrology 47 (1), 145-189. http://dx.doi.org/10.1093/petrology/egi071.

Hooper, A., Segall, P., Zebker, H., 2007. Persistent scatterer interferometric synthetic aperture radar for crustal displacement analysis, with application to Volcano Alcedo, Galapagos. J. Geophys. Res.-Solid Earth 112 (B7), B07407.

Hubbert, M. K., and W. W. Rubey (1959), Role of fluid pressure in mechanics of overthrust faulting, Geol. Soc. Am. Bull., 70, 115–166.

Hunt, J.E., Wynn, R.B., Masson, D.G., Talling, P.J. and Teagle, D.A.H., 2011. Sedimentological and geochemical evidence for multistage failure of volcanic island landslides: A case study from Icod landslide on north Tenerife, Canary Islands. Geochemistry Geophysics Geosystems 12 (12), Q12007. http://dx.doi.org/10.1029/2011GC003740.

Iverson, R.M., 1995. Can magma-injection and groundwater forces cause massive landslides on Hawaiian volcanoes? Journal of Volcanology and Geothermal Research 66, 295-308.

Jaeger, J.C., Cook, N.G.W., 1979. Fundamentals of Rock Mechanics. Chapman and Hall, New York.

Johnson, C.L., Wijbrans, J.R., Constable, C.G., Gee, J., Staudigel, H., Tauxe, L., Forjaz, V.H., Salgueiro, M., 1998. Ar-40/Ar-39 ages and paleomagnetism of Sao Miguel lavas, Azores. Earth Planet. Sci. Lett. 160, 637-649.

Kampes, B., Hanssen, R., Perski, Z., 2003. "Radar interferometry with public domain tools," in *Proc. FRINGE*, Frascati, Italy, Dec. 1–5, 2003.

Keating, B.H., McGuire, W.J., 2000. Island edifice failures and associated tsunami hazards. Pure and Applied Geophysics 157 (6-8), 899–955. http://dx.doi.org/10.1007/s000240050011.

Kelfoun, K., Giachetti, T., Labazuy, P., 2010. Landslide-generated tsunamis at Réunion Island. Journal of Geophysical Research 115, F04012, http://dx.doi.org/10.1029/2009JF001381.

King, R.W., Bock, Y., 2002. Documentation for the GAMIT analysis software, release 10.1: Cambridge, MA, Massachusetts Institute of Technology.

Klügel, A., Walter, T.R., Schwarz, S., Geldmacher, J., 2005. Gravitational spreading causes en-echelon diking along a rift zone of Madeira Archipelago: an experimental approach and implications for magma transport. Bulletin of Volcanology 68, 37–46, http://dx.doi.org/10.1007/s00445-005-0418-6.

Kongsberg, S., 2007. EM 120 Multibeam echo sounder, product description , Kongsberg Maritime AS, Norway, Bremerhaven, PANGAEA, 44 p. (available at http://epic.awi.de/26725/1/Kon2007a.pdf)

Krastel, S., Schmincke, H.U., 2002. The channel between Gran Canaria and Tenerife: constructive processes and destructive events during the evolution of volcanic islands. International Journal of Earth Sciences 91 (4), 629-641. http://dx.doi.org/10.1007/s00531-002-0285-8.Krastel, S., Schmincke, H.U., Jacobs, C.L., Rihm, R., Le Bas, T.P., Alibés, B., 2001. Submarine landslides around the Canary Islands. Journal of Geophysical Research 106 (B3), 3977–3997. http://dx.doi.org/10.1029/2000JB900413.

Krastel, S., Schmincke, H.U., Jacobs, C.L., Rihm, R., Le Bas, T.P., Alibes, B., 2001. Submarine landslides around the Canary Islands. Journal of Geophysical Research 106 (B3), 3977–3997. http://dx.doi.org/10.1029/2000JB900413.

Krause, D.C., Watkins, N.D., 1970. North Atlantic Crustal Genesis in the Vicinity of the Azores. Geophysical Journal International 19(3), 261–283. http://dx.doi.org/10.1111/j.1365-246X.1970.tb06046.x

Kvalstad, T.J., Andresena, L., Forsberga, C.F., Bergb, K., Brynb, P., Wangen, M., 2005a. The Storegga slide: evaluation of triggering sources and slide mechanics. Marine and Petroleum Geology 22, 245-256.

Kvalstad, T.J., Nadim, F., Kaynia, A.M., Mokkelbost, K.H., Bryn, P., 2005b. Soil conditions and slope stability in the Ormen Lange area. Marine and Petroleum Geology 22, 299-310. doi:10.1016/j.marpetgeo.2004.10.021

Lacoste, A., Loncke, L., Chanier, F., Bailleul, J., Vendeville, B.C., Mahieux, G., 2009. Morphology and structure of a landslide complex in an active margin setting: The Waitawhiti complex, North Island, New Zealand. Geomorphology 109, 184-196. doi:10.1016/j.geomorph.2009.03.001

Lacoste, A., Vendeville, B. C., Loncke, L., 2011. Influence of combined incision and fluid overpressure on slope stability: Experimental modelling and natural applications, J. Struct. Geol., 33, 731–742.

Lacoste, A., Vendeville, B. C. , Mourgues, R., Loncke, L., Lebacq, M., 2012. Gravitational instabilities triggered by fluid overpressure and downslope incision—Insights from analytical and analogue modelling, J. Struct. Geol., 42, 151–162.

Le Bas, T. P., Masson, D.G., Holtom, R.T., Grevemeyer, I., 2007. Slope failures on the flanks of the southern Cape Verde Islands. In edited by Lykousis, V., Sakellariou, D., Locat, J. (Eds.), Submarine Mass Movements and Their Consequences, Springer, Dordrecht, Netherlands, pp. 337–345.

Le Friant, A., Boudon, G., Deplus, C., and Villemant, B., 2003. Large-scale flank collapse events during the activity of Montagne Pelée, Martinique, Lesser Antilles. Journal of Geophysical Research - Solid Earth 108 (B1), 2055. http://dx.doi.org/10.1029/2001JB001624.

Legros, F., 2002. The mobility of long-runout landslides. Engineering Geology 63 (3-4), 301-331. http://dx.doi.org/10.1016/S0013-7952(01)00090-4.

Lehner, F. K., 1986. Comments on "noncohesive critical Coulomb wedges: An exact solution" by F.A. Dahlen. J. Geophys. Res. 91(B1), 793–796.

Lipman, P.W., Normark, W.R., Moore, J.G., Wilson, J.B., Gutmacher, C.E., 1988. The giant submarine Alika debris slide, Mauna Loa, Hawaii. J. Geophys. Res. Solid Earth 93 (B5), 4279–4299. http://dx.doi.org/10.1029/JB093iB05p04279.

López, D.L., Williams, S.N., 1993. Catastrophic Volcanic Collapse: Relation to Hydrothermal Processes. Science (New Series) 260, No. 5115, 1794-1796.

Lourenço, N., 2007. Tectono-magmatic Processes at the Azores Triple Junction. Ph.D. Thesis, Univ. Algarve, Faro, Portugal, 239 pp.

Lourenço, N., Miranda, J.M., Luis, J.F., Ribeiro, A.,Mendes Victor, L.A., Madeira, J., Needham, H.D., 1998. Morpho-tectonic analysis of the Azores Volcanic Plateau from a new bathymetric compilation of the area. Mar. Geophys. Res. 20 (3), 141–156. http://dx.doi.org/10.1023/A%3A1004505401547.

Luis, J.F., 2007. Mirone: A multi-purpose tool for exploring grid data. Computers & Geosciences 33, 31-41.

Luis, J.F., Miranda, J.M., 2008. Reevaluation of magnetic chrons in the North Atlantic between 35ºN and 47ºN:Implications for the formation of the Azores Triple Junction and associated plateau. J. Geophys. Res.113 (B10), B10105. http://dx.doi.org/10.1029/2007JB005573

Luis, J.F., Miranda, J.M., Galdeano, A., Patriat, P., 1998. Constraints on the structure of the Azores spreading center from gravity data. Mar. Geophys. Res. 20 (3), 157–170. http://dx.doi.org/10.1023/A:1004698526004

Luis, J.F., Miranda, J.M., Galdeano, A., Patriat, P., Rossignol, J.C., Victor, L.A.M., 1994. The Azores Triple Junction Evolution since 10-Ma from an Aeromagnetic Survey of the Mid-Atlantic Ridge. Earth Planet. Sci. Lett. 125, 439-459.

Maccaferri, F., Bonafede, M., Rivalta, E., 2011. A quantitative study of the mechanisms governing dike propagation, dyke arrest and sill formation. J. Volcanol. Geotherm. Res. 208, 39–50. doi:10.1016/j.jvolgeores.2011.09.001

MacDonald, G.A., 1972. Volcanoes. A discussion of volcanoes, volcanic products, and volcanic phenomena.Prentice-Hall, International, New Jersey, 510 pp.

Macdonald, K.C., Miller, S.P., Huestis, S.P., Spiess, F.N., 1980. 3-Dimensional Modeling of a Magnetic Reversal Boundary from Inversion of Deep-Tow Measurements. J. Geophys. Res. 85, 3670-3680.

Machado, F., 1955. The Fracture Pattern of Azorean Volcanoes. Bulletin Volcanologique 17(1), 119─125. http://dx.doi.org/10.1007/BF02596049

Machado, F., 1959. Submarine pits of the Azores Plateau. Bulletin Volcanologique 21 (1), 109─116. http://dx.doi.org/10.1007/BF02596510

Machado, F., Nascimento, J.M., Denis, A.F., 1959. Evolução Topografica do cone Vulcanico dos Capelinhos, Le Volcanisme de l'ile de Faial, Serv. Geol. Portugal, Mem. 4, 65–71.

Machado, F., Parsons, W., Richards, A., Mulford, J.W., 1962. Capelinhos eruption of Fayal Volcano, Azores, 1957–1958. J. Geophys. Res. 67(9), 3519–3529.

Machado, F., Trêpa, M.V., Férin, C., Nunes, J.C., 1974. Crise sísmica do Pico (Açores), Nov. 1973. Comunicações dos Serviços Geológicos de Portugal 57, 229–242.

Madeira, J., 1998. Estudos de neotectónica nas ilhas do Faial, Pico e S. Jorge: Uma contribuição para o conhecimento geodinâmico da junção tripla dos Açores. Ph.D. Thesis. Univ. Lisboa, Portugal, 481 pp.

Madeira, J., Ribeiro, A., 1990. Geodynamic models for the Azores triple junction: a contribution from tectonics. Tectonophysics 184, 405-415.

Madeira, J., Brum da Silveira, A., 2003. Active tectonics and first paleoseismological results in Faial, Pico and S. Jorge islands (Azores, Portugal). Ann. Geophys. 46 (5), 733–761. http://dx.doi.org/10.4401/ag-3453.

Madeira, J., Soares, A.M.M., Da Silveira, A.B., Serralheiro, A., 1995. Radiocarbon dating recent volcanic activity on Faial Island (Azores). Radiocarbon 37, 139-147.

Madureira, P., Moreira, M., Mata, J., Allègre, C.J., 2005. Primitive neon isotopes in Terceira Island (Azores archipelago). Earth and Planetary Science Letters 233, 429–440. http://dx.doi.org/10.1016/j.epsl.2005.02.030

Madureira, P., Mata, J., Mattielli, N., Queiroz, G., Silva, P., 2011. Mantle source heterogeneity, magma generation and magmatic evolution at Terceira Island (Azores archipelago): constraints from elemental and isotopic (Sr, Nd, Hf, and Pb) data. Lithos 126, 402–418. http://dx.doi.org/10.1016/j.lithos.2011.07.002

Manconi, A., Longpre, M.A., Walter, T.R., Troll, V.R., Hansteen, T.H., 2009. The effects of flank collapses on volcano plumbing systems. Geology 37 (12), 1099–1102. http://dx.doi.org/10.1130/G30104A.1

Mandl, G., Crans,W., 1981. Gravitational gliding in deltas. In: McClay, K.R., Price, N.J. (Eds.), Thrust and Nappe Tectonics. Geological Society Special Publication, vol. 9, pp. 41-54.

Marques, F.O., Catalão, J.C., DeMets, C., Costa, A.C.G., Hildenbrand, A., 2013a. GPS and tectonic evidence for a diffuse plate boundary at the Azores Triple Junction. Earth Planet. Sci. Lett. 381, 177–187. http://dx.doi.org/10.1016/j.epsl.2013.08.051.

Marques, F.O., Sibrant, A., Hildenbrand, A., Costa, A.C.G., 2013. Large-scale Sector Collapses in the Evolution of Santa Maria Island, Azores. AGU Fall Meeting 2013, Abstract V51D-2719, San Francisco, California, 9-13 Dec.

Marques, F.O., Catalão, J.C., DeMets, C., Costa, A.C.G., Hildenbrand, A., 2014a. Corrigendum to " GPS and tectonic evidence for a diffuse plate boundary at the Azores Triple Junction" [Earth Planet. Sci. Lett. 381 (2013) 177-187]. Earth Planet. Sci. Lett. 387, 1–3. http://dx.doi.org/10.1016/j.epsl.2013.11.029.

Marques, F.O., Catalão, J., Hildenbrand, A., Costa, A.C.G., Dias, N.A., 2014b. The 1998 Faial earthquake, Azores: Evidence for a transform fault associated with the Nubia-Eurasia plate boundary? Tectonophysics. http://dx.doi.org/10.1016/j.tecto.2014.06.024.

Masson, D.G., 1996. Catastrophic collapse of the volcanic island of Hierro 15 ka ago and the history of landslides in the Canary Islands. Geology 24 (3), 231-234. http://dx.doi.org/10.1130/0091-7613(1996)024<0231:CCOTVI>2.3.CO;2.

Masson, D.G., Watts, A.B., Gee, M.J.R., Urgeles, R., Mitchell, N.C., Le Bas, T.P., Canals, M., 2002. Slope failures on the flanks of the western Canary Islands. Earth-Science Reviews 57 (1–2), 1-35. http://dx.doi.org/10.1016/S0012-8252(01)00069-1

Masson, D.G., Harbitz, C.B., Wynn, R.B:, Pedersen, G., Lovholt, F., 2006. Submarine landslides: processes, triggers and hazard prediction. Phil. Trans. R. Soc. A 364, 2009-2039. doi: 10.1098/rsta.2006.1810

Masson, D. G., Le Bas, T. P., Grevemeyer, I., Weinrebe, W., 2008. Flank collapse and large-scale landsliding in the Cape Verde Islands, off West Africa. Geochemistry, Geophysics, Geosystems 9 (7), Q07015. doi: 10.1029/2008GC001983.

.Matias, L., Dias, N.A., Morais, I., Vales, D., Carrilho, F., Madeira, J., Gaspar, J., Senos, L., Silveira, A., 2007. The 9th of July 1998 Faial Island (Azores, North Atlantic) seismic sequence. J. Seismol. 11, 275–298. http://dx.doi.org/10.1007/s10950-007-9052-4

McClusky, S., Balassanian, S., Barka, A., Demir, C., Ergintav, S., Georgiev, I., Gurkan, O., Hamburger, M., Hurst, K., Kahle, H., Kastens, K., Kekelidze, G., King, R., Kotzev, V., Lenk, O., Mahmoud, S., Mishin, A., Nadariya, M., Ouzounis, A., Paradissis, D., Peter, Y., Prilepin, M., Reilinger, R., Sanli, I., Seeger, H., Tealeb, A., Toksoz, M., Veis, G., 2000. Global positioning system constraints on plate kinematics and dynamics in the eastern Mediterranean and Caucasus. J. Geophys. Res. 105, 5695-5719.

McGuire, W.J., 1996. Volcano instability: a review of contemporary themes. In: McGuire, W.J., Jones, A.P., Neuberg, J. (Eds.), Volcano Instability on the Earth and Other Planets. Geological Society Special Publication, London, 1–23.

McGuire, W.J., Pullen, A.D., 1989. Location and orientation of eruptive fissures and feeder-dykes at Mount Etna: influence of gravitational and regional stress regimes. J. Volcanol. Geotherm. Res. 38 (3–4), 325–344. http://dx.doi.org/10.1016/0377-0273(89)90046-2

McMurtry, G.M., Herrero-Bervera, E., Cremer, M.D., Smith, J.R., Sherman, C., Torresan, M.E., 1999. Stratigraphic constraints on the timing and emplacement of the Alika 2 giant Hawaiian submarine landslide. Journal of Volcanology and Geothermal Research 94, 35–58, http://dx.doi.org/10.1016/S0377-0273(99)00097-9.

McMurty, G.M., Fryer, G.J., Tappin, D.R., Wilkinson, I.P., Williams, M., Fietzke, J., Garbe-Schoenberg, D., Watts, P., 2004. Megatsunami deposits on Kohala volcano, Hawaii, from flank collapse of Mauna Loa. Geology 32(9), 741-744. http://dx.doi.org/10.1130/G20642.1.

Métrich, N., Zanon, V., Créon, L., Hildenbrand, A., Moreira, M., Marques, F.O., 2014. Is the "Azores hotspot" a wetspot? Insights from geochemistry of fluid and melt inclusions in olivine of Pico basalt. Journal of Petrology 55(2), 377–393. http://dx.doi.org/10.1093/petrology/egt071

Miranda, J.M., Freire Luis, J., Abreu, I., Mendes Victor, A., 1991. Tectonic framework of the Azores Triple Junction. Geophys. Res. Lett. 18, 1421-1424.

Miranda, J.M., Mendes Victor, L.A., Simões, J.Z., Luis, J.F., Matias, L., Shimamura, H., Shiobara, H., Nemoto, H., Mochizuki, H., Hirn, A., Lépine, J.C., 1998. Tectonic setting of the Azores Plateau deduced from a OBS survey. Mar. Geophys. Res. 20, 171–182.

Miranda, J.M., Luis, J.F., Lourenço, N., Goslin, J., 2014. Distributed deformation close to the Azores Triple "Point". Mar. Geol. 355, 27–35. http://dx.doi.org/10.1016/j.margeo.2014.05.006

Mitchell, N.C., 1998. Characterising the irregular coastlines of volcanic ocean islands. Geomorphology 23, 1-14.

Mitchell, N.C., 2001. The transition from circular to stellate forms of submarine volcanoes. Journal of Geophysical Research - Solid Earth 106 (B2), 1987-2003. http://dx.doi.org/10.1029/2000JB900263.

Mitchell, N.C., Masson, D.G., Watts, A.B., Gee, M.J.R., Urgeles, R., 2002. The morphology of the submarine flanks of volcanic ocean islands: A comparative study of the Canary and Hawaiian hotspot islands. Journal of Volcanology and Geothermal Research 115 ( 1–2), 83-107. http://dx.doi.org/10.1016/S0377-0273(01)00310-9.

Mitchell, N.C., 2003. Susceptibility of mid-ocean ridge volcanic islands and seamounts to large-scale landsliding. J. Geophys. Res. 108 (B8), 2397. http://dx.doi.org/10.1029/2002JB001997.

Mitchell, N.C., Beier, C., Rosin, P. L., Quartau, R., Tempera, F., 2008. Lava penetrating water: Submarine lava flows around the coasts of Pico Island, Azores. Geochemistry, Geophysics, Geosystems 9 (3), Q03024, http://dx.doi.org/10.1029/2007GC001725.

Mitchell, N.C., Stretch, R., Oppenheimer, C., Kay, D., Beier, C., 2012a. Cone morphologies associated with shallow marine eruptions: east Pico Island, Azores. Bull. Volcanol. 74 (10), 2289–2301. http://dx.doi.org/10.1007/s00445-012-0662-5

Mitchell, N.C., Quartau, R., Madeira, J., 2012b. Assessing landslide movements in volcanic islands using near-shore marine geophysical data: south Pico island, Azores. Bulletin of Volcanology 74 (2), 483-496. http://dx.doi.org/10.1007/s00445-011-0541-5.

Mitchell, N.C., Quartau, R., Madeira, J., 2013. Large-scale active slump of the southeastern flank of Pico Island, Azores: comment. Geology 41 (12), e301. http://dx.doi.org/10.1130/G34006C.1.

Montelli, R., Nolet, G., Dahlen, F.A., Masters, G., Engdahl, E.R., Hung, S.H., 2004. Finite-frequency tomography reveals a variety of plumes in the mantle. Science 303, 338-343.

Montelli, R., Nolet, G., Dahlen, F.A., Masters, G., 2006. A catalogue of deep mantle plumes: new results from finite frequency tomography. Geochemistry, Geophysics, Geosystems 7, Q11007. http://dx.doi.org/10.1029/2006GC001248.

Moore, J.G., 2001. Density of basalt core from Hilo drill hole, Hawaii. Journal of Volcanology and Geothermal Research 112, 221-230.

Moore, J.G., Moore, G.W., 1984. Deposit from a Giant Wave on the Island of Lanai, Hawaii. Science 226 (4680), 1312-1315.

Moore, G.W., Moore, J.G., 1988. Large-scale bedforms in boulder gravel produced by giant waves in Hawaii. Geological Society of America Special Paper 229, 101-110. http://dx.doi.org/10.1130/SPE229-p101.

Moore, J.G., Chadwick Jr., W.W., 1995. Offshore geology of Mauna Loa and adjacent area, Hawaii, In: Rhodes, J.M., and Lockwood, J.P. (Eds.), Mauna Loa revealed: Structure, Composition, History and Hazards. Geophysical Monograph 92, American Geophysical Union, Washington DC, pp. 21–44.

Moore, J.G., Clague, D.A., 2002. Mapping the Nuuanu and Wailau Landslides in Hawaii. In: Takahashi, E., Lipman, P.W., Garcia, M.O., Naka, J., Aramaki, S. (Eds.), Hawaiian Volcanoes: Deep Underwater Perspectives. Geophysical Monograph Series 128, American Geophysical Union, Washington D.C., pp. 223-244.http://dx.doi.org/10.1029/GM128.

Moore, J.G., Clague, D.A., Holcomb, R.T., Lipman, P.W., Normark,W.R., Torresan, M.E., 1989. Prodigious submarine landslides on the Hawaiian Ridge. J. Geophys. Res. Solid Earth 94 (B12), 17465–17484. http://dx.doi.org/10.1029/JB094iB12p17465.

Moore, I. D., A. Lewis, and J. C. Gallant, 1993. Terrain properties: Estimation Methods and Scale Effects. In Jakeman, A.J., Beck, M.B., MCaleer, M.J. (Eds.), Modelling Change in Environmental Systems, , John Wiley and Sons, New York.

Moore, J.G., Normark, W.R., Holcomb, R.T., 1994a. Giant Hawaiian Landslides. Annual Review Of Earth And Planetary Sciences 22, 119-144.

Moore, J.G., Bryan, W.B., Ludwig, K.R., 1994b. Chaotic deposition by a giant wave, Molokai, Hawaii. Geological Society of America Bulletin 106, 962-967.

Moore, J.G., Bryan, W.B., Beeson, M.H., Normark, W.R., 1995. Giant blocks in the South Kona landslide, Hawaii. Geology, 23 (2), 125-128. http://dx.doi.org/10.1130/0091-7613(1995)023<0125:GBITSK>2.3.CO;2.

Moreira, M., Doucelance, R., Kurz, M.D., Dupré, B., Allègre, C.J., 1999. Helium and lead isotope geochemistry of the Azores Archipelago. Earth and Planetary Science Letters 169 (1-2), 189–205. http://dx.doi.org/10.1016/S0012-821X(99)00071-0

Morgan, J.K., Clague, D.A., 2003. Volcanic spreading on Mauna Loa volcano, Hawaii: Evidence from accretion, alteration, and exhumation of volcaniclastic sediments. Geology 31 (5), 411-414.

Morgan, J. K., McGovern, P.J., 2005a. Discrete element simulations of gravitational volcanic deformation: 1. Deformation structures and geometries, J. Geophys. Res. 110, B05402. http://dx.doi.org/10.1029/2004JB003252.

Morgan, J.K., McGovern, P.J., 2005b. Discrete element simulations of gravitational volcanic deformation: 2. Mechanical analysis, J. Geophys. Res. 110, B05403. http://dx.doi.org/10.1029/2004JB003253.

Morgan, J.K., Moore, G.F., Hills, D.J., Leslie, S., 2000. Overthrusting and sediment accretion along Kilauea's mobile south flank, Hawaii: Evidence for volcanic spreading from marine seismic reflection: Geology 28, 667–670. http://dx.doi.org/10.1130/0091-7613(2000)28<667:OASAAK>2.0.CO;2.

Morgan, J.K., Moore, G.F., Clague, D.A., 2003. Slope failure and volcanic spreading along the submarine south flank of Kilauea volcano, Hawaii. Journal of Geophysical Research 108 (B9), 2415. http://dx.doi.org/10.1029/2003JB002411

Mourgues, R., and P. R. Cobbold (2003), Some tectonic consequences of fluid overpressures and seepage forces as demonstrated by sandbox modeling, Tectonophysics, 376, 75–97.

Mourgues, R., and P. R. Cobbold (2006a), Sandbox experiments on gravitational spreading and gliding in the presence of fluid overpressures, J. Struct. Geol., 28, 887–901.

Mourgues, R., and P. R. Cobbold (2006b), Thrust wedges and fluid overpressures: Sandbox models involving pore fluids, J. Geophys. Res., 111, B05404, http://dx.doi.org/10.1029/2004JB003441.

Mourgues, R., Lecomte, E., Vendeville, B., Raillard, S., 2009. An experimental investigation of gravity-driven shale tectonics in progradational delta. Tectonophysics 474, 643-656.

Mourgues, R., Lacoste, A., Garibaldi, C., 2014. The Coulomb critical taper theory applied to gravitational instabilities. Journal of Geophysical Research (Solid Earth) 119 (1), 754-765. http://dx.doi.org/10.1002/2013JB010359

Nadeau, P.H., 2011. Lessons Learned from the Golden Zone Concept for Understanding Overpressure Development, and Drilling Safety in Energy Exploration. Deepwater Horizon Study Group, Working Paper, 1-18, (available at: http://risk.berkeley.edu/pdfs_papers/DHSGWorkingPapersFeb16-2011/LessonsLearnedFromGoldenZoneConcept-PHN_DHSG-Jan2011-1.pdf)

Navarro, J.M. and Coello, J., 1989. Depressions originated by landslide processes in Tenerife, ESF Meeting on Canarian Volcanism, Lanzarote, pp. 150-152.

Neves, M.C., Miranda, J.M., Luis, J.F., 2013. The role of lithospheric processes on the development of linear volcanic ridges in the Azores. Tectonophysics 608, 376–388. http://dx.doi.org/10.1016/j.tecto.2013.09.016.

Niell, A.E., 1996. Global mapping functions for the atmosphere delay at radio wavelengths: Geophys. Res. 101, 3227–3246.

Nielson, D. L., Stiger, S.G., 1996. Drilling and evaluation of Ascension #1, a geothermal exploration well on Ascension Island, South Atlantic Ocean. Geothermics 25 (4/5), 543–560, 1996.

Normark, W.R., Moore, J.G., Torresan, M.E., 1993. Giant Volcano-Related Landslides and the Development of the Hawaiian Islands. In: Schwab, W.C., Lee, H.J., Twichell, D.C., Submarine Landslides: Selected Studies in the U.S. Exclusive Economic Zone, 2002, U.S. Geological Survey Bulletin, pp. 184-196.

Nunes, J.C., 1999. A actividade vulcânica na ilha do Pico do Plistocénico Superior ao Holocénico: Mecanismo eruptivo e hazard vulcânico. PhD thesis. Universidade dos Açores, Ponta Delgada, Portugal, 356 pp.(available at: http://www.jcnunes.uac.pt/principal.htm)

Nunes, J.C., 2002. Lateral collapse structures in Pico Island (Azores): Mechanism, constraints and age. 3ª Assembleia Luso Espanhola de Geodesia e Geofísica, Valencia, 731-735.

Nunes, J.C., França, Z., Cruz, J.V., Carvalho, M.R., Serralheiro, A., 1999a, Carta Vulcanológica da Ilha do Pico (Açores), In: Nunes, J.C., (Eds.), A actividade vulcânica na ilha do Pico do Plistocénico Superior ao Holocénico: Mecanismo eruptivo e hazard vulcânico, 1999, Ph.D. Thesis. Univ. Açores, Ponta Delgada, Portugal, 356 pp.

Nunes, J.C., França, Z., Cruz, J.V., Carvalho, M.R., Serralheiro, A., 1999b, Carta Morfo-tectónica da Ilha do Pico (Açores), In: Nunes, J.C., (Eds.), A actividade vulcânica na ilha do Pico do Plistocénico Superior ao Holocénico: Mecanismo eruptivo e hazard vulcânico, 1999, Ph.D. Thesis. Univ. Açores, Ponta Delgada, Portugal, 356 pp.

Nunes, J.C., Camacho, A., França, Z., Montesinos, F.G., Alves, M., Vieira, R., Velez, E, Ortiz, E., 2006. Gravity anomalies and crustal signature of volcano-tectonic structures of Pico Island (Azores). Journal of Volcanology and Geothermal Research 156 (1-2), 55-70. http://dx.doi.org/10.1016/j.jvolgeores.2006.03.023.

Oehler, J.F., van Wyk de Vries, B., Labazuy, P., 2005. Landslides and spreading of oceanic hot-spot and arc shield volcanoes on Low Strength Layers (LSLs): an analogue modelling approach. Journal of Volcanology and Geothermal Research 144, 169-189. http://dx.doi.org/10.1016/j.jvolgeores.2004.11.023.

Owen, S., Segall, P., Lisowski, M., Miklius, A., Denlinger, R., Sako, M., 2000. Rapid deformation of Kilauea Volcano: Global Positioning System measurements between 1990 and 1996. Journal of Geophysical Research 105 (B8), 18983-18998. http://dx.doi.org/10.1029/2000JB900109.

Pacheco, J.M.R., 2001. Processos associados ao desenvolvimento de erupções vulcânicas hidromagmáticas explosivas na ilha do Faial e sua interpretação numa perspectiva de avaliação do hazard e minimização do risco. PhD thesis. Azores University. Ponta Delgada. 300 pp.

Paris, R., Giachetti, T., Chevalier, J., Guillou, H., Frank, N., 2011. Tsunami deposits in Santiago Island (Cape Verde archipelago) as possible evidence of a massive flank failure of Fogo volcano. Sedimentary Geology 239 (3-4), 129-145. http://dx.doi.org/10.1016/j.sedgeo.2011.06.006

Paris, R., Kelfoun, K., Giachetti, T., 2013. Marine conglomerate and reef megaclasts at Mauritius Island: Evidences of a tsunami generated by a flank collapse of the Piton de La Fournaise volcano, Reunion Island? Science of Tsunami Hazards 32(4),281-291.

Pattier, F., Loncke, L., Gaullier, V., Vendeville, B., Maillard, A., Basile, C., Patriat, M., Roest, W.R., Loubrieu, B., 2011. Mass movements in a transform margin setting: The example of the Eastern Demerara Rise, in Submarine Mass Movements and Their Consequences, Advances in Natural and Technological Hazards Research, vol. 31, edited by Y. Yamada et al., pp. 331–339, Springer, Berlin, Germany.

Pérez-Torrado, F.J., Paris, R., Cabrera, M.C., Schneider, J.L., Wassmer, P., Carracedo, J.C., Rodríguez-Santana, A., Santana, F., 2006. Tsunami deposits related to flank collapse in oceanic volcanoes: The Agaete Valley evidence, Gran Canaria, Canary Islands. Marine Geology 227 (1-2), 135-149. http://dx.doi.org/10.1016/j.margeo.2005.11.008

Pilidou, S., Priestley, K., Debayle, E., Gudmundsson, O., 2005. Rayleigh wave tomography in the North Atlantic: high resolution images of the Iceland, Azores and Eifel mantle plumes. Lithos 79, 453–474. http://dx.doi.org/10.1016/j.lithos.2004.09.012

Pola, A., Crosta, G., Fusi, N., Barberini, V., Norini, G., 2012. Influence of alteration on physical properties of volcanic rocks. Tectonophysics 566-567, 67-86. http://dx.doi.org/10.1016/j.tecto.2012.07.017

Pola, A., Crosta, G.B., Fusi, N., Castellanza, R., 2014. General characterization of the mechanical behaviour of different volcanic rocks with respect to alteration. Engineering Geology 169, 1-13. http://dx.doi.org/10.1016/j.enggeo.2013.11.011

Quartau, R., Mitchell, N.C., 2013. Comment on "Reconstructing the architectural evolution of volcanic islands from combined K/Ar, morphologic, tectonic, and magnetic data: The Faial Island example (Azores)" by Hildenbrand et al. (2012) [J. Volcanol. Geotherm. Res. 241–242 (2012) 39–48]. Journal of Volcanology and Geothermal Research 255, 124-126. http://dx.doi.org/10.1016/j.jvolgeores.2012.12.020.

Quartau, R., Trenhaile, A.S., Mitchell, N.C., Tempera, F., 2010. Development of volcanic insular shelves: Insights from observations and modelling of Faial Island in the Azores Archipelago. Marine Geology 275 (1-4), 66-83, http://dx.doi.org/10.1016/j.margeo.2010.04.008.

Quartau, R., Tempera, F., Mitchell, N.C., Pinheiro, L.M., Duarte, H., Brito, P.O., Bates, C.R. Monteiro, J.H., 2012. Morphology of the Faial Island shelf (Azores) : The interplay between volcanic, erosional, depositional, tectonic and mass-wasting processes. Geochemistry Geophysics Geosystems 13, Q04012. http://dx.doi.org/10.1029/2011GC003987.

Quidelleur, X., Gillot, P.Y., Carlut, J., Courtillot, V., 1999. Link between excursions and paleointensity inferred from abnormal field directions recorded at La Palma around 600 ka. Earth Planet. Sci. Lett. 168, 233-242.

Quidelleur, X., Carlut, J., Soler, V., Valet, J.P., Gillot, P.Y., 2003. The age and duration of the Matuyama–Brunhes transition from new K–Ar data from La Palma (Canary Islands) and revisited Ar-40/Ar-19 ages. Earth Planet. Sci. Lett. 208, 149–163. http://dx.doi.org/10.1016/S0012-821X(03)00053-0

Quidelleur, X., Hildenbrand, A., Samper, A., 2008. Causal link between Quaternary paleoclimatic changes and volcanic islands evolution. Geophysical Research Letters 35, L02303, http://dx.doi.org/10.1029/2007GL031849.

Ramalho, R.S., Madeira, J., Helffrich, G.R., Schaefer, J.M., Winckler, G., Quartau, R., Adena, K., 2013. Evidence for a Mega-Tsunami Generated by Giant Flank Collapse of Fogo Volcano, Cape Verde. In proceeding of: AGU Fall Meeting 2013, San Francisco, poster NH41A-1690.

Reid, M.E., 2004. Massive collapse of volcano edifices triggered by hydrothermal pressurization. Geology 32 (5), 373–376. http://dx.doi.org/10.1130/G20300.1

Reid, M.E., Sisson, T.W., Brien, D.L., 2001. Volcano collapse promoted by hydrothermal alteration and edifice shape, Mount Rainier, Washington. Geology 29, 779-782.

Reid, M.E., Keith, T.E.C., Kayen, R.E., Iverson, N.R., Iverson, R.M., Brien, D.L., 2010. Volcano collapse promoted by progressive strength reduction: new data from Mount St. Helens. Bull Volcanol 72, 761-766. http://dx.doi.org/10.1007/s00445-010-0377-4

Saastamoinen, J., 1972. Atmospheric correction for the troposphere and stratosphere in radio ranging of satellites: in The Use of Artificial Satellites for Geodesy, Geophys. Monograph 15, p247–251.

Saffer, D. M., and B. A. Bekins (1998), Episodic fluid flow in the Nankai accretionary complex: Timescale, geochemistry, flow rates, and fluid budget, J. Geophys. Res., 103(B12), 30,351–30,370.

Saki, M., Thomas, C., Nippress, S.E.J., Lessing, S., 2015. Topography of upper mantle seismic discontinuities beneath the North Atlantic: The Azores, Canary and Cape Verde plumes. Earth and Planetary Science Letters 409, 193-202. http://dx.doi.org/10.1016/j.epsl.2014.10.052.

Samper, A., Quidelleur, X., Lahitte, P., Mollex, D., 2007, Timing of effusive volcanism and collapse events within an oceanic arc island: Basse-Terre, Guadeloupe archipelago (Lesser Antilles Arc). Earth and Planetary Science Letters 258 (1-2), 175–191. http://dx.doi.org/10.1016/j.epsl.2007.03.030.

Satake, K., Smith, J.R., Shinozaki, K., 2002. Three-dimensional reconstruction and tsunami model of the Nuuanu and Wailau giant landslides, Hawaii. In: Takahashi, E., Lipman, P.W., Garcia, M.O., Naka, J., Aramaki, S. (Eds.),Hawaiian Volcanoes: Deep Underwater Perspectives. Geophysical Monograph Series 128. American Geophysical Union, Washington D.C., pp. 333–346. http://dx.doi.org/10.1029/GM128.

Scheidegger, A. E., 1973. On the prediction of the reach and velocity of catastrophic landslides. Rock Mechanics 5 (4), 231-236. http://dx.doi.org/10.1007/BF01301796.

Schiffman, P., Watters, R.J., Thompson, N., Walton, A.W., 2006. Hyaloclastites and the slope stability of Hawaiian volcanoes: insights from the Hawaiian Scientific Drilling Project's 3-km drill core. Journal of Volcanology and Geothermal Research 151 (1–3), 217–228.

Schilling, J.-G., 1975. Azores mantle blob - rare earth evidence. Earth Planet. Sci. Lett. 25, 103-115.

Schilling, J.-G., Bergeron, M.B., Evans, R., 1980. Halogens in the mantle beneath the North Atlantic. Phil. Trans. R. Soc. Lond. A 297, 147-178.

Schmidt, R., Schminke, H.U., 1999. Seamounts and island building. In: Sigurdsson, H., Houghton, B., McNutt, S.R., Rymer, H., Stix, J. (Eds.), Encyclopedia of Volcanoes. Academic Press, pp. 383─402.

Schultz, R.A., 1995. Limits on strength and deformation properties of jointed basaltic rock masses. Rock Mechanics and Rock Engineering 28 (1), 1–15.

Schultz, R.A., 1996. Relative scale and the strength and deformability of rock masses. Journal of Structural Geology 18 (9), 1139–1149.

Searle, R., 1980, Tectonic pattern of the Azores spreading centre and triple junction. Earth Planet. Sci. Lett. 51, 415–434.

Serralheiro, A., Forjaz, V.H., Alves, C.A.M., Rodrigues, B., 1989. Carta Vulcanológica dos Açores – Ilha do Faial, Scale 1:15 000, Sheets 1, 2, 3 & 4. Centro de Vulcanologia do INIC, Serviço Regional de Protecção Civil dos Açores & Univ. of Azores (Ed.), Ponta Delgada.

Shi, Y., and C. Wang (1988), Generation of high pore pressures in accretionary prisms: Inferences from the Barbados subduction complex, J. Geophys. Res., 93(B8), 8893–8909.

Shirzaei, M., Walter, T.R., Nankali, H.R., Holohan, E., 2011. Gravity-driven deformation of Damavand volcano, Iran, detected through InSAR time series. Geology, 39, 251–254. http://dx.doi.org/10.1130/G31779.1.

Sibrant, A.L.R., Marques, F.O., Hildenbrand, A., 2014. Construction and destruction of a volcanic island developed inside an oceanic rift: Graciosa Island, Terceira Rift, Azores. J. Volcanol. Geotherm. Res. 284, 32-45. http://dx.doi.org/10.1016/j.jvolgeores.2014.07.014

Siebert, L., 1984. Large volcanic debris avalanches: characteristics of source areas, deposits and associated eruptions. J. Volcanol. Geotherm. Res. 22, 163–197.

Silva, P.F., Henry B., Marques F.O., Hildenbrand A., Marques F.O. (2008) New paleomagnetic and K/Ar on Faial Island (Azores Archipelago). Constraints on the spatio-temporal evolution of the on-land volcanism. 11th Castle meeting, Bojnice (Slovakia).

Silva, P.F., Henry B., Hildenbrand A., Madureira P., Marques F.O., Kratinová Z., Nunes J.C. (2010). Spatial/temporal evolution of Faial's onshore volcanism (Azores Archipelago). Joint AGU meeting, Foz de Iguassu.

Silva, P.F., Henry, B., Marques, F.O; Hildenbrand, A.; Madureira, P., Mériaux, C. A., and Z. Kratinová, 2012. Palaeomagnetic study of a sub-aerial volcanic ridge (São Jorge Island, Azores) for the past 1.3 Myr: evidences for the Cobb Mountain Subchron, volcano flank instability and tectono-magmatic implications. Geophys. J. Int., 188, 959-978. http://dx.doi.org/10.1111/j.1365-246X.2011.05320.x.

Silva, P.F., Miranda J.M., Henry B., Marques F.O., Hildenbrand A., Madureira P., Kratinová Z. (in preparation). Paleomagnetic and magnetic study of Faial island (Azores Archipelago). Geophys. J. Int.

Silveira, G., Stutzmann, E., 2002. Anisotropic tomography of the Atlantic Ocean.Phys. Earth Planet. Int. 132, 237-248.

Silveira, G., Stutzmann, E., Davaille, A., Montagner, J.-P., Mendes-Victor, L., Sebai, A., 2006. Azores hotspot signature in the upper mantle. Journal of Volcanology and Geothermal Research 156, 23–34. http://dx.doi.org/10.1016/j.jvolgeores.2006.03.022

Smith, J.R., Malahoff, A., Shor, A.N., 1999. Submarine geology of the Hilina slump and morpho-structural evolution of Kilauea volcano, Hawaii. Journal of Volcanology and Geothermal Research 94, 59–88. http://dx.doi.org/10.1016/10.1016/S0377-0273(99)00098-0.

Smith, D.E., Harrison, S., Jordan, J.T., 2013. Sea level rise and submarine mass failure on open continental margins. Quaternary Science Reviews 82, 93-103. http://dx.doi.org/10.1016/j.quascirev.2013.10.012

Sparks, R.S.J., 1997. Causes and consequences of pressurisation in lava dome eruptions. Earth and Planetary Science Letters 150, 177-189.

Staudigel, H., Schmincke, H.-U., 1984. The Pliocene Seamount Series of La Palma/Canary Islands. Journal of Geophysical Research 89 (B13), 11125-11215.

Steiger, R.H., Jäger, E., 1977. Subcommission on geochronology: Convention on the use of decay constants in geo- and cosmochronology. Earth and Planetary Science Letters 36 (3), 359-362. http://dx.doi.org/10.1016/0012-821X(77)90060-7.

Stretch, R., Mitchell, N.C., Portaro, R.A., 2006. A morphometric analysis of the submarine volcanic ridge of Pico Island. J. Volcanol. Geotherm. Res. 156(1–2), 35–54. http://dx.doi.org/10.1016/j.jvolgeores.2006.03.009

Tazieff, H.,1959. L'éruption de 1957–1958 et la tectonique de Faïal. In Memória Nº4 (nova série) Serv. Geol. Portugal, Lisboa, 71–88

Terakawa, T., Yamanaka, Y., Nakamichi, H., Watanabe, T., Yamazaki, F., Horikawa, S., Okuda, T., 2013. Effects of pore fluid pressure and tectonic stress on diverse seismic activities around the Mt. Ontake volcano, central Japan. Tectonophysics 608, 138-148. http://dx.doi.org/10.1016/j.tecto.2013.10.005.

Thomas, M.E., Petford, N., Bromhead, E.N., 2004a. The effect of internal gas pressurization on volcanic edifice stability: evolution towards a critical state. Terra Nova 16, 312-317. http://dx.doi.org/10.1111/j.1365-3121.2004.00567.x

Thomas, M.E., Petford, N., Bromhead, E.N., 2004b. Volcanic rock-mass properties from Snowdonia and Tenerife: implications for volcano edifice strength. Journal of the Geological Society, London, vol. 161, 1-8.

Thompson, N., Watters, R.J., Schiffman, P., 2008. Stability analysis of Hawaiian Island flanks using insight gained from strength testing of the HSDP core. Journal of Volcanology and Geothermal Research 171, 163–177. http://dx.doi.org/10.1016/j.jvolgeores.2007.11.008

Tilling, R.I., Koyanagi, R.Y., Lipman, P.W., Lockwood, J.P., Moore, J.G., Swanson, D.A., 1976. Earthquake and related catastrophic events, island of Hawaii, November 29, 1975: A preliminary report; U.S. Geological Survey Circular 740, 33 p.

Trippanera, D., Porreca, M., Ruch, J., Pimentel, A., Acocella, V., Pacheco, J., Salvatore, M., 2014. Relationships between tectonics and magmatism in a transtensive/transform setting: An example from Faial Island (Azores, Portugal). Geological Society of America Bulletin 126 (1-2), 164-181. http://dx.doi.org/10.1130/B30758.1

Turner, S., Hawkesworth, C., Rogers, N., King, P., 1997. U-Th isotope disequilibria and ocean island basalt generation in the Azores. Chem. Geol. 139, 145-164.

Urgeles, R., Masson, D.G., Canals, M., Watts, A.B., Le Bas, T., 1999. Recurrent large-scale landsliding on the west flank of La Palma, Canary Islands. J. Geophys. Res. Solid Earth 104 (B11), 25331–25348. http://dx.doi.org/10.1029/1999JB900243.

van Wyk de Vries, B., Borgia, A., 1996. The role of basement in volcano deformation. In: McGuire, W.J., Jones, A.P., Neuberg, J. (Eds.), Volcano Instability on the Earth and Other Planets. Geological Society Special Publication, London, 95–110.

van Wyk de Vries, B., Kerle, N., Petley, D., 2000. Sector collapse forming at Casita volcano, Nicaragua. Geology 28 (2), 167-170. http://dx.doi.org/10.1130/0091-7613(2000)28<167:SCFACV>2.0.CO;2

Voight, B., Elsworth, D., 1997. Failure of volcano slopes. Géotechnique 47 (1), 1-31.

Voight, B., Elsworth, D., 2000. Instability and collapse of hazardous gas-pressurized lava domes. Geophysical Research Letters 27 (1), 1-4.

Voight, B., Janda, R.J., Glicken, H., Douglass, P.M. 1983. Nature and mechanics of the Mt. St. Helens rockslide–avalanche of 18th May 1980. Géotechnique 33, 243–227.

Walder, J., Nur, A., 1984. Porosity reduction and crustal pore pressure development. Journal of Geophysical Research 89 (B13), 11539-11548.

Walker, G.P.L., 1999. Basaltic volcanoes and volcanic systems. In: Sigurdsson, H., Houghton, B., McNutt, S.R., Rymer, H., Stix, J. (Eds.), Encyclopedia of Volcanoes. Academic Press, pp. 283─290.

Walter, T.R., Schmincke, H.U., 2002. Rifting, recurrent landsliding and Miocene structural reorganization on NW-Tenerife (Canary Islands). International Journal of Earth Sciences 91, 615–628. http://dx.doi.org/10.1007/s00531-001-0245-8.

Walton, A.W., Schiffman, P., 2003. Alteration of hyaloclastites in the HSDP 2 Phase 1 Drill Core: 1. Description and paragenesis. Geochemistry, Geophysics, Geosystems 4 (5), 8709. http://dx.doi.org/10.1029/2002GC000368.

Watters, R.J., Zimbelman, D.R., Bowman, S.D., Crowley, J.K., 2000. Rock mass strength assessment and significance to edifice stability, Mount Rainier and Mount Hood, Cascade Range Volcanoes. Pure appl. geophys. 157, 957–976.

Watts, A.B. and Masson, D.G., 2001. New sonar evidence for recent catastrophic collapses of the north flank of Tenerife, Canary Islands. Bulletin of Volcanology 63 (1), 8-19.

White, W.M., Schilling, J.-G., Hart, S.R., 1976. Evidence for the Azores mantle plume from strontium isotope geochemistry of the Central North Atlantic. Nature 263, 659–663. http://dx.doi.org/10.1038/263659a0

White, W.M., Tapia, M.D.M., Schilling, J.-G., 1979. The petrology and geochemistry of the Azores Islands. Contrib. Mineral. Petrol. 69, 201-213.

Widom, E., Shirey, S.B., 1996. Os isotope systematics in the Azores: Implications for mantle plume sources. Earth Planet. Sci. Lett. 142, 451-465.

Woodhall, D., 1974. Geology and volcanic history of Pico Island Volcano, Azores. Nature 248, 663–665. http://dx.doi.org/10.1038/248663a0.

Yang, T., Shen, Y., van der Lee, S., Solomon, S.C., Hung, S.H., 2006. Upper mantle structure beneath the Azores hotspot from finite-frequency seismic tomography. Earth Planet. Sci. Lett. 250 (1–2), 11–26. http://dx.doi.org/10.1016/j.epsl.2006.07.031

Zanella, A., Cobbold, P.R., Rojas, L., 2014a. Beef veins and thrust detachments in Early Cretaceous source rocks, foothills of Magallanes-Austral Basin, southern Chile and Argentina: Structural evidence for fluid overpressure during hydrocarbon maturation. Marine and Petroleum Geology 55, 250-261. http://dx.doi.org/10.1016/j.marpetgeo.2013.10.006

Zanella, A., Cobbold, P.R., Le Carlier de Veslud, C., 2014b. Physical modelling of chemical compaction, overpressure development, hydraulic fracturing and thrust detachments in organic rich source rock. Marine and Petroleum Geology 55, 262-274. http://dx.doi.org/10.1016/j.marpetgeo.2013.12.017

Zbyszewsky, G., Da Veiga Ferreira, O., 1959. Rapport de la deuxième mission géologique sur le volcanisme de l'île de Faial. In Memória Nº4 (nova série) Le Volcanisme de l'Île de Faial et l'éruption du Volcan de Capelinhos, Serv. Geol. Portugal, Lisboa.

Zbyszewski, G., Ribeiro Ferreira, C., Veiga Ferreira, O., Torre de Assunção, C., 1963a. Notícia explicativa da Folha "B" da Ilha do Pico (Açores). Carta Geológica de Portugal na escala 1/50 000. Serviços Geológicos de Portugal. Lisbon, Portugal. 21 pp.

Zbyszewski, G., Ribeiro Ferreira, C., Veiga Ferreira, O., Torre de Assunção, C., 1963b. Notícia explicativa da Folha "A" da Ilha do Pico (Açores). Carta Geológica de Portugal na escala 1/50 000. Serviços Geológicos de Portugal. Lisbon, Portugal. 23 pp.

Zimbelman, D.R., Watters, R.J., Firth, I.R., Breit, G.N., Carrasco-Nunez, G., 2004. Stratovolcano stability assessment methods and results from Citlaltépetl, Mexico. Bull Volcanol 66, 66-79. http://dx.doi.org/10.1007/s00445-003-0296-8

# ANNEX I

## Reply to the comment by Quartau and Mitchell on "Reconstructing the architectural evolution of volcanic islands from combined K/Ar, morphologic, tectonic, and magnetic data: The Faial Island example (Azores)"

## (Hildenbrand et al., 2013a)

Journal of Volcanology and Geothermal Research 255 (2013) 127–130

Contents lists available at SciVerse ScienceDirect

Journal of Volcanology and Geothermal Research

journal homepage: www.elsevier.com/locate/jvolgeores

Discussion

# Reply to the comment by Quartau and Mitchell on "Reconstructing the architectural evolution of volcanic islands from combined K/Ar, morphologic, tectonic, and magnetic data: The Faial Island example (Azores)", J. Volcanol. Geotherm. Res. 241–242, 39–48, by Hildenbrand et al. (2012)

A. Hildenbrand [a,b,*], F.O. Marques [c], A.C.G. Costa [a,c], A.L.R. Sibrant [a,c], P.F. Silva [d], B. Henry [e], J.M. Miranda [c], P. Madureira [f,g]

[a] Univ Paris-Sud, Laboratoire IDES, UMR8148, 91405 Orsay, F-91405, France
[b] CNRS, Orsay, F-91405, France
[c] Universidade de Lisboa, IDL, Lisboa, Portugal
[d] ISEL/DEC and IDL/CGUL, Lisboa, Portugal
[e] Paleomagnetism, IPGP and CNRS, 4 Av. de Neptune, 94107 Saint-Maur cedex, France
[f] Centro de Geofísica de Évora and Dep. de Geociências da Univ. de Évora, R. Romão Ramalho, 59, 7000–671 Évora, Portugal
[g] Estrutura de Missão para a Extensão da Plataforma Continental, R. Costa Pinto, 165, 2770–047, Paço D'Arcos, Portugal

ARTICLE INFO

*Article history:*
Received 20 January 2013
Accepted 23 January 2013
Available online 31 January 2013

In our recent paper (Hildenbrand et al., 2012a), we used a panel of complementary approaches to reconstruct the architectural evolution of Faial oceanic island over the last 1 Myr. We showed that the present island has a complex architecture, which results from distinct and brief (<50 kyr) episodes of volcanic construction separated by long periods of volcanic inactivity, during which the edifices were extensively dismantled by erosion and tectonics. The upper part of the oldest volcanic system, especially, only crops out in the SE part of the island, whereas most of the original volcano was deeply modified by mass wasting processes and extensively covered by more recent volcanic products. The combination of our K/Ar, morphologic, tectonic and magnetic data suggests that the remnants of the old volcano are presently under most of Faial, and that this volcano had an elongated morphology slightly oblique with respect to the present WNW–ESE elongation of the island. In their comment, Quartau and Mitchell point out possible "problems" in our interpretations. Their only criticism lies on the extent and morphology of the old volcano, which they draw as a small conical edifice restricted to the eastern end of the island.

We thank Quartau and Mitchell for giving us the opportunity to clarify some important points and discuss significant problems regarding their interpretations:

(1) On-land and offshore topographic data, indeed, provide useful information regarding slope processes on oceanic islands (e.g., Hildenbrand et al., 2006). However, they only give an instantaneous picture of the present edifice morphology. In their comment, Quartau and Mitchell show the bathymetry close to the Faial Island shorelines, and focus more specifically on shallow insular shelves located a few hundred meters away from the present sea cliffs. In their interpretation, the distribution of these shelves would mimic the original slopes of the old volcano. In this interpretation, they assume that (a) the volcano has not experienced any subsequent morphological evolution throughout the lifetime of the island, and (b) the present morphology of the upper proximal submarine slopes is representative of the full geometry of the volcanic edifice. In Fig. 1 of their comment, Quartau and Mitchell present a close-up of the submarine flank, and draw two main volcanoes with a circular shape in plan view. From the extent of these circles, and consideration about statistical slope distribution (Fig. 2 of their comment), they claim that the 800 m isobath materializes the "bathymetric base" of the island. However, they restrict their analysis to the upper submarine slopes, especially in the southern sector, while deeper features on the northern flank are ignored. Previous data by Mitchell et al. (2003) provide a more coherent view at a more appropriate scale (Fig. 1). These clearly show that Faial is only the emerged western part of a much larger volcanic complex, the Pico–Faial ridge, which sits on top of the Azores plateau, down to depths between 1200 m and 1400 m below sea level. While the morphology of the southern flank is disturbed by submarine ridges parallel to the island, the distal bathymetry N of Faial shows a large low-slope relief (Fig. 1), which could either

DOI of original article: http://dx.doi.org/10.1016/j.jvolgeores.2012.06.019.
* Corresponding author at: Univ Paris-Sud, Laboratoire IDES, UMR8148, 91405 Orsay, F-91405, France. Tel.: +33 1 69 15 67 42; fax: +33 1 69 15 48 91.
*E-mail address:* anthony.hildenbrand@u-psud.fr (A. Hildenbrand).

0377-0273/$ – see front matter © 2013 Elsevier B.V. All rights reserved.
http://dx.doi.org/10.1016/j.jvolgeores.2013.01.015

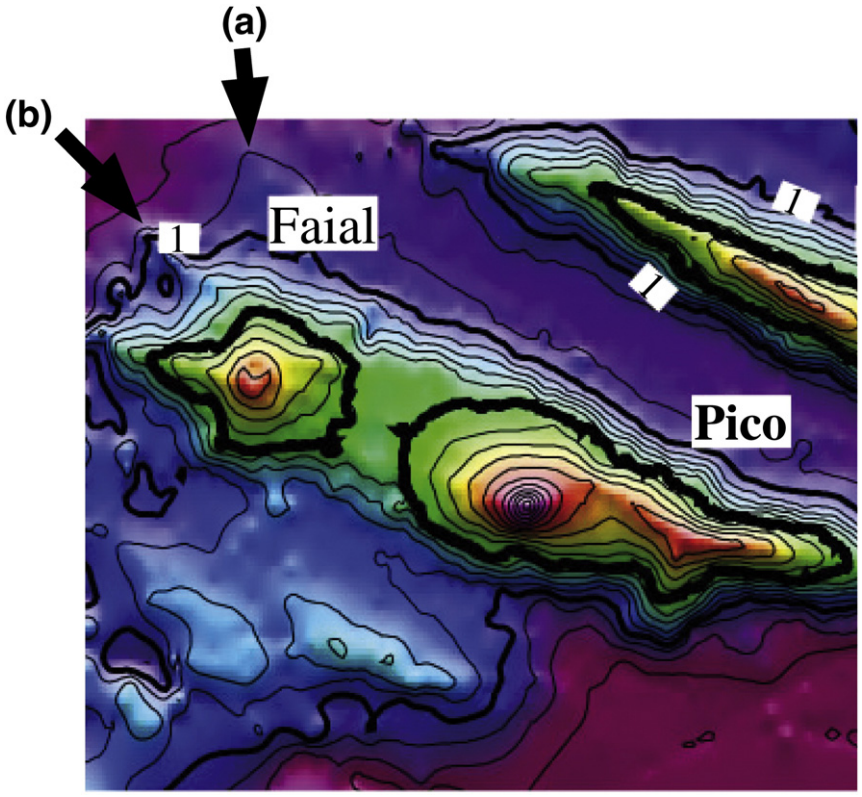


**Fig. 1.** Topographic and bathymetric map (contours every 200 m with bold contours annotated every 1 km) showing the overall morphology of the Pico-Faial volcanic ridge (after Mitchell et al., 2003, modified). Arrows in the North show important deep submarine features not considered by Quartau and Mitchell in their comment: (a) flat-top relief at the base of the island; (b) oblique elongated feature in the prolongation of the "ridge-like" old volcano proposed in our original paper (Hildenbrand et al., 2012a).

represent deep remnants of the old volcanic system, or remobilized material accumulated in response to destruction of the central parts of the volcano. Furthermore, the map evidences an oblique elongated ridge-like feature NW of Faial, which lies in the prolongation of the oblique ridge inferred from magnetic data (Hildenbrand et al., 2012a). Therefore, the deep submarine evidence appears highly consistent with onshore data, whereas the upper 800 m of the submarine flank on which Quartau and Mitchell focus their discussion most likely only records the younger evolution of the island.

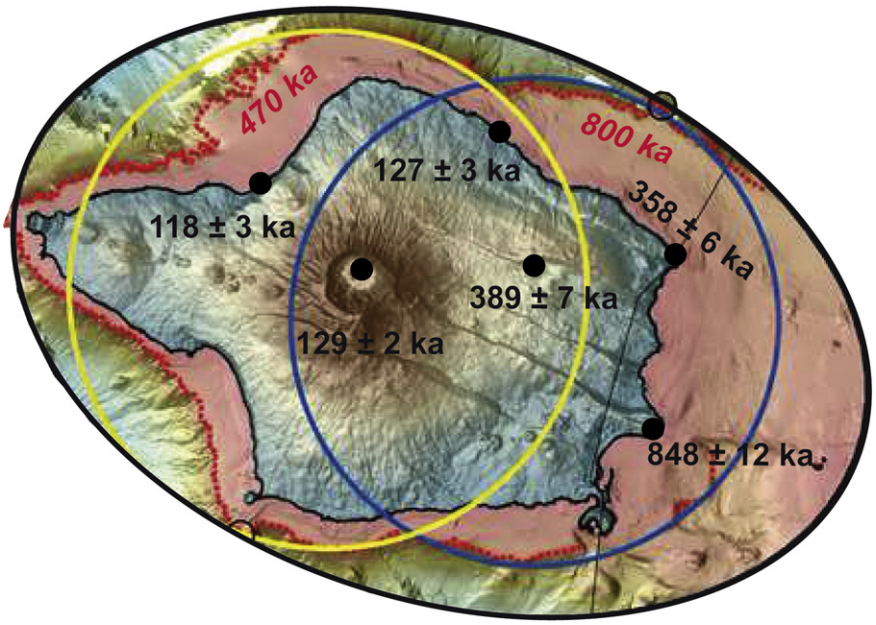


**Fig. 2.** Unspiked K/Ar ages measured on the main volcanic units of Faial island (data from Hildenbrand et al., 2012a, black numbers) vs age of formation of the shelves inferred by Quartau et al., (2010) and Quartau and Mitchell in their comment (red numbers, italic). Background image after Quartau and Mitchell (modified).

(2) The age of formation of the shelves studied by Quartau et al. (2010) and further considered by Quartau and Mitchell in their comment is highly discussible (Fig. 2). From previous K/Ar data (Féraud et al., 1980; Demande et al., 1982), the oldest volcanic system on Faial, the so-called "Galego volcano" (Féraud et al., 1980) or the "Ribeirinha volcano" (Madeira, 1998), was thought to be active between 800 ka and 560 ka. Based on these previous data, Quartau et al. (2010) modelled shelf formation in the NE sector of Faial over the last 800 kyr. They thus considered that the shelves immediately started to form around the emerging volcano ca. 800 ka ago, and that all the lava flows from subsequent eruptions between 800 ka and 560 ka stopped close to the shore level without significantly covering the shelves. Such a hypothesis seems rather implausible, as volcano growth on oceanic islands generally yield the accumulation of thick lava successions in only a few tens of kyr (e.g., Hildenbrand et al., 2004,2008; Boulesteix et al., 2012; Salvany et al., 2012; Silva et al., 2012). Our new data (Hildenbrand et al., 2012a) show that the whole NE slope of Faial is composed of more than 100 m-thick lava succession ca. 360 kyr old dipping towards the N. Therefore, in our interpretation, it materializes the northern slope of a relatively small edifice emplaced rapidly at that time, which therefore provides a maximum age for the development of the oldest shelves (Fig. 2). Similarly, we show that the young large Central Volcano composing the central sub-aerial part of Faial has been active during the last 130 kyr, instead of the 470 kyr previously proposed (Demande et al., 1982). Therefore, most of the shelves considered by Quartau et al. (2010) and Quartau and Mitchell in their comment, are much younger than supposed, which has a direct impact on shelf modelling and geological interpretation. We are fully aware that Quartau et al. (2010) used existing geochronological data available at the time of their study. However, Quartau and Mitchell should not claim in their present comment that shelf modelling is a way to help dating the volcanic formations, because they now know the revised age of the lavas (Hildenbrand et al., 2012a). If the position and width of the shelf break can provide information regarding the relative age between adjacent volcanoes, the model still needs to integrate updated geochronological evidence (Hildenbrand et al., 2012a) or, alternatively, to be calibrated by datable markers such as marine terraces including fossils/microfossils.

(3) The insular shelves studied by Quartau et al. (2010) and Quartau and Mitchell around the various sectors of Faial are presently located between 211 m and 27 m below sea level. Quartau et al. (2010) tentatively modelled shelf development assuming that they have been formed mostly by surf erosion in response to eustatic sea level variations, while the island is considered to have remained at the same vertical position during the last 800 kyr. This is a major problem, as most volcanic islands experience considerable vertical movements during their growth (e.g., Ludwig et al., 1991; Hildenbrand et al., 2003). We note that Quartau et al. (2010) estimated possible local vertical movements from the discrepancy between modelled shelves and actual shelf depth. However, such interpretation is biased by the over-estimated ages used in their modelling (see point (2)). The Pico–Faial ridge has developed over a young oceanic lithosphere, about 10 Ma in age (e.g., Miranda et al., 1991; Luis et al., 1994). Significant thermal subsidence due to lithosphere cooling is thus expected, at a typical rate on the order of a fraction of a mm/yr from the equations of Turcotte and Schubert (2002). Flexural load of the lithosphere by the whole volcanic edifice and additional tectonic subsidence must also be considered, and can be significant. The central Azores, indeed, have developed in a region subject to intense regional deformation, marked by recurrent medium/high-magnitude earthquakes (e.g., Catita et al., 2005; Borges et al., 2007), and by the development of numerous volcano-tectonic structures. Faial Island, specifically, is cut by a large graben bounded by numerous normal faults, which have accumulated important vertical offset over the last 400 kyr (Hildenbrand et al., 2012a). From the various sources of subsidence here considered (thermal, flexural and tectonic), an average long-term subsidence rate of 1 mm/yr appears plausible for Faial. Such value is a minimum, as present movement measured by GPS and radar interferometry (Catalão et al., 2011) show rates greater than or equal to 2 mm/yr for the Pico–Faial ridge as a whole, plus faster movements (ca 1 cm/yr) along some shorelines, especially on the northern coast of Faial and also on Pico, where active slumping is displacing the SE flank of the island at rates of up to 1 cm/yr (Hildenbrand et al., 2012b). From our new geochronological and magnetic data on Faial, the old volcano was completely built at ca 850 ka (Hildenbrand et al., 2012a). Assuming a long-term (conservative) subsidence rate of ~1 mm/yr yields an integrated downward movement of ca. 850 m. This suggests that the low-slope deep portion referred to as the "bathymetric base" of Faial by Quartau and Mitchell was formed close to shore level some 850 ka ago. It certainly cannot represent the bathymetric base of the island, unless we consider that any portion below sea level at a given time is not part of the volcanic edifice.

To summarize, the comment by Quartau and Mitchell addresses important questions, but is based on a number of misleading assumptions. In particular, they have used unreliable K/Ar ages acquired on whole-rock (see a review in Hildenbrand et al., 2012a) to support a study that requires very accurate dating, and have ignored vertical movements typical of volcanic islands built on top of young and thin lithosphere. From the several lines of evidence exposed above, in particular the new accurate geochronological data presented in Hildenbrand et al. (2012a), different conclusions can be reached: (i) the shelf at 211 m does not record the succession of construction and destruction episodes over the last 850 kyr. (ii) the shelves studied by Quartau and co-workers most likely formed during the last 400 kyr, and most of them during the last 120 kyr. Therefore, their distribution does not reflect the geometry of the initial volcano. In fact, they are parallel to the present island shape, which is not surprising, since the latter was roughly acquired since 120 ka, except the western end, which was active during the last 10 kyr. (iii) Average subsidence rates, along with eustatic sea level variations must be taken into account in shelf modelling. (iv) The flat portion at a depth of ca. 800 m around the island does not represent the base of the Pico–Faial ridge, but may alternatively represent a shelf formed rapidly after the rapid construction of the old volcano 850 ka ago, which then subsided down to 800 m bsl. (vi) If such a hypothesis is correct, it means that the old volcano was a large edifice (from the seafloor to asl), which appears consistent with magnetic data and the general morphology of oceanic islands. (vii) Bathymetric data at the full-scale of the whole Pico–Faial ridge support an oblique-ridge geometry and significant mass-wasting for the old Faial volcano. These clarifications will hopefully illustrate that on-land and offshore data need to be considered together, rather than separately to reconstruct, in a consistent way, the long-term architectural evolution of rapidly evolving oceanic islands like Faial. This is LGMT contribution 107.

## References

Borges, J.F., Bezzeghoud, M., Buforn, E., Pro, C., Fitas, A., 2007. The 1980, 1997 and 1998 Azores earthquakes and some seismo-tectonic implications. Tectonophysics 435, 37–54.

Boulesteix, T., Hildenbrand, A., Gillot, P.Y., Soler, V., 2012. Eruptive response of oceanic islands to giant landslides: new insights from the geomorphologic evolution of the Teide–Pico Viejo volcanic complex (Tenerife, Canary). Geomorphology 138 (1), 61–73.

Catalão, J., Nico, G., Hanssen, R., Catita, C., 2011. Merging GPS and atmospherically corrected InSAR data to map 3D terrain displacement velocity. IEEE Transactions

on Geoscience and Remote Sensing 49, 2354–2360. http://dx.doi.org/10.1109/TGRS.2010.2091963.
Catita, C., Feigl, K.L., Catalão, J., Miranda, J.M., Victor, L.M., 2005. Time series analysis of SAR data applied to the study of the co-seismic deformation of the 9th July 1998 Pico–Faial (Azores) earthquake. International Journal of Remote Sensing 26, 2715–2729. http://dx.doi.org/10.1080/01431160512331337835.
Demande, J., Fabriol, R., Gérard, A., Iundt, F., 1982. Prospection géothermique des Iles de Faial et Pico (Açores). 82SGN003GTH, Bureau de recherches géologiques et minières, Orléans.
Féraud, G., Kaneoka, I., Allègre, C.J., 1980. K/Ar ages and stress pattern in the Azores: geodynamic implications. Earth and Planetary Science Letters 46, 275–286.
Hildenbrand, A., Gillot, P.Y., Soler, V., Lahitte, P., 2003. Evidence for a persistent uplifting of La Palma (Canary Islands) inferred from morphological and radiometric data. Earth and Planetary Science Letters 210, 277–289.
Hildenbrand, A., Gillot, P.Y., Le Roy, I., 2004. Volcano–tectonic and geochemical evolution of an oceanic intra-plate volcano: Tahiti–Nui (French Polynesia). Earth and Planetary Science Letters 217, 349–365.
Hildenbrand, A., Gillot, P.Y., Bonneville, A., 2006. Off-shore evidence for a huge landslide of the northern flank of Tahiti–Nui (French Polynesia). Geochemistry, Geophysics, Geosystems 7 (3), 1–12. http://dx.doi.org/10.1029/2005GC001003.
Hildenbrand, A., Madureira, P., Ornelas Marques, F., Cruz, I., Henry, B., Silva, P., 2008. Multi-stage evolution of a sub-aerial volcanic ridge over the last 1.3 Myr: S. Jorge Island, Azores Triple Junction. Earth and Planetary Science Letters 273, 289–298.
Hildenbrand, A., Marques, F.O., Costa, A.C.G., Sibrant, A.L.R., Silva, P.F., Henry, B., Miranda, J.M., Madureira, P., 2012a. Reconstructing the architectural evolution of volcanic islands from combined K/Ar, morphologic, tectonic, and magnetic data: the Faial Island example (Azores). Journal of Volcanology and Geothermal Research 241–242, 39–48.
Hildenbrand, A., Marques, F.O., Fernandes, J.C.C.C., Catita, C.M.S., Costa, A.C.G., 2012b. Large-scale active slump of the southeastern flank of Pico Island, Azores. Geology 40 (10), 939–942.
Ludwig, K.R., Szabo, B.J., Moore, J.G., Simmons, K.R., 1991. Crustal subsidence rate off Hawaii, determined from $^{234}U/^{238}U$ ages of drowned coral reefs. Geology 19, 171–174.
Luis, J.F., Miranda, J.M., Galdeano, A., Patriat, P., Rossignol, J.C., Victor, L.A.M., 1994. The Azores Triple Junction evolution since 10-Ma from an aeromagnetic survey of the mid-Atlantic Ridge. Earth and Planetary Science Letters 125, 439–459.
Madeira, J., 1998. Estudos de neotectónica nas ilhas do Faial, Pico e S. Jorge: Uma contribuição para o conhecimento geodinâmico da junção tripla dos Açores, PhD thesis. Faculdade de Ciencias, Univ. of Lisboa, 481 pp.
Miranda, J.M., Freire Luis, J., Abreu, I., Mendes Victor, A., 1991. Tectonic framework of the Azores Triple Junction. Geophysical Research Letters 18, 1421–1424.
Mitchell, N.C., Schmidt, T., Isidro, E., Tempera, F., Cardigos, F., Nunes, J.C., Figueiredo, J., 2003. Multibeam sonar survey of the central Azores volcanic islands. InterRidge News 12 (2), 30–32.
Quartau, R., Trenhaile, A.S., Mitchell, N.C., Tempera, F., 2010. Development of volcanic insular shelves: insights from observations and modelling of Faial Island in the Azores Archipelago. Marine Geology 275, 66–83.
Salvany, T., Lahitte, P., Nativel, P., Gillot, P.-Y., 2012. Geomorphic evolution of the Piton des Neiges Volcano (Reunion Island, Indian Ocean): competition between volcanic construction and erosion since 1.4 Ma. Geomorphology 136, 132–147.
Silva, P.F., Henry, B., Marques, F.O., Hildenbrand, A., Madureira, P., Mériaux, C.A., Kratinová, Z., 2012. Palaeomagnetic study of a sub-aerial volcanic ridge (São Jorge Island, Azores) for the past 1.3 Myr: evidences for the Cobb Mountain Subchron, volcano flank instability and tectono-magmatic implications. Geophysical Journal International 188, 959–978.
Turcotte, D., Schubert, G., 2002. Geodynamics, Second ed. Cambridge University Press, pp. 456.

# ANNEX II

## Reply to comment (Mitchell et al., 2013) on “Large-scale active slump of the southeastern flank of Pico Island, Azores”

## (Hildenbrand et al., 2013b)

doi:10.1130/G34879Y.1

# Forum Reply

## Large-scale active slump of the southeastern flank of Pico Island, Azores

**A. Hildenbrand[1,2]*, F.O. Marques[3], J. Catalão[4], C.M.S. Catita[4], and A.C.G. Costa[1,4]**

[1]University of Paris-Sud, Laboratoire IDES, UMR8148, 91405 Orsay, France
[2]CNRS, 91405 Orsay, France
[3]Universidade Lisboa, 1749-016 Lisbon, Portugal
[4]Universidade Lisboa and IDL, 1749-016 Lisbon, Portugal

We thank Mitchell et al. (2013) for their Comment. It confirms that there is actually present movement on Pico Island's southeastern flank, and opens up the opportunity to clarify important points.

Mitchell et al. (2013) point out two eventual inaccuracies in our paper (Hildenbrand et al., 2012a): (1) in their opinion, we considered only one of the several options mentioned in their previous works. This is certainly not the case. In the section "Slump Mechanisms and Propagation" (p. 941), we first state "previous studies have considered that the present configuration of the southeastern flank of Pico could reflect vertical caldera collapse." A few lines after we state "lateral collapse has been proposed, but is considered as currently inactive," again citing Mitchell and co-workers. Therefore, the two main options they discussed have been clearly considered by us. (2) Mitchell first identified a submarine debris field, but because it is not visible on the multibeam acquired in 2003, Mitchell et al. (2012) suggested instead that the "traces" visible on the sidescan sonar data are from ancient material buried under a thin sedimentary cover, while the steep submarine slope of the island was created recently from lavas reaching the sea during the delta emplacement. The latter hypothesis is not inconsistent with our interpretation. We, indeed, proposed that the creation of the S3 scarp by recurrent detachment of blocks is "consistent with the presence of a moderate-sized debris field on the southern submarine slope of the ridge." Partial concealing of the debris field by fine-grained sediments and recent lava flows that cascaded on S3 seems plausible to us.

In their Comment, Mitchell et al. (2013) question the existence of an active slump and discuss the slumping mechanisms proposed by us. However, their arguments are rather disputable:

1) Mitchell et al. question the faults we mark as active, arguing that they did not find evidence for recent activity. We remind Mitchell et al. that the absence of evidence is not evidence of absence. Active faults in the slump area are hard to detect because the steep topography and dense vegetation do not offer easy access to the lava flows cascading over the various scars. It is fairly obvious to us that most of the young volcanic cones developed along the trace of the structures (main failure, S1, and S2) are associated with recurrent movements along the faults over the past few thousand years. The youngest lava flows (Hildenbrand et al., 2012a, their figure 2), especially, have apparently been erupted from lateral fissures at the foot of S2. Some recent flows also show signs of deformation, and clastic breccia deposits are being produced/accumulated at the foot of the scars. Overall, this points to very recent/active flank movements.

2) Mitchell et al. claim that our SAR data do not show evidence for rigid body movement. In Hildenbrand et al. (2012a, their figure 4), the sector west of the main scar shows very limited downward movements (green and yellow circles), whereas the portion east of the scar shows pronounced subsidence (blue points), with overall higher displacements southeast of S2 (dark blue circles). Therefore, the bulk of our data clearly shows differential movement. We did not say that present movement involves rigid body motion; instead, we stated that the main mode of deformation is creeping. Instantaneous measurements are rarely representative of long-term behavior. For instance, short-term differential deformation recorded by GPS and SAR data on active slumps such as the Hilina in Hawaii appear rather complex. On the longer term, block rotation may develop over several kilometers across the island flank, but may appear rather subtle at the foot of the fault headwall where downward motion dominates.

3) We are very pleased to read that one of Mitchell et al.'s co-authors measured deformation of a monument inside the slump area, and now concludes that GPS data acquired over 11 years confirm that there is actually present-day movement. This seems to complement our study, and contrasts with Mitchell et al.'s present Comment. Unfortunately, these data are not shown in the Comment or published elsewhere, so it is impossible to check their significance and examine in detail the possible mechanisms of present-day displacements. Noticeably, the now alleged horizontal displacement is in apparent contradiction with their argument of compaction.

4) In their Comment, and in previous papers, Mitchell et al. (2012, 2013) use a shallow platform located a few hundreds of meters from the island shore to assess potential recent movements. They assign an age of 7 ka to this platform, and claim that no visible fault in the platform reveals that any potential movement has to be very recent. If the abrasion shelf studied by Mitchell et al. (2012) were really 7 ka in age, which is merely speculative at this stage (absence of unambiguous datable markers), it certainly does not record the whole history of an island's flank, as recently shown by Hildenbrand et al. (2012b) on the neighboring Faial Island. The development of a slump is most likely discontinuous; i.e., it may involve the gradual development of curved fault structures, with alternating phases of activity and quiescence. On Pico, the overall prominent morphology of the main scar, and the various lava successions cut by the several faults point to an incremental process initiated well before 7 ka. We agree that active movement recorded in our study likely reveals a renewed phase of downward motion that started recently. This therefore deserves particular attention, especially as potential sudden detachment of part of the flank cannot be ruled out.

We thank Mitchell et al. for their suggestion of deploying a network of continuously recording seismic and GPS stations, but we already installed a dense network of new tiltmeters, microseismic stations, and GPS stations in 2012.

**REFERENCES CITED**

Hildenbrand, A., Marques, F.O., Catalão, J., Catita, C.M.S., and Costa, A.C.G., 2012a, Large-scale active slump of the southeastern flank of Pico Island, Azores: Geology, v. 40, p. 939–942, doi:10.1130/G33303.1.

Hildenbrand, A., Marques, F.O., Costa, A.C.G., Sibrant, A.L.R., Silva, P.F., Henry, B., Miranda, J.M., and Madureira, P., 2012b, Reconstructing the architectural evolution of volcanic islands from combined K/Ar, morphologic, tectonic, and magnetic data: The Faial Island example (Azores): Journal of Volcanology and Geothermal Research, v. 241–242, p. 39–48.

Mitchell, N.C., Quartau, R., and Madeira, J., 2012, Assessing landslide movements in volcanic islands using near-shore marine geophysical data: South Pico Island, Azores: Bulletin of Volcanology, v. 74, p. 483–496, doi:10.1007/s00445-011-0541-5.

Mitchell, N.C., Quartau, R., and Madeira, J., 2013, Large-scale active slump of the southeastern flank of Pico Island, Azores: Comment: Geology, v. 41, p. e301, doi:10.1130/G34006C.1.

*E-mail: anthony.hildenbrand@u-psud.fr.

© 2013 Geological Society of America. For permission to copy, contact Copyright Permissions, GSA, or editing@geosociety.org.

# ANNEX III

## GPS and tectonic evidence for a diffuse plate boundary at the Azores Triple Junction

## (Marques et al., 2013),

## and respective *corrigendum* (Marques et al., 2014a)

Earth and Planetary Science Letters 381 (2013) 177–187

Contents lists available at ScienceDirect

Earth and Planetary Science Letters

www.elsevier.com/locate/epsl

# GPS and tectonic evidence for a diffuse plate boundary at the Azores Triple Junction

F.O. Marques [a,*], J.C. Catalão [b], C. DeMets [c], A.C.G. Costa [b,d], A. Hildenbrand [d,e]

[a] Universidade de Lisboa, Lisboa, Portugal
[b] Universidade de Lisboa, Instituto Dom Luiz, Lisboa, Portugal
[c] Department of Geoscience, University of Wisconsin–Madison, Madison, USA
[d] Université Paris-Sud, Laboratoire IDES, UMR8148, Orsay, F-91405, France
[e] CNRS, Orsay, F-91405, France

ARTICLE INFO

*Article history:*
Received 14 March 2013
Received in revised form 29 August 2013
Accepted 31 August 2013
Available online xxxx
Editor: P. Shearer

*Keywords:*
GPS and structural data
plate boundary
Nubia and Eurasia
Azores Triple Junction
Terceira Rift
Mid-Atlantic Ridge (MAR)

ABSTRACT

We use GPS, bathymetric/structural, and seismic data to define the pattern of present deformation along the northern half of the Azores plateau, where the Nubia–Eurasia plate boundary terminates at the axis of the Mid-Atlantic Ridge (MAR). New and existing campaign GPS velocities from the Azores islands reveal extension oblique to a series of en échelon volcanic ridges occupied by Terceira, S. Jorge, Pico, and Faial islands. In a frame of reference defined by 69 continuous GPS stations on the Eurasia plate, Terceira Island moves $2 \pm 1$ mm/yr away from Eurasia, consistent with the island's location within the Terceira Rift and plate boundary structure. The volcanic ridges south of the Terceira Rift move toward WSW at progressively faster rates, reaching a maximum of $3.5 \pm 0.5$ mm/yr (2-$\sigma$) for the Pico/Faial volcanic ridge. The hypothesis that the Terceira Rift accommodates all Nubia–Eurasia plate motion is rejected at high confidence level based on the motions of sites on S. Jorge Island just west of Terceira Rift. All of the islands move relative to the Nubia plate, with Pico Island exhibiting the slowest motion, only $1 \pm 0.5$ mm/yr (2-$\sigma$). Detailed bathymetry from the interior of the hypothesized Azores microplate reveals faults that crosscut young MAR seafloor fabric. These observations and the GPS evidence for distributed deformation described above argue against the existence of a rigid or semi-rigid Azores microplate, and instead suggest that Nubia–Eurasia plate motion is accommodated by extension across a ~140-km-wide zone east of the MAR axis, most likely bounded to the north by the northern shoulder of the Terceira Rift. The MAR spreading rate along the western end of the Azores deformation zone (~38.5°N–39.5°N) is intermediate between the Eurasia–North America rate measured at 39.5°N and the Nubia–North America rate measured at 38.5°N, consistent with the joint conclusions that the Nubia–Eurasia boundary is broad where it intersects the MAR, and the Azores Triple Junction is diffuse rather than discrete.

© 2013 Elsevier B.V. All rights reserved.

## 1. Introduction

The Azores Triple Junction is located at the western end of the Nubia–Eurasia plate boundary, where the North America, Eurasia and Nubia plates meet (Fig. 1). Although its existence has long been recognized, there is as yet no consensus regarding its location and the nature of deformation in the vicinity of the triple junction (e.g. Krause and Watkins, 1970; Searle, 1980; Miranda et al., 1991; Luís et al., 1994; Lourenço et al., 1998; Luís and Miranda, 2008). The triple junction is marked by a ~15% decrease in MAR seafloor spreading rates from 39.5°N, where Eurasia–North America motion occurs, to ~38.5°N, where Nubia–North America plate motion occurs (DeMets et al., 2010). Along the ~100-km-long stretch of the ridge between ~38.5°N and 39.5°N, the average seafloor spreading rate is intermediate between that for Eurasia–North America and Nubia–North America motion (DeMets et al., 2010), suggesting that either a rigid or nearly rigid Azores microplate rotates independently east of the MAR axis between ~38.5°N and 39.5°N, or that distributed deformation occurs across a ~140-km-wide zone east of the MAR axis.

In this study, we present and interpret GPS observations from sites in the Azores archipelago in the context of existing bathymetric/structural and seismic data to address three fundamental questions related to the Azores Triple Junction: (1) Is the Nubia–Eurasia plate boundary discrete or diffuse near the Azores Triple Junction and, by implication, is the triple junction discrete or diffuse? (2) Where is the present Nubia–Eurasia plate boundary in this region? (3) Is there an Azores microplate? Previous authors have used a variety of data to address some of these questions, including seafloor spreading magnetic lineations (e.g. Krause and Watkins, 1970; Searle, 1980; Luís et al., 1994; Luís and Mi-

* Corresponding author. Tel.: +351 217500000; fax: +351 217500064.
*E-mail address:* fomarques@fc.ul.pt (F.O. Marques).

0012-821X/$ – see front matter © 2013 Elsevier B.V. All rights reserved.
http://dx.doi.org/10.1016/j.epsl.2013.08.051

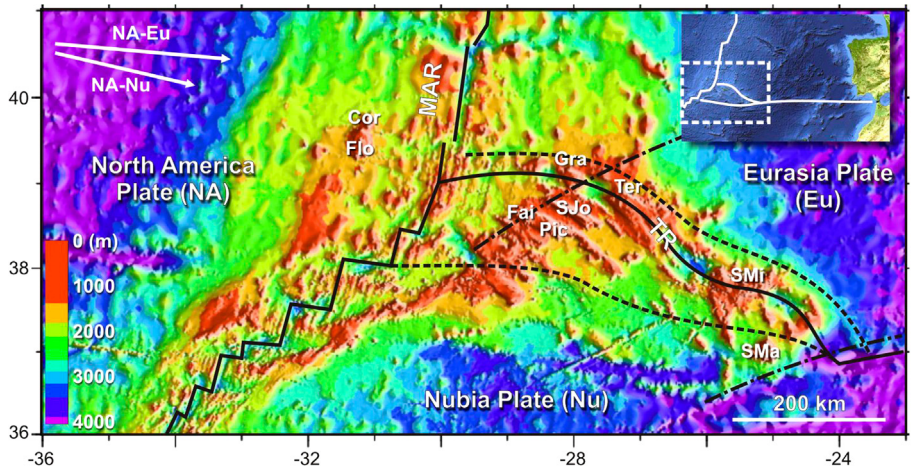


**Fig. 1.** Sketch illustrating the tectonic setting of the Azores Triple Junction. Inset on top right corner for location. Inset on top left corner for the kinematics of the Nubia and Eurasia lithospheric plates (DeMets et al., 2010). Dashed lines mark the boundaries of a hypothetical Azores microplate. Dash-dotted lines represent small circles around the MORVEL Nubia–Eurasia pole. The nine Azores islands are, from W to E, Corvo (Cor), Flores (Flo), Faial (Fai), Pico (Pic), S. Jorge (SJo), Graciosa (Gra), Terceira (Ter), S. Miguel (SMi), and Santa Maria (SMa).

randa, 2008), SONAR and marine bathymetry (e.g. Searle, 1980; Madeira and Ribeiro, 1990; Lourenço et al., 1998), bathymetric and seismic observations (Borges et al., 2007), and GPS (Fernandes et al., 2006). A key goal of this paper is to use a critical subset of observations to evaluate and refine the emerging view that Nubia–Eurasia plate motion is accommodated by deformation distributed across the northern half of the Azores plateau.

This paper is organized as follows. We first present and analyze the GPS observations that are the core of the study, including descriptions of newly estimated Nubia and Eurasia plate angular velocities in the ITRF2008 reference frame, and the resulting Nubia–Eurasia relative angular velocity. We next describe relevant bathymetric observations and the information they suggest about the character and location of regional deformation, albeit over time scales significantly longer than for the GPS observations. Finally, we discuss the implications of the GPS velocity field in the context of bathymetric/structural observations and seismic data.

## 2. GPS data

The GPS observations used in this study consist of the following: (1) new measurements at 35 campaign sites on Faial, Pico and Terceira islands (shown by red circles in Fig. 2A), (2) measurements at 117 continuous sites on the Nubia and Eurasia plates (Figs. 3 and 4), and (3) velocities for 15 GPS stations on S. Jorge Island from Mendes et al. (2013). Procedures for processing the new campaign and continuous data are described below.

### 2.1. Campaign GPS data

The Azores central group GPS geodetic–geodynamic network was established in 2001 in the aim of STAMINA and SARAZORES projects (Navarro et al., 2003; Catalão et al., 2006). It consists of 35 rock-anchored benchmarks on Faial, Pico and Terceira islands (14, 8 and 13 marks, respectively), with an average spacing of 5 km (Fig. 2A).

The principal data used for this study, from 35 stations on Faial, Pico and Terceira islands (locations shown in Fig. 2A and listed in Table 1), were acquired during seven surveys from 2001 to 2013. During each survey, every benchmark was occupied for two-to-four 24 h sessions with a sampling rate of 30 s and elevation mask of 15°. During each survey, at least six stations were observed simultaneously and one station per island was measuring continuously (FAIM for Faial, TOMA for Terceira and PPIL for Pico). For this

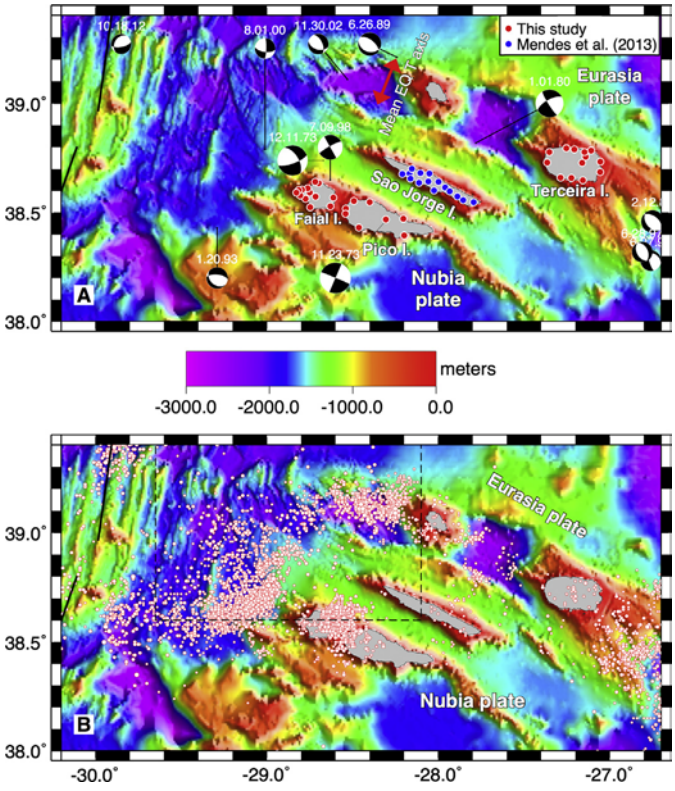


**Fig. 2.** A – locations of GPS sites used for this study and earthquake focal mechanisms for the study area. Bathymetry is a 1-km-resolution grid from J. Luis (http://w3.ualg.pt/~jluis/misc/ac_plateau1km.grd). Legend indicates source of the GPS velocities for Faial, Pico, S. Jorge and Terceira islands. Earthquake focal mechanisms are from the global centroid-moment tensor catalogue (Dziewonski et al., 1981; Ekstrom et al., 2012) and Borges et al. (2007 – labeled 11.23.73 and 12.11.73). Double-headed red arrow shows the average tension axis direction for the focal mechanisms of earthquakes in the diffuse deformation zone (29.5°W–27.5°W). B – epicentres of M > 1 earthquakes for the period 1998–2013, from the Portuguese IPMA catalogue, scaled by magnitude. Dashed rectangle indicates the region shown in Fig. 6. (For interpretation of the references to color in this figure legend, the reader is referred to the web version of this article.)

12-yr-long time series, each station was visited at least four times and observed for at least eight 24-h sessions.

GPS phase observations were analyzed using GAMIT software version 10.4 (Herring et al., 2010). The processing and analysis were made in two-step approach according to Dong et al. (1998).

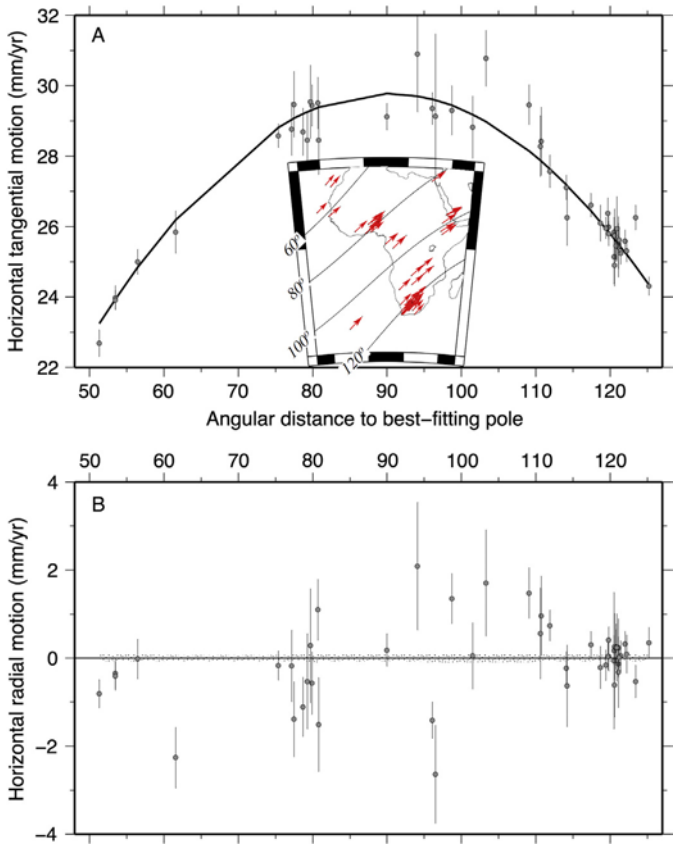


**Fig. 3.** Locations (map inset) and velocity components of 49 Nubia plate GPS sites used to estimate the instantaneous Nubia plate angular velocity relative to ITRF2008. Red arrows in map inset show GPS site velocities in ITRF2008. A – component of GPS station velocities parallel to small circles around the best-fitting Nubia-ITRF2008 pole. B – component of GPS station velocities orthogonal (radial) to small circles around the best-fitting pole. Vertical bars indicate 1-$\sigma$ rate uncertainties. Stippled pattern shows 1-$\sigma$ uncertainty in the predicted rates propagated from the angular velocity covariances. (For interpretation of the references to color in this figure legend, the reader is referred to the web version of this article.)

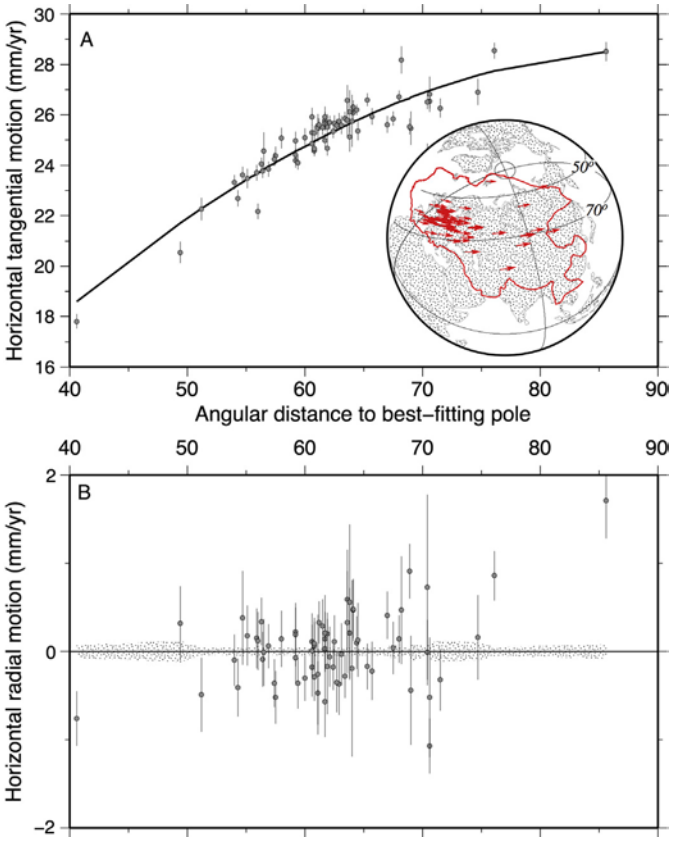


**Fig. 4.** Locations (map inset) and velocity components of 69 Eurasia plate GPS sites used to estimate the instantaneous Eurasia plate angular velocity relative to ITRF2008. Red arrows in map inset show GPS site velocities in ITRF2008. A – component of GPS station velocities parallel to small circles around the best-fitting Eurasia-ITRF2008 pole. B – component of GPS station velocities orthogonal (radial) to small circles around the best-fitting pole. Vertical bars indicate 1-$\sigma$ rate uncertainties. Stippled pattern shows 1-$\sigma$ uncertainty in the predicted rates propagated from the angular velocity covariances.

First, GPS phase observations from each day were used to estimate loosely constrained station coordinates, tropospheric zenith delay parameters and orbital and earth orientation parameters and associated variance–covariance matrices. We have included in the analysis 117 IGS continuous operating GPS stations in order to tie the regional measurements to a global reference frame. We have selected IGS stations distributed worldwide and stations from EUREF network. The GAMIT solution was computed using loose constraints on the *a priori* station coordinate (0.5 m), *a priori* hydrostatic and wet models from Saastamoinen (1972a, 1972b, 1973) and Global Mapping Functions (Böhm et al., 2006), solid earth tides according to IERS conventions (Petit and Luzum, 2010), ocean tidal loading from the FES2004 ocean tide model (Lyard et al., 2006) and receiver and satellite antenna phase centre corrections were modeled with IGS08 ANTEX files from IGS. We used SOPAC's final orbits generated under the scope of the IGS reprocessing analysis and coordinates for all the stations expressed in the ITRF2005 (Altamimi et al., 2007).

Following analysis of the raw GPS data, daily GAMIT solutions were used as quasi-observations in GLOBK to obtain position time series for all sites. In this solution, the regional daily solutions were combined with global daily solution from the IGS1, IGS2, IGS3 and EURA networks computed by SOPAC, the h-files (GAMIT interchange format). Position time series were analyzed to detect and remove outliers and detect possible vertical offsets caused by erroneous antenna height. After editing, site coordinates and velocities were estimated with respect to ITRF2008 reference frame from *a priori* values of coordinates and velocities of IGS permanent sites.

A second iteration of this process was made using GLOBK estimated coordinates and velocities as *a priori* in GAMIT, now with a constraint of 5 cm for coordinates of the surveyed sites. The final solution of site coordinates and velocities was computed by GLOBK using generalized constraints by minimizing the velocity for a large number of IGS stations and estimating a Helmert transformation. The ITRF2008 reference frame was adopted in this last step. The final solution combines seven survey-mode GPS campaigns with IGS stations globally between 2001 and 2013. The weighted RMS of the residual velocity for sites used to define the reference frame (IGS sites) are 0.78, 0.66, 1.2 mm/yr for east, north and vertical components, respectively. Table 1 gives the estimated velocities and formal 1-$\sigma$ uncertainties for GPS sites on Faial, Pico, and Terceira islands. The campaign velocity uncertainties are the formal errors derived from a weighted linear regression of each station time series. They depend on the time spanned by the observations as well as the number of site occupations and estimated location uncertainties.

The velocities for all campaign GPS sites on S. Jorge Island were taken from Mendes et al. (2013), who process their campaign GPS data with GAMIT using procedures the same as those outlined above (including the underlying geodetic reference frame ITRF2008). By implication, their velocities can be included with ours without concerns about inconsistencies between the two.

**Table 1**
GPS site velocities and 1-$\sigma$ uncertainties (units mm/yr).

| | Long. | Lat. | ve | vn | 1-$\sigma$-ve | 1-$\sigma$-vn |
|---|---|---|---|---|---|---|
| PRIB | 331.801 | 38.39558 | 11.46 | 14.43 | 0.15 | 0.16 |
| PPRN | 331.796 | 38.47172 | 10.82 | 14.3 | 0.11 | 0.13 |
| PBJQ | 331.695 | 38.46891 | 11.47 | 14.77 | 0.10 | 0.11 |
| PSLU | 331.601 | 38.54895 | 11.15 | 15.14 | 0.14 | 0.16 |
| PSMT | 331.536 | 38.4324 | 11.6 | 14.69 | 0.11 | 0.12 |
| PDRO | 331.507 | 38.55444 | 11.28 | 14.75 | 0.12 | 0.13 |
| PMAD | 331.461 | 38.51932 | 11.46 | 14.86 | 0.09 | 0.1 |
| PCAL | 331.460 | 38.49515 | 11.24 | 15.02 | 0.12 | 0.13 |
| TPVT | 332.945 | 38.73359 | 12.91 | 16.15 | 0.16 | 0.19 |
| TPOM | 332.944 | 38.68715 | 13.27 | 15.07 | 0.12 | 0.14 |
| TCAP | 332.892 | 38.78465 | 12.19 | 15.56 | 0.11 | 0.12 |
| TSBR | 332.860 | 38.75664 | 12.37 | 15.6 | 0.14 | 0.17 |
| TCAB | 332.854 | 38.77781 | 13.15 | 14.84 | 0.11 | 0.12 |
| TSER | 332.843 | 38.64884 | 12.27 | 16.22 | 0.18 | 0.22 |
| TGOL | 332.839 | 38.72859 | 13.01 | 16.04 | 0.14 | 0.16 |
| TQRB | 332.793 | 38.78996 | 14.06 | 14.65 | 0.13 | 0.14 |
| TOMA | 332.776 | 38.65864 | 13.02 | 17.31 | 0.09 | 0.09 |
| TBIS | 332.747 | 38.79645 | 14.5 | 13.77 | 0.10 | 0.11 |
| TCCD | 332.713 | 38.6611 | 13.46 | 16.51 | 0.10 | 0.11 |
| TRAM | 332.648 | 38.77842 | 15.57 | 14.79 | 0.16 | 0.20 |
| TPTE | 332.635 | 38.73034 | 14.36 | 15.67 | 0.16 | 0.18 |
| FFAR | 331.398 | 38.59532 | 13.2 | 14.74 | 0.14 | 0.16 |
| FPMG | 331.388 | 38.56857 | 11.99 | 15.3 | 0.20 | 0.22 |
| FAIM | 331.371 | 38.52952 | 11.42 | 14.89 | 0.09 | 0.10 |
| FCDR | 331.303 | 38.63617 | 12.53 | 15.83 | 0.15 | 0.16 |
| FCGO | 331.285 | 38.57371 | 11.4 | 14.12 | 0.15 | 0.17 |
| FPN2 | 331.282 | 38.6417 | 12.29 | 15.34 | 0.16 | 0.18 |
| FCBR | 331.253 | 38.52527 | 11.55 | 14.55 | 0.20 | 0.22 |
| FPCD | 331.250 | 38.59254 | 11.3 | 15.57 | 0.16 | 0.18 |
| FFAJ | 331.238 | 38.61159 | 11.1 | 14.88 | 0.15 | 0.16 |
| FVAR | 331.226 | 38.56446 | 11.96 | 15.98 | 0.12 | 0.14 |
| FPDN | 331.206 | 38.60598 | 11.55 | 15.13 | 0.23 | 0.27 |
| FVUS | 331.195 | 38.57873 | 12.43 | 16.37 | 0.23 | 0.26 |
| FVUN | 331.186 | 38.60447 | 12.1 | 15.24 | 0.14 | 0.16 |
| FVUL | 331.172 | 38.59247 | 12.65 | 16.11 | 0.21 | 0.23 |

### 2.2. Continuous GPS data for the Nubia and Eurasia plates

All of the continuous GPS data we used from sites on the Nubia and Eurasia plates are in the public domain and were procured variously from EUREF (epncb.oma.be), NGS (geodesy.noaa.gov/CORS), SOPAC (www.sopac.ucsd.edu), TRIGNET (trignet.co.za), and UNAVCO (unavco.org). The raw GPS data were processed with release 6.1 of the GIPSY software suite from the Jet Propulsion Laboratory (JPL). No-fiducial daily GPS station coordinates were estimated using a precise point-positioning strategy (Zumberge et al., 1997), including constraints on *a priori* tropospheric hydrostatic and wet delays from Vienna Mapping Function (VMF1) parameters (http://ggosatm.hg.tuwien.ac.at), elevation- and azimuthally-dependent GPS and satellite antenna phase centre corrections from IGS08 ANTEX files (available via ftp from sideshow.jpl.nasa.gov), and corrections for ocean tidal loading (http://holt.oso.chalmers.se). Phase ambiguities were resolved using GIPSY's single-station ambiguity resolution feature. Daily no-fiducial station location estimates were transformed to IGS08, which conforms to ITRF2008 (Altamimi et al., 2011), using daily seven-parameter Helmert transformations from JPL. We assume that the geocentre as defined in ITRF2008 is stable and make no correction for possible geocentral motion (Argus, 2007).

In light of compelling evidence that noise in the estimates of daily station coordinates remains strongly correlated out to inter-station distances of 3000 km (Marquez-Azua and DeMets, 2003), we used a straightforward method outlined by these authors to estimate and reduce spatially correlated noise between GPS sites. Interested readers are referred to Marquez-Azua and DeMets (2003) and references therein for details.

Prior to correcting any of our 119 GPS time series for spatially-correlated noise, their 1-$\sigma$ daily repeatabilities were 1.8 mm in both the northing and easting components. Time-correlated noise had average amplitudes of 4.4 mm and 4.5 mm in the north and east components. After correcting each time series for their spatially correlated noise, the average daily coordinate repeatability was reduced to 1.5 mm in both horizontal components and 3.5 mm and 3.7 mm in the northing and easting components of the time-correlated noise. Corrections for the common-mode noise thus effected ~20% reductions in the noise, which reduce the uncertainties in the site velocities described next.

Uncertainties in the velocities of the continuous GPS sites were estimated using an expression from Mao et al. (1999) that relates the velocity uncertainty to the length of a GPS station's time series, the number of time series measurements, and the magnitudes of the white, flicker, and random-walk noise per site. We approximated the respective amplitudes of the white and time-correlated noise at each site from the WRMS scatter of a site's daily locations relative to its monthly-average locations and the average amplitude of longer-period noise manifested in the site's coordinate time series. We assigned an average value of 1 mm/yr for the magnitude of the random-walk noise. Using this algorithm, the standard errors in the 119 continuous site velocities ranged from ±0.24 mm/yr to ±2 mm/yr for time series that span 2 yr to 19 yr. Inversions of the GPS velocities using these uncertainties (see below) return values of reduced chi-square (i.e. chi-square per degree of freedom) of 1.5 and 2.2, suggesting that the estimated uncertainties may be modestly underestimated (20–50%).

### 2.3. Motion of Nubia relative to ITRF2008

We determined the angular velocity for the Nubia plate relative to ITRF2008 (Table 2) from an inversion of the velocities of 49 stations (Fig. 3) west of the East Africa Rift (see map inset for Fig. 3) in nominally stable parts of the plate interior. The Nubia site velocities span a large angular distance with respect to their best-fitting pole (Fig. 3) and thus impose strong geometric constraints on both the pole location and angular rotation rate. The components of the 49 site velocities around the pole (tangential

**Table 2**
GPS angular velocities.

| Plate pair | Angular velocity ($\omega$) | | | Angular velocity covariances ($\sigma$) | | | | | | |
|---|---|---|---|---|---|---|---|---|---|---|
| | Latitude (°N) | Longitude (°E) | $\omega$ (°/Myr) | Sites | $\sigma_{xx}$ | $\sigma_{yy}$ | $\sigma_{zz}$ | $\sigma_{xy}$ | $\sigma_{xz}$ | $\sigma_{yz}$ |
| EU-ITRF08 | 54.5 | −99.1 | 0.257 | 69 | 2.67 | 0.52 | 3.92 | 0.56 | 2.83 | 0.72 |
| NU-ITRF08 | 49.1 | −80.8 | 0.268 | 49 | 4.37 | 1.36 | 1.58 | 0.96 | −1.20 | −0.43 |
| NU-EU | −6.8 | −26.5 | 0.058 | 118 | 7.08 | 1.88 | 5.55 | 1.53 | 1.67 | 0.30 |
| NU-EU (1) | 21.6 | −20.4 | 0.131 | | | | | | | |
| NU-EU (2) | −10.3 | −27.7 | 0.103 | | | | | | | |
| NU-EU (3) | −7.5 | −21.1 | 0.061 | | | | | | | |
| NU-EU (4) | −8.1 | −19.8 | 0.053 | | | | | | | |

Angular velocities describe counter clockwise rotation of the first plate relative to second. NU is Nubia plate; EU is Eurasia plate. Covariance units are $10^{-10}$ rad$^2$/Myr$^2$. Nubia–Eurasia angular velocities are as follows: (1) MORVEL – DeMets et al. (2010); (2) Calais et al. (2003); (3) Argus et al. (2010); (4) Altamimi et al. (2011).

component) and radial to the pole are well described by the best-fitting angular velocity (Fig. 3) and have a weighted RMS misfit of only 0.75 mm/yr. The GPS velocities are thus consistent with the hypothesis that the interior of the Nubia plate deforms slowly or not at all. Reduced chi-square for the 49 Nubia sites is 1.46, close to the value of 1.0 expected if the plate is not deforming and the GPS velocity uncertainties are approximately correct.

### 2.4. Motion of Eurasia relative to ITRF2008

The angular velocity for the Eurasia plate relative to ITRF2008 (Table 2) was determined from an inversion of the velocities of 69 stations (Fig. 4). The sites are distributed throughout the plate interior, but are heavily weighted toward European stations. Stations from Fennoscandia are excluded due to significant isostatic rebound in these areas (Nocquet et al., 2005). The components of the 69 site velocities around the pole (tangential component) and radial to the pole are well described by the best-fitting angular velocity (Fig. 4) and have a weighted RMS misfit of only 0.68 mm/yr, similar to that for the Nubia plate and consistent with little or no deformation within the areas of the Eurasia plate that are sampled by the 69 GPS sites. Reduced chi-square for the 29 Eurasia sites is 2.2, ∼50% larger than expected if the GPS velocity uncertainties were correct. Roughly half of the larger-than-expected misfit is attributable to three poorly fit velocities for GPS sites in NE Asia. Including or omitting these three site velocities has little impact on the resulting best-fitting angular velocity – we thus elected to use these three velocities.

### 2.5. Motion of Nubia relative to Eurasia

A simultaneous inversion of all 119 Eurasia and Nubia plate GPS velocities gives a best-fitting angular velocity for Nubia relative to Eurasia (Table 2) that lies ∼3000 km south of the MORVEL geologically-estimated Nubia–Eurasia pole (Table 2 and DeMets et al., 2010), but agrees well with poles estimated by other authors from GPS measurements on these two plates (Table 2). Despite the large difference between pole locations determined from GPS and that of the MORVEL geologic model, their respective angular velocities predict similar motions near the centre of the study area (Fig. 5C). Our new GPS-based angular velocity predicts that Nubia moves $4.6 \pm 0.3$ mm/yr toward S87.9°W $\pm$ 3.3° (95% uncertainties) relative to Eurasia. For comparison, MORVEL predicts $4.5 \pm 0.4$ mm/yr toward S68.1°W $\pm$ 2.8°. The difference in the predicted velocities is too small to affect any of the conclusions we reach below.

## 3. GPS velocity fields for Faial, Pico, S. Jorge and Terceira islands

### 3.1. GAMIT/GIPSY velocity field combination and velocity uncertainties

In order to evaluate the consistency of our velocity solutions from GAMIT and GIPSY, we compared the ITRF2008 velocities of 32 globally-distributed IGS stations for which we processed continuous data with both software packages. On average, the Cartesian components of the 32 station velocities differ by only −0.23, 0.17, and −0.17 mm/yr for the $X$, $Y$ and $Z$ velocity components, respectively. The close agreement between the two velocity solutions validates our respective processing methodologies and our separate realizations of the station velocities in ITRF08. From 38 continuous stations common to both analyses, we estimated and applied translational and rotational parameters to transform the GAMIT velocity solution onto the GIPSY solution. This altered the GAMIT velocities in the study area by only 0.07 mm/yr and 0.12 mm/yr in the east and north velocity components, reflecting the high degree of consistency in the solutions prior to their formal combination.

Whereas the uncertainties in the continuous GPS site velocities were estimated using a method that accounts for non-random sources of noise in GPS time series (described above), estimating realistic uncertainties for campaign site velocities is more difficult since the noise characteristics of campaign sites are poorly known. White-noise-only models, as assumed in estimating velocity uncertainties via standard linear regressions of station position time series, may underestimate velocity uncertainties by a factor of 5 to 11 (Mao et al., 1999). To approximate realistic velocity uncertainties at the campaign sites, we first determined formal velocity uncertainties via standard weighted linear regressions of the station coordinate time series. The formal uncertainties were typically $\pm 0.1$ to $\pm 0.2$ mm/yr, smaller than the velocity uncertainties for continuous sites with comparable time spans. We therefore increased the formal velocity uncertainties for the campaign sites by a factor of three, such that the adjusted velocity uncertainties were larger than for continuous GPS sites with comparable observation time spans (∼10 yr). Given the subjective nature of this adjustment, we also repeated the kinematic tests described below while using campaign velocity uncertainties that were increased by a factor of four. Using these more conservative error estimates did not however significantly alter any of the results or conclusions presented below.

### 3.2. Island motions relative to Nubia and Eurasia plates and the Pico–Faial volcanic ridge

In order to test a variety of hypotheses related to deformation in the Azores, we analyzed the campaign site velocities in three frames of reference, one fixed to the Eurasia plate (Figs. 5 C and D), one fixed to a frame of reference that minimizes the motion of stations on Pico and eastern Faial islands (Fig. 5a), and one fixed to the Nubia plate (not shown, but discussed below). The results for Terceira, S. Jorge, and Pico and Faial islands are described below. Note that Pico and Faial islands occupy the same volcanic ridge.

### 3.3. Terceira Island

The 13 GPS sites on Terceira Island move systematically faster to the west than predicted by the Eurasia plate angular velocity (Fig. 5C), at rates that vary between 1 and 2.8 mm/yr (Fig. 5D). The average rate near the centre of the island, $2 \pm 1$ mm/yr (2-$\sigma$), is nearly half of the Nubia–Eurasia rate at this location (Fig. 5d), consistent with the island's location inside the Terceira Rift and along the plate boundary (Fig. 2). Further discussion of this velocity field and its implications for the volcanotectonics of Terceira Island and vicinity will be presented in a future paper.

We tested for statistically significant motion of Terceira Island relative to the Eurasia plate using the Stein and Gordon (1984) test for an additional plate boundary, as follows: separate inversions of the 69 Eurasia plate site velocities and 13 Terceira site velocities were used to estimate best-fitting angular velocities and least-squares misfits for the Eurasia plate and an independently moving Terceira Island. A simultaneous inversion of all 82 velocities was used to a single angular velocity to describe Eurasia plate motion including Terceira Island. We then use the $F$-ratio test to evaluate whether the former, two-plate model improves the fit significantly relative to the latter one-plate model. The outcome, $F = 21.5$ for 3 versus 158 degrees of freedom, indicates that the one-plate model degrades the fit at high confidence level (much greater than 99%). The kinematic evidence thus strongly supports significant motion of Terceira Island relative to the Eurasia plate.

### 3.4. S. Jorge Island

On average, the 15 S. Jorge GPS sites move WSW away from the Eurasia plate at $2.7 \pm 0.7$ mm/yr (2-$\sigma$) (Figs. 5 B and C) and

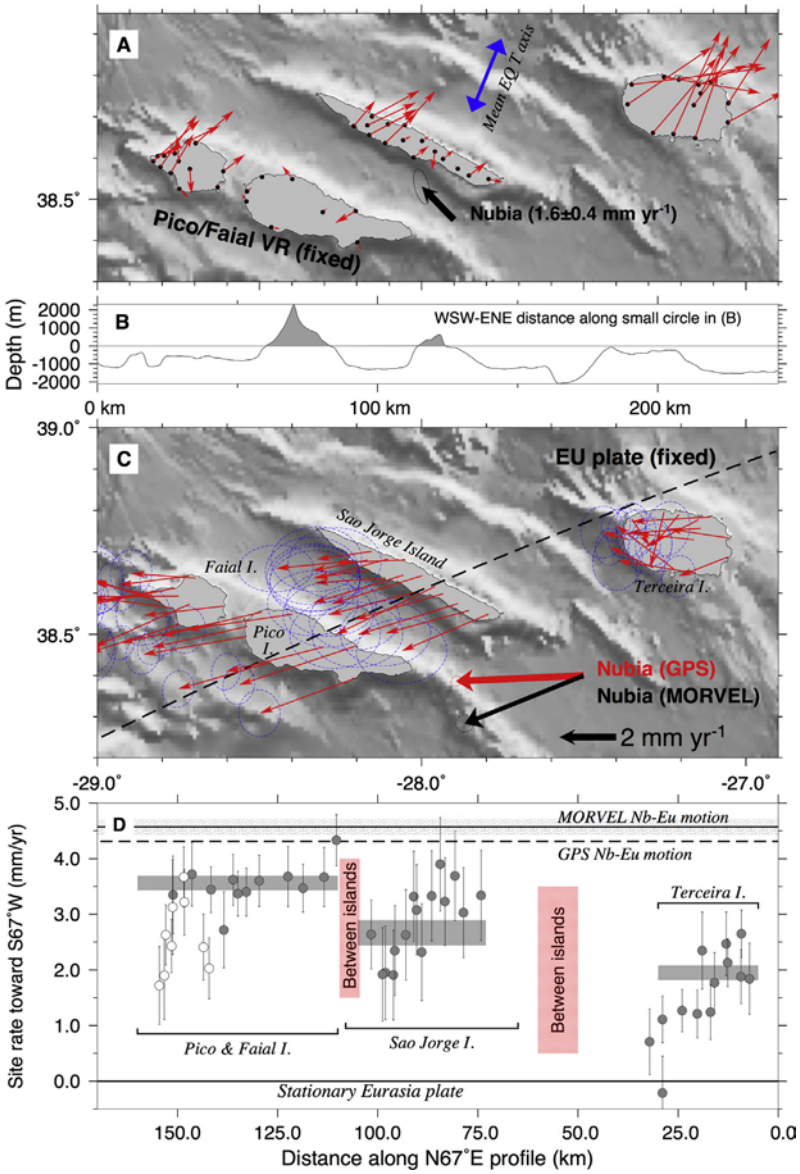


**Fig. 5.** A: GPS site velocities (red arrows) and Nubia plate motion (black arrow with 1-$\sigma$ uncertainty) relative to Pico/Faial volcanic ridge (VR). Black arrow gives the scale. Velocity error ellipses are omitted for clarity. Blue arrow indicates mean tensional axis for eight earthquakes shown in Fig. 2A (see text). B: Topography and bathymetry along the dashed line in Part C. C: GPS site velocities (red arrows) relative to Eurasia plate. Bold red and black arrows show Nubia plate motion predicted by the best-fitting GPS-derived Nubia–Eurasia angular velocity (Table 1) and MORVEL (DeMets et al., 2010). Blue velocity error ellipses are 1-$\sigma$. D: GPS site velocities collapsed onto a WSE-ENE transect of the islands (indicated by dashed line in C). Circles show site velocities from Panel B rotated onto N67°E, the Nubia–Eurasia plate slip direction predicted by MORVEL in the study area. Error bars are 1-$\sigma$. Sites on Terceira Island move ~1 mm/yr with respect to the Eurasia plate. Grey bars show weighted average rates and formal 1-$\sigma$ uncertainties. Open circles show site velocities on Faial Island possibly biased by recent volcanic deformation. (For interpretation of the references to color in this figure legend, the reader is referred to the web version of this article.)

~1 mm/yr to the WSW away from Terceira Island (Fig. 5D). The velocities of sites located in the NW and SE sectors of the island differ by ~1 mm/yr (Fig. 5A), indicating that slow intra-island deformation occurs (Mendes et al., 2013). In Section 5.2, we use velocities from S. Jorge to test the hypothesis that the Terceira Rift accommodates all Nubia–Eurasia motion.

Relative to the Nubia plate, sites in the NW sector of S. Jorge move 2–2.5 mm/yr toward the east, and sites in the SE sector move 1.5–2 mm/yr toward the SE (not shown), consistent with results reported by Mendes et al. (2013). The island therefore does not move with the Nubia plate, a conclusion that is independent of which sector of the island best represents its long-term motion. We refer readers to Mendes et al. (2013) for a more complete description of their GPS velocities and interpretation of the velocity field in the context of the volcanotectonic setting of the island.

### 3.5. Pico and Faial islands

Pico and Faial islands, which occupy the Pico/Faial volcanic ridge, move WSW away from the Eurasia plate (Fig. 5C) at rates of 2–4 mm/yr (Fig. 5D). Relative to the Eurasia plate, the velocities of the 8 Pico Island sites and 4 sites on the eastern half of Faial Island average $3.5 \pm 0.5$ mm/yr (2-$\sigma$), approximately 80% of the Nubia–Eurasia plate rate (Fig. 5D) and ~1 mm/yr faster than sites on S. Jorge Island. To test for significant motion of the Pico/Faial volcanic ridge relative to the Nubia plate, we repeated the statistical test for an additional plate using the 49 Nubia plate site velocities and 12 velocities from Pico and eastern Faial islands. The differ-

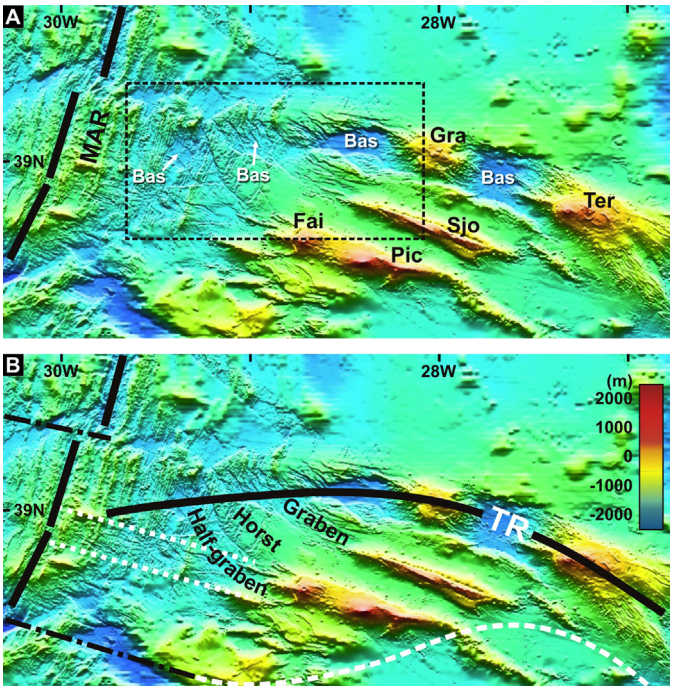


**Fig. 6.** Bathymetry of the western end of the TR, in its junction with the MAR axis. Black heavy lines – ridge axes (MAR and TR). Long-dashed white line – northern shoulder of the TR. Dashed white line – southern limit of deformation and seismicity, here proposed as the southern boundary of the diffuse Nubia–Eurasia boundary, based on extension-related structures, seismicity and GPS measurements. Dash-dot lines – transform faults. Dotted lines mark the limits of a strip of concentrated N110°normal faulting. Bas – basins. Lighting from N. Dashed rectangle marks the region shown in Fig. 7. JPG image made available by Joaquim Luis (http://w3.ualg.pt/~jluis/).

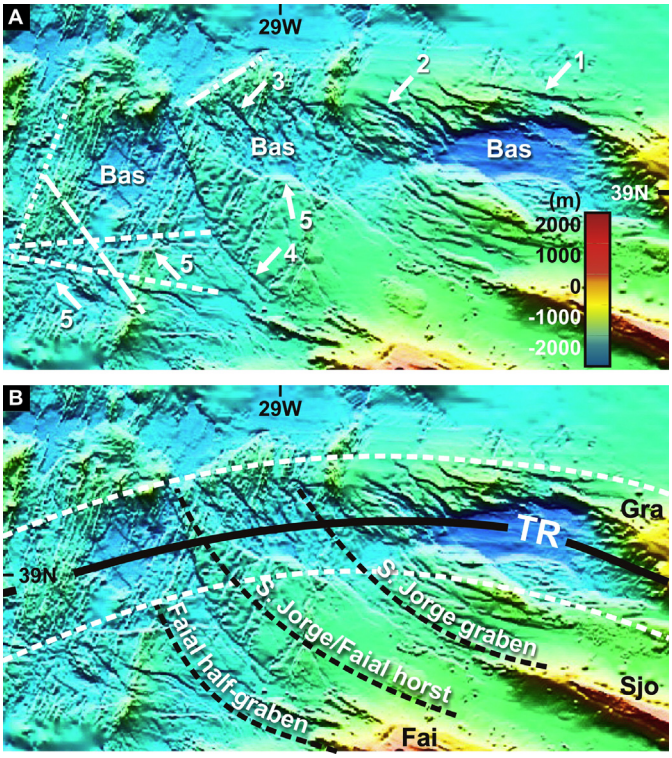


**Fig. 7.** Close up of Fig. 6, as marked by the dashed rectangle. Note: (1) the gradual change in orientation of faults marked 1 to 3 in A; (2) the main structural orientations – dominant faults striking N80–110° (dashed white lines in A) and N150° (long-dashed white line in A), N60° faults (e.g. dash-dotted line in A) bounding some basins, and MAR linear fabric (dotted line in A); (3) the curved graben-horst outlined in B; (4) suggested boundaries of western termination of the TR, with deformation mostly by en échelon normal faulting and formation of basins (Bas) (dashed thick white line in B); (5) the similarity between the shape and orientation of the two basins marked Bas in black. Full black line in B – axis of the TR. Lighting from N.

ence in the least-squares fits for models that fit these two velocity subsets with one or two angular velocities is significant at a confidence level much greater than 99%, with $F = 23.7$ for 3 versus 116 degrees of freedom. We conclude that the Pico/Faial volcanic ridge moves relative to the Nubia plate (also see black arrow in Fig. 5A).

Given the similarity of the velocities of stations on Pico Island and the eastern half of Faial Island, we inverted them together to construct a frame of reference tied to the Faial/Pico volcanic ridge. The resulting velocity field (Fig. 5a) clearly shows ~1 mm/yr of NE-directed extension between the Faial/Pico and S. Jorge volcanic ridges. It also illustrates that sites in western Faial move relative to the volcanic ridge farther east. Although the reasons for this movement are unclear, their proximity to the 1957/58 eruption that added 1.5 $km^2$ to western Faial suggests a volcanic origin for the anomalous GPS velocities.

## 4. Structural and seismic data

### 4.1. Structural data

In the mostly submarine Azores region, detailed bathymetric maps are useful for interpreting recent seafloor deformation because faults are abundant, young (as evidenced by the abundance of seismic activity), are clearly revealed due to low sedimentation rates, and are easily recognized due to their significant vertical offsets. We thus invest significant effort below in interpreting the available bathymetry to provide a framework for understanding both the regional-scale deformation at the western end of the Nubia–Eurasia boundary and for interpreting the GPS velocities.

The Nubia–Eurasia plate boundary in the Azores is defined by the following series of features, which are described below and illustrated in Figs. 6 and 7.

(1) The Terceira Rift is a prominent sigmoidal and deep graben, which extends several hundred km from the MAR axis (at ca. 39°N, 29.89°W) to the East Formigas Basin near the junction with the Azores–Gibraltar Fault (Figs. 1 and 6). The rift is filled at regular spaces (ca. 80 km) by concentrated volcanism forming islands or seamounts that rise near to the sea surface.
(2) A curved graben-horst structure (Figs. 6B and 7B), west of Faial and S. Jorge islands, bounded by faults that gradually change strike from azimuth N160° in the N to azimuth N110° in the S (marked 4 in Fig. 7A). The grabens are here called S. Jorge graben and Faial half-graben, and the intervening tectonic high here called the S. Jorge–Faial horst (Fig. 7B). The main fault scarps bounding these grabens are as high as 200 m.
(3) Smaller trapezoidal basins bounded on all four sides by faults (marked Bas in Figs. 6 and 7). These basins occur along two lineaments, mostly between Graciosa Island and MAR axis.
(4) Faults arranged en échelon in an ENE-WSW band running from the N edge of the West Graciosa Basin to close to the MAR axis (marked 1, 2 and 3 in Fig. 7A); fault strike varies gradually from N100° in the E to N145° in the W. From their bathymetric expressions, the faults appear to be normal faults dipping to W (mostly) and E, thus defining grabens (e.g. the S. Jorge graben), half grabens (e.g. the Faial half-graben) and horsts (e.g. the S. Jorge/Faial horst) (Figs. 6 and 7).
(5) Faults with different trends, mostly concentrated along the N110° (white dashed lines in Figs. 6 and 7), N150° long-dashed line) and N60° (dash-dotted line) directions.
(6) Close to the MAR axis, fractures and faults are mostly perpendicular to the ridge axis (parallel to transforms), and thus

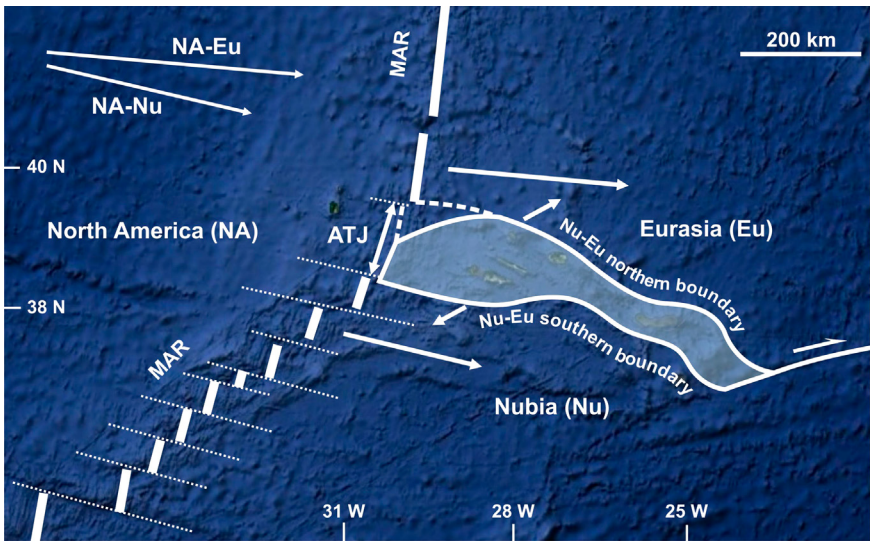


**Fig. 8.** Proposed Nu–Eu plate boundary in the Azores. Shadowed area is the diffuse plate boundary inferred from GPS, bathymetric, structural and seismic data. Inset on top left corner shows kinematics of the Nubia and Eurasia lithospheric plates (DeMets et al., 2010). Dotted lines represent transform faults. Background image is from Google.

strike between N80° and N110°. These fractures/faults are disrupted by the N150° aults (marked 5 in Fig. 7).

(7) Linear volcanic ridges that seem to have grown mostly along N110° fractures, at least during the last 400 kyr (Hildenbrand et al., 2008, 2012a, 2012b, 2013). The S. Jorge Island lies on top of the S. Jorge graben, and the Pico–Faial ridge sits on top of the northern edge of the Faial half graben.

(8) Strip of N110° normal faulting stretching from the MAR axis to the Faial-Pico ridge. This concentration of normal faulting can be the result of MAR change in strike at around 39°N (Fig. 6b).

Detailed bathymetric images of some of the major structures described above, as well as detailed bathymetry around some of the islands studied in the present work, can be found in Mitchell et al. (2008, 2012), Quartau and Mitchell (2013), Quartau et al. (2012), Stretch et al. (2006) and Tempera et al. (2012). Madeira and Brum da Silveira (2003) reported on the inland expression of some of the faults described above.

### 4.2. Seismic data

Earthquake epicentres and focal mechanisms offer useful information about the local tectonics (Fig. 2). In general, the widespread seismicity is consistent with the hypothesis that deformation in the study area is distributed rather than concentrated along a well-defined plate boundary. For example, earthquakes located west of the Pico–Faial ridge are most likely the result of extension within the Faial half-graben (Figs. 7 and 8), and earthquakes west of S. Jorge are probably related to opening across the S. Jorge graben (Figs. 7 and 8). Both support the GPS evidence for distributed oblique extension between Terceira, S. Jorge, and Pico/Faial islands.

The few available earthquake focal mechanisms (Fig. 2A) define two possible fault planes, N100–120° and N140–160°, both coinciding with the dominant orientations of faults in the bathymetry (Figs. 7 and 8). Analyses of body waves and aftershocks of the $M = 7.2$ 1980 earthquake (Hirn et al., 1980; Grimison and Chen, 1988; Borges et al., 2007) suggest that it ruptured an N150°-striking fault, thereby implying sinistral strike-slip motion (Fig. 2A). From body-wave modeling, Borges et al. (2007) also proposed that the $M_w = 6.2$ 1998 Faial Island earthquake ruptured a N150°-striking fault. Matias et al. (2007) also suggested that the 1998 Faial earthquake was a shallow (<5 km depth) sinistral strike-slip earthquake on a N150°-striking fault. In contrast, Fernandes et al. (2002) were unable to identify the rupture plane of the 1998 Faial earthquake based on ground motion and numerical modeling.

Assuming that both of these strike-slip earthquakes ruptured faults that strike ~N150°, the faults are oriented at a high angle to the Nubia–Eurasia plate direction (Fig. 4B) and thus cannot accommodate Nubia–Eurasia motion by themselves. By inference, other faults must accommodate some of the plate movement. Within the study area, the tensional axes for the eight strike-slip and normal-faulting earthquakes between 29.5°W and 27.5°W in Fig. 2A are nearly all oriented NNE–SSW. The average T axis orientation for these eight earthquakes, N22°E (indicated by double-headed arrows in Figs. 2 and 5B), is perpendicular to the volcanic ridges occupied by S. Jorge and Pico and Faial islands, which trend N110°E. The direction of principal instantaneous extensional strain indicated by the earthquakes is thus consistent with (i.e. orthogonal to) the trends of the main volcanic ridges. The average T axis is however oriented 45° and 70° counter clockwise from the Nubia–Eurasia directions predicted by the MORVEL and GPS angular velocities for Nubia–Eurasia motion, respectively.

The discrepancy between the predicted plate motion and the seismic deformation can be reconciled by one or more of the following: (1) The earthquakes recorded during the past few decades may not fully characterize the long-term deformation in the study area given the slow deformation rates, (2) crustal extension south of the Terceira Rift may be accompanied by aseismic block rotations, and (3) partitioning of the plate motion could occur, possibly between structures in the Terceira Rift and the volcanic ridges SW of Terceira Island.

In summary, well-constrained, high-magnitude earthquakes summarized in Borges et al. (2007) and augmented by more recent earthquakes (Fig. 2A) indicate that earthquakes are dominantly normal-faulting or strike slip. At least some of the latter record sinistral strike-slip motion along faults trending N150°, at high angle to the predicted plate motion. The bulk of the evidence suggests that deformation is diffuse and may include either block rotations south of the Terceira Rift or partitioning of distinctly different motions within different domains of the study area in order to accommodate the predicted motion between Nubia and Eurasia.

## 5. Discussion

### 5.1. GPS constraints on inter-island motions

A comparison of the GPS velocities of Pico, Faial, S. Jorge and Terceira islands with the Nubia–Eurasia velocity in the Azores region (ca. 4.5 mm/yr, DeMets et al., 2010) shows that the islands belong to neither the Eurasia nor Nubia plates. Relative to Eurasia, Terceira moves ca. 2 mm/yr to the west, a likely result of its location within the Terceira Rift. S. Jorge, which lies on the southern shoulder of the Terceira Rift WSW of Terceira Island, moves WSW at ca. 3 mm/yr relative to the Eurasia plate. S. Jorge thus moves away from Terceira at ca. 1 mm/yr, as the result of aggregate opening across the Terceira Rift and the S. Jorge graben (Figs. 5 and 8). Faial and Pico move to the WSW away from Eurasia at ca. 3.5 mm/yr faster than both S. Jorge and Terceira islands, and consistent with distributed oblique divergence between the NE edge of the Terceira Rift and Pico/Faial islands.

### 5.2. Is the Terceira Rift the Nubia–Eurasia plate boundary?

The new GPS velocities permit a strong test of the hypothesis that the Terceira Rift is the sole plate boundary structure. Since Terceira Island is located within the rift, GPS velocities from Terceira Island cannot be used for the test. Rather, GPS velocities from S. Jorge, the nearest island WSW of the Terceira Rift, must be used. As is shown in Fig. 5D, sites on S. Jorge Island move to the WSW from 2 to 4 mm/yr and average $2.7 \pm 0.7$ mm/yr, ca. 60% of the Nubia–Eurasia plate rate (Fig. 5D). A statistical test for significant motion between S. Jorge and the Nubia plate passes with high probability ($\gg$99% confidence level). The hypothesis that all Nubia–Eurasia motion is accommodated by the Terceira Rift, as suggested by Vogt and Jung (2004), is thus inconsistent with the current GPS data. The available data instead suggest a lower bound of $2 \pm 1$ mm/yr of extension across the Terceira Rift (Fig. 5D), and an upper bound of $2.7 \pm 0.7$ mm/yr based on GPS sites motions on S. Jorge Island and the unlikely assumption that no extension occurs across the S. Jorge graben between S. Jorge and Terceira islands.

### 5.3. Implications for Nubia–Eurasia plate boundary geometry

Taken together, the GPS, bathymetric, and seismic data define the volcanic and tectonic framework of the western end of the Nubia–Eurasia plate boundary. The central question of our analysis is whether these data favor a model in which deformation is distributed across a wide zone encompassing the northern half of the Azores plateau or a model in which most or all of the plate boundary slip is confined to a narrow zone. As described above, the GPS observations reject a narrow boundary that coincides with the prominent Terceira Rift. The existence of numerous ESE–WNW-trending faults that cross-cut the young abyssal hill fabric of the MAR between 38.4°N and 39.3°N (Figs. 7 and 8), within what would otherwise be defined as the Azores microplate, strongly argues against a narrow-boundary (or rigid microplate) model. The ESE-WNW-striking faults appear to connect the MAR to the zone of distributed oblique extension defined by Terceira, S. Jorge, Faial, and Pico islands, and thus define a diffuse boundary between the Nubia and Eurasia plates. The distributed seismicity in the same area as these crosscutting faults (Fig. 2B) constitutes additional evidence for distributed deformation, although the epicentral locations are too imprecise to strictly assign the earthquakes to well identified cross-cutting faults.

If the Nubia–Eurasia plate boundary were narrow at the triple junction, seafloor spreading rates would change suddenly along the MAR immediately north and south of the triple junction. The spreading rates instead change gradually (see Fig. 22 in DeMets et al., 2010), indicating there is either a rigid or nearly rigid Azores microplate moving independently of Nubia and Eurasia east of the MAR axis between ~38°N and 39.5°N, or that distributed deformation occurs across a ~140-km-wide zone east of the MAR axis. The evidence outlined in the previous paragraphs clearly favors the latter possibility.

The pattern of GPS velocities and horst-and-graben morphology between Terceira, S. Jorge, and Pico/Faial islands (Figs. 5, 7, 8) offer further evidence for an accommodation of Nubia–Eurasia motion across a wide rather than narrow zone. The GPS velocities clearly show that WSW-directed extension (relative to the Eurasia plate) is accommodated by a combination of opening across the Terceira Rift and smaller scale grabens WSW of the rift (Fig. 5). GPS site velocities only begin to reach the full Nubia–Eurasia plate rate at a distance greater than 140 km south of the Terceira Rift. The GPS velocities clearly show that the extension across the Terceira Rift does not account for all of the plate motion, hence the Eurasia-Nubia plate boundary is not discrete. Oblique extension is instead distributed across a plate boundary at least 140 km wide spanning the islands of Terceira, S. Jorge and Pico/Faial (Fig. 8).

Based on the GPS velocities, seismic data, and seafloor morphology, we hypothesize that Nubia–Eurasia plate motion in the Azores is accommodated by a wide zone of oblique extensional deformation limited by the MAR axis in the west, the northern shoulder of the Terceira Rift in the north, and in the south, by a line that connects the MAR axis at 38.4°N, 30.5°W to the East Formigas Basin (36.9°N, 23.6°W), passing south of the Pico–Faial ridge and SE of the S. Jorge Island. The southern boundary is defined by the transition from the concentration of faults and earthquakes in the north to an area in the south where there are few signs of active deformation.

The above interpretation implies that the Azores triple “point” is better thought of as a diffuse triple junction.

### 5.4. Limitations due to elastic effects of locked faults and volcanic processes

At least two factors limit our interpretations of the tectonic implications of the GPS velocity field. First, the influences of volcanic processes and mass wasting on the GPS velocity field are poorly understood, but may be potentially important on an island-by-island basis (Mendes et al., 2013; Miranda et al., 2012). Second, widespread earthquake activity in the Azores islands (Borges et al., 2007 and Fig. 2B) clearly suggests there are multiple locked faults within our study area. Interseismic elastic deformation associated with these faults and possible viscoelastic effects from large earthquakes during the past few decades both affect the GPS velocity field in the study area to an unknown degree. Depending on the spacing and geometry of the active faults, their elastic effects may overlap and give rise to a GPS velocity field more characteristic of continuous than discrete deformation.

Unfortunately, estimating these location-dependent elastic effects via forward modeling requires knowledge of the principal active faults and their long-term slip rates. Neither are well known – historic earthquakes near Pico, Faial, S. Jorge and Terceira islands are dominantly strike-slip events on submarine faults distributed within the study area (Fig. 2A and Borges et al., 2007). Given the uncertainties in modeling the elastic deformation and the sensitivity of the predicted elastic deformation to the input parameters, we elected not to model those effects.

Inverse modeling of the GPS velocity field and other kinematic constraints such as earthquake focal mechanisms could conceivably be used to discriminate between rigid or semi-rigid microplate and continuum or distributed deformation models for this region (e.g.

McCaffrey, 2002; Meade and Loveless, 2009). Such models however require information about the locations and geometry of the principal block-bounding faults, which, as noted above, remain poorly known for the study area.

## 6. Conclusions

From newly determined GPS velocities from the Azores archipelago, and Eurasia and Nubia plates, we find that oblique WSW-ENE extension between the Nubia and Eurasia plates is accommodated across a series of horsts and grabens that include the Pico/Faial volcanic ridge, which moves mostly with Nubia, Terceira Island, which moves mostly with Eurasia, and S. Jorge Island, whose motion is intermediate between that of Nubia and Eurasia. From these observations and existing bathymetric and seismic data, we conclude the following:

1. The Nubia–Eurasia plate boundary at the longitude of the Azores is diffuse, comprising a ca. 140-km-wide zone of deformation shown in Fig. 8.
2. The opening rate in the Terceira Rift is much smaller than previously thought, because it does not take up the whole deformation imposed by the motions of Nubia and Eurasia.
3. The Azores Triple Junction is diffuse, stretching along the MAR axis between 38.3°N, 30.3°W and 39.4°N, 29.7°W, where spreading rates decrease gradually from ca. 22.5 mm/yr N of 40°N to 19.5 mm/yr S of 38°N.
4. The new data do not require the existence of an independent Azores microplate.

## Acknowledgements

This is a contribution to Project MEGAHazards (PTDC/CTE-GIX/108149/2008) funded by FCT Portugal. Funding for C. DeMets was provided by U.S. National Science Foundation grant OCE-0926274. We are grateful to colleague Joaquim Luis (http://w3.ualg.pt/~jluis/) for kindly offering the higher resolution image of the Azores bathymetry. We thank Neil Mitchell and an anonymous reviewer for comments that helped improve the quality of this manuscript.

## References

Altamimi, Z., Collilieux, X., Legrand, J., Garayt, B., Boucher, C., 2007. ITRF2005: A new release of the international terrestrial reference frame based on time series of station positions and Earth orientation parameters. J. Geophys. Res. 112, B09401, http://dx.doi.org/10.1029/2007JB004949.

Altamimi, Z., Collilieux, X., Metivier, L., 2011. ITRF2008: An improved solution of the international terrestrial reference frame. J. Geod. 8, 457–473.

Argus, D.F., 2007. Defining the translational velocity of the reference frame of Earth. Geophys. J. Int. 169, 830–838.

Argus, D.F., Gordon, R.G., Heflin, M.B., Ma, C., Eanes, R., Willis, P., Peltier, W.R., Owen, S.E., 2010. The angular velocities of the plates and the velocity of Earth's centre from space geodesy. Geophys. J. Int. 180, 913–960.

Böhm, J., Werl, B., Schuh, H., 2006. Troposphere mapping functions for GPS and very long baseline interferometry from European Centre Medium-Range Weather Forecasts operational analysis data. J. Geophys. Res. 111, B02406, http://dx.doi.org/10.1029/2005JB003629.

Borges, J.F., Bezzeghoud, M., Buforn, E., Pro, C., Fitas, A., 2007. The 1980, 1997 and 1998 Azores earthquakes and some seismo-tectonic implications. Tectonophysics 435, 37–54.

Calais, E., DeMets, C., Nocquet, J.-M., 2003. Evidence for a post-3.16 Ma change in Nubia–Eurasia–North America plate motions? Earth Planet. Sci. Lett. 216, 81–92.

Catalão, J., Miranda, J.M., Lourenço, N., 2006. Deformation associated with the Faial (Capelinhos) 1956 eruption. Inferences from 1937–1997 geodetic measurements. J. Volcanol. Geotherm. Res. 155, 151–163.

DeMets, C., Gordon, R.G., Argus, D.F., 2010. Geologically current plate motions. Geophys. J. Int. 181, 1–80.

Dong, D., Herring, T.A., King, R.W., 1998. Estimating regional deformation from a combination of space and terrestrial geodetic data. J. Geod. 72, 200–214.

Dziewonski, A.M., Chou, T.-A., Woodhouse, J.H., 1981. Determination of earthquake source parameters from waveform data for studies of global and regional seismicity. J. Geophys. Res. 86, 2825–2852.

Ekstrom, G., Nettles, M., Dziewonski, A.M., 2012. The global CMT project 2004–2010: Centroid-moment tensors for 13,017 earthquakes. Phys. Earth Planet. Inter. 200–201, 1–9.

Fernandes, R.M.S., Miranda, J.M., Catalão, J., Luis, J.F., Bastos, L., Ambrosius, B.A.C., 2002. Coseismic displacements of the MW = 6.1, July 9, 1998, Faial earthquake (Azores, North Atlantic). Geophys. Res. Lett. 29, 1–4.

Fernandes, R.M.S., Bastos, L., Miranda, J.M., Lourenço, N., Ambrosius, B.A.C., Noomen, R., Simons, W., 2006. Defining the plate boundaries in the Azores region. J. Volcanol. Geotherm. Res. 156, 1–9.

Grimison, N., Chen, W., 1988. The Azores–Gibraltar plate boundary: focal mechanisms, depths of earthquakes and their tectonic implications. J. Geophys. Res. 91, 2029–2047.

Hirn, A., Haessler, J., Hoang Trong, P., Wittlinger, G., MendesVictor, L., 1980. Aftershock sequence of the January 1st, 1980 earthquake and present-day tectonics in the Azores. Geophys. Res. Lett. 7, 501–504.

Herring, T.A., King, R.W., McClusky, S.C., 2010. GLOBK Reference Manual Release 10.4. Department of Earth, Atmospheric, and Planetary Sciences, Massachusetts Institute of Technology, Cambridge.

Hildenbrand, A., Madureira, P., Marques, F.O., Cruz, I., Henry, B., Silva, P., 2008. Multistage evolution of a sub-aerial volcanic ridge over the last 1.3 Myr: S. Jorge Island, Azores Triple Junction. Earth Planet. Sci. Lett. 273, 289–298.

Hildenbrand, A., Marques, F.O., Fernandes, J.C.C.C., Catita, C.M.S., Costa, A.C.G., 2012a. Large-scale active slump of the southeastern flank of Pico Island, Azores. Geology 40, 939–942.

Hildenbrand, A., Marques, F.O., Costa, A.C.G., Sibrant, A.L.R., Silva, P.M.F., Henry, B., Miranda, J.M., Madureira, P., 2012b. Reconstructing the architectural evolution of volcanic islands from combined K/Ar, morphologic, tectonic, and magnetic data: the Faial Island example (Azores). J. Volcanol. Geotherm. Res. 241–242, 39–48.

Hildenbrand, A., Marques, F.O., Costa, A.C.G., Sibrant, A.L.R., Silva, P.M.F., Henry, B., Miranda, J.M., Madureira, P., 2013. Reply to the comment by Quartau and Mitchell on "Reconstructing the architectural evolution of volcanic islands from combined K/Ar, morphologic, tectonic, and magnetic data: The Faial Island example (Azores)". J. Volcanol. Geotherm. Res. 241–242, 39–48, by Hildenbrand et al., 2012. J. Volcanol. Geotherm. Res. 255, 127–130.

Krause, D.C., Watkins, N.D., 1970. North Atlantic crustal generation in the vicinity the Azores. Geophys. J. R. Astron. Soc. 19, 261–283.

Lourenço, N., Luis, J.F., Miranda, J.M., Ribeiro, A., Mendes Victor, L.A., Madeira, J., Needham, H.D., 1998. Morpho-tectonic analysis of the Azores Volcanic Plateau from a new bathymetric compilation of the area. Mar. Geophys. Res. 20, 141–156.

Luis, J.F., Miranda, J.M., 2008. Reevaluation of magnetic chrons in the North Atlantic between 35°N and 47°N: Implications for the formation of the Azores Triple Junction and associated plateau. J. Geophys. Res. 113, B10105, http://dx.doi.org/10.1029/2007JB005573.

Luis, J.F., Miranda, J.M., Galdeano, A., Patriat, P., Rossignol, J.C., Mendes Victor, L.A., 1994. The Azores Triple Junction evolution since 10 Ma from an aeromagnetic survey of the Mid-Atlantic Ridge. Earth Planet. Sci. Lett. 125, 439–459.

Lyard, F., Lefèvre, F., Letellier, T., Francis, O., 2006. Modelling the global ocean tides: a modern insight from FES2004. Ocean Dyn. 56, 394–415.

Madeira, J., Brum da Silveira, A., 2003. Active tectonics and first paleoseismological results in Faial, Pico and S. Jorge islands (Azores, Portugal). Ann. Geophys. 46, 733–761.

Madeira, J., Ribeiro, A., 1990. Geodynamic models for the Azores Triple Junction: a contribution from tectonics. Tectonophysics 184, 405–415.

Mao, A., Harrison, C.G.A., Dixon, T.H., 1999. Noise in GPS coordinate time series. J. Geophys. Res. 104, 2797–2816.

Marquez-Azua, B., DeMets, C., 2003. Crustal velocity field of Mexico from continuous GPS measurements, 1993 to June, 2001: Implications for the neotectonics of Mexico. J. Geophys. Res. 108, http://dx.doi.org/10.1029/2002JB002241.

Matias, L., Dias, N., Morais, I., Vales, D., Carrilho, F., Madeira, J., Gaspar, J., Senos, L., Silveira, A., 2007. The 9th of July 1998 Faial Island (Azores, North Atlantic) seismic sequence. J. Seismol. 11, 275–298.

McCaffrey, R., 2002. Crustal block rotations and plate coupling. In: Stein, S., Freymueller, J. (Eds.), Plate Boundary Zones. In: Geodynamics Series, vol. 30. American Geophysical Union, Washington, pp. 101–122.

Meade, B.J., Loveless, J.P., 2009. Block modeling with connected fault-network geometries and a linear elastic coupling estimator in spherical coordinates. Bull. Seismol. Soc. Am. 99, 3124–3239.

Mendes, V.B., Madeira, J., Brum da Silveira, A., Trota, A., Elosegui, P., Pagarete, J., 2013. Present-day deformation in São Jorge Island, Azores, from episodic GPS measurements (2001–2011). Adv. Space Res. 51, 1581–1592.

Miranda, J.M., Navarro, A., Catalão, J., Fernandes, R.M.S., 2012. Surface displacement field at Terceira Island deduced from repeated GPS measurements. J. Volcanol. Geotherm. Res. 217, 1–7.

Miranda, J.M., Luis, J.F., Abreu, I., Mendes Victor, L.A., Galdeano, Q., Rossignol, J.C., 1991. Tectonic framework of the Azores Triple Junction. Geophys. Res. Lett. 18, 1421–1424.

Mitchell, N.C., Beier, C., Rosin, P., Quartau, R., Tempera, F., 2008. Lava penetrating water: Submarine lava flows around the coasts of Pico Island, Azores. Geochem. Geophys. Geosyst. 9, http://dx.doi.org/10.1029/2007GC001725.

Mitchell, N.C., Stretch, R., Oppenheimer, C., Kay, D., Beier, C., 2012. Cone morphologies associated with shallow marine eruptions: east Pico Island, Azores. Bull. Volcanol. 74, 2289–2300.

Navarro, A., Catalão, J., Miranda, J.M., Fernandes, R.M.S., 2003. Estimation of the Terceira Island (Azores) main strain rates from GPS data. Earth Planets Space 55, 637–642.

Nocquet, J.-M., Calais, E., Parsons, B., 2005. Geodetic constraints on glacial isostatic adjustment in Europe. Geophys. Res. Lett. 32, L06308, http://dx.doi.org/10.1029/2004GL022174.

Petit, G., Luzum, B., 2010. IERS conventions, 2010. IERS Technical Note; No. 36. Verlag des Bundesamts fur Kartographie und Geodasie, Frankfurt am Main.

Quartau, R., Mitchell, N.C., 2013. Comment on "Reconstructing the architectural evolution of volcanic Islands from combined K/Ar, morphologic, tectonic, and magnetic data: The Faial Island example (Azores)". by Hildenbrand et al. 2012. J. Volcanol. Geotherm. Res. 241–242 (2012) 39–48. J. Volcanol. Geotherm. Res. 255, 124–126.

Quartau, R., Tempera, F., Mitchell, N.C., Pinheiro, L.M., Duarte, H., Brito, P.O., Bates, C.R., Monteiro, J.H., 2012. Morphology of Faial Island's shelf: The results of volcanic, erosional, depositional and mass-wasting processes. Geochem. Geophys. Geosyst. 13, http://dx.doi.org/10.1029/2011GC003987.

Saastamoinen, J., 1972a. Contributions to the theory of atmospheric refraction. Bull. Géod. 105, 279–298, I part.

Saastamoinen, J., 1972b. Contributions to the theory of atmospheric refraction. Bull. Géod. 106, 383–397, II part.

Saastamoinen, J., 1973. Contributions to the theory of atmospheric refraction. Bull. Géod. 107, 13–34, III part.

Searle, R., 1980. Tectonic pattern of the Azores spreading centre and triple junction. Earth Planet. Sci. Lett. 51, 415–434.

Stein, S., Gordon, R.G., 1984. Statistical tests of additional plate boundaries from plate motion inversions. Earth Planet. Sci. Lett. 69, 401–412.

Stretch, R., Mitchell, N.C., Portaro, R.A., 2006. A morphometric analysis of the submarine volcanic ridge of Pico Island. J. Volcanol. Geotherm. Res. 156, 35–54.

Tempera, F., Giacomello, E., Mitchell, N.C., Campos, A.S., Henriques, A.B., Martins, A., Bashmachnikov, I., Mendonça, A., Morato, T., Colaço, A., Porteiro, F.M., Catarino, D., Gonçalves, J., Pinho, M.R., Isidro, E.J., Santos, R.S., Menezes, G., 2012. Mapping the Condor seamount seafloor environment and associated biological assemblages (Azores, NE Atlantic). In: Harris, P.T., et al. (Eds.), Seafloor Geomorphology as Benthic Habitat: Geohab Atlas of Seafloor Geomorphic Features and Benthic Habitats. Elsevier, London, pp. 807–818.

Vogt, P.R., Jung, W.Y., 2004. The Terceira Rift as hyper-slow, hotspot-dominated oblique spreading axis: A comparison with other slow-spreading plate boundaries. Earth Planet. Sci. Lett. 218, 77–90.

Zumberge, J.F., Heflin, M.B., Jefferson, D.C., Watkins, M.M., Webb, F.H., 1997. Precise point positioning for the efficient and robust analysis of GPS data from large networks. J. Geophys. Res. 102, 5005–5017.

Earth and Planetary Science Letters 387 (2014) 1–3

Contents lists available at ScienceDirect

Earth and Planetary Science Letters

www.elsevier.com/locate/epsl

Corrigendum

# Corrigendum to "GPS and tectonic evidence for a diffuse plate boundary at the Azores Triple Junction" [Earth Planet. Sci. Lett. 381 (2013) 177–187]

F.O. Marques [a,*], J.C. Catalão [b], C. DeMets [c], A.C.G. Costa [b,d], A. Hildenbrand [d,e]

[a] Universidade de Lisboa, Lisboa, Portugal
[b] Universidade de Lisboa, Instituto Dom Luiz, Lisboa, Portugal
[c] Department of Geoscience, University of Wisconsin–Madison, Madison, USA
[d] Université Paris-Sud, Laboratoire IDES, UMR 8148, Orsay, F-91405, France
[e] CNRS, Orsay, F-91405, France

ARTICLE INFO

*Article history:*
Received 1 November 2013
Accepted 4 November 2013
Available online xxxx
Editor: P. Shearer

Figs. 6 and 7 of this paper are images of high-resolution bathymetry of the Azores Plateau, kindly provided to us by Dr. Joaquim Luis. However, because these data are not yet released or published, Dr. Luis did not intend to give formal permission to include the images in our paper. We therefore regret our premature publication, in Figs. 6 and 7, of parts of the image offered by Dr. Luis, and have revised our paper accordingly.

Below is the new text and new versions of Figs. 6 and 7, which should take the place of the original figures and text. The new figures were made using the low-resolution bathymetry made available by Luis at http://w3.ualg.pt/~jluis/misc/ac_plateau1km.grd (Lourenço et al., 1998).

### 4.1. Structural data

In the mostly submarine Azores region, bathymetric maps are useful for interpreting recent seafloor deformation, because faults are abundant, young (as evidenced by the abundance of seismic activity), clearly revealed due to low sedimentation rates, and easily recognized due to their significant vertical offsets. We thus invest significant effort below in interpreting the available bathymetry (http://w3.ualg.pt/~jluis/misc/ac_plateau1km.grd) to provide a framework for understanding both the regional-scale deformation at the western end of the Nubia–Eurasia boundary and for interpreting the GPS velocities. The Nubia–Eurasia plate boundary in the Azores is defined by the following series of features:

(1) The Terceira Rift, which is a prominent sigmoidal and deep graben that extends several hundred km from the MAR axis (at ca. 39°00′ N, 30°02′ W) to the East Formigas Basin near the junction with the Azores–Gibraltar Fault (Fig. 1 and Fig. 6). The rift is filled at regular spaces (ca. 80 km) by concentrated volcanism forming islands or seamounts that rise near to the sea surface.
(2) A curved graben-horst structure (Figs. 6A and 7), west of Faial and S. Jorge islands, bounded by faults that gradually change strike from azimuth N160° in the N to azimuth N110° in the S (Fig. 6B). The grabens are here called S. Jorge graben and Faial Half-graben, and the intervening tectonic high here called S. Jorge/Faial Horst (Fig. 7). The main fault scarps bounding these grabens are as high as 400 m.
(3) Smaller trapezoidal basins bounded on all four sides by faults (marked Ba in Fig. 6). These basins occur mostly between the Graciosa Island and the MAR axis.
(4) Faults arranged en échelon in an ENE-WSW band running from the N edge of the West Graciosa Basin to close to the MAR axis (dashed lines in Fig. 6B). Fault strike varies gradually from N100° in the E to N145° in the W. From their bathymetric expressions, the faults appear to be normal faults dipping to W (mostly) and E, thus defining grabens (e.g. the S. Jorge graben), half grabens (e.g. the Faial Half-graben) and horsts (e.g. the S. Jorge/Faial Horst) (Fig. 7).
(5) Faults with different trends, mostly concentrated along the azimuths N110° (long dashed lines in Fig. 6B) and N150° (long dash-dotted lines). The MAR fabric (dotted lines) is disrupted

DOI of original article: http://dx.doi.org/10.1016/j.epsl.2013.08.051.
* Corresponding author. Tel.: +351217500000; fax: +351217500064.
*E-mail address:* fomarques@fc.ul.pt (F.O. Marques).

0012-821X/$ – see front matter © 2013 Elsevier B.V. All rights reserved.
http://dx.doi.org/10.1016/j.epsl.2013.11.029

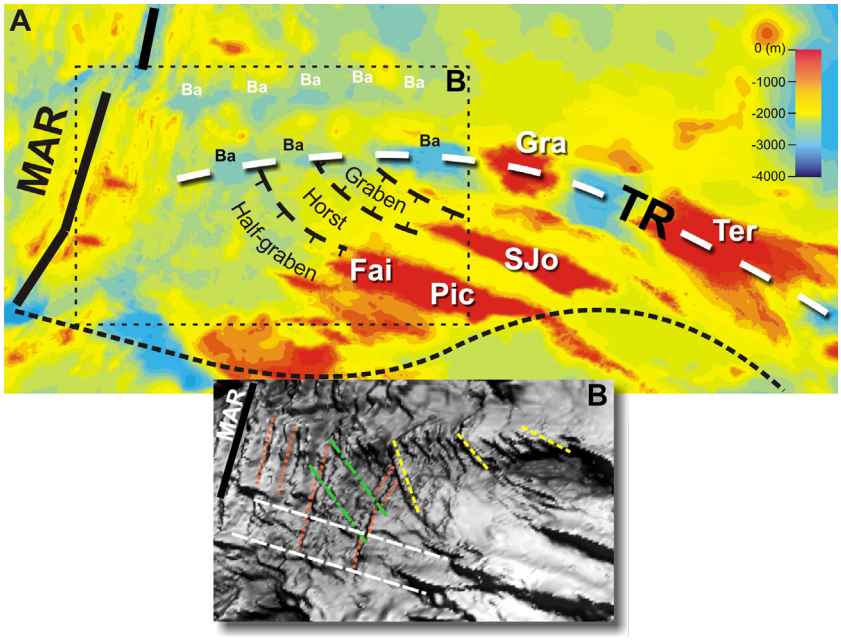


**Fig. 6.** Bathymetry (A) and shaded relief (B) built using available bathymetry data (http://w3.ualg.pt/~jluis/misc/ac_plateau1km.grd). A – Bathymetry of the western end of the Terceira Rift (TR), in its junction with the MAR axis. Note the succession of rhomboidal basins (black Ba) and seamounts/ridges making up the TR axis and shoulders, respectively. White long-dashed line – TR axis. Black dashed-line – southern limit of deformation and seismicity, here proposed as the southern boundary of the diffuse Nubia–Eurasia boundary, based on extension-related structures, seismicity and GPS measurements. Ba – basin. Dashed rectangle – position of B. B – Shaded relief (lighting from NE) of the area marked by dashed rectangle in A. Dotted orange lines – MAR fabric. Dashed yellow lines – en échelon faults with strike varying from N110° to N160°. Dash-dotted green lines – N150° fault system. Long-dashed white lines – N110° fault system, which also mark the limits of a strip of concentrated N110° normal faulting. (For interpretation of the references to color in this figure legend, the reader is referred to the web version of this article.)

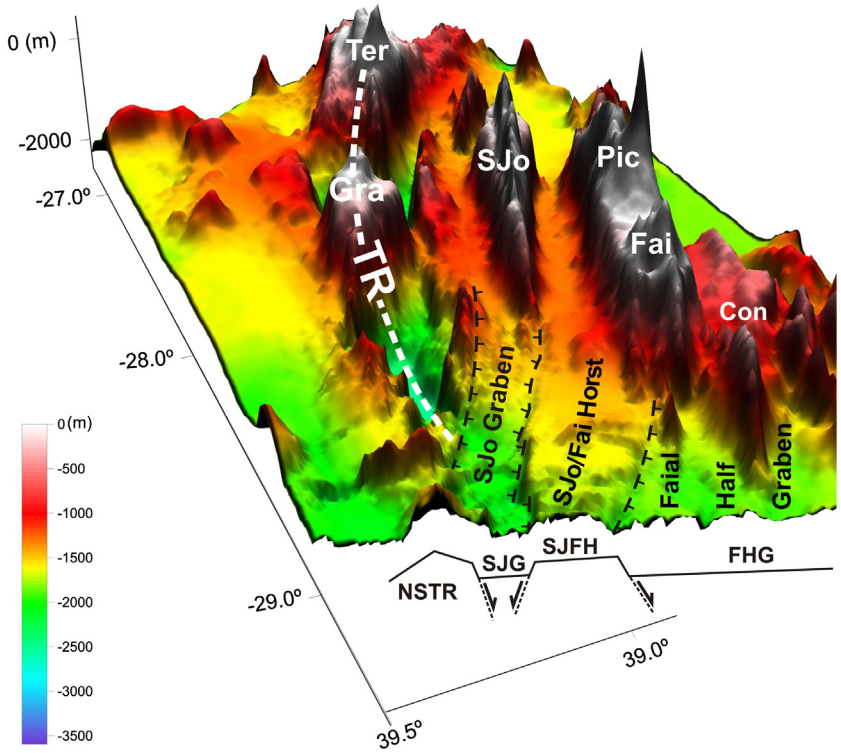


**Fig. 7.** 3D surface built using available bathymetry data (http://w3.ualg.pt/~jluis/misc/ac_plateau1km.grd). Note the prominent graben-horst structure close to the junction between the TR and the MAR. The islands of Terceira (Ter), Graciosa (Gra), S. Jorge (SJo), Pico (Pic) and Faial (Fai) are shown. Con – Condor seamount. NSTR – northern shoulder of the Terceira Rift (TR). SJG – S. Jorge Graben. SJFH – S. Jorge/Faial Horst. FHG – Faial Half-graben. Vertical lighting.

by the N110° and N150° faults. The S. Jorge/Faial Horst is bounded by faults that gradually change direction from N160° to N110° (Figs. 6 and 7).

(6) Linear volcanic ridges that seem to have grown mostly along N110° fractures/faults, at least during the last 400 kyr (Hildenbrand et al., 2008, 2012a, 2012b, 2013). The S. Jorge Island lies on top of the S. Jorge graben, and the Pico–Faial ridge sits on top of the northern edge of the Faial Half-graben.

(7) Strip of N110° normal faulting stretching from the MAR axis to the Faial–Pico ridge. This concentration of normal faulting

can be the result of MAR change in strike at around 39° N (Fig. 6B).

This proposed model of distributed deformation is consistent with high-resolution bathymetry (Luis, personal communication, 2012), which shows faults that crosscut the seafloor fabric.

## References

Hildenbrand, A., Madureira, P., Marques, F.O., Cruz, I., Henry, B., Silva, P., 2008. Multistage evolution of a sub-aerial volcanic ridge over the last 1.3 Myr: S. Jorge Island, Azores Triple Junction. Earth Planet. Sci. Lett. 273, 289–298.

Hildenbrand, A., Marques, F.O., Fernandes, J.C.C.C., Catita, C.M.S., Costa, A.C.G., 2012a. Large-scale active slump of the southeastern flank of Pico Island, Azores. Geology 40, 939–942.

Hildenbrand, A., Marques, F.O., Costa, A.C.G., Sibrant, A.L.R., Silva, P.M.F., Henry, B., Miranda, J.M., Madureira, P., 2012b. Reconstructing the architectural evolution of volcanic islands from combined K/Ar, morphologic, tectonic, and magnetic data: the Faial Island example (Azores). J. Volcanol. Geotherm. Res. 241–242, 39–48.

Hildenbrand, A., Marques, F.O., Costa, A.C.G., Sibrant, A.L.R., Silva, P.M.F., Henry, B., Miranda, J.M., Madureira, P., 2013. Reply to the comment by Quartau and Mitchell on "Reconstructing the architectural evolution of volcanic islands from combined K/Ar, morphologic, tectonic, and magnetic data: The Faial Island example (Azores)". J. Volcanol. Geotherm. Res. 241–242, 39–48, by Hildenbrand et al., 2012. J. Volcanol. Geotherm. Res. 255, 127–130.

Lourenço, N., Luis, J.F., Miranda, J.M., Ribeiro, A., Mendes Victor, L.A., Madeira, J., Needham, H.D., 1998. Morpho-tectonic analysis of the Azores Volcanic Plateau from a new bathymetric compilation of the area. Mar. Geophys. Res. 20, 141–156.

# ANNEX IV

## The 1998 Faial earthquake, Azores: Evidence for a transform fault associated with the Nubia–Eurasia plate boundary? (Marques et al., 2014b)

Tectonophysics 633 (2014) 115–125

Contents lists available at ScienceDirect

Tectonophysics

journal homepage: www.elsevier.com/locate/tecto

# The 1998 Faial earthquake, Azores: Evidence for a transform fault associated with the Nubia–Eurasia plate boundary?

F.O. Marques [a,*], J. Catalão [b], A. Hildenbrand [c,d], A.C.G. Costa [b,c], N.A. Dias [b,e]

[a] Universidade de Lisboa, Lisboa, Portugal
[b] IDL, Universidade de Lisboa, Lisboa, Portugal
[c] Université Paris-Sud, Laboratoire IDES, UMR8148, Orsay F-91405, France
[d] CNRS, Orsay F-91405, France
[e] Instituto Superior de Engenharia de Lisboa, Lisboa, Portugal

ARTICLE INFO

*Article history:*
Received 19 March 2014
Received in revised form 4 June 2014
Accepted 22 June 2014
Available online 28 June 2014

*Keywords:*
Azores Triple Junction
1998 Faial earthquake
Transform fault
Block rotation and fault termination
Faial Graben
Terceira Rift

ABSTRACT

With very few exceptions, M > 4 tectonic earthquakes in the Azores show normal fault solution and occur away from the islands. Exceptionally, the 1998 shock was pure strike-slip and occurred within the northern edge of the Pico–Faial Ridge. Fault plane solutions show two possible planes of rupture striking ENE–WSW (dextral) and NNW–SSE (sinistral). The former has not been recognised in the Azores, but is parallel to the transform direction related to the relative motion between the Eurasia and Nubia plates. Therefore, the main question we address in the present study is: do transform faults related to the Eurasia/Nubia plate boundary exist in the Azores? Knowing that the main source of strain is related to plate kinematics, we conclude that the sinistral strike-slip NNW–SSE fault plane solution is not consistent with either the fault dip (ca. 65°, which is typical of a normal fault) or the ca. ENE–WSW direction of maximum extension; both are consistent with a normal fault, as observed in most major earthquakes on faults striking around NNW–SSE in the Azores. In contrast, the dextral strike-slip ENE–WSW fault plane solution is consistent with the transform direction related to the anticlockwise rotation of Nubia relative to Eurasia. Altogether, tectonic data, measured ground motion, observed destruction, and modelling are consistent with a dextral strike-slip source fault striking ENE–WSW. Furthermore, the bulk clockwise rotation measured by GPS is typical of bookshelf block rotations observed at the termination of such master strike-slip faults. Therefore, we suggest that the 1998 earthquake can be related to the WSW termination of a transform (ENE–WSW fault plane solution) associated with the Nubia–Eurasia diffuse plate boundary.

© 2014 Elsevier B.V. All rights reserved.

## 1. Introduction

The Central Azores Islands (Faial, Pico, S. Jorge, Graciosa and Terceira islands, Figs. 1 and 2) were born during the Quaternary at the Azores Triple Junction (ATJ), more specifically within the boundary between the Eurasia (Eu) and Nubia (Nu) plates. The ATJ is currently of the rift–rift–rift type. The Middle-Atlantic Rift makes the northern and southern arms, and the eastern arm is made of the Terceira Rift (TR), which connects to the Gloria Fault and the Azores Gibraltar Fault Zone in the east (Fig. 1). According to DeMets et al. (2010), there should be an Azores microplate interacting differently with the neighbouring Eu and Nu plates (Fig. 1): the Azores–Eu motion should be dextral oblique extension, and the Azores–Nu motion should be dextral strike-slip along an ENE–WSW direction. Based on GPS, tectonic and seismic data, Marques et al. (2013) concluded that the Nu–Eu boundary in the Azores is not discrete, and therefore the existence of an intervening Azores microplate is unlikely. Instead, the boundary is diffuse in its western half, with deformation accommodated by a ca. 150 km wide strip extending south of the western half of the TR. This has major implications in the distribution of strain, because maximum extension (approximately ENE–WSW) should be similar all over the diffuse boundary. The general structure in the diffuse boundary (Central Azores) is that of a sequence of WNW–ESE grabens and horsts (Fig. 2): the Graciosa and Terceira islands grew inside the TR; the Pico–Faial volcanic ridge sits on the master fault bounding the Faial Half-graben in the north; and the S. Jorge Island developed in the middle of a narrow graben, the S. Jorge Graben.

With the exception of the very small area of the islands (Fig. 1), the Azores crust lies below sea level, which is a strong limitation to directly observe and characterise deformation. Moreover, appreciable surface rupture related to main tectonic and M > 4 earthquakes has not been observed within the islands. Even if there were minor surface rupture, the superficial effects of very slow deformation imposed by the hyper-slow differential motion between Eurasia and Nubia (ca. 4 mm/yr) would not survive, because erosion, sedimentation and volcanic rates are much faster than the tectonic rate. For instance, Costa et al. (2014) and Hildenbrand et al. (2008, 2012a,b) have shown that major periods of massive island destruction (mostly large-scale landslides and flank

* Corresponding author. Tel.: +351 217500000; fax: +351 217500064.
*E-mail address:* fomarques@fc.ul.pt (F.O. Marques).

http://dx.doi.org/10.1016/j.tecto.2014.06.024
0040-1951/© 2014 Elsevier B.V. All rights reserved.

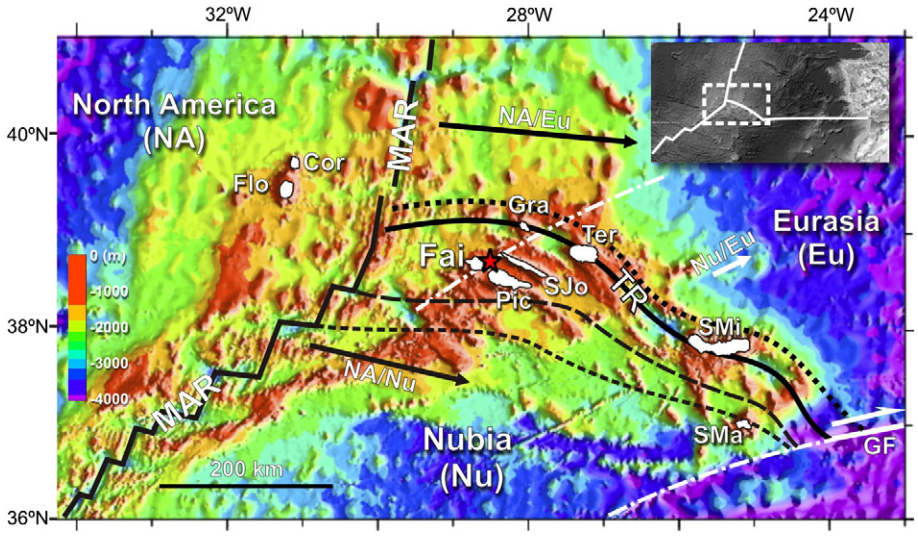


**Fig. 1.** Sketch of the general framework of the Azores Triple Junction. Black-rimmed red star marks the 1998 Faial earthquake. MAR and TR are the Mid-Atlantic and Terceira rifts, respectively. GF is the dextral strike-slip Gloria Fault. Full black arrows represent the velocity vectors of Eurasia (Eu) and Nubia (Nu) relative to North America (NA). Full white arrow represents the velocity vector of Eu relative to Nu. Dotted black line marks the northern shoulder of the TR, which represents the northern Nu/Eu plate boundary for both the diffuse boundary and the microplate scenarios. Black dashed and black long-dashed lines mark the southern boundaries of the hypothetical Azores microplate and the diffuse Nu/Eu plate boundary, respectively. White dash-dotted lines represent small circles around the MORVEL Nu/Eu pole (DeMets et al., 2010), which represent the transform direction related to the Nu/Eu boundary. From W to E, the Azores Islands are Flores (Flo), Corvo (Cor), Faial (Fai), Pico (Pic), S. Jorge (SJo), Graciosa (Gra), Terceira (Ter), S. Miguel (SMi), and Santa Maria (SMa).
Background image built with data retrieved from http://topex.ucsd.edu/marine_topo/mar_topo.html (Smith and Sandwell, 1997).

collapses) are intercalated with short periods of fast volcanic construction, which are able to mask intra-island evidence of the effects of large-scale tectonics occurring in the underlying plateau.

The Azores earthquakes show a few characteristics that make the 1998 Faial shock unique: (1) it has been reported since the early 1930s that very rare earthquakes (i.e. of tectonic origin, and M > 4) have seemingly occurred inside the islands (e.g. Agostinho, 1931; Borges et al., 2007; Machado, 1959). In fact, no major intra-island tectonic earthquake has been recorded in the Azores since earthquakes can be measured instrumentally. Locally, earthquakes occur inside the islands, but they are mostly related to volcanism rather than tectonics, which is the case, for instance, of the ongoing seismic crisis in the S. Miguel Island (e.g. Silva et al., 2012). (2) From a total of 24 major earthquakes for which the focal mechanisms have been computed (e.g. Borges et al., 2007), very few tectonic and M > 4 earthquakes are strike-slip (4 out of 24), and by far the large majority shows normal fault kinematics (16 out of 24) (e.g. Borges et al., 2007; Buforn et al., 1988, 2004; Grimison and Chen, 1988; Hirn et al., 1980; McKenzie, 1972; Miranda et al., 1998; Moreira, 1985; Udías et al., 1976 for a synthesis). (3) The main fault trends associated with tectonic M > 4 earthquakes are the WNW–ESE and NNW–SSE trends. The exception to this most common scenario can be the Faial 1998 shock, because deformation propagated inland, and the main source fault is pure strike-slip. Furthermore, this peculiar earthquake occurred within the Pico–Faial volcanic ridge (although close to the northern edge) and it can be related to a different trend (ENE–WSW), overlooked in the Azores, although of probable large-scale tectonic meaning as argued in the present paper. These characteristics, together with the relationship with plate kinematics and strains, support and justify the importance of studying the 1998 Faial shock.

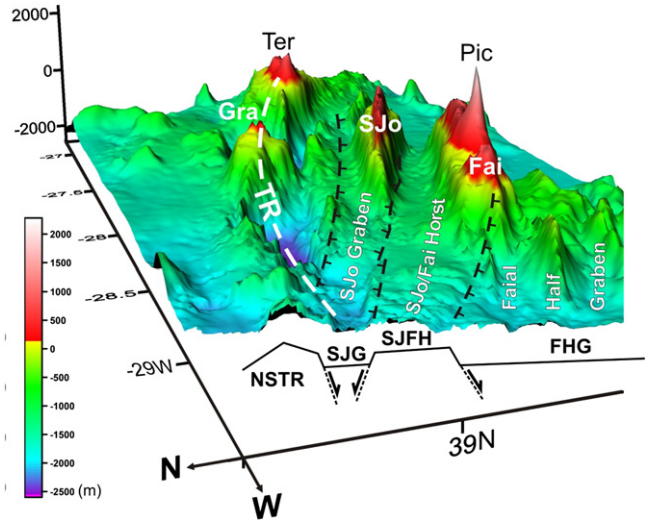


**Fig. 2.** 3D surface with interpreted main tectonic framework (viewed from WNW). TR is the Terceira Rift. Fai, Pic, SJo, Gra and Ter correspond to the islands of Faial, Pico, S. Jorge, Graciosa and Terceira, respectively.
3D surface built using topographic data available at http://w3.ualg.pt/~jluis/misc/ac_plateau1km.grd (Lourenço et al., 1998).

The TR is a ca. 620 km-long sigmoidal graben filled at regular spaces (ca. 80 km) by large-volume central volcanism making up islands and large seamounts (Fig. 1). Here we hypothesise that the regular spacing is due to concentrated volcanism at the intersection between the TR and transform faults related to the Nu/Eu plate boundary, thus making up privileged conduits. However, such transforms have never been recognised, which could be due in part to the low resolution of the bathymetry. Therefore, we looked for different evidence, in the form of earthquakes, like the 1998 Faial earthquake, which can be related to transform motion due to the Nu/Eu interaction in the Azores.

Given the premises and current knowledge outlined above, the questions we address in this article are: (1) which was the fault responsible for the earthquake? The sinistral NNW–SSE or the dextral ENE–WSW? (2) Which one is consistent (or inconsistent) with the known plate kinematics in the Azores? (3) What kind of fault is it? Are there transform faults associated with the Nu/Eu plate boundary? (4) What is the meaning of the measured ground deformation? (5) What are the sources of strain/stress? Our ultimate objective is a better understanding of strain (mostly faults) in the Azores Triple Junction, in terms of typology,

distribution, geometry, kinematics, earthquake generation and sources of stress.

In order to tackle these problems, we used: (1) a 50 m resolution DEM to evaluate the topography and interpret the main tectonic lineaments; (2) a detailed structural analysis to recognise and characterise the main faults, and interpret their tectonic meaning; (3) GPS data to measure, characterise and interpret the ground motion due to the main shock and subsequent aftershocks; (4) seismic data to characterise the main rupture and aftershocks in terms of position, nodal planes, and fault geometry and kinematics; and (5) modelling to test the consistency between fault plane solutions, aftershocks, tectonic data, and ground motion measured from GPS data.

## 2. Geological setting

Faial constitutes one of the emerged parts of a single volcanic ridge, the Pico–Faial Ridge, which is elongated along azimuth N110°. According to Hildenbrand et al. (2012a,b), Faial has three main volcanic complexes: a dismantled volcano older than ca. 850 ka, unconformably overlain by two volcanic complexes, one ca. 360 ka old, and another younger than ca. 120 ka. The most prominent tectonic feature in Faial is the central graben affecting the whole island. The fault scarps are clearly visible in the Faial Graben (Fig. 3), but the actual fault surfaces are only visible locally, mostly along sea cliffs. Faults and fault scarps strike N110°–120° on average, and faults dip steeply (60°–70°) to the NNE (in the S) or SSW (in the N). According to Hildenbrand et al. (2012a,b), the Faial Graben is younger than 360 ka.

The main geological features in the neighbourhood of the 1998 shock are the prominent Faial Graben in Faial Island, and the Pico Volcano (2351 m above sea level) in western Pico Island.

The 9th July 1998 earthquake (ML = 5.8) was shortly preceded by a 4.9 earthquake, and the combined effect of these two shocks impeded the adequate registration of the events by the local seismic network. Only 4 stations were able to record these events, and, as a consequence, the available hypocentre solution still has a great uncertainty, particularly the focal depth and the fault orientation (Matias et al., 2007). Following the main shock, thousands of aftershocks were recorded by the local seismic network in the following months. These data were used by Matias et al. (2007) to relocate the main aftershocks, recorded in the first 20 days following the main shock, by joint inversion of hypocentres and 1D velocity models. After relocation, the aftershocks present a complex shape, with the majority distributed along a main N–S direction, therefore making an angle >20° with one of the fault planes (N151°) of the centroid moment tensor (CMT, Harvard University) solution for the main shock. Refined hypocentral solutions, derived from 3D tomographic inversion, were later presented by Dias et al. (2007), with decreased spatial dispersion and showing an aftershock distribution in two main directions: N–S and ENE–WSW. In terms of focal depth, most aftershocks are located between 3 and 13 km, with shallower events occurring inland Faial. Events with focal depths less than 6 km occur in the NE sector of the island, associated with the main faults bounding the Faial Graben in the N.

Fernandes et al. (2002) used a set of GPS data acquired in 1997 and 1998 (one month after the main event) in a network of marks distributed all over Faial, in order to constrain the parameters that define the fault that generated the main shock. They analysed two solutions, the N61° dextral strike-slip, and the N151° sinistral strike-slip computed by CMT, and concluded that, from geodetic data and statistical criteria, it was not possible to decide for the strike direction of the main shock. Anyway, Fernandes et al. (2002) estimated the fault geometry for both hypotheses. In the model, triggering effects were not considered, resulting in poor model fit to the observations in NE and SW Faial. Neighbouring geodetic marks in NE Faial show opposite displacement directions, which were interpreted by Fernandes et al. (2002) as a possible interaction of the main rupture with the Faial Graben. In the present study we used tectonic and seismic data, and numerical modelling to show how the main shock interacted with the two master faults bounding the Faial Graben in the north.

Interferometric synthetic aperture radar (InSAR) was applied to the available set of ERS images, aimed at mapping the deformation resulting from the 1998 seismic crisis (Catita et al., 2005). Despite the adverse circumstances, mainly due to the reduced number of SAR images and large areas with vegetation, Catita et al. (2005) managed to build fringe patterns with approximately 3 cm of range change between 1992 and 1998. Although correlation breaks down in many areas, the fringe pattern is legible in NW Pico Island. The fringe pattern detected in this

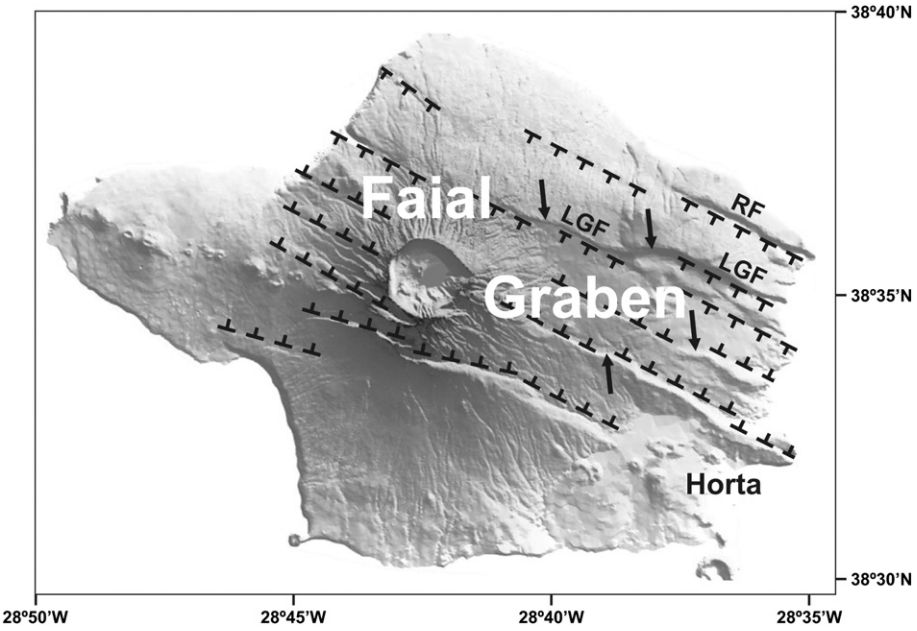


**Fig. 3.** Tectonic framework of the Faial Island, where the fault scarps making up the Faial Graben stand out. RF — Ribeirinha Fault. LGF — Lomba Grande Fault. Arrows mark bends (in plan view) on normal faults, which indicate a sinistral strike-slip component. Lighting from NE.

part of Pico can be related to the synthetic model computed from the fault parameters of Fernandes et al. (2002) (see Fig. 9), and Catita et al. (2005) concluded that the observed interferometric fringes generally agree with the synthetic models and, therefore, are coherent with the available seismic and GPS data.

## 3. Data

### 3.1. GPS velocities

A dense geodetic network was installed on the islands of Faial and Pico, in the early years of the 20th century. The network was first surveyed with GPS, on regular campaigns, in 1995 (Pico Island) and 1997 (Faial). In 1998, one month after the earthquake, the network was again surveyed with GPS, but only occupying 32 stations (29 on Faial and 3 on Pico). All the surveys were performed with dual-frequency GPS receivers, collecting data every 15 s and occupying stations for 1 to 4 h. The mean baseline length between stations is ca. 3000 m.

The GPS data were analysed and processed by Fernandes et al. (2002) using Bernese software. The mean position of the geodetic marks was estimated by least squares adjustment of the GPS baselines, fixing the position of FAIM station (in Horta) on the three campaigns. The displacement field was calculated as the difference between the estimated coordinates for the 32 stations in 1995, 1997 and in 1998. The displacement vectors are shown in Fig. 4.

### 3.2. Main earthquake and aftershocks

The CMT solution for the Faial earthquake (Figs. 5 and 6D) shows the existence of two nodal planes where the main shock may have occurred: N61° (ENE–WSW) and N151° (NNW–SSE). The fault plane solution indicates vertical dip and almost pure strike-slip motion in both faults: left-lateral in the NNW–SSE fault, and right-lateral in the ENE–WSW fault.

The relocation of aftershocks with the 3D tomographic model (Dias et al., 2007, and this work) (Fig. 5) shows a pattern that is only seemingly simple to interpret. Relocated aftershocks also show the reactivation of the two WNW–ESE main faults making up the northern boundary of the Faial Graben. Two main trends strike approximately orthogonal to each other: one ENE–WSW (blue line in Fig. 5), and the other NNW–SSE (yellow line in Fig. 5). However, both trends are composed of two main concentrations of aftershocks: (1) one offshore (where the main shock occurred) that trends ENE–WSW, and the other onshore trending WNW–ESE and reactivating the northernmost faults of the Faial Graben. (2) The NNW–SSE trend shows two concentrations of aftershocks, both offshore: one in the south, more linear and striking ca. N175° (black line in Fig. 5), and the other in the north and approximately circular. Both NNW–SSE and ENE–WSW trends show a wide distribution of aftershocks, not the discrete linear concentration expected for single and vertical faults (the CMT solution for the Faial earthquake). Therefore, we made three seismic sections across the two main trends to find the dip of the main faults (Fig. 6). The seismic sections show an ENE-WSW fault dipping ca. 80° to the SSE (Fig. 6B), a NNW–SSE fault dipping ca. 65° to the WSW (Fig. 6C), and a WNW–ESE fault (Faial Graben) dipping ca. 65° to the SSW (Fig. 6A). The NNW–SSE and WNW–ESE faults have the typical dip of normal faults, while the ENE–WSW fault dips steeply like a strike-slip fault.

### 3.3. Seismic intensity

As shown by the isoseismal maps in Matias et al. (2007), Oliveira et al. (2012), Senos et al. (1998) and Zonno et al. (2010), the main destruction occurred in Faial, especially in the NE corner of the island where destruction was maximal (Fig. 7). In contrast, damage in Pico and S. Jorge islands was reduced or even minimal, and mainly concentrated on the capital village in westernmost Pico, and confined to a small village in WNW S. Jorge.

## 4. Co-seismic modelling/GPS data inversion

The co-seismic displacements were determined by coordinate difference of the GPS surveys carried out in 1995 (Pico, 3 geodetic marks), 1997 (Faial, 29 geodetic marks) (Catalão et al., 2006), and 1998 (in the same geodetic marks, one month after the earthquake), assuming that there were no other significant volcanic or seismic events in those periods. For more detailed information see Fernandes et al. (2002).

The spatial distribution of the observations is asymmetric relative to the ENE–WSW fault plane, with few observations on the northern block. Moreover, the epicentre is in the ocean, on the northern flank of the Pico–Faial Ridge, and so does most of the rupture surface. According to the isoseismal information, the earthquake was weakly felt in S. Jorge Island (NE of Faial), with minimal observed damage only in the NW

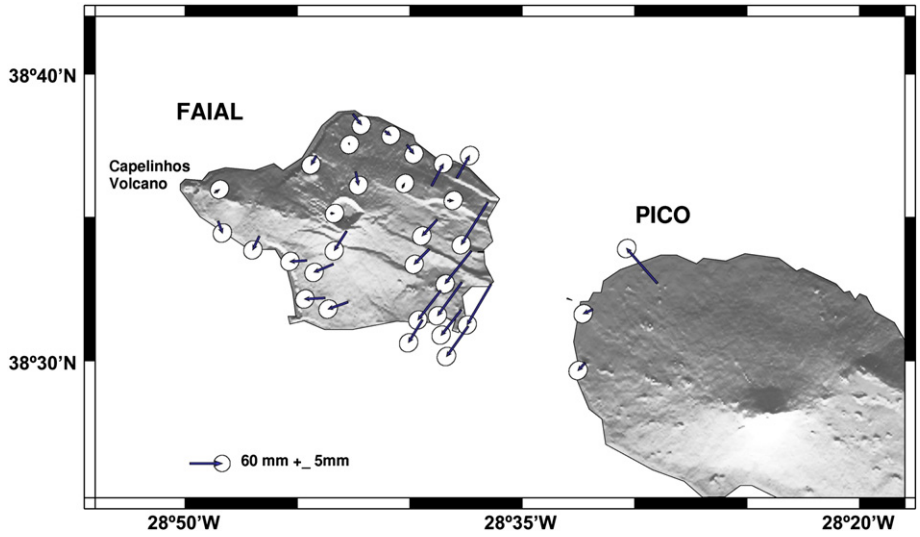


**Fig. 4.** The measured displacements (blue arrows) show three main features: (1) clockwise rotation of the island southwest of the fault that bounds the Faial Graben in the N (RF). (2) Opposite displacements to south and north of the RF fault in NE Faial. (3) Counter clockwise rotation of western Pico. GPS surveyed in 1997 and 1998.

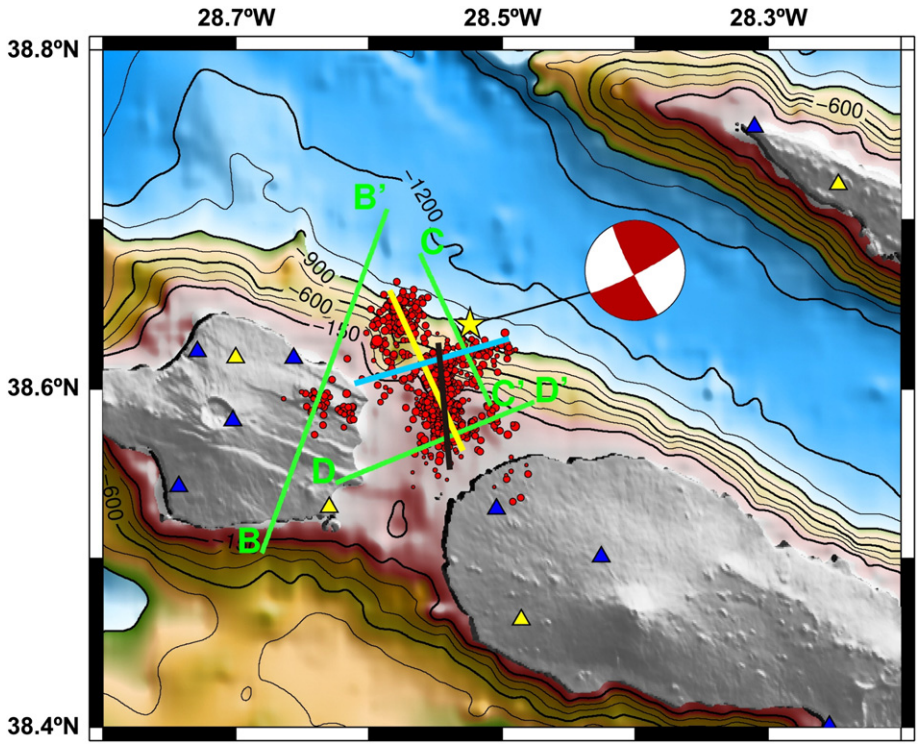


**Fig. 5.** Map with location of the main shock (yellow star) and respective fault plane solution (beach-ball, from Borges et al., 2007), representation of the relocated aftershocks (red dots), seismic stations (blue and yellow triangles, the latter used to locate the main shock), and the seismic profiles shown in Fig. 6. The yellow, black and blue full lines represent the N155°, N175° and N75° possible fault planes. Background DEM of the islands built from topographic data supplied by Instituto Geográfico do Exército (IGeoE, Portugal), with vertical and horizontal resolutions of 10 m and 50 m, respectively.
Background bathymetry from Lourenço et al. (1998), with 100 m resolution.

sector of the island (e.g. Matias et al., 2007); therefore, we can assume that there was negligible deformation in S. Jorge.

In order to constrain the mathematical model, we used: (1) the measured ground motion (Fernandes et al., 2002); (2) the direction and dip of the faults inferred from the seismic data (this study); (3) the structural data regarding onshore faults where seismicity was observed (Hildenbrand et al., 2012a,b); (4) the depth estimated from the seismic data (Dias et al., 2007; Matias et al., 2007); (5) the earthquake magnitude (Borges et al., 2007; Matias et al., 2007) to estimate the corresponding rupture surface (e.g. Wells and Coppersmith, 1994, their Fig. 16); and (6) the line of sight deformation measured with SAR interferometry (Catalão et al., 2011; Catita et al., 2005). The inclusion of these measurements in the model results in a directional and positional constraint for the estimated fault parameters of the main shock. Contrary to previous studies (Dias et al., 2007; Fernandes et al., 2002; Matias et al., 2007), in this study we assume that the main event interacted with the fault system of the Faial Graben, causing displacement on its northern faults, as observed in the aftershocks. The problem is the actual kinematics of these faults: the main component is that of normal faults, but the horizontal component is not obvious. From the bends marked with arrows in Fig. 3, we can deduce a left-lateral strike-slip component, which is in agreement with the bookshelf structure expected at the termination of a strike-slip fault or fault rupture (e.g. Lin et al., 2010; Ron et al., 1986, their Figure 6).

We modelled the observed coseismic displacement using a rectangular model fault, along which the displacement is uniform and the top is parallel to the Earth's surface, according to Okada's (1985) algorithm. An elastic, homogeneous and isotropic half-space with a rigidity of 30 GPa was assumed. The inversion was done using the non-linear generalised inverse algorithm developed by Briole et al. (1986), which estimates the parameters of the fault and fault plane displacement that best fit the GPS data. The fault parameters were estimated using weighted least squares inversion of the east and north displacement vectors, with the data weighted by the reciprocal of the square of the

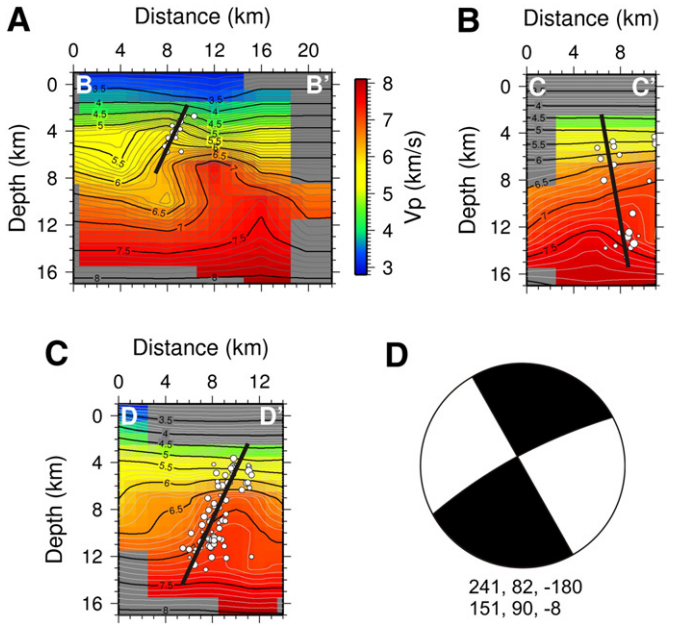


**Fig. 6.** A, B and C — Seismic profiles B–B′, C–C′ and D–D′, respectively, showing the distribution of aftershocks at depth, overlying the tomographic model of Dias et al. (2007). Inferred faults are represented by black full lines. D — Fault plane solution according to the CMT solution of Harvard University.

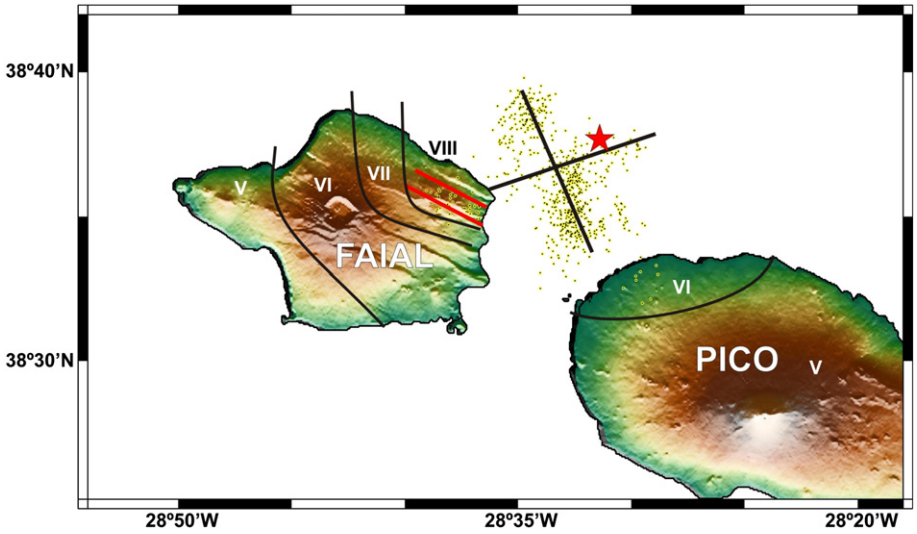


**Fig. 7.** Macroseismic intensity (modified Mercalli scale) inferred for the Faial and Pico islands (modified after Senos et al., 1998). Red star marks the location of the 1998 Faial main shock. Black straight lines represent the nodal planes. Red lines mark the faults in the Faial Graben where aftershocks occurred. Yellow-rimmed black dots represent the relocated aftershocks.

estimated error. The estimated error for each campaign is between 1 mm and 7 mm for the horizontal component (with an average of 4 mm), and between 3 and 14 mm for the vertical component.

The inversion process was performed in three steps. (1) In the first step, we used the initial solution given in the CMT catalogue and estimated the 8 parameters describing the fault of the main event (location, depth, length, width, strike, dip, strike-slip, dip-slip) by changing the original position of the epicentre (latitude, longitude, depth) supplied by SIVISA, which is feasible considering the uncertainties of ca. 5 km associated with that solution (Matias et al., 2007). Given the geological setting, the ground motion, and the isoseismal distribution, we considered for the initial solution the ENE–WSW right lateral fault (fault 1a in Table 1). (2) In the second step, the residuals of the first inversion (computed as the difference between GPS and modelled displacements) were used to estimate the parameters of the two northernmost main faults of the Faial Graben: the Ribeirinha and Lomba Grande faults, which strike N120° and dip 60°–70° to the SSW (Hildenbrand et al., 2012a,b). The evidence of the displacement on these structures is given in Figs. 5 and 6. Some of the relocated seismic events are shallow events (about 4 km) and inside the island. In the inversion process, some of the parameters of these two faults were constrained: the position, and strike and dip obtained by field measurements (Hildenbrand et al., 2012a,b); the depth of the fault (ca. 4 km given in Dias et al., 2007), and the length estimated by the trace at the surface. (3) In the third step, the position, direction and size of the three faults were fixed, and the slip parameters estimated on a single system of equations. The results are shown in Table 1. The measure of misfit, given by the reduced chi-square, was computed as the ratio between the weighted residual sum of squares and degrees of freedom (number of data − number of parameters). The reduced chi-square was determined for the 3-fault model solution based on the data uncertainties (10 mm for the horizontal and 21 mm for the vertical), and on the number of 32 stations and 9 parameters. For this model the reduced chi-square was 1.8. A misfit of 1 would indicate that the residuals are statistically consistent with the data errors. In this case we have assumed that data uncertainties are too optimistic, and we decided to scale the uncertainties by two (~1.8). The obtained reduced chi-square is now 1.06. If we assume only the main event, and using the same data uncertainties, the misfit increases to 1.4, meaning that this fault model does not fit the physical phenomenon as well as the proposed 3-fault model.

The optimal uniform-slip dislocation closely follows the displacement measured in the field, and is consistent with the alignment of aftershocks. Furthermore, this 3-fault model is able to reproduce the measured dislocation in NE Faial. In this model, the largest surface deformation occurs onshore NE Faial, as confirmed by the high level of destruction in this area (e.g. Oliveira et al., 2012). The geodetic moment magnitude is Mw = 6.18, consistent with the CMT catalogue. The surface projections of the three dislocations are shown in Figs. 8 and 9. They closely follow the coseismic events relocated by Dias et al. (2007).

Following the same procedure, we also modelled the two other possible solutions, as indicated by the CMT fault plane solutions and the aftershock sequence: the long N155° sinistral strike-slip fault (fault 1c in Table 1, and red in Fig. 10), and the short N175° sinistral strike-slip fault (fault 1b in Table 1, and green in Fig. 10).

## 5. Discussion

The motions between Azores–Eurasia (dextral oblique extension) and Azores–Nubia (dextral strike-slip), shown by DeMets et al. (2010) in a scenario with an Azores microplate, have to be reconfigured in a

**Table 1**
Fault parameters determined from inversion of GPS data. Depth refers to the top of the fault.

| Fault | Length (km) | Width (km) | Dip (°) | Strike (°) | Lat (°N) | Lon (°W) | Depth (km) | Dip-slip (cm) | Strike slip (cm) | Kinematics |
|---|---|---|---|---|---|---|---|---|---|---|
| 1a | 12 | 5.5 | 83 | 264 | 38.6184 | 28.5550 | 5 | 0 | −117 | Dextral |
| 1b | 6 | 5.5 | 89 | 175 | 38.5964 | 28.5446 | 4 | 0 | 147 | Sinistral |
| 1c | 10.6 | 5.5 | 89 | 155 | 38.6118 | 28.5597 | 4 | 0 | 99 | Sinistral |
| 2 | 2 | 1 | 70 | 118 | 38.5986 | 28.6306 | 2 | 15 | 0 | Normal/sinistral |
| 3 | 2.2 | 1 | 70 | 118 | 38.5932 | 28.6573 | 2 | 34 | 14 | Normal/sinistral |

Using the same data uncertainties, the reduced chi-square is: fault 1a = 1.06; fault 1b = 1.6; and fault 1c = 2.15.

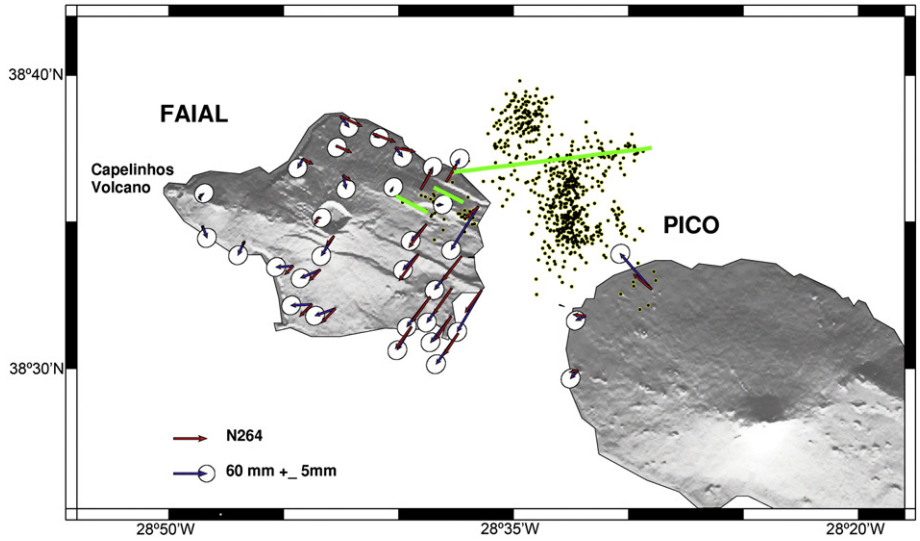


**Fig. 8.** Comparison of measured and modelled station displacements for the 3-fault model, with the main ENE–WSW fault. Blue arrows: displacement measured with GPS. Red arrows: modelled displacement. Red lines: faults.

scenario without the Azores microplate (Marques et al., 2013). The TR seems to be taking up most of the oblique extension, as shown by the prominent graben comprising the TR; therefore, the dextral strike-slip motion (transform motion) should be taking place south of the TR, where the boundary with Nubia is diffuse. Here, as in the case of the Faial 1998 earthquake, the transform direction works as a dextral strike-slip fault, similarly to the Gloria Fault (GF in Fig. 11), as expected from the counter clockwise rotation of Nubia relative to Eurasia.

The aftershock sequence shows two main lineaments, from which we infer the position and geometry of two main faults making an angle of ca. 90° between them (ENE–WSW and NNW–ESE). However, classical rock mechanics predicts conjugate faults at an angle of ca. 60°. Therefore, we infer that the faults should be the result of a more complex stress field or of mixing of structures inherited from the MAR with structures generated by the Nu/Eu kinematics. Two main fault systems have been recognised in the Azores (WNW–ESE and NNW–SSE), and a third is being proposed in the present work (ENE–WSW) (Fig. 11): (1) the best-known fault system in Central Azores strikes WNW–ESE, which is responsible for the horst–graben structure shown in Fig. 2. (2) The NNW–SSE fault system could be generated by the differential motion between Eurasia and Nubia, and work as pure normal as shown by most of the available fault plane solutions. (3) The ENE–WSW fault system has not been recognised in the Azores, but it is predicted by the plate velocities reported in DeMets et al. (2010), and in the fault plane solutions of major earthquakes (e.g. Borges et al., 2007; Hirn et al., 1980). The transform direction is produced by the rotation of Nubia relative to Eurasia, and changes strike along the TR, as shown by the plate velocity configuration in the Azores (DeMets et al., 2010). Locally, as in the case of the Faial 1998 earthquake, the transform direction works as a dextral strike-slip fault, similarly to the Gloria Fault (Fig. 11), as expected from the counter clockwise rotation of Nubia relative to Eurasia.

The NNW–SSE faults in the Azores, dipping to the WSW or ENE, are typically normal faults according to the fault plane solutions available (cf. Figure 8 in Borges et al., 2007). This is consistent with the relative motion between Eu and Nu (DeMets et al., 2010), because the NNW–SSE trend is orthogonal to the principal extension in the diffuse Nu/Eu

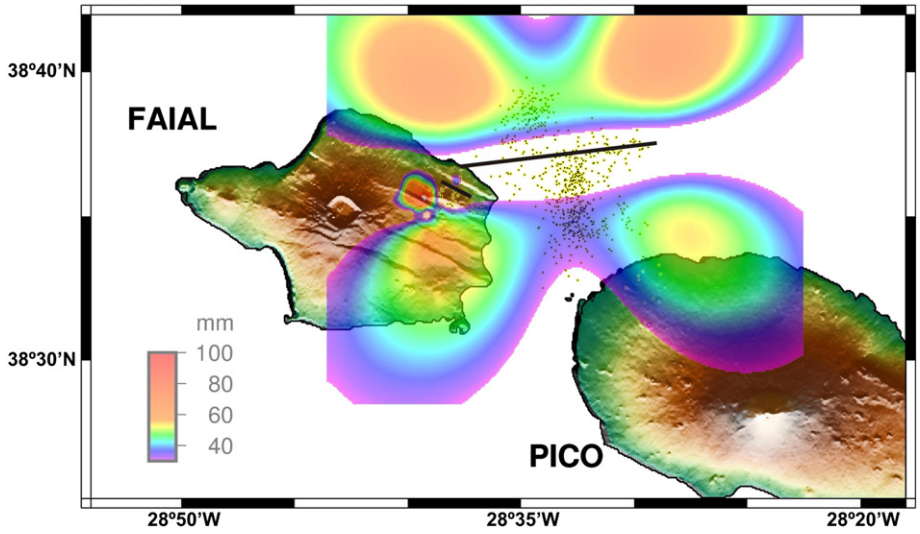


**Fig. 9.** Comparison of model fault location (represented by thick red lines) and seismic events (represented by yellow-rimmed black dots). Coloured overlay is modelled station displacements for the 3-fault model.

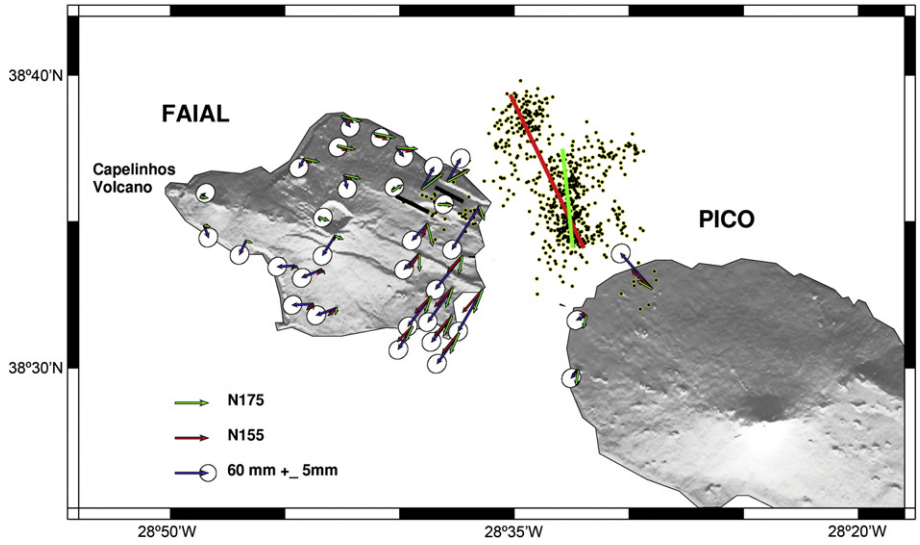


**Fig. 10.** Comparison of measured and modelled station displacements for a 3-fault model, with a main short N175° sinistral strike-slip fault (green), or a main long N155° sinistral strike-slip fault (red). Note that: (1) the long N155° fault model solution cannot reproduce the measured ground displacement (black arrows), with displacement directions everywhere at high angle to the measured displacement; and (2) the short N175° fault model solution cannot reproduce the measured ground displacement, with displacement magnitude everywhere much smaller than the measured displacements.

boundary. Given that the two NNW–SSE fault plane solutions correspond to normal faults, it is not relevant if the normal fault dips to the ENE or to the WSW; it is normal fault in any case. In contrast, when the fault plane solution shows two vertical pure strike-slip faults, one sinistral (striking NNW–SSE) and the other dextral (striking ENE–WSW), then a problem of consistency arises: the NNW–SSE fault strikes orthogonal to the maximum extension, and thus should not be a pure strike-slip fault; it should be a pure normal fault, as observed when the two fault plane solutions trend NNW–SSE and dip around 65°. In fact, the NNW–SSE fault inferred from the 1998 Faial aftershock sequence dips ca. 65°, which means that it is consistent with normal faulting. The alternative, which is the main thesis of the present paper, is that the main shock occurred on the fault corresponding to the fault plane solution that trends ENE–WSW, which is coincident with the transform direction related to the rotation of Nu relative to Eu in the Azores, and therefore consistent with plate kinematics and induced strain. Similarly to the Gloria Fault (Fig. 11), the faults trending ENE–WSW should be vertical and pure dextral strike-slip.

Two main features stand out from the measured velocity field in Faial (Fig. 4): (1) the opposite velocities in Faial's NE corner, to each side of the RF and LGF faults, and (2) the concentric velocities in central Faial. The possible kinematics of the faults making up the Faial Graben (WNW–ESE) are: (1) pure normal (as observed in fault plane solutions of major earthquakes in the Azores); (2) normal/dextral as inferred from the angular relationship between fault strike (WNW–ESE) and direction of maximum extension (ENE–WSW) (Fig. 11); and (3) normal/sinistral if there is clockwise bookshelf rotation related to the differential motion between NA/Eu and NA/Nu. Note that the sinistral strike-slip component is consistent with the release bends shown in Fig. 3. As shown by modelling, the velocities in NE Faial can only be explained if there is oblique displacement on the northernmost faults of the Faial Graben, i.e. only if a sinistral strike-slip component is

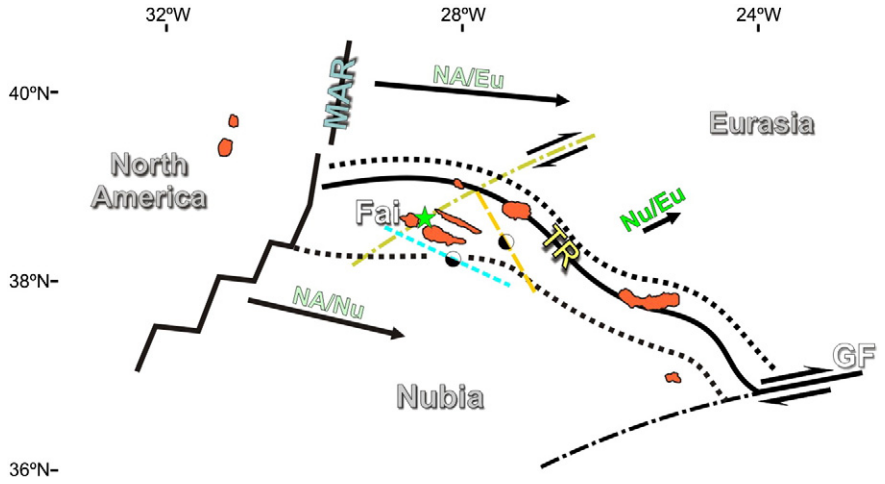


**Fig. 11.** Schematic representation of plate distribution and kinematics (arrows with reference to the involved plates, DeMets et al., 2010), Nu/Eu boundary (marked by dotted black lines), the small circles related to rotation of Nu relative to Eu (dash-dot lines), and main fault systems (NNW–SSE marked by long-dashed yellow line; WNW–ESE marked by dashed blue line; ENE–WSW marked by dash-dot green line). Strike-slip kinematics indicated by black half arrows, and normal fault kinematics indicated by half white/half black circles. MAR and TR represent the Mid-Atlantic and Terceira rifts, respectively.

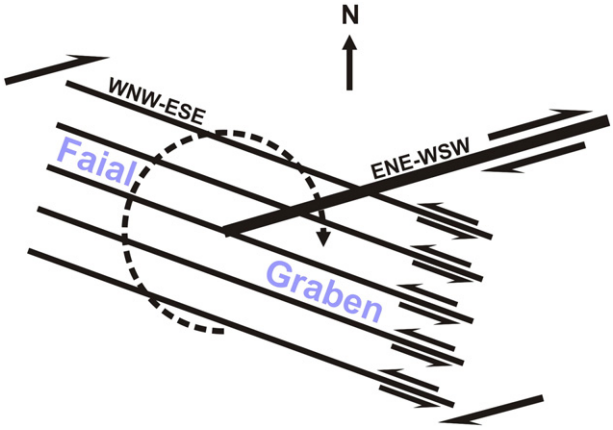


**Fig. 12.** Sketch with kinematic interpretation of the measured ground motions and estimated movement on the main fault. Note that the WNW–ESE fault system (making the Faial Graben and sketched here) works as a bookshelf in response to the observed clockwise rotation imposed by the dextral movement in the main ENE–WSW fault.

added to the main normal component, which is consistent with the tectonics inferred from fault geometry. Although not clearly reproduced in the model, the concentric velocity field in central Faial can be explained if the Faial Graben corresponds to the termination of the ENE–WSW dextral strike-slip fault (Fig. 12). Similar fault and kinematic configurations (block rotations associated with the termination of strike-slip faults) have been observed and reported by Ron et al. (1986), and measured by GPS by Lin et al. (2010). Noticeably, the prominent faults onshore Faial are not visible offshore in the channel between Faial and Pico islands (Figure 4 in Tempera, 2009). This is consistent with our hypothesis of a fault termination, because in such a configuration the displacement on the WNW–ESE graben faults is attenuated by the displacement on the ENE–WSW fault. In contrast, it is not consistent with the N175° fault, because there is no direct interaction with the Faial Graben faults.

The continuation of the ENE–WSW fault to the ENE, toward the TR, is not clear. On the one hand, its strike may be affected by the local stress field imposed by the massive Pico stratovolcano, deflecting it toward a more E–W trend. On the other hand, there is no clear evidence of the fault trace on the available bathymetry. However, in the nearby S. Jorge Island (to the ENE of the epicentre) there is a clean-cut jump in GPS velocities in the middle of the island (Marques et al., 2013; Mendes et al., 2013), which could be explained by an ENE–WSW transform. GPS velocities in Figure 5a and c in Marques et al. (2013) show that there is dextral strike-slip motion along a line passing where the 1998 shock occurred and through the middle of the S. Jorge Island (Fig. 13). Coincidently, this line is the transform direction predicted by Morvel for this region, and also the direction of one of the fault plane solutions of the Faial 1998 shock, the ENE–WSW fault.

The N75° fault inferred from the aftershock sequence is at a small angle to the local transform direction, which is closer to ENE–WSW in the Faial area (DeMets et al., 2010). Based on the radial stress field that develops around conical loads (e.g. Duran, 2000; Marques and Cobbold, 2002, 2006), we argue that the N75° strike is a local deflection of the general ENE–WSW transform direction, due to stresses born at the massive Pico stratovolcano (Fig. 13). Such stresses could also be responsible for the southwards dip of the N75° fault, by addition of a vertical component of compression to the far field stresses.

According to the CMT fault plane solutions, the main rupture may have occurred on two fault planes, the ENE–WSW or the NNW–SSE. The aftershocks also occurred along two main lineaments, which strike ca. N75° and N175°. From a geophysical point of view, the main shock may have occurred on either of the two faults. However, the numerical modelling using the three possible main faults (N155° long sinistral fault, N175° short sinistral fault, and N84° dextral fault), constrained by the aftershock sequence (Figs. 8 and 10), indicates that: (1) the long N155° fault model solution is not consistent with the measured ground displacement, because displacement directions are everywhere at a high angle to the measured displacement (Fig. 10). (2) The short N175° fault model solution cannot reproduce the measured ground displacement, because displacement magnitude is everywhere much smaller than the measured displacement (Fig. 10). (3) The N84° model fault is the one that best reproduces the measured displacements, in both direction and magnitude (Fig. 8). Furthermore: (1) the major destruction was observed in NE Faial, to the W of the epicentre. (2) The N175° fault deduced from the seismicity alignment shows no spatial interaction with the Faial Graben faults (Fig. 13). (3) The N175° fault can only generate an M ~ 6 event if we assume either that the fault extends to the north (with the NW cluster deviated from it), or that the fault ruptures the entire crust (which has a thickness here of ~14 km according to Dias et al., 2007). The proposed ENE–WSW fault has the

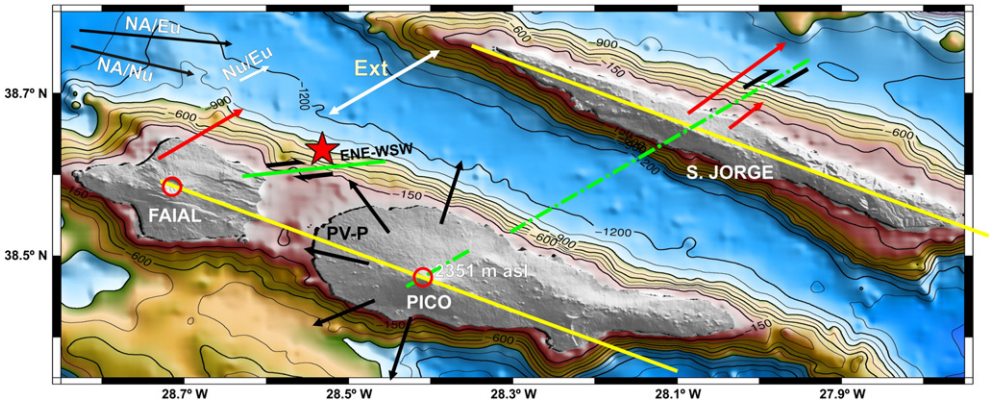


**Fig. 13.** Schematic representation of the main volcano/tectonic structures and GPS velocities. Note that the ENE–WSW fault (green full line) is aligned with the main volcano in Faial (Caldera Volcano, red circle), and that the line separating the jump in GPS velocities in S. Jorge (green dash-dot line, which represents a small circle around the MORVEL Nubia–Eurasia pole — DeMets et al., 2010) is aligned with the Caldera in the Pico Volcano (red circle). The yellow lines through the main volcanoes in Pico–Faial and S. Jorge ridges are the surface expressions of the main tectonic horst/graben structure in the basement (Fig. 2). The red arrows correspond to the GPS velocities with fixed Pico (Marques et al., 2013). It seems therefore that the main volcanoes in the Pico–Faial Ridge developed at the intersection between the WNW–ESE and the ENE–WSW fault systems. Morvel plate velocities (DeMets et al., 2010) are represented at the top-left corner. Black full arrows represent the radial stresses induced by the Pico volcano on the surrounding lithosphere. Black half arrows indicate fault kinematics. The red star marks the location of the Faial 1998 earthquake. PV-P is the topographic force exerted by the Pico Volcano, a volcanic cone with top at 2351 m above sea level (asl).

advantage of not requiring a rupture of the entire crust. (4) Last but most importantly, the Morvel plate velocities and the GPS velocities shown in Figure 5 of Marques et al. (2013) and reproduced in Fig. 13 are not consistent with a pure strike-slip motion on the NNW–SSE fault, because maximum extension is orthogonal to the fault plane. In fact, most of the ca. NNW–SSE fault plane solutions for tectonic earthquakes with M > 4 have normal fault kinematics (cf. Borges et al., 2007), as expected from the known plate kinematics (ENE–WSW extension). Putting all data together, we conclude that the main shock occurred on the ENE–WSW fault. Knowing that the ENE–WSW fault is approximately along the transform direction related to the Nu/Eu plate boundary, we conclude that the fault responsible for the 1998 Faial earthquake strikes ENE–WSW and can be a transform associated with the TR.

The differences between measured ground motion and model velocities can be the result of model insufficiencies, mostly flat surface (therefore lack of island topography effects), rigidity in the model, and small number of faults in the model as compared to nature. The fact that the NNW–SSE aftershock sequence is more prominent than the ENE–WSW is not, by itself, guarantee that the main shock occurred on a NNW–SSE fault. In fact, stress triggering has become a common observation. For instance, the 1992 M = 7.4 Landers earthquake changed the failure stress on the southern San Andreas fault system (King et al., 1994; Stein et al., 1992). Similarly, many other earthquakes have been triggered by its predecessors (e.g. Freed, 2005; Stein, 1999; Stein et al., 1994, 1997 for a review). We conclude that the concentration of aftershocks along the N175° fault could well mean that it readjusted to motion along the N75° fault during the main earthquake.

From the complex geometry of the aftershock pattern and continued seismicity from 1998 to present-day, the aftershock swarm could well correspond to volcanic seismicity triggered by the main earthquake and subsequent aftershocks.

## 6. Conclusions

The fault plane solution and the aftershock sequence of the 1998 Faial earthquake in the Azores show that the main shock occurred on two possible vertical faults striking NNW–SSE (sinistral strike-slip) and ENE–WSW (dextral strike-slip). Given that the main earthquake and aftershocks occurred within the diffuse Nu/Eu plate boundary, and that the maximum extension there is approximately orthogonal to the NNW–SSE fault plane solution, we conclude that the vertical and sinistral strike-slip NNW–SSE solution is inconsistent with the known plate kinematics in the Azores. There, the main earthquakes on faults trending close to NNW–SSE, for which the focal mechanisms are known, show that the faults are neither vertical nor strike-slip; they dip like classical normal faults, and have the kinematics of normal faults. In contrast, the ENE–WSW fault is sub-vertical and dextral strike-slip, thus consistent with the rotation of Nu relative to Eu and the transform direction in the diffuse Nu/Eu boundary. Therefore, we conclude that the main earthquake occurred on the ENE–WSW fault, which is a transform related to the Nu/Eu diffuse boundary.

The tectonics observed onshore Faial, the measured displacements, and the observed destruction, all point to the ENE–WSW fault as the source fault of the 1998 Faial earthquake, and therefore corroborate the conclusion reached from plate kinematics and strain. The dextral clockwise motion and clockwise rotation measured by GPS are typical of block rotations associated with the termination of strike-slip faults. Based on the known plate kinematics, fault geometry and kinematics, we conclude that the ENE–WSW dextral strike-slip fault can be a transform associated with the Nubia–Eurasia plate boundary.

The numerical three-fault models used to test the consistency of the possible fault planes with the measured ground displacement indicate that the ENE–WSW dextral strike-slip fault is the best-fitting solution.

## Acknowledgements

This is a contribution to projects TEAMINT (POCTI/CTE/48137/2002) and MEGAHazards (PTDC/CTE-GIX/108149/2008) funded by FCT, Portugal. We thank the two anonymous reviewers for the comments that helped to substantially improve the final manuscript.

## References

Agostinho, J., 1931. The volcanoes of the Azores Islands. Bull. Volcanol. 8, 123–138.
Borges, J.F., Bezzeghoud, M., Buforn, E., Pro, C., Fitas, A., 2007. The 1980, 1997 and 1998 Azores earthquakes and some seismo-tectonic implications. Tectonophysics 435, 37–54.
Briole, P., De Natale, G., Gaulon, R., Pingue, F., Scarpa, R., 1986. Inversion of geodetic data and seismicity associated with the Friuli earthquake sequence (1976–1977). Ann. Geophys. 4, 481–492.
Buforn, E., Udías, A., Colombás, M.A., 1988. Seismicity, source mechanisms and seismotectonics of the Azores–Gibraltar plate boundary. Tectonophysics 152, 89–118.
Buforn, E., Bezzeghoud, M., Udías, A., Pro, C., 2004. Seismic sources on the Iberia–African plate boundary and their tectonic implications. Pure Appl. Geophys. 161, 623–646.
Catalão, J., Miranda, J.M., Lourenco, N., 2006. Deformation associated with the Faial (Capelinhos) 1957–1958 eruption: inferences from 1937–1997 geodetic measurements. J. Volcanol. Geotherm. Res. 155, 151–163.
Catalão, J., Nico, G., Hanssen, R., Catita, C., 2011. Merging GPS and atmospherically corrected InSAR data to map 3D terrain displacement velocity. IEEE Trans. Geosci. Remote Sens. 49, 2354–2360. http://dx.doi.org/10.1109/TGRS.2010.2091963.
Catita, C., Feigl, K.L., Catalão, J., Miranda, J.M., Victor, L.M., 2005. InSAR time series analysis of the 9th July 1998 Azores earthquake. Int. J. Remote Sens. 26. http://dx.doi.org/10.1080/01431160512331337835.
Costa, A.C.G., Marques, F.O., Hildenbrand, A., Sibrant, A.L.R., Catita, C.M.S., 2014. Large-scale flank collapses in a steep volcanic ridge: Pico-Faial Ridge, Azores Triple Junction. J. Vol. Geotherm. Res. 272, 111–125.
DeMets, C., Gordon, R.G., Argus, D.F., 2010. Geologically current plate motions. Geophys. J. Int. 181, 1–80.
Dias, N.A., Matias, L., Lourenço, N., Madeira, J., Carrilho, F., Gaspar, J.L., 2007. Crustal seismic velocity structure near Faial and Pico Islands (Azores), from local earthquake tomography. Tectonophysics 445, 301–317.
Duran, J., 2000. Sands, Powders, and Grains: An Introduction to the Physics of Granular Materials. Springer-Verlag, New York (214 pages).
Fernandes, R.M.S., Miranda, J.M., Catalão, J., Luis, J.F., Bastos, L., Ambrosius, B., 2002. Coseismic displacements of the Mw = 6.1, July 9, 1998, Faial earthquake (Azores, North Atlantic). Geophys. Res. Lett. 29. http://dx.doi.org/10.1029/2001GL014415.
Freed, A., 2005. Earthquake triggering by static, dynamic and postseismic stress transfer. Annu. Rev. Earth Planet. Sci. 33, 335–367.
Grimison, N., Chen, W., 1988. The Azores–Gibraltar plate boundary: focal mechanisms, depths of earthquakes and their tectonic implications. J. Geophys. Res. 91, 2029–2047.
Hildenbrand, A., Madureira, P., Marques, F.O., Cruz, I., Henry, B., Silva, P., 2008. Multi-stage evolution of a sub-aerial volcanic ridge over the last 1.3 Myr: S. Jorge Island, Azores Triple Junction. Earth Planet. Sci. Lett. 273, 289–298.
Hildenbrand, A., Marques, F.O., Catalão, J., Catita, C.M.S., Costa, A.C.G., 2012a. Large-scale active slump of the SE flank of Pico Island (Azores). Geology 40, 939–942.
Hildenbrand, A., Marques, F.O., Costa, A.C.G., Sibrant, A.L.R., Silva, P.F., Henry, B., Miranda, J. M., Madureira, P., 2012b. Reconstructing the architectural evolution of volcanic islands from combined K/Ar, morphologic, tectonic, and magnetic data: the Faial Island example (Azores). J. Volcanol. Geotherm. Res. 241–242, 39–48.
Hirn, A., Haessler, J., Hoang Trong, P., Wittlinger, G., MendesVictor, L., 1980. Aftershock sequence of the January 1st, 1980 earthquake and present-day tectonics in the Azores. Geophys. Res. Lett. 7, 501–504.
King, G.C.P., Stein, R.S., Lin, J., 1994. Static stress changes and the triggering of earthquakes. Bull. Seismol. Soc. Am. 84, 935–953.
Lin, K.-C., Hu, J.-C., Ching, K.-E., Angelier, J., Rau, R.-J., Yu, S.-B., Tsai, C.-H., Shin, T.-C., Huang, M.-H., 2010. GPS crustal deformation, strain rate, and seismic activity after the 1999 Chi-Chi earthquake in Taiwan. J. Geophys. Res. 115, B07404. http://dx.doi.org/10.1029/2009JB006417.
Lourenço, N., Miranda, J.M., Luis, J.F., Ribeiro, A., Victor, L.A.M., Madeira, J., Needham, H.D., 1998. Morpho-tectonic analysis of the Azores Volcanic Plateau from a new bathymetric compilation of the area. Mar. Geophys. Res. 20 (3), 141–156.
Machado, F., 1959. Submarine pits of the Azores plateau. Bull. Volcanol. 21, 109–116.
Marques, F.O., Cobbold, P.R., 2002. Topography as a major factor in the development of arcuate thrust belts: insights from sandbox experiments. Tectonophysics 348, 247–268.
Marques, F.O., Cobbold, P.R., 2006. Effects of topography on the curvature of fold-and-thrust belts during shortening of a 2-layer model of continental lithosphere. Tectonophysics 415, 65–80.
Marques, F.O., Catalão, J.C., DeMets, C., Costa, A.C.G., Hildenbrand, A., 2013. GPS and tectonic evidence for a diffuse plate boundary at the Azores Triple Junction. Earth Planet. Sci. Lett. 381, 177–187.
Matias, L., Dias, N.A., Morais, I., Vales, D., Carrilho, F., Madeira, J., Gaspar, J., Senos, L., Silveira, A., 2007. The 9th of July 1998 Faial Island (Azores, North Atlantic) seismic sequence. J. Seismol. 11, 275–298.
McKenzie, D., 1972. Active tectonics of the Mediterranean region. Geophys. J. R. Astron. Soc. 30, 109–185.
Mendes, V.B., Madeira, J., Brum da Silveira, A., Trota, A., Elosegui, P., Pagarete, J., 2013. Present-day deformation in São Jorge Island, Azores, from episodic GPS measurements (2001–2011). Adv. Space Res. 51, 1581–1592.

Miranda, J.M., Mendes Victor, L., Simoes, J.Z., Luis, J.F., Matías, L., Shimamura, H., Shiobara, H., Nemoto, H., Mochizuki, H., Hirn, A., Lepine, J.C., 1998. Tectonic setting of the Azores Plateau deduced from OBS survey. Mar. Geophys. Res. 20, 171–182.
Moreira, V.S., 1985. Seismotectonics of Portugal and its adjacent area in the Atlantic. Tectonophysics 117, 85–96.
Okada, Y., 1985. Surface deformation due to shear and tensile faults in a half space. Bull. Seismol. Soc. Am. 75, 1135–1154.
Oliveira, C.S., Ferreira, M.A., Mota-de-Sá, F., Neves, F., 2012. The concept of a disruption index: application of the overall impact of the July 9, 1998 Faial earthquake (Azores Islands). Bull. Earthq. Eng. 10, 7–25.
Ron, H., Aydin, A., Nur, A., 1986. Strike-slip faulting and block rotation in the Lake Mead fault system. Geology 14, 1020–1023.
Senos, M.L., Gaspar, J.L., Cruz, J., Ferreira, T., Nunes, J.C., Pacheco, J.M., Alves, P., Queiroz, G., Dessai, P., Coutinho, R., Vales, D., Carrilho, F., 1998. O terramoto do Faial de 9 de Julho de 1998. 1° Simpósio de Meteorologia e Geofísica da APMG, Lagos, Portugal, pp. 61–67.
Silva, R., Havskov, J., Bean, C., Wallenstein, N., 2012. Seismic swarms, fault plane solutions, and stress tensors for São Miguel Island central region (Azores). J. Seismol. 16, 389–407.
Smith, W.H.F., Sandwell, D.T., 1997. Global seafloor topography from satellite altimetry and ship depth soundings. Science 277, 1957–1962.
Stein, R.S., 1999. The role of stress transfer in earthquake occurrence. Nature 402, 605–609.
Stein, R.S., King, G.C.P., Lin, J., 1992. Change in failure stress in southern San Andreas fault system caused by the 1992 Magnitude = 7.4 Landers earthquake. Science 258, 1328–1332.
Stein, R.S., King, G.C.P., Lin, J., 1994. Stress triggering of the 1994 M = 6.7 Northridge, California, earthquake by its predecessors. Science 265, 1432–1435.
Stein, R.S., Barka, A.A., Dieterich, J.H., 1997. Progressive failure on the Northern Anatolian Fault since 1939 by earthquake stress triggering. Geophys. J. Int. 128, 594–604.
Tempera, F., 2009. Benthic Habitats of the Extended Faial Island Shelf and Their Relationship to Geologic, Oceanographic and Infralittoral Biologic Features(PhD. Thesis) University of St. Andrews, Scotland, UK.
Udías, A., López Arroyo, A., Mézcua, J., 1976. Seismotectonics of the Azores–Alboran region. Tectonophysics 31, 259–289.
Wells, D.L., Coppersmith, K.J., 1994. New empirical relationships among magnitude, rupture length, rupture width, rupture area, and surface displacement. Bull. SSA 84, 974–1002.
Zonno, G., Oliveira, C.S., Ferreira, M.A., Musachio, G., Meroni, F., Mota-de-Sá, F., Neves, F., 2010. Assessing seismic damage through stochastic simulation of ground shaking: the case of the 1998 Faial earthquake (Azores Islands). Surv. Geophys. 31, 361–381.